University of Lille

Faculty of Sciences and Technologies

Doctoral School 104 – Science of the Matter, of the Radiation, and of the Environment

Doctoral Thesis

by

Nishith MAITY

to obtain the degree of

Doctor of the University of Lille

Discipline: Physical, analytical and theoretical chemistry

Characterization of the polarity, reorientation dynamics and photophysics of indoline based solar cell dyes in ionic liquid-molecular solvent mixtures: steadystate UV-visible, EPR, time resolved fluorescence, femtosecond transient absorption and optical Kerr effect spectroscopic analysis

Date of defense: 01 April 2022

Bożena	**RATAJSKA-GADOMSKA** *Associate Professor, University of Warsaw (Poland)*	**Referee**
Thomas	**LENZER** *Professor, University of Siegen (Germany)*	**Referee**
Abdenacer	**IDRISSI** *Professor, University of Lille*	**Supervisor**
François-Alexandre	**MIANNAY** *Associate Professor, University of Lille*	**Co-supervisor**
Sophie	**FOURMENTIN-LAMOTTE** *Professor, University of Littoral Côte d'Opale*	**President**
Bertrand	**CHAZALLON** *Professor, University of Lille*	**Examiner**
Kamil	**POLOK** *Associate Professor, University of Warsaw (Poland)*	**Examiner**
Minh-Huong	**HA-THI** *Associate Professor, Paris-Saclay University*	**Examiner**

Université de Lille

Faculté des Sciences et des Technologies

École Doctorale 104 – Science de la matière, du rayonnement et de l'environnement

Thèse

par

Nishith MAITY

pour obtenir le degré de

Docteur de l'Université de Lille

Discipline : Chimie physique, analytique et théorique

Caractérisation de la polarité, dynamique de réorientation et photophysique des colorants à base d'indoline dans des mélanges de liquide ionique/solvant : analyse par spectroscopie UV-visible, RPE, fluorescence résolue en temps et absorption transitoire et effet Kerr optique femtoseconde

Date de soutenance: 01 Avril 2022

Bożena	**RATAJSKA-GADOMSKA**	**Rapporteur**
	Professeur associé, Université de Varsovie (Pologne)	
Thomas	**LENZER**	**Rapporteur**
	Professeur, Université de Siegen (Allemagne)	
Abdenacer	**IDRISSI**	**Directeur de thèse**
	Professeur, Université de Lille	
François-Alexandre	**MIANNAY**	**Co-encadrant de thèse**
	Maître de conférences, Université de Lille	
Sophie	**FOURMENTIN-LAMOTTE**	**Président**
	Professeur, Université de Littoral Côte d'Opale	
Bertrand	**CHAZALLON**	**Examinateur**
	Professeur, Université de Lille	
Kamil	**POLOK**	**Examinateur**
	Maître de conférences, Université de Varsovie (Pologne)	
Minh-Huong	**HA-THI**	**Examinateur**
	Maître de conférences, Université Paris-Saclay	

Acknowledgements

I like to acknowledge Prof. Abdenacer Idrissi and Dr. François-Alexandre Miannay for their help and supports during my Ph.D. I am truly grateful to have them as my thesis supervisor and co-supervisor respectively. I have learned a lot from them regarding academics. The scientific insights I have learned from both of them during my working days are immeasurable.

I would also like to thank my collaborators Dr. Kamil Polok and Dr. Piotr Piatkowski for their help during the working days at the University of Warsaw. Their invaluable guidance alongside scientific inputs was truly helpful for performing experiments using two important time-resolved spectroscopic techniques, namely transient absorption, and optical Kerr effect spectroscopy.

I would also like to thank Spectroscopy Laboratory for Interactions, Reactivity and the Environment (LASIR UMR 8516) at the University of Lille and the institute director Dr. Hervé Vezin, where I carried out most of the work of this thesis. I should also acknowledge the help from the InFemto laboratory at the University of Warsaw and the head of the group Prof. Wojciech Gadomski because there I had spent about 6 months of my doctoral years for carrying out the transient absorption and OKE experiments. I am also grateful to the University of Lille, PHC Polonium, and the French National Agency for Research for funding my research work during these years.

Assoc. Prof. Bożena Ratajska-Gadomska and Prof. Thomas Lenzer were the referees of my thesis. Therefore, I would like to thank them for agreeing to be the referees and also for their precious time and effort to examine the thesis. Besides, I should also acknowledge the other jury members, namely Prof. Bertrand Chazallon, Prof. Sophie Fourmentin-Lamotte, Dr. Kamil Polok and Dr. Minh-Huang Ha-Thi for carefully reading my thesis.

My special thanks to all my past and present lab members, especially to Yevhenii, Balint, and Akos for their support during my work. I should also not forget the help from Julien Dubois, Myriam Moreau, Hania Ahouari, and Jeremy Gaillard, who helped me regarding various experimental setups in the LASIR laboratory.

Last but not least, I want to express my deepest gratitude to my parents and also to my beloved Jayashrita for their help and support and also for being there with me through thick and thin. This journey would have been very difficult without them.

Abstract

Dye sensitized solar cell (DSSC) is one of the available renewable energy sources which are intensively investigated. There are many directions of research to improve the efficiency of these DSSCs. In this thesis, we have chosen to focus on the photosensitizers and the electrolytes with the objective of characterizing the polarity and the reorientation dynamics of the ionic liquid-molecular solvent (IL-MS) mixtures and also to investigate the effect of the mixture composition on the photophysics of the sensitizers. For this purpose, few spectroscopic techniques were used, including steadystate UV-visible, electron paramagnetic resonance (EPR), picosecond time-resolved fluorescence, femtosecond optical Kerr effect (OKE) and femtosecond transient absorption (TA). The studied sensitizers are organic indoline dyes D102, D149 and D205 and the electrolytes are [Bmim][BF_4/PF_6/TFO/TFSI]-ACN/γ-BL/PC mixtures. These indoline derivatives are used as the sensitizer in a DSSC. In addition, IL-MS mixtures are considered as suitable replacement for the viscous ILs due to some of their advantageous properties. Various types of interactions like ion-ion, ion-solvent, solvent-solvent, dye-solvent are modulated by changing the IL mole fraction (X_{IL}), which helps to disentangle the contribution of these interactions on the structure of the IL-MS mixture and also on the photophysics of the studied dyes.
Therefore, part of this thesis is devoted to the analysis of the effect of the composition of IL-MS mixtures on their physicochemical properties. OKE study in time and frequency domain was used to characterize the effect of the mixture composition on the reorientation dynamics in BmimPF_6-ACN mixture. Time domain study reveals three relaxation times. While two longer ones are attributed to the reorientation of the cation and acetonitrile molecules in the vicinity of the imidazolium ring, shortest one is associated with cation rotation and the reorientation of ACN near alkyl chains of the cation. With the help of MD simulations, we have developed a new interpretation of the low frequency response as obtained by OKE. Furthermore, EPR study using the spin probe TEMPO in the IL-MS mixtures helped us to study mixture composition effect on the values of hyperfine coupling constant (A_N) and rotational correlation time (τ_R) of the probe. Careful fitting of the EPR signals have showed that, both A_N and τ_R values are slightly affected at X_{IL} range between 1 and 0.4 while it strongly decreases for further dilution of the IL. We have also discussed the correlation between A_N and Reichardt polarity parameter. In addition, using the picosecond time-resolved fluorescence, we have found that the solvation dynamics of C153 in IL-MS mixture becomes slower while increasing X_{IL} and the solvation time follows the fraction power law dependence with the mixture's viscosity.
We have also characterized excited state dynamics of three indoline dyes in the whole composition range of the IL-MS mixtures using femtosecond TA technique. The steady-state absorption and emission maxima, Stokes shift and the relative quantum yield values undergo a large change at low X_{IL} region. Furthermore, global analysis reveals four relaxation times to characterize dye excited state dynamics. We have noticed an overall decrease of their values while diluting IL and their values go through the minima at X_{IL}~0.1 for the two slower ones. The viscosity and polarity dependence of these four times were also discussed. The presence of the minima in the emission lifetime and relative quantum yield values at low X_{IL} region indicates the presence of different interactions between the dye and the neighboring medium.
The overall results from this thesis constitute a useful basis in the case of further studies where the Dye-IL-MS mixture is at the interface of the electrode.

Keywords: Ionic liquids, indoline, DSSC, transient absorption, TCSPC, EPR, OKE, solvation, reorientation, photophysics

Résumé

Parmi les différentes sources d'énergie renouvelables disponibles, les cellules solaires dopées à colorants font l'objet d'études approfondies. Il existe de nombreuses directions de recherche pour améliorer l'efficacité de ces cellules. Dans cette thèse, nous avons choisi de nous concentrer sur les photosensibilisateurs et les électrolytes (mélange de liquides ioniques (LI) et de solvants aprotiques polaires (SM)). L'objectif étant de caractériser la polarité et la dynamique de réorientation de ces mélanges et également d'étudier l'effet de la composition du mélange sur la photophysique des sensibilisateurs. À cette fin, un ensemble de techniques spectroscopiques avancées ont été utilisées, qui comprennent l'absorption UV-visible et la fluorescence en régime stationnaire, la résonance paramagnétique électronique (RPE), la spectroscopie résolue en temps (la fluorescence, l'effet Kerr optique (EKO) et l'absorption transitoire (AT)). Les sensibilisateurs étudiés sont des colorants organiques à base d'indoline D102, D149 et D205 et les électrolytes sont des mélanges [Bmim][BF_4/PF_6/TFO/TFSI]-ACN/γ-BL/PC (LI-SM). Les différents types d'interactions comme ion-ion, ion-solvant, solvant-solvant, colorant-solvant sont modulées en changeant la fraction molaire du liquide ionique (X_{IL}). Ceci permet de démêler la contribution de chaque type de ces interactions sur les propriétés physico-chimiques des mélanges LI-SM et également sur la photo physique des colorants étudiés.

Par conséquent, dans une partie de cette thèse est consacrée à l'analyse de l'effet de la composition des mélanges LI-SM sur leurs propriétés physico-chimiques. Nous avons commencé par utiliser l'effet EKO résolu en temps pour caractériser l'effet de la composition du mélange sur la dynamique de réorientation dans le mélange [Bmim][PF_6]-ACN. Nous avons analysé le signal EKO dans les domaines temporel et fréquentiel. Trois temps de relaxation ont été identifiés. Avec l'aide de la simulation de dynamique moléculaire, nous avons proposé une interprétation de ces temps de relaxation ainsi que de la réponse en basses fréquences du signal EKO. Par ailleurs, nous avons aussi utilisé la spectroscopie RPE pour analyser la polarité des mélanges LI-SM. Nous avons donc analysé l'effet de la composition du mélange LI-SM sur la constante de couplage hyperfine (A_N), et sur les temps de corrélation rotationnels (τ_R) de la sonde de spin TEMPO. Notre analyse montre que les valeurs de ces deux paramètres changent faiblement entre X_{IL} =1 et 0.4, alors qu'elles diminuent fortement en diluant le mélange. Nous avons discuté de la corrélation entre la polarité quantifiée par la sonde magnétique et le paramètre de polarité déterminé par une sonde optique. De plus, en utilisant la fluorescence résolue en temps picoseconde, nous avons constaté que la dynamique de solvatation de C153 dans ces mélanges devient plus lente tout en augmentant X_{IL} et dépendent de façon non linéaire de la viscosité des mélanges.
Dans l'autre partie de cette thèse, nous avons caractérisé la dynamique de l'état excité de trois colorants indolines dans la composition complète des mélanges LI-SM, en utilisant des techniques de spectroscopie UV visible et de fluorescence en régime stationnaire et d'AT. Nous avons montré, en considérant les maximas des spectres stationnaires d'absorption et d'émission, que les déplacements de Stokes et les valeurs du rendement quantique relatif subissent un changement important principalement pour les plus valeurs de $X_{IL} < 0.1$. En outre, sur la base de l'ajustement global des données AT, quatre temps de relaxation caractérisent la dynamique de l'état excité. Nous avons remarqué une diminution globale de leurs valeurs lors de la dilution du LI et pour les deux plus lents, leurs valeurs passent par des minima à X_{IL} autour de 0.1. Nous avons également discuté de la dépendance de la viscosité et de la polarité de ces quatre composantes du temps de relaxation.

Mots clés: D205, D102, D149, indoline, liquides ioniques, DSSC, absorption transitoire, TCSPC, RPE, EKO, solvatation, réorientation, photo-physique

Table of contents

INTRODUCTION **7**
CHAPTER 1. Steady State Behavior of Indoline dyes in Ionic Liquid-Molecular Solvent Mixture: An Experimental Study **16**

1.1. Introduction **17**
1.2. Experimental section **21**
1.2.1. Chemicals 21
1.2.2. Experimental Setups 22
1.3. Results and discussions **22**
1.3.1. Absorption and fluorescence spectra 22
1.3.2. Stokes shift 29
1.2.1. Relative quantum yield 31
1.4. Conclusions **33**
CHAPTER 2. Characterization of the Excited State Dynamics of Indoline dyes in Imidazolium Ionic Liquid-Molecular Solvent mixtures: Study using Transient Absorption Spectroscopy **40**

2.1. Introduction **41**
2.2. Experimental section **44**
2.2.1. Chemicals 44
2.2.2. Experimental Setups 44
2.3. Results and discussions **44**
2.3.1. Time dependent spectral changes of TAS 44
2.3.2. Composition dependent spectral changes of TAS 46
2.3.2.1. Effect of changing the molecular solvents on the TA spectra 47
2.3.2.2. Effect of changing the ionic liquids on the TA spectra 48
2.3.3. Global analysis of TAS 49
2.3.4. Discussions 50
2.4. Conclusions **57**
CHAPTER 3. Comment on Polarity and Heterogeneity in Ionic Liquid - Molecular Solvent Mixtures: EPR Study **71**

3.1. Introduction **71**
3.2. Sample preparation **73**
3.3. Results and discussions **73**
3.3.1. CW-EPR spectral discussion 73
3.3.2. The hyperfine coupling constant 75
3.3.3. Rotational correlation time 77

3.4. A particular case study: BmimBF$_4$-ACN mixture 80
3.4.1. Correlation between two spectroscopic polarity parameter 81
3.4.2. Correlation between A_N and ε: Modified Onsager equation 82
3.3.3. Rotational relaxation time 85
3.5. Conclusions 86
CHAPTER 4. Composition Dependence on the Solvation and Reorientation Dynamics in BmimPF$_6$-ACN mixture 101
4.1. Introduction 101
4.2. Literature preview 104
4.3. Sample preparation 106
4.4. Experimental setups 106
4.5. Results and discussions 106
4.5.1. Steady state measurements 106
4.5.2. TCSPC measurements 108
4.5.2.1. Reconstruction of Time-Resolved Emission spectra 108
4.5.2.2. Calculation of the Solvation response function 109
4.5.2.3. Discussions 110
4.5.3. Femtosecond optical Kerr-effect spectroscopy 112
4.5.3.1. Orientational diffusion study 112
4.5.3.2. OKE low frequency response 116
4.5.3.2.1. Pure components 116
4.5.3.2.2. Composition dependence of low frequency OKE response 117
4.6. Conclusions 120
CHAPTER 5. Experimental Techniques 130
Conclusions and Perspectives 139
Appendices 142
A. Steadystates 143
B. Transient absorption 154
C. EPR study 269
D. Solvation and reorientation dynamics 273

List of Abbreviations

UV	Ultraviolet
Vis	Visible
IR	Infrared
CW-EPR	Continuous wave-electron paramagnetic resonance
IL	Ionic liquid
MS	Molecular solvent
$BmimBF_4$	1-Butyl-3-methylimidazolium tetrafluoroborate
$BmimPF_6$	1-Butyl-3-methylimidazolium hexafluorophosphate
BmimTFO	1-Butyl-3-methylimidazolium trifluoromethanesulfonate
BmimTFSI	1-Butyl-3-methylimidazolium bis(trifluoromethanesulfonyl)imide
ACN	Acetonitrile
γ-BL	γ-Butyrolactone
PC	Propylene carbonate
TCSPC	Time correlated single photon counting
TRES	Time resolved emission spectra
IRF	Instrument response function
GSB	Ground state bleach
ESA	Excited state absorption
SE	Stimulated emission
TAS	Transient absorption spectra
DAS	Decay associated spectra
GVD	Group velocity dispersion
C153	Coumarin 153
OKE	Optical Kerr effect spectroscopy
RSD	Reduced spectral density
MD	Molecular dynamics
TEMPO	(2,2,6,6-Tetramethylpiperidin-1-yl)oxyl radical

Introduction

Among different forms of renewable energy sources, solar energy is the most effective one. Sun is the main source of energy on earth. To capture the solar energy, we need to have photovoltaic cell called solar cell. Photovoltaic cells work according to the principle of photovoltaic effect which is nothing but conversion of photon energy to electrical energy. First silicon crystalline solar cell was invented by Chaplin et al. at Bell Lab in 1954 with 6% light to electric conversion efficiency.[1] After this ground-breaking discovery, we have come through a long period of time and different types of solar cells have been invented. Throughout the years, different types of photovoltaic cells were invented and many research attempts are going on optimization of their efficiencies.

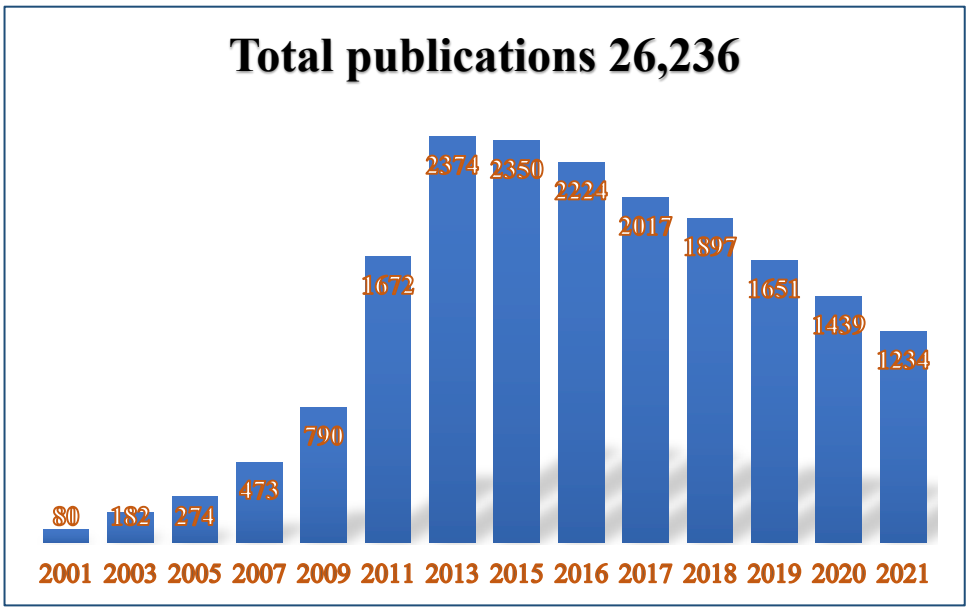

Figure 1: Number of publications per year as a result of the literature search using the keywords "dye sensitized" and "solar" (Source Clarivate Web of Science)

Dye sensitized solar cell is one of among the available solar cells nowadays which is a third generation solar cell with power conversion efficiency (PCE) exceeds 14%.[2–4] It was invented by Gratzel and O'Regan in the year 1991.[5] This third-generation cell is low cost and easy to prepare and handle and it gives good performance. Also this type of cell is a greener option than traditional photovoltaic cells. All these properties draw more and more interests nowadays and the figure below will show how the research on this type of solar cells are growing day by day. There are still many areas of improvement in the efficiency of these types of solar cells.

In Figure 2, the scheme of a typical DSSC is shown. After the sunlight absorption by the sensitizer molecules, which is adsorbed on a film consisting of n-type nanoparticles like TiO_2, ZnO etc., it reaches to its excited state. The excited state of the dye then transfer an electron to the conduction band of the semiconductor whose fermi energy is lower than the electron energy of the excited state of the dye. This electron then travels through the external

circuit which helps to get the power from the cell. On the other hand, the redox couple present in the electrolyte solution helps the oxidized dye to return to its initial state by transferring an electron, which in turn takes an electron from the photocathode.

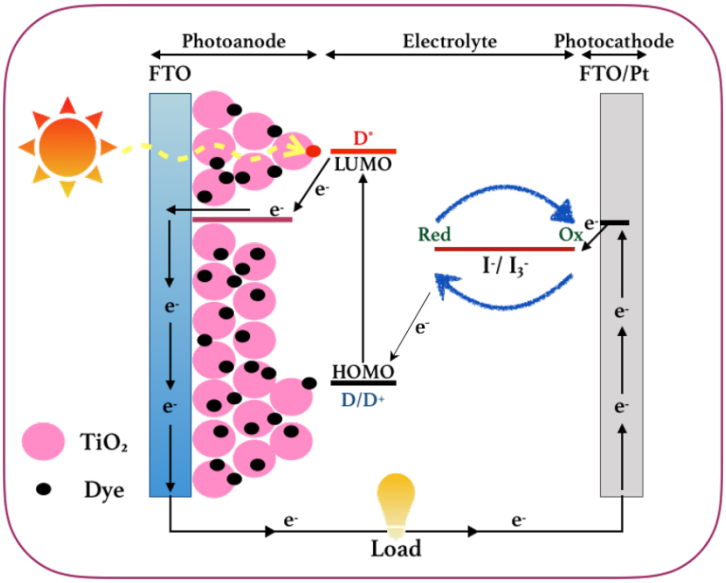

Figure 2: Scheme of a typical dye sensitized solar cell

These set of reactions are known as forward reaction and they are helpful for the efficiency of the DSSC. However, the reasons behind the decrease in the efficiency of DSSC are the occurrence of the backward/reverse reactions in the cell, mainly the charge back transfers to sensitizer and direct recombination between electron and hole transporting layers. Few previous reports show a scheme of different dynamical processes within a typical DSSC with corresponding timescales.[6–8] According to these studies, all the forward reactions that are helpful for the higher efficiency of DSSC are quite fast as compared to the unfavorable electron recombination from semiconductor conduction band to the sensitizer or to the redox pair. Hence, these reverse processes are not very disadvantageous to DSSC. However, sometimes the lifetime of the excited state of the sensitizer molecule, which varies with the type of sensitizers, becomes comparable to the timescales of forward reactions in DSSC and can cause decrease in the efficiency of the solar cell.[9]

A conventional DSSC contains mainly five components, namely photoanode, mesoporous semiconductor metal oxide film, sensitizer, redox electrolyte and counter electrode, whose properties must be optimized to get optimum output from the cell. Among them, the studies in this thesis are mainly concentrated on the characterization of the electrolyte and the sensitizer of the DSSC using various spectroscopic techniques which includes steadystate UV-visible, EPR, time resolved transient absorption, TCSPC and OKE techniques.

To be considered as a good sensitizer for DSSC, a molecule must have some properties. They should have high quantum yield and high redox potential and they should absorb all wavelengths till 920 nm. In addition, the highest occupied molecular orbital (HOMO) energy level of the sensitizer/dye should lie below the energy level of the hole-transporter/redox material so that the oxidized dyes after electron donation to the conduction band of TiO_2 can be regenerated effectively.[10] Besides that, they should also have an anchor group by which they can attach with the semiconductor layer. Over the years, different types of sensitizers are being

used by scientists, lots of articles and reviews were also published mainly on this topic[10–18] and many are still going on with the goal to improve various properties of the DSSC sensitizers. Many different types of dyes are available nowadays starting from the traditional metal-centered ones to organic dyes.[10–18] Among them, organic sensitizers are quite popular nowadays as a greener alternative of traditional metal-centered ones.[11,12] Among the available organic dyes, indoline derivatives have greater power conversion efficiency (PCE) compared to othes.[19] These indoline dyes have common donor-π-bridge-acceptor (D-π-A) type structures with common donor group D with different acceptor groups. One rhodanine ring acts as an acceptor in case of D102, whereas an extra rhodanine ring with two different alkyl extensions (ethyl in D149 and n-octyl in D205) are used as acceptors in D149 and D205.[14,20–22] The octyl chain in D205 was introduced to hinder the undesired electron recombination process of the dye by creating some space between the dye and semiconductor.[23] Besides, a common –COOH group is present in the structure of all these dyes, which can act as an anchor group and help them to stick to the semiconductor surface in DSSC and facilitates the electron injection process from the dye to the semiconductor surface at the same time.

As the dye excited state is mainly involved in the reactions of the DSSC, one need to characterize their exited state relaxation dynamics. In this aspect, various studies have been performed.[24–33] In particular, the excited state dynamics of D149 was very extensively studied. For instance, Fakis et al.,[26] Lohse et al.[27] had studied the excited state dynamics of indoline dye D149 in various organic solvents using transient absorption (TA) spectroscopy, followed by a series of studies by El-Zohry et al.[25,28,29] These studies also discussed about different ways to stabilize the excited state of the organic D149 dye. However, in case of other indoline dyes like D102, D131, D205 etc., the number of reports about their excited state dynamics is quite small.[30–33] Similarly, the number of literatures explaining the excited state dynamics of the organic dyes in IL-MS mixtures is still quite small.[24]

Furthermore, the story is also the same in the case of electrolytes. As DSSC is a photoelectrochemical cell, the primary role of electrolyte is to carry the electrons between cathode and anode. A good electrolyte provides good ionic conductivity in the cell. Besides that, the electrolyte in DSSC also carries the red-ox pair molecules. A good electrolyte must have these following properties: (a) low viscosity and high conductivity, (b) low volatility, (c) high thermal and electrochemical stability, (d) optical transparency, and (e) low cost of purification. There are many choices of electrolytes available nowadays starting from liquid state to solid state. Many quasi-solid electrolytes are also useful due to their favorable properties. Many articles and reviews were also published on this topic also.[12,34–39] Among all the available electrolytes nowadays, ionic liquids (IL) are used extensively in the DSSC as well as in many other electrochemical devises due to some of their interesting properties like non-flammability, low vapor pressure, high electrochemical and thermal stability, large electrochemical potential window, high conductivity etc.[39] However, high viscosity and cost of purification of ILs are the main drawbacks of using them as electrolyte. Therefore, ILs are generally mixed with conventional molecular solvents (MS) like acetonitrile (ACN), γ-butyrolactone (γ-BL), propylene carbonate (PC) etc. to overcome these drawbacks of using ILs as electrolytes. These types of MSs are also chosen among other available solvents due to their profitable properties like wide electrochemical window, relatively high dielectric constant, low

viscosity, wide liquid state temperature range, nontoxicity etc.[40–44] The structures of the used ILs and MSs in this thesis can be noticed in Figure 3.

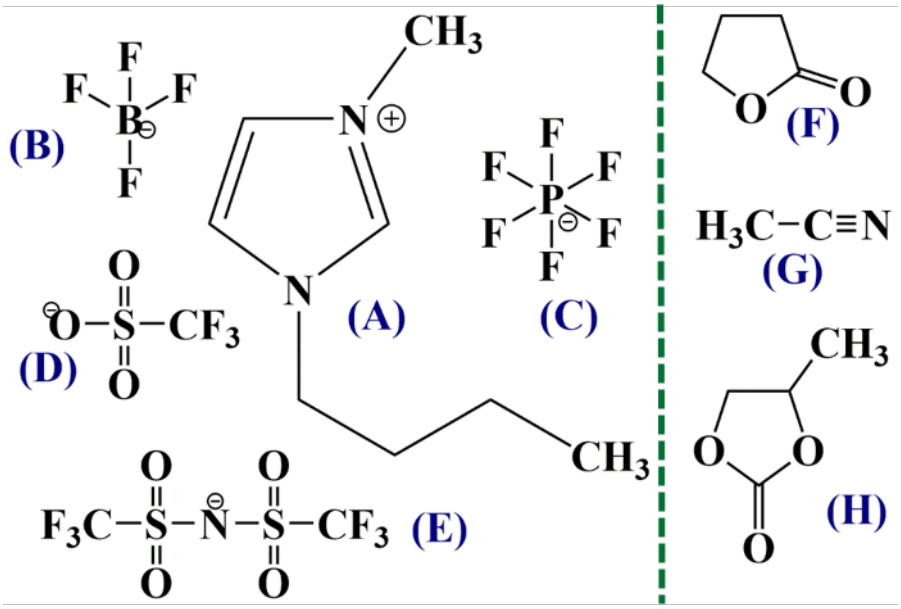

Figure 3: Structures of ILs containing (A) Bmim cation, (B) BF_4^-, (C) PF_6^-, (D) $TFO^-$and (E) $TFSI^-$anions; also three different MSs, (F) γ-BL, (G) ACN and (H) PC

Lots of studies have been performed regarding various properties of the IL-MS mixtures. Composition dependent values of some properties of the IL-MS mixtures like viscosity,[45–52] conductivity[45,47,51–53] and density[54,55] are well-documented. However, there are still differences about the notion of polarity of the IL-MS mixtures, which is important while studying the photophysics of the sensitizer/dye molecule. While the solvatochromic polarity parameter values suggest that ILs are quite polar (polarity in the range of short chain alcohols), static dielectric constant values indicate the polarity of ILs are in the range of medium chain alcohols like n-pentanol.[56] Indeed, the idea of polarity in ILs as well as in IL-MS mixtures is not the same as that in conventional solvents due to the presence of ions in the medium.[56,57] Furthermore, mixing MSs in ILs can not only change the values of the macroscopic properties like viscosity, density, polarity, conductivity etc., but also can modulate the overall microscopic structures because of the composition dependent changes of interactions between the mixture components. In this aspect, while dipole-dipole interactions are predominant in the case of polar aprotic molecular solvents, ionic interactions are the most effective ones in case of ILs. Therefore, it is important to consider all these factors while characterizing various properties of the IL-MS mixtures. Furthermore, the situation become more complicated while the dipolar dye/sensitizer molecules are present in a typical IL-MS mixtures.

Therefore, the overall aim regarding the thesis is mainly two-fold. First, to characterize various physicochemical properties of these IL-MS mixtures which have potential to be used as electrolytes in DSSC and second, to study the photophysics of organic indoline dyes in these IL-MS mixtures. The overall results from this thesis can give us an idea about these systems before using them in the presence of electrodes and other components in the DSSC.

Organization of the thesis

This thesis mainly presents the characterization of the polarity, solvation and reorientation dynamics in imidazolium IL-MS mixtures alongside with the study of photophysics of organic sensitizers used in DSSC in these IL-MS mixtures. The overall thesis is divided in the following manner.

To start with, the study of organic indoline dyes in the IL-MS mixtures using the steadystate UV-visible absorption and fluorescence spectroscopy is presented in Chapter 1. The effect of mixture compositions on the steadystate properties like absorption and emission maxima, Stokes shift and relative quantum yield is described in this chapter. In addition, Chapter 2 consists of the femtosecond transient absorption studies of the similar types of indoline dyes in the same sets of IL-MS mixtures to study the composition dependency on the excited state dynamics of those dyes. In this chapter, special attention was given to various relaxation timescales and their changes with mixture properties during the discussion. The studies in these two chapters will help us to understand the effect of interactions between the dye and neighboring medium on both the ground state and excited state of the dye molecules.

Furthermore, the characterization of mixture polarity and microheterogeneity in the IL-MS mixtures is presented in Chapter 3 using CW-EPR spectroscopy. The correlation between different polarity parameters alongside with the mixture viscosity dependence of the rotational relaxation times of the probe molecule in IL-MS mixtures is shown in this chapter.

In addition, the complete reorientation dynamics in a particular IL-MS mixture, namely BmimPF_6-ACN mixture, is discussed in chapter 4. Besides, picosecond solvation dynamics of the fluorescent probe C153 is also discussed in the case of BmimPF_6-ACN mixture in this chapter. The effect of changing the IL-MS mixture compositions is mainly discussed in the case of both solvation and reorientation dynamics study in this chapter of the thesis. Moreover, there is one chapter (Chapter 5) which is mainly dedicated to the various experimental techniques alongside with the data analysis processes used in this thesis. At the end of this thesis, a collective conclusion alongside with the future perspectives of these studies are jotted down thoroughly.

Finally, all the tables and figures, which are not eligible for the main text of the thesis but important enough to explain the results, are placed in the Appendices.

Bibliography

(1) Chapin, D. M.; Fuller, C. S.; Pearson, G. L. A New Silicon P-n Junction Photocell for Converting Solar Radiation into Electrical Power. *J. Appl. Phys.* **1954**, *25* (5), 676–677. https://doi.org/10.1063/1.1721711.

(2) Mathew, S.; Yella, A.; Gao, P.; Humphry-Baker, R.; Curchod, B. F. E.; Ashari-Astani, N.; Tavernelli, I.; Rothlisberger, U.; Nazeeruddin, M. K.; Grätzel, M. Dye-Sensitized Solar Cells with 13% Efficiency Achieved through the Molecular Engineering of Porphyrin Sensitizers. *Nat. Chem.* **2014**, *6* (3), 242–247. https://doi.org/10.1038/nchem.1861.

(3) Eom, Y. K.; Kang, S. H.; Choi, I. T.; Yoo, Y.; Kim, J.; Kim, H. K. Significant Light Absorption Enhancement by a Single Heterocyclic Unit Change in the π-Bridge Moiety from Thieno[3,2-b]Benzothiophene to Thieno[3,2-b]Indole for High Performance Dye-Sensitized and Tandem Solar Cells. *J. Mater. Chem. A* **2017**, *5* (5), 2297–2308. https://doi.org/10.1039/C6TA09836C.

(4) Yella, A.; Lee, H.-W.; Tsao, H. N.; Yi, C.; Chandiran, A. K.; Nazeeruddin, M. K.; Diau, E. W.-G.; Yeh, C.-Y.; Zakeeruddin, S. M.; Grätzel, M. Porphyrin-Sensitized Solar Cells with Cobalt (II/III)–Based Redox Electrolyte Exceed 12 Percent Efficiency. *Science (80-.).* **2011**, *334* (6056), 629–634. https://doi.org/10.1126/science.1209688.

(5) O'Regan, B.; Grätzel, M. A Low-Cost, High-Efficiency Solar Cell Based on Dye-Sensitized Colloidal TiO2 Films. *Nature* **1991**, *353* (6346), 737–740. https://doi.org/10.1038/353737a0.

(6) Wu, J.; Lan, Z.; Lin, J.; Huang, M.; Huang, Y.; Fan, L.; Luo, G. Electrolytes in Dye-Sensitized Solar Cells. *Chem. Rev.* **2015**, *115* (5), 2136–2173. https://doi.org/10.1021/cr400675m.

(7) Hagfeldt, A.; Boschloo, G.; Sun, L.; Kloo, L.; Pettersson, H. Dye-Sensitized Solar Cells. *Chem. Rev.* **2010**, *110* (11), 6595–6663. https://doi.org/10.1021/cr900356p.

(8) Boschloo, G.; Hagfeldt, A. Characteristics of the Iodide/Triiodide Redox Mediator in Dye-Sensitized Solar Cells. *Acc. Chem. Res.* **2009**, *42* (11), 1819–1826. https://doi.org/10.1021/ar900138m.

(9) Shalini, S.; Balasundaraprabhu, R.; Kumar, T. S.; Prabavathy, N.; Senthilarasu, S.; Prasanna, S. Status and Outlook of Sensitizers/Dyes Used in Dye Sensitized Solar Cells (DSSC): A Review. *Int. J. Energy Res.* **2016**, *40* (10), 1303–1320. https://doi.org/10.1002/er.3538.

(10) Mishra, A.; Fischer, M. K. R.; Bäuerle, P. Metal-Free Organic Dyes for Dye-Sensitized Solar Cells: From Structure: Property Relationships to Design Rules. *Angew. Chemie Int. Ed.* **2009**, *48* (14), 2474–2499. https://doi.org/10.1002/anie.200804709.

(11) Robertson, N. Optimizing Dyes for Dye-Sensitized Solar Cells. *Angew. Chemie Int. Ed.* **2006**, *45* (15), 2338–2345. https://doi.org/10.1002/anie.200503083.

(12) Wang, P.; Klein, C.; Humphry-Baker, R.; Zakeeruddin, S. M.; Grätzel, M. A High Molar Extinction Coefficient Sensitizer for Stable Dye-Sensitized Solar Cells. *J. Am. Chem. Soc.* **2005**, *127* (3), 808–809. https://doi.org/10.1021/ja0436190.

(13) Ito, S.; Zakeeruddin, S. M.; Humphry-Baker, R.; Liska, P.; Charvet, R.; Comte, P.; Nazeeruddin, M. K.; Péchy, P.; Takata, M.; Miura, H.; Uchida, S.; Grätzel, M. High-Efficiency Organic-Dye- Sensitized Solar Cells Controlled by Nanocrystalline-TiO2 Electrode Thickness. *Adv. Mater.* **2006**, *18* (9), 1202–1205. https://doi.org/10.1002/adma.200502540.

(14) Ito, S.; Miura, H.; Uchida, S.; Takata, M.; Sumioka, K.; Liska, P.; Comte, P.; Péchy, P.; Grätzel, M. High-Conversion-Efficiency Organic Dye-Sensitized Solar Cells with a Novel Indoline Dye. *Chem. Commun.* **2008**, No. 41, 5194. https://doi.org/10.1039/b809093a.

(15) Hara, K.; Dan-oh, Y.; Kasada, C.; Ohga, Y.; Shinpo, A.; Suga, S.; Sayama, K.; Arakawa, H. Effect of Additives on the Photovoltaic Performance of Coumarin-Dye-Sensitized

Nanocrystalline TiO 2 Solar Cells. *Langmuir* **2004**, *20* (10), 4205–4210. https://doi.org/10.1021/la0357615.
(16) Koumura, N.; Wang, Z.-S.; Mori, S.; Miyashita, M.; Suzuki, E.; Hara, K. Alkyl-Functionalized Organic Dyes for Efficient Molecular Photovoltaics. *J. Am. Chem. Soc.* **2006**, *128* (44), 14256–14257. https://doi.org/10.1021/ja0645640.
(17) Thomas, K. R. J.; Lin, J. T.; Hsu, Y.-C.; Ho, K.-C. Organic Dyes Containing Thienylfluorene Conjugation for Solar Cells. *Chem. Commun.* **2005**, No. 32, 4098. https://doi.org/10.1039/b506732d.
(18) Hagberg, D. P.; Marinado, T.; Karlsson, K. M.; Nonomura, K.; Qin, P.; Boschloo, G.; Brinck, T.; Hagfeldt, A.; Sun, L. Tuning the HOMO and LUMO Energy Levels of Organic Chromophores for Dye Sensitized Solar Cells. *J. Org. Chem.* **2007**, *72* (25), 9550–9556. https://doi.org/10.1021/jo701592x.
(19) Tyagi, H.; Agarwal, A. K.; Chakraborty, P. R.; Powar, S. Introduction to Advances in Solar Energy Research. In *Advances in Solar Energy*; 2019; Vol. 17, pp 3–11. https://doi.org/10.1007/978-981-13-3302-6_1.
(20) Kuang, D.; Uchida, S.; Humphry-Baker, R.; Zakeeruddin, S. M.; Grätzel, M. Organic Dye-Sensitized Ionic Liquid Based Solar Cells: Remarkable Enhancement in Performance through Molecular Design of Indoline Sensitizers. *Angew. Chemie* **2008**, *120* (10), 1949–1953. https://doi.org/10.1002/ange.200705225.
(21) Lee, C.-L.; Lee, W.-H.; Yang, C.-H. High Efficiency of Dye-Sensitized Solar Cells Based on Ruthenium and Metal-Free Dyes. *Int. J. Photoenergy* **2013**, *2013*, 1–6. https://doi.org/10.1155/2013/250397.
(22) Horiuchi, T.; Miura, H.; Uchida, S. Highly-Efficient Metal-Free Organic Dyes for Dye-Sensitized Solar Cells. *ChemInform* **2004**, *35* (15), 3036–3037. https://doi.org/10.1002/chin.200415171.
(23) Kuang, D.; Uchida, S.; Humphry-Baker, R.; Zakeeruddin, S. M.; Grätzel, M. Organic Dye-Sensitized Ionic Liquid Based Solar Cells: Remarkable Enhancement in Performance through Molecular Design of Indoline Sensitizers. *Angew. Chemie* **2008**, *120* (10), 1949–1953. https://doi.org/10.1002/ange.200705225.
(24) Maity, N.; Piatkowski, P.; Polok, K.; Miannay, F.-A.; Idrissi, A. Effect of the Mixture Composition of BmimBF 4 –Acetonitrile on the Excited-State Relaxation Dynamics of a Solar-Cell Dye D149: An Ultrafast Transient Absorption Study. *J. Phys. Chem. C* **2021**, *125* (32), 17841–17852. https://doi.org/10.1021/acs.jpcc.1c05008.
(25) El-Zohry, A.; Orthaber, A.; Zietz, B. Isomerization and Aggregation of the Solar Cell Dye D149. *J. Phys. Chem. C* **2012**, *116* (50), 26144–26153. https://doi.org/10.1021/jp306636w.
(26) Fakis, M.; Stathatos, E.; Tsigaridas, G.; Giannetas, V.; Persephonis, P. Femtosecond Decay and Electron Transfer Dynamics of the Organic Sensitizer D149 and Photovoltaic Performance in Quasi-Solid-State Dye-Sensitized Solar Cells. *J. Phys. Chem. C* **2011**, *115* (27), 13429–13437. https://doi.org/10.1021/jp201143n.
(27) Lohse, P. W.; Kuhnt, J.; Druzhinin, S. I.; Scholz, M.; Ekimova, M.; Oekermann, T.; Lenzer, T.; Oum, K. Ultrafast Photoinduced Relaxation Dynamics of the Indoline Dye D149 in Organic Solvents. *Phys. Chem. Chem. Phys.* **2011**, *13* (43), 19632. https://doi.org/10.1039/c1cp22429h.
(28) El-Zohry, A. M.; Roca-Sanjuán, D.; Zietz, B. Ultrafast Twisting of the Indoline Donor Unit Utilized in Solar Cell Dyes: Experimental and Theoretical Studies. *J. Phys. Chem. C* **2015**, *119* (5), 2249–2259. https://doi.org/10.1021/jp505649s.
(29) El-Zohry, A. M.; Zietz, B. Concentration and Solvent Effects on the Excited State Dynamics of the Solar Cell Dye D149: The Special Role of Protons. *J. Phys. Chem. C* **2013**, *117* (13), 6544–6553. https://doi.org/10.1021/jp400782g.
(30) Ohta, N.; Awasthi, K.; Okoshi, K.; Manseki, K.; Miura, H.; Inoue, Y.; Nakamura, K.; Kono, H.; Diau, E. W.-G. Stark Spectroscopy of Absorption and Emission of Indoline Sensitizers: A Correlation with the Performance of Photovoltaic Cells. *J. Phys. Chem. C* **2016**, *120* (46), 26206–26216. https://doi.org/10.1021/acs.jpcc.6b08531.
(31) Matsui, M.; Tanaka, N.; Funabiki, K.; Haishima, Y.; Manseki, K.; Jin, J.; Inoue, Y.; Higashijima, S.; Kubota, Y. Application of Indoline Dyes Attached with Strongly Electron-Withdrawing Carboxylated Indan-1,3-Dione Analogues Linked with a Hexylthiophene Ring to

Dye-Sensitized Solar Cells. *Tetrahedron* **2018**, *74* (27), 3498–3506. https://doi.org/10.1016/j.tet.2018.04.077.
(32) El-Zohry, A. M. The Origin of Slow Electron Injection Rates for Indoline Dyes Used in Dye-Sensitized Solar Cells. *Dye. Pigment.* **2019**, *160* (July 2018), 671–674. https://doi.org/10.1016/j.dyepig.2018.09.002.
(33) El-Zohry, A. M.; Agrawal, S.; De Angelis, F.; Pastore, M.; Zietz, B. Critical Role of Protons for Emission Quenching of Indoline Dyes in Solution and on Semiconductor Surfaces. *J. Phys. Chem. C* **2020**, *124* (39), 21346–21356. https://doi.org/10.1021/acs.jpcc.0c07099.
(34) MacFarlane, D. R.; Huang, J.; Forsyth, M. Lithium-Doped Plastic Crystal Electrolytes Exhibiting Fast Ion Conduction for Secondary Batteries. *Nature* **1999**, *402* (6763), 792–794. https://doi.org/10.1038/45514.
(35) Fung, Y. S.; Chad, S. M. Investigation of the 1-Methyl-3-Ethylimidazolium Chloride-AlCl3/LiAlCl4 System for Lithium Battery Application Part I: Physical Properties and Preliminary Chronopotentiometric Study. *J. Appl. Electrochem.* **1993**, *23* (4), 346–351. https://doi.org/10.1007/BF00296690.
(36) Shin, J. Ionic Liquids to the Rescue? Overcoming the Ionic Conductivity Limitations of Polymer Electrolytes. *Electrochem. commun.* **2003**, *5* (12), 1016–1020. https://doi.org/10.1016/j.elecom.2003.09.017.
(37) Shin, J.-H.; Henderson, W. A.; Tizzani, C.; Passerini, S.; Jeong, S.-S.; Kim, K.-W. Characterization of Solvent-Free Polymer Electrolytes Consisting of Ternary PEO–LiTFSI–PYR[Sub 14] TFSI. *J. Electrochem. Soc.* **2006**, *153* (9), A1649. https://doi.org/10.1149/1.2211928.
(38) Tedla, A.; Tai, Y. Influence of Binary Solvent System on the Stability and Efficiency of Liquid Dye Sensitized Solar Cells. *J. Photochem. Photobiol. A Chem.* **2018**, *358*, 70–75. https://doi.org/10.1016/j.jphotochem.2018.03.005.
(39) Kawano, R.; Matsui, H.; Matsuyama, C.; Sato, A.; Susan, M. A. B. H.; Tanabe, N.; Watanabe, M. High Performance Dye-Sensitized Solar Cells Using Ionic Liquids as Their Electrolytes. *J. Photochem. Photobiol. A Chem.* **2004**, *164* (1–3), 87–92. https://doi.org/10.1016/j.jphotochem.2003.12.019.
(40) Chagnes, A.; Diaw, M.; Carré, B.; Willmann, P.; Lemordant, D. Imidazolium-Organic Solvent Mixtures as Electrolytes for Lithium Batteries. *J. Power Sources* **2005**, *145* (1), 82–88. https://doi.org/10.1016/j.jpowsour.2004.12.035.
(41) Chagnes, A.; Carré, B.; Willmann, P.; Lemordant, D. Modeling Viscosity and Conductivity of Lithium Salts in γ-Butyrolactone. *J. Power Sources* **2002**, *109* (1), 203–213. https://doi.org/10.1016/S0378-7753(02)00073-3.
(42) Chagnes, A.; Carré, B.; Willmann, P.; Dedryvère, R.; Gonbeau, D.; Lemordant, D. Cycling Ability of γ-Butyrolactone-Ethylene Carbonate Based Electrolytes. *J. Electrochem. Soc.* **2003**, *150* (9), A1255. https://doi.org/10.1149/1.1597882.
(43) Chagnes, A.; Carré, B.; Willmann, P.; Lemordant, D. Ion Transport Theory of Nonaqueous Electrolytes. LiClO4 in γ-Butyrolactone: The Quasi Lattice Approach. *Electrochim. Acta* **2001**, *46* (12), 1783–1791. https://doi.org/10.1016/S0013-4686(00)00718-0.
(44) Chagnes, A.; Allouchi, H.; Carré, B.; Odou, G.; Willmann, P.; Lemordant, D. Γ-Butyrolactone-Ethylene Carbonate Based Electrolytes for Lithium-Ion Batteries. *J. Appl. Electrochem.* **2003**, *33* (7), 589–595. https://doi.org/10.1023/A:1024904918401.
(45) Li, W.; Zhang, Z.; Han, B.; Hu, S.; Xie, Y.; Yang, G. Effect of Water and Organic Solvents on the Ionic Dissociation of Ionic Liquids. *J. Phys. Chem. B* **2007**, *111* (23), 6452–6456. https://doi.org/10.1021/jp071051m.
(46) Zafarani-Moattar, M. T.; Majdan-Cegincara, R. Viscosity, Density, Speed of Sound, and Refractive Index of Binary Mixtures of Organic Solvent + Ionic Liquid, 1-Butyl-3-Methylimidazolium Hexafluorophosphate at 298.15 K. *J. Chem. Eng. Data* **2007**, *52* (6), 2359–2364. https://doi.org/10.1021/je700338t.
(47) Vraneš, M.; Zec, N.; Tot, A.; Papović, S.; Dožić, S.; Gadžurić, S. Density, Electrical Conductivity, Viscosity and Excess Properties of 1-Butyl-3-Methylimidazolium Bis(Trifluoromethylsulfonyl)Imide+propylene Carbonate Binary Mixtures. *J. Chem. Thermodyn.* **2014**, *68*, 98–108. https://doi.org/10.1016/j.jct.2013.08.034.

(48) Wang, J.; Tian, Y.; Zhao, Y.; Zhuo, K. A Volumetric and Viscosity Study for the Mixtures of 1-n-Butyl-3-Methylimidazolium Tetrafluoroborate Ionic Liquid with Acetonitrile, Dichloromethane, 2-Butanone and N, N ? Dimethylformamide. *Green Chem.* **2003**, *5* (5), 618. https://doi.org/10.1039/b303735e.
(49) Khupse, N. D.; Kumar, A. Dramatic Change in Viscosities of Pure Ionic Liquids upon Addition of Molecular Solvents. *J. Solution Chem.* **2009**, *38* (5), 589–600. https://doi.org/10.1007/s10953-009-9390-7.
(50) Rizzuto, A. M.; Pennington, R. L.; Sienerth, K. D. Study of the BMIM-PF6: Acetonitrile Binary Mixture as a Solvent for Electrochemical Studies Involving CO2. *Electrochim. Acta* **2011**, *56* (14), 5003–5009. https://doi.org/10.1016/j.electacta.2011.03.106.
(51) Zhu, A.; Wang, J.; Han, L.; Fan, M. Measurements and Correlation of Viscosities and Conductivities for the Mixtures of Imidazolium Ionic Liquids with Molecular Solutes. *Chem. Eng. J.* **2009**, *147* (1), 27–35. https://doi.org/10.1016/j.cej.2008.11.013.
(52) Canongia Lopes, J. N.; Costa Gomes, M. F.; Husson, P.; Pádua, A. A. H.; Rebelo, L. P. N.; Sarraute, S.; Tariq, M. Polarity, Viscosity, and Ionic Conductivity of Liquid Mixtures Containing [C 4 C 1 Im][Ntf 2] and a Molecular Component. *J. Phys. Chem. B* **2011**, *115* (19), 6088–6099. https://doi.org/10.1021/jp2012254.
(53) Stoppa, A.; Hunger, J.; Buchner, R. Conductivities of Binary Mixtures of Ionic Liquids with Polar Solvents. *J. Chem. Eng. Data* **2009**, *54* (2), 472–479. https://doi.org/10.1021/je800468h.
(54) Stoppa, A.; Hunger, J.; Buchner, R. Conductivities of Binary Mixtures of Ionic Liquids with Polar Solvents. *J. Chem. Eng. Data* **2009**, *54* (2), 472–479. https://doi.org/10.1021/je800468h.
(55) Tariq, M.; Forte, P. A. S.; Gomes, M. F. C.; Lopes, J. N. C.; Rebelo, L. P. N. Densities and Refractive Indices of Imidazolium- and Phosphonium-Based Ionic Liquids: Effect of Temperature, Alkyl Chain Length, and Anion. *J. Chem. Thermodyn.* **2009**, *41* (6), 790–798. https://doi.org/10.1016/j.jct.2009.01.012.
(56) Wakai, C.; Oleinikova, A.; Weingärtner, H. Reply to "Comment On 'How Polar Are Ionic Liquids? Determination of the Static Dielectric Constant of an Imidazolium-Based Ionic Liquid by Microwave Spectroscopy''''." *J. Phys. Chem. B* **2006**, *110* (11), 5824–5824. https://doi.org/10.1021/jp0601973.
(57) Znamenskiy, V.; Kobrak, M. N. Molecular Dynamics Study of Polarity in Room-Temperature Ionic Liquids. *J. Phys. Chem. B* **2004**, *108* (3), 1072–1079. https://doi.org/10.1021/jp035891m.

Chapter 1

Steady State Behavior of Indoline dyes in Ionic Liquid-Molecular Solvent Mixture: An Experimental Study

This chapter is the basis of the paper titled-

Effect of the Mixture Composition of $BmimBF_4$–Acetonitrile on the Excited-State Relaxation Dynamics of a Solar-Cell Dye D149: An Ultrafast Transient Absorption Study

Nishith Maity, Piotr Piatkowski, Kamil Polok, François-Alexandre Miannay, and Abdenacer Idrissi
The Journal of Physical Chemistry C 2021 *125* (32), 17841-17852

Indoline-based organic dyes are being used as the replacement of the traditional metal-based complexes as the photosensitizers in a DSSC. Thus, it is important to characterize their spectroscopic properties especially when they are dissolved in the electrolyte in the cell. In this aspect, ionic liquid-molecular solvent mixtures also have the potential to be used as the electrolyte in the DSSC due to some of their advantageous properties. Therefore, we have studied the steady state properties of three solar cell dyes D102, D149 and D205 in various imidazolium ionic liquid-molecular solvent mixtures in this chapter. We have shown the effect of the change of composition on the spectroscopic properties like absorption and emission maxima, Stokes shift and relative quantum yield values. All the steady-state properties show noticeable changes in their values at the low mole fraction (X_{IL}) region of ionic liquids in the mixtures. In addition, the presence of extrema at the low X_{IL} region in the values of the emission maxima, Stokes shift and relative quantum yield indicates the presence of interactions between the dye and neighboring medium. The results from this chapter will be quite useful for the study of excited state dynamics which is going to be discussed in the next chapter.

1.1. Introduction:

After the invention of DSSC in the year 1991 by Grätzel and O'Regan, the optimization of the solar cell is one of the rising interests nowadays. Among the commercially available ones, organic indoline based dyes D102, D149, D205 and D131 are used also as photosensitizer in a DSSC. In the case of organic dyes, the indoline dyes have greater power conversion efficiency (PCE) compared to other available organic dyes.[1] These indoline based dyes have donor-π-bridge-acceptor (D-π-A) type structures with common donor group D (Figure 1.1) with different acceptor groups. One single rhodanine ring acts as an acceptor in the case of D102, whereas an extra rhodanine ring with two different alkyl extensions (-C_2H_5 in case of D149 and -C_8H_{17} in the case of D205) are used as acceptors in D149 and D205.[2–5] The n-octyl chain in D205 was introduced to stop the undesired electron recombination process of the dye by creating some gap between the dye and semiconductor surface.[3] Besides, a common –COOH group is present in the structure of all these dyes, which helps these dyes to anchor them to the semiconductor surface in DSSC and also speeds up the process of electron injection from the dye to the semiconductor surface at the same time.

There are a few reports about the photophysical properties of these types of indoline dyes.[6–10] However, their photophysics is still not completely clear. Especially, when the surrounding medium is ionic liquid and even a particular mole fraction of IL-MS mixtures, the study of photophysics of these dyes become quite complicated. To study the photophysics of these dyes in ILs and in IL-MS mixtures, one must study their steady state properties by studying the experimental absorption and emission spectra. By studying these time integrated spectra, we can get an idea about the exact values of changes of absorption and emission maxima, Stokes shift, relative quantum yield. These types of steady state information will be helpful for further time resolved studies like transient absorption and TCSPC studies.

Among the available reports about the steady state properties of the indoline dyes, Fakis et al. had performed both experimental and quantum calculation studies of the indoline dye D149.[9,11] According to their study,[9] when the dye molecule is adsorbed on TiO_2 and Al_2O_3 and dispersed in PMMA, it shows broader S_0-S_1 absorption band than that in organic solvents which in turn suggests the presence of aggregates in those mediums. In addition, according to them, the S_0-S_1 absorption peak of the dye also shows a typical blue shift in case of TiO_2 than that in pure organic solvents. Both the broader absorption band and blue shift of absorption peak can be due to the presence of hydrogen bonding between parallelly arranged D149 molecules. The absorption spectra contain two peaks. The shorter wavelength S_0-S_2 peak (~390 nm) has lower intensity than the longer wavelength S_0-S_1 (~520-550 nm) peak. Both of them have charge transfer (CT) characteristics.[10–12] The S_0-S_2 absorption peak of D149 does not show much changes with the change of solvents, whereas the S_0-S_1 peak show a non-monotonic dependence on the solvent polarity.[9–11] In this regard, Lohse et al. had showed the dependence of the S_0-S_1 absorption peak shift of D149 with the polarizability parameter [($\Delta R = n^2 - 1/n^2 + 2$), n =medium refractive index] in case of pure solvents[10] and also in case of another dye 12'CA in HmimNTf_2-ACN mixture.[13] In addition, the dependency of the polarizability parameter values of the mediums can also be noticed in case of polyene and carotenoid type dyes in different organic solvents, ILs and also in IL-MS mixtures.[13–18]

In the case of emission study, they also found the evidence of aggregation on the emission maxima values in various types of solvents. Due to the aggregation on TiO_2 and Al_2O_3, the dye emission (S_1-S_0) peaks are quenched and red-shifted compared to that in pure solvents. Among the organic solvents, they have found the prolific effect of polarity on the emission maxima values also. While increasing the polarity of the solvent, the emission maxima values show red shift. In addition, the effect of the dye concentration on the emission spectra is also quite noticeable. For instance, the fluorescence peak of D149 in chloroform is found at 620 nm by Fakis et al.[9,11], while it was found at 636 nm by Dentani et al.[19] and at 643 nm by Lohse et al.[10] Also, the fluorescence peak of D149 in MeOH was found at 644 nm by Le-Bahers et al.[12] and at 670 nm by Lohse et al.[10] These types of discrepancy in the emission maxima values was attributed to different experimental conditions, especially due to the concentration of the dyes in the solution. The concentration of the dyes varies between 0.2 - 1×10^{-5}(M) in these studies. In addition to the prominent S_1-S_0 peak, while exciting at 390 nm, there exists another peak with much lower intensity in the wavelength range 430-460 nm. This peak is attributed to the S_2-S_0 emission of the dye. Another important property of D149 is that, it follows the Lippert-Mataga equation in case of pure solvents which results in the value of dipole moment change ($\Delta\mu$) upon excitation up to 13.2D.[11] This value is in agreement with the theoretically calculated values of 10.8D and 11.6D using PBE0/6-311þG (d, p) and RI-CC2/TZVP levels of theory respectively. In this aspect, this change of the transition dipole moment measured and calculated by Fakis et al.[11] was quite small compared the one calculated by Le-Bahers et al.[12], because the later calculation was based on a different conformation of the dye D149 and also due to the choice of different solvation model (PCM model). In this aspect, a comparison between different theoretical and experimental values of the absorption spectra of the dye D149 in different organic solvents were performed which resulted that M05 exchange-correlation functional[20] gave the best results in comparison to experimental one.[21] Previously, this M05 functional also gave excitation energies similar to the experimental values for the dye D149.[22] All the values of steady state properties gathered from previous studies are given in the following table (Table 1.1).

Table 1.1: Previous literature data about steady state properties of the dyes D102, D149 and D205

Medium	λ_{Max}^{Abs} (nm)	λ_{Max}^{Em} (nm)	ν_S (cm^{-1})	λ_{Max}^{Abs} (nm)	λ_{Max}^{Em} (nm)	ν_S (cm^{-1})	λ_{Max}^{Abs} (nm)	λ_{Max}^{Em} (nm)	ν_S (cm^{-1})	Ref
	D102			**D149**			**D205**			
C_6H_6				540, 532, 529	590, 571, 597	1570, 1284				9,11, 23
ACN	503	626	4182	526, 530, 522, 538, 529,	640, 661, 615, 607, 664	3749, 3740, 2897, 4050	525	640	3616	9,11, 21–24

				524, 528						
MeOH	497,523	617, 616	4044, 0.55 ev	525, 528, 561, 527	647, 670, 640, 644	3684, 4015, 4260, 0.42 ev, 0.27 ev	524	671	4269	10,21,23, 25
$CHCl_3$	515	622	3644	552, 548, 534, 549, 550	627, 620, 601, 643	2167, 2119, 2780	550	638	2606	10,11,19, 21
THF	501, 532	597	3349	528, 526, 536, 531	618, 601, 605, 621	2913, 2372, 2870	528	618	2862.4	3,10, 11,21
DCM	512	616	3531	540, 544, 537	629, 625, 606	2918, 2382	544	645	2926	11,21
ACT				528, 538, 530	614, 607, 659	2652, 3860				10,11
EtOH				531	664	4020	527	645	3684	10,21
PC	507	635	3976	538	649	3527	532	650	3622	21
γ-BL	508	635	3937	538	645	3273	515	631	3744	21
5-ol	488.5	610	4211	530	631	3169	515	624	3620	21
DMSO	509	630	3972	542	651	3367	541	653	3332	
CX	490	518	1103	524	545	735	524	545	735	
TLN	505	560	2008	539	582	1430	538	581	1376	
DMF	500	635	4375	532	652	3714	531	652	3726	
n-3ol							534	644	3483	
n-4ol							530	637	3316	
TFE							557	691	3647	
PMMA				533	591	1840				23
PS				540	605	1990				
ZnO				513, 521, 505						19,26,27

TiO_2				518, 541, 516		2,9,27
Al_2O_3				507		27
Vacuum	506			505		28
1:1 ACN, t-BuOH				527, 526		2,26

All three indoline dyes used for our study (D102, D149 and D205) have large excited state dipole moment than ground state dipole moment, according to previous reports.[11,12] Also Lippert-Mataga equation was helpful in the calculation of the dipole moment change between excited state and ground state.[21] According to that, $\Delta\mu^{D205}$ (16.7 D) > $\Delta\mu^{D149}$ (15.5 D) > $\Delta\mu^{D102}$ (14.1 D). In addition, multivariate regression analysis suggested the effect of polarizability on the absorption spectra, which also suggests the dominance of dispersion interaction in the ground state.[21] However, similar analysis also suggested the effect of dipolarity of surrounding medium is more important over the polarizability while explaining emission spectra in various solvents.[21] Later in this chapter, we will find out the similar effect of polarizability parameters in absorption spectra and effect of polarity on the emission spectra. Furthermore, hydrogen bonding interactions between dye excited state and solvents are also important, which is the outcome from the fact that alcohols with small dipole moment show more red-shift in the emission maxima values compared to aprotic solvents with higher dipole moments. Besides that, the gas phase Stokes shift values increase following the order D205 ≈ D149 < D102.[21]

As discussed earlier, concentration dependency on the dye performance was also noticed in some of the studies. The high concentration of the dyes trigger dye aggregation which was studied by some previous experimental and theoretical studies. In general, this aggregation process affect the electron injection process. A study by Sobuś et al.,[27] by creating the whole DSSC cell using D149 dye (D149, TiO_2/ZnO and commercial iodide-based electrolyte), also suggested the presence of singlet-singlet annihilation process as a method of self-quenching of the dye excited state in presence of semiconductor in the medium. Another study by El-Zohry et al. suggested that, high concentration of the dye helps the self-quenching process of the dye which eventually affects the photophysics of D149.[29] Therefore, besides the electron injection, the high concentration of the dye also affects the excited state dynamics of the dye. To get rid of this dye aggregation process, anti-aggregating agent like CDCA (chenodeoxycholic acid) helps to increase the efficiency of the cell.[30,31]

Furthermore, various properties of a particular IL-MS mixture like density, viscosity, conductivity etc. have been already measured experimentally by various groups.[32–44] Changes of the values of these properties have already been settled. As an example, Stoppa et al. had measured the conductivities of the IL-MS mixtures. According to their study, conductivity of IL-MS mixtures starts to increase at the lower X_{IL} region due to increase of ions in the mixtures. However, after reaching at the maximum value at particular X_{IL} (at X_{IL} ≈ 0.1-0.25, varies

between binary mixtures), the conductivity starts to decrease while increasing X_{IL} due to increase of viscosity (i.e. decrease of speed of the ions) of the mixtures.[42] In addition, according to Buchner et al., IL-MS mixtures behave like lubricated ionic liquid down to $X_{IL} \approx 0.2$. Below that concentration, their properties are similar to the weakly associated electrolyte solutions. In the transition region at $X_{IL} \approx 0.2$, the re-dissociation of the ion pairs of IL occurs which eventually helps to build the IL-like "lubricated" structure.[39]

In addition, the concept of polarity of the IL-MS mixture is still quite contradictory. Indeed, the solvatochromic polarity parameter (E_T^N) values of ILs are quite high (same range as short chain alcohols), whereas their static dielectric constants are comparatively low (same range as medium chain-length alcohols like n-pentanol). According to Wakai et al., due to the presence of ions in the IL-MS mixtures, the concept of polarity is not similar to the one which are used to describe polarity of conventional solvents.[45] Therefore, these is a contradiction in the composition dependent change of polarity parameters in a typical IL-MS mixture. For instance, in case of $BmimBF_4$-ACN mixture, the solvatochromic polarity parameter value (E_N^T) of pure $BmimBF_4$ is greater than that of pure ACN.[46–48] Besides, according to Manchini et al., E_N^T values of $BmimBF_4$-ACN mixtures also increases while increasing X_{IL}.[49] However, Stoppa et al.[39] had measured dielectric constant (ε) of $BmimBF_4$-ACN binary mixture at different X_{IL} using dielectric relaxation spectroscopy (DRS). Although there is an initial increase at very low X_{IL} of $BmimBF_4$ ($X_{IL} \leq 0.01$), overall values of ε show a gradual decrease from pure ACN to pure $BmimBF_4$. Overall, these previous studies in different IL-MS mixtures show some peculiar characteristics about these mixtures.

Therefore, in this chapter, we are going to show the experimental study of the steady state photophysical properties of the three organic solar cell dyes D102, D149 and D205 in different IL-MS mixtures. Four different imidazolium based ILs and three different polar aprotic solvents (ACN, γ-BL and PC) were used to make overall twelve different IL-MS mixtures. By discussing the steady state properties of these three indoline-based dyes in these IL-MS mixtures, we can understand how the solvent and solvent mixture properties effect the steady state photophysical properties of the dyes.

This chapter proceeds as follows: first we will discuss the changes of steady state absorption and emission spectra and maxima values in pure components as well as in the studied IL-MS mixtures. Then, we will discuss the same for the Stokes shift values and finally we will make a general conclusion after discussing the variation of the relative quantum yield values of the dyes in the IL-MS mixtures and their pure counterparts.

1.2. Experimental section:

1.2.1. Chemicals:

The dyes D102, D149, and D205 and all molecular solvents (acetonitrile, ACN (≥ 99.5%), γ-butyrolactone, γ-BL (≥ 99%) and propylene carbonate, PC (99.7%) were bought from Sigma Aldrich. The Imidazolium ionic liquids 1-butyl-3-methylimidazolium tetrafluoroborate, $BmimBF_4$ (≥ 98%), 1-butyl-3-methylimidazolium hexafluorophosphate, $BmimPF_6$ (99.5%), 1-butyl-3-methylimidazolium trifluoromethanesulfonate, BmimTFO (99.5%) and 1-butyl-3-

methylimidazolium bis(trifluoromethylsulfonyl)imide, BmimTFSI (99.5%) were bought from Solvionic. All the ionic liquids and molecular solvents were stored under inert argon atmosphere to keep them away from the moisture. All binary solvents mixtures were prepared and kept inside the argon atmosphere glove box. The optical cuvettes were also filled with the samples inside the glove box just before the experiment to minimize the risk of introducing impurities. The structures of all the three dyes and other chemicals are shown in Figure 1.1 and in Figure 3 in the Introduction.

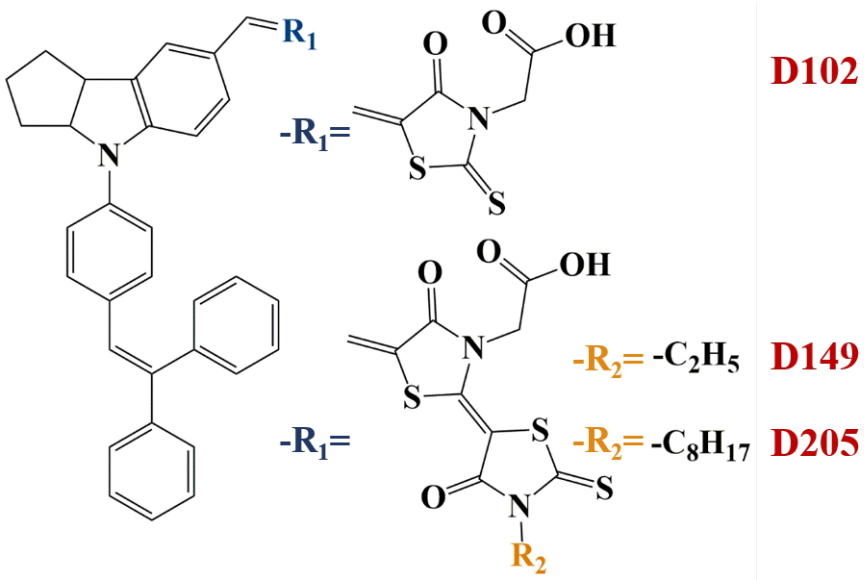

Figure 1.1: Structures of the organic indoline dyes D102, D149 and D205

1.2.2. Experimental Setups:

All the steady state absorption and emission experiments are performed by using Varian Cary 100 and on Jobin Yvon Fluoromax respectively.

1.3. Results and Discussions:

Our results can be divided into three main parts. Steady state absorption and emission spectra, Stokes Shift and relative quantum yields of the dyes in all IL-MS mixtures.

1.3.1. Absorption and Emission Spectra:

General Characteristics:

In this section, we will show all the steady state absorption and emission spectra and discuss about their different changes while changing the mixture composition. There are some general features of these absorption and emission spectra of the dyes (D102, D149 and D205) in IL-MS mixtures. Similar to previous reports,[7,50–52] all the absorption spectra (right spectra in Figures 1.2, A1 and A2) in this study consist of two peaks corresponding two electronic transition, namely higher energy S_0-S_2 peak and lower energy S_0-S_1 peak. According to Le-Bahers et al.,[50]

both these electronic transitions are π-π^*transitions and they have charge transfer (CT) characteristics also.

Furthermore, the emission spectra of these dyes (left spectra in Figures 1.2, A1 and A2) can be obtained by excitation of the sample using 460 nm light wavelength. The excitation wavelength was chosen in a way that the sample can be excited to S_1 state, as we are mainly interested to study the relaxation dynamics from first excited state of the dye. Similar excitation wavelengths were chosen mainly to get better comparison among all the samples using all three studied dyes. Thus, emission spectra contains one peak corresponds to S_1-S_0 transition with very weak vibronic shoulder.[6]

Composition dependent absorption and emission spectra:

In case of the absorption and emission spectra of D102, D149 and D205 in different IL-MS mixtures, we have to take a look at Figures 1.2, 1.3 and A1-A4. However, for the discussion, we have chosen to discuss about the absorption and emission spectra of D102 in various IL-MS mixtures and also in pure components because the spectra in case of the other two dyes behave almost similarly (Figures A1-A4 in the appendix).

In case of D102 in different IL-MS mixtures, for the sake of better comparison, we have divided the figures of steady state spectra into two main categories. First one contains the spectra of D102 in IL-MS mixtures containing a particular IL. As we have four different ILs, four subfigures (Figure 1.2) are possible to prepare in this category. Describing them will help us to get an idea about the effect of changing MSs (ACN, γ-BL and PC) on the steady state behavior in case of each ILs used in this study. The other category contains the spectra of D102 in IL-MS mixtures containing a particular MS. Three different subfigures (Figure 1.3) containing three different MSs will help us to understand the effect of changing four ILs ($BmimBF_4$, $BmimPF_6$, BmimTFO and BmimTFSI) on the steady state properties of each particular MS in this study.

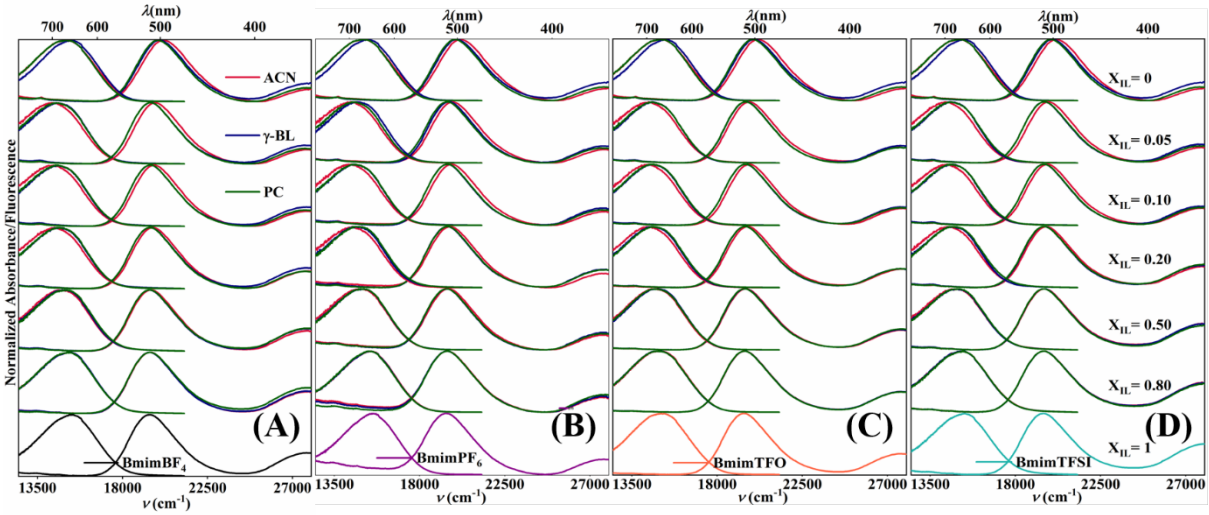

Figure 1.2: Normalized steady state absorption (right) and emission (left) spectra of D102 in (A) $BmimBF_4$-MS, (B) $BmimPF_6$-MS, (C) BmimTFO-MS and (D) BmimTFSI-MS mixtures ($\lambda_{excitation}$= 460 nm).

In Figure 1.2 [(A), (B), (C) and (D)], we can see the absorption and emission spectra of D102 in $BmimBF_4$-MS, $BmimPF_6$-MS, BmimTFO-MS and BmimTFSI-MS mixtures (where MS = ACN, γ-BL and PC) respectively. As discussed earlier, the general characteristics of these spectra are similar in case of all the spectra. In addition, if we try to compare the steady state spectra of the dye in three different MSs keeping same IL, we can see a common trend in all the subfigures of Figure 1.2. Mainly in the regions with lower X_{IL} values ($X_{IL} \leq 0.20$), the absorption and emission spectra are little shifted with respect to each other while changing the three molecular solvents because the mixture at lower X_{IL} region has more MS characteristics. As the X_{IL} increases ($X_{IL} > 0.20$), both the absorption and emission spectra of the dye in three different solvents start to merge and after $X_{IL} = 0.50$, it's really difficult to find out differences among these spectra as they almost look similar to each other.

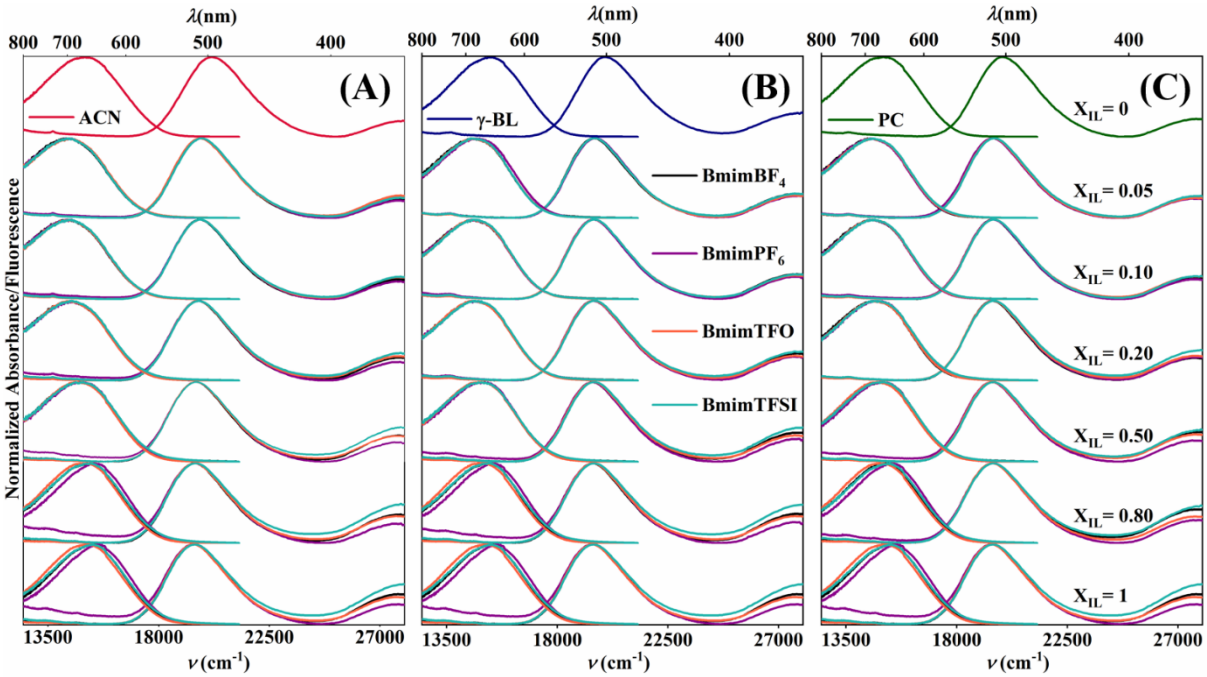

Figure 1.3: Normalized steady state absorption (right) and emission (left) spectra of D102 in (A) IL-ACN, (B) IL-γ-BL and (C) IL-PC mixtures ($\lambda_{excitation}$= 460 nm).

Moreover, we have also plotted the absorption and emission spectra of D102 in IL-MS mixtures keeping MSs constant. Figure 1.3 [(A), (B) and (C)] show the steady state spectral changes of this type. As each subfigure contains one particular solvent, it is expected that the absorption and emission spectra should show almost similar peaks in different ILs in lower X_{IL} ($X_{IL} \leq 0.20$) regions, where the MS characteristics are dominant in the mixture and exactly the same thing happens in this case. However, increasing X_{IL} starts to show the differences in both the absorption and emission spectra in four different ILs as the IL characteristics of the IL-MS mixtures starts to dominate. In the case of absorption spectra, the S_0-S_1 peaks remains almost at the same position while the other peak (S_0-S_2) intensity starts to show the differences. Furthermore, the position of emission maxima also show the shift while changing the ILs in the case of each of these subfigures [(A), (B) and (C)] which becomes evident at $X_{IL} > 0.50$.

These type of steady state spectral behavior clearly suggests the presence of two different regions in a particular IL-MS mixture, which was previously suggested by many previous

studies.[39,53–58] Before X_{IL} = 0.20, the MS characteristics of a particular IL-MS mixture is more prominent in the mixture whereas the IL characteristics starts to dominate after X_{IL} = 0.20. In the transition region at $X_{IL} \approx 0.20$, there exists a particular mixture composition from where the mixture behavior started to show IL dominated behavior from MS dominated behavior.

Correspondingly, the change of absorption and emission maxima should be discussed now as we have discussed about the spectra already. Values of the steady state properties of the dyes in IL-MS mixtures have been shown in Tables A1-A35 in the appendix.

Table 1.2: Steady state properties of the studied indoline dyes in pure solvents and ILs

Solvs/ ILs	λ_{Max}^{Abs} (nm)			λ_{Max}^{Em} (nm)			$\nu_{Stokes}(cm^{-1})$		
	D102	D149	D205	D102	D149	D205	D102	D149	D205
ACN	494.1	531.0	527.9	633.6	665.0	646.8	5101.1	4285.5	3980.9
γ-BL	499.5	538.1	533.9	631.6	661.3	642.3	4611.6	3749.1	3485.5
PC	501.7	532.9	534.6	633.2	646.1	643.1	4798.9	3695.6	3998.4
Bmim BF_4	512.7	542.3	543.4	630.5	644.0	641.5	4051.0	3328.4	3242.5
Bmim PF_6	513.5	542.6	543.2	622.9	637.9	639.1	3818.3	3075.8	3377.8
Bmim TFO	513.5	540.5	542.4	631.3	640.7	638.5	4259.5	3116.7	3078.9
Bmim TFSI	512.4	540.5	541.7	630.8	643.9	640.1	4074.6	3367.0	3174.1

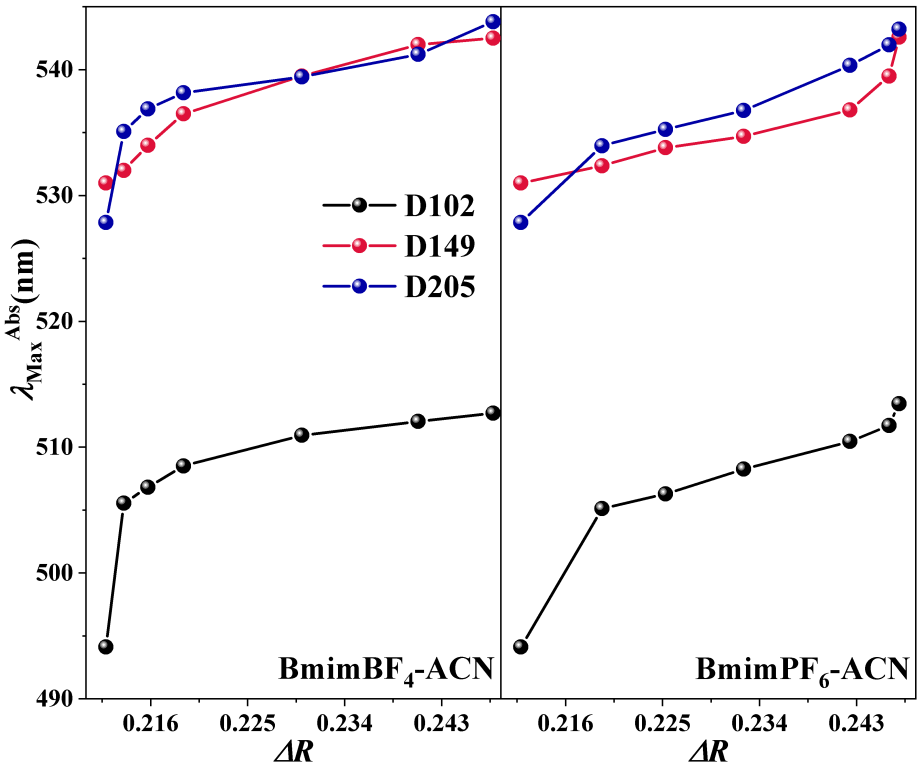

Figure 1.4: Variation of absorption maxima with polarizability parameters (ΔR) of the medium

For the discussion of S_0-S_1 absorption maxima of three studied indoline dyes in pure solvents and in pure ILs, one can easily notice that, the values of λ_{Max}^{Abs} are red-shifted in case of pure ILs compared to that in pure MSs. In this regard, previous studies showed that the absorption maxima of these D-dyes are weakly solvent dependent in case of pure solvents. However, this typical red shift of the absorption maxima of the dyes in ILs compared to that in pure organic solvents can be explained considering the presence of interactions between the dyes and the ions in ILs. Indeed, previous studies[18,59,60] also found this typical red shift of λ_{Max}^{Abs} in pure ILs compared to that in pure solvents using pyrene and 12'-CA probes and gave similar types of descriptions behind their observation. All the values of absorption maxima in pure solvents and pure ILs are given in Table 1.2, while previous reports are shown in Table 1.1.

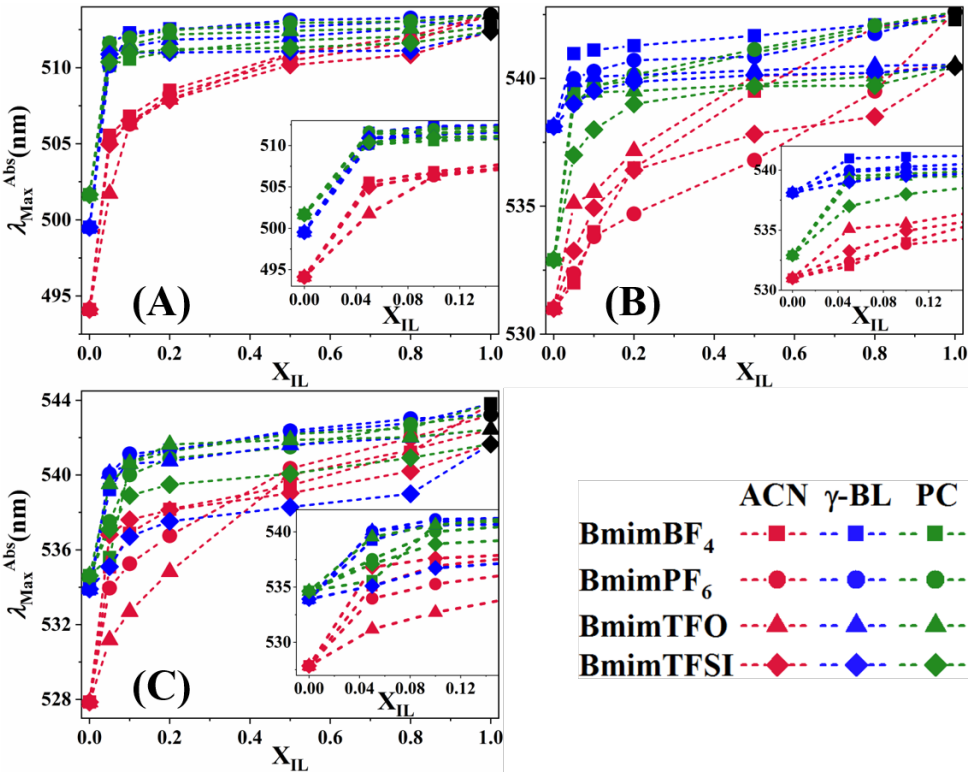

Figure 1.5: Change of absorption maxima of (A) D102, (B) D149 and (C) D205 in IL-MS mixtures

In case of absorption maxima, generally in the range of X_{IL} between 1 and 0.1, we notice that the values of λ_{Max}^{Abs} of D-dyes are comparatively less affected (Figure 1.5). It seems that in this range of mole fraction, the interactions between the dye and the mixture components are not affected while changing mixture compositions. The exception to this general trend is observed when the dyes are dissolved in IL-ACN mixtures. In addition, for further decrease of X_{IL} ($0.1 \geq X_{IL} \geq 0$) the decrease of λ_{Max}^{Abs} is quite noticeable. This observation gives a hint that in this range of mole fraction (X_{IL}=0-0.1), a strong change in the local structure around these dyes occurs which may be due to stronger interaction between the dye and the dye surrounding medium.

In addition to that, Figure 1.5 and Tables A1-A35 (Appendix) show the typical red shift while increasing X_{IL} in case of all three indoline dyes in all imidazolium IL-MS mixtures. This red

shift of absorption maxima was also observed in the case of different polyene and carotenoid type dyes in different organic solvents and in HmimNTf$_2$-ACN binary mixture.[14,17,61,62] This typical red shift was attributed to the increase of polarizability of the surrounding medium of the dye. In addition, multivariate regression analysis also showed the effect of polarizability on this shift of absorption maxima suggesting the effect of dispersion interaction in the ground state of the dyes.[21] We can also calculate the value of polarizability parameter ($\Delta R(n)$) if we have the idea about experimental refractive index of these IL-MS mixtures in our study. To our knowledge, the experimental values of both refractive index (n) of BmimBF$_4$-ACN[39] and BmimPF$_6$-ACN[34] mixtures are only reported till date. We have calculated the values of ΔR and found a non-linear increase of absorption maxima while increasing the polarizability parameter of these two IL-MS mixtures (Figure 1.4, Table 1.3). In case of other IL-MS mixtures, the observed redshift of the absorption maxima is similar to the red shift in BmimBF$_4$-ACN and BmimPF$_6$-ACN mixtures. Another possible reason of this typical red shift of $\lambda_{\mathrm{Max}}^{\mathrm{Abs}}$ of D-dyes in the IL-MS mixtures while increasing X_{IL} can be due to the interactions present in the medium. In previous studies related to the pyrene dye in various pyridinium and imidazolium-based IL-MS mixtures, Zhu et al.[59] and Carrete et al.[60] have also noticed this typical red shift of $\lambda_{\mathrm{Max}}^{\mathrm{Abs}}$ while increasing IL-concentration in the mixtures and described viscosity increase and interactions between the dye and ionic liquid as the origin of this behavior.

Another important aspect can be discussed from Figure 1.4 considering the non-linear mixing behavior in IL-MS mixtures. In case of these two IL-MS mixtures (BmimBF$_4$-ACN[39] and BmimPF$_6$-ACN[34]), The absorption maxima values show non-linear change while changing the solvent polarizability function (ΔR). This non-linear dependence indicates that, the bulk composition of the mixture is not similar to the composition of the mixture in the cybotactic region i.e. in the vicinity of the probe, which in turn indicates that, there exists preferential solvation type behavior of the probe/dye molecule by the mixture components.

Table 1.3: Absorption maxima of three dyes and polarizability parameter values in BmimBF$_4$-ACN and BmimPF$_6$-ACN mixtures.

X_{IL}	**BmimBF$_4$-ACN Mixture**					**BmimPF$_6$-ACN Mixture**				
	n	ΔR^*	$\lambda_{\mathrm{Max}}^{\mathrm{Abs}}$			n	ΔR^*	$\lambda_{\mathrm{Max}}^{\mathrm{Abs}}$		
			D102	**D149**	**D205**			**D102**	**D149**	**D205**
0.00	1.344	0.212	494.12	531.00	527.86	1.344	0.212	494.12	531.00	527.86
0.05	1.347	0.214	505.56	532.00	535.09	1.358	0.219	505.13	532.37	533.96
0.10	1.351	0.216	506.82	534.00	536.89	1.368	0.225	506.29	533.81	535.26
0.20	1.357	0.219	508.52	536.50	538.17	1.382	0.232	508.26	534.70	536.76
0.50	1.377	0.230	510.95	539.50	539.44	1.399	0.242	510.46	536.80	540.35
0.80	1.397	0.241	512.05	542.00	541.22	1.407	0.246	511.73	539.50	541.98
1.00	1.410	0.248	512.71	542.50	543.82	1.408	0.247	513.47	542.60	543.22

*$\Delta R = (n^2-1)/(n^2+2)$, here n are the values of refractive indices[34,39] of the binary mixtures of different compositions

Additionally, the absorption maxima of D149 and D205 are more red-shifted than that of D102 in all the pure solvents, ILs and in the IL-MS mixtures. This can be described

considering the structures of these dyes (Figure 1.1). The extra rhodanine ring in the acceptor unit of both D149 and D205 helps to increase the π-conjugation[3] which results in the red-shift of the absorption maxima compared to D102.

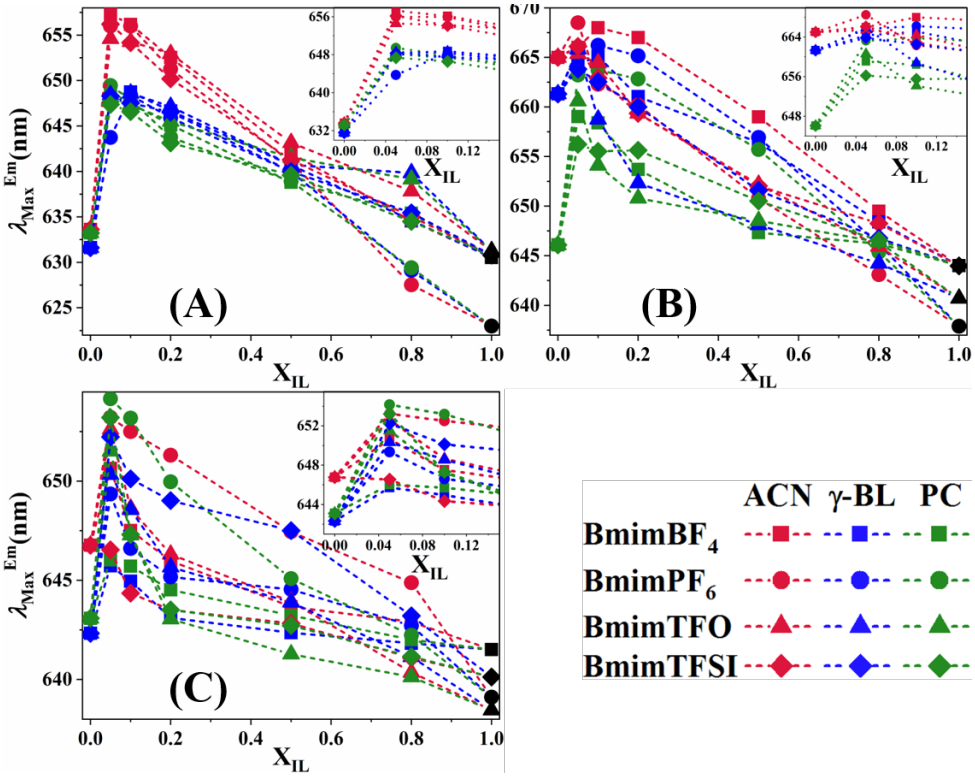

Figure 1.6: Change of emission maxima of (A) D102, (B) D149 and (C) D205 in IL-MS mixtures

In Figure 1.6, the emission maxima values of the dyes are plotted against composition of the IL-MS mixtures. From this figure, we can notice that the emission maxima of the dyes in pure ILs are blue shifted compared to that in pure MSs. In addition, ACN has the most red-shifted emission maxima value compared to other MSs. The λ_{Max}^{Em} values of the dyes in pure solvents and ionic liquids are shown in Table 1.1 and Table 1.2 respectively.

In the case of the IL-MS mixtures, Figure 1.6 clearly shows the red-shift of emission maxima values while decreasing X_{IL} until X_{IL}=0.10. This red shift can be described considering the increase of medium polarity. Table 1.4 shows that MSs used in this study are more polar than the used ILs. In addition, DRS spectroscopic technique showed an overall increase of medium polarity values while decreasing X_{IL} of the IL-MS mixtures, especially in $EmimBF_4$, $BmimBF_4$, $HmimBF_4$-ACN[39] and $HmimNTf_2$-ACN[62] mixtures. However, the λ_{Max}^{Em} values of the three used dyes go through maxima at X_{IL} = 0.05-0.10 in case of all the studied IL-MS mixtures and show a further blue shift while decreasing X_{IL} to 0. In this regard, emission process of a dye is generally more sensitive towards the change of local environment of the dye compared to the absorption. Previous studies have already shown that, the cation-anion interactions in the studied IL-MS mixtures are weaker at the lower X_{IL} region compared to higher X_{IL} region. This in turn indicates that, competitive dye-ion interactions are comparatively stronger at lower X_{IL} region of the mixture. Therefore, this presence of maxima in the values of λ_{Max}^{Em} of the dyes at the low X_{IL} region of the studied IL-MS mixtures may indicates the presence of interactions

(dipole-dipole/ H-bonding/ Van der Waals) between the solute (dye) and the surrounding mediums. There are mainly two reasons behind this previous statement. First, the viscosity change in this low X_{IL} region of the mixture is negligible and second, the values of dielectric constants of the IL-MS mixtures pass through maxima at $X_{IL} \sim 0.01$.[39,62] Although experimental data are not available for all the studied mixtures, this behavior of the composition dependence of the dielectric constant values in IL-MS mixtures can be correlated with the composition dependent change of emission maxima here.

Table 1.4 : Polarity parameters (Δf) and polarizability parameter (ΔR) of pure solvents and ILs used in this study.

Liquids	ε	n	ΔR	Δf
ACN	35.96	1.34	0.21	0.71
γ-BL	41.70	1.44	0.26	0.67
PC	64.96	1.42	0.25	0.70
$BmimBF_4$	11.70	1.42	0.25	0.53
$BmimPF_6$	11.40	1.41	0.25	0.53
BmimTFO	13.20	1.44	0.26	0.54
BmimTFSI	11.60	1.43	0.26	0.52

$\Delta f = (\varepsilon\text{-}1)/(\varepsilon+2)\text{-}(n^2\text{-}1)/(n^2+2)$, $\Delta R = (n^2\text{-}1)/(n^2+2)$, here ε and n are the values of dielectric constants[39,63–65] and refractive indices[32–34,39,44] of the binary mixtures of different compositions

1.3.2. Stokes Shift:

Generally the emission spectra are red-shifted compared to absorption spectra. In other words, energy of emission is less than the energy of absorption. Upon excitation into higher energy levels, the excess energy is quickly dissipated, which helps the dye molecule to reach in the lowest vibrational level of its first excited state.[66,67] Therefore, the emission maxima values indicate the energy gap between the lowest vibrational level of the excited state and the ground state of the dye, and the energy difference between the absorption and emission for a particular dye/chromophore is known as Stokes shift, named after the first observer of this phenomena sir G. G. Stokes.[68] The extent of Stokes shift depends on the nature of fluorophore and its solvation environment. Indeed, more stabilized excited state due to various reasons would help to increase the Stokes shift values of a particular dye/fluorophore.

While comparing the Stokes shift values of pure solvents and pure ionic liquids, it can be clearly noticed that the values of ν_{Stokes} in pure solvents are larger than that in pure ILs. (Table 1.2) This can be described considering the values of polarity parameter (Δf) of the surrounding medium of the dye (Table 1.4). The polarity parameter as well as the Stokes shift values are greater in pure molecular solvents than in pure ionic liquids. In addition, dyes in acetonitrile has higher values of Stokes shift because it is more polar (higher Δf) than other two molecular solvents (γ-BL and PC) used in our study.

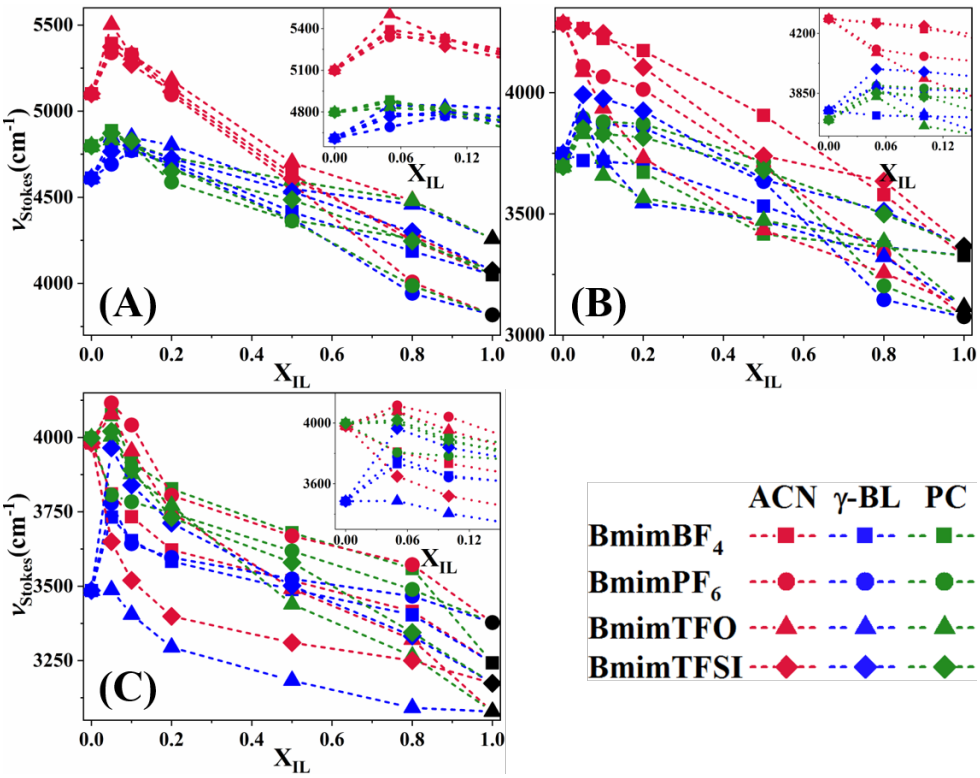

Figure 1.7: Change of Stokes shift values of (A) D102, (B) D149 and (C) D205 in IL-MS mixtures

In Figure 1.7, we can see the change of Stokes shift values of D102, D149 and D205 with increasing X_{IL} in the IL-MS mixtures. Besides, all the Stokes shift values are shown in Tables A1-A35. The change of Stokes shift values behaves differently in case of the IL-MS mixtures used in this study while using the three different dyes. From Figure 1.7, starting from pure ILs, we can see an overall increase of the values of Stokes shift with dilution of the ILs which can be correlated with an overall increase of polarity parameter values (Δf). However, in the case of some IL-MS mixtures (example: $BmimBF_4$-ACN mixture), the Stokes shift values go through a maximum at around X_{IL} =0.05-0.1. This type of maxima in Stokes shift values of the three dyes at the lower X_{IL} region of some IL-MS mixtures can be the outcome of the stronger dye-ion interactions due to weaker cation-anion interactions especially at the lower X_{IL} region of the IL-MS mixtures.

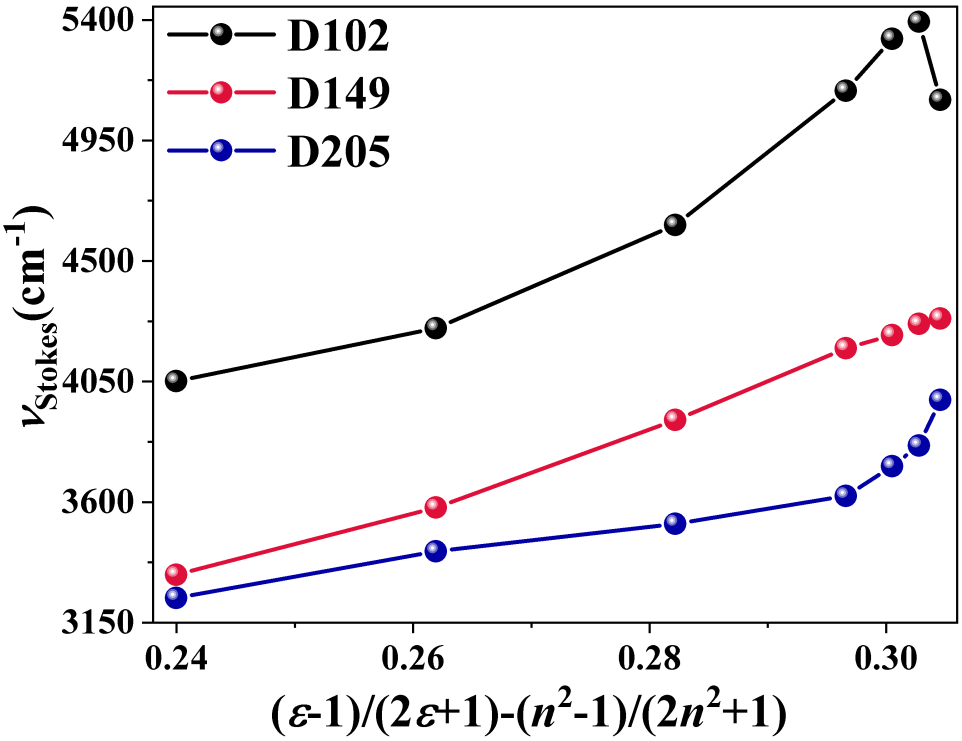

Figure 1.8: Lippert-Mataga plot for three dyes in $BmimBF_4$-ACN mixtures. ε and n values of the mixtures are taken from a previous report[39]

Another way to observe the solvent effect on steady state spectral shifts is to follow the Lippert-Mataga equation for these three dyes D102, D149 and D205. The actual derivation of the equation are described elsewhere.[69,70] However, the final form of this equation looks like the following:

$$\bar{\nu}_{Stokes} = \bar{\nu}_A - \bar{\nu}_F = \frac{2}{hc}\left(\frac{\varepsilon-1}{2\varepsilon+1} - \frac{n^2-1}{2n^2+1}\right)\frac{(\mu_E-\mu_G)^2}{a^3} + constant \qquad (1.1)$$

Here ε and n are dielectric constant and refractive index of the medium and μ_E and μ_G are excited and ground state dipole moments of the dye respectively. Besides, h is Planck's constant, c is the speed of light and a is the radius of the dye molecule. Furthermore, $\bar{\nu}_A$ and $\bar{\nu}_F$ are absorption and emission wavenumbers respectively.

In Figure 1.8, we have shown the Lippert-Mataga plot for three dyes in $BmimBF_4$-ACN mixtures as the experimental values of ε and n in case of other IL-MS mixtures are not available. From this figure, we can see an almost linear relation only in case of D149. However, in case of other two dyes, the Lippert-Mataga plots are non-linear. On this note, it is worth mentioning that the Lippert-Mataga equation only considers dipole-dipole and dispersion interactions between dye and the surrounding medium. Thus, non-linear Lippert-Mataga plots of D102 and D205 in $BmimBF_4$-ACN mixture also suggests that other specific interactions like hydrogen bonding and electron pair donor/acceptor interactions may be present between the dye and the surrounding medium.

1.3.3. Relative Quantum Yield:

From the steady state absorption and emission spectra, we can also get an idea about relative quantum yield (ϕ_{Relative}) of the dyes in solvents and solvent mixtures. This can be expressed as the area under the emission spectra normalized with respect to absorption intensity at the excitation wavelength. Previously this type of relative quantum yield calculation was shown in case of D149 in pure solvents by El-Zohry et al.[8] In case of our study, we are extrapolating this concept in case of other dyes D102, D149[71] and D205 in various imidazolium IL-MS mixtures. To get a better comparison, we have set the value of ϕ_{Relative} of D149 in ACN to 1 in order to get an idea of the comparative changes of ϕ_{Relative} values while changing the dyes, MSs, ILs and also the compositions of IL-MS mixtures. However, the reported experimental quantum yield of D149 in ACN is 4.64%.[72]

ϕ_{Relative} values in Figure 1.9 of the dyes in different IL-MS mixtures show a decrease from X_{IL}=1 to X_{IL}=0.1 and minima at X_{IL} ~ 0.05-0.1. In general, ϕ_{Relative} values increase when the rate of non-radiative processes decreases and vice versa. This minimum in ϕ_{Relative} suggests that at this specific range of mixture composition, the relaxation of the excited state prefers non-radiative process over radiative decay. This minimum can't also be explained regarding the viscosity of the surrounding medium as there is no presence of minimum in the composition dependence of the viscosity values of these IL-MS mixtures.[34–38,40,41,43,73] Based only on these spectroscopic data, it is difficult to interpret the appearance of this minimum in the quantum yield. However, in some previous studies,[74–78] the change in the conformation of the dye molecules, the hydrogen bonding between the dye and the surrounding medium are also regarded as reasons for the decrease in quantum yield. To get further idea about dye conformation change or hydrogen bonding interactions in our case, we need to do further molecular level calculations, which is out of the scope of this study.

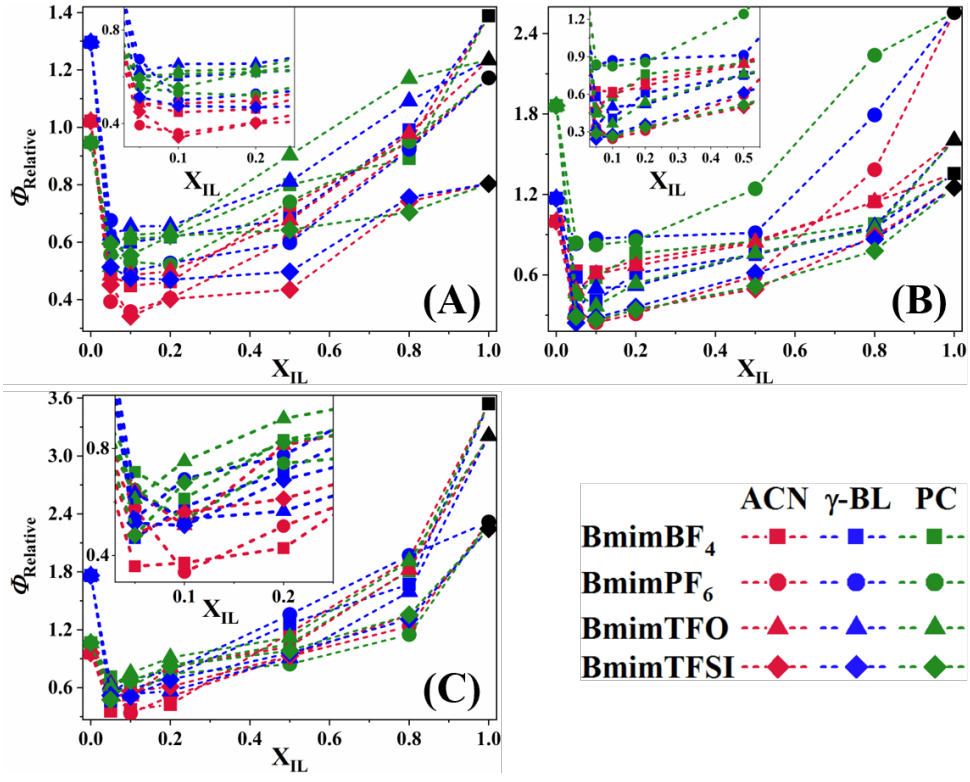

Figure 1.9: Relative quantum yield values of (A) D102, (B) D149 and (C) D205 in IL-MS mixtures

1.4. Conclusions:

In this chapter, we have comprehensively discussed about the steady state properties of the three organic indoline based solar cell dyes D102, D149 and D205 in various imidazolium-based ionic liquid-polar aprotic molecular solvent mixtures. To conclude, we would like to summarize what we have discussed throughout this chapter. First, the composition dependence of the absorption maxima values of all three dyes show and overall red-shift while increasing X_{IL} and also a noticeable change in the mole fraction range 0 to 0.1 in the studied IL-γ-BL,PC mixtures, whereas it is not exactly true in case of IL-ACN mixtures. In addition, this typical red shift of absorption maxima is also correlated with the calculated values of the polarizability parameter in case of only available $BmimBF_4$, $BmimPF_6$-ACN mixtures.

In the case of composition emission maxima change, although a polarity dependent overall blue shift occurred while increasing the X_{IL} values, an initial red shift indicates the effect of interactions in the local environment of the dyes in case of all the studied IL-MS mixtures. Similar type of the presence of the maxima at lower X_{IL} region also suggests the effect of local environment on the values of the Stokes shift (ν_{Stokes}) of the studied dyes in the solvent mixtures. In addition, the non-linear Lippert-Mataga plots of D102, D149 and D205 in $BmimBF_4$-ACN mixture also indicates the presence of other specific interactions like hydrogen bonding and electron pair donor/acceptor interactions between the dye and the neighboring medium. Furthermore, the relative quantum yield (ϕ_{Relative}) values also show the presence of a clear minima at the similar mole fraction range, which is another proof of the presence of stronger interactions between the dye and surrounding medium especially at the lower X_{IL} region due to the presence of weaker cation-anion interactions in the similar mixture composition range.

Overall, all these steady state properties of the dyes in the IL-MS mixtures suggests the presence of specific interactions between the dye and neighboring medium in the lower X_{IL} region. From this, we might also expect the similar type of behavior in case of fluorescence lifetimes of these dyes in the solvent mixtures. The outcome from this chapter surely creates the baseline for the further study. Talking about further study, the more detailed study of the excited state dynamics as a result of the photo-excitation of the indoline dyes, will be discussed in the following chapter.

Bibliography

(1) Tyagi, H.; Agarwal, A. K.; Chakraborty, P. R.; Powar, S. Introduction to Advances in Solar Energy Research. In *Advances in Solar Energy*; 2019; Vol. 17, pp 3–11. https://doi.org/10.1007/978-981-13-3302-6_1.

(2) Lee, C.-L.; Lee, W.-H.; Yang, C.-H. High Efficiency of Dye-Sensitized Solar Cells Based on Ruthenium and Metal-Free Dyes. *Int. J. Photoenergy* **2013**, *2013*, 1–6. https://doi.org/10.1155/2013/250397.

(3) Kuang, D.; Uchida, S.; Humphry-Baker, R.; Zakeeruddin, S. M.; Grätzel, M. Organic Dye-Sensitized Ionic Liquid Based Solar Cells: Remarkable Enhancement in Performance through Molecular Design of Indoline Sensitizers. *Angew. Chemie* **2008**, *120* (10), 1949–1953. https://doi.org/10.1002/ange.200705225.

(4) Ito, S.; Miura, H.; Uchida, S.; Takata, M.; Sumioka, K.; Liska, P.; Comte, P.; Péchy, P.; Grätzel, M. High-Conversion-Efficiency Organic Dye-Sensitized Solar Cells with a Novel Indoline Dye. *Chem. Commun.* **2008**, No. 41, 5194. https://doi.org/10.1039/b809093a.

(5) Horiuchi, T.; Miura, H.; Uchida, S. Highly-Efficient Metal-Free Organic Dyes for Dye-Sensitized Solar Cells. *ChemInform* **2004**, *35* (15), 3036–3037. https://doi.org/10.1002/chin.200415171.

(6) El-Zohry, A. M.; Roca-Sanjuán, D.; Zietz, B. Ultrafast Twisting of the Indoline Donor Unit Utilized in Solar Cell Dyes: Experimental and Theoretical Studies. *J. Phys. Chem. C* **2015**, *119* (5), 2249–2259. https://doi.org/10.1021/jp505649s.

(7) El-Zohry, A. M.; Zietz, B. Concentration and Solvent Effects on the Excited State Dynamics of the Solar Cell Dye D149: The Special Role of Protons. *J. Phys. Chem. C* **2013**, *117* (13), 6544–6553. https://doi.org/10.1021/jp400782g.

(8) El-Zohry, A.; Orthaber, A.; Zietz, B. Isomerization and Aggregation of the Solar Cell Dye D149. *J. Phys. Chem. C* **2012**, *116* (50), 26144–26153. https://doi.org/10.1021/jp306636w.

(9) Fakis, M.; Stathatos, E.; Tsigaridas, G.; Giannetas, V.; Persephonis, P. Femtosecond Decay and Electron Transfer Dynamics of the Organic Sensitizer D149 and Photovoltaic Performance in Quasi-Solid-State Dye-Sensitized Solar Cells. *J. Phys. Chem. C* **2011**, *115* (27), 13429–13437. https://doi.org/10.1021/jp201143n.

(10) Lohse, P. W.; Kuhnt, J.; Druzhinin, S. I.; Scholz, M.; Ekimova, M.; Oekermann, T.; Lenzer, T.; Oum, K. Ultrafast Photoinduced Relaxation Dynamics of the Indoline Dye D149 in Organic Solvents. *Phys. Chem. Chem. Phys.* **2011**, *13* (43), 19632. https://doi.org/10.1039/c1cp22429h.

(11) Fakis, M.; Hrobárik, P.; Stathatos, E.; Giannetas, V.; Persephonis, P. A Time Resolved Fluorescence and Quantum Chemical Study of the Solar Cell Sensitizer D149. *Dye. Pigment.* **2013**, *96* (1), 304–312. https://doi.org/10.1016/j.dyepig.2012.07.025.

(12) Le Bahers, T.; Pauporté, T.; Scalmani, G.; Adamo, C.; Ciofini, I. A TD-DFT Investigation of Ground and Excited State Properties in Indoline Dyes Used for Dye-Sensitized Solar Cells. *Phys. Chem. Chem. Phys.* **2009**, *11* (47), 11276. https://doi.org/10.1039/b914626a.

(13) Lohse, P. W.; Bartels, N.; Stoppa, A.; Buchner, R.; Lenzer, T.; Oum, K. Dielectric Relaxation and Ultrafast Transient Absorption Spectroscopy of [C6mim]+[Tf2N]−/Acetonitrile Mixtures. *Phys. Chem. Chem. Phys.* **2012**, *14* (10), 3596. https://doi.org/10.1039/c2cp23704k.

(14) Andersson, P. O.; Gillbro, T.; Ferguson, L.; Cogdell, R. J. ABSORPTION SPECTRAL SHIFTS OF CAROTENOIDS RELATED TO MEDIUM POLARIZABILITY. *Photochem. Photobiol.* **1991**, *54* (3), 353–360. https://doi.org/10.1111/j.1751-1097.1991.tb02027.x.

(15) Chen, Z.; Lee, C.; Lenzer, T.; Oum, K. Solvent Effects on the S 0 (1A g -) → S 2 (1 1 B u +) Transition of β-Carotene, Echinenone, Canthaxanthin, and Astaxanthin in Supercritical CO 2 and CF 3 H. *J. Phys. Chem. A* **2006**, *110* (39), 11291–11297. https://doi.org/10.1021/jp0643247.

(16) Golibrzuch, K.; Ehlers, F.; Scholz, M.; Oswald, R.; Lenzer, T.; Oum, K.; Kim, H.; Koo, S. Ultrafast Excited State Dynamics and Spectroscopy of 13,13′-Diphenyl-β-Carotene. *Phys. Chem. Chem. Phys.* **2011**, *13* (13), 6340. https://doi.org/10.1039/c0cp02525a.

(17) Hudson, B. S.; Kohler, B. E. Polyene Spectroscopy: The Lowest Energy Excited Singlet State of Diphenyloctatetraene and Other Linear Polyenes. *J. Chem. Phys.* **1973**, *59* (9), 4984–5002. https://doi.org/10.1063/1.1680717.

(18) Lohse, P. W.; Bürsing, R.; Lenzer, T.; Oum, K. Exploring 12‘-Apo-β-Carotenoic-12‘-Acid as an Ultrafast Polarity Probe for Ionic Liquids. *J. Phys. Chem. B* **2008**, *112* (10), 3048–3057. https://doi.org/10.1021/jp710766z.

(19) Dentani, T.; Kubota, Y.; Funabiki, K.; Jin, J.; Yoshida, T.; Minoura, H.; Miura, H.; Matsui, M. Novel Thiophene-Conjugated Indolinedyes for Zinc Oxide Solar Cells. *New J. Chem.* **2009**, *33* (1), 93–101. https://doi.org/10.1039/B808959K.

(20) Zhao, Y.; Schultz, N. E.; Truhlar, D. G. Exchange-Correlation Functional with Broad Accuracy for Metallic and Nonmetallic Compounds, Kinetics, and Noncovalent Interactions. *J. Chem. Phys.* **2005**, *123* (16), 161103. https://doi.org/10.1063/1.2126975.

(21) Smortsova, Y. Thèse de Yevheniia Smortsova, Université de Lille, 2018. **2018**.

(22) Fukunishi, H.; Nakamura, S.; Fujieda, S. Influence of Conformation on the Absorption Spectra of Flexible Organic Dyes Used in Dye-Sensitized Solar Cells. *Comput. Theor. Chem.* **2013**, *1014*, 29–36. https://doi.org/10.1016/j.comptc.2013.03.021.

(23) El-Zohry, A.; Orthaber, A.; Zietz, B. Isomerization and Aggregation of the Solar Cell Dye D149. *J. Phys. Chem. C* **2012**, *116* (50), 26144–26153. https://doi.org/10.1021/jp306636w.

(24) Lohse, P. W.; Kuhnt, J.; Druzhinin, S. I.; Scholz, M.; Ekimova, M.; Oekermann, T.; Lenzer, T.; Oum, K. Ultrafast Photoinduced Relaxation Dynamics of the Indoline Dye D149 in Organic Solvents. *Phys. Chem. Chem. Phys.* **2011**, *13* (43), 19632–19640. https://doi.org/10.1039/c1cp22429h.

(25) Le Bahers, T.; Pauporté, T.; Scalmani, G.; Adamo, C.; Ciofini, I. A TD-DFT Investigation of Ground and Excited State Properties in Indoline Dyes Used for Dye-Sensitized Solar Cells. *Phys. Chem. Chem. Phys.* **2009**, *11* (47), 11276–11284. https://doi.org/10.1039/b914626a.

(26) Rohwer, E.; Richter, C.; Heming, N.; Strauch, K.; Litwinski, C.; Nyokong, T.; Schlettwein, D.; Schwoerer, H. Ultrafast Photodynamics of the Indoline Dye D149 Adsorbed to Porous ZnO in Dye-Sensitized Solar Cells. *ChemPhysChem* **2013**, *14* (1), 132–139. https://doi.org/10.1002/cphc.201200715.

(27) Sobuś, J.; Karolczak, J.; Komar, D.; Anta, J. A.; Ziółek, M. Transient States and the Role of Excited State Self-Quenching of Indoline Dyes in Complete Dye-Sensitized Solar Cells. *Dye. Pigment.* **2015**, *113*, 692–701. https://doi.org/10.1016/j.dyepig.2014.10.008.

(28) Baryshnikov, G. V.; Minaev, B. F.; Minaeva, V. A. Quantum-Chemical Study of the Structure and Optical Properties of Sensitized Dyes of an Indoline-Thiazolidine Series. *Opt. Spectrosc.* **2010**, *108* (1), 16–22. https://doi.org/10.1134/S0030400X10010042.

(29) El-Zohry, A. M.; Zietz, B. Concentration and Solvent Effects on the Excited State Dynamics of the Solar Cell Dye D149: The Special Role of Protons. *J. Phys. Chem. C* **2013**, *117* (13), 6544–6553. https://doi.org/10.1021/jp400782g.

(30) Wang, Z.-S.; Cui, Y.; Dan-oh, Y.; Kasada, C.; Shinpo, A.; Hara, K. Thiophene-Functionalized Coumarin Dye for Efficient Dye-Sensitized Solar Cells: Electron Lifetime Improved by Coadsorption of Deoxycholic Acid. *J. Phys. Chem. C* **2007**, *111* (19), 7224–7230. https://doi.org/10.1021/jp067872t.

(31) Selvaraj, A. R. K.; Hayase, S. Molecular Dynamics Simulations on the Aggregation Behavior of Indole Type Organic Dye Molecules in Dye-Sensitized Solar Cells. *J. Mol. Model.* **2012**, *18* (5), 2099–2104. https://doi.org/10.1007/s00894-011-1230-1.

(32) Srinivasa Krishna, T.; Nain, A. K.; Chentilnath, S.; Punyaseshudu, D.; Munibhadrayya, B. Densities, Ultrasonic Speeds, Refractive Indices, Excess and Partial Molar Properties of Binary Mixtures of Imidazolium Based Ionic Liquid with Pyrrolidin-2-One at Temperatures from 298.15 L to 323.15 K. *J. Chem. Thermodyn.* **2016**, *101*, 103–114. https://doi.org/10.1016/j.jct.2016.05.021.

(33) Carissimi, G.; Montalbán, M. G.; Díaz Banos, F. G.; Víllora, G. Density, Refractive Index and Volumetric Properties of Water-Ionic Liquid Binary Systems with Imidazolium-Based Cations and Tetrafluoroborate, Triflate and Octylsulfate Anions at T = 293 to 343 K and p = 0.1 MPa. *J. Chem. Eng. Data* **2019**, *64* (3), 979–994. https://doi.org/10.1021/acs.jced.8b00854.

(34) Zafarani-Moattar, M. T.; Majdan-Cegincara, R. Viscosity, Density, Speed of Sound, and Refractive Index of Binary Mixtures of Organic Solvent + Ionic Liquid, 1-Butyl-3-Methylimidazolium Hexafluorophosphate at 298.15 K. *J. Chem. Eng. Data* **2007**, *52* (6), 2359–2364. https://doi.org/10.1021/je700338t.

(35) Zhu, A.; Wang, J.; Han, L.; Fan, M. Measurements and Correlation of Viscosities and Conductivities for the Mixtures of Imidazolium Ionic Liquids with Molecular Solutes. *Chem. Eng. J.* **2009**, *147* (1), 27–35. https://doi.org/10.1016/j.cej.2008.11.013.

(36) Rizzuto, A. M.; Pennington, R. L.; Sienerth, K. D. Study of the BMIM-PF6: Acetonitrile Binary Mixture as a Solvent for Electrochemical Studies Involving CO2. *Electrochim. Acta* **2011**, *56* (14), 5003–5009. https://doi.org/10.1016/j.electacta.2011.03.106.

(37) Canongia Lopes, J. N.; Costa Gomes, M. F.; Husson, P.; Pádua, A. A. H.; Rebelo, L. P. N.; Sarraute, S.; Tariq, M. Polarity, Viscosity, and Ionic Conductivity of Liquid Mixtures Containing [C 4 C 1 Im][Ntf 2] and a Molecular Component. *J. Phys. Chem. B* **2011**, *115* (19), 6088–6099. https://doi.org/10.1021/jp2012254.

(38) Vraneš, M.; Zec, N.; Tot, A.; Papović, S.; Dožić, S.; Gadžurić, S. Density, Electrical Conductivity, Viscosity and Excess Properties of 1-Butyl-3-Methylimidazolium Bis(Trifluoromethylsulfonyl)Imide+propylene Carbonate Binary Mixtures. *J. Chem. Thermodyn.* **2014**, *68*, 98–108. https://doi.org/10.1016/j.jct.2013.08.034.

(39) Stoppa, A.; Hunger, J.; Hefter, G.; Buchner, R. Structure and Dynamics of 1- N -Alkyl-3- N -Methylimidazolium Tetrafluoroborate + Acetonitrile Mixtures. *J. Phys. Chem. B* **2012**, *116* (25), 7509–7521. https://doi.org/10.1021/jp3020673.

(40) Wang, J.; Tian, Y.; Zhao, Y.; Zhuo, K. A Volumetric and Viscosity Study for the Mixtures of 1-n-Butyl-3-Methylimidazolium Tetrafluoroborate Ionic Liquid with Acetonitrile, Dichloromethane, 2-Butanone and N, N ? Dimethylformamide. *Green Chem.* **2003**, *5* (5), 618. https://doi.org/10.1039/b303735e.

(41) Li, W.; Zhang, Z.; Han, B.; Hu, S.; Xie, Y.; Yang, G. Effect of Water and Organic Solvents on the Ionic Dissociation of Ionic Liquids. *J. Phys. Chem. B* **2007**, *111* (23), 6452–6456. https://doi.org/10.1021/jp071051m.

(42) Stoppa, A.; Hunger, J.; Buchner, R. Conductivities of Binary Mixtures of Ionic Liquids with Polar Solvents. *J. Chem. Eng. Data* **2009**, *54* (2), 472–479. https://doi.org/10.1021/je800468h.

(43) Khupse, N. D.; Kumar, A. Dramatic Change in Viscosities of Pure Ionic Liquids upon Addition of Molecular Solvents. *J. Solution Chem.* **2009**, *38* (5), 589–600. https://doi.org/10.1007/s10953-009-9390-7.

(44) Tariq, M.; Forte, P. A. S.; Gomes, M. F. C.; Lopes, J. N. C.; Rebelo, L. P. N. Densities and Refractive Indices of Imidazolium- and Phosphonium-Based Ionic Liquids: Effect of Temperature, Alkyl Chain Length, and Anion. *J. Chem. Thermodyn.* **2009**, *41* (6), 790–798. https://doi.org/10.1016/j.jct.2009.01.012.

(45) Wakai, C.; Oleinikova, A.; Weingärtner, H. Reply to "Comment On 'How Polar Are Ionic Liquids? Determination of the Static Dielectric Constant of an Imidazolium-Based Ionic Liquid by Microwave Spectroscopy'"". *J. Phys. Chem. B* **2006**, *110* (11), 5824–5824. https://doi.org/10.1021/jp0601973.

(46) Reichardt, C. Solvatochromic Dyes as Solvent Polarity Indicators. *Chem. Rev.* **1994**, *94* (8), 2319–2358. https://doi.org/10.1021/cr00032a005.

(47) Poole, C. F. Chromatographic and Spectroscopic Methods for the Determination of Solvent Properties of Room Temperature Ionic Liquids. *J. Chromatogr. A* **2004**, *1037* (1–2), 49–82. https://doi.org/10.1016/j.chroma.2003.10.127.

(48) Lee, J.-M.; Ruckes, S.; Prausnitz, J. M. Solvent Polarities and Kamlet−Taft Parameters for Ionic Liquids Containing a Pyridinium Cation. *J. Phys. Chem. B* **2008**, *112* (5), 1473–1476. https://doi.org/10.1021/jp076895k.

(49) Mancini, P. M.; Fortunato, G. G.; Adam, C. G.; Vottero, L. R. Solvent Effects on Chemical Processes: New Solvents Designed on the Basis of the Molecular–microscopic Properties of (Molecular Solvent + 1,3-Dialkylimidazolium) Binary Mixtures. *J. Phys. Org. Chem.* **2008**, *21* (2), 87–95. https://doi.org/10.1002/poc.1227.

(50) Le Bahers, T.; Pauporté, T.; Scalmani, G.; Adamo, C.; Ciofini, I. A TD-DFT Investigation of Ground and Excited State Properties in Indoline Dyes Used for Dye-Sensitized Solar Cells. *Phys. Chem. Chem. Phys.* **2009**, *11* (47), 11276. https://doi.org/10.1039/b914626a.

(51) Lohse, P. W.; Kuhnt, J.; Druzhinin, S. I.; Scholz, M.; Ekimova, M.; Oekermann, T.; Lenzer, T.; Oum, K. Ultrafast Photoinduced Relaxation Dynamics of the Indoline Dye D149 in Organic Solvents. *Phys. Chem. Chem. Phys.* **2011**, *13* (43), 19632. https://doi.org/10.1039/c1cp22429h.

(52) Fakis, M.; Stathatos, E.; Tsigaridas, G.; Giannetas, V.; Persephonis, P. Femtosecond Decay and Electron Transfer Dynamics of the Organic Sensitizer D149 and Photovoltaic Performance in Quasi-Solid-State Dye-Sensitized Solar Cells. *J. Phys. Chem. C* **2011**, *115* (27), 13429–13437. https://doi.org/10.1021/jp201143n.

(53) Koverga, V. A.; Smortsova, Y.; Miannay, F. A.; Kalugin, O. N.; Takamuku, T.; Jedlovszky, P.; Marekha, B.; Cordeiro, M. N. D. S.; Idrissi, A. Distance Angle Descriptors of the Interionic and Ion–Solvent Interactions in Imidazolium-Based Ionic Liquid Mixtures with Aprotic Solvents: A Molecular Dynamics Simulation Study. *J. Phys. Chem. B* **2019**, *123* (28), 6065–6075. https://doi.org/10.1021/acs.jpcb.9b03838.

(54) Nordness, O.; Brennecke, J. F. Ion Dissociation in Ionic Liquids and Ionic Liquid Solutions. *Chem. Rev.* **2020**, *120* (23), 12873–12902. https://doi.org/10.1021/acs.chemrev.0c00373.

(55) Lee, B.-S.; Lin, S.-T. The Origin of Ion-Pairing and Redissociation of Ionic Liquid. *J. Phys. Chem. B* **2017**, *121* (23), 5818–5823. https://doi.org/10.1021/acs.jpcb.7b01189.

(56) Stoppa, A.; Hunger, J.; Buchner, R. Conductivities of Binary Mixtures of Ionic Liquids with Polar Solvents. *J. Chem. Eng. Data* **2009**, *54* (2), 472–479. https://doi.org/10.1021/je800468h.

(57) Schröer, W.; Weingärtner, H. Structure and Criticality of Ionic Fluids. *Pure Appl. Chem.* **2004**, *76* (1), 19–27. https://doi.org/10.1351/pac200476010019.

(58) Boruń, A. Conductance and Ionic Association of Selected Imidazolium Ionic Liquids in Various Solvents: A Review. *J. Mol. Liq.* **2019**, *276*, 214–224. https://doi.org/10.1016/j.molliq.2018.11.140.

(59) Zhu, G.; Zhang, L.; Wang, Y.; Xu, X.; Peng, X. Interactions between Pyrene and Pyridinium Ionic Liquids Studied by Ultraviolet–visible Spectroscopy. *J. Mol. Liq.* **2016**, *213*, 289–293. https://doi.org/10.1016/j.molliq.2015.11.026.

(60) Carrete, J.; Méndez-Morales, T.; Cabeza, Ó.; Lynden-Bell, R. M.; Gallego, L. J.; Varela, L. M. Investigation of the Local Structure of Mixtures of an Ionic Liquid with Polar Molecular Species through Molecular Dynamics: Cluster Formation and Angular Distributions. *J. Phys. Chem. B* **2012**, *116* (20), 5941–5950. https://doi.org/10.1021/jp301309s.

(61) Golibrzuch, K.; Ehlers, F.; Scholz, M.; Oswald, R.; Lenzer, T.; Oum, K.; Kim, H.; Koo, S. Ultrafast Excited State Dynamics and Spectroscopy of 13,13′-Diphenyl- β-Carotene. *Phys. Chem. Chem. Phys.* **2011**, *13* (13), 6340–6351. https://doi.org/10.1039/c0cp02525a.

(62) Lohse, P. W.; Bartels, N.; Stoppa, A.; Buchner, R.; Lenzer, T.; Oum, K. Dielectric Relaxation and Ultrafast Transient Absorption Spectroscopy of [C6mim]+[Tf2N]−/Acetonitrile Mixtures. *Phys. Chem. Chem. Phys.* **2012**, *14* (10), 3596. https://doi.org/10.1039/c2cp23704k.

(63) Mialkowski, C.; Chagnes, A.; Carré, B.; Lemordant, D.; Willmann, P. Excess Thermodynamic Properties of Binary Liquid Mixtures Containing Dimethylcarbonate and γ-Butyrolactone. *J. Chem. Thermodyn.* **2002**, *34* (11), 1847–1856. https://doi.org/10.1016/S0021-9614(02)00232-X.

(64) Weingärtner, H. The Static Dielectric Constant of Ionic Liquids. *Zeitschrift für Phys. Chemie* **2006**, *220* (10), 1395–1405. https://doi.org/10.1524/zpch.2006.220.10.1395.

(65) Barthel, J.; Neueder, R.; Roch, H. Density, Relative Permittivity, and Viscosity of Propylene Carbonate+dimethoxyethane Mixtures from 25 °C to 125 °C. *J. Chem. Eng. Data* **2000**, *45* (6), 1007–1011. https://doi.org/10.1021/je000098x.

(66) Eaborn, C. Compendium of Chemical Terminology: IUPAC Recommendations. *J. Organomet. Chem.* **1988**, *356* (2), C76–C77. https://doi.org/10.1016/0022-328X(88)83113-9.

(67) Kasha, M. Characterization of Electronic Transitions in Complex Molecules. *Discuss. Faraday Soc.* **1950**, *9*, 14. https://doi.org/10.1039/df9500900014.

(68) G.G.Stokes. XXX. On the Change of Refrangibility of Light. *Philos. Trans. R. Soc. London* **1852**, *142* (June 1848), 463–562. https://doi.org/10.1098/rstl.1852.0022.

(69) Lippert, E. Spektroskopische Bestimmung Des Dipolmomentes Aromatischer Verbindungen Im Ersten Angeregten Singulettzustand. *Zeitschrift für Elektrochemie, Berichte der Bunsengesellschaft für Phys. Chemie* **1957**, *61* (8), 962–975. https://doi.org/10.1002/bbpc.19570610819.

(70) Mataga, N.; Kaifu, Y.; Koizumi, M. Solvent Effects upon Fluorescence Spectra and the Dipolemoments of Excited Molecules. *Bull. Chem. Soc. Jpn.* **1956**, *29* (4), 465–470. https://doi.org/10.1246/bcsj.29.465.

(71) Maity, N.; Piatkowski, P.; Polok, K.; Miannay, F.-A.; Idrissi, A. Effect of the Mixture Composition of BmimBF 4 –Acetonitrile on the Excited-State Relaxation Dynamics of a Solar-Cell Dye D149: An Ultrafast Transient Absorption Study. *J. Phys. Chem. C* **2021**, *125* (32), 17841–17852. https://doi.org/10.1021/acs.jpcc.1c05008.

(72) El-Zohry, A. M.; Roca-Sanjuán, D.; Zietz, B. Ultrafast Twisting of the Indoline Donor Unit

Utilized in Solar Cell Dyes: Experimental and Theoretical Studies. *J. Phys. Chem. C* **2015**, *119* (5), 2249–2259. https://doi.org/10.1021/jp505649s.

(73) Wang, H.; Liu, S.; Wang, N.; Liu, Y. Vinylene Carbonate Modified 1-Butyl-3-Methyle-Imidazolium Tetrafluoroborate Ionic Liquid Mixture as Electrolyte. *Int. J. Electrochem. Sci.* **2012**, *7* (8), 7579–7586.

(74) Uesaka, T.; Ishitani, T.; Sawada, R.; Maeda, T.; Yagi, S. Fluorescent 2-Phenyl-2H-Benzotriazole Dyes with Intramolecular N–H···N Hydrogen Bonding: Synthesis and Modulation of Fluorescence Properties by Proton-Donating Substituents. *Dye. Pigment.* **2020**, *183* (March), 108672. https://doi.org/10.1016/j.dyepig.2020.108672.

(75) Yu, B.; Liu, D.; Zhang, J.; Li, Z.; Zhang, Y.-M.; Li, M.; Zhang, S. X.-A. Emissions and the Application of a Series of Twisted Fluorophores with Intramolecular Weak Hydrogen Bonds. *RSC Adv.* **2019**, *9* (23), 13214–13219. https://doi.org/10.1039/C9RA01244C.

(76) Kijak, M.; Petkova, I.; Toczek, M.; Wiosna-Sałyga, G.; Zielińska, A.; Herbich, J.; Thummel, R. P.; Waluk, J. Conformation-Dependent Photophysics of Bifunctional Hydrogen Bond Donor/Acceptor Molecules. *Acta Phys. Pol. A* **2007**, *112* (Supplement), S-105-S-120. https://doi.org/10.12693/APhysPolA.112.S-105.

(77) Kielesiński, Ł.; Gryko, D. T.; Sobolewski, A. L.; Morawski, O. W. Effect of Conformational Flexibility on Photophysics of Bis-Coumarins. *Phys. Chem. Chem. Phys.* **2018**, *20* (21), 14491–14503. https://doi.org/10.1039/C8CP01084F.

(78) Dahiya, P.; Kumbhakar, M.; Maity, D. K.; Mukherjee, T.; Tripathi, A. B. R.; Chattopadhyay, N.; Pal, H. Solvent Polarity and Intramolecular Hydrogen Bonding Effects on the Photophysical Properties of 1-Amino-9,10-Anthraquinone Dye. *J. Photochem. Photobiol. A Chem.* **2006**, *181* (2–3), 338–347. https://doi.org/10.1016/j.jphotochem.2005.12.016.

Chapter 2

Characterization of the Excited State Dynamics of Indoline dyes in Imidazolium Ionic Liquid-Molecular Solvent mixtures: Study using Transient Absorption Spectroscopy

This chapter is the basis of the paper titled-

Effect of the Mixture Composition of $BmimBF_4$–Acetonitrile on the Excited-State Relaxation Dynamics of a Solar-Cell Dye D149: An Ultrafast Transient Absorption Study

Nishith Maity, Piotr Piatkowski, Kamil Polok, François-Alexandre Miannay, and Abdenacer Idrissi
The Journal of Physical Chemistry C 2021 *125* (32), 17841-17852

In this chapter, we are going to discuss about the study of the excited state relaxation dynamics of three metal-free substituted indoline dyes D102, D149 and D205 in whole mixture composition range of various IL-MS mixtures containing four different imidazolium-based ionic liquids (ILs) and three different polar aprotic molecular solvents (MSs) binary mixtures using femtosecond transient absorption (TA) spectroscopy. We have already discussed about the steady state properties of these dyes in previous chapter. Here we will discuss about their excited state relaxation dynamics after the excitation to their first excited state using a femtosecond pump pulse. The global analysis of the TA spectra reveals us about the presence of four different time components in the relaxation process of all three dyes in all the studied IL-MS mixtures. First, we have discussed about the origin of these four timescales in the mixtures as well as in the pure components. Then, we have described the composition, polarity and viscosity dependence of these four timescales. The viscosity and polarity dependence of these four relaxation time components indicates the importance of local structures of the surrounding medium in describing the behavior of these four timescales. Furthermore, in case of the composition dependence of the longest global analysis timescale, related to the emission lifetime of the dye, there exist minima at lower X_{IL} region (X_{IL}=0.05-0.10) of the mixtures, which can be an indication of the presence of stronger interactions between the dye and the neighboring medium due to the weaker cation-anion interactions in ILs especially at the lower X_{IL} region. The modulation of the preferential interactions between the ions, ion-solvent and ion-dye interactions play an important role in describing the composition dependent change of emission lifetime of the dyes. This typical behavior of the excited state of the dyes can be correlated to the steady state emission, Stokes shift and also relative quantum yield of the dyes which was described in previous chapter.

2.1. Introduction:

As we have discussed the steady state properties of the organic solar cell dyes in the previous chapter, we are now going to study the excited state dynamics of these dyes in various IL-MS mixtures to get further idea about the photophysics of the excited state.

To start with, there are mainly two important components of DSSC cell, electrolyte and the photosensitizer. ILs are used nowadays as electrolytes due to some advantageous properties of them. Indeed, in recent years, we have seen a rise of interest in the research on ILs.[1,2,11–16,3–10] Due to some very interesting properties of ILs like non-flammability, negligible vapor pressure, large electrochemical potential window, high thermal stability, high electrical conductivity etc., they are quite useful in various types of chemical and biological applications.[17–25] In particular, the family of 1-alkyl-3-methylimdazolium (C_4mim^+) cation combined with perfluorinated anions (PF_6^-, BF_4^-, $CF_3SO_3^-$, $(CF_3SO_2)_2N^-$) are mainly used in various electrochemical devices such as supercapacitors or electrochemical actuators due to their high electrical conductivity.[2,10,26–29] Moreover, they also have many other applications.[30,31,40–42,32–39] However, the high viscosity of ILs alongside high purification cost can causes a hindrance to their applications. The viscosity can be reduced to only one order of magnitude by varying the temperature.[43] Therefore, the problem regarding the high viscosity of ILs can be solved by mixing the ILs with low-viscous MSs, which leads to an almost exponential decay of the viscosity as a function of molar fraction of the IL (X_{IL}).[44–46] this decrease of viscosity helps to improve the electrical conductivity of the resulting IL-MS mixtures. Therefore, various polar aprotic solvents like acetonitrile (ACN), γ-butyrolactone (γ-BL) and propylene carbonate (PC) can be a reasonable choice as MSs for mixing with the ILs. In particular, in the field of electrochemical applications,[47–49] these polar aprotic solvents also possess several advantageous properties like wide electrochemical window, relatively high dielectric constant and low viscosity for which they can be easily dissolved in the ILs. Moreover, wide temperature range of the liquid state, nontoxicity along with environmental friendliness of cyclic organic esters and carbonates (like γ-BL and PC) are the reasons behind their usage as electrolytes media in many electrochemical devices.

In general, mixing molecular solvents with ILs changes the overall microscopic structures because of the presence of composition dependent interactions between the mixture components. While ion-ion interactions are more prominent in case of ILs, dipole-dipole interactions are dominant in case of the polar aprotic MSs. Therefore, depending upon the tendency of the pure components to give up their intrinsic interaction patterns to help the solvation process, one can expect the presence of different concentration regime over the whole composition range in a typical IL-MS mixture.[50] Therefore, it is important to analyze the IL-MS mixtures based on different microscopic interactions between the mixture components to predict their different macroscopic properties. The composition dependent spectroscopic and physicochemical data of IL-MS can be summarized as follow. From pure IL to pure MS, a composition dependent characteristic red shift of C-H vibration mode was noticed in case of some IL-MS mixtures, like $BmimBF_4$-DMSO, EmimTFSI-PEO, and $BmimPF_6/BF_4$-PEO,[51–55]

while no apparent shift can be observed in some of the them, like $C_n$mimBF_4-H_2O, EmimTFSI-MeOH, RmimBF_4-EG etc.[52,56–63] Similar behavior of ^{1}H chemical shift can also be noticed in various IL-MS mixtures.[59,64,73–81,65–72] In particular, the corresponding values of the C-H vibration mode and the double difference of the ^{1}H chemical shift values are relatively unaffected in the X_{IL} range between 1.0 and 0.3 in those studies. However, with further decrease of X_{IL}, large changes are observed in the case of both spectroscopic parameters. This typical behavior of the spectroscopic data can also be correlated to the composition dependence of static dielectric constant values in BmimBF_4-ACN mixture.[82] These changes are compatible with the physical picture that the solvent molecules compete with the anions to occupy positions close to the cation ring hydrogen atoms. The presence of two competitive interactions, ion-ion and ion-solvent interactions, in the IL-MS mixture make the interactions between the cations and anions in ILs weaker. In fact, at a specific low mole fraction of a particular IL-MS mixture, a crossover between the average distance between the cation and anion and between the solvent and the ion indicates that the solvent molecules can dissociate the cation-anion interactions in the ILs at a certain dilution.[83]

Another important component of the DSSC cell is the photosensitizer. The sunlight helps the dye/sensitizer molecule to reach its excited state and from there the other reactions in the cell initiates. Therefore, the excited state of the dye is mainly involved in the DSSC cell reactions and we have to characterize their exited state relaxation dynamics. Many studies have been performed in this matter.[84–90] In particular, the excited state relaxation dynamics of the dye D149 was very extensively studied in recent years. For instance, Fakis et al., Lohse et al. had studied the excited state dynamics of indoline dye D149 in various organic solvents with different polarity, viscosity and H-bond formation ability. Fakis et al. used femtosecond up-conversion spectroscopy to study the excited state dynamics of D149 dye in various organic solvents and also on TiO_2, Al_2O_3 and in PMMA films.[84,85] Lohse et al. used femtosecond pump-supercontinuum probe (PSCP) spectroscopy and time correlated single photon counting (TCSPC) to study the photophysics of D149 also in various organic solvents.[86] El-Zohry et al. had also published a few articles related to the excited state of the dye D149. All of these reports together give an overall idea about the present excited state processes in the D149 dye like photo-isomerization and aggregation,[87] excited state proton transfer (ESPT)[88] and ultrafast twisting in D149 donor moiety.[90] Furthermore, Lin et al. had also showed the effect of the presence of isomerization process in the sensitizer on the efficiency of the cell.[89] Overall, all these processes which are competitive to the radiative relaxation lifetime of the dye excited state result in decrease in the efficiency of the solar cell. The authors also suggested that, these non-radiative competitive processes of the dye can be overcome by using some methods like attaching the dye to a semiconductor oxide electrode[87] and introducing quasi-solid[84] and solid[87] states as the medium surrounding the dye molecules. However, in case of other indoline dyes like D102, D131, D205 etc., the number of reports about their excited states are quite small.[91–95] In addition, in most of the studies, the conventional organic polar and non-polar solvents were used as the local environments of the dye.

These previous studies about the excited state dynamics of D149 in various solvents also indicated the presence of four different relaxation timescales among which two faster ones are related to solvation dynamics.[84–87,90] In addition, the slowest one was previously attributed

to S_1-S_0 decay of the dye molecule.[84,86,90] This slow S_1-S_0 decay time of the dye also depends on the polarity of the surrounding medium.[84,86] However, two different ideas are present about the origin of the third and moderately longer timescale. Fakis et al.[84] and Lohse et al.[86] had attributed this timescale to the vibrational relaxation/structural relaxation of the dye excited state, whereas El-Zohry et al.[90] suggested that this fast relaxation timescale is due to a twisting motion around the double bond in the donor unit of the dye.

As the two faster relaxation timescales of the dye are related to the solvation process, one need to study the solvation dynamics more thoroughly. In this regard, there are few studies present where the solvation dynamics in ILs were rationalized using Coumarin 153 (C153) as a model dye.[96–101] The interpretations regarding the two solvation dynamics timescales are following. While the faster sub-picosecond relaxation time is related to the inertial motions of the solvent and ions, the slower one is originated from the structural reorganization of the ions surrounding the dye molecule.[96–101] In addition, the solvation dynamics in ILs is much slower compared to that in common solvents such as acetonitrile, methanol, and water, which can be described considering very high viscosity of ILs compared to conventional solvents. As an example, the solvation dynamics of C153 in $BmimBF_4$ showed that the overall solvation process has two time constants of 278 ps and 3.98 ns.[102] Maroncelli et al. had also showed that the solvation times of C153 display an approximate power law relationship with viscosity in case of $BmimBF_4$-ACN solvent mixture.[101,103] Furthermore, According to a review by Samanta, solvation process in ionic liquids is not similar to that in organic solvents. While the dipole-dipole interactions are dominant in the case of pure organic solvents, the interactions between charged groups of the ions and polar molecules of solute play the major role in the solvation process in ionic liquid.[96]

As it was pointed out above, most of the studies about the excited state dynamics of the dyes are carried out when they are dissolved in conventional organic solvents which are chosen to mimic different polar and non-polar environmental conditions of the dye. To our best knowledge, there are very few reports where the photophysics of the dye dissolved in a IL-MS mixtures were studied.[104–107] Therefore, the goal of this chapter is to fill the gap and provide a systematic study of three indoline-based dyes namely, the D102, D149 and D205 dissolved in various IL-MS mixtures where IL represents four different 1-butyl-3-methylimdazolium ILs with four different perfluorinated anions and MS represents three polar aprotic molecular solvents, such as acetonitrile (ACN), γ-butyrolactone (γ-BL), and propylene carbonate (PC). In case of each of these three studied dyes, twelve sets of IL-MS mixtures, each containing five intermediate compositions in addition to seven pure components were used. The ultimate goal was to get an overall idea about the excited state dynamics of the three indoline dyes dissolved in various intermediate compositions of the IL-MS mixtures. In the previous studies, different solvents with different properties like polarity, viscosity, hydrogen bonding ability etc. were used to study the excited state relaxation dynamics of the dye molecule. However, here we are using different intermediate compositions of IL-MS mixtures with varying solvent mixture properties and interactions (ion-ion, ion-solvent and solute-solvent) as the surrounding medium of the dye molecule. This also suggests that, the physicochemical properties of the pure components of the mixtures remain similar yet they are regulated by the change of the mixture composition. We have used femtosecond transient absorption (TA) spectroscopic technique to

study the excited state dynamics of the dyes in these systems. It is also noteworthy that, this type of study of the excited relaxation dynamics of these organic dyes in the chosen IL-MS mixtures is considered as the initial stage of research related to DSSC before exploring their exited state relaxation dynamics at the interface of an electrode.[108–111]

This chapter consists of these different sections. First, we will take a short look on the used chemicals, experimental setups and data analysis methods. Then, we will present and analyze the experimental results which will eventually leads us to our final conclusions from this study.

2.2. Experimental Section:

2.2.1. Chemicals:

All the details about the dyes and ionic liquids were already described in the previous chapter (Chapter 1, section 1.2).

2.2.2. TA setup and data analysis:

The scheme of transient absorption setup with the description is discussed in the experimental techniques chapter (Chapter 5, section 5.1).

2.3. Results and Discussions:

2.3.1. Time dependent spectral changes of TAS:

In this section, all the time dependent changes of the experimental TAS are going to be discussed. As the general characteristics of the femtosecond TA spectra of the three indoline dyes are used for our study are very similar, the discussion in this section is going to be concentrated only on one of the three used dyes D102. The TA spectra of other two dyes (D149 and D205) in the IL-MS mixtures are shown in the Appendix (Figures B3, B4, B6, B7 and B27-B66). In case of D102, the overall TA spectra are also divided into three different sub-sections where each of them contains the time dependent spectral changes of TAS at a particular mole fraction (X_{IL}=0.10) of $BmimPF_6$-ACN, $BmimPF_6$-γ-BL and $BmimPF_6$-PC mixtures. As the overall spectral changes are disentangled into time and composition dependent changes, we have only chosen one particular mole fraction (X_{IL}=0.10) of the mixture to show only the time dependent changes. However, the figures of the time dependency of the TAS of D102 in case of other compositions of the IL-MS mixtures are also shown in the Appendix (Figures B2, B5 and B8-B26).

In Figure 2.1, all the time dependent TAS of D102 in $BmimPF_6$-ACN/γ-BL/PC mixtures are shown respectively and each of them is divided into few subfigures for better and easier discussion.

The faster timescale TAS spectra can be divided into two different wavelength regions. In the shorter wavelength region of the Figures 2.1 [(A), (B), (C)], a negative ground state bleach (GSB) band emerges and starts to increase initially with the increase of time delay. This negative GSB is mainly due to depopulation of the ground state (S_0) of the dye. The spectral overlap between the GSB band and steady state absorption spectra (black dotted one in each

subfigures) also supports the fact that the former one is due to ground state absorption of the dye. After a few hundred femtoseconds (fs), this GSB band intensity starts to decrease due to ground state recovery of the dye molecule. Additionally, a positive excited state absorption (ESA) band appears in the first few fs in the longer wavelength region of the TA spectra. Due to a few fs delayed arrival of negative stimulated emission (SE) band, we can finally notice three distinct wavelength regions (480-530 nm GSB, 530-630 nm ESA and 630-750 nm SE respectively) within 1 picosecond (ps) of time delay between probe and pump pulse in the case of $BmimPF_6$-ACN mixture [Figure 2.1(A)]. However, these three distinct wavelength regions are not clearly formed within 1 ps delay time in case of other two IL-MS mixtures containing γ-BL and PC mixtures [Figures 2.1(B) and 2.1(C)].

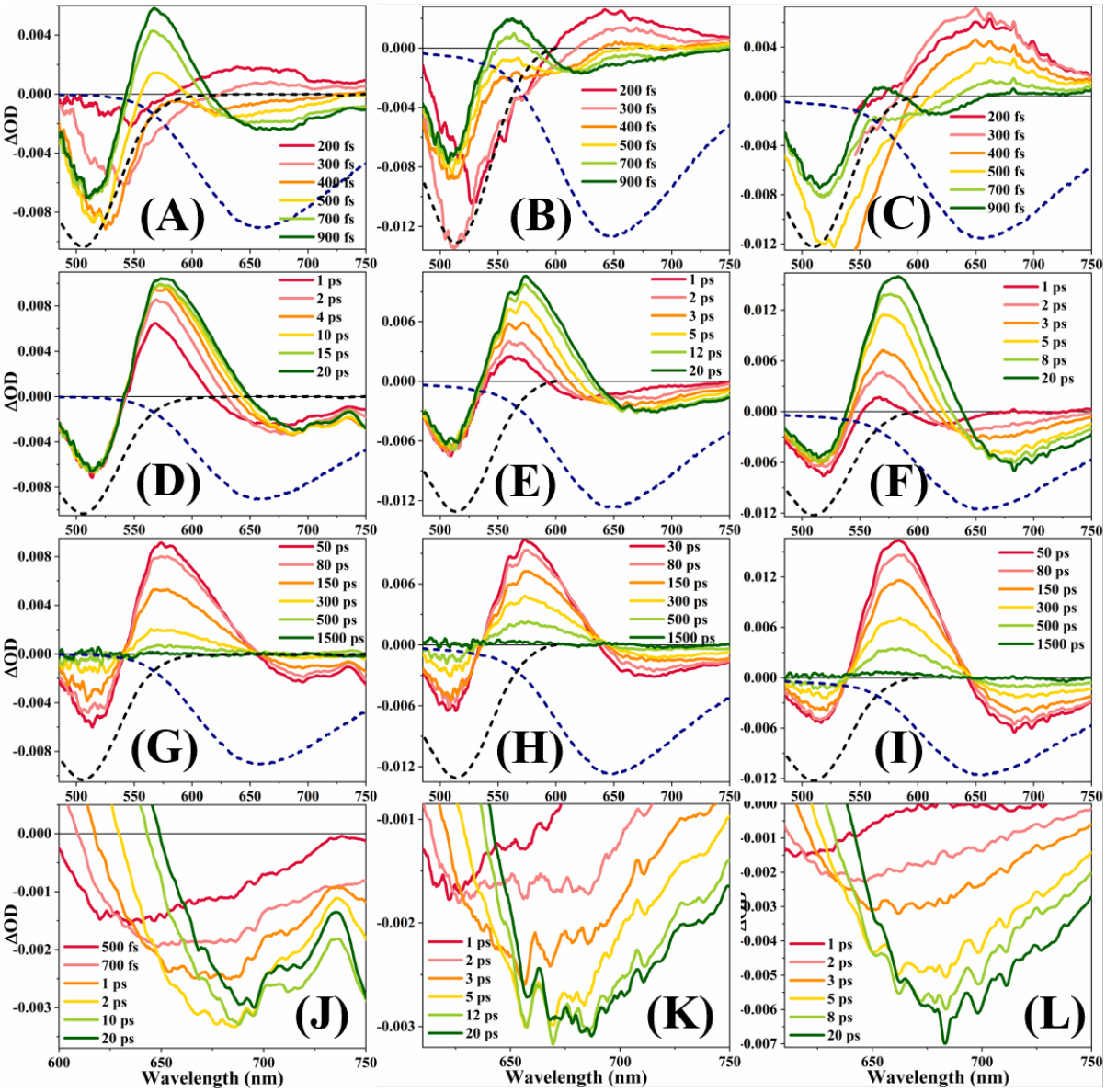

Figure 2.1: Transient Absorption spectra of D102 in $BmimPF_6$–ACN [(A), (D), (G), (J)], in $BmimPF_6$-γ-BL [(B), (E), (H), (K)] and in $BmimPF_6$-PC [(C), (F), (I), (L)] mixtures (X_{IL}= 0.10). [(A), (B), (C)] short timescale (200-900 fs), [(D), (E), (F)] middle timescale (1-20 ps), [(G), (H), (I)] long timescale (50-1500 ps) and [(J), (K), (L)] solvation timescale. Dashed spectra are steady state absorption (black) and emission (blue) spectra.

In Figure 2.1(D), the negative GSB band doesn't show any significant change in this time region, whereas a small GSB intensity decrease happened in both $BmimPF_6$-γ-BL/PC mixtures due to continuation of ground state recovery process of the dye (Figures 2.1(E) and 2.1(F)). However, positive ESA shows a gradual increase in all three IL-MS mixtures (Figures 2.1[(D), (E), (F)]) and it is mainly due to the geometric relaxation of the excited state of the dye *(vide infra)*. In addition, a clear negative SE band is also observed at higher wavelength region in $BmimPF_6$-ACN mixture (Figure 2.1(D)), whereas distinct SE band can only be noticed in the other two IL-MS mixtures after ~2 ps delay time (Figures 2.1(E) and 2.1(F)). The origin of this negative signal is nothing but stimulated emission (SE) of the excited state (S_1) of the dye. Furthermore, the typical spectral overlap between the negative SE bands and the steady state emission also solidifies the same fact. The negative SE peaks show a gradual red shift with the increase of time in this time delay range (1-20 ps). This can be described in two ways. Firstly, a gradual red shift of SE bands while ESA intensity remains almost same with time and then it can be described as a solvent relaxation process. Secondly, the increase of ESA intensity while SE band position remains almost similar with time and then it can be described due to structural/vibrational relaxation of the dye molecule (Figure B1, Appendix B). Noticing the changes happening in our study [Figures 2.1((J),(K),(L))], both solvent relaxation and vibrational/structural relaxation of the dye can be regarded as the possible explanations in the case of our studied dyes in the IL-MS mixtures.

Finally, an overall decrease of TA signal in the whole spectral region is observed (Figures 2.1[(G), (H), (I)]) which is due to the excited state relaxation to the ground state (S_1-S_0 transition) with corresponding time constants. This is also supported by previous studies (*vide infra*).[87,105,112–114]

Overall, after this discussion related to the time dependent TAS, we can certainly generalize the time dependent spectral changes in case of all the other samples (Figures B2-B66). However, there is a slight difference among all these TAS figures, which is mainly related to the rate of the increase of TA signals in the ESA region and decrease in SE region at the middle timescales (Figures 2.1, and B2-B26), which are different for different samples even while using a particular dye like D102. This certainly indicates the fact that, the excited state processes of the dyes are dependable on the properties of surrounding medium. This similar type of difference in the rate of the TA signal increase/decrease mainly in the ESA and SE regions at middle timescales can also be noticed in case of the other two dyes also (Figure B27-B66). While discussing the composition dependent changes of the TAS in the next sub-section, this behavior of the spectra can be described more thoroughly.

2.3.2. Composition dependent spectral changes of TAS:

Beside the time evolution of the TA spectra, the composition dependence of TAS is shown and discussed in four different timescales which consist of two shorter timescales (500 fs and 1 ps) and two comparatively longer timescales (30 ps and 150 ps). In this section, we will get an idea about the effect of changing the mixture compositions on the TAS in case of all the studied IL-MS mixtures while using the same three indoline dyes D102, D149 and D205. Similar to the previous section, we would like to discuss about the composition dependent changes of D102 only because similar changes can be shown in the cases of the other two dyes. All the figures

using D149 and D205 dyes are shown in the appendix. To show the effect of changing MS and changing IL separately, here in this section, we will divide the discussion into two subsections. To initiate we will discuss about effect of changing three molecular solvents in the TAS of D102 in $BmimPF_6$-MS mixtures. As the composition dependent spectral discussions for the other three ILs are similar, only the figures are shown in the Appendix (Figures B67-B69). Then we will discuss about the effect of changing four ionic liquids in the TAS of D102 in IL-ACN mixtures. Similarly, the figures of the TAS of D102 containing IL-γ-BL/PC mixtures are also shown in the appendix (Figures B70, B71).

2.3.2.1. Effect of changing the MSs on the TA spectra:

Figure 2.2 will show the composition dependent changes of TAS of D102 in binary mixtures with $BmimPF_6$ and all three MSs used in our study.

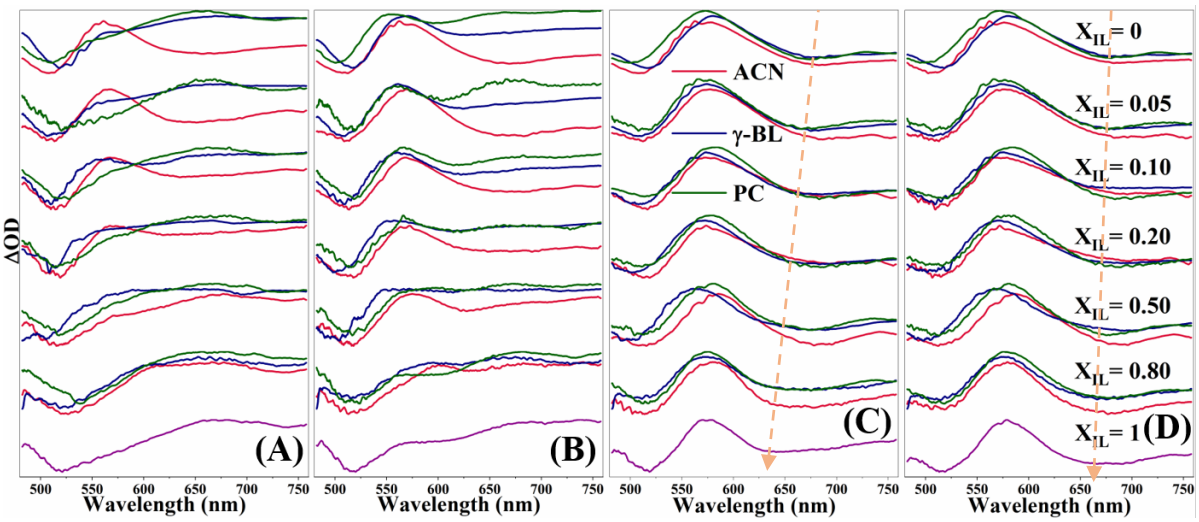

Figure 2.2: Composition dependent TAS of D102 in $BmimPF_6$-MS mixtures at (A) 500 fs, (B) 1 ps, (C) 30 ps and (D) 150 ps

At the shorter times (500 fs and 1ps, Figures 2.2(A), 2.2(B)), the TAS show large difference in shape at the lower X_{IL} ($X_{IL} \leq 0.20$) region of $BmimPF_6$-ACN mixtures compared to the other two IL-MS mixtures. The reason behind this can be due to the faster dynamics in ACN compared to that in γ-BL and PC. The faster excited state dynamics of the dye in ACN helps to form definite SE regions in case of IL-ACN mixtures at low X_{IL} regions ($X_{IL} \leq 0.20$) compared to that in IL-γ-BL and IL-PC mixtures. We have also noticed the similar effect while discussing time evolution of TAS in fast timescales in case of three different IL-MS mixtures with three different MSs. Figures 2.1((A), (B) and (C)) clearly show that, in case of $BmimPF_6$-ACN mixture (Figures 2.1(A)) the TAS have already formed the negative SE region and the positive ESA region within 1 ps. However, in case of $BmimPF_6$-γ-BL and $BmimPF_6$-PC mixtures (Figures 2.1(B) and 2.1(C)), it takes more than 1 ps time to form negative SE and positive ESA region (~ 2 ps) in the TAS spectra. Furthermore, the Figures in the appendix section (Figures B67-B69) also confirms the fact that this change in the shape of TAS is not due to the IL present in the mixtures, as the similar changes can also be noticed in case of IL-ACN mixtures containing $BmimBF_4$, BmimTFO and BmimTFSI as the IL. Therefore, the different TAS shape of $BmimPF_6$-ACN mixtures compared to that in $BmimPF_6$-γ-BL,PC mixtures at lower X_{IL} at

faster times (before ~1 ps) is mainly due to the effect of the MS used in the IL-MS mixtures. (Figures 2.2(A) and 2.2(B)). On the contrary, at higher X_{IL} ($X_{IL} \geq 0.50$), the TAS show almost similar shapes in case of three different MSs (Figures 2.2(A) and 2.2(B)), which can be due to the increased viscosity of surrounding medium while increasing X_{IL} of the mixtures and dominance of viscosity effect in changing the shapes of TAS. Moreover, there is not much of difference in the shapes of the TAS in Figures 2.2(C) and 2.2(D), i.e. at the longer time regions (30 ps and 150 ps), as positive ESA and negative SE bands are already formed at these times.

2.3.2.2. Effect of changing the ILs on the TA spectra:

As we have discussed about the effect of changing MSs on the TAS of D102 in the previous sub-section, we can now show the effect of changing four different ILs on the shape of the TAS of the dye D102 while keeping ACN as the same molecular solvent. In Figure 2.3, we have shown the TAS of the dye D102 in all the four IL-ACN mixtures at four different times starting from very fast 0.5 ps and 1 ps to comparatively slower 30 ps and 150 ps. From Figures 2.3(A) and 2.3(B), we can see the change of the shape of TAS while changing X_{IL} at two shorter times. The TA spectra below $X_{IL} = 0.20$ show nicely formed positive ESA and negative SE, while both the positive ESA and negative SE bands are not completely formed in the higher concentration regions of IL ($X_{IL} > 0.20$) in case of all four IL-ACN mixtures. Similar types of observations can be noticed in case of IL-γ-BL (Figure B70(B)) and IL-PC (Figure B71(B)) mixtures while using D102 dye, as the spectral shapes at 1 ps show the differences with the mixture compositions. This is mainly due to the fast relaxation dynamics in three solvents compared to highly viscous ILs. Due to faster dynamics in MSs, the formation of ESA and SE bands are faster at the lower X_{IL} region (where the mixture properties are mainly dominated by the solvents due to the abundance), which eventually slows down with the increase of X_{IL}. In addition, the shapes of the TAS are almost similar in the whole composition range of IL-ACN mixtures at the other two comparatively longer times (30 ps and 150 ps, Figures 2.3(C) and 2.3(D)). In these two cases, the formation of ESA and SE bands already can be noticed due to longer delay time.

Furthermore, the polarity dependent shift of negative SE peaks in the longer wavelength region (> 600 nm), where they are formed already in Figure 2.3, is not visible while changing the ILs in the IL-ACN mixtures because of almost similar polarity of four ILs used in this study. However, the composition dependent blue shift of SE peaks while increasing X_{IL} of the mixtures can be noticed while increasing X_{IL} of the IL-ACN mixtures at two slower delay times (dashed arrows to show the blue shift of SE regions in Figures 2.2 and 2.3), which is due to the decrease of the polarity of the surrounding medium of the dye while increasing X_{IL} of the mixtures. This type of polarity dependent shift of SE bands was also noticed in previous study.[112]

Overall, the composition dependent changes of TAS in BmimPF_6-MS and in IL-ACN mixtures mainly show the effect of surrounding mediums on the TAS shape changes. Similar types of changes can also be noticed in case of other two dyes in other IL-MS mixtures. Thus, they are not worthy for further discussions. The Figures are given in the appendix (Figures B72-B85).

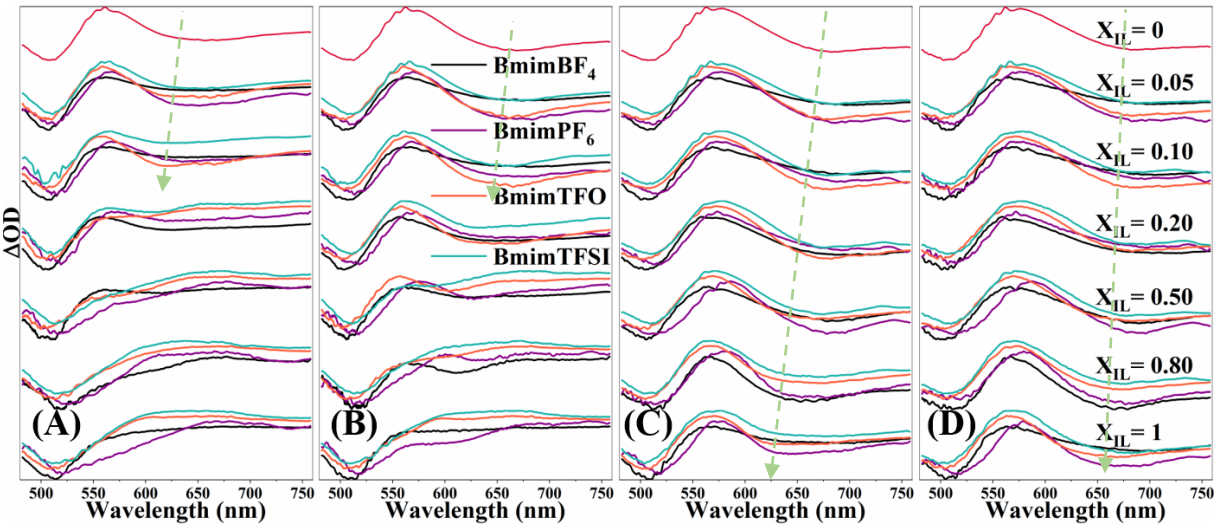

Figure 2.3: Composition dependent TAS of D102 in IL-ACN mixtures at (A) 500 fs, (B) 1 ps, (C) 30 ps and (D) 150 ps

2.3.3. Global analysis:

The global analysis of the TA spectra of the samples was performed in the following way.

First, the experimental data were corrected using a LabVIEW tool for the GVD correction. The full details of the GVD correction process is described in another chapter (Chapter 5, Section 5.1). After that, the GVD corrected data were fitted by using a global analysis software called Ultrafast Toolbox. The basic principles and related equations of the global analysis process are described in Chapter 5, Section 5.1, which also contains the IRF measurement of the TA setup.

The global analysis of TA spectra gives us two important information about the excited state dynamics. The first one is number of excited state processes and corresponding time components (τ_i) and the other one is the amplitude of the global fit ($A_i(\lambda)$). All the values of global analysis time components of the dyes D102, D149 and D205 in the IL-MS mixtures used in this study are shown in the Tables B2-B37 in the Appendix section. In addition, the wavelength dependent plot of the pre-exponential factors, which are also known as decay associated spectra (DAS), are shown in Figures 2.4 and B86-B152 in the Appendix. Next, we would like to discuss more about the outcome of the global analysis procedure.

Decay Associated Spectra (DAS):

Our global analysis of TAS also results in four different DAS corresponding to four time-components (τ_i) in case of each studied mixture. In this section, we would like to discuss about the behavior of these four DAS related to four time-components (Figure 2.4). All the DAS related to the time components in case of three dyes used in our study can be divided into two sets. Here, we are going to give a comparative discussion about these two sets of DAS by discussing one representative from each of the two sets in case of three dyes. Other DAS figures are shown in the Appendix (Figures B86-B152).

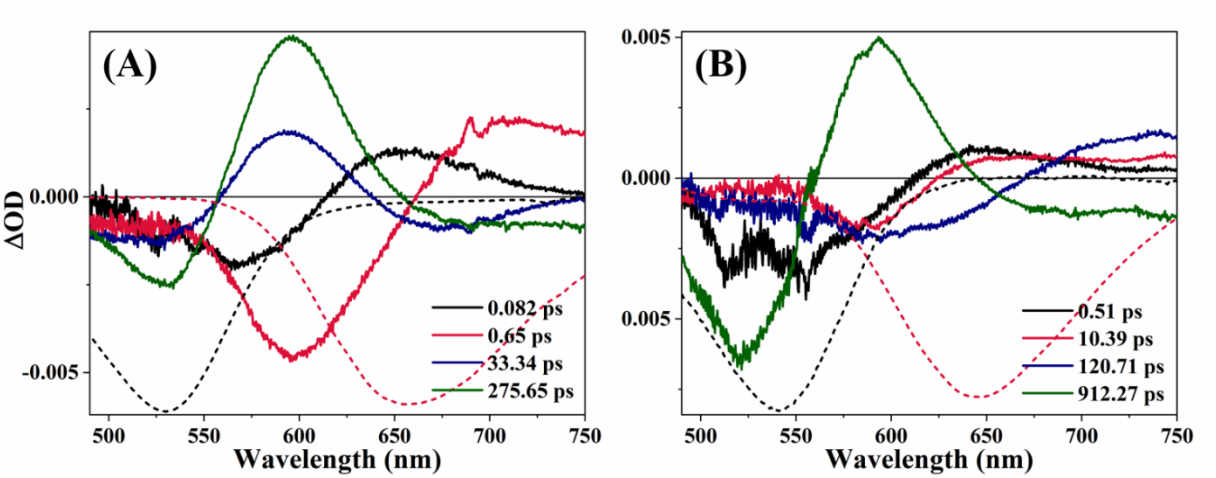

Figure 2.4: DAS of D149 in (A) ACN, (B) $BmimBF_4$. Absorption and emission spectra are shown in black and red dashed lines respectively.

In Figures 2.4(A) and 2.4(B), the DAS of D149 in pure ACN and in pure $BmimBF_4$ are shown respectively. The discussion about the similarities and dis-similarities between these two DAS will cover the DAS of these dyes in the other studied samples. Firstly, DAS related to the longest τ_4 (Figures 2.4, B86-B152, green) have negative GSB, SE and positive ESA in case of all the samples and both GSB and SE overlaps with time-integrated absorption (black dashed line) and emission (blue dashed line) spectra respectively. Therefore, this τ_4 DAS is due to nothing but the excited state decay (S_1-S_0 transition) of the dye.[105] In the same figures, we can also see that the signs of both τ_1 and τ_2 DAS (Figures 2.4, B86-B152, red and black) are opposite to τ_4 DAS, evidently in the ESA and SE regions (~ 550-750 nm). This indicates that both of them are rise components and related to the excited state processes of the dye molecules. In addition, these two DAS corresponding to τ_1 and τ_2 have blue-shifted SE regions compared to steady state emission spectra which are also indications that these two time components can be due to the solvent relaxation in the surrounding mediums.[115] However, the DAS of τ_3 (Figures 2.4, B86-B152, blue) shows different behavior in case of different samples. For most of the samples, DAS of τ_3 shows similar behavior to that of τ_2 (characteristic blue shift of negative SE region compared to steady state emission spectra) which certainly suggest the involvement of excited state of the dye. However, for some of the samples (Figures 2.4(A), B108-B112), where common molecular solvent is ACN, τ_3 DAS shows the similar sign to τ_4 DAS, which also indicate that τ_3 is a decay timescale in case of those samples. In this regard, previous study by El-Zohry et al.[90] had attributed this τ_3 as a non-radiative decay timescale in ACN related to the twisting of a bond in the donor moiety of the D149 dye while Fakis et al.[114] and Lohse et al.[112] had attributed this τ_3 to the vibrational relaxation process of the excited state of D149 molecule. Thus, determining the nature of τ_3 remains unclear from this DAS analysis. Further studies are necessary in this aspect to get a better insight about the origin of τ_3. For this work, we are mainly interested in the composition dependent changes of the four global analysis time components for the three studied indoline dyes in the studied IL-MS mixtures.

2.3.4. Discussions:

In the first step of this discussion , we will compare the obtained relaxation times by the global analysis with those obtained in the literature for the same dyes used in this study. In Figure 2.5 and Table B1, we can see the previous values and values from this study of these relaxation times as a function of both the viscosity and polarity in different pure MSs and ILs. It is true that the conventional organic solvents, where the excited state dynamics of these dyes studied previously, have very low viscosity values compared to the ionic liquids used in our study. For instance, the highest viscous IL used for our study, $BmimPF_6$, has ~750 times higher viscosity then lowest viscous MS, ACN, and the lowest viscous used IL, BmimTFSI, has almost 20 times higher viscosity than highest viscous MS, PC. Moreover, the viscosity values of other organic solvents shown in Figure 2.6 are quite similar and are below 2 cP.

The dependence of these four relaxation times on viscosity is very difficult to rationalize [Figures 2.5((A), (B), (C) and (D))]. One reason behind this is the large scattering of the previous reported literature values. As an illustration, in the same solvent, namely ACN, the values of τ_1 varies from 0.11 to 0.21ps for D102 and from 0.08 to 0.45 ps for D149. Analyzing the general trend of these relaxation times as a function of viscosity, it can be noticed that, for organic solvents the viscosity values of which are below 1 cP, the values of τ_1, τ_2 , τ_3 and τ_4 increase to reach maximum values of 0.19, 2.31, 40, 720 ps respectively. Although there is no particular correlation between the viscosity values and these four relaxation times values, one can notice the increase of these four relaxation timescales in more viscous ILs compared to the MSs [Figures 2.5((A), (B), (C) and (D))].

In this aspect, the viscosity dependence of these relaxation times of the excited state dynamics were also analyzed in the previous reports. For instance, the solvation dynamics studies using C153 dyes in various organic solvents[116] and ILs[96,99,100,117–120] and even in IL-MS mixtures[121–123] showed the viscosity dependence of these solvation time components. El Zohry et al.[87] had also studied the effect of viscosity by introducing highly viscous mediums like polymer matrices and ZrO_2. They have noticed an increase of excited state relaxation time of D149 up to 2 ns. They have attributed this increase of lifetime of the dye to blocked internal motion of the dye while increasing medium viscosity. In addition, excited state relaxation dynamics study of a metal(Re)-based dye in ionic liquid showed that the lifetime of the excited state increases with the viscosity increase of the medium, and the decay time follows the series $EmimBF_4$ (330 ps) < $BmimBF_4$ (470 ps) < $BmimPF_6$ (1570 ps).[124] To sum up, the literature data also show that, by increasing the viscosity (although the extent of this increase is small in comparison to that when considering ionic liquids) the relaxation times of the excited state increases.

Now, if we consider the effect of the polarity as quantified by the dielectric constant values, Figures 2.5 [(E), (F), (G) and (H)] show that, for organic solvents (for which we recall that the viscosity values are smaller than 2cP), there exists no particular correlation between the solvent polarity and the values of these four relaxation time constants. In addition, while considering the ILs, it is the viscosity and not the polarity that determines the values of these relaxation times. These findings are also consistent with the literature data. Indeed, Fakis et al.[84,85] and Lohse et al.[112] have found that with the increase of the solvent polarity, the excited state lifetime (τ_4 in our case) of the dye decreases. Similar type of solvent polarity dependence was also noticed in case of carotenoid-type dyes also.[125–129] In addition to polarity, the solvents with

possibility of the formation of hydrogen bond between the dye and the solvent also have an impact on the values of these relaxation times. Therefore, the excited state relaxation times of the dye D149 is lower in different alcohols than that in aprotic solvents.[112] In addition, Lohse et al.[130] also found that the relaxation time of 12'-CA decreases with the increase of medium polarity in case of pure organic solvents, whereas there is no particular correlation between the medium polarity and the dye relaxation times in case of the ILs. According to them, the main reason behind this type of behavior in ILs is the presence of dominant probe/dye-cation interactions in them, which can't be quantified by the microscopic properties.[130]

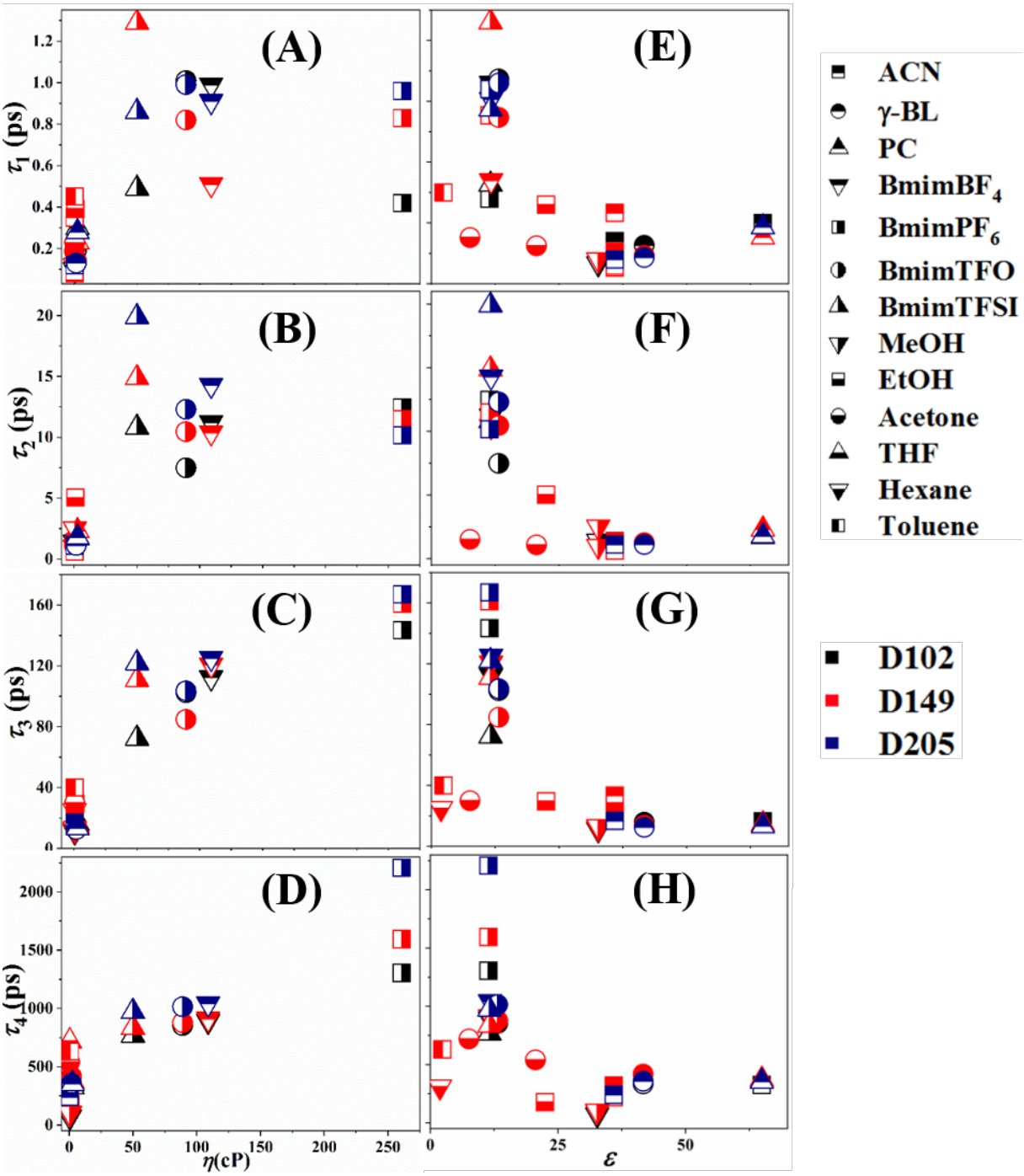

Figure 2.5: Different time-components of D102, D149 and D205 in various pure solvents with respect to [(A), (B), (C) and (D)] viscosity and [(E), (F), (G) and (H)] dielectric constant [84,86,87,94]

This previous discussion about the dependence of the dye relaxation times on the polarity and viscosity of pure ILs and MSs mainly point out the fact that, it is really difficult to interpret the excited state relaxation times considering only the macroscopic properties like the polarity and the viscosity of the surrounding medium of the dyes. In case of viscosity dependence, the high values of the viscosity (such as in ILs) results in high values of these relaxation times and objectively this is associated with the hindrance of the change of the conformation of flexible molecules (such as our chosen dyes). Similarly, we didn't find any correlation between these four relaxation time values and the polarity as determined by the dielectric constant of the mediums. Therefore, we conjecture that, these relaxation times are mainly determined considering the local distribution of the solvent or the ions (hydrogen bonding, stacking interactions etc.) around the given dye, not by the values of macroscopic parameters like polarity and viscosity.

When it comes to the physical meaning of the four relaxation times after the global analysis, there is agreement in the interpretation of the τ_1, τ_2 and τ_4 in the previous studies.[84,86,87,90] While both τ_1 and τ_2 are considered due to solvation in the medium, the longest τ_4 was regarded as a decay timescale from the excited state to the ground state. However, there is disagreement regarding the origin of τ_3. Indeed, Fakis et al.[84] and Lohse et al.[86] had attributed this τ_3 to the vibrational/structural relaxation of the excited state of the dye, whereas El-Zohry et al.[90] had described this timescale as a relaxation timescale due to a twisting process in the donor unit of the dye.

By studying the mixtures composition dependence of these relaxation times, our goal is to get more insight about the behavior of these relaxation times. Therefore, we have their behavior as a function of the mixture composition for the three studied dyes reported in Figures 2.7, 2.8, 2.9 and 2.10. In addition, all the values of global analysis timescales are given in Tables B2-B37. Of course it is true that, the change of the composition of the mixture helps in the gradual modulation of the properties of the IL-MS mixtures like polarity, viscosity, hydrogen bond, the interionic, ion-solvent, dye-ion and dye-solvent interactions. In general, we notice an overall decrease of these four relaxation time values (Figures 2.7, 2.8, 2.9 and 2.10) when the X_{IL} of the mixtures decrease. However, the rate of this decrease is high in the range of X_{IL} between 1 and 0.2 while it slows down for further dilution of IL. This decrease can be correlated with the gradual decrease of the viscosity and increase in the polarity of the mixture. Indeed, the polarity of the solvent measured by dielectric constant being higher by a factor of 3 to 6 than that of the used ILs while the viscosity of the latter's are higher by a factor of 50 to 100 than the formers. In particular, this is the case of τ_1 and τ_2 relaxation times. They decrease with the decrease of the viscosity and the increase of the polarity which indicates that the composition dependent changes of these two timescales are modulated by the gradual change of the viscosity/polarity of the corresponding mixtures. However, the presence of a minimum in the case of the values of both τ_3 and τ_4 at $X_{IL} \sim 0.05$ suggests the fact that this excited state dynamics is not only dependent on mixture polarity and viscosity. In addition, it is also true that the values of τ_4 also go through a minimum for D102, and D149 in all the studied IL-MS mixtures while this minimum is not very well-defined for the D205. The occurrence of the minima in the values of τ_3 is also observed but to a less extent, even not present in some mixtures (in most of the mixtures while the dye is D102). This type of overall increase and also the presence of the

minima in the composition dependence of the dye relaxation time using the dye 12'-CA was also observed in the case of $HmimNTf_2$-ACN mixture.[104] The authors described this overall increase with respect to the medium polarity parameter (Δf) and the presence of the minima due to ion pair interactions in the surroundings of the dye.[104] A careful analysis of the literature data shows that by increasing the viscosity[131–137] (the high viscosity hinders the change of the conformation of the dye[87,90] and also reduces its diffusion) while the polarity increase[84,86,104] of the surroundings help to open up non-radiative decay channels of the excited state of the studied dyes. Considering the polarity of our studied mixtures, the experimental values of the dielectric constant as a function the mixture composition are only available for $BmimBF_4$-ACN mixtures to our best knowledge.[138] These values increase with dilution and go through a maximum at $X_{IL} \sim 0.01$.[139] This indicates that, at this range of mole fraction, particular interactions between the components of the IL-MS mixture and the dye are present in considerate amount to effect the medium polarity. Although the experimental data on dielectric constant of the other mixtures used in our study are not available, we can expect the similar behavior of the dielectric constant may occur in our other studied mixtures, as the trend is similar in case of other IL-MS mixtures like $EmimBF_4$-ACN, $HmimBF_4$-ACN, $HmimNTf_2$-ACN and $EmimEtSO_4$-DCM mixtures.[138–140] Furthermore, various other properties of IL-MS mixtures also show drastic changes in this low X_{IL} region.[82,141–146] Indeed, in this mole fraction range, the spectroscopic studies reported a noticeable change of the vibration mode and NMR chemical shift and conductivity of the mixtures. One of the possible explanation was also given in a previous work by Marekha et al.,[83] where the average distance between the ions, the ions and the solvent were calculated through MD simulations at different mixture compositions in case of the IL-MS mixtures similar to our study. A crossover between the cation-anion distance and that between the cation-solvent and anion-solvent was noticed in that study. The mole fraction at which this crossover occurs depend on how the solvent is competing on the cation-anion interactions, it is higher in the case of PC and γ-BL than in ACN.[83]

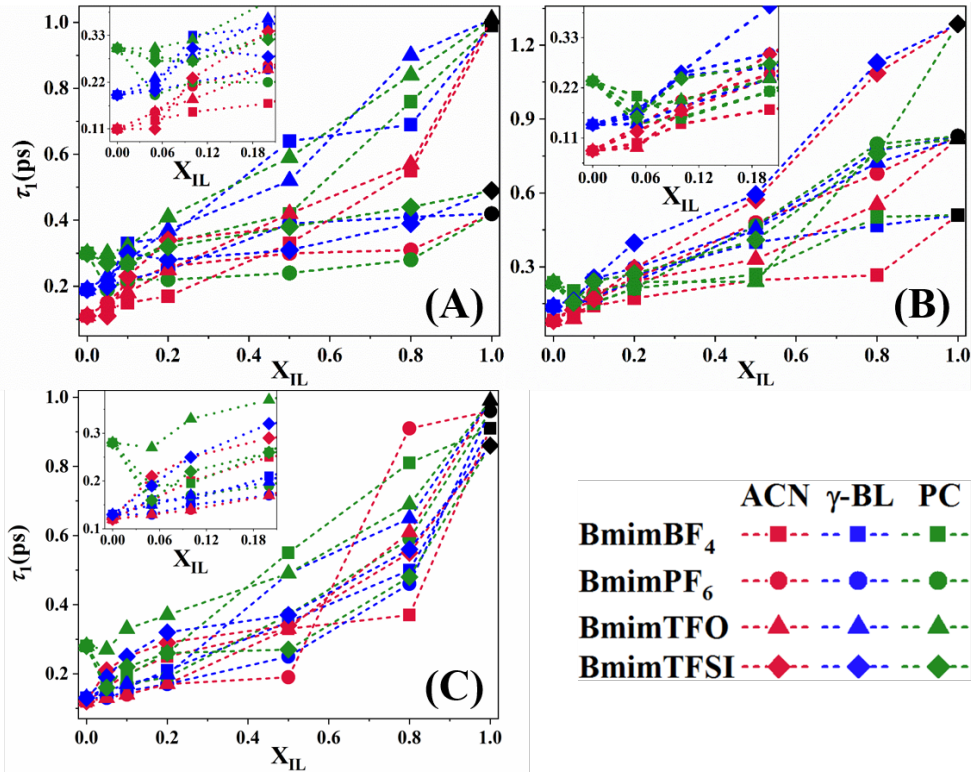

Figure 2.7: Change of τ_1 of (A) D102, (B) D149 and (C) D205 with the composition of IL-MS Mixtures

In the mixture of the dye-IL-MS, the same crossover in the hydrogen bonding between the dye and the ions and the solvent molecules may occur at this range of mole fractions. Preliminary results of the molecular dynamics simulation of a D205 in a mixture with $BmimBF_4$-ACN, show that the average distance between the dye and the ions remains same as it is in the neat IL at the higher mole fraction region of the IL-MS mixtures. However, the average cation-anion distance increases drastically for X_{IL} below 0.2. Concomitantly, the average distance between the dye and the ions decreases to be lower than that between the cations and the anions. These results indicate that the structural changes occurring especially at the low range of mole fraction of the IL-MS mixture correlates well with behavior of the relaxation dynamics of the excited state. The dye is acting as a probe of this crossover region of the mixtures and it is expressed by the occurrence of the minima in case of τ_3 and τ_4. However, we don't have any microscopic explanations regarding various interactions in the medium and we believe that further investigation using MD simulations of these dyes in the case of these studied mixtures are needed to clarify the origin of the minimum observed particularly for the two larger relaxation time components (τ_3 and τ_4).

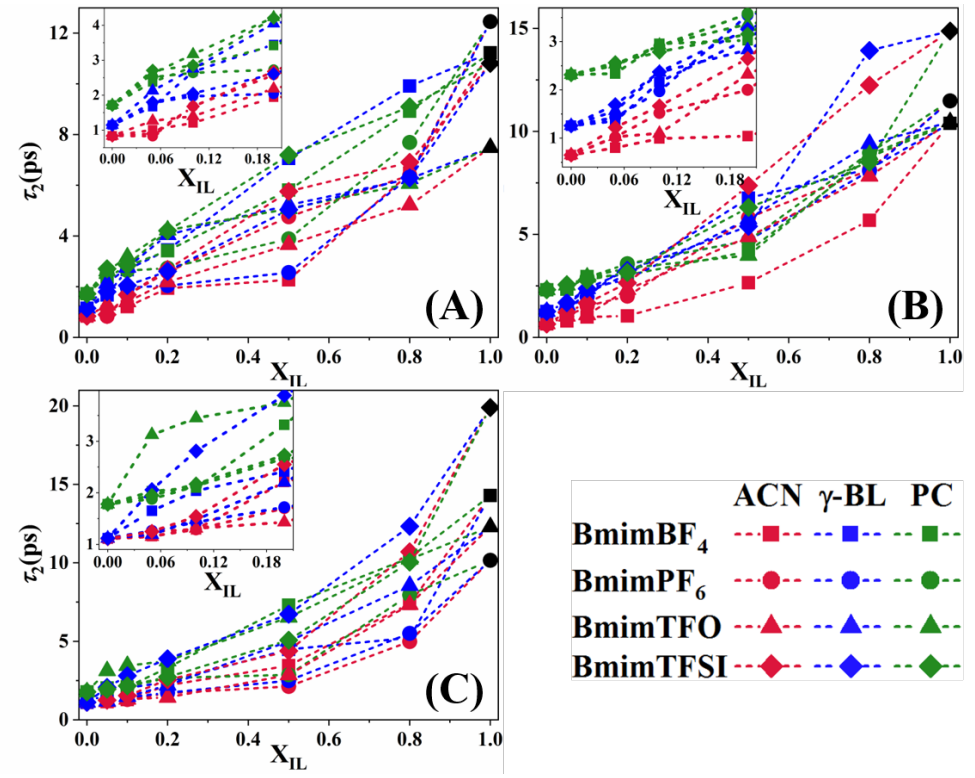

Figure 2.8: Change of τ_2 of (A) D102, (B) D149 and (C) D205 with the composition of IL-MS Mixtures

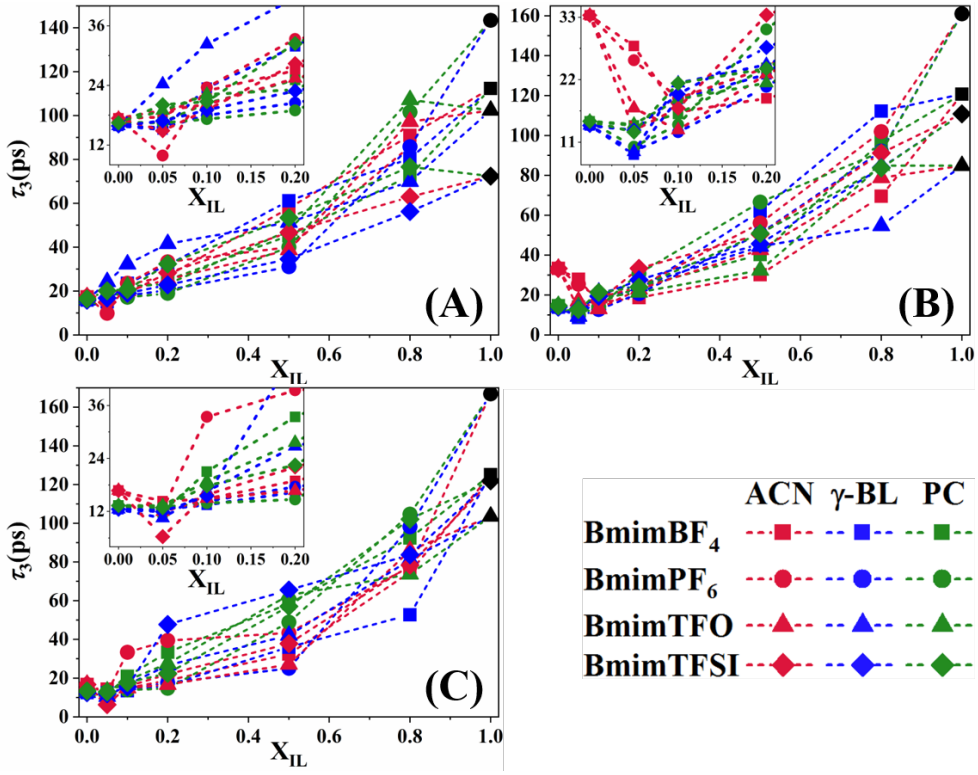

Figure 2.9: Change of τ_3 of (A) D102, (B) D149 and (C) D205 with the composition of IL-MS Mixtures.

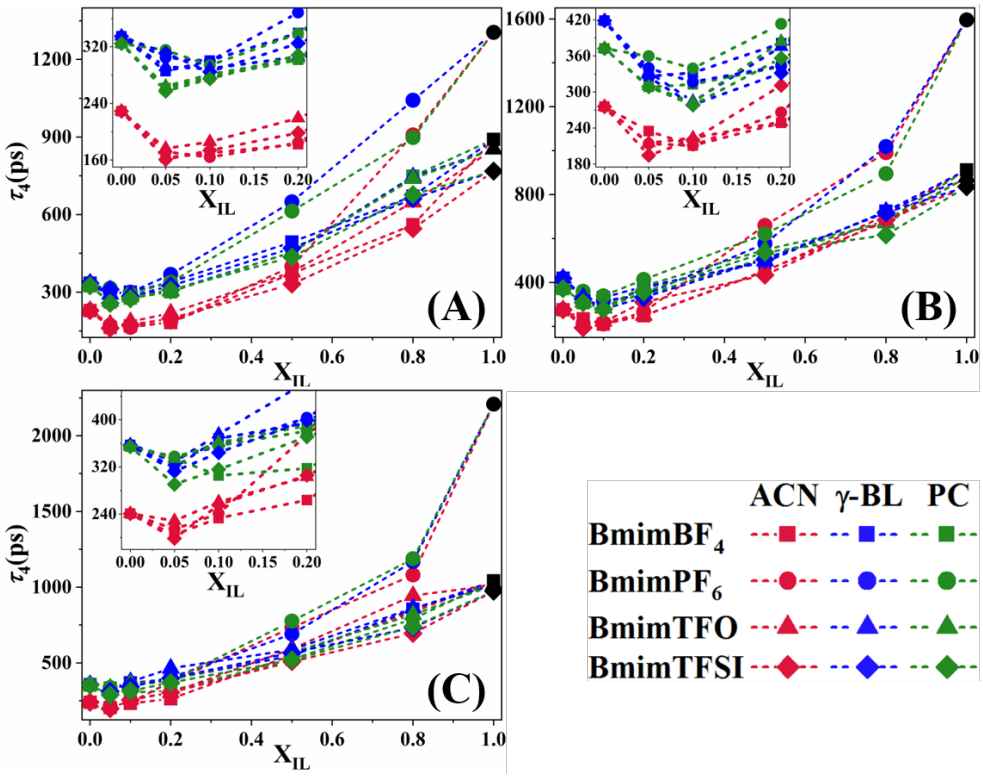

Figure 2.10: Change of τ_4 of (A) D102, (B) D149 and (C) D205 with the composition of IL-MS Mixtures.

2.4. Conclusions:

In this chapter, we have studied the excited state relaxation dynamics of indoline dyes, namely the D102, D139 and D205 in different IL-MS mixtures containing four different imidazolium cation based ILs and three different polar aprotic MSs using time-resolved transient absorption spectroscopy. The time dependent TA spectral analysis showed us the time dependent changes of three overlapping regions consist of negative GSB, positive ESA and negative SE regions in case of all three studied dyes. In addition, the composition dependent TAS analysis helped us to understand the effect of both ILs and MSs in the IL-MS mixtures in determining the shapes of the dye TA spectra at different delay times. Furthermore, the global analysis of experimental TA data reveals that the excited state relaxation occurs through four relaxation times. The viscosity and polarity dependence of these four timescales are not fully understood; however, the high viscosity, particularly in pure ILs and also at the higher mole fraction region ($X_{IL} \geq 0.50$) of ILs, causes the hindrance in the conformational change of such flexible dyes and also in slowing down its diffusion. Besides, the increasing polarity induces an overall decrease of the slowest relaxation time (τ_4). This lack of both polarity and viscosity correlations of these four timescales in pure components and also in the mixtures suggest the need of introduction of the interactions between the dye and surrounding mediums in the discussion of these four timescales. Moreover, the composition dependence of the values of excited state decay timescale τ_4 pass through a minimum in case of D102, D149 and D205 in all the studied IL-MS mixtures. The occurrence of a minimum in the values of τ_3 also is observed but to a less extent. Similar to the two longer excited state relaxation times of the dyes, this occurrence of extrema was also noticed in the case of steady-state properties like emission maxima, Stokes

shift, the minimum in the relative quantum yield as well (Chapter 1). This typical behavior of the dye at low X_{IL} indicates that, the dye is experiencing a change in the constitution of its local structure from being dominated by the ions in ionic liquids to the one dominated by the solvent molecules, which is behind the regulation of the interactions between the dye and the surrounding environment. However, to know further about the types of interactions present in between the dye and surroundings, detailed molecular dynamics simulation studies are needed, which is mainly the next goal regarding this study.

Bibliography

(1) Germani, R.; Mancini, M. V.; Spreti, N.; Profio, P. Di; Savelli, G. Cu(II) Extraction in Ionic Liquids and Chlorinated Solvents: Temperature Effect. *Green Sustain. Chem.* **2011**, *01* (04), 155–164. https://doi.org/10.4236/gsc.2011.14024.

(2) Kawano, R.; Matsui, H.; Matsuyama, C.; Sato, A.; Susan, M. A. B. H.; Tanabe, N.; Watanabe, M. High Performance Dye-Sensitized Solar Cells Using Ionic Liquids as Their Electrolytes. *J. Photochem. Photobiol. A Chem.* **2004**, *164* (1–3), 87–92. https://doi.org/10.1016/j.jphotochem.2003.12.019.

(3) Zhao, H. Effect of Ions and Other Compatible Solutes on Enzyme Activity, and Its Implication for Biocatalysis Using Ionic Liquids. *J. Mol. Catal. B Enzym.* **2005**, *37* (1–6), 16–25. https://doi.org/10.1016/j.molcatb.2005.08.007.

(4) Zhao, H. Effect of Ions and Other Compatible Solutes on Enzyme Activity, and Its Implication for Biocatalysis Using Ionic Liquids. *J. Mol. Catal. B Enzym.* **2005**, *37* (1–6), 16–25. https://doi.org/10.1016/j.molcatb.2005.08.007.

(5) Matsuda, T. *Future Directions in Biocatalysis*; Elsevier, 2007. https://doi.org/10.1016/B978-0-444-53059-2.X5000-6.

(6) Plechkova, N. V.; Seddon, K. R. Applications of Ionic Liquids in the Chemical Industry. *Chem. Soc. Rev.* **2008**, *37* (1), 123–150. https://doi.org/10.1039/b006677j.

(7) Zhao, H. Methods for Stabilizing and Activating Enzymes in Ionic Liquids - A Review. *J. Chem. Technol. Biotechnol.* **2010**, *85* (7), 891–907. https://doi.org/10.1002/jctb.2375.

(8) Cui, X.; Zhang, S.; Shi, F.; Zhang, Q.; Ma, X.; Lu, L.; Deng, Y. The Influence of the Acidity of Ionic Liquids on Catalysis. *ChemSusChem* **2010**, *3* (9), 1043–1047. https://doi.org/10.1002/cssc.201000075.

(9) Feng, R.; Zhao, D.; Guo, Y. Revisiting Characteristics of Ionic Liquids: A Review for Further Application Development. *J. Environ. Prot. (Irvine,. Calif).* **2010**, *01* (02), 95–104. https://doi.org/10.4236/jep.2010.12012.

(10) Armel, V.; Pringle, J. M.; Forsyth, M.; MacFarlane, D. R.; Officer, D. L.; Wagner, P. Ionic Liquid Electrolyte Porphyrin Dye Sensitised Solar Cells. *Chem. Commun.* **2010**, *46* (18), 3146. https://doi.org/10.1039/b926087k.

(11) Suresh; Sandhu, J. S. Recent Advances in Ionic Liquids: Green Unconventional Solvents of This Century: Part I. *Green Chem. Lett. Rev.* **2011**, *4* (4), 289–310. https://doi.org/10.1080/17518253.2011.572294.

(12) Patel, D. D.; Lee, J. M. Applications of Ionic Liquids. *Chem. Rec.* **2012**, *12* (3), 329–355. https://doi.org/10.1002/tcr.201100036.

(13) Sheldon, R. A. Biocatalysis in Ionic Liquids. *RSC Catal. Ser.* **2014**, *2014–Janua* (15), 20–43. https://doi.org/10.1007/978-981-10-6739-6_77-1.

(14) Greer, A. J.; Jacquemin, J.; Hardacre, C. Industrial Applications of Ionic Liquids. *Molecules* **2020**, *25* (21), 5207. https://doi.org/10.3390/molecules25215207.

(15) Sakhno, T. V.; Barashkov, N. N.; Irgibaeva, I. S.; Mendigaliyeva, S.; Bostan, D. S. Ionic

Liquids and Deep Eutectic Solvents and Their Use for Dissolving Animal Hair. *Adv. Chem. Eng. Sci.* **2020**, *10* (01), 40–51. https://doi.org/10.4236/aces.2020.101003.

(16) Seddon, K. R. Ionic Liquids for Clean Technology. *J. Chem. Technol. Biotechnol.* **1997**, *68* (4), 351–356. https://doi.org/10.1002/(SICI)1097-4660(199704)68:4<351::AID-JCTB613>3.0.CO;2-4.

(17) Ignatyev, I. A.; Mertens, P. G. N.; Van Doorslaer, C.; Binnemans, K.; de Vos, D. E. Cellulose Conversion into Alkylglycosides in the Ionic Liquid 1-Butyl-3-Methylimidazolium Chloride. *Green Chem.* **2010**, *12* (10), 1790. https://doi.org/10.1039/c0gc00192a.

(18) Moniruzzaman, M.; Nakashima, K.; Kamiya, N.; Goto, M. Recent Advances of Enzymatic Reactions in Ionic Liquids. *Biochem. Eng. J.* **2010**, *48* (3), 295–314. https://doi.org/10.1016/j.bej.2009.10.002.

(19) Lozano, P. Enzymes in Neoteric Solvents: From One-Phase to Multiphase Systems. *Green Chem.* **2010**, *12* (4), 555. https://doi.org/10.1039/b919088k.

(20) Laali, K. K. Ionic Liquids in Synthesis. *Synthesis (Stuttg).* **2003**, *2003* (11), 1752–1752. https://doi.org/10.1055/s-2003-40869.

(21) Chowdhury, S.; Mohan, R. S.; Scott, J. L. Reactivity of Ionic Liquids. *Tetrahedron* **2007**, *63* (11), 2363–2389. https://doi.org/10.1016/j.tet.2006.11.001.

(22) Garcia, S.; Lourenço, N. M. T.; Lousa, D.; Sequeira, A. F.; Mimoso, P.; Cabral, J. M. S.; Afonso, C. A. M.; Barreiros, S. A Comparative Study of Biocatalysis in Non-Conventional Solvents: Ionic Liquids, Supercritical Fluids and Organic Media. *Green Chem.* **2004**, *6* (9), 466–470. https://doi.org/10.1039/B405614K.

(23) Yau, H. M.; Croft, A. K.; Harper, J. B. Investigating the Origin of Entropy-Derived Rate Accelerations in Ionic Liquids. *Faraday Discuss.* **2012**, *154*, 365–371. https://doi.org/10.1039/C1FD00060H.

(24) Gyton, M. R.; Cole, M. L.; Harper, J. B. Ionic Liquid Effects on Mizoroki–Heck Reactions: More than Just Carbene Complex Formation. *Chem. Commun.* **2011**, *47* (32), 9200. https://doi.org/10.1039/c1cc12082d.

(25) Chen, Q.; Wang, Q.; Mitsumura, N.; Niida, H. Improved Cellulose by Ionic Liquid Mixture with Solid Acid Catalysis and Its Application in Polyethylene Glycol Liquefaction. *Mater. Sci. Appl.* **2013**, *04* (12), 839–845. https://doi.org/10.4236/msa.2013.412107.

(26) Shin, J.-H.; Henderson, W. A.; Tizzani, C.; Passerini, S.; Jeong, S.-S.; Kim, K.-W. Characterization of Solvent-Free Polymer Electrolytes Consisting of Ternary PEO–LiTFSI–PYR[Sub 14] TFSI. *J. Electrochem. Soc.* **2006**, *153* (9), A1649. https://doi.org/10.1149/1.2211928.

(27) Shin, J. H.; Henderson, W. A.; Passerini, S. Ionic Liquids to the Rescue? Overcoming the Ionic Conductivity Limitations of Polymer Electrolytes. *Electrochem. commun.* **2003**, *5* (12), 1016–1020. https://doi.org/10.1016/j.elecom.2003.09.017.

(28) Fung, Y. S.; Chad, S. M. Investigation of the 1-Methyl-3-Ethylimidazolium Chloride-AlCl3/LiAlCl4 System for Lithium Battery Application Part I: Physical Properties and Preliminary Chronopotentiometric Study. *J. Appl. Electrochem.* **1993**, *23* (4), 346–351. https://doi.org/10.1007/BF00296690.

(29) MacFarlane, D. R.; Huang, J.; Forsyth, M. Lithium-Doped Plastic Crystal Electrolytes Exhibiting Fast Ion Conduction for Secondary Batteries. *Nature* **1999**, *402* (6763), 792–794. https://doi.org/10.1038/45514.

(30) Alonso, L.; Arce, A.; Francisco, M.; Soto, A. Solvent Extraction of Thiophene from N-Alkanes (C7, C12, and C16) Using the Ionic Liquid [C8mim][BF4]. *J. Chem. Thermodyn.* **2008**, *40* (6), 966–972. https://doi.org/10.1016/j.jct.2008.01.025.

(31) Zhang, Z.; Zhao, Z. K. Microwave-Assisted Conversion of Lignocellulosic Biomass into Furans in Ionic Liquid. *Bioresour. Technol.* **2010**, *101* (3), 1111–1114. https://doi.org/10.1016/j.biortech.2009.09.010.

(32) Gupta, S.; Moulik, S. P. Biocompatible Microemulsions and Their Prospective Uses in Drug Delivery. *J. Pharm. Sci.* **2008**, *97* (1), 22–45. https://doi.org/10.1002/jps.21177.

(33) Sekhon, S. S.; Krishnan, P.; Singh, B.; Yamada, K.; Kim, C. S. Proton Conducting Membrane Containing Room Temperature Ionic Liquid. *Electrochim. Acta* **2006**, *52* (4), 1639–1644. https://doi.org/10.1016/j.electacta.2006.03.095.

(34) de Souza, R. F.; Padilha, J. C.; Gonçalves, R. S.; Dupont, J. Room Temperature Dialkylimidazolium Ionic Liquid-Based Fuel Cells. *Electrochem. commun.* **2003**, *5* (8), 728–731. https://doi.org/10.1016/S1388-2481(03)00173-5.

(35) Chagnes, A.; Carré, B.; Willmann, P.; Lemordant, D. Ion Transport Theory of Nonaqueous Electrolytes. LiClO4 in γ-Butyrolactone: The Quasi Lattice Approach. *Electrochim. Acta* **2001**, *46* (12), 1783–1791. https://doi.org/10.1016/S0013-4686(00)00718-0.

(36) Visser, A. E.; Swatloski, R. P.; Reichert, W. M.; Mayton, R.; Sheff, S.; Wierzbicki, A.; Davis, J. H.; Rogers, R. D. Task-Specific Ionic Liquids Incorporating Novel Cations for the Coordination and Extraction of Hg 2+ and Cd 2+ : Synthesis, Characterization, and Extraction Studies. *Environ. Sci. Technol.* **2002**, *36* (11), 2523–2529. https://doi.org/10.1021/es0158004.

(37) Huddleston, J. G.; Willauer, H. D.; Swatloski, R. P.; Visser, A. E.; Rogers, R. D. Room Temperature Ionic Liquids as Novel Media for 'Clean' Liquid–liquid Extraction. *Chem. Commun.* **1998**, No. 16, 1765–1766. https://doi.org/10.1039/A803999B.

(38) Quinn, B. M.; Ding, Z.; Moulton, R.; Bard, A. J. Novel Electrochemical Studies of Ionic Liquids. *Langmuir* **2002**, *18* (5), 1734–1742. https://doi.org/10.1021/la011458x.

(39) Wei, G.-T.; Yang, Z.; Chen, C.-J. Room Temperature Ionic Liquid as a Novel Medium for Liquid/Liquid Extraction of Metal Ions. *Anal. Chim. Acta* **2003**, *488* (2), 183–192. https://doi.org/10.1016/S0003-2670(03)00660-3.

(40) Borra, E. F.; Seddiki, O.; Angel, R.; Eisenstein, D.; Hickson, P.; Seddon, K. R.; Worden, S. P. Deposition of Metal Films on an Ionic Liquid as a Basis for a Lunar Telescope. *Nature* **2007**, *447* (7147), 979–981. https://doi.org/10.1038/nature05909.

(41) Hough, W. L.; Smiglak, M.; Rodríguez, H.; Swatloski, R. P.; Spear, S. K.; Daly, D. T.; Pernak, J.; Grisel, J. E.; Carliss, R. D.; Soutullo, M. D.; Davis, Jr., J. H.; Rogers, R. D. The Third Evolution of Ionic Liquids: Active Pharmaceutical Ingredients. *New J. Chem.* **2007**, *31* (8), 1429. https://doi.org/10.1039/b706677p.

(42) Weyershausen, B.; Lehmann, K. Industrial Application of Ionic Liquids as Performance Additives. *Green Chem.* **2005**, *7* (1), 15. https://doi.org/10.1039/b411357h.

(43) Canongia Lopes, J. N.; Costa Gomes, M. F.; Husson, P.; Pádua, A. A. H.; Rebelo, L. P. N.; Sarraute, S.; Tariq, M. Polarity, Viscosity, and Ionic Conductivity of Liquid Mixtures Containing [C 4 C 1 Im][Ntf 2] and a Molecular Component. *J. Phys. Chem. B* **2011**, *115* (19), 6088–6099. https://doi.org/10.1021/jp2012254.

(44) Rizzuto, A. M.; Pennington, R. L.; Sienerth, K. D. Study of the BMIM-PF6: Acetonitrile Binary Mixture as a Solvent for Electrochemical Studies Involving CO2. *Electrochim. Acta* **2011**, *56* (14), 5003–5009. https://doi.org/10.1016/j.electacta.2011.03.106.

(45) Li, W.; Zhang, Z.; Han, B.; Hu, S.; Xie, Y.; Yang, G. Effect of Water and Organic Solvents on the Ionic Dissociation of Ionic Liquids. *J. Phys. Chem. B* **2007**, *111* (23), 6452–6456. https://doi.org/10.1021/jp071051m.

(46) Wang, J.; Tian, Y.; Zhao, Y.; Zhuo, K. A Volumetric and Viscosity Study for the Mixtures of 1-n-Butyl-3-Methylimidazolium Tetrafluoroborate Ionic Liquid with Acetonitrile, Dichloromethane, 2-Butanone and N, N ? Dimethylformamide. *Green Chem.* **2003**, *5* (5), 618. https://doi.org/10.1039/b303735e.

(47) Stoppa, A.; Hunger, J.; Buchner, R. Conductivities of Binary Mixtures of Ionic Liquids with Polar Solvents. *J. Chem. Eng. Data* **2009**, *54* (2), 472–479. https://doi.org/10.1021/je800468h.

(48) Chagnes, A.; Diaw, M.; Carré, B.; Willmann, P.; Lemordant, D. Imidazolium-Organic Solvent Mixtures as Electrolytes for Lithium Batteries. *J. Power Sources* **2005**, *145* (1), 82–88. https://doi.org/10.1016/j.jpowsour.2004.12.035.

(49) Trivedi, S.; Sarkar, A.; Pandey, S. Solvatochromic Absorbance Probe Behavior within 1-Butyl-3-Methylimidazolium Hexafluorophosphate+propylene Carbonate: Preferential Solvation or Solvent–solvent Interaction? *Chem. Eng. J.* **2009**, *147* (1), 36–42. https://doi.org/10.1016/j.cej.2008.11.014.

(50) Koverga, V. A.; Voroshylova, I. V.; Smortsova, Y.; Miannay, F.-A.; Cordeiro, M. N. D. S.; Idrissi, A.; Kalugin, O. N. Local Structure and Hydrogen Bonding in Liquid γ-Butyrolactone and Propylene Carbonate: A Molecular Dynamics Simulation. *J. Mol. Liq.* **2019**, *287*, 110912. https://doi.org/10.1016/j.molliq.2019.110912.

(51) Chang, H.-C.; Tsai, T.-T.; Kuo, M.-H. Using High-Pressure Infrared Spectroscopy to Study the Interactions between Triblock Copolymers and Ionic Liquids. *Macromolecules* **2014**, *47* (9), 3052–3058. https://doi.org/10.1021/ma500493p.

(52) Jiang, J. C.; Li, S. C.; Shih, P. M.; Hung, T. C.; Chang, S. C.; Lin, S. H.; Chang, H. C. A High-Pressure Infrared Spectroscopic Study on the Interaction of Ionic Liquids with PEO-PPO-PEO Block Copolymers and 1,4-Dioxane. *J. Phys. Chem. B* **2011**, *115* (5), 883–888. https://doi.org/10.1021/jp109600c.

(53) Zhang, L.; Wang, Y.; Xu, Z.; Li, H. Comparison of the Blue-Shifted C-D Stretching Vibrations for DMSO-d 6 in Imidazolium-Based Room Temperature Ionic Liquids and in Water. *J. Phys. Chem. B* **2009**, *113* (17), 5978–5984. https://doi.org/10.1021/jp900139z.

(54) Zheng, Y. Z.; He, H. Y.; Zhou, Y.; Yu, Z. W. Hydrogen-Bonding Interactions between [BMIM][BF4] and Dimethyl Sulfoxide. *J. Mol. Struct.* **2014**, *1069* (1), 140–146. https://doi.org/10.1016/j.molstruc.2014.01.013.

(55) Jiang, J.-C.; Lin, K.-H.; Li, S.-C.; Shih, P.-M.; Hung, K.-C.; Lin, S. H.; Chang, H.-C.

Association Structures of Ionic Liquid/DMSO Mixtures Studied by High-Pressure Infrared Spectroscopy. *J. Chem. Phys.* **2011**, *134* (4), 044506. https://doi.org/10.1063/1.3526485.

(56) Jeon, Y.; Sung, J.; Kim, D.; Seo, C.; Cheong, H.; Ouchi, Y.; Ozawa, R.; Hamaguchi, H. O. Structural Change of 1-Butyl-3-Methylimidazolium Tetrafluoroborate + Water Mixtures Studied by Infrared Vibrational Spectroscopy. *J. Phys. Chem. B* **2008**, *112* (3), 923–928. https://doi.org/10.1021/jp0746650.

(57) Jeon, Y.; Sung, J.; Seo, C.; Lim, H.; Cheong, H.; Kang, M.; Moon, B.; Ouchi, Y.; Kim, D. Structures of Ionic Liquids with Different Anions Studied by Infrared Vibration Spectroscopy. *J. Phys. Chem. B* **2008**, *112* (15), 4735–4740. https://doi.org/10.1021/jp7120752.

(58) Roth, C.; Appelhagen, A.; Jobst, N.; Ludwig, R. Microheterogeneities in Ionic-Liquid-Methanol Solutions Studied by FTIR Spectroscopy, DFT Calculations and Molecular Dynamics Simulations. *ChemPhysChem* **2012**, *13* (7), 1708–1717. https://doi.org/10.1002/cphc.201101022.

(59) Singh, T.; Rao, K. S.; Kumar, A. Polarity Behaviour and Specific Interactions of Imidazolium-Based Ionic Liquids in Ethylene Glycol. *ChemPhysChem* **2011**, *12* (4), 836–845. https://doi.org/10.1002/cphc.201000826.

(60) Bhat, M. A.; Dutta, C. K.; Rather, G. M. Exploring Physicochemical Aspects of N-Alkylimidazolium Based Ionic Liquids. *J. Mol. Liq.* **2013**, *181*, 142–151. https://doi.org/10.1016/j.molliq.2013.02.021.

(61) Takamuku, T.; Kyoshoin, Y.; Shimomura, T.; Kittaka, S.; Yamaguchi, T. Effect of Water on Structure of Hydrophilic Imidazolium-Based Ionic Liquid. *J. Phys. Chem. B* **2009**, *113* (31), 10817–10824. https://doi.org/10.1021/jp9042667.

(62) Cha, S.; Ao, M.; Sung, W.; Moon, B.; Ahlström, B.; Johansson, P.; Ouchi, Y.; Kim, D. Structures of Ionic Liquid-Water Mixtures Investigated by IR and NMR Spectroscopy. *Phys. Chem. Chem. Phys.* **2014**, *16* (20), 9591–9601. https://doi.org/10.1039/c4cp00589a.

(63) Snežzana Miljanić, Leo Frkanec, Tomislav Biljan, 3 Zlatko Meić Mladen Žini ć. Recent Advances in Linear and Nonlinear Raman Spectroscopy I. *J. Raman Spectrosc.* **2007**, *38* (April), 1538–1553. https://doi.org/10.1002/jrs.

(64) Li, X.; Zhang, Y.; Tang, J.; Lan, A.; Yang, Y.; Gibril, M.; Yu, M. Efficient Preparation of High Concentration Cellulose Solution with Complex DMSO/ILs Solvent. *J. Polym. Res.* **2016**, *23* (2), 32. https://doi.org/10.1007/s10965-016-0922-8.

(65) Majhi, D.; Pabbathi, A.; Sarkar, M. Probing the Aggregation Behavior of Neat Imidazolium-Based Alkyl Sulfate (Alkyl = Ethyl, Butyl, Hexyl, and Octyl) Ionic Liquids through Time Resolved Florescence Anisotropy and NMR and Fluorescence Correlation Spectroscopy Study. *J. Phys. Chem. B* **2016**, *120* (1), 193–205. https://doi.org/10.1021/acs.jpcb.5b10137.

(66) Zheng, Y. Z.; Zhou, Y.; Deng, G.; Yu, Z. W. Hydrogen-Bonding Interactions between a Nitrile-Based Functional Ionic Liquid and DMSO. *J. Mol. Struct.* **2016**, *1124*, 207–215. https://doi.org/10.1016/j.molstruc.2016.01.071.

(67) Radhi, A.; Le, K. A.; Ries, M. E.; Budtova, T. Macroscopic and Microscopic Study of 1-Ethyl-3-Methyl-Imidazolium Acetate–DMSO Mixtures. *J. Phys. Chem. B* **2015**, *119* (4), 1633–1640. https://doi.org/10.1021/jp5112108.

(68) Katsyuba, S. A.; Griaznova, T. P.; Vidis, A.; Dyson, P. J. Structural Studies of the Ionic Liquid 1-Ethyl-3-Methylimidazolium Tetrafluoroborate in Dichloromethane Using a Combined DFT-NMR Spectroscopic Approach. *J. Phys. Chem. B* **2009**, *113* (15), 5046–5051. https://doi.org/10.1021/jp8083327.

(69) Cade, E. A.; Petenuci, J.; Hoffmann, M. M. Aggregation Behavior of Several Ionic Liquids in Molecular Solvents of Low Polarity - Indication of a Bimodal Distribution. *ChemPhysChem* **2016**, *17* (4), 520–529. https://doi.org/10.1002/cphc.201500990.

(70) Zheng, Y.-Z.; Wang, N.-N.; Luo, J.-J.; Zhou, Y.; Yu, Z.-W. Hydrogen-Bonding Interactions between [BMIM][BF4] and Acetonitrile. *Phys. Chem. Chem. Phys.* **2013**, *15* (41), 18055. https://doi.org/10.1039/c3cp53356e.

(71) Zhai, C.; Wang, J.; Xuan, X.; Wang, H.; Chen, M. Interactions of 1-Hexyl-3-Methylimidazolium Bromide with Acetone. *Chinese J. Chem. Phys.* **2006**, *19* (5), 447–450. https://doi.org/10.1360/cjcp2006.19(5).447.4.

(72) Zhang, Q.-G.; Wang, N.-N.; Wang, S.-L.; Yu, Z.-W. Hydrogen Bonding Behaviors of Binary Systems Containing the Ionic Liquid 1-Butyl-3-Methylimidazolium Trifluoroacetate and Water/Methanol. *J. Phys. Chem. B* **2011**, *115* (38), 11127–11136. https://doi.org/10.1021/jp204305g.

(73) Marekha, B. A.; Kalugin, O. N.; Bria, M.; Idrissi, A. Probing Structural Patterns of Ion Association and Solvation in Mixtures of Imidazolium Ionic Liquids with Acetonitrile by Means of Relative 1H and 13C NMR Chemical Shifts. *Phys. Chem. Chem. Phys.* **2015**, *17* (35), 23183–23194. https://doi.org/10.1039/c5cp02748a.

(74) Remsing, R. C.; Liu, Z.; Sergeyev, I.; Moyna, G. Solvation and Aggregation of N,N′ -Dialkylimidazolium Ionic Liquids: A Multinuclear NMR Spectroscopy and Molecular Dynamics Simulation Study. *J. Phys. Chem. B* **2008**, *112* (25), 7363–7369. https://doi.org/10.1021/jp800769u.

(75) Scharf, N. T.; Stark, A.; Hoffmann, M. M. Ion Pairing and Dynamics of the Ionic Liquid 1-Hexyl-3-Methylimidazolium Bis(Irifluoromethylsulfonyl)Amide ([C6mim][NTf2]) in the Low Dielectric Solvent Chloroform. *J. Phys. Chem. B* **2012**, *116* (37), 11488–11497. https://doi.org/10.1021/jp3047592.

(76) Marekha, B. A.; Kalugin, O. N.; Bria, M.; Takamuku, T.; Gadžurić, S.; Idrissi, A. Competition between Cation–Solvent and Cation–Anion Interactions in Imidazolium Ionic Liquids with Polar Aprotic Solvents. *ChemPhysChem* **2017**, *18* (7), 718–721. https://doi.org/10.1002/cphc.201601445.

(77) D'Anna, F.; Cascino, M.; Meo, P. Lo; Riela, S.; Noto, R. The Effect of Some Amines and Alcohols on the Organized Structure of [Bmim][BF4] Investigated by 1H NMR Spectroscopy. *Arkivoc* **2008**, *2009* (8), 30–46. https://doi.org/10.3998/ark.5550190.0010.804.

(78) Su, B. M.; Zhang, S.; Zhang, Z. C. Structural Elucidation of Thiophene Interaction with Ionic Liquids by Multinuclear NMR Spectroscopy. *J. Phys. Chem. B* **2004**, *108* (50), 19510–19517. https://doi.org/10.1021/jp0490271.

(79) Zheng, Y. Z.; Wang, N. N.; Luo, J. J.; Zhou, Y.; Yu, Z. W. Hydrogen-Bonding Interactions between [BMIM][BF4] and Acetonitrile. *Phys. Chem. Chem. Phys.* **2013**, *15* (41), 18055–18064. https://doi.org/10.1039/c3cp53356e.

(80) Bonhôte, P.; Dias, A.-P.; Papageorgiou, N.; Kalyanasundaram, K.; Grätzel, M. Hydrophobic, Highly Conductive Ambient-Temperature Molten Salts. *Inorg. Chem.* **1996**, *35* (5), 1168–1178. https://doi.org/10.1021/ic951325x.

(81) Avent, A. G.; Chaloner, P. A.; Day, M. P.; Seddon, K. R.; Welton, T. Evidence for Hydrogen Bonding in Solutions of 1-Ethyl-3-Methylimidazolium Halides, and Its Implications for Room-Temperature Halogenoaluminate(III) Ionic Liquids. *J. Chem. Soc. Dalt. Trans.* **1994**, No. 23, 3405. https://doi.org/10.1039/dt9940003405.

(82) Stoppa, A.; Hunger, J.; Hefter, G.; Buchner, R. Structure and Dynamics of 1- N -Alkyl-3- N -Methylimidazolium Tetrafluoroborate + Acetonitrile Mixtures. *J. Phys. Chem. B* **2012**, *116* (25), 7509–7521. https://doi.org/10.1021/jp3020673.

(83) Koverga, V. A.; Smortsova, Y.; Miannay, F. A.; Kalugin, O. N.; Takamuku, T.; Jedlovszky, P.; Marekha, B.; Cordeiro, M. N. D. S.; Idrissi, A. Distance Angle Descriptors of the Interionic and Ion–Solvent Interactions in Imidazolium-Based Ionic Liquid Mixtures with Aprotic Solvents: A Molecular Dynamics Simulation Study. *J. Phys. Chem. B* **2019**, *123* (28), 6065–6075. https://doi.org/10.1021/acs.jpcb.9b03838.

(84) Fakis, M.; Stathatos, E.; Tsigaridas, G.; Giannetas, V.; Persephonis, P. Femtosecond Decay and Electron Transfer Dynamics of the Organic Sensitizer D149 and Photovoltaic Performance in Quasi-Solid-State Dye-Sensitized Solar Cells. *J. Phys. Chem. C* **2011**, *115* (27), 13429–13437. https://doi.org/10.1021/jp201143n.

(85) Fakis, M.; Hrobárik, P.; Stathatos, E.; Giannetas, V.; Persephonis, P. A Time Resolved Fluorescence and Quantum Chemical Study of the Solar Cell Sensitizer D149. *Dye. Pigment.* **2013**, *96* (1), 304–312. https://doi.org/10.1016/j.dyepig.2012.07.025.

(86) Lohse, P. W.; Kuhnt, J.; Druzhinin, S. I.; Scholz, M.; Ekimova, M.; Oekermann, T.; Lenzer, T.; Oum, K. Ultrafast Photoinduced Relaxation Dynamics of the Indoline Dye D149 in Organic Solvents. *Phys. Chem. Chem. Phys.* **2011**, *13* (43), 19632. https://doi.org/10.1039/c1cp22429h.

(87) El-Zohry, A.; Orthaber, A.; Zietz, B. Isomerization and Aggregation of the Solar Cell Dye D149. *J. Phys. Chem. C* **2012**, *116* (50), 26144–26153. https://doi.org/10.1021/jp306636w.

(88) El-Zohry, A. M.; Zietz, B. Concentration and Solvent Effects on the Excited State Dynamics of the Solar Cell Dye D149: The Special Role of Protons. *J. Phys. Chem. C* **2013**, *117* (13), 6544–6553. https://doi.org/10.1021/jp400782g.

(89) Lin, Y.-D.; Chow, T. J. Geometrical Effect of Stilbene on the Performance of Organic Dye-Sensitized Solar Cells. *J. Mater. Chem.* **2011**, *21* (38), 14907. https://doi.org/10.1039/c1jm11623a.

(90) El-Zohry, A. M.; Roca-Sanjuán, D.; Zietz, B. Ultrafast Twisting of the Indoline Donor Unit Utilized in Solar Cell Dyes: Experimental and Theoretical Studies. *J. Phys. Chem. C* **2015**, *119* (5), 2249–2259. https://doi.org/10.1021/jp505649s.

(91) El-Zohry, A. M.; Agrawal, S.; De Angelis, F.; Pastore, M.; Zietz, B. Critical Role of Protons for Emission Quenching of Indoline Dyes in Solution and on Semiconductor Surfaces. *J. Phys. Chem. C* **2020**, *124* (39), 21346–21356. https://doi.org/10.1021/acs.jpcc.0c07099.

(92) El-Zohry, A. M. The Origin of Slow Electron Injection Rates for Indoline Dyes Used in Dye-Sensitized Solar Cells. *Dye. Pigment.* **2019**, *160* (August 2018), 671–674.

https://doi.org/10.1016/j.dyepig.2018.09.002.

(93) Pastore, M.; Fantacci, S.; De Angelis, F. Modeling Excited States and Alignment of Energy Levels in Dye-Sensitized Solar Cells: Successes, Failures, and Challenges. *J. Phys. Chem. C* **2013**, *117* (8), 3685–3700. https://doi.org/10.1021/jp3095227.

(94) El-Zohry, A. M.; Roca-Sanjuán, D.; Zietz, B. Ultrafast Twisting of the Indoline Donor Unit Utilized in Solar Cell Dyes: Experimental and Theoretical Studies. *J. Phys. Chem. C* **2015**, *119* (5), 2249–2259. https://doi.org/10.1021/jp505649s.

(95) El-Zohry, A. M.; Zietz, B. Concentration and Solvent Effects on the Excited State Dynamics of the Solar Cell Dye D149: The Special Role of Protons. *J. Phys. Chem. C* **2013**, *117* (13), 6544–6553. https://doi.org/10.1021/jp400782g.

(96) Samanta, A. Solvation Dynamics in Ionic Liquids: What We Have Learned from the Dynamic Fluorescence Stokes Shift Studies. *J. Phys. Chem. Lett.* **2010**, *1* (10), 1557–1562. https://doi.org/10.1021/jz100273b.

(97) Samanta, A. Dynamic Stokes Shift and Excitation Wavelength Dependent Fluorescence of Dipolar Molecules in Room Temperature Ionic Liquids. *J. Phys. Chem. B* **2006**, *110* (28), 13704–13716. https://doi.org/10.1021/jp060441q.

(98) Sahu, P. K.; Das, S. K.; Sarkar, M. Fluorescence Response of a Dipolar Organic Solute in a Dicationic Ionic Liquid (IL): Is the Behavior of Dicationic IL Different from That of Usual Monocationic IL? *Phys. Chem. Chem. Phys.* **2014**, *16* (25), 12918–12928. https://doi.org/10.1039/C4CP01053A.

(99) Paul, A.; Samanta, A. Solute Rotation and Solvation Dynamics in an Alcohol-Functionalized Room Temperature Ionic Liquid †. *J. Phys. Chem. B* **2007**, *111* (18), 4724–4731. https://doi.org/10.1021/jp065790z.

(100) Paul, A.; Samanta, A. Effect of Nonpolar Solvents on the Solute Rotation and Solvation Dynamics in an Imidazolium Ionic Liquid. *J. Phys. Chem. B* **2008**, *112* (3), 947–953. https://doi.org/10.1021/jp077536s.

(101) Liang, M.; Zhang, X.-X.; Kaintz, A.; Ernsting, N. P.; Maroncelli, M. Solvation Dynamics in a Prototypical Ionic Liquid + Dipolar Aprotic Liquid Mixture: 1-Butyl-3-Methylimidazolium Tetrafluoroborate + Acetonitrile. *J. Phys. Chem. B* **2014**, *118* (5), 1340–1352. https://doi.org/10.1021/jp412086t.

(102) Karmakar, R.; Samanta, A. Steady-State and Time-Resolved Fluorescence Behavior of C153 and PRODAN in Room-Temperature Ionic Liquids. *J. Phys. Chem. A* **2002**, *106* (28), 6670–6675. https://doi.org/10.1021/jp0143591.

(103) Horng, M. L.; Gardecki, J. A.; Papazyan, A.; Maroncelli, M. Subpicosecond Measurements of Polar Solvation Dynamics: Coumarin 153 Revisited. *J. Phys. Chem.* **1995**, *99* (48), 17311–17337. https://doi.org/10.1021/j100048a004.

(104) Lohse, P. W.; Bartels, N.; Stoppa, A.; Buchner, R.; Lenzer, T.; Oum, K. Dielectric Relaxation and Ultrafast Transient Absorption Spectroscopy of [C6mim]+[Tf2N]−/Acetonitrile Mixtures. *Phys. Chem. Chem. Phys.* **2012**, *14* (10), 3596. https://doi.org/10.1039/c2cp23704k.

(105) Maity, N.; Piatkowski, P.; Polok, K.; Miannay, F.-A.; Idrissi, A. Effect of the Mixture Composition of BmimBF 4 –Acetonitrile on the Excited-State Relaxation Dynamics of a Solar-

Cell Dye D149: An Ultrafast Transient Absorption Study. *J. Phys. Chem. C* **2021**, *125* (32), 17841–17852. https://doi.org/10.1021/acs.jpcc.1c05008.

(106) Paul, S.; Panda, A. K. Physicochemical Investigations on the Aqueous Solution of an Ionic Liquid, 1-Butyl-3-Methylimidazolium Methanesulfonate, [Bmim][MS], in a Concentrated and Dilute Regime. *Colloids Surfaces A Physicochem. Eng. Asp.* **2012**, *404*, 1–11. https://doi.org/10.1016/j.colsurfa.2012.01.034.

(107) Gautam, R. K.; Bapli, A.; Jana, R.; Seth, D. Photophysics and Rotational Dynamics of Nile Red in Room Temperature Ionic Liquid (RTIL) and RTIL-Cosolvents Binary Mixtures. *J. Photochem. Photobiol. A Chem.* **2020**, *399* (April), 112550. https://doi.org/10.1016/j.jphotochem.2020.112550.

(108) Bangle, R. E.; Meyer, G. J. Factors That Control the Direction of Excited-State Electron Transfer at Dye-Sensitized Oxide Interfaces. *J. Phys. Chem. C* **2019**, *123* (42), 25967–25976. https://doi.org/10.1021/acs.jpcc.9b06755.

(109) Hsu, H.-Y.; Wang, C.-Y.; Fathi, A.; Shiu, J.-W.; Chung, C.-C.; Shen, P.-S.; Guo, T.-F.; Chen, P.; Lee, Y.-P.; Diau, E. W.-G. Femtosecond Excitonic Relaxation Dynamics of Perovskite on Mesoporous Films of Al 2 O 3 and NiO Nanoparticles. *Angew. Chemie* **2014**, *126* (35), 9493–9496. https://doi.org/10.1002/ange.201404213.

(110) Zhang, L.; Yang, X.; Wang, W.; Gurzadyan, G. G.; Li, J.; Li, X.; An, J.; Yu, Z.; Wang, H.; Cai, B.; Hagfeldt, A.; Sun, L. 13.6% Efficient Organic Dye-Sensitized Solar Cells by Minimizing Energy Losses of the Excited State. *ACS Energy Lett.* **2019**, *4* (4), 943–951. https://doi.org/10.1021/acsenergylett.9b00141.

(111) Zhang, M.; Yang, L.; Yan, C.; Ma, W.; Wang, P. Multiple-State Interfacial Electron Injection Competes with Excited State Relaxation and de-Excitation to Determine External Quantum Efficiencies of Organic Dye-Sensitized Solar Cells. *Phys. Chem. Chem. Phys.* **2014**, *16* (38), 20578–20585. https://doi.org/10.1039/C4CP03230F.

(112) Lohse, P. W.; Kuhnt, J.; Druzhinin, S. I.; Scholz, M.; Ekimova, M.; Oekermann, T.; Lenzer, T.; Oum, K. Ultrafast Photoinduced Relaxation Dynamics of the Indoline Dye D149 in Organic Solvents. *Phys. Chem. Chem. Phys.* **2011**, *13* (43), 19632. https://doi.org/10.1039/c1cp22429h.

(113) Oum, K.; Lohse, P. W.; Flender, O.; Klein, J. R.; Scholz, M.; Lenzer, T.; Du, J.; Oekermann, T. Ultrafast Dynamics of the Indoline Dye D149 on Electrodeposited ZnO and Sintered ZrO2 and TiO2 Thin Films. *Phys. Chem. Chem. Phys.* **2012**, *14* (44), 15429. https://doi.org/10.1039/c2cp42961f.

(114) Fakis, M.; Stathatos, E.; Tsigaridas, G.; Giannetas, V.; Persephonis, P. Femtosecond Decay and Electron Transfer Dynamics of the Organic Sensitizer D149 and Photovoltaic Performance in Quasi-Solid-State Dye-Sensitized Solar Cells. *J. Phys. Chem. C* **2011**, *115* (27), 13429–13437. https://doi.org/10.1021/jp201143n.

(115) Smortsova, Y. Thèse de Yevheniia Smortsova, Université de Lille, 2018. **2018**.

(116) Maroncelli, M.; Fleming, G. R. Picosecond Solvation Dynamics of Coumarin 153: The Importance of Molecular Aspects of Solvation. *J. Chem. Phys.* **1987**, *86* (11), 6221–6239. https://doi.org/10.1063/1.452460.

(117) Chowdhury, P. K.; Halder, M.; Sanders, L.; Calhoun, T.; Anderson, J. L.; Armstrong, D. W.;

Song, X.; Petrich, J. W. Dynamic Solvation in Room-Temperature Ionic Liquids. *J. Phys. Chem. B* **2004**, *108* (29), 10245–10255. https://doi.org/10.1021/jp0376828.

(118) Karmakar, R.; Samanta, A. Steady-State and Time-Resolved Fluorescence Behavior of C153 and PRODAN in Room-Temperature Ionic Liquids. *J. Phys. Chem. A* **2002**, *106* (28), 6670–6675. https://doi.org/10.1021/jp0143591.

(119) Maroncelli, M.; Zhang, X.-X.; Liang, M.; Roy, D.; Ernsting, N. P. Measurements of the Complete Solvation Response of Coumarin 153 in Ionic Liquids and the Accuracy of Simple Dielectric Continuum Predictions. *Faraday Discuss.* **2012**, *154*, 409–424. https://doi.org/10.1039/C1FD00058F.

(120) Samanta, A. Dynamic Stokes Shift and Excitation Wavelength Dependent Fluorescence of Dipolar Molecules in Room Temperature Ionic Liquids. *J. Phys. Chem. B* **2006**, *110* (28), 13704–13716. https://doi.org/10.1021/jp060441q.

(121) Chakrabarty, D.; Chakraborty, A.; Seth, D.; Hazra, P.; Sarkar, N. Dynamics of Solvation and Rotational Relaxation of Coumarin 153 in 1-Butyl-3-Methylimidazolium Hexafluorophosphate [Bmim][PF6]–water Mixtures. *Chem. Phys. Lett.* **2004**, *397* (4–6), 469–474. https://doi.org/10.1016/j.cplett.2004.08.141.

(122) Smortsova, Y.; Miannay, F.-A.; Oher, H.; Marekha, B.; Dubois, J.; Sliwa, M.; Kalugin, O.; Idrissi, A. Solvation Dynamics and Rotation of Coumarin 153 in a New Ionic Liquid/Molecular Solvent Mixture Model: [BMIM][TFSI]/Propylene Carbonate. *J. Mol. Liq.* **2017**, *226*, 48–55. https://doi.org/10.1016/j.molliq.2016.10.008.

(123) Liang, M.; Zhang, X. X.; Kaintz, A.; Ernsting, N. P.; Maroncelli, M. Solvation Dynamics in a Prototypical Ionic Liquid + Dipolar Aprotic Liquid Mixture: 1-Butyl-3-Methylimidazolium Tetrafluoroborate + Acetonitrile. *J. Phys. Chem. B* **2014**, *118* (5), 1340–1352. https://doi.org/10.1021/jp412086t.

(124) Blanco-Rodríguez, A. M.; Ronayne, K. L.; Záliš, S.; Sýkora, J.; Hof, M.; Vlček, A. Solvation-Driven Excited-State Dynamics of [Re(4-Et-Pyridine)(CO) 3 (2,2‘-Bipyridine)] + in Imidazolium Ionic Liquids. A Time-Resolved Infrared and Phosphorescence Study. *J. Phys. Chem. A* **2008**, *112* (16), 3506–3514. https://doi.org/10.1021/jp710442v.

(125) Flender, O.; Scholz, M.; Klein, J. R.; Oum, K.; Lenzer, T. Excited-State Relaxation of the Solar Cell Dye D49 in Organic Solvents and on Mesoporous Al 2 O 3 and TiO 2 Thin Films. *Phys. Chem. Chem. Phys.* **2016**, *18* (37), 26010–26019. https://doi.org/10.1039/C6CP05167G.

(126) Stalke, S.; Wild, D. A.; Lenzer, T.; Kopczynski, M.; Lohse, P. W.; Oum, K. Solvent-Dependent Ultrafast Internal Conversion Dynamics of N′-Apo-β-Carotenoic-N′-Acids (n = 8, 10, 12). *Phys. Chem. Chem. Phys.* **2008**, *10* (16), 2180. https://doi.org/10.1039/b720037d.

(127) Kopczynski, M.; Ehlers, F.; Lenzer, T.; Oum, K. Evidence for an Intramolecular Charge Transfer State in 12‘-Apo-β-Caroten-12‘-Al and 8‘-Apo-β-Caroten-8‘-Al: Influence of Solvent Polarity and Temperature. *J. Phys. Chem. A* **2007**, *111* (25), 5370–5381. https://doi.org/10.1021/jp0672252.

(128) Ehlers, F.; Wild, D. A.; Lenzer, T.; Oum, K. Investigation of the S 1 /ICT → S 0 Internal Conversion Lifetime of 4‘-Apo-β-Caroten-4‘-Al and 8‘-Apo-β-Caroten-8‘-Al: Dependence on Conjugation Length and Solvent Polarity. *J. Phys. Chem. A* **2007**, *111* (12), 2257–2265. https://doi.org/10.1021/jp0676888.

(129) Wild, D. A.; Winkler, K.; Stalke, S.; Oum, K.; Lenzer, T. Extremely Strong Solvent Dependence of the S 1 → S 0 Internal Conversion Lifetime of 12′-Apo-β-Caroten-12′-Al. *Phys. Chem. Chem. Phys.* **2006**, *8* (21), 2499–2505. https://doi.org/10.1039/B601669C.

(130) Lohse, P. W.; Bürsing, R.; Lenzer, T.; Oum, K. Exploring 12‘-Apo-β-Carotenoic-12‘-Acid as an Ultrafast Polarity Probe for Ionic Liquids. *J. Phys. Chem. B* **2008**, *112* (10), 3048–3057. https://doi.org/10.1021/jp710766z.

(131) Das, S. K.; Sarkar, M. Steady-State and Time-Resolved Fluorescence Behavior of Coumarin-153 in a Hydrophobic Ionic Liquid and Ionic Liquid–toluene Mixture. *J. Mol. Liq.* **2012**, *165*, 38–43. https://doi.org/10.1016/j.molliq.2011.10.004.

(132) Dutta, R.; Jana, G.; Mondal, D.; Pyne, A.; Sil, S.; Chattaraj, P. K.; Sarkar, N. The Role of Viscosity in Various Dynamical Processes of Different Fluorophores in Ionic Liquid–cosolvent Mixtures: A Femtosecond Fluorescence Upconversion Study. *Photochem. Photobiol. Sci.* **2019**, *18* (6), 1359–1372. https://doi.org/10.1039/C9PP00045C.

(133) Nandi, S.; Parui, S.; Jana, B.; Bhattacharyya, K. Local Environment of Organic Dyes in an Ionic Liquid-Water Mixture: FCS and MD Simulation. *J. Chem. Phys.* **2018**, *149* (5), 054501. https://doi.org/10.1063/1.5027458.

(134) Panigrahi, M.; Dash, S.; Patel, S.; Mishra, B. K. Preferential Solvation of Styrylpyridinium Dyes in Binary Mixtures of Alcohols with Hexane, Dioxane, and Dichloromethane. *J. Phys. Chem. B* **2011**, *115* (1), 99–108. https://doi.org/10.1021/jp108002e.

(135) Prabhu, S. R.; Dutt, G. B. Rotational Diffusion of Organic Solutes in 1-Methyl-3-Octylimidazolium Tetrafluoroborate–Diethylene Glycol Mixtures: Influence of Organic Solvent on the Organized Structure of the Ionic Liquid. *J. Phys. Chem. B* **2014**, *118* (20), 5562–5569. https://doi.org/10.1021/jp5032459.

(136) Sarkar, S.; Pramanik, R.; Ghatak, C.; Setua, P.; Sarkar, N. Probing the Interaction of 1-Ethyl-3-Methylimidazolium Ethyl Sulfate ([Emim][EtSO 4]) with Alcohols and Water by Solvent and Rotational Relaxation. *J. Phys. Chem. B* **2010**, *114* (8), 2779–2789. https://doi.org/10.1021/jp907936s.

(137) Seth, D.; Sarkar, S.; Pramanik, R.; Ghatak, C.; Setua, P.; Sarkar, N. Photophysical Studies of a Hemicyanine Dye (LDS-698) in Dioxane−Water Mixture, in Different Alcohols, and in a Room Temperature Ionic Liquid. *J. Phys. Chem. B* **2009**, *113* (19), 6826–6833. https://doi.org/10.1021/jp810045h.

(138) Lohse, P. W.; Bartels, N.; Stoppa, A.; Buchner, R.; Lenzer, T.; Oum, K. Dielectric Relaxation and Ultrafast Transient Absorption Spectroscopy of [C6mim]+[Tf2N]−/Acetonitrile Mixtures. *Phys. Chem. Chem. Phys.* **2012**, *14* (10), 3596. https://doi.org/10.1039/c2cp23704k.

(139) Stoppa, A.; Hunger, J.; Hefter, G.; Buchner, R. Structure and Dynamics of 1- N -Alkyl-3- N -Methylimidazolium Tetrafluoroborate + Acetonitrile Mixtures. *J. Phys. Chem. B* **2012**, *116* (25), 7509–7521. https://doi.org/10.1021/jp3020673.

(140) Hunger, J.; Stoppa, A.; Buchner, R.; Hefter, G. Dipole Correlations in the Ionic Liquid 1-N-Ethyl-3-N-Methylimidazolium Ethylsulfate and Its Binary Mixtures with Dichloromethane. *J. Phys. Chem. B* **2009**, *113* (28), 9527–9537. https://doi.org/10.1021/jp9024574.

(141) Koel, M. Solvatochromic Study on Binary Solvent Mixtures with Ionic Liquids. *Zeitschrift für*

Naturforsch. A **2008**, *63* (7–8), 505–512. https://doi.org/10.1515/zna-2008-7-818.

(142) Ando, M.; Kawano, M.; Tashiro, A.; Takamuku, T.; Shirota, H. Low-Frequency Spectra of 1 - Methyl-3-Octylimidazolium Tetra Fl Uoroborate Mixtures with Methanol , Acetonitrile , and Dimethyl Sulfoxide : A Combined Study of Femtosecond Raman- Induced Kerr E Ff Ect Spectroscopy and Molecular Dynamics Simulations. **2020**. https://doi.org/10.1021/acs.jpcb.0c04870.

(143) Kawano, M.; Sadakane, K.; Iwase, H.; Matsugami, M.; Marekha, B. A.; Idrissi, A.; Takamuku, T. Assessment of the UCST-Type Liquid–liquid Phase Separation Mechanism of Imidazolium-Based Ionic Liquid, [C 8 Mim][TFSI], and 1,4-Dioxane by SANS, NMR, IR, and MD Simulations. *Phys. Chem. Chem. Phys.* **2021**, *23* (42), 24449–24463. https://doi.org/10.1039/D1CP01940F.

(144) Carissimi, G.; Montalbán, M. G.; Díaz Banos, F. G.; Víllora, G. Density, Refractive Index and Volumetric Properties of Water-Ionic Liquid Binary Systems with Imidazolium-Based Cations and Tetrafluoroborate, Triflate and Octylsulfate Anions at T = 293 to 343 K and p = 0.1 MPa. *J. Chem. Eng. Data* **2019**, *64* (3), 979–994. https://doi.org/10.1021/acs.jced.8b00854.

(145) Srinivasa Krishna, T.; Nain, A. K.; Chentilnath, S.; Punyaseshudu, D.; Munibhadrayya, B. Densities, Ultrasonic Speeds, Refractive Indices, Excess and Partial Molar Properties of Binary Mixtures of Imidazolium Based Ionic Liquid with Pyrrolidin-2-One at Temperatures from 298.15 L to 323.15 K. *J. Chem. Thermodyn.* **2016**, *101*, 103–114. https://doi.org/10.1016/j.jct.2016.05.021.

(146) Mancini, P. M.; Fortunato, G. G.; Adam, C. G.; Vottero, L. R. Solvent Effects on Chemical Processes: New Solvents Designed on the Basis of the Molecular–microscopic Properties of (Molecular Solvent + 1,3-Dialkylimidazolium) Binary Mixtures. *J. Phys. Org. Chem.* **2008**, *21* (2), 87–95. https://doi.org/10.1002/poc.1227.

Chapter 3

Comment on Polarity and Heterogeneity in Ionic Liquid - Molecular Solvent Mixtures: EPR Study

This chapter is mainly dedicated to the analysis of polarity of IL-MS mixtures in the whole mixture composition range using the Electron Paramagnetic Resonance (EPR) spectroscopy of a magnetic probe TEMPO. We have chosen the similar set of IL-MS mixtures i.e. four imidazolium ILs containing same Bmim cation and four different anions (BF_4, PF_6, TFO and TFSI) and three molecular solvents (ACN, γ-BL and PC) for this study also. We have two main goals to achieve through this EPR study. Firstly, to study and comment on the hyperfine coupling constant values, which is considered as a polarity parameter, of the EPR probe in these set of IL-MS mixtures. Secondly, to calculate and comment on the rotational relaxation time constant (τ_R) values of the probe molecules in the same set of mixtures. In addition, a detailed analysis about various polarity parameters while using the probe TEMPO is also carried out in case of $BmimBF_4$-ACN mixture.

3.1. Introduction:

While discussing the photophysics of the spectroscopic probes in different pure ILs and in various IL-MS mixtures, one need to characterize the polarity of these mediums first. Polarity of ILs and IL-MS mixtures had been measured using various solvatochromic[1–5] and EPR[6–10] probes and also using FT-IR,[11] RAMAN,[12] DRS[13,14] spectroscopic techniques. There are various ways of measuring the polarity of a solvent such as dipole moment, kinetic rate constant, Hildebrand solubility parameter, dielectric constant (ε), spectroscopic polarity parameters (magnetic A_N and optical E_T^N). There are various studies about the polarity of ionic liquids and their mixtures with molecular solvents. Two different set of polarity parameters give different results. While dielectric constants denote ILs as moderately polar (i.e. similar to n-pentanol), solvatochromic polarity parameters suggests that ILs are as polar as primary alcohols. Even there are two sets of results regarding these two polarity parameters in $BmimBF_4$-ACN mixtures. While the DRS study by Stoppa et al.,[14] showed an overall decrease of dielectric constant values from pure ACN to pure IL, solvatochromic polarity parameter (E_T^N) measured by Manchini et al.[15] had displayed an overall increase of E_T^N values while increasing X_{IL}. Thus, apparently the probe independent and probe dependent polarity parameters give us different ideas about the polarity of ILs and IL-MS mixtures. In this aspect, there also exists some previous reports by Wang et al.,[16,17] which suggest correlation between hyperfine coupling constant (A_N) measured by EPR and solvatochromic polarity parameter (E_T^N) measured by UV-Visible spectroscopy. However, all the studies related to the correlation between different polarity parameters were only shown in the case of pure solvents and in pure ionic liquids. To our knowledge, there are no studies related to the correlation between the polarity parameters in IL-MS mixtures.

In addition to the polarity, microheterogeneity is also an important property in the case of the imidazolium IL-MS mixtures. There are various previous experimental studies which suggest the presence of heterogeneities in imidazolium ILs.[6,10,26–29,18–25] As a result, non-Gaussian type rotational and translation diffusions are present in case of ILs. Indeed, Maroncelli et al. had showed that the rotational correlation time was acquired from the stretched exponential fitting of the fluorescence anisotropy decay of the dye C153.[19] Hu et al. had also showed the presence of dynamics heterogeneity which is the main reason behind the red edge effect (REE) in room temperature ILs by using MD simulations.[20] In a series of papers from Samanta group, it was described that the presence of heterogeneity in ILs is the main reason behind the excitation wavelength dependent fluorescence spectra in ILs.[21,23,30] Using EPR paramagnetic probe studies, one can also monitor the heterogeneities in ILs and also in IL-MS mixtures. The interactions between the EPR probe and the nearby microenvironment can give us idea about the microheterogeneity in the medium. Various EPR studies have also reported microheterogeneities in case of both in ILs and IL-MS mixtures.[6,6,37–46,10,47,48,26,31–36]

On the account of the EPR paramagnetic probe, nitroxide radicals are one of the most used among the available paramagnetic species. In general, radicals are very reactive species and unstable in the nature. However, nitroxide radicals are stable in room temperature. Therefore, these types of stable radicals are used in numerous chemical reactions. Besides this, due to the presence of unpaired electron in the anti-bonding orbital (SOMO)[49], nitroxide radicals also exhibit significant EPR signal and they are used as paramagnetic probes for EPR studies.[6,10,43,46,50–55,22,25,27–29,31,32,42] Various types of stable nitroxide radicals are used as spin levels for the EPR study, like TEMPO, TEMPOL, ATEMPO etc. to name a few. Among these available nitroxide probes, TEMPO has least number of interactions with the surrounding mediums (IL-MS mixtures in our case) due to absence of any substituted groups in the structure. As there exists various types of interactions in the IL-MS mixtures, other EPR probes with different substituted groups can complicate the situation by adding more and more interactions with the substituted groups in them. Therefore, we have used TEMPO for our study.

Furthermore, when a solute molecule is present in IL-MS mixtures, there exists various types of interactions in the medium. Although the electrostatic interactions are the most dominant one due to presence of ions in the mixture, other types of interactions like H-bonding, Van der Waals and even hydrophobic interactions (interaction by using hydrophobic moiety in the structure) are also present.[31,56] Various molecular modeling and simulations were also used to study the structures and interactions in ILs and IL-MS mixtures.[57–62] According to Tokuda et al.,[58] ILs are defined as self-organized phases with polar charged zones and non-polar regions containing the alkyl extensions. The size of alkyl extensions determines the size of nonpolar domains in different ionic liquids. The presence of both polar and nonpolar regions in ILs also explains the solvation of different types of solutes in them.

Another important information which can also be extracted from the spectral analysis of the EPR line-shape is the rotational correlation time (τ_R) of the probe. Various studies have been performed to show the viscosity dependence of the τ_R values in different solvents and ILs while using solvatochromic and EPR probes. In case of solvatochromic probes, fluorescence anisotropy studies are performed in general to study τ_R,[63,64,73–76,65–72] whereas the analysis of

the spectral broadening of EPR hyperfine lines can provide us the same information while using the EPR probes.[10,27,48,50,55,77–82,31,35,39,41–44,46] Khara et al. had shown that the temperature dependence of the τ_R values of C153 in various ILs follows the Stokes-Einstein-Debye (SED) relation in between stick and slip boundary conditions.[68] In a similar type of temperature dependent fluorescence anisotropy study using another fluorescence probe 9-PA, Dutt et al.[65] had shown the effect of cation and anion determining τ_R values in case of a set of imidazolium based ILs. Super-stick behavior of the temperature dependence of τ_R values was also noticed in case of various ILs.[71,76,83] In addition, Gierer-Wirtz type of viscosity dependence of τ_R values was also noticed in case of pure ILs.[43,46,48,53,54,82,84,85] However, the number of studies related to the rotational correlation times in the whole mixture compositions of IL and MS are quite low.[70,74,75,86–88] In general, composition and viscosity dependent changes of τ_R values were studied in those studies. Similar to the spectroscopic probes, the number of studies related to the EPR probes in IL-MS mixtures are also quite small,[37,89,90] and also, to our knowledge, there are no EPR studies in IL-MS mixtures other than IL-water mixture till now.

As we have discussed earlier about the correlation between the different polarity parameters in the case of IL-MS mixtures, the correlation between spectroscopic polarity parameters (A_N and E_T^N) and dielectric constant (ε) was shown using a modified Onsager's reaction field model.[16,17] Generally, Onsager's reaction field model is considered as a classic model to correlate the spectroscopic polarity parameters with the dielectric constant values of the medium. According to Onsager's reaction field theory,[91] a solute molecule polarizes the solvent surrounding it and this polarization generates an electric field, known as the reaction field. In this aspect, according to the linear solvation energy relationships (LSERs), the spectroscopic polarity parameters such as E_T^N and A_N are regarded as a sum of electrostatic interactions, hydrogen bonding and other specific interactions. However, the reaction field according to the Onsager's theory can be applied for electrostatic interaction term. Without other terms like hydrogen bonding and other specific interaction terms, these spectroscopic polarity parameters would be proportional to the reaction field. As the hydrogen bonding and other types of specific interactions can't be ignored while discussing about the ILs and IL-MS mixtures, the modified Onsager's reaction field model[16,17] should be applied while correlating the polarity parameters.

Considering the Onsager's reaction field, the molecular model of solvation[92] of molecules suggests the presence of three important components in a solute-solvent system which are solute, first solvation sphere and bulk solvent. Generally, radius of solute was used as the radius of reaction field in the Onsager equation. However, there are some modifications of Onsager's reaction field. Wang et al. introduced the primary solvation sphere alongside the radius of the probe/solute as the reaction field in applying Onsager model in correlating E_T^N and A_N with dielectric constant of different organic solvents and they found good agreement with experimental value.[16] They even extended their work by applying Onsager's theory in ionic liquids by modifying the reaction field.[17] However, due to the less-availability of experimental values of various polarity parameters like E_T^N, A_N and ε, this type of correlation wasn't performed yet in the case of IL-MS mixtures.

To sum up, in this chapter, we are going to discuss an overall CW-EPR study of the spin probe TEMPO in various imidazolium IL-MS mixtures. First, we will discuss composition dependent

changes of hyperfine coupling constants and rotational correlation times in the IL-MS mixtures. Then, we are going to discuss about a particular case, the EPR study of TEMPO in $BmimBF_4$-ACN mixture. In the case of this particular IL-MS mixture, we are going to use the similar type of correlation between A_N and ε values which were already used in case of pure counterparts. In addition, the relation between two spectroscopic polarity parameters (i.e. E_T^N and A_N) in case of $BmimBF_4$-ACN mixture is also discussed in this chapter. Besides, we are going to get further idea about the composition and viscosity dependence of the rotational relaxation time (τ_R) of the probe molecule while comparing with that of UV-visible probe coumarin 153 in the case of same binary mixture.

3.2. Sample Preparation:

The EPR probe TEMPO (purity 98%) was bought from Sigma Aldrich (Figure 3.1). All the ionic liquids and solvents were bought from the same places as discussed in chapter 1, section 1.2. All the samples were stored inside the glove box in inert gas atmosphere. In doing so, we can remove two sources of impurity in the EPR spectra. Firstly, the moisture of the air can't impure the ILs and solvents and also the probe. Secondly, the oxygen in the air can't also intervene the EPR signal. In addition, all the sample preparation processes were performed inside the inert atmosphere (argon filled) glove box. All the sample capillaries were vacuum-sealed inside the glove box. After all these steps, the tubes with samples and EPR probes became ready for the experiment. In this regard, the concentration of the EPR probe TEMPO in the solvents and solvent mixtures were $3 \times 10^{-4} - 5 \times 10^{-4}$ (M). This probe concentrations were kept almost similar throughout our whole sets of measurements.

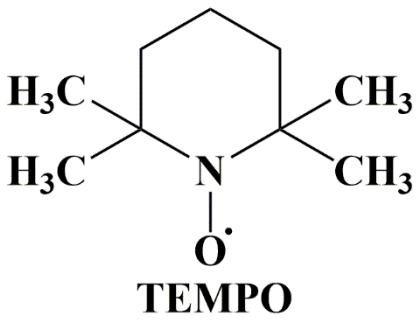

Figure 3.1: Structure of the EPR probe TEMPO

3.3. Results and discussion:

3.3.1. CW-EPR spectra:

In Figure 3.2, we can see the CW-EPR spectra of TEMPO in a particular IL-MS mixture ($BmimBF_4$-ACN). Other spectra are shown in the appendix and have similar characteristics as Figure 3.2. Therefore, they don't need further discussion (Figures C1-C4). In Figure 3.2, one can clearly notice the change of the shapes of the spectra while increasing X_{IL}. In pure solvents like ACN, γ-BL and PC, the TEMPO EPR spectra are symmetrical. However, while increasing IL mole fractions, the symmetry of the EPR spectra starts to decrease as the heights and width of the three EPR peaks start to become dissimilar. The two higher field peaks become wider

and the intensities start to decrease more and more as X_{IL} increases. This type of solvent dependent changes in EPR spectra was also noticed in previous studies. Mladenova et al.,[43,44] Akdogan et al.,[31] Dhale et al.[25] have also seen this type of broadening of EPR spectra in different ILs while using different EPR probes.

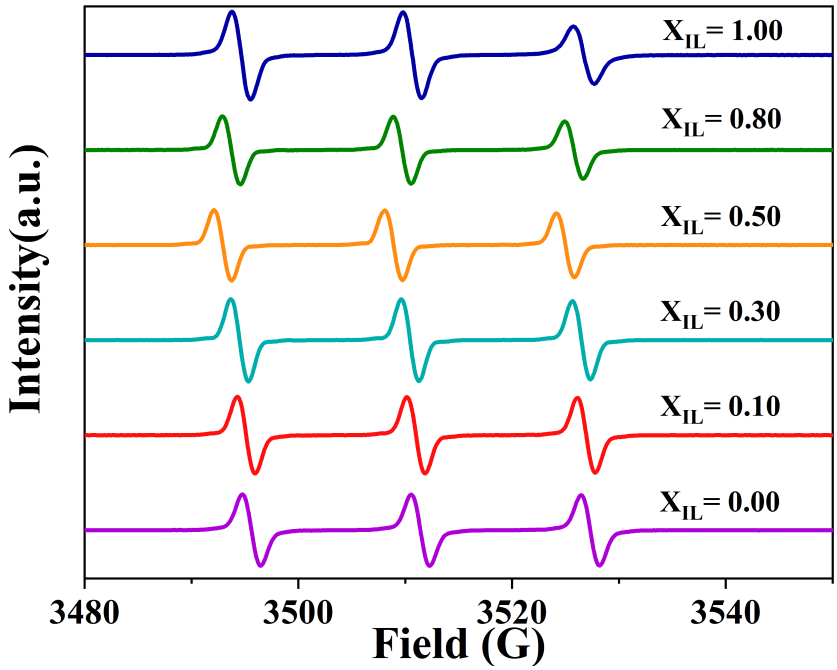

Figure 3.2: EPR signal of TEMPO in $BmimBF_4$-ACN mixture

Discussion about the shape of EPR spectra:

To describe this composition dependent spectral behavior, we need to consider heterogeneity in IL mediums. The EPR probe TEMPO is quite sensitive towards the changes in the surrounding mediums. As discussed earlier, ILs are mostly known as heterogeneous mediums. Moreover, EPR spectroscopy can probe this heterogeneity in ILs and IL-MS mixtures. Thus, previous EPR studies in pure ILs and also in IL-MS mixtures showed this type of decrease of symmetry and broadening of peaks of the EPR spectra.[6,10,30,35,18–21,23,25–27] The similar effect also has been noticed in case of our study. While increasing the X_{IL} of the IL-MS mixtures, the heterogeneity is increased in the surrounding mediums of the probe molecule (TEMPO). This increase of heterogeneity in the IL-MS mixtures eventually causes the decrease of symmetry of the EPR spectra. Now, to discuss more about heterogeneity in ILs, we need to take a look at their molecular structures. Although they are present as ions in the medium, they are not at all similar to the conventional salt solutions containing metal cations and different anions. The main structural characteristic of ILs that distinguishes them from conventional solvents is that they have a structure consisting of polar and non-polar domains. The latter domains are generally associated with the correlated position of the neutral alkyl side chains of the cations, which self-associate particularly for long alkyl chains (despite the expected repulsion forces) to form spatially heterogeneous domains. On the other hand, the polar domains, associated with both the positions of the cation rings as well as of the anions, are governed mainly by their attractive interactions. This induces a sort of charge ordering at the level of local structure. This heterogeneity creates inherent interfaces, which should influence the solvation process in such

media.[6,10,35,38,18–21,23–26] Indeed, the solvation of a solute depends strongly on its preferential localization in these different regions of the IL (i.e., within the polar network, in the non-polar domains, or at the interface between the polar and non-polar domains). This heterogeneity in ILs makes them interesting and difficult to study at the same time.[22,37,93–97] This type of heterogeneity in ILs eventually causes the decrease of symmetry in the EPR spectral shape.[6,10,30,35,18–21,23,25–27] Similar to these studies, while increasing X_{IL}, the heterogeneity increases in our case and the broadening of EPR spectral line-shapes increases eventually.

The EPR spectral shape showed that the spectral broadening is inevitable while increasing X_{IL} of all the studied IL-MS mixtures. When this spectral broadening happens to an EPR spectra, calculation of A_N values directly from the experimental EPR peaks is not accurate.[27] One needs to consider the average distance between the centers of the hyperfine lines in an EPR spectra to get the correct value of A_N.[25,44,98] Therefore, to get the correct analysis of the EPR spectra, we have used the SimLabel[99] tool which is basically a graphical user interface for the Easyspin[100] program. All the data analysis procedure is given in the EPR data analysis section of theories and experimental techniques chapter (Chapter 5, Section 5.4). In addition, an example of EPR spectral fitting is given in Figure C1(C) in the Appendix.

As a result of the EPR spectral fitting, one can get idea about the hyperfine coupling constant (A_N) and rotational relaxation time (τ_R) of the probe molecule TEMPO in the studied mixtures. First, we are going to discuss about the values of A_N of TEMPO in different pure components as well as in different IL-MS mixtures. Then we will do the same type of discussion in case of the τ_R of the probe molecule TEMPO.

3.3.2. The hyperfine coupling constant (A_N):

The hyperfine coupling constant of a particular EPR probe is the measure of the perturbation of its spin density distribution in a medium. In the viewpoint of the EPR spectra, the hyperfine coupling constant is nothing but the average distance between two EPR hyperfine lines. These A_N values have a physical importance. This is the EPR parameter which can be correlated to the medium polarity and they are considered as polarity parameter using probe molecules, similar to the solvatochromic polarity parameter E_T^N. It has been previously described that the A_N values are intimately related to the charge transfer (CT) nature of the EPR probe.[51,101] The more polar the solvent is, the more it can stabilize the CT structure of the EPR probes, which also has higher electron spin density on the nitrogen atom and higher A_N values.[51,101] Thus, the change of A_N values of the EPR probe can give us an idea about polarity of the medium.

First, we have tried to compare the values of A_N in pure solvents and also in pure ILs with previous results. In doing that, we have found a good agreement between the previous studies and our results.[25,28] All the analyzed A_N values of TEMPO in various IL-MS mixtures and previous values of A_N of TEMPO in pure solvents and ILs are shown in Tables C1, C2 and 3.2. The hyperfine coupling constant values in pure MSs used in this study are smaller than that in pure ILs, similar to the values of other spectroscopic polarity parameter E_N^T (Table 3.2). Similar type of correlations can also be noticed for the other EPR probes in pure solvents and also in ILs.[25,102] In this regard, it is pertinent to discuss that the dielectric constant values (ε) of pure ILs are quite smaller than that of pure MSs used in this study.[103–106] Thus, probe independent

(ε) and probe dependent (E_N^T and A_N) polarity parameters give us a conflicting idea about polarity of ILs and IL-MS mixtures. In addition, it is also true that, the concept of polarity in ionic liquids is dissimilar to that in conventional solvents due to their complex nanostructure and presence of charged species in the medium.[107] Therefore, it is important to get a correlation between these types of polarity parameters (probe dependent and probe independent). We will get further insights about the correlation between these polarity parameters in case of IL-MS mixtures while discussing the EPR study in $BmimBF_4$-ACN mixture (section 3.4).

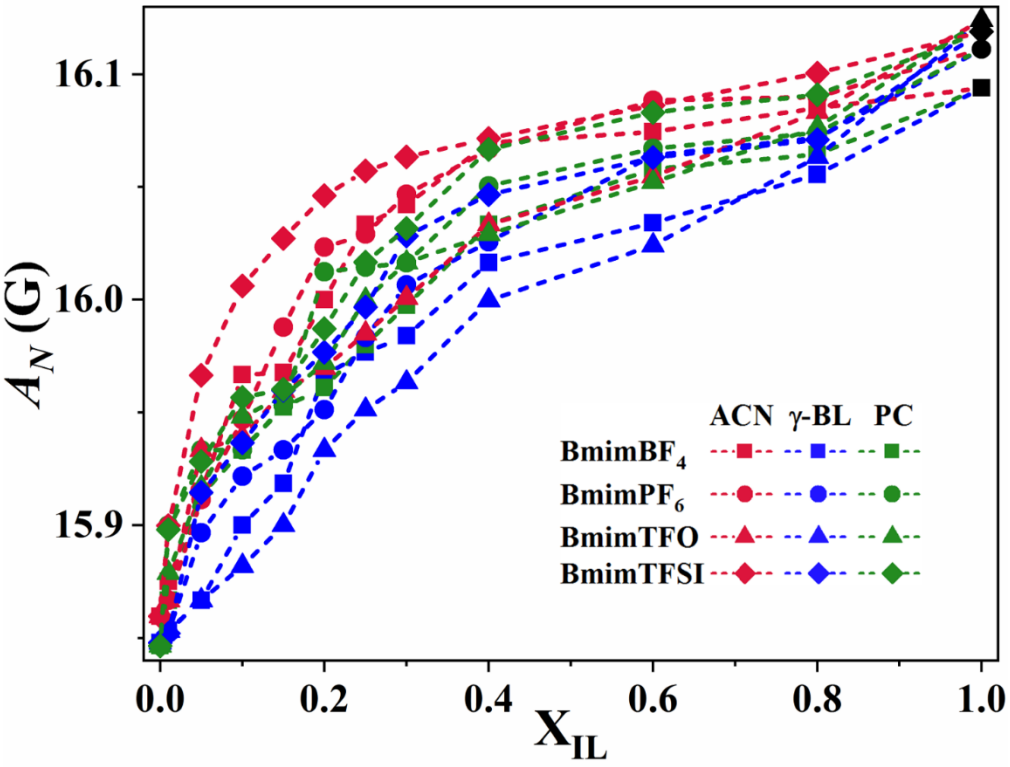

Figure 3.3: Composition dependence of the A_N values in IL-MS mixtures

Similar to the EPR study in different pure solvents and in pure ILs, we have studied using EPR probe TEMPO in various IL-MS mixtures containing imidazolium-based ILs and three different polar aprotic solvents. Our EPR spectral analysis also resulted in the values of hyperfine coupling constants (A_N) depending upon the mixture compositions. All the analyzed A_N values are shown in Table C2 in the Appendix.

In addition, considering IL-MS mixtures, a typical non-linear increase of A_N values is noticed while increasing the X_{IL} of the mixture. If we notice the composition dependence of A_N values in the studied IL-MS mixtures, we can see a common trend. The A_N values show a noticeable change in the lower mole fraction range of all the mixtures ($0 \leq X_{IL} \leq 0.4$). After that, the change in the A_N values are quite small. This type of composition dependence of A_N values are quite similar with the changes of other physicochemical and spectroscopic properties in IL-MS mixtures, where most of the changes in the values happen at the lower X_{IL} regions.[14,108–113] This type of changes in various properties in the IL-MS mixtures can be originated from the local interactions between the probes and the surrounding medium especially in the lower mole fraction range.

3.3.3. Rotational correlation time (τ_R):

Besides isotropic hyperfine coupling constant (A_N) values, the analysis of CW-EPR spectra results in rotational correlation time (τ_R) values of the probe TEMPO in various studied mixtures. In the fast-motion region (τ_R< 3 ns), the rotational correlation time of the probe can be determined using motional narrowing theory,[114] where the EPR spectral line width (ΔH_{PP}) can be obtained by asymmetric line broadening in EPR quantum number $m_I = \pm 1,0$ for the nitroxide radical TEMPO.

$$\Delta H_{PP}(m_I) = A + Bm_I + Cm_I^2 \quad (3.1)$$

Here, the parameters *A, B* and *C* can be expressed by the formula which contains anisotropic rotational correlation time, *g*-tensor values (arises from the interaction of the electron spin with external magnetic field) and hyperfine coupling constant values of the radical TEMPO in various mixtures. In this regard, various previous reports have already nicely described the calculation of rotational relaxation time.[44,100,101,115–117] Only the basic equations are going to be discussed here, which will help us to understand the process.

Firstly, in the absence of paramagnetic broadening of the EPR spectra, the parameters B and C become B_{uncorr} and C_{uncorr} , which can be expressed as-

$$B_{uncorr} = 0.5\Delta H_0 \left(\sqrt{\frac{V_0}{V_{+1}}} - \sqrt{\frac{V_0}{V_{-1}}}\right) \quad (3.2)$$

$$C_{uncorr} = 0.5\Delta H_0 \left(\sqrt{\frac{V_0}{V_{+1}}} + \sqrt{\frac{V_0}{V_{-1}}} - 2\right) \quad (3.3)$$

Here ΔH_0 is the overall linewidth of the central line and $V_{-1,0,+1}$ is the peak-to-peak intensity of the high, middle and low field EPR spectral lines respectively (corresponding to the spin states of the N atom). To understand the parameters in equation 3.2 and 3.3, a scheme of EPR signal is shown here (Scheme 3.1).

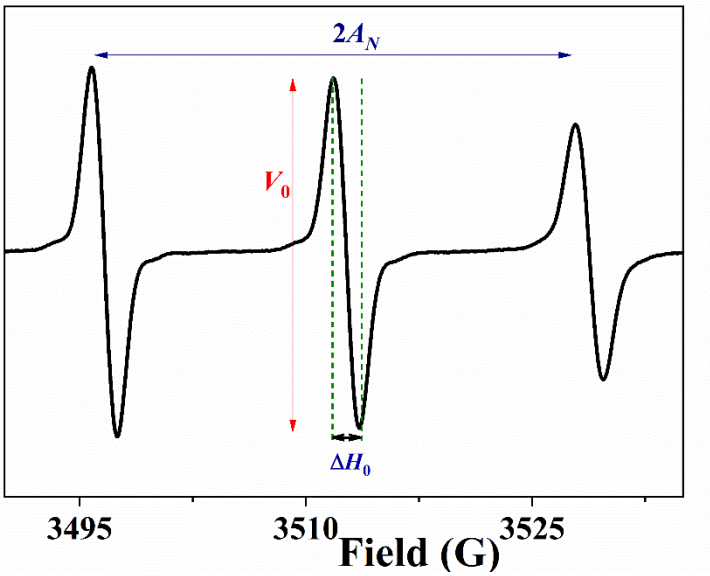

Scheme 3.1: Parameters in a typical EPR spectrum of TEMPO

However, the hyperfine coupling between the electron and the neighboring protons makes the EPR line broadening inhomogeneous in nature. Indeed, the subscript in equation 3.2 and 3.3 'uncorr' indicates the fact that the correlation for the inhomogeneous broadening of the hyperfine lines is not yet performed so far.[101] To consider the case of inhomogeneous broadening in the EPR signal, one need to make some corrections in equations 3.2 and 3.3.

$$B = QSB_{uncorr} \tag{3.4}$$

$$C = QSC_{uncorr} \tag{3.5}$$

Where,

$$Q = \frac{\left[-1+\sqrt{(1+4\chi^2)}\right]}{2\chi^2} \tag{3.6}$$

$$S = \frac{\left[1+1.78\chi+1.85\chi^2\right]}{(1+2.08\chi)} \tag{3.7}$$

$$\text{And } \chi = \left(\frac{\Delta H_0}{\Delta H_G} - \frac{\Delta H_G}{\Delta H_0}\right) \tag{3.8}$$

Here ΔH_G is the Gaussian contribution in the hyperfine lines and χ represents the Voigt parameter.

Finally, the rotational correlation times can be calculated using the following equations:

$$\tau_b = C_1.B \tag{3.9}$$

$$\tau_c = C_2.C \tag{3.10}$$

$$\tau_R = \sqrt{\tau_b \tau_c} \tag{3.11}$$

Here C_1 and C_2 are constants whose values are dependent on exact values of the hyperfine coupling constant (A_N) and g-tensor elements.[101,118,119] All these calculations were performed internally during the process of the fitting of experimental EPR spectra by using the SimLabel[99] tool and EasySpin[100] program.

After the thorough analysis of the CW-EPR spectra of TEMPO using the SimLabel toolbox, we have also found the values of the weighted average of τ_R values of the probe TEMPO in all the studied IL-MS mixtures. Similar to the discussion related to the hyperfine coupling constant in the mixtures, the discussion related to τ_R values are also divided into two parts. First, we will discuss about the changes of τ_R values in case of pure solvents used in our study. Then, we will concentrate our discussion on the changes of τ_R values in the studied IL-MS mixtures while using the EPR probe TEMPO.

In case of pure components, the τ_R values in pure ILs are much higher than those in pure MSs used in this study (Figure 3.4). In this aspect, previous studies also showed higher viscosity of the surrounding medium of the probe molecules can be the reason behind higher τ_R values.[28,29,43,46,48,53,54,82,84,120] Similarly, highly viscous ILs show longer rotational relaxation time values of the probe than that of low viscous molecular solvents.

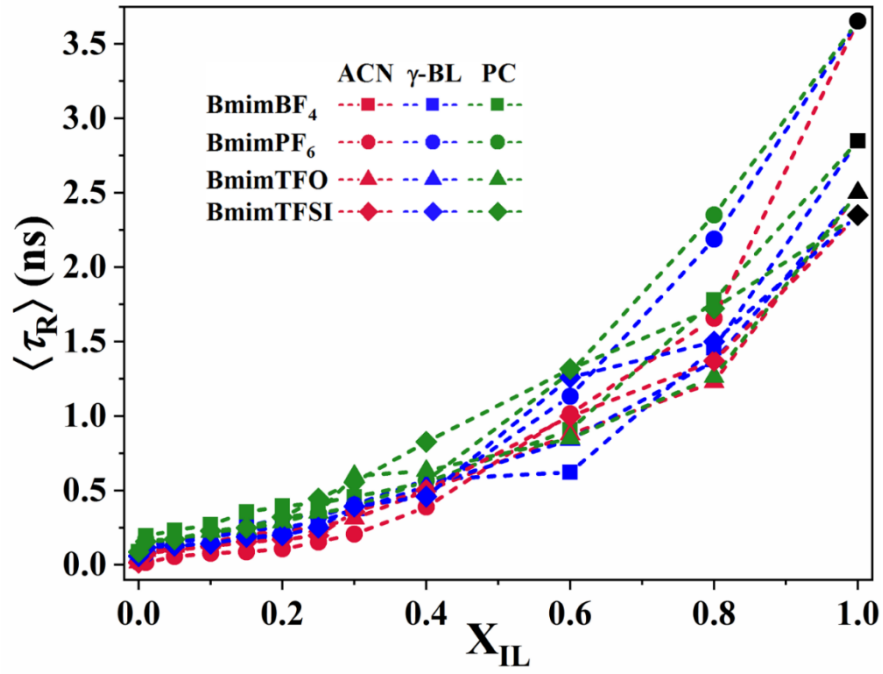

Figure 3.4: Mixture composition dependence of the τ_R values of TEMPO in IL-MS mixtures

Furthermore, in the case of IL-MS mixtures, a non-linear increase of τ_R values can be noticed in the case of the composition dependence of τ_R values (Figure 3.4). The increase of viscosity of the mixtures while increasing X_{IL} can be a reason behind that. Indeed, previous spectroscopic studies also showed the viscosity dependence of τ_R values in case of various IL-MS mixtures.[86,88,121–124] Therefore, we have also plotted these τ_R values of the probe in various IL-MS mixtures with respect to the mixture viscosity values. Although available for most of the studied IL-MS mixtures[125–133], the viscosity values of some of the mixtures ($BmimBF_4$-PC, BmimTFO-PC and BmimTFSI-γ-BL) were unavailable. Therefore, this viscosity correlation is impossible to show for these three mixtures. The viscosity dependence of τ_R values in the nine IL-MS mixtures with available viscosity values can be noticed in Figure 3.5.

Two interesting points can be made from this Figure. Firstly, the viscosity dependence of τ_R follows fractional Stokes-Einstein-Debye (SED) law, i.e. $\langle\tau_R\rangle \propto \eta^p$, where $p < 1$ (Table 3.1) , similar to some of the previous studies.[52,55,84,86,121,134]

Secondly, the viscosity dependence is not similar in all the intermediate mole fractions of the mixtures. While the IL-MS mixtures with X_{IL} ranging from 0.1 to 1 follows fractional SED relation with mixture viscosity, the mixtures before this composition range ($0 \leq X_{IL} < 0.1$), doesn't follow the same trend. We are going to discuss about it more while discussing about the particular case of $BmimBF_4$-ACN mixture in the next section.

Table 3.1: Viscosity dependence of τ_R values of TEMPO in IL-MS mixtures

Subfigure number	Mixtures	Fractional SED power/ p
3.5(A)	$BmimBF_4$-γ-BL	0.70
3.5(B)	$BmimPF_6$-ACN	0.72
3.5(C)	$BmimPF_6$- γ-BL	0.73

3.5(D)	$BmimPF_6$-PC	0.70
3.5(E)	BmimTFO-ACN	0.56
3.5(F)	BmimTFO- γ-BL	0.74
3.5(G)	BmimTFSI-ACN	0.75
3.5(H)	BmimTFSI-PC	0.99

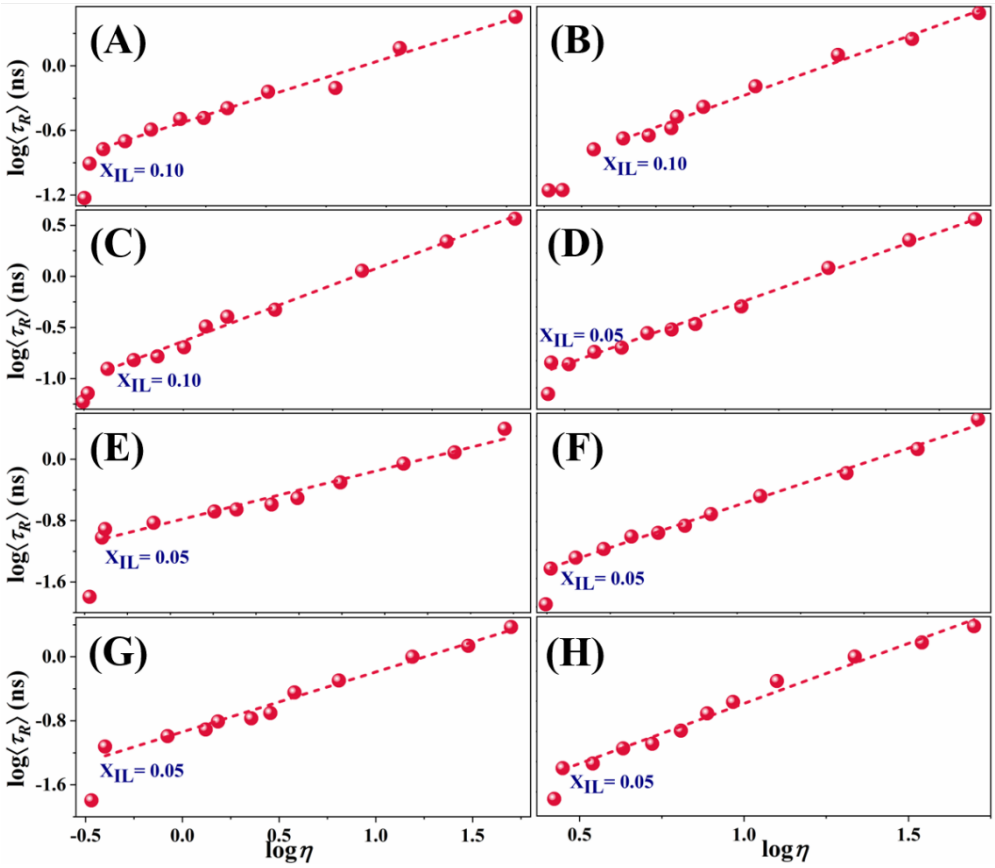

Figure 3.5: Viscosity dependence of τ_R values of TEMPO in IL-MS mixtures. (A) $BmimBF_4$-γ-BL, (B) $BmimPF_6$-ACN, (C) $BmimPF_6$- γ-BL, (D) $BmimPF_6$-PC, (E) BmimTFO- ACN, (F) BmimTFO- γ-BL, (G) BmimTFSI-ACN and (H) BmimTFSI-ACN

3.4. A particular case study: TEMPO in $BmimBF_4$-ACN mixture

Among the imidazolium based IL-MS mixtures, $BmimBF_4$-ACN mixture is the mostly studied one. Various physicochemical and spectroscopic properties (density, conductivity, viscosity, static dielectric constant, solvatochromic polarity parameter, E_T^N etc.) are already published in case of $BmimBF_4$-ACN mixture.[112,113,133,135,136,125–132] Among them, composition dependent values of different polarity parameters are not yet settled. While spectroscopic polarity parameter E_T^N increases with the increase of IL concentration,[15] static dielectric constant (ε) values show a decrease with the increase of X_{IL}.[104] In this section, we would like to address this problem regarding the medium polarity in $BmimBF_4$-ACN mixtures through this EPR analysis. In addition, we are going to show the correlation between two probe dependent spectroscopic polarity parameters (E_T^N and A_N) in the aforementioned IL-MS mixture, as shown recently in case of pure solvents and also in pure ionic liquids.[25,27,28]

3.4.1. Correlation between two spectroscopic polarity parameters in BmimBF$_4$-ACN mixture:

Table 3.2 and Figure 3.6 shows that the correlation between the E_N^T and A_N values in BmimBF$_4$-ACN mixture also follows the line which correlates these two spectroscopic polarity parameters in case of previously known pure solvents and pure ILs.[25,51] As the similar type of linear correlation in pure ILs and MSs are followed in case of one of the studied IL-MS mixtures (BmimBF$_4$-ACN mixture), this result can be extrapolated in case of other IL-MS mixtures. However, we need more experimental data points for proving that. Although the values of E_N^T are unknown in case of other imidazolium IL-MS mixtures, the measured experimental values of A_N (Tables C2) and this linear correlation in Figure 3.6 can help us to predict the values of E_N^T in other IL-MS mixtures.

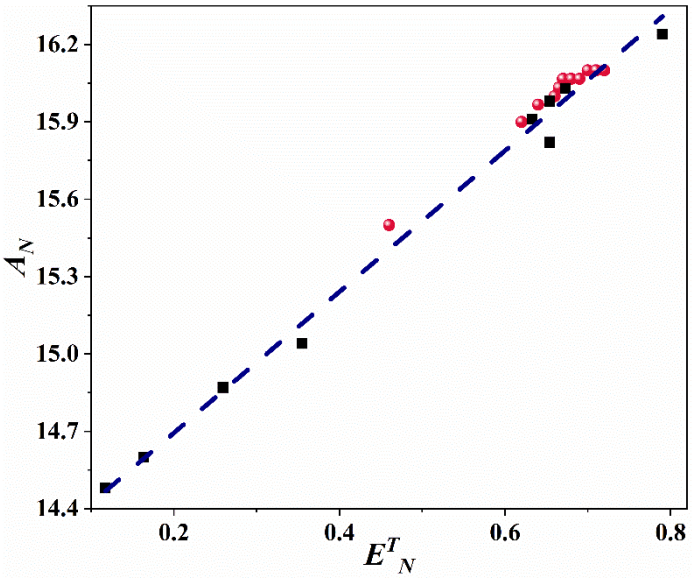

Figure 3.6: Correlation between E_T^N and A_N values in BmimBF$_4$-ACN mixture. The red circles represent the values for BmimBF$_4$-ACN mixtures, whereas black squares are for known values in different solvents and ILs [25,51,137]

Table 3.2: Values of solvatochromic polarity parameters in pure solvents, ILs and BmimBF$_4$-ACN mixtures (X_{IL} = IL mole fraction in the mixtures)

Pure solvents/Mixtures	E_N^T*	A_N(G)
ACN	0.46 [15]	15.50
X_{IL}=0.05	0.62 [15]	15.90
X_{IL}=0.10	0.64 [15]	15.97
X_{IL}=0.20	0.66 [15]	16.00
X_{IL}=0.25	0.67 [15]	16.03
X_{IL}=0.30	0.67 [15]	16.06
X_{IL}=0.40	0.68 [15]	16.07
X_{IL}=0.50	0.69 [15]	16.07
X_{IL}=0.60	0.70 [15]	16.10

X_{IL}=0.80	0.71 [15]	16.10
X_{IL}=0.90	0.72 [15]	16.10
$BmimBF_4$	0.67 [15]	16.20
$BmimBF_4$ [51]	0.64	15.91
$BmimPF_6$ [51]	0.65	15.98
BmimTFSI [51]	0.67	16.03
Ethylene glycol [51]	0.79	16.24
1,4-dioxane [51]	0.16	14.60
Chloroform [51]	0.26	14.87
Acetone [51]	0.35	15.04
Ethyl alcohol [51]	0.65	15.82
Benzene [25,137]	0.12	14.48

$*E_T^N = \frac{E_T(30)_{Solvent} - E_T(30)_{TMS})}{(E_T(30)_{Water} - E_T(30)_{TMS})} = \frac{E_T(30)_{Solvent} - 30.7)}{32.4}$

So far, we have discussed about the two solvatochromic polarity parameters and the relation between them. However, the concept of polarity in ILs and in IL-MS mixtures is quite difficult to understand. These type of spectroscopic polarity parameters give us an idea that these imidazolium ILs are as polar as short chain alcohols like methanol, ethanol. However, the dielectric constant values in IL and also in IL-MS mixtures suggest that ILs are not that polar. These types of discrepancy in the polarity parameter values in case of IL and IL-MS mixtures lead us to make a correlation between them. In this regard, there are some studies which also correlate these two types of polarity parameters, i.e. the probe dependent parameters (E_N^T and A_N) and probe independent parameters (ε), in case of pure solvents and in pure ILs.[16,17] In these two studies, the authors used modified Onsager equation to create a relation between these polarity parameters. We are going to extend that particular type of studies in case of $BmimBF_4$-ACN mixtures.

3.4.2. Correlation between A_N and ε: Modified Onsager equation

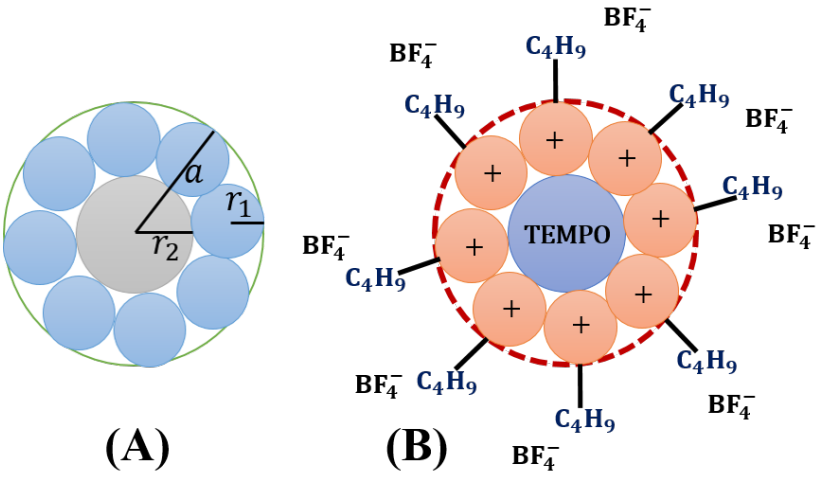

Figure 3.7: (A) Molecular model for modified reaction field in the Onsager model, (B) Modified reaction field in case of pure $BmimBF_4$

Onsager's reaction field model[91] is the most used one to understand the relation between the dielectric constant of the medium and the probe dependent solvent polarity parameter (A_N).

It has been already known that, in the absence of hydrogen bonding between probe and solvent molecules, the spectroscopic polarity parameter (Y) is approximately proportional to the reaction field (E_R)[16,17,138,139] using the following equation:

$$Y = Y_0 + K_v . E_R \tag{3.12}$$

Here, Y_0 is the value of solvent dependent spectroscopic polarity parameter in a region with no external electric field, K_v is a constant which is probe dependent. This reaction field can be expressed using Onsager equation in the following way:

$$E_R = -\frac{2\mu}{r^3} . \frac{\varepsilon - 1}{2\varepsilon + 1} \tag{3.13}$$

According to Onsager theory,[91] ε is the dielectric constant of the medium, μ is the dipole of the probe molecule and r is the radius of reaction field. The equation 3.12 works well for non-hydrogen bonding solvents. However, in the case of hydrogen bonding solvents, this equation failed to give a good fit,[16,17,138]

In general, the radius of solute molecule is chosen as the radius of the reaction field, especially in case of non-hydrogen bonding solvents. In this regard, according to molecular model of solvation, solvation of a solute in a solvent consists of the solute molecule, first solvation shell and the bulk solvent.[140] Previous studies by Wang et al.[16,17] related to the correlation among these solvent parameters had already modified the radius of the reaction field by including the primary solvation shell while calculating the values of the radius of the reaction field. The modified equation 3.12 can be written as-

$$Y = Y_0 - K_v . \frac{2\mu}{a^3} . \frac{\varepsilon - 1}{2\varepsilon + 1} \tag{3.14}$$

Here,

$$a = r_2 + 2r_1 \tag{3.15}$$

r_2 and r_1 the radius of solute and solvent respectively and a is the radius of primary solvation shell

To calculate the radius of primary solvation shell (a), one need to consider the values of molar volumes. As our target mixture contains ACN and $BmimBF_4$, we need to concentrate on the values of molar volumes of these two pure components. In case of ACN, the molar volume V_M is 52.86 $cm^3 mol^{-1}$[16], which was used for this calculation also. However, the value of the molar volume calculated in case of $BmimBF_4$ (V_1) is 31.25 $cm^3 mol^{-1}$[17] which is much smaller than its actual molar volume i.e. 188.1 $cm^3 mol^{-1}$. In this aspect, it is important to know that, in case of pure $BmimBF_4$, the effective radius is nothing but the distance of the first chemical bond further from the interaction site.[17] Therefore, only the cation without the butyl extension can be considered for the calculation of the effective radius in case of ILs (Figure 3.7 (B)).[17] Using the values of modified molar volume as well as the effective radius of the modified reaction fields, the experimental results were fitted in a better way in case of ILs.

Now, while A_N is the chosen spectroscopic parameter, the simplified equation 3.14 will be,

$$A_N = A_{N_0} + K.\frac{R}{a^3} \quad (3.18)$$

Here $R = \frac{\varepsilon-1}{2\varepsilon+1}$ and $K = -2\mu K_v$ and K is a constant for a particular probe molecule (TEMPO in our case)

For this study, we have used the previous values of molar volumes[16,17] of pure ACN and $BmimBF_4$ to calculate the values of A_{N_0} and K in the equation 3.7. The whole calculation is shown in Appendix C.1.

Thus, the equation 3.18 will look like-

$$A_N = 14.987 + 914.94 \times {}^{R}/_{a^3} \quad (3.19)$$

Our goal is to use this equation in case of intermediate mixtures between $BmimBF_4$ and ACN. We already have experimental values of dielectric constant of the mixture to calculate R values in case of each mixture compositions. Besides, after the fitting of experimental EPR hyperfine lines, we have already collected the A_N values for the same intermediate mixture compositions (Table C2 in the Appendix). Therefore, using equation 3.19, we can calculate the values of a, which is nothing but the radius of first solvation shell in case of each intermediate mixture composition.

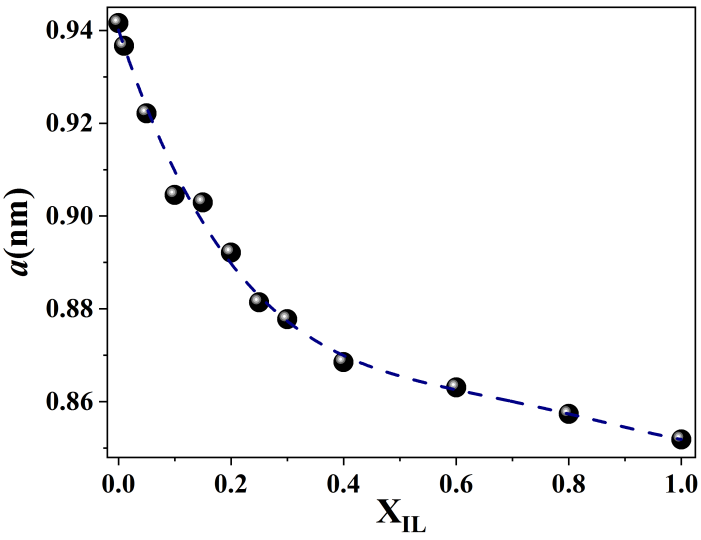

Figure 3.8: Radius of first solvation sphere in $BmimBF_4$-ACN mixtures using TEMPO as a probe.

From Figure 3.8, we can see an overall decrease of the radius of the first solvation sphere while increasing X_{IL}. However, this decrease is not linear. At low X_{IL} ($0 \leq X_{IL} < 0.2$) region, the rate of decrease is greater compared to that in higher X_{IL} regions. This type of composition dependence show similarities with previously discussed composition dependence of steady-state properties while using UV-Vis probes (Chapter 1). Similarly, various measured physicochemical and spectroscopic properties in IL-MS mixtures[14,108–113] also show noticeable

change in the low X_{IL} regions. In this regard, it is worthy to remember that the main reason behind the smaller effective molar volume (V_M) as well as the effective radius values in $BmimBF_4$ compared to that in pure ACN is due to the presence of dominant electrostatic interactions over H-bonding and Van der Waals interactions in the medium.[17] Now, according to that logic, the high rate of decrease of a values at low X_{IL} regions in Figure 3.8 also can suggest a dominance of ionic interactions in these mixture compositions. On the other hand, the extent of decrease of the radius of first solvation sphere is comparatively less at higher X_{IL} regions ($X_{IL} \geq 0.2$) which in turn shows large interactions between the ions of ILs especially at the higher X_{IL} regions.

Rotational relaxation time:

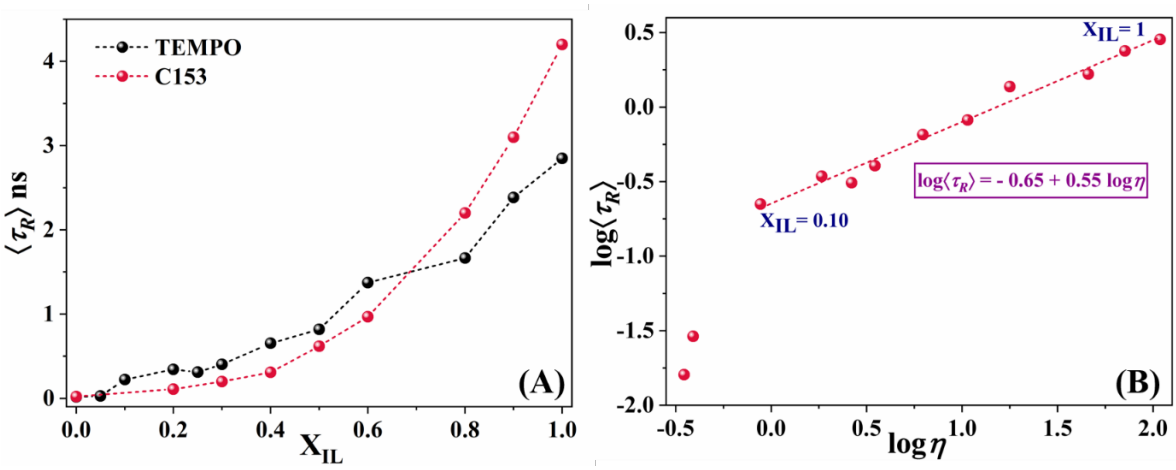

Figure 3.9: (A) Composition and (B) Viscosity dependence of τ_R values of TEMPO in $BmimBF_4$-ACN mixtures

In addition, the EPR data fitting also results in the weighted average rotational relaxation time (τ_R) values which is shown in Table C3. In addition to that, we have plotted (Figure 3.9) the values of τ_R to show both composition and viscosity dependence in $BmimBF_4$-ACN mixtures. From Figure 3.9 (A), we can clearly see the overall composition dependent changes of rotational relaxation time of TEMPO in $BmimBF_4$-ACN mixtures. In addition, we have also tried to compare this composition dependent change of the EPR probe with that of previously published spectroscopic probe C153.[17] From Figure 3.9, it can be noticed that, the rate of the composition dependent change of τ_R values of the EPR probe TEMPO is not exactly similar to that of UV-Vis probe C153. While the difference is smaller at lower X_{IL} regions, the deviation is quite large at very high X_{IL} regions and also in pure $BmimBF_4$. To get further idea about the changes of τ_R values in the mixture, we have also shown the viscosity dependence of τ_R values in $BmimBF_4$-ACN mixture. As it can be seen from Figure 3.9 (B), the values of τ_R starting from X_{IL}=0.1 ($X_{IL} \geq 0.1$) can be fitted using the following equation-

$$\log\langle\tau_R\rangle = 0.65 + 0.55\log\eta \qquad (3.20)$$

Therefore, the viscosity dependence of rotational relaxation time of TEMPO is not linear and it follows the following relation in the region $X_{IL} \geq 0.1$-

$$\langle\tau_R\rangle \propto \eta^p \text{ with } p = 0.55 \qquad (3.21)$$

In this regard, this type of viscosity dependence can be noticed while using UV-Vis spectroscopic probe C153 as a probe in $BmimBF_4$-ACN mixture[86] and even in $BmimBF_4$-PC mixture[121] throughout the whole mole fraction range of these mixtures. However, unlike C153, τ_R values of TEMPO can't be fitted using the same straight line in the whole intermediate X_{IL} range. At low X_{IL} ($0 \leq X_{IL} \leq 0.1$) region, the values of τ_R are comparatively small. In this regard, it is also important to mention that, Maroncelli et al. have shown the viscosity dependence of τ_R of C153 in the X_{IL} range from 0.2 to 1 in $BmimBF_4$-ACN mixtures.[86] Furthermore, Stoppa et al.[14] had also noticed that, the correlation times follow the SED model in the composition range $0.2 \leq X_{IL} \leq 1$ in their DRS study in $BmimBF_4$-ACN mixture. In addition, although not much but a deviation from the fitted line in the similar type of plot like Figure 3.9(B) was also noticed in the viscosity dependent change of τ_R values of C153 dye in $BmimBF_4$-PC mixture.[121] To describe this deviation from linearity and not following the viscosity dependence at low X_{IL} regions may suggests that, one need to consider the effect of local and specific interactions like H-bonding, dipole-dipole, Van der Waals interactions etc. while describing τ_R values in these mixture compositions.

Overall, according to the modified Onsager equation used in case of $BmimBF_4$-ACN mixture, the reason behind the overall increase of A_N value in $BmimBF_4$ despite the decrease of dielectric constant ε is the decrease of the radius of the reaction field surrounding the probe. As the modified reaction field is nothing but the radius of first solvation sphere surrounding the probe molecule, its value in $BmimBF_4$ is less than that in ACN. The radius of the first solvation shell revealed from this study in case of $BmimBF_4$-ACN mixture can be useful in studying the solvation process in these mixtures. Indeed, various previous studies discussed about the composition of solvation shell in different IL-MS mixtures.[141–143] Also, the composition dependence of the radius of reaction field give us an idea about the present interactions in a typical IL-MS mixture. In addition, the viscosity dependence of rotational relaxation times of TEMPO also showed unusual deviation at low X_{IL} region of $BmimBF_4$-ACN mixture, which can be explained considering the presence of local and specific interactions in the mixture.

3.5. Conclusions:

In conclusion, in this chapter, we have performed CW-EPR experiments using a paramagnetic probe TEMPO to study different imidazolium ionic liquid-molecular solvent mixtures. We have noticed a significant change of the shapes of EPR hyperfine lines while increasing the mole fractions of ionic liquids. In case of each studied IL-MS mixtures, addition of IL in the mixtures increases the heterogeneity in the medium, which is the main cause of the EPR spectral broadening while increasing X_{IL}. Spectral analysis results in two different properties named the hyperfine coupling constant (A_N) and rotational relaxation time (τ_R) of the probe molecule. We have showed the composition dependent changes of the A_N values in case of studied IL-MS mixtures. In addition, we have made a correlation between different polarity parameters for the very first time in case of $BmimBF_4$-ACN mixture using TEMPO as a probe. Besides, the composition and viscosity dependence of the τ_R values of TEMPO was also studied in this

chapter. In the case of viscosity dependence, the rotational correlation times of the probe molecules follow the fractional SED equation only in a particular X_{IL} range ($0.1 \leq X_{IL} \leq 1$).

As an extension of this study, we can do some high-field EPR measurements to study the polarity and hydrogen bonding effects simultaneously by studying the changes of g_{xx} and A_{zz} parameters.[31] Similarly, temperature dependent changes of rotational relaxation time values of the EPR probe in the IL-MS mixtures can also be performed while doing variable temperature EPR studies, which will give us an idea about activation energy of the rotation process of the probe molecules in the IL-MS mixtures. In addition, varying nitroxide EPR probes with different substituents in the IL-MS mixtures and studying their EPR spectra can give us idea about types of interaction presents in between the probes and the IL-MS mixtures. Therefore, there are various ways to follow up this type of EPR study discussed in this chapter. Furthermore, very recently an article was published to study the structural anomaly in a $BmimBF_4$-water mixture using pulsed and CW-EPR spectroscopic techniques.[37] These type of studies using pulsed EPR techniques can also be helpful to get an idea about the peculiar behavior of the EPR probes in the IL-MS systems used in our study.

Bibliography

(1) Aki, S. N. V. K.; Brennecke, J. F.; Samanta, A. How Polar Are Room-Temperature Ionic Liquids? *Chem. Commun.* **2001**, No. 5, 413–414. https://doi.org/10.1039/b008039j.

(2) Carmichael, A. J.; Seddon, K. R. Polarity Study of Some 1-Alkyl-3-Methylimidazolium Ambient-Temperature Ionic Liquids with the Solvatochromic Dye, Nile Red. *J. Phys. Org. Chem.* **2000**, *13* (10), 591–595. https://doi.org/10.1002/1099-1395(200010)13:10<591::AID-POC305>3.0.CO;2-2.

(3) Karmakar, R.; Samanta, A. Steady-State and Time-Resolved Fluorescence Behavior of C153 and PRODAN in Room-Temperature Ionic Liquids. *J. Phys. Chem. A* **2002**, *106* (28), 6670–6675. https://doi.org/10.1021/jp0143591.

(4) Muldoon, M. J.; Gordon, C. M.; Dunkin, I. R. Investigations of Solvent–solute Interactions in Room Temperature Ionic Liquids Using Solvatochromic Dyes. *J. Chem. Soc. Perkin Trans. 2* **2001**, No. 4, 433–435. https://doi.org/10.1039/b101449h.

(5) Ingram, J. A.; Moog, R. S.; Ito, N.; Biswas, R.; Maroncelli, M. Solute Rotation and Solvation Dynamics in a Room-Temperature Ionic Liquid. *J. Phys. Chem. B* **2003**, *107* (24), 5926–5932. https://doi.org/10.1021/jp034231e.

(6) Strehmel, V.; Laschewsky, A.; Stoesser, R.; Zehl, A.; Herrmann, W. Mobility of Spin Probes in Ionic Liquids. *J. Phys. Org. Chem.* **2006**, *19* (5), 318–325. https://doi.org/10.1002/poc.1072.

(7) Kawai, A.; Hidemori, T.; Shibuya, K. Electron Spin Dynamics of Triplet and Doublet Molecules in Room Temperature Ionic Liquids Studied by a Time-Resolved EPR Method. *Mol. Phys.* **2006**, *104* (10–11), 1573–1579. https://doi.org/10.1080/00268970500513602.

(8) Kawai, A.; Hidemori, T.; Shibuya, K. Solvation of α-Hydroxydiphenylmethyl Radical in Room Temperature Ionic Liquids Studied by Transient FT-EPR Spectroscopy. *Chem. Phys. Lett.* **2005**, *414* (4–6), 378–383. https://doi.org/10.1016/j.cplett.2005.08.030.

(9) Owenius, R.; Engström, M.; Lindgren, M.; Huber, M. Influence of Solvent Polarity and Hydrogen Bonding on the EPR Parameters of a Nitroxide Spin Label Studied by 9-GHz and 95-GHz EPR Spectroscopy and DFT Calculations. *J. Phys. Chem. A* **2001**, *105* (49), 10967–10977. https://doi.org/10.1021/jp0116914.

(10) Stoesser, R.; Herrmann, W.; Zehl, A.; Laschewsky, A.; Strehmel, V. Microviscosity and Micropolarity Effects of Imidazolium Based Ionic Liquids Investigated by Spin Probes Their Diffusion and Spin Exchange. *Zeitschrift für Phys. Chemie* **2006**, *220* (10), 1309–1342. https://doi.org/10.1524/zpch.2006.220.10.1309.

(11) Tao, G.; Zou, M.; Wang, X.; Chen, Z.; Evans, D. G.; Kou, Y. Comparison of Polarities of Room-Temperature Ionic Liquids Using FT-IR Spectroscopic Probes. *Aust. J. Chem.* **2005**, *58* (5), 327. https://doi.org/10.1071/CH05025.

(12) Kimura, Y.; Hamamoto, T.; Terazima, M. Raman Spectroscopic Study on the Solvation of N , N -Dimethyl- p -Nitroaniline in Room-Temperature Ionic Liquids. *J. Phys. Chem. A* **2007**, *111* (30), 7081–7089. https://doi.org/10.1021/jp072020u.

(13) Lohse, P. W.; Bartels, N.; Stoppa, A.; Buchner, R.; Lenzer, T.; Oum, K. Dielectric Relaxation and Ultrafast Transient Absorption Spectroscopy of [C6mim]+[Tf2N]−/Acetonitrile Mixtures. *Phys. Chem. Chem. Phys.* **2012**, *14* (10), 3596. https://doi.org/10.1039/c2cp23704k.

(14) Stoppa, A.; Hunger, J.; Hefter, G.; Buchner, R. Structure and Dynamics of 1- N -Alkyl-3- N -Methylimidazolium Tetrafluoroborate + Acetonitrile Mixtures. *J. Phys. Chem. B* **2012**, *116* (25), 7509–7521. https://doi.org/10.1021/jp3020673.

(15) Mancini, P. M.; Fortunato, G. G.; Adam, C. G.; Vottero, L. R. Solvent Effects on Chemical Processes: New Solvents Designed on the Basis of the Molecular–microscopic Properties of (Molecular Solvent + 1,3-Dialkylimidazolium) Binary Mixtures. *J. Phys. Org. Chem.* **2008**, *21* (2), 87–95. https://doi.org/10.1002/poc.1227.

(16) Wang, X.; Dao, R.; Yao, J.; Peng, D.; Li, H. Modification of the Onsager Reaction Field and Its Application on Spectral Parameters. *ChemPhysChem* **2017**, *18* (7), 763–771. https://doi.org/10.1002/cphc.201601093.

(17) Wang, X.; Zhang, S.; Yao, J.; Li, H. The Polarity of Ionic Liquids: Relationship between Relative Permittivity and Spectroscopic Parameters of Probe. *Ind. Eng. Chem. Res.* **2019**, *58* (17), 7352–7361. https://doi.org/10.1021/acs.iecr.9b00485.

(18) Nicolau, B. G.; Sturlaugson, A.; Fruchey, K.; Ribeiro, M. C. C.; Fayer, M. D. Room Temperature Ionic Liquid−Lithium Salt Mixtures: Optical Kerr Effect Dynamical Measurements. *J. Phys. Chem. B* **2010**, *114* (25), 8350–8356. https://doi.org/10.1021/jp103810r.

(19) Jin, H.; Baker, G. A.; Arzhantsev, S.; Dong, J.; Maroncelli, M. Solvation and Rotational Dynamics of Coumarin 153 in Ionic Liquids: Comparisons to Conventional Solvents. *J. Phys. Chem. B* **2007**, *111* (25), 7291–7302. https://doi.org/10.1021/jp070923h.

(20) Hu, Z.; Margulis, C. J. Heterogeneity in a Room-Temperature Ionic Liquid: Persistent Local Environments and the Red-Edge Effect. *Proc. Natl. Acad. Sci.* **2006**, *103* (4), 831–836. https://doi.org/10.1073/pnas.0507364103.

(21) Paul, A.; Samanta, A. Photoinduced Electron Transfer Reaction in Room Temperature Ionic Liquids: A Combined Laser Flash Photolysis and Fluorescence Study. *J. Phys. Chem. B* **2007**, *111* (8), 1957–1962. https://doi.org/10.1021/jp067481e.

(22) Evans, R. G.; Wain, A. J.; Hardacre, C.; Compton, R. G. An Electrochemical and ESR Spectroscopic Study on the Molecular Dynamics of TEMPO in Room Temperature Ionic Liquid Solvents. *ChemPhysChem* **2005**, *6* (6), 1035–1039. https://doi.org/10.1002/cphc.200500157.

(23) Mandal, P. K.; Samanta, A. Fluorescence Studies in a Pyrrolidinium Ionic Liquid: Polarity of the Medium and Solvation Dynamics. *J. Phys. Chem. B* **2005**, *109* (31), 15172–15177. https://doi.org/10.1021/jp051844d.

(24) Samanta, A. Dynamic Stokes Shift and Excitation Wavelength Dependent Fluorescence of Dipolar Molecules in Room Temperature Ionic Liquids. *J. Phys. Chem. B* **2006**, *110* (28), 13704–13716. https://doi.org/10.1021/jp060441q.

(25) Dhale, R. S.; Sahu, P. K.; Sarkar, M. Understanding the Microscopic Behavior of the Mixture of Ionic Liquid/Ethylene Glycol/Lithium Salt through Time-Resolved Fluorescence, Nuclear

Magnetic Resonance (NMR), and Electron Paramagnetic Resonance (EPR) Studies. *J. Phys. Chem. B* **2017**, *121* (33), 7934–7945. https://doi.org/10.1021/acs.jpcb.7b04585.

(26) Kundu, K.; Kattnig, D. R.; Mladenova, B. Y.; Grampp, G.; Das, R. Electron Spin–Lattice Relaxation Mechanisms of Nitroxyl Radicals in Ionic Liquids and Conventional Organic Liquids: Temperature Dependence of a Thermally Activated Process. *J. Phys. Chem. B* **2015**, *119* (12), 4501–4511. https://doi.org/10.1021/acs.jpcb.5b00431.

(27) Kawai, A.; Hidemori, T.; Shibuya, K. Polarity of Room-Temperature Ionic Liquid as Examined by EPR Spectroscopy. *Chem. Lett.* **2004**, *33* (11), 1464–1465. https://doi.org/10.1246/cl.2004.1464.

(28) Chakraborty, M.; Ahmed, T.; Dhale, R. S.; Majhi, D.; Sarkar, M. Understanding the Microscopic Behavior of Binary Mixtures of Ionic Liquids through Various Spectroscopic Techniques. *J. Phys. Chem. B* **2018**, *122* (50), 12114–12130. https://doi.org/10.1021/acs.jpcb.8b09699.

(29) Dhale, R. S.; Sahu, P. K.; Sarkar, M. Understanding the Microscopic Behavior of the Mixture of Ionic Liquid/Ethylene Glycol/Lithium Salt through Time-Resolved Fluorescence, Nuclear Magnetic Resonance (NMR), and Electron Paramagnetic Resonance (EPR) Studies. *J. Phys. Chem. B* **2017**, *121* (33), 7934–7945. https://doi.org/10.1021/acs.jpcb.7b04585.

(30) Samanta, A. Dynamic Stokes Shift and Excitation Wavelength Dependent Fluorescence of Dipolar Molecules in Room Temperature Ionic Liquids. *J. Phys. Chem. B* **2006**, *110* (28), 13704–13716. https://doi.org/10.1021/jp060441q.

(31) Akdogan, Y.; Heller, J.; Zimmermann, H.; Hinderberger, D. The Solvation of Nitroxide Radicals in Ionic Liquids Studied by High-Field EPR Spectroscopy. *Phys. Chem. Chem. Phys.* **2010**, *12* (28), 7874. https://doi.org/10.1039/c001602k.

(32) Bordignon, E.; Brutlach, H.; Urban, L.; Hideg, K.; Savitsky, A.; Schnegg, A.; Gast, P.; Engelhard, M.; Groenen, E. J. J.; Möbius, K.; Steinhoff, H.-J. Heterogeneity in the Nitroxide Micro-Environment: Polarity and Proticity Effects in Spin-Labeled Proteins Studied by Multi-Frequency EPR. *Appl. Magn. Reson.* **2010**, *37* (1–4), 391–403. https://doi.org/10.1007/s00723-009-0072-9.

(33) Clark, R.; Nawawi, M. A.; Dobre, A.; Pugh, D.; Liu, Q.; Ivanov, A. P.; White, A. J. P.; Edel, J. B.; Kuimova, M. K.; McIntosh, A. J. S.; Welton, T. The Effect of Structural Heterogeneity upon the Microviscosity of Ionic Liquids. *Chem. Sci.* **2020**, *11* (24), 6121–6133. https://doi.org/10.1039/D0SC02009E.

(34) de Jesus, J. C.; Pires, P. A. R.; Mustafa, R.; Riaz, N.; El Seoud, O. A. Experimental and Theoretical Studies on Solvation in Aqueous Solutions of Ionic Liquids Carrying Different Side Chains: The n-Butyl-Group versus the Methoxyethyl Group. *RSC Adv.* **2017**, *7* (26), 15952–15963. https://doi.org/10.1039/C7RA00273D.

(35) Evans, R. G.; Wain, A. J.; Hardacre, C.; Compton, R. G. An Electrochemical and ESR Spectroscopic Study on the Molecular Dynamics of TEMPO in Room Temperature Ionic Liquid Solvents. *ChemPhysChem* **2005**, *6* (6), 1035–1039. https://doi.org/10.1002/cphc.200500157.

(36) Ivanov, M. Y.; Krumkacheva, O. A.; Dzuba, S. A.; Fedin, M. V. Microscopic Rigidity and Heterogeneity of Ionic Liquids Probed by Stochastic Molecular Librations of the Dissolved

Nitroxides. *Phys. Chem. Chem. Phys.* **2017**, *19* (38), 26158–26163. https://doi.org/10.1039/C7CP04890D.

(37) Ivanov, M. Y.; Prikhod'ko, S. A.; Adonin, N. Y.; Fedin, M. V. Structural Anomalies in Binary Mixtures of Ionic Liquid [Bmim]BF 4 with Water Studied by EPR. *J. Phys. Chem. B* **2019**, *123* (46), 9956–9962. https://doi.org/10.1021/acs.jpcb.9b08933.

(38) Kawai, A.; Hidemori, T.; Shibuya, K. Polarity of Room-Temperature Ionic Liquid as Examined by EPR Spectroscopy. *Chem. Lett.* **2004**, *33* (11), 1464–1465. https://doi.org/10.1246/cl.2004.1464.

(39) Kokorin, A. Peculiarities of Intramolecular Motions in Ionic Liquids. In *Ionic Liquids: Theory, Properties, New Approaches*; InTech, 2011. https://doi.org/10.5772/15170.

(40) McClung, R. E. D.; Kivelson, D. ESR Linewidths in Solution. V. Studies of Spin–Rotational Effects Not Described by Rotational Diffusion Theory. *J. Chem. Phys.* **1968**, *49* (8), 3380–3391. https://doi.org/10.1063/1.1670611.

(41) Merunka, D.; Peric, M.; Peric, M. Study of Nanostructural Organization of Ionic Liquids by Electron Paramagnetic Resonance Spectroscopy. *J. Phys. Chem. B* **2015**, *119* (7), 3185–3193. https://doi.org/10.1021/jp512487y.

(42) Miyake, Y.; Kawai, A. Solvation and Rotational Diffusion of Solutes in Room Temperature Ionic Liquids as Studied by EPR Spectroscopy with Nitroxide Spin Probing Method. *Appl. Magn. Reson.* **2018**, *49* (8), 825–835. https://doi.org/10.1007/s00723-018-1025-y.

(43) Mladenova, B. Y.; Chumakova, N. A.; Pergushov, V. I.; Kokorin, A. I.; Grampp, G.; Kattnig, D. R. Rotational and Translational Diffusion of Spin Probes in Room-Temperature Ionic Liquids. *J. Phys. Chem. B* **2012**, *116* (40), 12295–12305. https://doi.org/10.1021/jp306583g.

(44) Mladenova, B. Y.; Kattnig, D. R.; Grampp, G. Room-Temperature Ionic Liquids Discerned Via Nitroxyl Spin Probe Dynamics. *J. Phys. Chem. B* **2011**, *115* (25), 8183–8198. https://doi.org/10.1021/jp201703c.

(45) Noel, M. A. M.; Allendoerfer, R. D.; Osteryoung, R. A. Solvation in Ionic Liquids: An EPR Study. *J. Phys. Chem.* **1992**, *96* (5), 2391–2394. https://doi.org/10.1021/j100184a070.

(46) Stoesser, R.; Herrmann, W.; Zehl, A.; Strehmel, V.; Laschewsky, A. ESR Spin Probes in Ionic Liquids. *ChemPhysChem* **2006**, *7* (5), 1106–1111. https://doi.org/10.1002/cphc.200500651.

(47) Stout, G.; Engberts, J. B. F. N. Medium Effects on the Electron Spin Resonance Hyperfine Splitting Constants of Tert-Butyl Nitroxide in Mixed Aqueous Solvents. *J. Org. Chem.* **1974**, *39* (25), 3800–3802. https://doi.org/10.1021/jo00939a050.

(48) Strehmel, V.; Berdzinski, S.; Rexhausen, H. Interactions between Ionic Liquids and Radicals. *J. Mol. Liq.* **2014**, *192*, 153–170. https://doi.org/10.1016/j.molliq.2013.12.007.

(49) Likhtenshtein, G. I. *Nitroxides*; Springer Series in Materials Science; Springer International Publishing: Cham, 2020; Vol. 292. https://doi.org/10.1007/978-3-030-34822-9.

(50) Zhu, G.; Wang, Y.; Fu, H.; Xu, X.; Cui, Z.; Ji, X.; Wu, G. Photoinduced Electron Transfer between 2-Methylanthraquinone and Triethylamine in an Ionic Liquid: Time-Resolved EPR and Transient Absorption Spectroscopy Study. *Spectrochim. Acta Part A Mol. Biomol. Spectrosc.* **2015**, *137*, 148–153. https://doi.org/10.1016/j.saa.2014.08.021.

(51) Chakraborty, M.; Ahmed, T.; Dhale, R. S.; Majhi, D.; Sarkar, M. Understanding the Microscopic Behavior of Binary Mixtures of Ionic Liquids through Various Spectroscopic Techniques. *J. Phys. Chem. B* **2018**, *122* (50), 12114–12130. https://doi.org/10.1021/acs.jpcb.8b09699.

(52) Karve, L.; Dutt, G. B. Rotational Diffusion of Neutral and Charged Solutes in 1-Butyl-3-Methylimidazolium-Based Ionic Liquids: Influence of the Nature of the Anion on Solute Rotation. *J. Phys. Chem. B* **2012**, *116* (6), 1824–1830. https://doi.org/10.1021/jp208394n.

(53) Strehmel, V. Radicals in Ionic Liquids. *ChemPhysChem* **2012**, *13* (7), 1649–1663. https://doi.org/10.1002/cphc.201100982.

(54) Mladenova, B. Y.; Kattnig, D. R.; Grampp, G. Room-Temperature Ionic Liquids Discerned Via Nitroxyl Spin Probe Dynamics. *J. Phys. Chem. B* **2011**, *115* (25), 8183–8198. https://doi.org/10.1021/jp201703c.

(55) Miyake, Y.; Hidemori, T.; Akai, N.; Kawai, A.; Shibuya, K.; Koguchi, S.; Kitazume, T. EPR Study of Rotational Diffusion in Viscous Ionic Liquids: Analysis by a Fractional Stokes–Einstein–Debye Law. *Chem. Lett.* **2009**, *38* (2), 124–125. https://doi.org/10.1246/cl.2009.124.

(56) Israelachvili, J. N. *Intermolecular and Surface Forces*; Elsevier, 2011. https://doi.org/10.1016/C2011-0-05119-0.

(57) Pádua, A. A. H.; Costa Gomes, M. F.; Canongia Lopes, J. N. A. Molecular Solutes in Ionic Liquids: A Structural Perspective. *Acc. Chem. Res.* **2007**, *40* (11), 1087–1096. https://doi.org/10.1021/ar700050q.

(58) Tokuda, H.; Hayamizu, K.; Ishii, K.; Susan, M. A. B. H.; Watanabe, M. Physicochemical Properties and Structures of Room Temperature Ionic Liquids. 1. Variation of Anionic Species. *J. Phys. Chem. B* **2004**, *108* (42), 16593–16600. https://doi.org/10.1021/jp047480r.

(59) Kwac, K.; Geva, E. Solvation Dynamics of Formylperylene Dissolved in Methanol–Acetonitrile Liquid Mixtures: A Molecular Dynamics Study. *J. Phys. Chem. B* **2013**, *117* (34), 9996–10006. https://doi.org/10.1021/jp405818f.

(60) Ravi Kumar, V.; Verma, C.; Umapathy, S. Molecular Dynamics and Simulations Study on the Vibrational and Electronic Solvatochromism of Benzophenone. *J. Chem. Phys.* **2016**, *144* (6), 064302. https://doi.org/10.1063/1.4941058.

(61) Blazhynska, M. M.; Stepaniuk, D. S.; Koverga, V.; Kyrychenko, A.; Idrissi, A.; Kalugin, O. N. Structure and Dynamics of TiO2-Anchored D205 Dye in Ionic Liquids and Acetonitrile. *J. Mol. Liq.* **2021**, *332*, 115811. https://doi.org/10.1016/j.molliq.2021.115811.

(62) Koverga, V. A.; Smortsova, Y.; Miannay, F. A.; Kalugin, O. N.; Takamuku, T.; Jedlovszky, P.; Marekha, B.; Cordeiro, M. N. D. S.; Idrissi, A. Distance Angle Descriptors of the Interionic and Ion–Solvent Interactions in Imidazolium-Based Ionic Liquid Mixtures with Aprotic Solvents: A Molecular Dynamics Simulation Study. *J. Phys. Chem. B* **2019**, *123* (28), 6065–6075. https://doi.org/10.1021/acs.jpcb.9b03838.

(63) Das, S. K.; Sarkar, M. Rotational Dynamics of Coumarin-153 and 4-Aminophthalimide in 1-Ethyl-3-Methylimidazolium Alkylsulfate Ionic Liquids: Effect of Alkyl Chain Length on the Rotational Dynamics. *J. Phys. Chem. B* **2012**, *116* (1), 194–202. https://doi.org/10.1021/jp207528p.

(64) Das, S. K.; Sarkar, M. Probing Solute-Solvent Interaction in 1-Ethyl-3-Methylimidazolium-Based Room Temperature Ionic Liquids: A Time-Resolved Fluorescence Anisotropy Study. *J. Fluoresc.* **2014**, *24* (2), 455–463. https://doi.org/10.1007/s10895-013-1311-x.

(65) Gangamallaiah, V.; Dutt, G. B. Fluorescence Anisotropy of a Nonpolar Solute in 1-Alkyl-3-Methylimidazolium-Based Ionic Liquids: Does the Organized Structure of the Ionic Liquid Influence Solute Rotation? *J. Phys. Chem. B* **2013**, *117* (17), 5050–5057. https://doi.org/10.1021/jp401487r.

(66) Jas, G. S.; Wang, Y.; Pauls, S. W.; Johnson, C. K.; Kuczera, K. Influence of Temperature and Viscosity on Anthracene Rotational Diffusion in Organic Solvents: Molecular Dynamics Simulations and Fluorescence Anisotropy Study. *J. Chem. Phys.* **1997**, *107* (21), 8800–8812. https://doi.org/10.1063/1.475172.

(67) Karve, L.; Dutt, G. B. Rotational Diffusion of Neutral and Charged Solutes in Ionic Liquids: Is Solute Reorientation Influenced by the Nature of the Cation? *J. Phys. Chem. B* **2011**, *115* (4), 725–729. https://doi.org/10.1021/jp110119a.

(68) Khara, D. C.; Samanta, A. Fluorescence Response of Coumarin-153 in N -Alkyl- N -Methylmorpholinium Ionic Liquids: Are These Media More Structured than the Imidazolium Ionic Liquids? *J. Phys. Chem. B* **2012**, *116* (45), 13430–13438. https://doi.org/10.1021/jp3054058.

(69) Khara, D. C.; Samanta, A. Rotational Dynamics of Positively and Negatively Charged Solutes in Ionic Liquid and Viscous Molecular Solvent Studied by Time-Resolved Fluorescence Anisotropy Measurements. *Phys. Chem. Chem. Phys.* **2010**, *12* (27), 7671. https://doi.org/10.1039/b925099a.

(70) Kundu, N.; Roy, A.; Dutta, R.; Sarkar, N. Translational and Rotational Diffusion of Two Differently Charged Solutes in Ethylammonium Nitrate–Methanol Mixture: Does the Nanostructure of the Amphiphiles Influence the Motion of the Solute? *J. Phys. Chem. B* **2016**, *120* (24), 5481–5490. https://doi.org/10.1021/acs.jpcb.6b02251.

(71) Majhi, D.; Pabbathi, A.; Sarkar, M. Probing the Aggregation Behavior of Neat Imidazolium-Based Alkyl Sulfate (Alkyl = Ethyl, Butyl, Hexyl, and Octyl) Ionic Liquids through Time Resolved Florescence Anisotropy and NMR and Fluorescence Correlation Spectroscopy Study. *J. Phys. Chem. B* **2016**, *120* (1), 193–205. https://doi.org/10.1021/acs.jpcb.5b10137.

(72) Majhi, D.; Sahu, P. K.; Seth, S.; Sarkar, M. Probing the Interactions of Structurally Similar but Chemically Distinguishable Organic Solutes with 1-Ethyl-3-Methylimidazolium Alkyl Sulfate (Alkyl = Ethyl, Hexyl and Octyl) Ionic Liquids through Fluorescence, NMR and Fluorescence Correlation Spectrosco. *Phys. Chem. Chem. Phys.* **2016**, *18* (32), 22343–22354. https://doi.org/10.1039/C6CP03006H.

(73) Mali, K. S.; Dutt, G. B.; Mukherjee, T. Do Organic Solutes Experience Specific Interactions with Ionic Liquids? *J. Chem. Phys.* **2005**, *123* (17), 174504. https://doi.org/10.1063/1.2102847.

(74) Mandal, S.; Ghosh, S.; Banerjee, C.; Kuchlyan, J.; Sarkar, N. Roles of Viscosity, Polarity, and Hydrogen-Bonding Ability of a Pyrrolidinium Ionic Liquid and Its Binary Mixtures in the Photophysics and Rotational Dynamics of the Potent Excited-State Intramolecular Proton-Transfer Probe 2,2′-Bipyridine-3,3′-Diol. *J. Phys. Chem. B* **2013**, *117* (22), 6789–6800. https://doi.org/10.1021/jp4025443.

(75) Prabhu, S. R.; Dutt, G. B. Rotational Diffusion of Charged and Nondipolar Solutes in Ionic Liquid–Organic Solvent Mixtures: Evidence for Stronger Specific Solute–Solvent Interactions in Presence of Organic Solvent. *J. Phys. Chem. B* **2015**, *119* (33), 10720–10726. https://doi.org/10.1021/acs.jpcb.5b06297.

(76) Waluk, J. Conformational Analysis of Molecules in Excited States. **2000**, 297–366.

(77) Kattnig, D. R.; Akdogan, Y.; Bauer, C.; Hinderberger, D. High-Field EPR Spectroscopic Characterization of Spin Probes in Aqueous Ionic Liquid Mixtures. *Zeitschrift für Phys. Chemie* **2012**, *226* (11–12), 1363–1378. https://doi.org/10.1524/zpch.2012.0272.

(78) Majhi, D.; Seth, S.; Sarkar, M. Differences in the Behavior of Dicationic and Monocationic Ionic Liquids as Revealed by Time Resolved-Fluorescence, NMR and Fluorescence Correlation Spectroscopy. *Phys. Chem. Chem. Phys.* **2018**, *20* (11), 7844–7856. https://doi.org/10.1039/C7CP08630J.

(79) Sengupta, A.; RM, K. Electron Paramagnetic Resonance Spectroscopic Investigation of the Dynamics of Spin Probe in Room Temperature Ionic Liquid. *Mod. Chem. Appl.* **2016**, *04* (04). https://doi.org/10.4172/2329-6798.1000189.

(80) Strehmel, V. Radicals in Ionic Liquids. *ChemPhysChem* **2012**, *13* (7), 1649–1663. https://doi.org/10.1002/cphc.201100982.

(81) Strehmel, V.; Rexhausen, H.; Strauch, P. Synthesis of 4-Trimethylammonio-2,2,6,6-Tetramethylpiperidine-1-Yloxyl with Various Anions for Investigation of Ionic Liquids. *Tetrahedron Lett.* **2008**, *49* (20), 3264–3267. https://doi.org/10.1016/j.tetlet.2008.03.073.

(82) Strehmel, V.; Rexhausen, H.; Strauch, P.; Görnitz, E.; Strehmel, B. Temperature Dependence of Interactions between Stable Piperidine-1-Yloxyl Derivatives and an Ionic Liquid. *ChemPhysChem* **2008**, *9* (9), 1294–1302. https://doi.org/10.1002/cphc.200800068.

(83) Fleming, G. Chemical Applications of Ultrafast Spectroscopy.

(84) Strehmel, V.; Rexhausen, H.; Strauch, P. Synthesis of 4-Trimethylammonio-2,2,6,6-Tetramethylpiperidine-1-Yloxyl with Various Anions for Investigation of Ionic Liquids. *Tetrahedron Lett.* **2008**, *49* (20), 3264–3267. https://doi.org/10.1016/j.tetlet.2008.03.073.

(85) Kumar Das, S.; Sarkar, M. Studies on the Solvation Dynamics of Coumarin 153 in 1-Ethyl-3-Methylimidazolium Alkylsulfate Ionic Liquids: Dependence on Alkyl Chain Length. *ChemPhysChem* **2012**, *13* (11), 2761–2768. https://doi.org/10.1002/cphc.201200185.

(86) Liang, M.; Zhang, X.-X.; Kaintz, A.; Ernsting, N. P.; Maroncelli, M. Solvation Dynamics in a Prototypical Ionic Liquid + Dipolar Aprotic Liquid Mixture: 1-Butyl-3-Methylimidazolium Tetrafluoroborate + Acetonitrile. *J. Phys. Chem. B* **2014**, *118* (5), 1340–1352. https://doi.org/10.1021/jp412086t.

(87) Smortsova, Y.; Miannay, F.-A.; Koverga, V.; Dubois, J.; Kalugin, O.; Idrissi, A. Fluorescent Probe Dependence of the Solvation Dynamics in Ionic Liquid BmimBF4 and Propylene Carbonate Mixtures: A Time-Resolved Fluorescence and Quantum Chemistry Study. *J. Mol. Liq.* **2019**, *282*, 39–50. https://doi.org/10.1016/j.molliq.2019.02.123.

(88) Zhang, X.-X.; Liang, M.; Hunger, J.; Buchner, R.; Maroncelli, M. Dielectric Relaxation and Solvation Dynamics in a Prototypical Ionic Liquid + Dipolar Protic Liquid Mixture: 1-Butyl-3-Methylimidazolium Tetrafluoroborate + Water. *J. Phys. Chem. B* **2013**, *117* (49), 15356–

15368. https://doi.org/10.1021/jp4043528.

(89) Ivanov, M. Y.; Polienko, Y. F.; Kirilyuk, I. A.; Prikhod'ko, S. A.; Adonin, N. Y.; Fedin, M. V. Peek Inside the Water Mixtures of Ionic Liquids at Molecular Level: Microscopic Properties Probed by EPR Spectroscopy. *Int. J. Mol. Sci.* **2021**, *22* (21), 11900. https://doi.org/10.3390/ijms222111900.

(90) Kattnig, D. R.; Akdogan, Y.; Lieberwirth, I.; Hinderberger, D. Spin Probing of Supramolecular Structures in 1-Butyl-3-Methyl-Imidazolium Tetrafluoroborate/Water Mixtures. *Mol. Phys.* **2013**, *111* (18–19), 2723–2737. https://doi.org/10.1080/00268976.2013.793420.

(91) Onsager, L. Electric Moments of Molecules in Liquids. *J. Am. Chem. Soc.* **1936**, *58* (8), 1486–1493. https://doi.org/10.1021/ja01299a050.

(92) Schuster, P.; Jakubetz, W.; Marius, W. Molecular Models for the Solvation of Small Ions and Polar Molecules. In *Topics in Current Chemistry*; Springer Berlin Heidelberg: Berlin, Heidelberg, 1975; pp 1–107.

(93) Hardacre, C.; Holbrey, J. D.; McMath, S. E. J.; Nieuwenhuyzen, M. Small-Angle Scattering from Long-Chain Alkylimidazolium-Based Ionic Liquids. In *ACS Symposium Series*; 2002; Vol. 818, pp 400–412. https://doi.org/10.1021/bk-2002-0818.ch031.

(94) Downard, A.; Earle, M. J.; Hardacre, C.; McMath, S. E. J.; Nieuwenhuyzen, M.; Teat, S. J. Structural Studies of Crystalline 1-Alkyl-3-Methylimidazolium Chloride Salts. *Chem. Mater.* **2004**, *16* (1), 43–48. https://doi.org/10.1021/cm034344a.

(95) Abdallah, D. J.; Robertson, A.; Hsu, H.-F.; Weiss, R. G. Smectic Liquid-Crystalline Phases of Quaternary Group VA (Especially Phosphonium) Salts with Three Equivalent Long n -Alkyl Chains. How Do Layered Assemblies Form in Liquid-Crystalline and Crystalline Phases? *J. Am. Chem. Soc.* **2000**, *122* (13), 3053–3062. https://doi.org/10.1021/ja994055g.

(96) Nagana Gowda, G. A.; Chen, H.; Khetrapal, C. L.; Weiss, R. G. Amphotropic Ionic Liquid Crystals with Low Order Parameters. *Chem. Mater.* **2004**, *16* (11), 2101–2106. https://doi.org/10.1021/cm034963j.

(97) Chen, H.; Kwait, D. C.; Gönen, Z. S.; Weslowski, B. T.; Abdallah, D. J.; Weiss, R. G. Phase Characterization and Properties of Completely Saturated Quaternary Phosphonium Salts. Ordered, Room-Temperature Ionic Liquids. *Chem. Mater.* **2002**, *14* (10), 4063–4072. https://doi.org/10.1021/cm010930x.

(98) Mladenova, B. Y.; Chumakova, N. A.; Pergushov, V. I.; Kokorin, A. I.; Grampp, G.; Kattnig, D. R. Rotational and Translational Diffusion of Spin Probes in Room-Temperature Ionic Liquids. *J. Phys. Chem. B* **2012**, *116* (40), 12295–12305. https://doi.org/10.1021/jp306583g.

(99) Etienne, E.; Le Breton, N.; Martinho, M.; Mileo, E.; Belle, V. SimLabel: A Graphical User Interface to Simulate Continuous Wave EPR Spectra from Site-Directed Spin Labeling Experiments. *Magn. Reson. Chem.* **2017**, *55* (8), 714–719. https://doi.org/10.1002/mrc.4578.

(100) Stoll, S.; Schweiger, A. EasySpin, a Comprehensive Software Package for Spectral Simulation and Analysis in EPR. *J. Magn. Reson.* **2006**, *178* (1), 42–55. https://doi.org/10.1016/j.jmr.2005.08.013.

(101) Persson, K.; Bales, B. L. EPR Study of an Associative Polymer in Solution: Determination of Aggregation Number and Interactions with Surfactants. *J. Chem. Soc. Faraday Trans.* **1995**, *91*

(17), 2863. https://doi.org/10.1039/ft9959102863.

(102) Knauer, B. R.; Napier, J. J. The Nitrogen Hyperfine Splitting Constant of the Nitroxide Functional Group as a Solvent Polarity Parameter. The Relative Importance for a Solvent Polarity Parameter of Its Being a Cybotactic Probe vs. Its Being a Model Process. *J. Am. Chem. Soc.* **1976**, *98* (15), 4395–4400. https://doi.org/10.1021/ja00431a010.

(103) Weingärtner, H. The Static Dielectric Constant of Ionic Liquids. *Zeitschrift für Phys. Chemie* **2006**, *220* (10), 1395–1405. https://doi.org/10.1524/zpch.2006.220.10.1395.

(104) Stoppa, A.; Hunger, J.; Hefter, G.; Buchner, R. Structure and Dynamics of 1- N -Alkyl-3- N -Methylimidazolium Tetrafluoroborate + Acetonitrile Mixtures. *J. Phys. Chem. B* **2012**, *116* (25), 7509–7521. https://doi.org/10.1021/jp3020673.

(105) Mialkowski, C.; Chagnes, A.; Carré, B.; Lemordant, D.; Willmann, P. Excess Thermodynamic Properties of Binary Liquid Mixtures Containing Dimethylcarbonate and γ-Butyrolactone. *J. Chem. Thermodyn.* **2002**, *34* (11), 1847–1856. https://doi.org/10.1016/S0021-9614(02)00232-X.

(106) Barthel, J.; Neueder, R.; Roch, H. Density, Relative Permittivity, and Viscosity of Propylene Carbonate+dimethoxyethane Mixtures from 25 °C to 125 °C. *J. Chem. Eng. Data* **2000**, *45* (6), 1007–1011. https://doi.org/10.1021/je000098x.

(107) Wakai, C.; Oleinikova, A.; Weingärtner, H. Reply to "Comment On 'How Polar Are Ionic Liquids? Determination of the Static Dielectric Constant of an Imidazolium-Based Ionic Liquid by Microwave Spectroscopy'''''." *J. Phys. Chem. B* **2006**, *110* (11), 5824–5824. https://doi.org/10.1021/jp0601973.

(108) Koel, M. Solvatochromic Study on Binary Solvent Mixtures with Ionic Liquids. *Zeitschrift für Naturforsch. A* **2008**, *63* (7–8), 505–512. https://doi.org/10.1515/zna-2008-7-818.

(109) Ando, M.; Kawano, M.; Tashiro, A.; Takamuku, T.; Shirota, H. Low-Frequency Spectra of 1-Methyl-3-Octylimidazolium Tetrafluoroborate Mixtures with Methanol, Acetonitrile, and Dimethyl Sulfoxide: A Combined Study of Femtosecond Raman-Induced Kerr Effect Spectroscopy and Molecular Dynamics Simulations. *J. Phys. Chem. B* **2020**, *124* (36), 7857–7871. https://doi.org/10.1021/acs.jpcb.0c04870.

(110) Carissimi, G.; Montalbán, M. G.; Díaz Baños, F. G.; Víllora, G. Density, Refractive Index and Volumetric Properties of Water–Ionic Liquid Binary Systems with Imidazolium-Based Cations and Tetrafluoroborate, Triflate and Octylsulfate Anions at T = 293 to 343 K and p = 0.1 MPa. *J. Chem. Eng. Data* **2019**, *64* (3), 979–994. https://doi.org/10.1021/acs.jced.8b00854.

(111) Kawano, M.; Sadakane, K.; Iwase, H.; Matsugami, M.; Marekha, B. A.; Idrissi, A.; Takamuku, T. Assessment of the UCST-Type Liquid–liquid Phase Separation Mechanism of Imidazolium-Based Ionic Liquid, [C 8 Mim][TFSI], and 1,4-Dioxane by SANS, NMR, IR, and MD Simulations. *Phys. Chem. Chem. Phys.* **2021**, *23* (42), 24449–24463. https://doi.org/10.1039/D1CP01940F.

(112) Srinivasa Krishna, T.; Nain, A. K.; Chentilnath, S.; Punyaseshudu, D.; Munibhadrayya, B. Densities, Ultrasonic Speeds, Refractive Indices, Excess and Partial Molar Properties of Binary Mixtures of Imidazolium Based Ionic Liquid with Pyrrolidin-2-One at Temperatures from 298.15 L to 323.15 K. *J. Chem. Thermodyn.* **2016**, *101*, 103–114. https://doi.org/10.1016/j.jct.2016.05.021.

(113) Mancini, P. M.; Fortunato, G. G.; Adam, C. G.; Vottero, L. R. Solvent Effects on Chemical Processes: New Solvents Designed on the Basis of the Molecular–microscopic Properties of (Molecular Solvent + 1,3-Dialkylimidazolium) Binary Mixtures. *J. Phys. Org. Chem.* **2008**, *21* (2), 87–95. https://doi.org/10.1002/poc.1227.

(114) Dalton, L. R. *EPR and Advanced EPR Studies of Biological Systems*; Dalton, L. R., Ed.; CRC Press, 2018. https://doi.org/10.1201/9781351071871.

(115) Bales, B. L.; Meyer, M.; Smith, S.; Peric, M. EPR Line Shifts and Line Shape Changes Due to Spin Exchange of Nitroxide Free Radicals in Liquids: 6. Separating Line Broadening Due to Spin Exchange and Dipolar Interactions. *J. Phys. Chem. A* **2009**, *113* (17), 4930–4940. https://doi.org/10.1021/jp8093947.

(116) Bales, B. L.; Peric, M.; Lamy-Freund, M. T. Contributions to the Gaussian Line Broadening of the Proxyl Spin Probe EPR Spectrum Due to Magnetic-Field Modulation and Unresolved Proton Hyperfine Structure. *J. Magn. Reson.* **1998**, *132* (2), 279–286. https://doi.org/10.1006/jmre.1998.1414.

(117) Halpern, H. J.; Peric, M.; Yu, C.; Bales, B. L. Rapid Quantitation of Parameters from Inhomogeneously Broadened EPR Spectra. *J. Magn. Reson. Ser. A* **1993**, *103* (1), 13–22. https://doi.org/10.1006/jmra.1993.1125.

(118) Schreier, S.; Polnaszek, C. F.; Smith, I. C. P. Spin Labels in Membranes Problems in Practice. *Biochim. Biophys. Acta - Rev. Biomembr.* **1978**, *515* (4), 395–436. https://doi.org/10.1016/0304-4157(78)90011-4.

(119) Gaffney, B. J.; McConnell, H. M. The Paramagnetic Resonance Spectra of Spin Labels in Phospholipid Membranes. *J. Magn. Reson.* **1974**, *16* (1), 1–28. https://doi.org/10.1016/0022-2364(74)90193-0.

(120) Ivanov, M. Y.; Veber, S. L.; Prikhod'ko, S. A.; Adonin, N. Y.; Bagryanskaya, E. G.; Fedin, M. V. Probing Microenvironment in Ionic Liquids by Time-Resolved EPR of Photoexcited Triplets. *J. Phys. Chem. B* **2015**, *119* (42), 13440–13449. https://doi.org/10.1021/acs.jpcb.5b06792.

(121) Smortsova, Y.; Miannay, F.-A.; Gustavsson, T.; Sauvage, F.; Ingrosso, F.; Kalugin, O.; Idrissi, A. Interrogating the Mechanism of the Solvation Dynamics in BmimBF4/PC Mixtures: A Cooperative Study Employing Time-Resolved Fluorescence and Molecular Dynamics. *J. Mol. Liq.* **2021**, *340*, 117163. https://doi.org/10.1016/j.molliq.2021.117163.

(122) Kundu, N.; Roy, A.; Dutta, R.; Sarkar, N. Translational and Rotational Diffusion of Two Differently Charged Solutes in Ethylammonium Nitrate–Methanol Mixture: Does the Nanostructure of the Amphiphiles Influence the Motion of the Solute? *J. Phys. Chem. B* **2016**, *120* (24), 5481–5490. https://doi.org/10.1021/acs.jpcb.6b02251.

(123) Prabhu, S. R.; Dutt, G. B. Rotational Diffusion of Charged and Nondipolar Solutes in Ionic Liquid–Organic Solvent Mixtures: Evidence for Stronger Specific Solute–Solvent Interactions in Presence of Organic Solvent. *J. Phys. Chem. B* **2015**, *119* (33), 10720–10726. https://doi.org/10.1021/acs.jpcb.5b06297.

(124) Mandal, S.; Ghosh, S.; Banerjee, C.; Kuchlyan, J.; Sarkar, N. Roles of Viscosity, Polarity, and Hydrogen-Bonding Ability of a Pyrrolidinium Ionic Liquid and Its Binary Mixtures in the Photophysics and Rotational Dynamics of the Potent Excited-State Intramolecular Proton-

Transfer Probe 2,2′-Bipyridine-3,3′-Diol. *J. Phys. Chem. B* **2013**, *117* (22), 6789–6800. https://doi.org/10.1021/jp4025443.

(125) Zafarani-Moattar, M. T.; Majdan-Cegincara, R. Viscosity, Density, Speed of Sound, and Refractive Index of Binary Mixtures of Organic Solvent + Ionic Liquid, 1-Butyl-3-Methylimidazolium Hexafluorophosphate at 298.15 K. *J. Chem. Eng. Data* **2007**, *52* (6), 2359–2364. https://doi.org/10.1021/je700338t.

(126) Canongia Lopes, J. N.; Costa Gomes, M. F.; Husson, P.; Pádua, A. A. H.; Rebelo, L. P. N.; Sarraute, S.; Tariq, M. Polarity, Viscosity, and Ionic Conductivity of Liquid Mixtures Containing [C 4 C 1 Im][Ntf 2] and a Molecular Component. *J. Phys. Chem. B* **2011**, *115* (19), 6088–6099. https://doi.org/10.1021/jp2012254.

(127) Rizzuto, A. M.; Pennington, R. L.; Sienerth, K. D. Study of the BMIM-PF6: Acetonitrile Binary Mixture as a Solvent for Electrochemical Studies Involving CO2. *Electrochim. Acta* **2011**, *56* (14), 5003–5009. https://doi.org/10.1016/j.electacta.2011.03.106.

(128) Zhu, A.; Wang, J.; Han, L.; Fan, M. Measurements and Correlation of Viscosities and Conductivities for the Mixtures of Imidazolium Ionic Liquids with Molecular Solutes. *Chem. Eng. J.* **2009**, *147* (1), 27–35. https://doi.org/10.1016/j.cej.2008.11.013.

(129) Vraneš, M.; Zec, N.; Tot, A.; Papović, S.; Dožić, S.; Gadžurić, S. Density, Electrical Conductivity, Viscosity and Excess Properties of 1-Butyl-3-Methylimidazolium Bis(Trifluoromethylsulfonyl)Imide+propylene Carbonate Binary Mixtures. *J. Chem. Thermodyn.* **2014**, *68*, 98–108. https://doi.org/10.1016/j.jct.2013.08.034.

(130) Wang, H.; Liu, S.; Wang, N.; Liu, Y. Vinylene Carbonate Modified 1-Butyl-3-Methyle-Imidazolium Tetrafluoroborate Ionic Liquid Mixture as Electrolyte. *Int. J. Electrochem. Sci.* **2012**, *7* (8), 7579–7586.

(131) Li, W.; Zhang, Z.; Han, B.; Hu, S.; Xie, Y.; Yang, G. Effect of Water and Organic Solvents on the Ionic Dissociation of Ionic Liquids. *J. Phys. Chem. B* **2007**, *111* (23), 6452–6456. https://doi.org/10.1021/jp071051m.

(132) Khupse, N. D.; Kumar, A. Dramatic Change in Viscosities of Pure Ionic Liquids upon Addition of Molecular Solvents. *J. Solution Chem.* **2009**, *38* (5), 589–600. https://doi.org/10.1007/s10953-009-9390-7.

(133) Wang, J.; Tian, Y.; Zhao, Y.; Zhuo, K. A Volumetric and Viscosity Study for the Mixtures of 1-n-Butyl-3-Methylimidazolium Tetrafluoroborate Ionic Liquid with Acetonitrile, Dichloromethane, 2-Butanone and N, N ? Dimethylformamide. *Green Chem.* **2003**, *5* (5), 618. https://doi.org/10.1039/b303735e.

(134) Dutt, G. B. Rotational Diffusion of Nondipolar Solutes in Ionic Liquids: Influence of Nature of Anion on Solute Rotation. *Indian J. Chem. - Sect. A Inorganic, Phys. Theor. Anal. Chem.* **2010**, *49* (5–6), 705–713.

(135) Stoppa, A.; Hunger, J.; Buchner, R. Conductivities of Binary Mixtures of Ionic Liquids with Polar Solvents. *J. Chem. Eng. Data* **2009**, *54* (2), 472–479. https://doi.org/10.1021/je800468h.

(136) Kawano, M.; Sadakane, K.; Iwase, H.; Matsugami, M.; Marekha, B. A.; Idrissi, A.; Takamuku, T. Assessment of the UCST-Type Liquid–liquid Phase Separation Mechanism of Imidazolium-Based Ionic Liquid, [C 8 Mim][TFSI], and 1,4-Dioxane by SANS, NMR, IR, and MD

Simulations. *Phys. Chem. Chem. Phys.* **2021**, *23* (42), 24449–24463. https://doi.org/10.1039/D1CP01940F.

(137) Dzyuba, S. V.; Bartsch, R. A. Expanding the Polarity Range of Ionic Liquids. *Tetrahedron Lett.* **2002**, *43* (26), 4657–4659. https://doi.org/10.1016/S0040-4039(02)00858-4.

(138) Cerón-Carrasco, J. P.; Jacquemin, D.; Laurence, C.; Planchat, A.; Reichardt, C.; Sraïdi, K. Determination of a Solvent Hydrogen-Bond Acidity Scale by Means of the Solvatochromism of Pyridinium- N -Phenolate Betaine Dye 30 and PCM-TD-DFT Calculations. *J. Phys. Chem. B* **2014**, *118* (17), 4605–4614. https://doi.org/10.1021/jp501534n.

(139) Griffith, O. H.; Dehlinger, P. J.; Van, S. P. Shape of the Hydrophobic Barrier of Phospholipid Bilayers (Evidence for Water Penetration in Biological Membranes). *J. Membr. Biol.* **1974**, *15* (1), 159–192. https://doi.org/10.1007/BF01870086.

(140) Schuster, P.; Jakubetz, W.; Marius, W. Molecular Models for the Solvation of Small Ions and Polar Molecules. In *Topics in Current Chemistry*; Springer-Verlag: Berlin/Heidelberg, 1975; pp 1–107. https://doi.org/10.1007/BFb0045206.

(141) Otero-Mato, J. M.; Lesch, V.; Montes-Campos, H.; Smiatek, J.; Diddens, D.; Cabeza, O.; Gallego, L. J.; Varela, L. M. Solvation in Ionic Liquid-Water Mixtures: A Computational Study. *J. Mol. Liq.* **2019**, *292*, 111273. https://doi.org/10.1016/j.molliq.2019.111273.

(142) Semino, R.; Zaldívar, G.; Calvo, E. J.; Laria, D. Lithium Solvation in Dimethyl Sulfoxide-Acetonitrile Mixtures. *J. Chem. Phys.* **2014**, *141* (21), 214509. https://doi.org/10.1063/1.4902837.

(143) Migliorati, V.; Lapi, A.; D'Angelo, P. Unraveling the Solvation Geometries of the Lanthanum(<scp>iii</Scp>) Bistriflimide Salt in Ionic Liquid/Acetonitrile Mixtures. *Phys. Chem. Chem. Phys.* **2020**, *22* (36), 20434–20443. https://doi.org/10.1039/D0CP03977B.

Chapter 4

Composition Dependence on the Solvation and Reorientation Dynamics in $BmimPF_6$-ACN mixture

A part of this chapter (optical Kerr effect study) is the basis of the publication-

Dynamics in the $BmimPF_6$/acetonitrile mixtures observed by femtosecond optical Kerr effect and molecular dynamics simulations.

Phys. Chem. Chem. Phys., 2020, 22, 24544-24554

DOI: 10.1039/d0cp03847d

Getting an idea about the excited state dynamics of the sensitizers present in the electrolyte medium is one of the important aspects for the optimization of the efficiency of the DSSC. In this chapter, we will discuss the solvation and reorientational dynamics in a particular IL-MS mixture, i.e. $BmimPF_6$-ACN mixture. For the steady-state and time resolved solvation dynamics study, we have used the so called 'golden' probe coumarin 153 and we have performed this study only using the TCSPC technique with picosecond time resolution. In addition, by using the femtosecond Kerr-effect spectroscopy, we have also studied the complete reorientational dynamics in the same IL-MS mixture.[1] By combining these two types of spectroscopic techniques, we can get an idea about both the solvation and reorientational relaxation dynamics with and without the probe molecules respectively. In this regard, it is worth mentioning that, I was involved in preparing the samples and the measurements of experimental OKE signals by using the oscillator and amplifier modes of measurements. The other parts (molecular dynamics simulation and experimental data analysis) of the optical Kerr effect spectroscopic study were performed by our collaborators. Therefore, in this chapter, the results from the OKE study will be discussed without much details on the data analysis and MD simulation process.

4.1. Introduction:

The chapter containing the transient absorption studies of the indoline photosensitizers in the IL-MS mixtures (Chapter 2) showed us the importance of solvation processes in the excited state relaxation dynamics of the dye molecules. Therefore, it is important to study the solvation dynamics and orientational relaxation of the solvent molecules in case of the IL-MS mixtures to get better insights about these mixtures.

To do an experimental study about the solvation dynamics, first we need to get an idea about the origin of the solvation dynamics process.

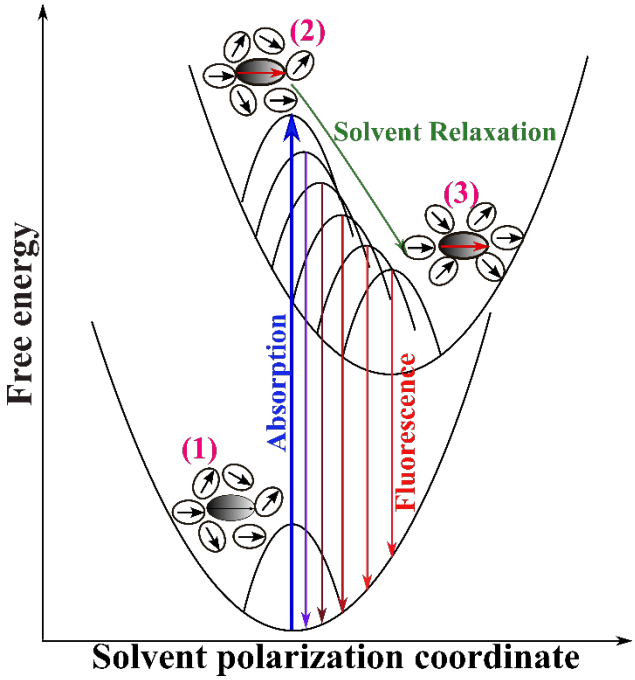

Figure 4.1: A schematic description of the physical processes involved in the solvation dynamics process

This Figure (Figure 4.1) will depict the solvation dynamics in the best way. In general, the dyes or fluorophores show a big change in their dipole moments (μ) while they become excited. This process of dipole moment change of the fluorophores is very fast. It happens just after the photoexcitation. However, as the movements of atoms are much slower than the movement of electrons, the surrounding medium can't show that fast change in their positions compared to the dipole moment change of the excited fluorophores. The surrounding atoms were in statistic equilibrium with the ground state dipole initially before the photoexcitation (state 1). They still remains in the Franck-Condon state of the ground state of the fluorophore just after the photoexcitation (at time t = 0, state 2).[2] After the photoexcitation, to accommodate and to recreate the statistic equilibrium with this newly generated dipole, the surrounding atoms have to reorient themselves (State 3). Unlike the photoexcitation of the dye, this process is not instant and is known as the solvation dynamics. This process of solvation can be detected experimentally by studying the time dependent fluorescence Stokes shift of the dye/fluorophore molecule. This process can cover multiple timescales (from picosecond to nanosecond).

In theory, the solvation dynamics process is a probe independent process, i.e. it is an inherent property of solvent. However, there are quite a few exceptions. The solvation times vary while varying the dye/probe molecules.[3–10] In general, these probe dependency of the solvation process arises when there is a possibility of the solvent-probe interactions[8–10] and also due to the rotational motion[5,6] of the probe molecules. Therefore, choosing a suitable probe molecule for studying the solvation dynamics is quite tricky. Previous study showed that, for studying the solvation process in ILs on in IL-MS mixtures, coumarin 153 (C153) is the most efficient probe among the available probes due to its rigid structure and simple two electronic state model for S_0-S_1 transition.[11] Therefore, we will also use C153 molecule for the study of solvation dynamics in BmimPF_6-ACN mixtures.

As we have discussed about the probe used for our study, we can describe our choice of IL-MS mixture for this study, i.e. BmimPF_6-ACN mixture. To initiate, ILs are very interesting mediums for various physical and electrochemical applications due to their interesting properties like high conductivity, thermal stability, low vapor pressure etc. However, their abnormally high viscosity is the reason for their limit in some electrochemical applications. One can overcome the limit in their applications by mixing them with different molecular solvents like ACN, γ-BL, PC etc.[12–17] The solvation response in these types of IL-MS mixtures normally varies from several picoseconds to several nanoseconds. These type of solvation dynamics in the IL-MS mixtures strongly varies on the mixture compositions and also the microviscosity of the mixtures.[18–20] Among the imidazolium ILs and MSs, there are various options of IL-MS mixtures by changing the ions and MSs in the mixture. However, we have chosen only one of them out of all the options which is BmimPF_6-ACN mixture. The main reason behind choosing this mixture to study the solvation process lies in the presence of different interactions between the mixture components in a typical IL-MS mixture. A previous theoretical study (using MD simulations) by Koverga et al.[21] had showed that, the IL-MS mixtures with common cation $Bmim^+$ can be divided into two sets of mixtures depending upon the cation-anion interaction strength and it depends on the size of anions. First set consists of ILs like BmimBF_4 and BmimTFO where the cation-anion interactions are relatively strong due to smaller anions whereas the second set contains BmimPF_6 and BmimTFSI with weaker cation-anion interactions due to larger anion size. Therefore, the probe molecule used for solvation dynamics study should interact more with the ions in the IL-MS mixtures containing BmimPF_6 and BmimTFSI as the ILs than those consist of BmimBF_4 and BmimTFO as ILs. Besides, different molecular solvents should also have different effect on the solvation process. In this aspect, the solvation dynamics studies have been already performed in the case of IL-MS mixtures containing BmimBF_4 and BmimTFSI as ILs.[18–20,22]

In addition to the solvation dynamics study using C153 probe and TCSPC technique, optical Kerr effect study was also performed to study complete reorientation dynamics of BmimPF_6-ACN mixture. During the OKE discussion, our main goal will be to explain the OKE response and its composition dependence in case of the BmimPF_6-ACN mixture. The slow dynamics, which is due to the reorientation in molecules, was analyzed using a multi-exponential decay. The resulting decay times were then attempted to connect with the relaxation of mixture components. In addition, the low frequency spectra, containing the information about

intermolecular dynamics, were also analyzed. This type of low frequency OKE spectral analysis was achieved by following steps. First, the low frequency spectra in ACN and in pure $BmimPF_6$ were interpreted in terms of rotations and translations of the components. Then, the composition dependence of the rotational and translational spectra was discussed describing the changes in the OKE spectra.

This chapter is organized as follows: in the next section, we will give a comprehensive literature review about previous solvation dynamics study and reorientation dynamics study in solvents and solvent mixtures. Next, we will discuss our experimental results, we will start our discussion with the steady state and TCSPC results and discuss about them and then we will elaborate our results and discussions about the OKE study. Finally, we will give an overall conclusion about this chapter.

4.1. Literature preview:

There are already quite a few previous reports present describing the solvation dynamics process in various solvents, ionic liquids and even in the mixtures between them. We will try to revisit these previous studies in this section. This literature survey can educate us about the solvation dynamics process which is going to be very useful for the solvation and reorientation dynamics study in $BmimPF_6$-ACN mixture.

The solvation dynamics studies using various picosecond and femtosecond time-resolved fluorescence spectroscopic techniques were performed already in different organic solvents,[5,9,10,23–26] ionic liquids,[27–36] solvent mixtures,[3,37] IL/MS mixtures,[18–20,22,38,39] micelle[40] and also in protein[40]. The probe dependent solvation dynamics study was performed using various fluorescent probe molecules like substituted coumarins, 3-aminopthalimide (3AP), 4-aminopthalimide (4AP), 4-amino-N-methyl pthalimide (4ANMP), aniline, dimethyl aniline, 1-aminonapthalene, 2-aminoanthrcene, 1-aminopyrene and others.[3,5,23–30,32,33,6,34–39,41–44,7,45,46,8,9,11,18–20] In the case of pure $BmimPF_6$ ionic liquid, there exist also a few literature data related to its solvation dynamics.[33,36] In this regard, the other imidazolium ILs like $BmimBF_4$ and BmimTFSI, there exist a few previous reports about the solvation process in the mixtures with these ILs and different solvents like water, ACN and PC.[18–20]

In addition to the pioneering study of solvation dynamics in various organic solvents,[25] Maroncelli group had published an article on the study of solvation in different ILs (pyrrolidinium, imidazolium ILs and others) using TCSPC and broadband ultrafast fluorescence up-conversion technique.[47] This study reveals the bimodal nature of the solvation process in ILs, similar to their previous study using only the TCSPC technique.[48] While the faster solvation component are attributed to the inertial motion of the components in the medium, the slower component can be described due to the structural organization of ILs in the medium and strongly correlated with the medium viscosity in the case of different ILs.[42] In addition, the rotational relaxation times of C153 in ILs behave similar to that in pure conventional solvents. Furthermore, the non-exponential character of the anisotropy decay was due to non-Markovian friction effects due to abnormally high viscosity of ILs. Similarly, various solvation dynamics studies by Paul et al.,[31] Karmakar et al.[44] and Samanta et al.[49] also found biexponential solvation dynamics of various ILs while fitting the solvent response

functions of them. Although the solvation in some of the ILs can easily be fitted by biexponential function, thinking the solvation in ILs similar to that in conventional molecular solvents is naive from our part. According to a review article by Samanta,[50] even if we don't think about the heterogeneity in a particular IL, the solvent reorganization process in ILs is quite complex and assignment of these different solvation timescales are even more challenging.

There are also other studies regarding the assignment of two solvation dynamics timescales in the case of different ILs. In contrary to the results from Maroncelli work in ILs, works by Headley et al.[46] and Mukherjee et al.[45] had claimed a faster solvation response which finished in 100 ps time range. The main reason behind the difference between these two sets of results originated from the difference in the solvation response function (SRF) formation. In addition, a study by Muramatsu et al.[30] revealed that the origin of faster component in solvation process is due to anions' inertial motion and the longer component originates from motions of the other components including the cations.

Unlike the pure components, the number of reports regarding the solvation dynamics in different IL-MS mixtures is comparatively less.[18–20,22,38,39] All the reports have the solvation dynamics study using the similar probe molecule C153. While both reports from Maroncelli group was concentrated on $BmimBF_4$-ACN[18] and $BmimBF_4$-water[20] mixtures, Smortsova et al.[19] had studied the solvation in BmimTFSI-PC mixture using different time-resolved spectroscopic techniques. However, before all these works, Paul et al.[38] and Chakrabarty et al.[39] had published another work regarding the solvation in $BmimPF_6$-nonpolar solvent and $BmimPF_6$-water mixtures respectively. The similarities in all of these works is the presence of two different time scales in all the intermediate mole fractions in the IL-MS mixtures. Moreover, the average solvation time values in $BmimBF_4$-ACN/PC/water mixtures maintain the power law relation with the medium viscosity, whereas this type of power law relation with mixture viscosity was not followed in case of the solvation in $BmimPF_6$-nonpolar solvent mixtures. On the similar note, theoretical calculations[51] using dielectric continuum model and semi-molecular theories did not give satisfactory predictions of the experimental results in case of the IL-MS mixtures initially. Later, a modified semi-molecular theory[52] had almost predicted the experimental results in case of $BmimBF_4$-ACN/water mixtures. In addition, MD simulations suggests the role of translational and rotational motions in the solvation process.[53–55] As a result, translational motion, anion translation to be precise, is more important in case of IL solvation process.

Similar to the probe dependent solvation dynamics study, there are also quite a few literature data related to the optical Kerr effect study of the reorientation dynamics in various pure solvents, ILs and IL-MS mixtures. In the case of pure ACN, previous OKE studies[56–63] revealed that the diffusive reorientation component can be fitted using single exponential decay and the relaxation time range is between 1.4-1.98 ps. The low-frequency part of the OKE response also has only one peak at 50 cm^{-1},[61] which is a combination of translational (peak at 10 cm^{-1}) and librational (peak at 50 cm^{-1}) bands.[62–64] These experimental results were also supported by simulation studies.[65,66] In addition, there are also a few studies related to the OKE response in pure $BmimPF_6$. However, none of them could capture the whole dynamics as up to a few

nanoseconds of delay times are needed.[67–73] In this regard, OKE response of another IL $BmimBF_4$ was also studied by Fayer et al.,[74,75] which suggested the presence of longest decay time of 1400 ps. However, the lower frequency OKE response study showed the presence of a bimodal intermolecular band and also the presence of low frequency interionic modes.[68,76–80] Generally, the low-frequency part of the intermolecular band is described due to translational motion while the high-frequency one is due to librational motion. However, there are some disputes about this assignment.[68,78,80–82] Giraud et al. had also described additional libration bands at 30 and 65 cm^{-1}.[76] In addition to the intermolecular band, presence of an intramolecular band between 85-111 cm^{-1} was also found and it was ascribed to the bending motion between butyl group an imidazolium ring.[69,76,83,84] Ishida et al. had showed in their combined theoretical and experimental study of the low-frequency OKE response that while both cations and anions show the lower frequency part of the intermolecular spectrum, only the cation translation is the reason behind the higher frequency part of the spectra.[68]

4.2. Sample preparation:

The ionic liquid $BmimPF_6$ (Purity 99.5%, Solvionic) and acetonitrile (99%, Sigma Aldrich) were kept in a glove box in an argon atmosphere. All the mixtures were prepared inside the glove box for the optical Kerr effect measurements to minimize the impurity from the air. In case of TCSPC experiments, mother solutions of pure $BmimPF_6$ and pure ACN were prepared separately containing the dye molecule C153. Then they were mixed accordingly inside the glove box to prepare the particular mole fractions of $BmimPF_6$-ACN mixture containing the dye.

4.3. Experimental setups:

The TCSPC setup used for this study is built in the LASIR unit. The detailed description of this setup is described in the experimental details chapter (chapter 5, section 5.2). The data analysis method using the TCSPC setup after the experiments is also discussed at the same place (chapter 5, section 5.2). In addition, the OKE measurements were performed using the femtosecond OKE setup situated in the InFemto laboratory, University of Warsaw. Similar to the TCSPC setup, the detailed OKE setup is also described in the experimental details chapter (chapter 5, section 5.3).

4.4. Results:

4.4.1. Steady state measurements:

Before getting an idea about the solvation dynamics, one should have an idea about the steady state behaviors of the same dye C153 in the studied IL-MS mixtures. In Figure 4.2(A), the absorption and emission spectra of the dye can be noticed in the whole composition range of $BmimPF_6$-ACN mixtures. From this figure, one can easily notice that only the transition between S_0 and S_1 contributes to the absorption and emission process in this wavelength region, as there is only one peak in case of both absorption and emission spectra. In addition to the steady-state absorption and emission spectra, the positions of the peaks in the absorption and emission spectra can also be discussed. All the values of the steady-state properties are shown

in Table 4.1. Furthermore, the values of absorption and emission maxima and the Stokes shift values in pure components are quite similar to the previous studies.[18,42]

Table 4.1: Steady state properties of Coumarin 153 in $BmimPF_6$-ACN mixture. All the values of wavenumbers and wavelengths are given in 10^3 cm^{-1} and nm respectively.

X_{IL}	λ_{Abs}^{Max}	ν_{Abs}^{Max}	λ_{Em}^{Max}	ν_{Em}^{Max}	ν_{Stokes}
0	418.57	23.68	518.45	18.53	5.15
0.05	420.92	23.57	524.64	18.45	5.12
0.1	422.8	23.46	526.57	18.33	5.13
0.2	421.61	23.44	528.31	18.27	5.17
0.3	422.88	23.4	530.68	18.18	5.22
0.4	423.01	23.45	529.79	18.21	5.24
0.5	424.56	23.38	530.38	18.13	5.25
0.65	424.37	23.39	530.81	18.11	5.28
0.8	424.89	23.37	531.11	18.06	5.31
1	425	23.36	531.68	17.92	5.44

In the case of the absorption and emission maxima (Figure 4.2 (B) and Table 4.1), both of them show an overall composition dependent red shift in their values while increasing the X_{IL} of the mixture. Similar type of composition dependent shift was also noticed in the case of previous studies using C153 dye in other IL-MS mixtures.[18–20,22] In addition, the composition dependent Stokes shift values of the dye in the studied IL-MS mixtures also show an overall increase in their values while increasing the IL-concentration in the mixture, similar to previous studies.[18–20,22] This type of red-shift in absorption and emission maxima as well as the increase of the Stokes shift values while increasing the X_{IL} was previously described considering the increase of polarity of the IL-MS mixtures while increasing IL concentration. Indeed, the solvatochromic polarity parameter (E_T^N) values of ILs are greater than that of the polar aprotic MSs like (ACN, γ-BL and PC) and are in the range of primary alcohols. However, another probe independent solvent polarity parameter, static dielectric constant (ε) values of ILs are much smaller than that of MSs. Therefore, it is quite difficult to describe this type of red-shift in absorption and emission maxima and the increase in the Stokes shift values while increasing X_{IL} only by considering the polarity of the IL-MS mixture, because a clear idea about the polarity parameter values in the ILs as well as in the IL-MS mixtures is still not available. As there are ions in the medium, one should also consider about the fact that, the other type of possible interactions like ion-ion, ion-solvent and dye-solvent interactions may play an important role in describing the steady state behaviors of the C153 dye.

Furthermore, both absorption and emission maxima values show the non-linear composition dependent red-shift while increasing the IL-mole fractions in $BmimPF_6$-ACN mixtures (Figure 4.2 (B)). In this aspect, Zhang et al.[20] had suggested that this type of non-linear dependency can be an indication of preferential solvation in the medium. In the case of both the absorption and emission maxima (Figure 4.2(B)), a rapid change is observed at the low X_{IL} region, which was also observed previously.[18,19,22]

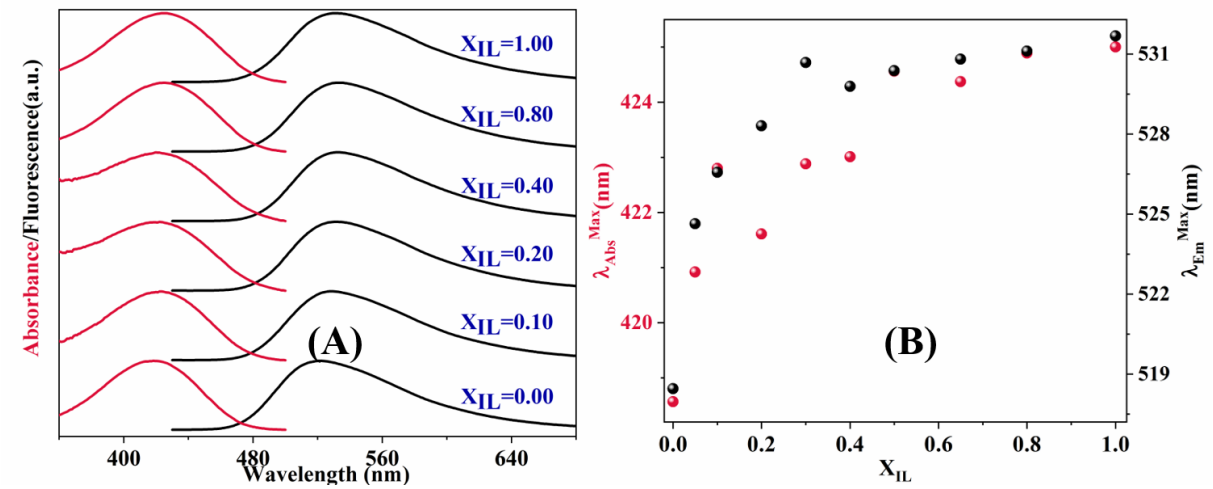

Figure 4.2: (A) Normalized absorption and emission spectra, (B) absorption and emission maxima of C153 in $BmimPF_6$-ACN mixture

With these background knowledge about the steady state behavior of the dye in the studied IL-MS mixtures, we can now proceed to discuss time resolved fluorescence measurements using the TCSPC techniques which is in the next sub-section.

4.4.2. TCSPC measurements:

Here we will discuss about the procedure to calculate the solvation dynamics of C153 dye in $BmimPF_6$-ACN mixtures. The overall process passes through two important steps. First, the reconstruction and fitting of time resolved emission spectra (TRES) from the experimental TCSPC time-dependent decays and second, the calculation of the solvation response function as well as the solvation dynamics. It is important to mention that, we could not get the complete solvation using the TCSPC setup as the previous studies mentioned that the overall solvation dynamics of C153 extends from femtoseconds to nanoseconds time region and the instrumental response function (IRF) of our TCSPC setup is 32 ps. For the femtosecond timescale solvation dynamics study, we need to use the femtosecond up-conversion setup, which is out of the scope of this study. By combining the results from both TCSPC and up-conversion setups, we can get the complete idea about the solvation dynamics in $BmimPF_6$-ACN mixture.

4.4.2.1. Reconstruction of Time-Resolved Emission spectra (TRES):

As an outcome of the deconvolution and multi-exponential fitting (described in chapter 5, section 5.2) of TCSPC decays at different wavelengths throughout the whole emission spectrum of a sample, one can have different values of time components ($\tau_i(\lambda_j)$), corresponding amplitude ($A_i(\lambda_j)$) and number of components (n) for a particular wavelength λ_j. These fitted parameters are then used to scale the steady-state emission spectrum for a particular sample using the equation 4.1.

$$I_{corr}(t,\lambda_j) = \frac{S(\lambda_j)}{\sum_{i=1}^{n} A_i(\lambda_j)\tau_i(\lambda_j)} \sum_{i=1}^{n} A_i(\lambda_j)\exp\left(-\frac{t}{\tau_i(\lambda_j)}\right) \quad (4.1)$$

Where $S(\lambda_j)$ is nothing but the steady-state emission intensity at that particular wavelength λ_j. Using these corrected intensities at particular time and wavelength $[I_{corr}(t,\lambda_j)]$ we can

construct a time-wavelength matrix in the time range 32 ps – 10 ns with varying time steps, considering time resolution of the TCSPC setup and lifetimes of these indoline-based dyes. Then, each of these wavelength-dependent spectrum was converted into wavenumber-dependent one by multiplying with a λ^2 conversion factor. The overall procedure finally leads us to the construction of time dependent emission spectra (TRES) in case of each sample. After the re-construction of TRES, each of these time-resolved emission spectra was then fitted by using a lognormal function, leading to the time dependent values of the mean wavenumbers (ν_{mean}(t)) alongside with other parameters. These ν_{mean}(t) values are used to calculate the solvation response function (SRF). The time resolved emission spectra of C153 in pure $BmimPF_6$ can be noticed from Figure 4.3. The evolution of the values of ν_{mean}(t) and ν_{max}(t) after fitting the time-resolved fluorescence in pure $BmimPF_6$ is shown in the appendix D (Figure D1).

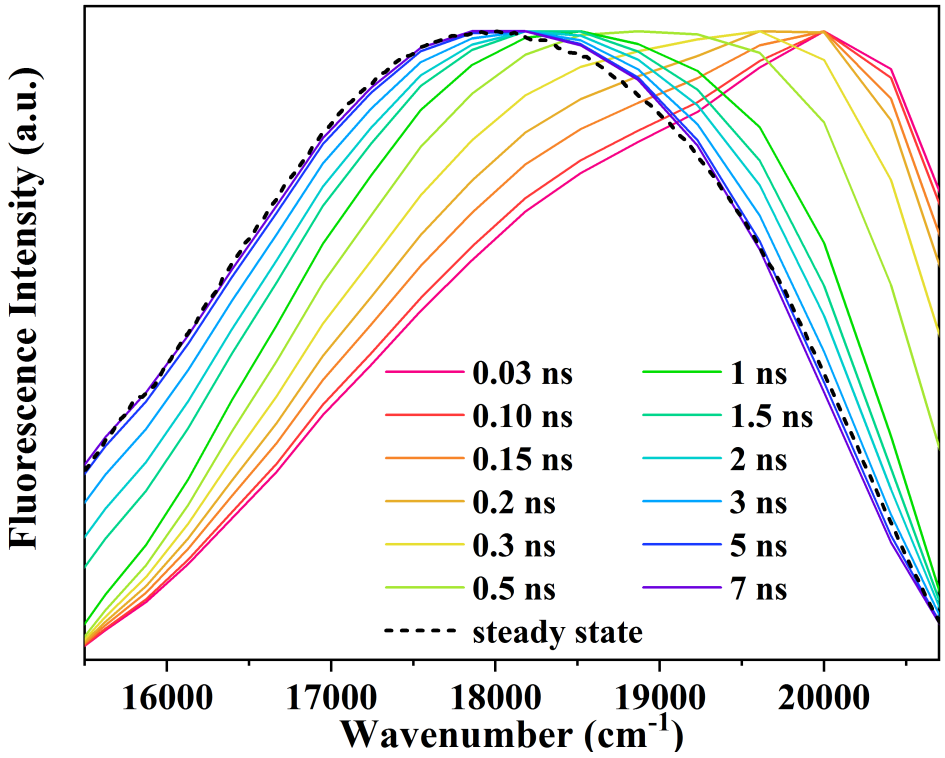

Figure 4.3: Time resolved emission spectra of C153 in pure $BmimPF_6$. The black dotted one is the steady state emission spectra.

4.4.2.2. Calculation and fitting of the Solvation response function (SRF):

The solvation response function (C(t)) corresponding to each studied samples can be created using the equation 4.2.

$$C(t) = \frac{\nu(t)-\nu(\infty)}{\nu(0)-\nu(\infty)} \qquad (4.2)$$

Here, $\nu(t)$ is the time dependent mean wavenumbers and $\nu(\infty)$ is the same at a very large time (10 ns in our case). The determination of $\nu(0)$ is the most uncertain thing because of the time-resolution of the setup. Therefore, we have followed the method suggested by Fee and Maroncelli, to calculate the values of $\nu(0)$.[85] According to them, the steady-state absorption

and emission spectra in given polar and non-polar solvents can be used to calculate $\nu(0)$ values for a particular sample. Therefore, equation 4.3 is used to calculate the $\nu(0)$ values for a given sample.

$$\nu(0) \approx \nu_{abs} - \left[(\nu_{abs})_{np} - (\nu_{em})_{np}\right] \quad (4.3)$$

$(\nu_{abs})_{np}$ and $(\nu_{em})_{np}$ are values of absorption and emission maxima of same dye molecule in a non-polar solvent. Cyclohexane was used as a non-polar solvent in this case. This method of calculation from the steady-state spectrum provides us the values of $\nu(0)$ with the error range of ~ $\pm$ 200 cm^{-1}.

After the calculation of SRF for the studied samples, it is fitted by using multi-exponential functions. The number of exponentials was chosen considering the values of χ^2. In Table 4.2, all the fitting parameters are shown.

Table 4.2: Best fit parameters of the SRFs of C153 using multi-exponential functions

X_{IL}	$y_0 . 10^4$	A_1	τ_1(ps)	A_2	τ_2(ps)	A_3	τ_3(ps)	χ^2
0.2	12±2	0.25±0.04	172±15.02	0.21±0.05	29±0.51	0.12±0.04	9±0.03	0.0031
0.3	10.1±3.1	0.28±0.05	252±20.53	0.18±0.04	43±0.98	0.11±0.02	12±0.05	0.0021
0.4	15.1±4.5	0.26±0.07	349±29.51	0.19±0.03	60±1.01	0.09±0.01	16±0.08	0.0038
0.5	20.1±5.3	0.41±0.05	430±31.61	0.22±0.04	86±1.63	0.10±0.02	24±0.11	0.0026
0.65	12.6±3.3	0.42±0.08	668±42.35	0.21±0.05	103±2.84	0.12±0.01	31±0.25	0.0034
0.8	11.9±4	0.35±0.13	926±51.61	0.28±0.04	181±3.61	0.08±0.01	50±0.34	0.0041
1	5.89±1.2	0.31±0.05	1743±100.52	0.26±0.06	376±5.86	0.20±0.04	92±1.31	0.0013

4.4.2.3. Discussions:

From Figure 4.4, one can clearly notice the effect of mixture composition on the solvation process, as well as on the values of solvation response functions (SRF). The solvation dynamics are getting longer while adding more and more ILs in the mixtures. To get a further idea about this solvation dynamics, the weighted average solvation times are calculated from the fitted parameters using the multi-exponential functions shown in Table 4.2. We have also tried to compare the average solvation times of C153 in pure $BmimPF_6$ with previous literature values, which also results in a quite good similarities. (0.85 ps in this study compared to 1 ns in previous studies[7,43]). In addition, the viscosity dependence of the average solvation time values in case of $BmimPF_6$-ACN mixtures is plotted alongside with the previous results in Figure 4.5. The

viscosity dependence of the average solvation time values (τ_{solv}) can be modelled by using the power law function shown following-

$$\tau_{solv} \propto \eta^{p} \quad (4.4)$$

Where p=0.48

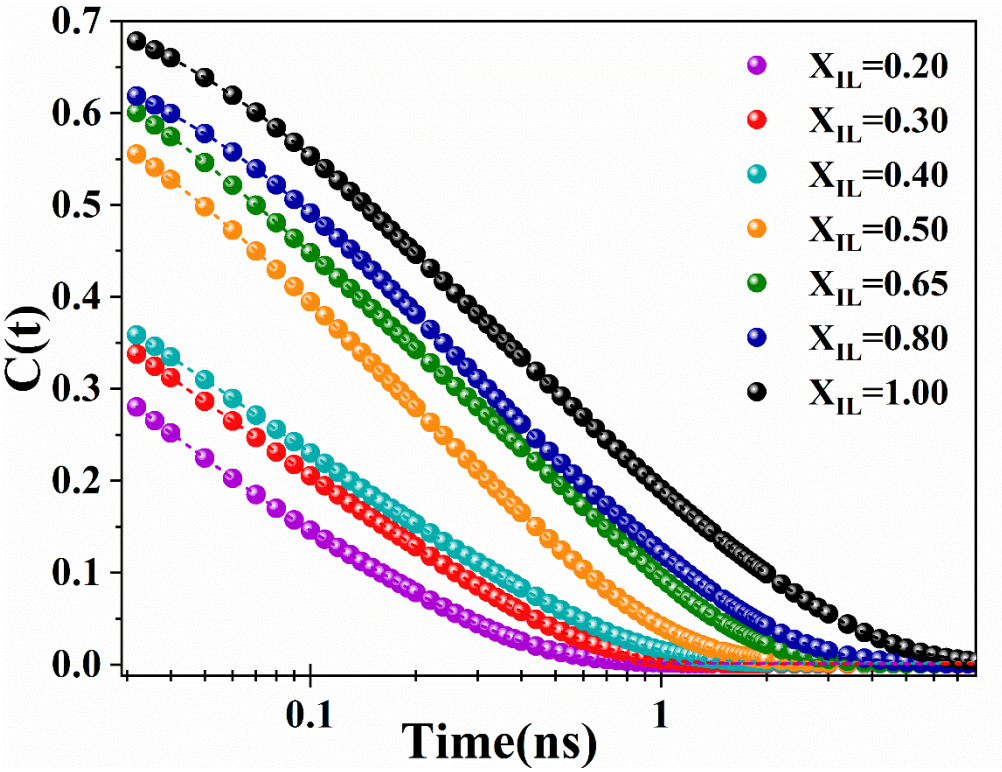

Figure 4.4: Observed solvation response functions (circles) in $BmimPF_6$-ACN mixture. The dashed lines refer to the fits of SRF using multi-exponential function

It this important to mention that, this fractional p value doesn't fall in the range between 0.7-0.8 which is the case for other IL-polar-aprotic MS mixtures.[18,19,22] In this regard, Smortsova et al.[19] had also mentioned that, the p value of 0.8 is the characteristics of $Bmim^+$ cation, as the viscosity dependence of average solvation times in IL-MS mixtures containing $Bmim^+$ cation follows the power law dependence with $p \sim 0.8$. To explain this deviation in our study, we need to consider the fact that, this study was performed only with the TCSPC setup with 32 ps time resolution. Therefore, we were unable to consider the faster time components present in the solvation process. To get a much better idea about the complete solvation process, we need to carry out the solvation dynamics measurements with sub-picosecond time resolution, i.e. the up-conversion setup, which is our next goal regarding this study. Only then, the complete solvation dynamics process in $BmimPF_6$-ACN mixture can be captured.

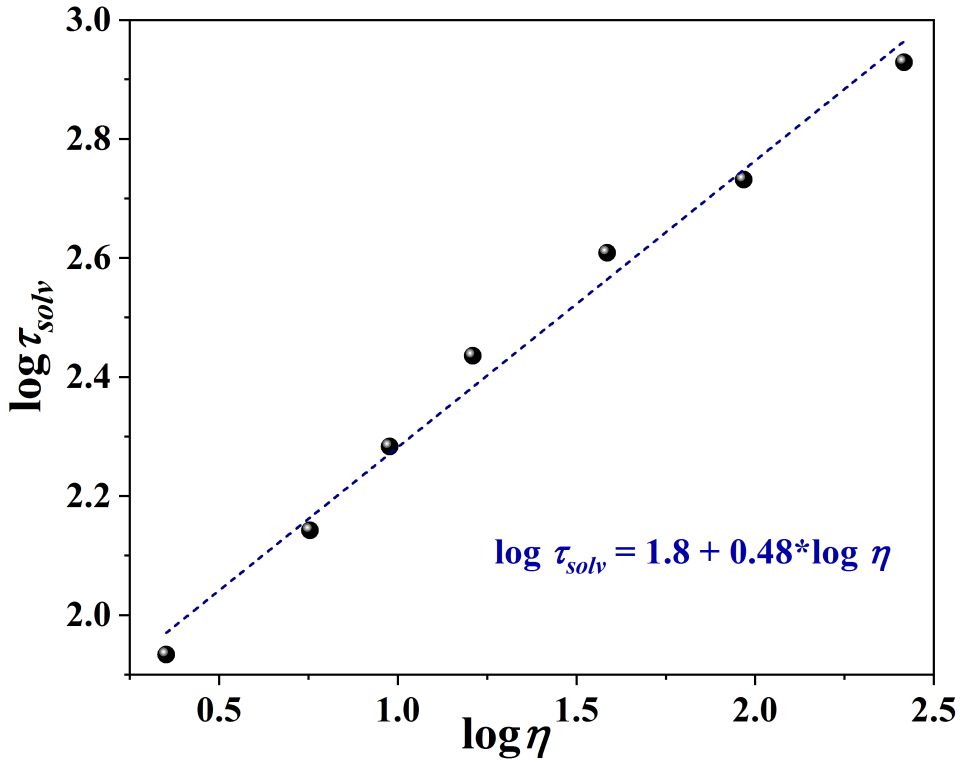

Figure 4.5: Viscosity dependence of the average solvation times in $BmimPF_6$-ACN mixture

In the next sub-section, we are going to discuss about the results from the complete reorientational dynamics study of the same IL-MS mixtures using the femtosecond OKE technique.

4.4.3. Femtosecond optical Kerr-effect spectroscopy:

4.4.3.1. Orientational diffusion study:

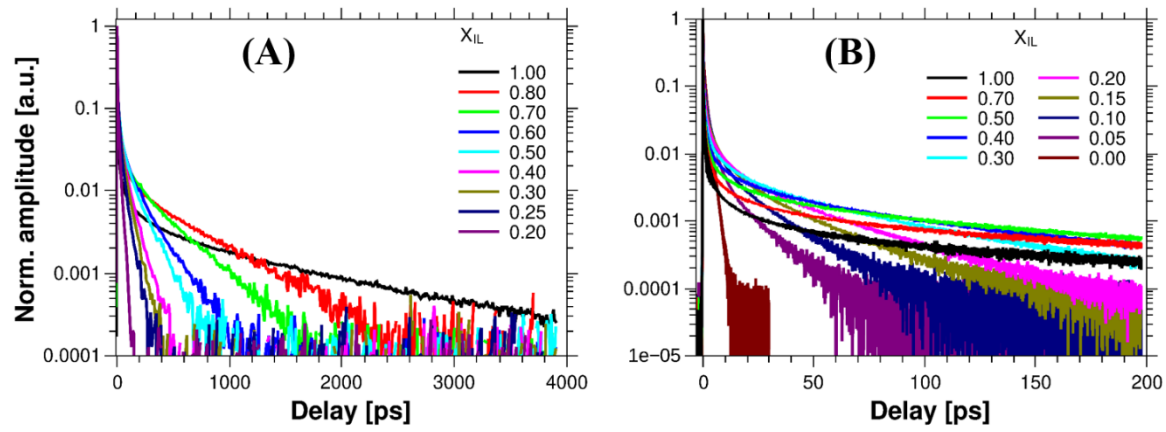

Figure 4.6: The OKE signals measured using (A) amplifier and (B) oscillator setups

In Figure 4.6, we can notice the OKE signals in the logarithmic scale both in the amplifier and oscillator modes of measurements. From this figure, it can be clearly noticed that, the long-time decay, which is associated to the orientation relaxation, decreases while decreasing the ionic liquid mole fraction. The main reason behind this decrease is the decrease of medium viscosity

while decreasing X_{IL} of the IL-MS mixture. To get a quantitative idea about the rate of decrease of the OKE signal, a multi-exponential fit was performed which resulted in three distinct relaxation times. The values are shown in Tables 4.3 and 4.4 and also in Figure 4.7.

Table 4.3: Composition dependent values of the decay times after fitting OKE signals measured with amplifier setup.

X_{IL}	τ_1(ps)	τ_2(ps)	$a_1.10^2$	$a_2.10^2$
0.20	60.8	28.8	2.42	5.95
0.25	72.2	31.3	3.43	5.11
0.30	92.9	34.9	2.98	5.21
0.40	146	48.9	2.8	4.09
0.50	222	61.5	1.79	4.61
0.60	362	77.7	1.59	2.54
0.80	648	105	1.07	1.75
1.00	1637	346	0.291	0.356

Table 4.4: Composition dependent values of the decay times after fitting OKE signals measured with oscillator setup.

X_{IL}	τ_1(ps)	τ_2(ps)	τ_3(ps)	τ_4(ps) [a]	$a_1.10^4$	$a_2.10^4$	$a_3.10^4$	$a_4.10^4$ [a]
0.00	-	-	1.62	-	-	-	103	-
0.05	17.4	5.55	2.08	-	2.48	8.29	57.3	-
0.10	22.8	6.63	2.34	-	3.89	11.1	40.6	-
0.15	43.9	17.2	5.27	1.98	1.91	5.47	15.9	29.9
0.20	55.7	21.9	6.5	2.14	2.25	4.94	12.9	25.3
0.30	92.9	34.9	9.56	2.59	1.99	3.86	8.74	19.3
0.40	146	48.9	13	3.15	1.91	2.76	6	15.2
0.50	222	61.5	14.4	3.28	1.75	2.05	4.93	13.5
0.70	475	90.3	19.5	4.28	0.867	1.75	3.49	10.5
1.00	1637	346	42.8	6.77	0.356	0.434	2.64	7.68

[a] This component was not involved in the analysis of reorientation. However, it is taken into account while removing the picosecond components from OKE signal before calculation of the reduced spectral density

From this Figure (Figure 4.7), one can clearly notice that each of these three relaxation time components overall increase up to two order of magnitudes while increasing X_{IL}. However, there is only one relaxation time in case of pure ACN and its value is 1.62 ps, which is in perfect agreement with the previous studies by Loughnane et al.[60] and Bardak et al.[64] In addition, the longest relaxation time in case of pure $BmimPF_6$ is 1637 ps, which is also in the similar range of 1400 ps in pure $BmimBF_4$.[86,87] As the viscosity of $BmimPF_6$ is higher than that of $BmimBF_4$, one can expect the increase of the orientational relaxation time. In addition, the 1.17 fold increase of the longest relaxation time is lower than the viscosity increase from $BmimBF_4$ to $BmimPF_6$.

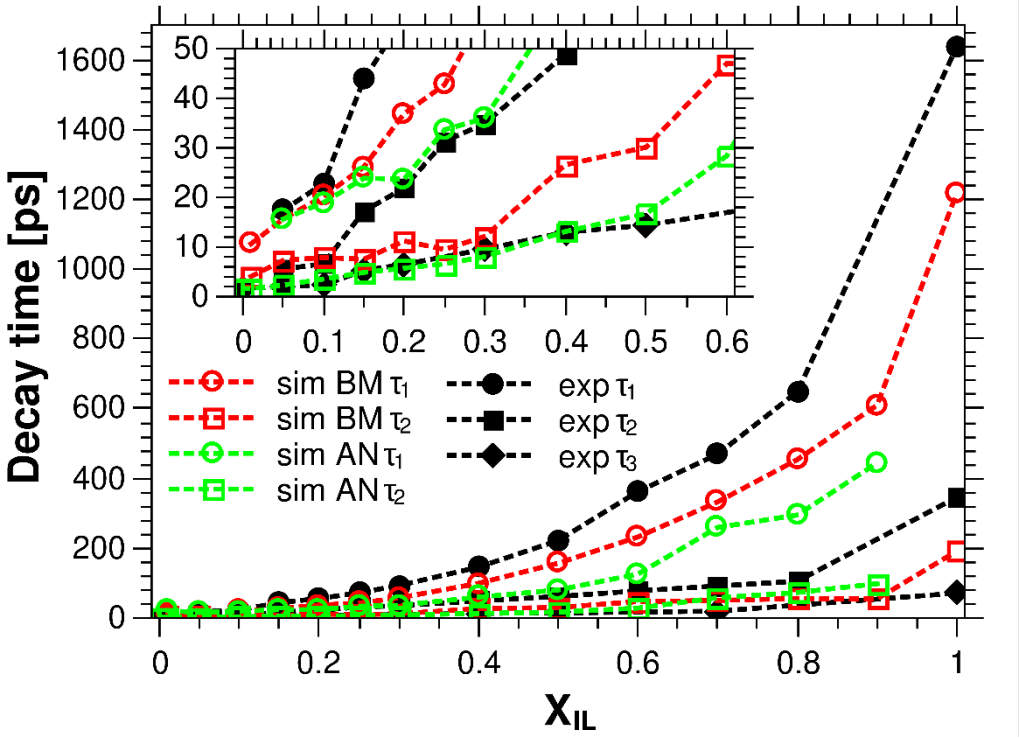

Figure 4.7: The decay times after fitting the experimental OKE response and simulated polarizability correlation function $\psi^{mol,ACN}(t)$ and $\psi^{mol,BM}(t)$ due to the rotation of ACN and Bmim cation respectively. The part of the plot until $X_{IL} \leq 0.60$ is zoomed in the inset.

Indeed, the change of the behavior of local environment plays an important role in case of simple liquids which results in non-SED type viscosity dependence of the reorientational time values.[88,89] This can also be applied in case of ionic liquids to describe the non-SED behavior of the longest orientational time. One more aspect to be considered for the sake of this discussion. Due to the symmetry of the anions present in the IL-MS mixtures, only the cations and ACN molecules can contribute in the values of three orientational time components. It can be safely stated that, the origin of longest one (τ_3) is associated to the ionic liquid cations, whereas the effect of the ACN dynamics can't be ignored in case of the other two timescales (τ_1 and τ_2).

To support this analysis, we have also used molecular dynamics simulation to calculate the contributions of both ACN ($\psi^{mol,ACN}(t)$) and IL ($\psi^{mol,BM}(t)$) cations (as the anions are symmetric, no contributions) to the total polarizability correlation function ($\psi^{tot}(t)$) of the system. (Figure 4.8) The reason behind calculating the overall polarizability correlation function is that this gives us an idea about collective reorientation observed in the OKE response. While the time dependent decay of $\psi^{mol,BM}(t)$ can be fitted by using 2 exponential decay, the decay of $\psi^{mol,ACN}(t)$ function can be fitted by using both single ($X_{IL} \leq 0.01$) and double exponentials ($X_{IL} > 0.01$). All the fitted values of relaxation times are shown in Figure 4.7 and Tables D1 and D2 in the appendix. Although the MD simulation of the studied systems is not a part of this thesis, we can get the correlation with the experimental findings through the MD simulation outcome.

From the MD simulations, the following interpretations of the experimental OKE response can be achieved.

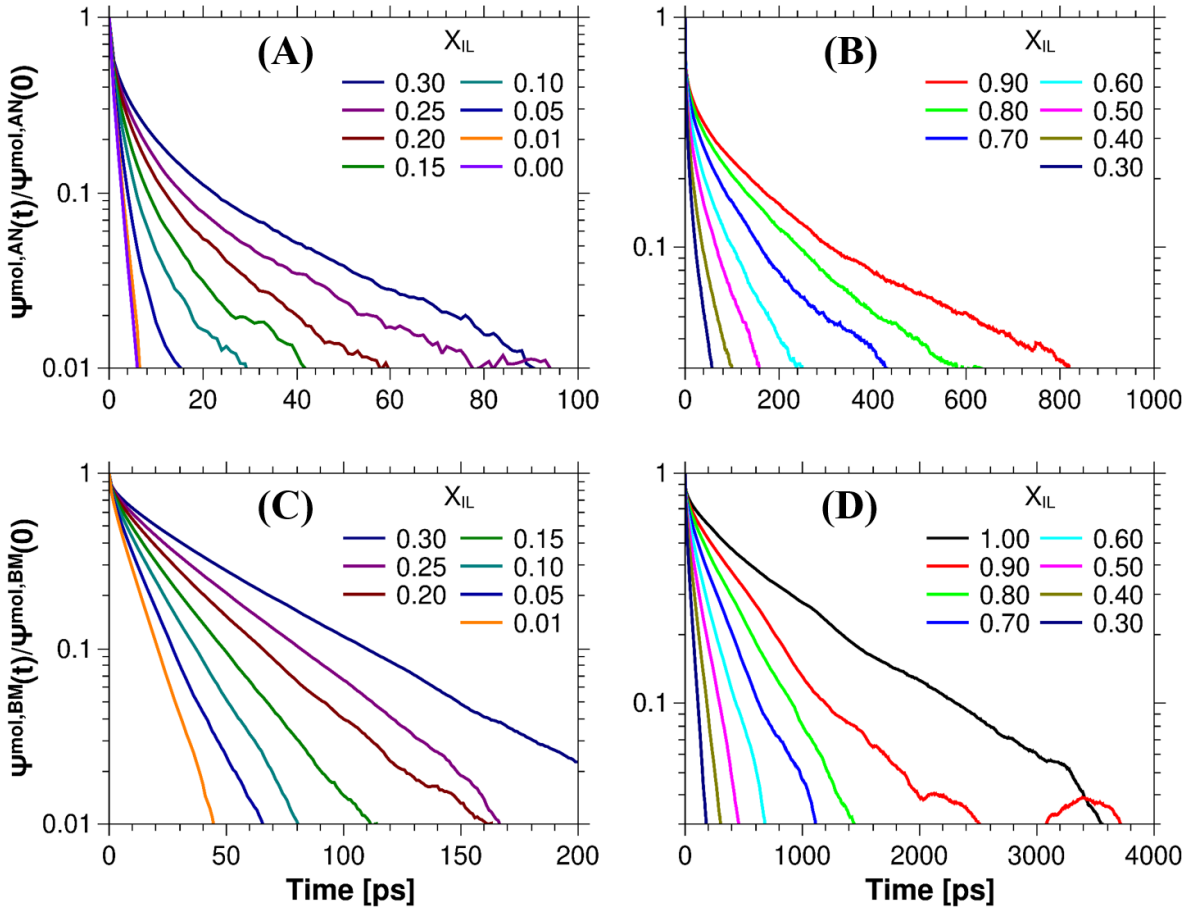

Figure 4.8: Time dependent decay of correlation function of the molecular contributions to the total polarizability of the system due to ACN [(A), (B)] and Bmim cation [(C), (D)] at different mixture compositions in $BmimPF_6$-ACN mixture

Firstly, the long and intermediate relaxation times after the fitting of OKE decay can be attributed to the reorientation of the Bmim cation and ACN molecules which are present near the imidazolium ring. In addition, the cation contribution is dominant in case of all the compositions of the mixtures.

Secondly, the experimental short decay time of the fitted OKE response is mainly due to the reorientation of ACN molecules in the bulk or in the neighborhood of the alkyl chain extension of the cation.

In addition to that, it was also noticed during this theoretical study that, the ACN contribution towards the fast relaxation is greater than the cation contribution up to X_{IL}=0.15. (Figure 4.9) Furthermore, the acetonitrile relaxation dynamics is also slowed down by more than 2 orders of magnitude starting from 1.6 ps in pure ACN to 444 ps at X_{IL}=0.90, which was also noticed in case of ACN in $BmimBF_4$[90] and also in silica nanopores[91–96] previously. Besides, from the previous discussion about decay times, it can be noticed that two different decay times (intermediate and short) are originating from ACN molecules in different environments in $BmimPF_6$-ACN mixture. This similar type of results were also noticed in the case of $BmimBF_4$-ACN mixture in the study by Stoppa et al.[97] and also in silica nanopores[91–96].

For the further validation of these interpretations from the fitted experimental OKE response and MD simulations, we need to do a more detailed study of the reorientation dynamics, which is going to be discussed later.

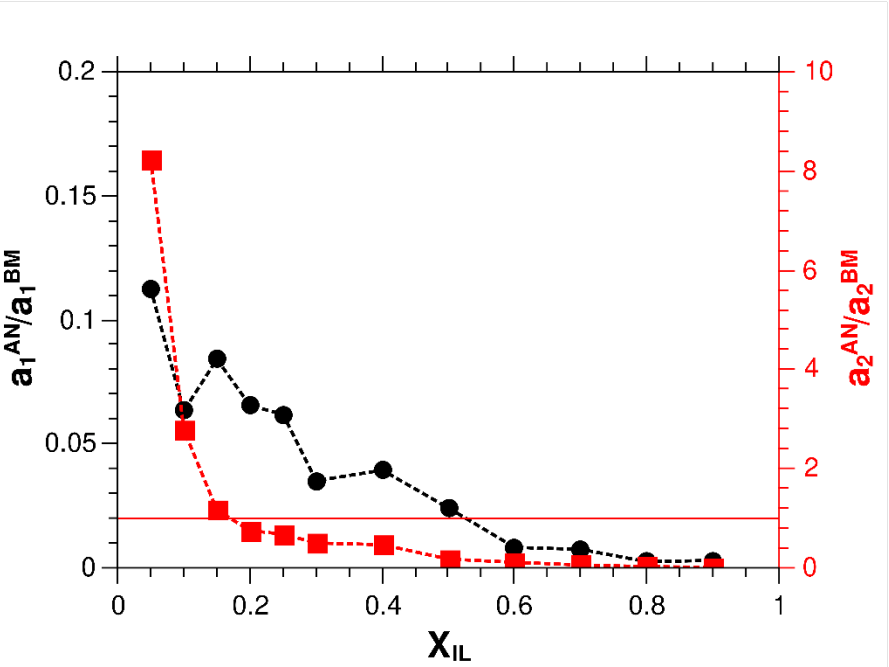

Figure 4.9: Ratio of the amplitudes of the fast and slow components after the fitting of $\psi^{mol,ACN}(t)$ and $\psi^{mol,BM}(t)$

4.4.3.2. OKE low frequency response:

The low frequency OKE response was calculated by using the Fourier transform deconvolution after subtraction of the slow picosecond timescale decay from the whole OKE response. In a typical low frequency OKE response, reduced spectral density (RSD) is generally plotted against wavenumber (ν (cm^{-1})). In this section, we are going to discuss the low frequency OKE response in the following way. First, we would like to describe the RSD function in case of pure components, i.e. in pure ACN and pure $BmimPF_6$. Later, we will show the composition dependence of the OKE low frequency response in the mixture between $BmimPF_6$ and ACN.

4.4.3.2.1. Pure components:

The OKE reduced spectral densities in pure components are shown in Figure 4.10. We are going to focus only on the intermolecular part of the figures which can be seen as a broad band below 200 cm^{-1}. In case of pure ACN (Figure 4.10(A)), the intermolecular RSD can be distinguished by the presence of a wide band with the maximum at 41 cm^{-1}. From Figure 4.10, one can also notice that the OKE responses were also calculated theoretically (blue) using the polarizability correlations. Although the simulated signals are quite noisy, they can give us the correlation between the experiments and theory. From the simulated RSD, we can notice a clear agreement with the experimental one in case of pure ACN. Similarly, the simulated signals are also quite similar in pure $BmimPF_6$. However, the higher frequency side of the wide band peak at 85 cm^{-1} of the experimental RSD spectra in $BmimPF_6$ became shifted towards lower frequency (65 cm^{-1}) in the simulated spectra.

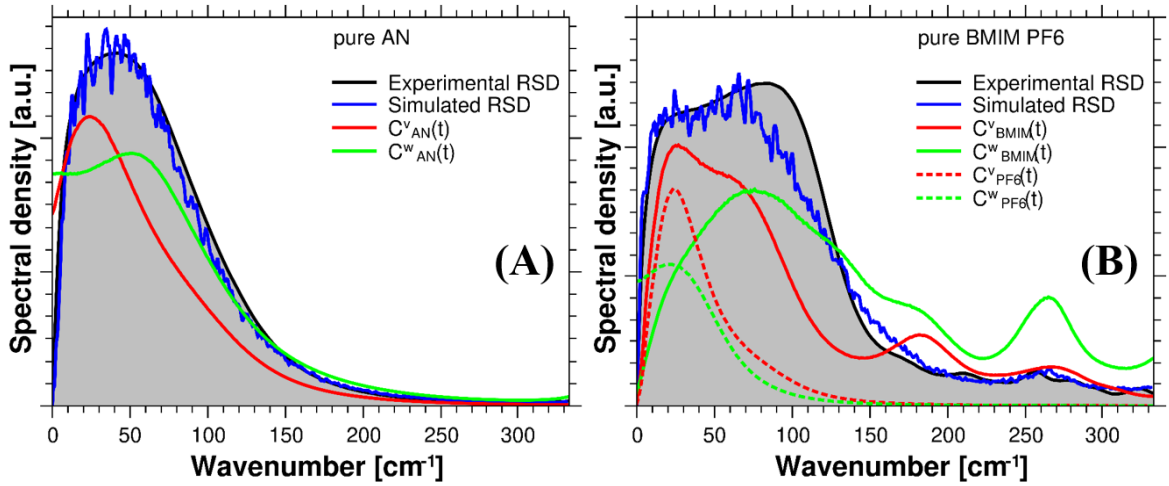

Figure 4.10: Experimental RSD (black) and simulated RSD (blue) in pure (A) ACN and in pure (B) $BmimPF_6$. They are also overlapped with the velocity (red) and angular velocity (green) correlation functions calculated for (A) ACN and (B) $BmimPF_6$

In addition, the intermolecular RSD of $BmimPF_6$ (Figure 4.10(B)) can be recognized by the occurrence of wide band with two peaks at ~ 25 cm^{-1} and ~ 85 cm^{-1}. Not only are these two peaks available in the OKE low frequency response of $BmimPF_6$, but five other small peaks are also visible in 150-300 cm^{-1} wavenumber range.[69,78]

In addition, it was also previously shown that, there exists a resemblance between the simulated low frequency response using the Fourier transform of the polarizability and the velocity and angular velocity correlation functions of the mixture components.[98] Therefore, all the calculations of velocity (C^V) and angular velocity (C^W) correlations in case of pure ACN, Bmim cation and PF_6 anion can be noticed in Figure 4.10. These two sub-figures corresponding to pure ACN and pure $BmimPF_6$ show that, the spectral contributions due to translation starts at lower frequency values than that due to rotation. In addition, the high frequency shoulders in velocity contribution of the Bmim cation suggests the presence of specific interactions like H-bonding. The 65 cm^{-1} peak in case of the velocity contribution of the cation is due to specific interactions, whereas the other peak at 25 cm^{-1} is due to translations dominated by weaker interactions. It is also worth noting that, the position of the C^V peak at 65 cm^{-1} corresponds to the peak of spectral contribution due to angular velocity (C^W).
Therefore, this previous interpretation of the low frequency OKE response with respect to the linear (C^V) and angular (C^W) velocity correlations is not straightforward due to overlapping of translational and rotational contributions. While the low frequency side of the spectral density function is related to the oscillation of mixture components in a cage formed by neighboring molecules, the high frequency part has the signature of both the rotational and specific interactions (H-bonding and anion-solvent interactions).

4.4.3.2.2. Composition dependence of low frequency OKE response:

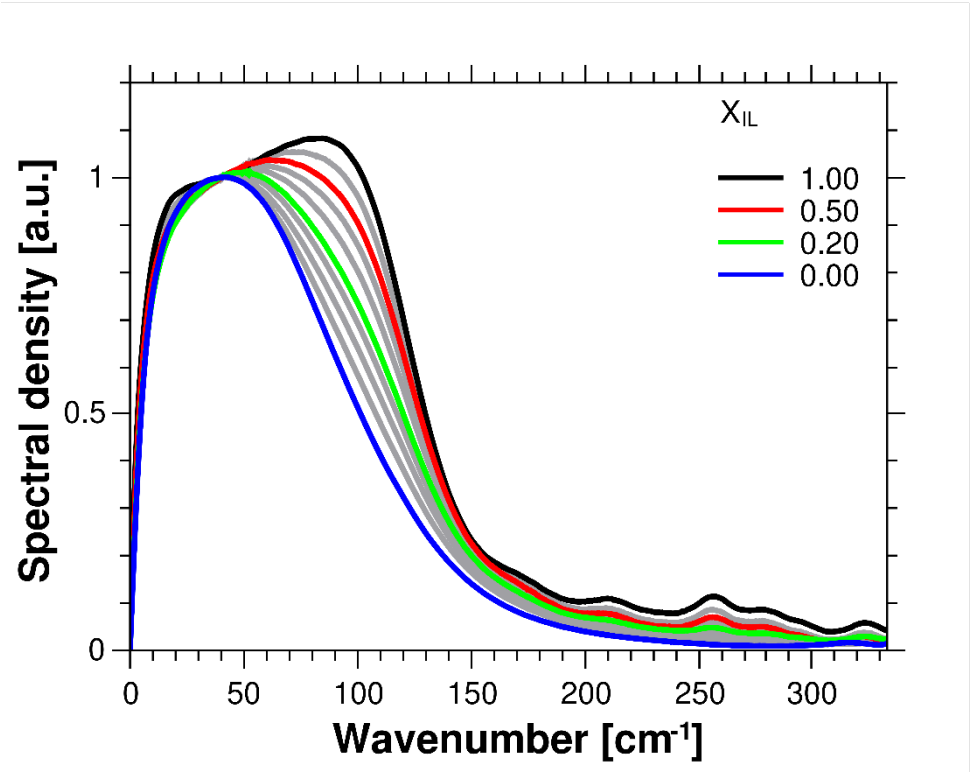

Figure 4.11: Mole fraction dependence of the experimental OKE reduced spectral density

In Figure 4.11, the variation of the low frequency OKE response (i.e. the reduced spectral density) can be noticed while changing the composition of the mixture between $BmimPF_6$ and ACN. For the ease of comparison, the spectral amplitudes are normalized at 40 cm^{-1}. From the previous discussion about low frequency OKE response in pure components, we came to know that while RSD of pure ACN has only one peak, RSD of pure $BmimPF_6$ has two peaks. In addition, the lower frequency RSD peak also overlaps with the RSD peak in pure ACN. From Figure 4.11, it can be easily observed that, while the lower frequency part shows very less variation, the higher frequency OKE response become more and more shifted towards lower wavenumber region while decreasing X_{IL} of the mixture.

Similar to the study of low frequency OKE response in pure components, the MD simulation was also performed in the case of the mixtures by calculating the translational and rotational spectral densities for different mixture components (ACN, Bmim cation and PF_6 anion) at various intermediate mole fractions of the IL-MS mixture. We can now discuss the results of these MD simulations in case of the mixtures.

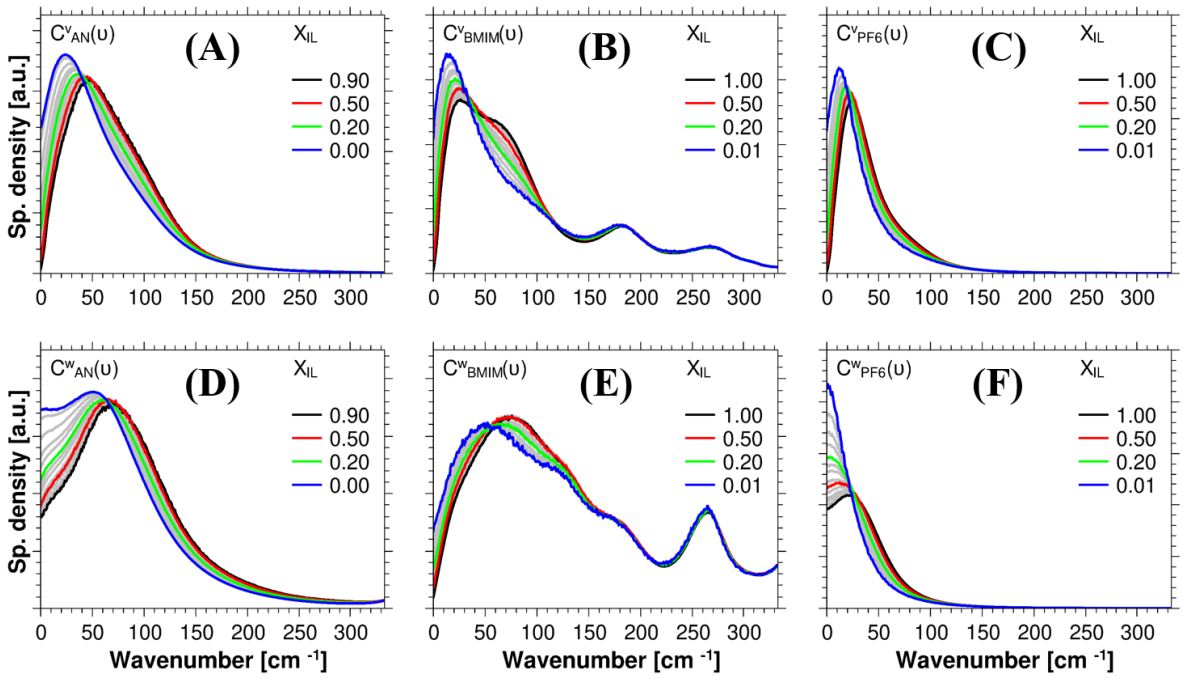

Figure 4.12: Simulated correlation function of velocity (top panel) and angular velocity (bottom panel) for the centers of mass of acetonitrile [(A), (D)] Bmim cation [(B), (E)] and PF_6 anion [(C), (F)]

In Figure 4.12 ((A), (D)), in case of both velocity (C^V) and angular velocity (C^W) correlations of ACN, we can clearly see the shift of the peak towards higher wavenumber regions while increasing IL concentration in the mixture. At the same time, a very weak shoulder can also be seen at around 90 cm^{-1}. These observations of the translational spectral density function in ACN indicates that the cage surrounding the ACN molecules is getting more and more rigid while increasing X_{IL}. Similar type of cage stiffening while increasing X_{IL} was observed in previous studies related to C_5mimNTf$_2$ ionic liquid.[64,99] Also, the weak shoulder at 90 cm^{-1} is an indication of the interactions between the ions and ACN molecules. Similar to translation spectral density, the rotational one also shifts towards higher frequency compared to pure ACN while increasing X_{IL} of the mixture. This observation indicates an increase of rotational hindrance while increasing the mole fraction of the IL-MS mixture.

Moreover, while decreasing X_{IL}, both the velocity and angular velocity correlations of the cations [Figures 4.12 ((B), (E))] and anions [Figures 4.12 ((C), (F))] show the shift of the peak towards lower wavenumbers. In the case of cation, the translational spectral density function shows a noticeable decrease of the higher wavenumber peak (65 cm^{-1}) while the weak shoulder remains visible at 90 cm^{-1} while decreasing the X_{IL} of the mixture. This decrease of intensity of the peak at 65 cm^{-1} is an indication that the specific interactions involving the cations are getting weakened while decreasing X_{IL}. In addition, similar to the translational spectral density function, this 90 cm^{-1} weak shoulder indicates the interactions between the ions and ACN molecules in the medium. Another important finding from these MD simulations is that, the rotational spectral density function (C^W) of the anions shows a center at around 0 cm^{-1}, which eventually suggests that the rotational motion of anions at lower X_{IL} regions become almost free. Similar to the ACN molecules, the shift of both the translational and rotational spectral

density function towards lower wavelength regions mainly indicates that the surrounding cages are getting more and more loose while decreasing X_{IL}. Furthermore, these findings about the local cage strengths from the low frequency OKE signal study can be correlated with the composition dependence of experimental diffusion coefficients of solvents, cations and anions.[100,101]

4.5. Conclusions:

In this chapter, we have discussed both the probe dependent solvation dynamics and probe independent OKE study of the completer reorientational relaxation dynamics using TCSPC and OKE techniques respectively in case of $BmimPF_6$-ACN mixture. The overall conclusions from this chapter is mainly divided into two parts.

4.5.1. Conclusions from TCSPC study:

Few points can be pointed out from this steady-state and solvation dynamics study using C153 probe. Firstly, the C153 solvation dynamics get slower while increasing the X_{IL} of $BmimPF_6$-ACN mixture. This is mainly due to the increase of the viscosity of the surrounding medium while increasing the IL-concentration in the mixture. Secondly, the average solvation time values follow the power law viscosity dependence, where p is the fractional power value, with mixture viscosity, similar to the other studied IL-MS mixtures. However, p value doesn't fall in the same range as suggested in the previous studies[18–20,22] containing the solvation dynamics of other IL-MS mixtures. This in turn suggests the importance of using faster sub-picosecond timescale measurements in addition to this study to get an idea about complete solvation process in the mixture.

4.5.2. Conclusions from OKE study:

In the femtosecond optical Kerr effect study, we have measured the complete reorientational dynamics in case of the same IL-MS mixture ($BmimPF_6$-ACN). We have used two types of measurements to accumulate the OKE response, namely the high resolution oscillator setup and low resolution amplifier setup. The low resolution amplifier setup was used to collect the completer decay process due to the reorientation of the molecules. Firstly, the slow orientational relaxation component in the time domain was discussed. Later, we have subtracted the slow component from the OKE response and carry our discussion for the faster component in the frequency domain. In addition, MD simulations were also provided to correlate with the experimental OKE response.

In case of the time domain slow orientational component study, we have found the presence of three distinguished relaxation times after fitting the experimental OKE decay. With the help of MD simulations, we concluded that the long and intermediate relaxation times can be attributed to the reorientation of the Bmim cation and ACN molecules which are in the vicinity of the imidazolium ring, whereas the experimental short decay time of the fitted OKE response can be attributed to cation rotations and the reorientation of ACN molecules in the bulk or in the neighborhood of the alkyl chain extension of the cation.

In the case of frequency domain measurements of the low frequency OKE response, first we have discussed about the frequency dependent changes of reduced spectral density function (RSD) in pure components. While the RSD in pure ACN has only one peak, the RSD of pure $BmimPF_6$ showed the bimodal nature. In addition, the MD simulation results also agrees with the experimental one in case of pure ACN, whereas the higher frequency peak of the simulated intermolecular band shows 20 cm^{-1} downshift from the experimental value in case of pure $BmimPF_6$. In this regard, the similarities between the experimental and MD simulation results are better than previous studies in case of pure $BmimPF_6$.[66,68] Then the velocity and angular velocity correlation functions are also calculated in case of pure components for further analysis. This helped us to conclude that, while the intermolecular band of ACN is dominated by translations and rotations at the low wavenumber side and high wavenumber side respectively, the high frequency side of ionic liquid RSD is associated to both librations of the cation and translations governed by specific interactions like H-bonding and anion-π^+ interactions.

Furthermore, we have also studied the composition dependence of the low frequency OKE response of different intermediate mole fractions of $BmimPF_6$-ACN mixtures. The experimental data of RSD showed that while the lower frequency part of the spectra remains less affected, the higher frequency part showed noticeable decrease in its intensity while decreasing X_{IL}. Similar to the pure ACN and $BmimPF_6$, the velocity and angular velocity contributions of the mixture components (solvents, cations and anions) were also analyzed in case of IL-MS mixtures. This type of analysis revealed that the lower frequency band, related to rattling of the molecule in the cage created by neighboring molecules, shows its position change towards higher wavenumbers in case of ACN while increasing X_{IL} and towards lower wavenumbers in case of IL ions while decreasing X_{IL} of the mixture. In addition, the disappearance of the high-frequency RSD in $BmimPF_6$ while decreasing X_{IL} can be described due to decrease of the imidazolium ring libration frequency and also due to the decrease of cation-anion interactions.

Therefore, as an outlook from this chapter, the sub-picosecond solvation dynamics alongside with the fluorescence anisotropy study to get an idea about rotational relaxation times (τ_R) and also to get a correlation between the solvation and rotational dynamics need to be performed to get a complete idea in these systems. In addition, the OKE study describes the general results regarding the contributions of rotational and translational motions to the OKE response in $BmimPF_6$-ACN mixture. However, a further detailed study is needed for better idea about these systems.

Bibliography

(1) Polok, K.; Beisert, M.; Świątek, A.; Maity, N.; Piatkowski, P.; Gadomski, W.; Miannay, F. A.; Idrissi, A. Dynamics in the BMIM PF 6 /Acetonitrile Mixtures Observed by Femtosecond Optical Kerr Effect and Molecular Dynamics Simulations. *Phys. Chem. Chem. Phys.* **2020**, *22* (42), 24544–24554. https://doi.org/10.1039/D0CP03847D.

(2) Bagchi, B.; Jana, B. Solvation Dynamics in Dipolar Liquids. *Chem. Soc. Rev.* **2010**, *39* (6), 1936. https://doi.org/10.1039/b902048a.

(3) Kaur, H.; Koley, S.; Ghosh, S. Probe Dependent Solvation Dynamics Study in a Microscopically Immiscible Dimethyl Sulfoxide–Glycerol Binary Solvent. *J. Phys. Chem. B* **2014**, *118* (27), 7577–7585. https://doi.org/10.1021/jp502003x.

(4) Karmakar, R.; Samanta, A. Steady-State and Time-Resolved Fluorescence Behavior of C153 and PRODAN in Room-Temperature Ionic Liquids. *J. Phys. Chem. A* **2002**, *106* (28), 6670–6675. https://doi.org/10.1021/jp0143591.

(5) Sajadi, M.; Weinberger, M.; Wagenknecht, H.-A.; Ernsting, N. P. Polar Solvation Dynamics in Water and Methanol: Search for Molecularity. *Phys. Chem. Chem. Phys.* **2011**, *13* (39), 17768. https://doi.org/10.1039/c1cp21794a.

(6) Zhang, X.-X.; Breffke, J.; Ernsting, N. P.; Maroncelli, M. Observations of Probe Dependence of the Solvation Dynamics in Ionic Liquids. *Phys. Chem. Chem. Phys.* **2015**, *17* (19), 12949–12956. https://doi.org/10.1039/C5CP00814J.

(7) Ito, N.; Arzhantsev, S.; Maroncelli, M. The Probe Dependence of Solvation Dynamics and Rotation in the Ionic Liquid 1-Butyl-3-Methyl-Imidazolium Hexafluorophosphate. *Chem. Phys. Lett.* **2004**, *396* (1–3), 83–91. https://doi.org/10.1016/j.cplett.2004.08.018.

(8) Kumpulainen, T.; Rosspeintner, A.; Vauthey, E. Probe Dependence on Polar Solvation Dynamics from Fs Broadband Fluorescence. *Phys. Chem. Chem. Phys.* **2017**, *19* (13), 8815–8825. https://doi.org/10.1039/C7CP00706J.

(9) Gustavsson, T.; Cassara, L.; Gulbinas, V.; Gurzadyan, G.; Mialocq, J.-C.; Pommeret, S.; Sorgius, M.; van der Meulen, P. Femtosecond Spectroscopic Study of Relaxation Processes of Three Amino-Substituted Coumarin Dyes in Methanol and Dimethyl Sulfoxide. *J. Phys. Chem. A* **1998**, *102* (23), 4229–4245. https://doi.org/10.1021/jp980282d.

(10) Chapman, C. F.; Fee, R. S.; Maroncelli, M. Measurements of the Solute Dependence of Solvation Dynamics in 1-Propanol: The Role of Specific Hydrogen-Bonding Interactions. *J. Phys. Chem.* **1995**, *99* (13), 4811–4819. https://doi.org/10.1021/j100013a060.

(11) Lewis, J. E.; Maroncelli, M. On the (Uninteresting) Dependence of the Absorption and Emission Transition Moments of Coumarin 153 on Solvent. *Chem. Phys. Lett.* **1998**, *282* (2), 197–203. https://doi.org/10.1016/S0009-2614(97)01270-0.

(12) Trivedi, S.; Sarkar, A.; Pandey, S. Solvatochromic Absorbance Probe Behavior within 1-Butyl-3-Methylimidazolium Hexafluorophosphate+propylene Carbonate: Preferential Solvation or Solvent–solvent Interaction? *Chem. Eng. J.* **2009**, *147* (1), 36–42. https://doi.org/10.1016/j.cej.2008.11.014.

(13) Chagnes, A.; Diaw, M.; Carré, B.; Willmann, P.; Lemordant, D. Imidazolium-Organic Solvent Mixtures as Electrolytes for Lithium Batteries. *J. Power Sources* **2005**, *145* (1), 82–88. https://doi.org/10.1016/j.jpowsour.2004.12.035.

(14) Stoppa, A.; Hunger, J.; Buchner, R. Conductivities of Binary Mixtures of Ionic Liquids with

Polar Solvents. *J. Chem. Eng. Data* **2009**, *54* (2), 472–479. https://doi.org/10.1021/je800468h.

(15) Wang, J.; Tian, Y.; Zhao, Y.; Zhuo, K. A Volumetric and Viscosity Study for the Mixtures of 1-n-Butyl-3-Methylimidazolium Tetrafluoroborate Ionic Liquid with Acetonitrile, Dichloromethane, 2-Butanone and N, N ? Dimethylformamide. *Green Chem.* **2003**, *5* (5), 618. https://doi.org/10.1039/b303735e.

(16) Li, W.; Zhang, Z.; Han, B.; Hu, S.; Xie, Y.; Yang, G. Effect of Water and Organic Solvents on the Ionic Dissociation of Ionic Liquids. *J. Phys. Chem. B* **2007**, *111* (23), 6452–6456. https://doi.org/10.1021/jp071051m.

(17) Rizzuto, A. M.; Pennington, R. L.; Sienerth, K. D. Study of the BMIM-PF6: Acetonitrile Binary Mixture as a Solvent for Electrochemical Studies Involving CO2. *Electrochim. Acta* **2011**, *56* (14), 5003–5009. https://doi.org/10.1016/j.electacta.2011.03.106.

(18) Liang, M.; Zhang, X.-X.; Kaintz, A.; Ernsting, N. P.; Maroncelli, M. Solvation Dynamics in a Prototypical Ionic Liquid + Dipolar Aprotic Liquid Mixture: 1-Butyl-3-Methylimidazolium Tetrafluoroborate + Acetonitrile. *J. Phys. Chem. B* **2014**, *118* (5), 1340–1352. https://doi.org/10.1021/jp412086t.

(19) Smortsova, Y.; Miannay, F.-A.; Oher, H.; Marekha, B.; Dubois, J.; Sliwa, M.; Kalugin, O.; Idrissi, A. Solvation Dynamics and Rotation of Coumarin 153 in a New Ionic Liquid/Molecular Solvent Mixture Model: [BMIM][TFSI]/Propylene Carbonate. *J. Mol. Liq.* **2017**, *226*, 48–55. https://doi.org/10.1016/j.molliq.2016.10.008.

(20) Zhang, X.-X.; Liang, M.; Hunger, J.; Buchner, R.; Maroncelli, M. Dielectric Relaxation and Solvation Dynamics in a Prototypical Ionic Liquid + Dipolar Protic Liquid Mixture: 1-Butyl-3-Methylimidazolium Tetrafluoroborate + Water. *J. Phys. Chem. B* **2013**, *117* (49), 15356–15368. https://doi.org/10.1021/jp4043528.

(21) Koverga, V. A.; Smortsova, Y.; Miannay, F. A.; Kalugin, O. N.; Takamuku, T.; Jedlovszky, P.; Marekha, B.; Cordeiro, M. N. D. S.; Idrissi, A. Distance Angle Descriptors of the Interionic and Ion–Solvent Interactions in Imidazolium-Based Ionic Liquid Mixtures with Aprotic Solvents: A Molecular Dynamics Simulation Study. *J. Phys. Chem. B* **2019**, *123* (28), 6065–6075. https://doi.org/10.1021/acs.jpcb.9b03838.

(22) Smortsova, Y. Thèse de Yevheniia Smortsova, Université de Lille, 2018. **2018**.

(23) Reynolds, L.; Gardecki, J. A.; Frankland, S. J. V.; Horng, M. L.; Maroncelli, M. Dipole Solvation in Nondipolar Solvents: Experimental Studies of Reorganization Energies and Solvation Dynamics. *J. Phys. Chem.* **1996**, *100* (24), 10337–10354. https://doi.org/10.1021/jp953110e.

(24) Laitinen, E.; Salonen, K.; Harju, T. Solvation Dynamics Study of 4-amino- N -methyl-phthalimide in n -alcohol Solutions. *J. Chem. Phys.* **1996**, *104* (16), 6138–6148. https://doi.org/10.1063/1.471279.

(25) Horng, M. L.; Gardecki, J. A.; Papazyan, A.; Maroncelli, M. Subpicosecond Measurements of Polar Solvation Dynamics: Coumarin 153 Revisited. *J. Phys. Chem.* **1995**, *99* (48), 17311–17337. https://doi.org/10.1021/j100048a004.

(26) Song, X.; Chandler, D. Dielectric Solvation Dynamics of Molecules of Arbitrary Shape and Charge Distribution. *J. Chem. Phys.* **1998**, *108* (6), 2594–2600. https://doi.org/10.1063/1.475644.

(27) Muramatsu, M.; Morishima, S.; Katayama, T.; Ito, S.; Nagasawa, Y.; Miyasaka, H. The Effect of Pre-Solvation in the Ground State on Photoinduced Electron Transfer in Ionic Liquids. *J. Solution Chem.* **2014**, *43* (9–10), 1550–1560. https://doi.org/10.1007/s10953-014-0227-7.

(28) Shim, Y.; Kim, H. J. Dielectric Relaxation and Solvation Dynamics in a Room-Temperature

Ionic Liquid: Temperature Dependence. *J. Phys. Chem. B* **2013**, *117* (39), 11743–11752. https://doi.org/10.1021/jp406353j.

(29) Schmollngruber, M.; Schröder, C.; Steinhauser, O. Polarization Effects on the Solvation Dynamics of Coumarin C153 in Ionic Liquids: Components and Their Cross-Correlations. *J. Chem. Phys.* **2013**, *138* (20), 204504. https://doi.org/10.1063/1.4807013.

(30) Muramatsu, M.; Nagasawa, Y.; Miyasaka, H. Ultrafast Solvation Dynamics in Room Temperature Ionic Liquids Observed by Three-Pulse Photon Echo Peak Shift Measurements. *J. Phys. Chem. A* **2011**, *115* (16), 3886–3894. https://doi.org/10.1021/jp108282v.

(31) Paul, A.; Samanta, A. Solute Rotation and Solvation Dynamics in an Alcohol-Functionalized Room Temperature Ionic Liquid. *J. Phys. Chem. B* **2007**, *111* (18), 4724–4731. https://doi.org/10.1021/jp065790z.

(32) Maroncelli, M.; Zhang, X.-X.; Liang, M.; Roy, D.; Ernsting, N. P. Measurements of the Complete Solvation Response of Coumarin 153 in Ionic Liquids and the Accuracy of Simple Dielectric Continuum Predictions. *Faraday Discuss.* **2012**, *154*, 409–424. https://doi.org/10.1039/C1FD00058F.

(33) Chakrabarty, D.; Hazra, P.; Chakraborty, A.; Seth, D.; Sarkar, N. Dynamics of Solvent Relaxation in Room Temperature Ionic Liquids. *Chem. Phys. Lett.* **2003**, *381* (5–6), 697–704. https://doi.org/10.1016/j.cplett.2003.10.029.

(34) Daschakraborty, S.; Pal, T.; Biswas, R. Stokes Shift Dynamics of Ionic Liquids: Solute Probe Dependence, and Effects of Self-Motion, Dielectric Relaxation Frequency Window, and Collective Intermolecular Solvent Modes. *J. Chem. Phys.* **2013**, *139* (16), 164503. https://doi.org/10.1063/1.4825195.

(35) Karmakar, R.; Samanta, A. Solvation Dynamics of Coumarin-153 in a Room-Temperature Ionic Liquid. *J. Phys. Chem. A* **2002**, *106* (18), 4447–4452. https://doi.org/10.1021/jp011498+.

(36) Ingram, J. A.; Moog, R. S.; Ito, N.; Biswas, R.; Maroncelli, M. Solute Rotation and Solvation Dynamics in a Room-Temperature Ionic Liquid. *J. Phys. Chem. B* **2003**, *107* (24), 5926–5932. https://doi.org/10.1021/jp034231e.

(37) Wetzler, D. E.; Chesta, C.; Fernández-Prini, R.; Aramendía, P. F. Dynamic Solvation of Aminophthalimides in Solvent Mixtures. *J. Phys. Chem. A* **2002**, *106* (11), 2390–2400. https://doi.org/10.1021/jp0118423.

(38) Paul, A.; Samanta, A. Effect of Nonpolar Solvents on the Solute Rotation and Solvation Dynamics in an Imidazolium Ionic Liquid. *J. Phys. Chem. B* **2008**, *112* (3), 947–953. https://doi.org/10.1021/jp077536s.

(39) Chakrabarty, D.; Chakraborty, A.; Seth, D.; Hazra, P.; Sarkar, N. Dynamics of Solvation and Rotational Relaxation of Coumarin 153 in 1-Butyl-3-Methylimidazolium Hexafluorophosphate [Bmim][PF6]–water Mixtures. *Chem. Phys. Lett.* **2004**, *397* (4–6), 469–474. https://doi.org/10.1016/j.cplett.2004.08.141.

(40) Lang, M. J.; Jordanides, X. J.; Song, X.; Fleming, G. R. Aqueous Solvation Dynamics Studied by Photon Echo Spectroscopy. *J. Chem. Phys.* **1999**, *110* (12), 5884–5892. https://doi.org/10.1063/1.478488.

(41) Hazra, P.; Chakrabarty, D.; Sarkar, N. Solvation Dynamics of Coumarin 153 in Aqueous and Non-Aqueous Reverse Micelles. *Chem. Phys. Lett.* **2003**, *371* (5–6), 553–562. https://doi.org/10.1016/S0009-2614(03)00304-X.

(42) Jin, H.; Baker, G. A.; Arzhantsev, S.; Dong, J.; Maroncelli, M. Solvation and Rotational Dynamics of Coumarin 153 in Ionic Liquids: Comparisons to Conventional Solvents. *J. Phys. Chem. B* **2007**, *111* (25), 7291–7302. https://doi.org/10.1021/jp070923h.

(43) Chowdhury, P. K.; Halder, M.; Sanders, L.; Calhoun, T.; Anderson, J. L.; Armstrong, D. W.; Song, X.; Petrich, J. W. Dynamic Solvation in Room-Temperature Ionic Liquids. *J. Phys. Chem. B* **2004**, *108* (29), 10245–10255. https://doi.org/10.1021/jp0376828.

(44) Karmakar, R.; Samanta, A. Steady-State and Time-Resolved Fluorescence Behavior of C153 and PRODAN in Room-Temperature Ionic Liquids. *J. Phys. Chem. A* **2002**, *106* (28), 6670–6675. https://doi.org/10.1021/jp0143591.

(45) Mukherjee, P.; Crank, J. A.; Sharma, P. S.; Wijeratne, A. B.; Adhikary, R.; Bose, S.; Armstrong, D. W.; Petrich, J. W. Dynamic Solvation in Phosphonium Ionic Liquids: Comparison of Bulk and Micellar Systems and Considerations for the Construction of the Solvation Correlation Function, C (T). *J. Phys. Chem. B* **2008**, *112* (11), 3390–3396. https://doi.org/10.1021/jp7107126.

(46) Headley, L. S.; Mukherjee, P.; Anderson, J. L.; Ding, R.; Halder, M.; Armstrong, D. W.; Song, X.; Petrich, J. W. Dynamic Solvation in Imidazolium-Based Ionic Liquids on Short Time Scales. *J. Phys. Chem. A* **2006**, *110* (31), 9549–9554. https://doi.org/10.1021/jp0606964.

(47) Zhang, X. X.; Liang, M.; Ernsting, N. P.; Maroncelli, M. Complete Solvation Response of Coumarin 153 in Ionic Liquids. *J. Phys. Chem. B* **2013**, *117* (16), 4291–4304. https://doi.org/10.1021/jp305430a.

(48) Ingram, J. A.; Moog, R. S.; Ito, N.; Biswas, R.; Maroncelli, M. Solute Rotation and Solvation Dynamics in a Room-Temperature Ionic Liquid. *J. Phys. Chem. B* **2003**, *107* (24), 5926–5932. https://doi.org/10.1021/jp034231e.

(49) Samanta, A. Dynamic Stokes Shift and Excitation Wavelength Dependent Fluorescence of Dipolar Molecules in Room Temperature Ionic Liquids. *J. Phys. Chem. B* **2006**, *110* (28), 13704–13716. https://doi.org/10.1021/jp060441q.

(50) Samanta, A. Solvation Dynamics in Ionic Liquids: What We Have Learned from the Dynamic Fluorescence Stokes Shift Studies. *J. Phys. Chem. Lett.* **2010**, *1* (10), 1557–1562. https://doi.org/10.1021/jz100273b.

(51) Daschakraborty, S.; Ranjit, B. Stokes Shift Dynamics in (Ionic Liquid + Polar Solvent) Binary Mixtures: Composition Dependence. *J. Phys. Chem. B* **2011**, *115* (14), 4011–4024. https://doi.org/10.1021/jp200407m.

(52) Daschakraborty, S.; Biswas, R. Composition Dependent Stokes Shift Dynamics in Binary Mixtures of 1-Butyl-3-Methylimidazolium Tetrafluoroborate with Water and Acetonitrile: Quantitative Comparison between Theory and Complete Measurements. *J. Phys. Chem. B* **2014**, *118* (5), 1327–1339. https://doi.org/10.1021/jp4093628.

(53) Kobrak, M. N. Characterization of the Solvation Dynamics of an Ionic Liquid via Molecular Dynamics Simulation. *J. Chem. Phys.* **2006**, *125* (6), 064502. https://doi.org/10.1063/1.2227026.

(54) Kobrak, M. N. A Comparative Study of Solvation Dynamics in Room-Temperature Ionic Liquids. *J. Chem. Phys.* **2007**, *127* (18), 184507. https://doi.org/10.1063/1.2790425.

(55) Terranova, Z. L.; Corcelli, S. A. On the Mechanism of Solvation Dynamics in Imidazolium-Based Ionic Liquids. *J. Phys. Chem. B* **2013**, *117* (49), 15659–15666. https://doi.org/10.1021/jp406419y.

(56) Chang, Y. J.; Castner, E. W. Femtosecond Dynamics of Hydrogen-bonding Solvents. Formamide and N -methylformamide in Acetonitrile, DMF, and Water. *J. Chem. Phys.* **1993**, *99* (1), 113–125. https://doi.org/10.1063/1.465790.

(57) Cho, M.; Du, M.; Scherer, N. F.; Fleming, G. R.; Mukamel, S. Off-resonant Transient Birefringence in Liquids. *J. Chem. Phys.* **1993**, *99* (4), 2410–2428.

https://doi.org/10.1063/1.465256.

(58) Ernsting, N. P.; Photiadis, G. M.; Hennig, H.; Laurent, T. Rotational Friction Kernel in Water from the Femtosecond Time-Resolved Optical Kerr Effect of Acetonitrile/Water Mixtures. *J. Phys. Chem. A* **2002**, *106* (40), 9159–9173. https://doi.org/10.1021/jp0260649.

(59) Fecko, C. J.; Eaves, J. D.; Tokmakoff, A. Isotropic and Anisotropic Raman Scattering from Molecular Liquids Measured by Spatially Masked Optical Kerr Effect Spectroscopy. *J. Chem. Phys.* **2002**, *117* (3), 1139–1154. https://doi.org/10.1063/1.1485070.

(60) Loughnane, B. J.; Scodinu, A.; Farrer, R. A.; Fourkas, J. T.; Mohanty, U. Exponential Intermolecular Dynamics in Optical Kerr Effect Spectroscopy of Small-Molecule Liquids. *J. Chem. Phys.* **1999**, *111* (6), 2686–2694. https://doi.org/10.1063/1.479544.

(61) McMorrow, D.; Lotshaw, W. T. Intermolecular Dynamics in Acetonitrile Probed with Femtosecond Fourier-Transform Raman Spectroscopy. *J. Phys. Chem.* **1991**, *95* (25), 10395–10406. https://doi.org/10.1021/j100178a029.

(62) Park, S.; Flanders, B. N.; Shang, X.; Westervelt, R. A.; Kim, J.; Scherer, N. F. Solvent Intermolecular Polarizability Response in Solvation. *J. Chem. Phys.* **2003**, *118* (9), 3917–3920. https://doi.org/10.1063/1.1555804.

(63) Shirota, H.; Fujisawa, T.; Fukazawa, H.; Nishikawa, K. Ultrafast Dynamics in Aprotic Molecular Liquids: A Femtosecond Raman-Induced Kerr Effect Spectroscopic Study. *Bull. Chem. Soc. Jpn.* **2009**, *82* (11), 1347–1366. https://doi.org/10.1246/bcsj.82.1347.

(64) Bardak, F.; Xiao, D.; Hines, L. G.; Son, P.; Bartsch, R. A.; Quitevis, E. L.; Yang, P.; Voth, G. A. Nanostructural Organization in Acetonitrile/Ionic Liquid Mixtures: Molecular Dynamics Simulations and Optical Kerr Effect Spectroscopy. *ChemPhysChem* **2012**, *13* (7), 1687–1700. https://doi.org/10.1002/cphc.201200026.

(65) Ladanyi, B. M.; Liang, Y. Q. Interaction-induced Contributions to Polarizability Anisotropy Relaxation in Polar Liquids. *J. Chem. Phys.* **1995**, *103* (15), 6325–6332. https://doi.org/10.1063/1.470413.

(66) Elola, M. D.; Ladanyi, B. M. Polarizability Response in Polar Solvents: Molecular-Dynamics Simulations of Acetonitrile and Chloroform. *J. Chem. Phys.* **2005**, *122* (22), 224506. https://doi.org/10.1063/1.1925275.

(67) Dhumal, N. R.; Kiefer, J.; Turton, D.; Wynne, K.; Kim, H. J. Dielectric Relaxation of the Ionic Liquid 1-Ethyl-3-Methylimidazolium Ethyl Sulfate: Microwave and Far-IR Properties. *J. Phys. Chem. B* **2017**, *121* (18), 4845–4852. https://doi.org/10.1021/acs.jpcb.7b00160.

(68) Ishida, T.; Nishikawa, K.; Shirota, H. Atom Substitution Effects of [XF 6] − in Ionic Liquids. 2. Theoretical Study. *J. Phys. Chem. B* **2009**, *113* (29), 9840–9851. https://doi.org/10.1021/jp8098818.

(69) Shirota, H.; Kakinuma, S.; Takahashi, K.; Tago, A.; Jeong, H.; Fujisawa, T. Ultrafast Dynamics in Aromatic Cation Based Ionic Liquids: A Femtosecond Raman-Induced Kerr Effect Spectroscopic Study. *Bull. Chem. Soc. Jpn.* **2016**, *89* (9), 1106–1128. https://doi.org/10.1246/bcsj.20160085.

(70) Sonnleitner, T.; Turton, D. A.; Hefter, G.; Ortner, A.; Waselikowski, S.; Walther, M.; Wynne, K.; Buchner, R. Ultra-Broadband Dielectric and Optical Kerr-Effect Study of the Ionic Liquids Ethyl and Propylammonium Nitrate. *J. Phys. Chem. B* **2015**, *119* (29), 8826–8841. https://doi.org/10.1021/jp502935t.

(71) Sonnleitner, T.; Turton, D. A.; Waselikowski, S.; Hunger, J.; Stoppa, A.; Walther, M.; Wynne, K.; Buchner, R. Dynamics of RTILs: A Comparative Dielectric and OKE Study. *J. Mol. Liq.* **2014**, *192*, 19–25. https://doi.org/10.1016/j.molliq.2013.09.019.

(72) Turton, D. A.; Hunger, J.; Stoppa, A.; Hefter, G.; Thoman, A.; Walther, M.; Buchner, R.; Wynne, K. Dynamics of Imidazolium Ionic Liquids from a Combined Dielectric Relaxation and Optical Kerr Effect Study: Evidence for Mesoscopic Aggregation. *J. Am. Chem. Soc.* **2009**, *131* (31), 11140–11146. https://doi.org/10.1021/ja903315v.

(73) Turton, D. A.; Sonnleitner, T.; Ortner, A.; Walther, M.; Hefter, G.; Seddon, K. R.; Stana, S.; Plechkova, N. V.; Buchner, R.; Wynne, K. Structure and Dynamics in Protic Ionic Liquids: A Combined Optical Kerr-Effect and Dielectric Relaxation Spectroscopy Study. *Faraday Discuss.* **2012**, *154*, 145–153. https://doi.org/10.1039/C1FD00054C.

(74) Bailey, H. E.; Wang, Y.-L.; Fayer, M. D. The Influence of Hydrophilicity on the Orientational Dynamics and Structures of Imidazolium-Based Ionic Liquid/Water Binary Mixtures. *J. Chem. Phys.* **2018**, *149* (4), 044501. https://doi.org/10.1063/1.5038563.

(75) Cang, H.; Li, J.; Fayer, M. D. Orientational Dynamics of the Ionic Organic Liquid 1-Ethyl-3-Methylimidazolium Nitrate. *J. Chem. Phys.* **2003**, *119* (24), 13017–13023. https://doi.org/10.1063/1.1628668.

(76) Giraud, G.; Gordon, C. M.; Dunkin, I. R.; Wynne, K. The Effects of Anion and Cation Substitution on the Ultrafast Solvent Dynamics of Ionic Liquids: A Time-Resolved Optical Kerr-Effect Spectroscopic Study. *J. Chem. Phys.* **2003**, *119* (1), 464–477. https://doi.org/10.1063/1.1578056.

(77) Iwata, K.; Okajima, H.; Saha, S.; Hamaguchi, H. Local Structure Formation in Alkyl-Imidazolium-Based Ionic Liquids as Revealed by Linear and Nonlinear Raman Spectroscopy. *Acc. Chem. Res.* **2007**, *40* (11), 1174–1181. https://doi.org/10.1021/ar700074c.

(78) Kakinuma, S.; Ishida, T.; Shirota, H. Femtosecond Raman-Induced Kerr Effect Study of Temperature-Dependent Intermolecular Dynamics in Imidazolium-Based Ionic Liquids: Effects of Anion Species and Cation Alkyl Groups. *J. Phys. Chem. B* **2017**, *121* (1), 250–264. https://doi.org/10.1021/acs.jpcb.6b11009.

(79) Urahata, S. M.; Ribeiro, M. C. C. Single Particle Dynamics in Ionic Liquids of 1-Alkyl-3-Methylimidazolium Cations. *J. Chem. Phys.* **2005**, *122* (2), 024511. https://doi.org/10.1063/1.1826035.

(80) Xiao, D.; Rajian, J. R.; Hines, L. G.; Li, S.; Bartsch, R. A.; Quitevis, E. L. Nanostructural Organization and Anion Effects in the Optical Kerr Effect Spectra of Binary Ionic Liquid Mixtures. *J. Phys. Chem. B* **2008**, *112* (42), 13316–13325. https://doi.org/10.1021/jp804417t.

(81) Shirota, H. Comparison of Low-Frequency Spectra between Aromatic and Nonaromatic Cation Based Ionic Liquids Using Femtosecond Raman-Induced Kerr Effect Spectroscopy. *ChemPhysChem* **2012**, *13* (7), 1638–1648. https://doi.org/10.1002/cphc.201100731.

(82) Shirota, H.; Matsuzaki, H.; Ramati, S.; Wishart, J. F. Effects of Aromaticity in Cations and Their Functional Groups on the Low-Frequency Spectra and Physical Properties of Ionic Liquids. *J. Phys. Chem. B* **2015**, *119* (29), 9173–9187. https://doi.org/10.1021/jp509412z.

(83) Rajesh Rajian, J.; Li, S.; Bartsch, R. A.; Quitevis, E. L. Temperature-Dependence of the Low-Frequency Spectrum of 1-Pentyl-3-Methylimidazolium Bis(Trifluoromethanesulfonyl)Imide Studied by Optical Kerr Effect Spectroscopy. *Chem. Phys. Lett.* **2004**, *393* (4–6), 372–377. https://doi.org/10.1016/j.cplett.2004.06.068.

(84) Xiao, D.; Hines, L. G.; Holtz, M. W.; Song, K.; Bartsch, R. A.; Quitevis, E. L. Effect of Cation Symmetry on the Low-Frequency Spectra of Imidazolium Ionic Liquids: OKE and Raman Spectroscopic Measurements and DFT Calculations. *Chem. Phys. Lett.* **2010**, *497* (1–3), 37–42. https://doi.org/10.1016/j.cplett.2010.07.085.

(85) Fee, R. S.; Maroncelli, M. Estimating the Time-Zero Spectrum in Time-Resolved Emmsion Measurements of Solvation Dynamics. *Chem. Phys.* **1994**, *183* (2–3), 235–247.

https://doi.org/10.1016/0301-0104(94)00019-0.

(86) Sturlaugson, A. L.; Fruchey, K. S.; Fayer, M. D. Orientational Dynamics of Room Temperature Ionic Liquid/Water Mixtures: Water-Induced Structure. *J. Phys. Chem. B* **2012**, *116* (6), 1777–1787. https://doi.org/10.1021/jp209942r.

(87) Fayer, M. D. Dynamics and Structure of Room Temperature Ionic Liquids. *Chem. Phys. Lett.* **2014**, *616–617*, 259–274. https://doi.org/10.1016/j.cplett.2014.09.062.

(88) Turton, D. A.; Wynne, K. Stokes–Einstein–Debye Failure in Molecular Orientational Diffusion: Exception or Rule? *J. Phys. Chem. B* **2014**, *118* (17), 4600–4604. https://doi.org/10.1021/jp5012457.

(89) Diaw, M.; Chagnes, A.; Carré, B.; Willmann, P.; Lemordant, D. Mixed Ionic Liquid as Electrolyte for Lithium Batteries. *J. Power Sources* **2005**, *146* (1–2), 682–684. https://doi.org/10.1016/j.jpowsour.2005.03.068.

(90) Conway, B.; Uitvlugt, C.; Maroncelli, M. Simulations of 1-Butyl-3-Methylimidazolium Tetrafluoroborate + Acetonitrile Mixtures: Force-Field Validation and Frictional Characteristics. *J. Phys. Chem. B* **2018**, *122* (29), 7385–7393. https://doi.org/10.1021/acs.jpcb.8b04341.

(91) Norton, C. D.; Thompson, W. H. Reorientation Dynamics of Nanoconfined Acetonitrile: A Critical Examination of Two-State Models. *J. Phys. Chem. B* **2014**, *118* (28), 8227–8235. https://doi.org/10.1021/jp501363q.

(92) Morales, C. M.; Thompson, W. H. Simulations of Infrared Spectra of Nanoconfined Liquids: Acetonitrile Confined in Nanoscale, Hydrophilic Silica Pores. *J. Phys. Chem. A* **2009**, *113* (10), 1922–1933. https://doi.org/10.1021/jp8072969.

(93) Milischuk, A. A.; Ladanyi, B. M. Polarizability Anisotropy Relaxation in Nanoconfinement: Molecular Simulation Study of Water in Cylindrical Silica Pores. *J. Chem. Phys.* **2014**, *141* (18), 18C513. https://doi.org/10.1063/1.4896218.

(94) Cheng, L.; Morrone, J. A.; Berne, B. J. Structure and Dynamics of Acetonitrile Confined in a Silica Nanopore. *J. Phys. Chem. C* **2012**, *116* (17), 9582–9593. https://doi.org/10.1021/jp301007k.

(95) Loughnane, B. J.; Farrer, R. A.; Scodinu, A.; Fourkas, J. T. Dynamics of a Wetting Liquid in Nanopores: An Optical Kerr Effect Study of the Dynamics of Acetonitrile Confined in Sol-Gel Glasses. *J. Chem. Phys.* **1999**, *111* (11), 5116–5123. https://doi.org/10.1063/1.479768.

(96) Loughnane, B. J.; Farrer, R. A.; Scodinu, A.; Reilly, T.; Fourkas, J. T. Ultrafast Spectroscopic Studies of the Dynamics of Liquids Confined in Nanoporous Glasses. *J. Phys. Chem. B* **2000**, *104* (23), 5421–5429. https://doi.org/10.1021/jp000323h.

(97) Stoppa, A.; Hunger, J.; Hefter, G.; Buchner, R. Structure and Dynamics of 1- N -Alkyl-3- N -Methylimidazolium Tetrafluoroborate + Acetonitrile Mixtures. *J. Phys. Chem. B* **2012**, *116* (25), 7509–7521. https://doi.org/10.1021/jp3020673.

(98) Idrissi, A.; Damay, P. Interpretation of the Low Frequency Response of Aqueous Solutions: A Molecular Dynamics Analysis. *J. Non. Cryst. Solids* **2006**, *352* (42–49), 4486–4489. https://doi.org/10.1016/j.jnoncrysol.2006.01.146.

(99) Quitevis, E. L.; Bardak, F.; Xiao, D.; Hines, L. G.; Son, P.; Bartsch, R. A.; Yang, P.; Voth, G. A. OKE Spectroscopy and Molecular Dynamics Simulations of Nonpolar and Polar Molecules in Ionic Liquids. In *ACS Symposium Series*; 2012; Vol. 1117, pp 271–287. https://doi.org/10.1021/bk-2012-1117.ch013.

(100) Chalyi, A. V. *Modern Problems of Molecular Physics*; Bulavin, L. A., Chalyi, A. V., Eds.;

Springer Proceedings in Physics; Springer International Publishing: Cham, 2018; Vol. 197. https://doi.org/10.1007/978-3-319-61109-9.

(101) Marekha, B. A.; Kalugin, O. N.; Bria, M.; Buchner, R.; Idrissi, A. Translational Diffusion in Mixtures of Imidazolium ILs with Polar Aprotic Molecular Solvents. *J. Phys. Chem. B* **2014**, *118* (20), 5509–5517. https://doi.org/10.1021/jp501561s.

Chapter 5

Experimental Techniques

5.1. Transient Absorption (TA):

5.1.1. Theory:

In case of the transient absorption spectroscopy, a part of the molecules is excited using the excitation pulse. Then, the excited molecules are probed using time-delayed probe pulse with a time delay τ with respect to the pump pulse. In a transient absorption experiment, mainly the difference absorption spectrum is calculated. The difference absorption spectrum (ΔA) is nothing but the difference between the absorption spectrum of excited sample and the ground state sample. This ΔA spectrum is collected while changing experimental wavelength (λ) and time delay (τ). This $\Delta A(\lambda, \tau)$ spectrum has the information about the excited state dynamics of the probe molecule in the medium. In case of our studied dyes, the $\Delta A(\lambda, \tau)$ spectrum has mainly three regions:

(a) Negative ground state bleach (GSB) – When the probe/dye molecule become excited by using the probe pulse, a fraction of these molecules are promoted to the excited state and the number of ground state molecules become decreased. That is the reason, this GSB signals are negative.

(b) Negative stimulated emission (SE) – Stimulated emission occurs only if there are some population of the excited state. Then the probe pulse goes through the excited state population to create the stimulated emission signal to the ground state. This, SE signal indicates that more light comes to detector when the probe/dye molecule is excited than the ground state sample, which indicates that, the ΔA signal should also be negative.

(c) Positive excited state absorption (ESA) – Upon excitation using the pump beam, the excited fraction of the sample also can absorb the probe pulse energy to go to higher excited state. This is the origin of ESA signal and this signal exists in certain wavelength range. The ΔA signal in this wavelength range is positive.

5.1.2. Experimental setup:

Femtosecond transient absorption setup is home-built and situated in the InFemto laboratory at the University of Warsaw. The full description of this setup used for our study has been stated elsewhere.[1] In short, the initial output of Coherent sapphire oscillator Micra 10 is amplified using 1 KHz regenerative amplifier Coherent Legend Elite. Then, the output pulse with 3.5 mJ energy and 45 fs time duration at 800 nm is divided into two pulses with different energy using a beam splitter. The stronger one with energy $\leq$ 15 μJ travels through the optical parametric amplifier (Opera Solo) to create the pump pulse at a particular wavelength for the excitation of the sample. In addition, the weaker pulse with < 1 μJ energy passes through a CaF_2 crystal to generate the white light supercontinuum probe pulse. Initially, the pump pulse at 460 nm excites the sample. After that, the delayed probe pulse passes through the same excited cross-section of the sample to create the transient absorption (TA) spectra which is then collected by using a spectrometer. The delay time between the pump and the probe pulse was controlled by using a mechanical delay line situated in the path of the probe pulse. The covered wavelength range of

the probe beam for our experiment was chosen from 470 nm to 750 nm. The instrument response function (IRF) of the setup is 90 fs which was calculated from the TA signal of pure acetonitrile at short time delay range (this way pump-probe cross-correlation was detected and fitted using a Gaussian function). The simplified figure of the transient absorption setup is shown in Figure 5.1 and a more detailed scheme of the TA setup is shown in Figure 5.2.

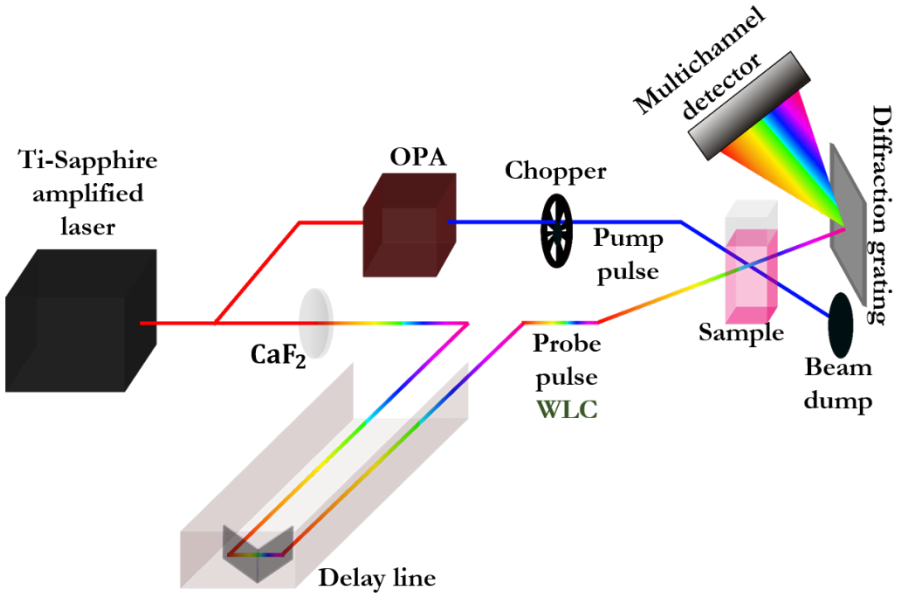

Figure 5.1: Simplified diagram of the TA setup used in our study

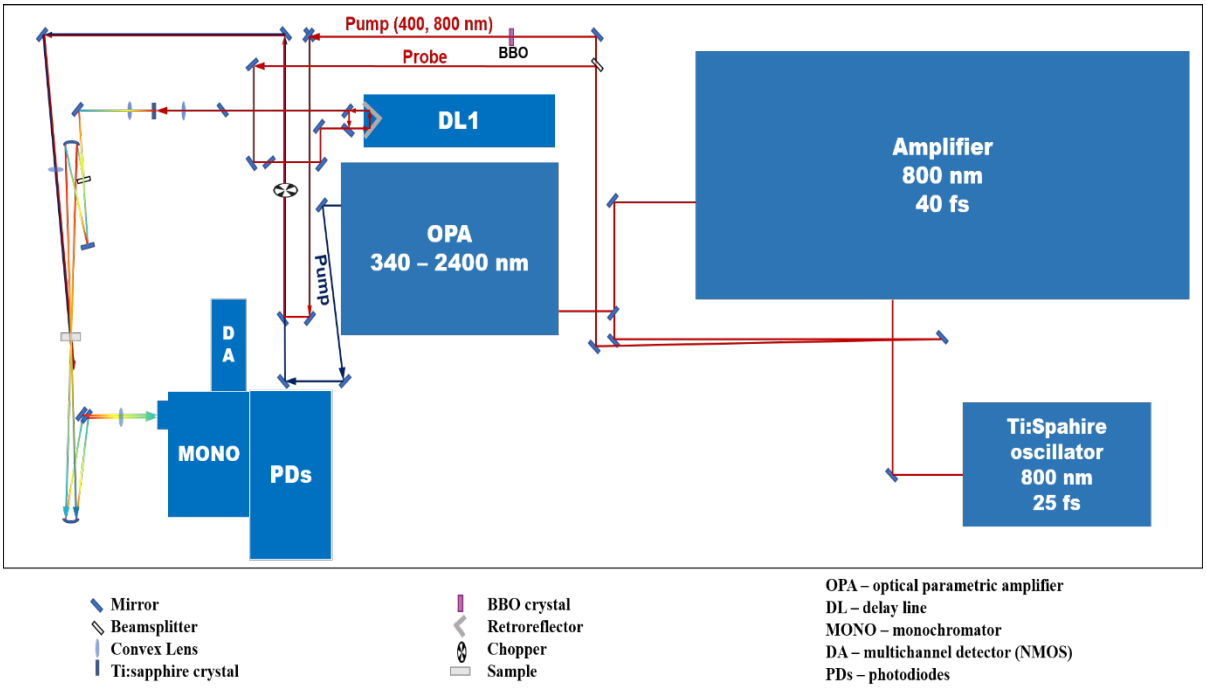

Figure 5.2: A detailed scheme of the femtosecond transient absorption setup. This Figure is prepared by Dr. Piotr Piatkowski

5.1.3. Data analysis:

5.1.3.1. Chirp correction:

The white light is chirped in general by the nature of the white light generation process, i.e. the blue wavelengths are generated later in time compared to the red wavelengths in a white light continuum. However, specific temporal properties of white light depends upon the conditions during the generation. Thus, the white light continuum has an intrinsic group velocity dispersion (GVD). This GVD becomes enhanced up to picoseconds when the white light passes through optically dense materials like lenses and cuvettes.[2]

Therefore, in the case of femtosecond TA setup, there also exists a significant amount of chirp in the experimental data. Although by using the parabolic mirrors in the setup, this effect can be minimized, but not completely ignored. Thus, one need to do a chirp-correction before analyzing the experimental TA "raw" data. Correction of GVD is not an easy task. In this work, it was performed using a LabVIEW software. The chirp correction process contains a shift in time of the kinetics at different wavelengths in a way that, they have the time zero at the same time. In our case, the TA signal of pure acetonitrile molecule was used to correct the chirp in the experimental data. The chirp coefficients were obtained after fitting using a polynomial function. After that, these sets of coefficients were used to correct all the experimental data used in our study. The chirp uncorrected (Figure 5.3(A)) and corrected (Figure 5.3(B)) TA signals can be noticed in Figure 5.3 in the case of pure acetonitrile using our TA setup.

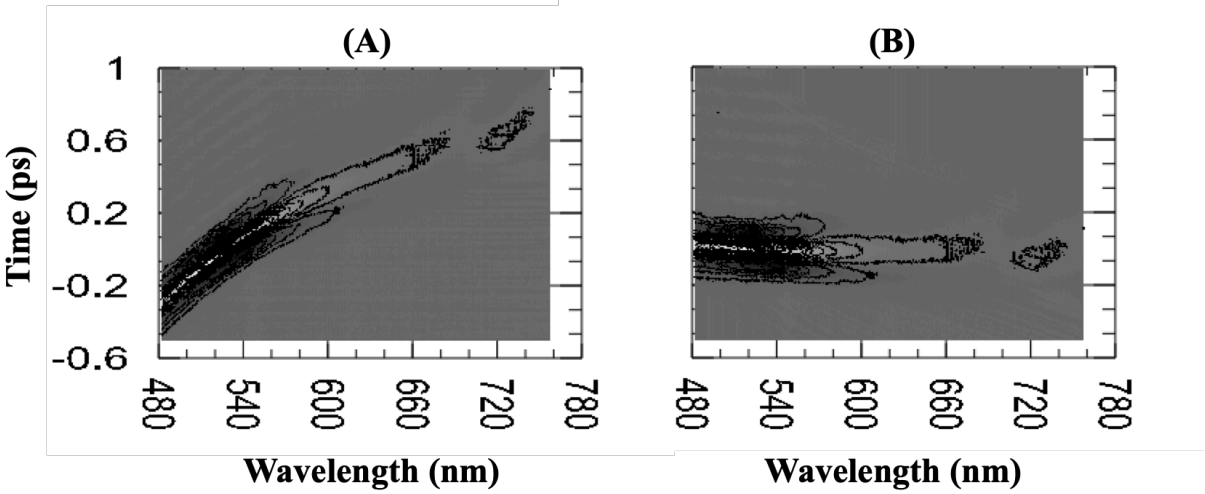

Figure 5.3: (A) Uncorrected and (B) chirp-corrected signals of pure ACN, λ_{Ex}= 460 nm

5.1.3.2. Global analysis:

The global analysis of the chirp-corrected experimental TA data was done using a MATLAB based tool called ultrafast Toolbox.[3] In this type of analysis, generally we can refine the enormous amount of data into relatively small number of time independent spectra, each of them associated with a particular excited state process or more than one excited state processes, characterized by a time constant. Therefore, the transient absorption signal is described as a sum of first order processes shown in equation 5.1 each characterized by a rate constant k_i.

$$\Delta A(t) = I_0 + \int_{-\infty}^{\infty} dt' \sum_{i=0}^{m} A_i(\lambda) e^{-k_i t'} I_{rf}(t - t') \qquad (5.1)$$

Where I_0 is the offset, m is the number of processes and I_{rf} is the instrumental response function (IRF)

$$I_{rf}(t) = \exp\left(-\left(\frac{t}{\tau_{irf}}\right)^2\right) \quad (5.2)$$

The IRF is obtained from the transient absorption signal of pure acetonitrile on very fast timescale where τ_{irf} is the instrument response time. The wavelength dependent pre-exponential factor $A_i(\lambda)$ forms a separate time independent decay associated spectrum (DAS) for each rate constants k_i, that corresponds to a decay time $\tau_i = (k_i)^{-1}$.

5.2. Time-Correlated Single-Photon Counting (TCSPC):

5.2.1. Experimental setup:

The TCSPC setup in LASIR was described elsewhere previously.[4] Here we will discuss about the setup in brief. A Ti:sapphire laser (Coherent Chameleon Ultra II, 200 fs, 3.8 W) with the repetition rate of 80 MHz and tunable output wavelength range of 700- 1200 nm is used as the excitation source for this setup. This 80 MHz output beam from the source become the input of a pulse picker where the repetition rate become 1/20th of the input beam. The output beam with 4 MHz repetition rate then goes through a second harmonic generator (SHG/THG, APE) which helps to generate the excitation pulse with the wavelength range 350-600 nm. The fluorescence lifetimes are recorded using FT200 PicoQuant spectrometer. The emission is collected at right angle with respect to incident beam using a Czerny-Turner type monochromator where the detection wavelengths can be chosen by computer. A polarizer between output beam and monochromator at magic angle (54.7°) helps to get rid of the anisotropy effects. Finally, the photons are detected by using a microchannel plate (Hamamatsu R3809U) cooled by using Peltier effect. A neutral density filter on the way of the excitation beam path helps to control the intensity of the incident beam and helps not to damage the microchannel plate. PicoHarp 300 TCSPC system helps to detect the time correlation of the photons. The time resolution or instrument response function (IRF) of this TCSPC setup is 32 ps which is excitation wavelength dependent and determined by measuring the signal of Ludox solution. Ludox solution (aqueous dispersion of silica particles) is used to disperse the excitation beam so that we can get the time resolution of the setup. A schematic diagram of the TCSPC setup in LASIR is shown in Figure 5.4.

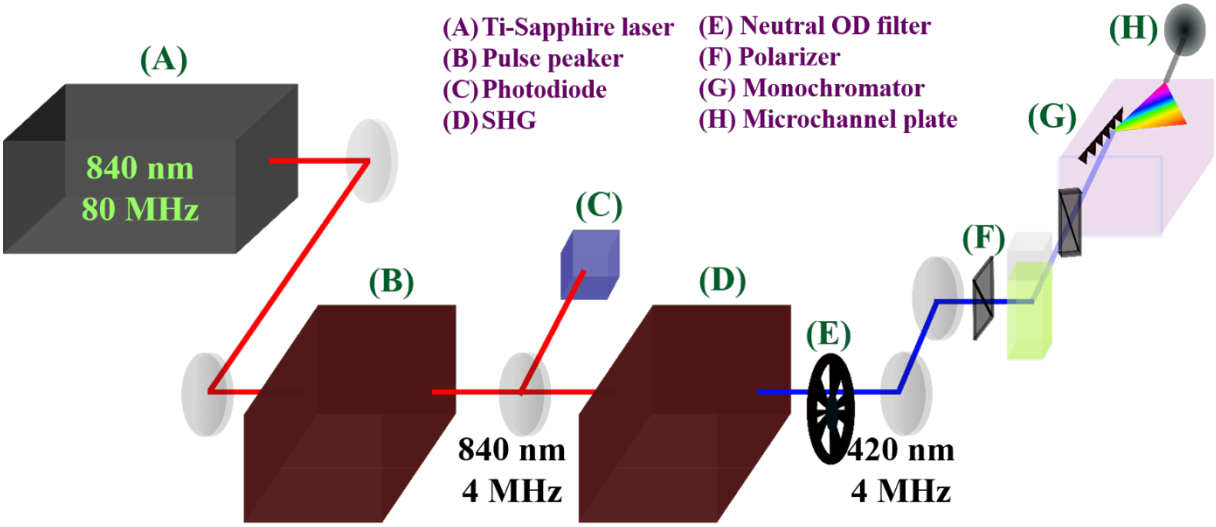

Figure 5.4: TCSPC setup in LASIRE

5.2.2. Data collection and analysis:

5.2.2.1. Data collection:

For the reconstruction of TRES, one needs to gather the time-dependent decay of the sample containing the dye molecule at different wavelengths spanning the whole range of the steady-state fluorescence spectrum. As the overall range of the emission spectrum of each studied samples was from 480 nm to 650 nm, we have gathered time-dependent decays at 18 different intermediate wavelengths with 10 nm wavelength steps in case of each studied sample. The intermediate mole fractions (X_{IL}) between pure ACN and pure $BmimPF_6$ are 0.05, 0.10, 0.20, 0.50 and 0.80.

5.2.2.2. Data analysis:

These experimental TCSPC decays at 18 intermediate wavelengths spanning the emission spectrum were then fitted after the deconvolution of the IRF spectrum. Here, in this data analysis section, we will discuss about the deconvolution and data fitting of the TCSPC decay at a particular wavelength. Fluofit[5] software from PicoQuant GmbH was used to fit all the experimental TCSPC decays. In Figure 5.5, we can see an example of the experimental and fitted data after deconvolution of the instrument response function (IRF) of our TCSPC setup.

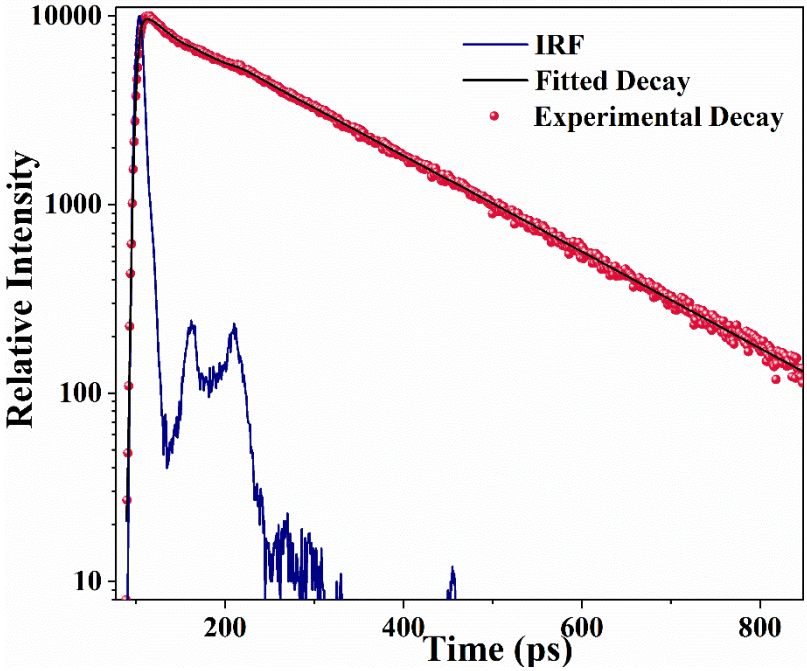

Figure 5.5: Representative experimental TCSPC decay (red circle), IRF (navy) and fitted trace (black)

To start with the data fitting procedure, deconvolution is mainly used to get rid of the finite time resolution of a particular TCSPC setup. All the experimental TCSPC data are fitted after getting deconvoluted by the Instrument response function of the setup. The instrument response function (R(t)) is generally measured from the TCSPC response through a scattering medium (Ludox solution in our case). The experimental fluorescence decay is inherently convoluted[6] as following:

$$I_M(t) = \int_0^t I_R(t - t')R(t')dt' \qquad (5.3)$$

Here, $I_M(t)$ is the measured TCSPC decay which is a convolution of 'real' decay $I_R(t)$ and the instrument response function R(t). After the deconvolution of the experimental decay function, the 'real' decay $I_R(t)$ is then fitted by using multi-exponential function. A non-linear least square analysis method is used to calculate the goodness of the fit parameter χ^2. In general, as the number of data points (n) in TCSPC measurements is very much higher than the number of fitting parameters, χ_R^2 is used instead of χ^2 where ($\chi_R^2 = \chi^2/n$) as the goodness of fit parameter. Typically, for TCSPC data the value of $\chi_R$remains in the range 0.8-1.2. The closer the value of χ_R is to 1, the better the quality of the TCSPC data fit.

5.3. Femtosecond Optical Kerr Effect Spectroscopy (OKE):

5.3.1. Experimental setup:

The overall femtosecond optical Kerr effect measurements were performed using two different types of experimental setups. The first one, based on sapphire oscillator, is already discussed comprehensively in a previous article by Polok et al.[7] In short, the initial femtosecond pulse is divided to pump and probe pulses by using a beam splitter. The relative polarization between the pump and probe pulses are fixed to 45°. The pump pulse is used mainly to generate the birefringence in the sample. After the generation of the birefringence in the sample, the pump pulse is blocked. The sample is placed right between a set of crossed polarizers for the probe pulse. For the heterodyne detection of the OKE signal, a wave plate is placed before the last polarizer whose optical axis is set at 45° with respect to the probe polarization before entering in the sample cuvette. The signal is then detected using a homebuilt balanced photodiode detector. The time delay between pump and probe pulse is created using a delay line whose maximum range is ~ 260 ps. The FWHM (full width half maxima) of the pulse was 23 fs. Using this oscillator setup, two different types of measurements were done for the sample. First, a high-resolution measurement with 1 fs steps until 50 ps pump-probe delay and second, a low-resolution measurement with 5 fs steps until 250 ps delay time. The figure of the setup is shown in Figure 5.6.

Beside this oscillator setup, another amplifier-based setup was also used to measure the OKE signals in case of sample containing ionic liquids because the orientational relaxation times in case of these highly viscous samples are quite slow (as long as a few nanoseconds). The amplifier used for this type of measurements is Coherent Legend Elite, with 1 kHz repetition rate and output power of 2.9 Watts. To get rid of the sample degradation and other additional effects during the experiments using this setup, the much higher energy of the input pulse is stretched to ~ 2 ps. This setup was mainly used to study the slow orientational dynamics of the samples with higher ionic liquid mole fraction ($X_{IL} \geq 0.20$) because the oscillator setup was unable to collect the complete orientational dynamics for these samples. The temperature of the samples was kept constant at 295±1 K for the oscillator setup and 297±1 K for the amplifier setup. The power of the pump pulses was ≤ 500 kW in both setups, whereas the power of the probe pulses was more than one order of magnitude lower than that of the pump pulses. Therefore, under all these measurement conditions, the other nonlinear processes can be neglected.

5.3.2. Data collection:

For the time-dependent OKE data collection, two separate sample sets were prepared for measurements on two different OKE setups. In case of the sample set for oscillator setup measurements, the intermediate ionic liquid mole fractions (X_{IL}) were 0.05, 0.10, 0.15, 0.20, 0.30, 0.40, 0.50 and 0.70 alongside the pure components. Besides, we have also used X_{IL} = 0.20, 0.25, 0.30, 0.40, 0.50, 0.60, 0.80, and 1.00 for the amplifier setup.

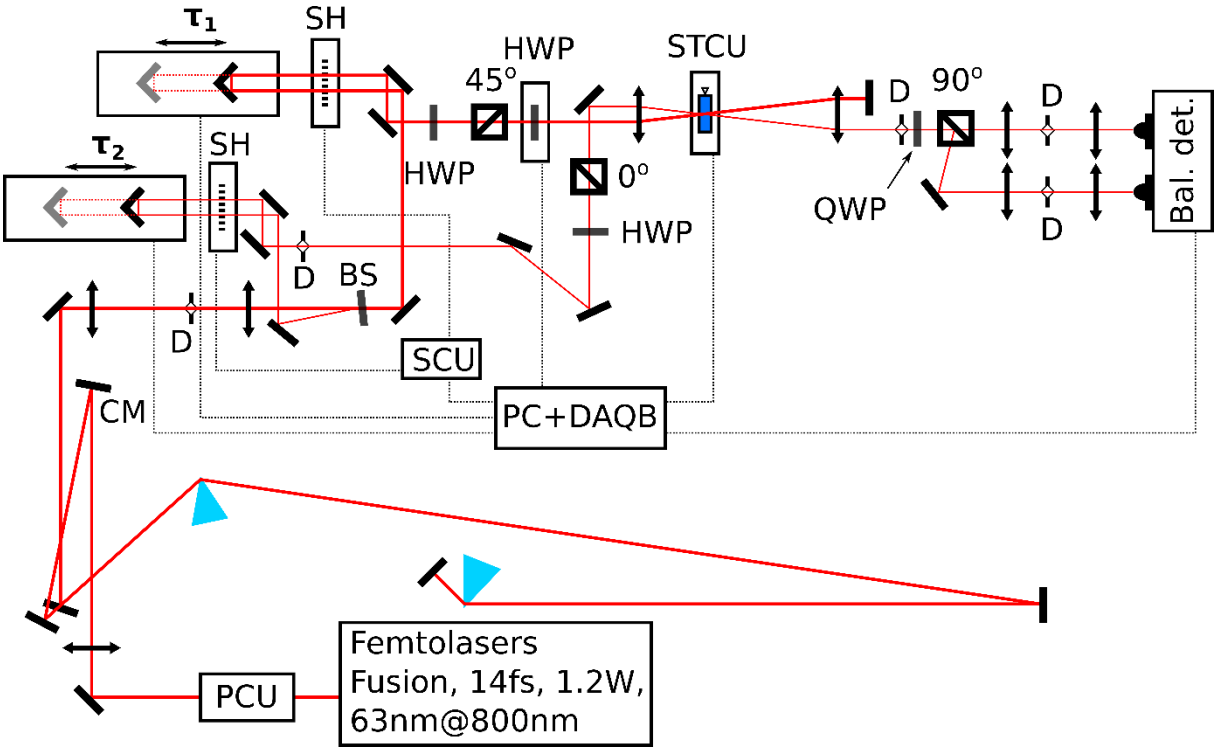

Figure 5.6: Femtosecond OKE setup in InFemto, Warsaw. PCU - power control unit, SCU - shutter control unit, PC+DAQB - computer with data acquisition board, BS - beam splitter , SH - shutter, HWP – half-waveplate, STCU - sample temperature control unit, QWP – Quarter-waveplate , τ_1- Fast variable delay, τ_2 - Slow variable delay, D - diaphragm and Bal. det.- balanced detector. This Figure is prepared by Dr. Kamil Polok.

5.3.3. Data analysis:

Each of the slow picosecond dynamics was fitted with a multi-exponential function. The slow picosecond orientational diffusion part of the signal was fitted using two decay times for X_{IL} > 0.20, whereas the number of time components vary from 1 to 4 in the case of OKE decay fitting using the oscillator setup in the whole composition range. In addition, the higher resolution data was used to obtain the OKE low frequency spectra using the McMorrow and Lotshaw deconvolution procedure.[8] Also, the pump-probe cross-correlation was measured using the CaF_2 crystal whose orientation was in a way that the nuclear contribution is minimized and the signal only consists of the response from the electron cloud.[7,9] Furthermore, to obtain the reduced spectral density (RSD), the fit of the slow picosecond component was subtracted from overall OKE response in the time domain in the following way:

$$r(t) = \left(1 - e^{-\frac{t}{\tau_r}}\right) \sum_{i=1}^{n} A_i e^{-\frac{t}{\tau_i}} \quad (5.4.1)$$

Here A_i and τ_i are the amplitude and time constant corresponding to each component of the fit of the slow picosecond dynamics respectively, and τ_r is the inertial rise time which was kept constant at 200 fs for our study.

5.4. CW-EPR Spectroscopy:

5.4.1. Experimental setup:

CW-EPR experiments were performed with a Bruker Elexsys E500 spectrometer operating at with X-band at 9.862 GHz at room temperature. For measurement of probes in solution, a solution of 300-500 μM of was filled into a glass capillary of 50 μL inside the glove box, which was in turn, placed in 4 mm quartz EPR tubes before EPR experiment. All the CW-EPR spectra were recorded using 0.02 mW of microwave power and 2 G of modulation amplitude with the sweeping field range of 3480 G – 3560 G.

5.4.2. Data simulation:

All the experimental EPR spectra were simulated using Matlab (The Mathworks, Inc.) in combination with the SimLabel[10] tool. In this aspect, SimLabel is nothing but a graphical user interface (GUI) of the EasySpin[11] program. In the Easyspin program, for analyzing the hyperfine splitting in the EPR spectra in liquid state, Easyspin uses the simulation function named "garlic". By using the "garlic" function, the resonance fields are computed by using the Brett-Rabi expression for the different energy levels as a function of external magnetic field (B) and it is solved for B by using the fixed-point iteration method.[11] As an output of this fitting of the EPR hyperfine lines, optimized values of all the other important parameters like the g-matrix, the hyperfine coupling constant (A_N), both the homogeneous and inhomogeneous broadening contributions (considering a mixture of both the Lorentzian and Gaussian functions) are found. In addition, the values of the average rotational relaxation time values are also calculated as an outcome of this fitting procedure. For the calculation of rotational relaxation time (τ_r), "garlic" uses the so-called Kivelson's formula in the fast motion regime.[11]

Biblioghraphy

(1) Piątkowski, P.; Ratajska-Gadomska, B.; Gadomski, W. Probing Slow Dynamics by Ultrafast Process: Sol–Gel Transition Detected by Transient Absorption Spectroscopy of Quantum Dots. *J. Mol. Liq.* **2012**, *176*, 106–111. https://doi.org/10.1016/j.molliq.2012.06.027.

(2) Berera, R.; van Grondelle, R.; Kennis, J. T. M. Ultrafast Transient Absorption Spectroscopy: Principles and Application to Photosynthetic Systems. *Photosynth. Res.* **2009**, *101* (2–3), 105–118. https://doi.org/10.1007/s11120-009-9454-y.

(3) van Wilderen, L. J. G. W.; Lincoln, C. N.; van Thor, J. J. Modelling Multi-Pulse Population Dynamics from Ultrafast Spectroscopy. *PLoS One* **2011**, *6* (3), e17373. https://doi.org/10.1371/journal.pone.0017373.

(4) Smortsova, Y.; Miannay, F.-A.; Oher, H.; Marekha, B.; Dubois, J.; Sliwa, M.; Kalugin, O.; Idrissi, A. Solvation Dynamics and Rotation of Coumarin 153 in a New Ionic Liquid/Molecular Solvent Mixture Model: [BMIM][TFSI]/Propylene Carbonate. *J. Mol. Liq.* **2017**, *226*, 48–55. https://doi.org/10.1016/j.molliq.2016.10.008.

(5) New Release 3.2 of FluoFit: Multiexponential Fluorescence Decay Fit Software. *J. Fluoresc.* **2003**, *13* (5), 451. https://doi.org/10.1023/A:1026173124577.

(6) Lakowicz, J. R. *General Features of Protein Fluorescence*; 2006.

(7) Polok, K.; Gadomski, W.; Ratajska-Gadomska, B. Femtosecond Optical Kerr Effect Setup with Signal "Live View" for Measurements in the Solid, Liquid, and Gas Phases. *Rev. Sci. Instrum.* **2015**, *86* (10), 103109. https://doi.org/10.1063/1.4932531.

(8) McMorrow, D.; Lotshaw, W. T. Intermolecular Dynamics in Acetonitrile Probed with Femtosecond Fourier-Transform Raman Spectroscopy. *J. Phys. Chem.* **1991**, *95* (25), 10395–10406. https://doi.org/10.1021/j100178a029.

(9) Taschin, A.; Bartolini, P.; Eramo, R.; Righini, R.; Torre, R. Evidence of Two Distinct Local Structures of Water from Ambient to Supercooled Conditions. *Nat. Commun.* **2013**, *4* (1), 2401. https://doi.org/10.1038/ncomms3401.

(10) Etienne, E.; Le Breton, N.; Martinho, M.; Mileo, E.; Belle, V. SimLabel: A Graphical User Interface to Simulate Continuous Wave EPR Spectra from Site-Directed Spin Labeling Experiments. *Magn. Reson. Chem.* **2017**, *55* (8), 714–719. https://doi.org/10.1002/mrc.4578.

(11) Stoll, S.; Schweiger, A. EasySpin, a Comprehensive Software Package for Spectral Simulation and Analysis in EPR. *J. Magn. Reson.* **2006**, *178* (1), 42–55. https://doi.org/10.1016/j.jmr.2005.08.013.

(12) Weil, J. A. The Analysis of Large Hyperfine Splitting in Paramagnetic Resonance Spectroscopy. *J. Magn. Reson.* **1971**, *4* (3), 394–399. https://doi.org/10.1016/0022-2364(71)90049-7.

Conclusions and perspectives

This thesis consists of the study of the spectroscopic and physical properties of ionic liquid-molecular solvent (IL-MS) mixtures and indoline-based dyes D102, D149 and D205 by using various time-integrated and time-resolved spectroscopic techniques. These spectroscopic techniques include steady-state UV-visible, electron paramagnetic resonance (EPR), picosecond time-resolved fluorescence and femtosecond optical Kerr effect (OKE) and transient absorption (TA). The studied organic indoline dyes are used as the photosensitizer in the so-called dye sensitized solar cell (DSSC) as they are considered as one of the most efficient among the available organic dyes used in DSSC. In addition, the studied IL-MS mixtures contain the imidazolium-based (Bmim) ionic liquids containing four different perfluorinated anions (BF_4^-, PF_6^-, $TFO^-$and $TFSI^-$) and three polar aprotic solvents (ACN, γ-BL and PC), which are considered as suitable replacement for the viscous ILs due to some of their advantageous properties like lower viscosity and cost over pure ILs. In is aspect, ionic liquids are already been used as electrolyte medium in DSSC and also other electrochemical devices due to their high conductivity, high thermal electrochemical stability and low volatility. Therefore, before using in a DSSC as an electrolyte, it is necessary to study different physical and spectrochemical properties in the IL-MS mixtures to optimize their useful properties. Of note is that, the presence of various types of interactions like ion-ion, ion-solvent, dye-solvent interactions makes the investigations challenging, which also explains the scarce number of previous studies about these IL-MS mixtures compared to that in pure solvents and ILs.

Therefore, part of the thesis was related to the characterization of the effect of the composition of IL-MS mixtures on their physicochemical properties. To start with, we have characterized polarity, one of the important property in ILs and also in the IL-MS mixtures, by using CW-EPR spectroscopy. As a result of this study, we have showed the composition dependent changes of the spectroscopic polarity parameter, hyperfine coupling constant (A_N), and rotational relaxation time (τ_R) values of the paramagnetic probe molecule TEMPO in case of all the aforementioned IL-MS mixtures. The careful EPR spectral fitting of the corresponding signals have resulted that, A_N values are less affected in the mole fraction (X_{IL}) range between 1 and 0.4, whereas it strongly decreases with further dilution of the IL. Besides, the similar trend can also be observed in case of the composition dependent τ_R values. In addition, we have showed the correlation between two probe dependent polarity parameters A_N and the UV-visible one (E_T^N) in case of a particular IL-MS mixture, namely $BmimBF_4$-ACN mixture. Furthermore, using the previously described modified Onsager field model as a correlation between A_N and static dielectric constant (ε) we have been able to explain the possible reason behind the discrepancy between the composition dependent changes of these two polarity parameter values in case of $BmimBF_4$-ACN mixture.

Furthermore, using femtosecond OKE technique, the complete reorientational dynamics in $BmimPF_6$-ACN mixture have been studied thoroughly, which was also supported by the molecular dynamics simulations. The overall OKE study was carried out in two domains, namely time domain and frequency domain. Firstly, three different relaxation times have been found from the time domain picosecond slow orientational OKE decay. Among them, the two slower ones have been attributed to the reorientation of the cation and the acetonitrile molecules which are in the vicinity of the imidazolium ring whereas, the fastest one is associated to the cation rotations and the reorientation of acetonitrile molecules near the bulk or the alkyl

extension of the cations. Secondly, the low frequency OKE response was studied experimentally and also using MD simulations in the frequency domain to interpret the intermolecular bands in the form of reduced spectral density (RSD) spectra. This combined analysis of the low frequency OKE response indicates that the low frequency side of the RSD spectra is dedicated to the oscillations of one of the mixture components in the cage formed by other neighbors, whereas the high frequency side is attributed to the librational motions of the cations and ACN molecules along with the intermolecular oscillations of the components. In addition, the composition dependent changes of the experimental RSD spectra was also obtained from the frequency domain analysis which was described considering the simulated velocity and angular velocity correlations in case of the mixture.

In addition to the reorientational dynamics, the solvation dynamics study was also performed using picosecond TCSPC technique and C153 as a probe in case of the similar IL-MS mixture, i.e. $BmimPF_6$-ACN mixture. This study reveals that the C153 solvation dynamics get slower while increasing the X_{IL} of $BmimPF_6$-ACN mixture, which is due to the increase of the viscosity of the surrounding medium while increasing the IL-concentration in the mixture. Moreover, the average solvation time values follow the power law viscosity dependence with mixture viscosity, similar to the other studied IL-MS mixtures. However, the fractional power value p in our study is not in the same range as suggested in the previous studies containing the solvation dynamics of other imidazolium based IL-MS mixtures. This indicates the presence of some shorter solvation time component in the solvation process which in turn suggests the importance of using sub-picosecond timescale measurements in addition to this study to get an idea about complete solvation process in the mixture.

In the other part of this thesis, the excited state dynamics of three organic indoline based dyes D102, D149 and D205 was characterized using the steadystate and femtosecond transient absorption spectroscopic techniques. All the values of steadystate absorption and emission maxima, Stokes shift and the relative quantum yield of these three studied dyes show large changes at low X_{IL} regions of all the above mentioned imidazolium IL-MS mixtures. The first excited (S_1) state of the dyes became accessible by exciting them using ultrashort laser pulses at 460 nm. As a result of the careful fitting of experimental TA spectra using the global analysis (GA) method, four distinguished characteristic relaxation timescales were found to describe the excited state dynamics of these three dyes in case of all IL-MS mixtures and corresponding pure components. The composition dependence of these four timescales shows an overall decay while decreasing the X_{IL} of the mixtures. Moreover, in the case of two slower ones among them, the composition dependence pass thorough the characteristic minima at $X_{IL} \sim 0.10$. In addition to the composition dependence, the viscosity and polarity dependence of these relaxation time components were also discussed which helped us to understand that fact that there is no particular correlation between the GA time components and the polarity and viscosity of pure components as well as in the mixtures. The outcomes from this study alongside with the appearance of the extrema in case of steadystate properties like the emission lifetime, Stokes shift and relative quantum yield values at the lower X_{IL} region mainly indicates the presence of different specific and non-specific interactions between the dye and the neighboring medium. However, the types of interactions between the dye and local medium which eventually have an effect on the excited state dynamics is yet be determined. Further theoretical studies are needed to be performed to get a deep insight about this matter.

In short, thorough the various studies presented in this thesis, we can get an overall idea about composition dependence of different spectrochemical properties in case of imidazolium IL-MS mixtures, a potential candidate to replace pure ILs as electrolyte in electrochemical cell. Besides, the excited state dynamics of organic indoline-based solar cell dyes were also studied in these IL-MS mixtures.

In perspectives, the work presented in this thesis can be the cause of these following developments:

- Study on the excited state dynamics of the studied dyes in the solvent mixtures between polar protic and aprotic solvents (for example, methanol-acetone mixture) to speculate the effect of the composition dependence on the relaxation times of the dyes.
- Dye concentration dependent change of the excited state dynamics in the case of studied indoline dyes as the aggregation due to higher concentration of the dye can affect the radiative relaxation process.
- Study the effect of addition of acids and bases in the solutions on the excited state relaxation process of the studied dyes.
- Finally, all the results in this thesis should be useful as the basis when the Dye-IL-MS mixture systems are present at the interface of the electrodes.

Appendices

Appendix A: Steadystate properties of indoline dyes in IL-MS mixtures

Table A1 : Steady state properties of D102 in $BmimBF_4$-ACN mixtures.

X_{IL}	λ_{Max}^{Abs} (nm)	ν_{Max}^{Abs} (cm^{-1})	λ_{Max}^{Em} (nm)	ν_{Max}^{Em} (cm^{-1})	ν_{Stokes} (cm^{-1})
0	494.12	20131.16	633.62	15030.10	5101.06
0.05	505.56	19691.16	657.30	14297.95	5393.21
0.10	506.82	19646.36	656.18	14316.84	5329.52
0.20	508.52	19567.54	652.55	14431.89	5135.65
0.50	510.95	19470.99	642.00	14836.79	4634.20
0.80	512.05	19440.10	634.55	15191.18	4248.92
1	512.71	19389.08	630.54	15338.05	4051.03

Table A2 : Steady state properties of D102 in $BmimBF_4$-γ-BL mixtures.

X_{IL}	λ_{Max}^{Abs} (nm)	ν_{Max}^{Abs} (cm^{-1})	λ_{Max}^{Em} (nm)	ν_{Max}^{Em} (cm^{-1})	ν_{Stokes} (cm^{-1})
0	499.52	19923.01	631.62	15311.41	4611.60
0.05	511.59	19468.81	648.41	14678.49	4790.32
0.10	512.30	19441.18	648.74	14668.17	4773.01
0.20	512.56	19426.41	646.66	14717.70	4708.71
0.50	512.68	19387.70	640.69	14971.45	4416.25
0.80	513.07	19401.39	634.64	15213.99	4187.40
1	512.71	19389.08	630.54	15338.05	4051.03

Table A3 : Steady state properties of D102 in $BmimBF_4$-PC mixtures.

X_{IL}	λ_{Max}^{Abs} (nm)	ν_{Max}^{Abs} (cm^{-1})	λ_{Max}^{Em} (nm)	ν_{Max}^{Em} (cm^{-1})	ν_{Stokes} (cm^{-1})
0	501.66	19839.72	633.25	15040.81	4798.91
0.05	510.14	19465.68	648.71	14578.59	4887.09
0.10	510.57	19455.25	647.52	14647.45	4807.80
0.20	511.07	19430.07	645.11	14758.63	4671.44
0.50	511.79	19389.25	638.82	15022.31	4366.94
0.80	512.07	19411.01	635.41	15149.19	4261.82
1	512.71	19389.08	630.54	15338.05	4051.03

Table A4 : Steady state properties of D102 in $BmimPF_6$-ACN mixtures.

X_{IL}	λ_{Max}^{Abs} (nm)	ν_{Max}^{Abs} (cm^{-1})	λ_{Max}^{Em} (nm)	ν_{Max}^{Em} (cm^{-1})	ν_{Stokes} (cm^{-1})
0	494.12	20131.16	633.62	15030.10	5101.06
0.05	505.13	19710.10	656.00	14371.14	5338.96

0.10	506.29	19656.29	656.00	14326.65	5329.64
0.20	508.26	19586.29	651.26	14490.62	5095.67
0.50	510.46	19505.61	641.04	14925.37	4580.24
0.80	511.73	19459.32	627.54	15450.98	4008.34
1	513.47	19381.70	622.99	15563.44	3818.26

Table A5 : Steady state properties of D102 in $BmimPF_6$-γ-BL mixtures.

X_{IL}	λ_{Max}^{Abs} (nm)	ν_{Max}^{Abs} (cm^{-1})	λ_{Max}^{Em} (nm)	ν_{Max}^{Em} (cm^{-1})	ν_{Stokes} (cm^{-1})
0	499.52	19923.01	631.62	15311.41	4611.60
0.05	510.12	19512.14	643.75	14819.80	4692.34
0.10	512.22	19439.31	648.40	14668.19	4771.12
0.20	512.45	19428.27	645.90	14738.12	4690.15
0.50	513.13	19408.03	640.00	15030.19	4377.84
0.80	513.27	19391.01	629.11	15448.11	3942.90
1	513.47	19381.70	622.99	15563.44	3818.26

Table A6 : Steady state properties of D102 in $BmimPF_6$-PC mixtures.

X_{IL}	λ_{Max}^{Abs} (nm)	ν_{Max}^{Abs} (cm^{-1})	λ_{Max}^{Em} (nm)	ν_{Max}^{Em} (cm^{-1})	ν_{Stokes} (cm^{-1})
0	501.66	19839.72	633.25	15040.81	4798.91
0.05	511.63	19455.15	649.45	14585.34	4869.81
0.10	511.95	19450.57	647.89	14648.05	4802.52
0.20	512.46	19420.23	643.76	14831.72	4588.51
0.50	512.95	19400.14	638.91	15037.59	4362.55
0.80	513.04	19390.17	629.41	15402.93	3987.24
1	513.47	19381.70	622.99	15563.44	3818.26

Table A7 : Steady state properties of D102 in BmimTFO-ACN mixtures.

X_{IL}	λ_{Max}^{Abs} (nm)	ν_{Max}^{Abs} (cm^{-1})	λ_{Max}^{Em} (nm)	ν_{Max}^{Em} (cm^{-1})	ν_{Stokes} (cm^{-1})
0	494.12	20131.16	633.62	15030.10	5101.06
0.05	501.74	19858.60	654.61	14356.05	5502.55
0.10	506.28	19681.90	654.28	14356.70	5325.20
0.20	507.91	19585.05	652.96	14405.76	5179.29
0.50	510.86	19500.60	643.17	14798.07	4702.53
0.80	512.07	19434.60	637.83	14952.72	4481.88
1	513.52	19379.84	631.27	15120.30	4259.54

Table A8 : Steady state properties of D102 in BmimTFO-γ-BL mixtures.

X_{IL}	λ_{Max}^{Abs} (nm)	ν_{Max}^{Abs} (cm^{-1})	λ_{Max}^{Em} (nm)	ν_{Max}^{Em} (cm^{-1})	ν_{Stokes} (cm^{-1})

0	499.52	19923.01	631.62	15311.41	4611.60
0.05	510.90	19493.15	648.43	14645.65	4847.50
0.10	511.37	19468.31	648.60	14619.88	4848.43
0.20	511.84	19462.71	647.14	14660.59	4802.12
0.50	512.04	19454.58	640.73	14905.80	4548.78
0.80	512.58	19436.78	639.84	14977.78	4459.00
1	513.52	19379.84	631.27	15120.30	4259.54

Table A9 : Steady state properties of D102 in BmimTFO-PC mixtures.

$\mathbf{X_{IL}}$	$\boldsymbol{\lambda^{Abs}_{Max}}$ **(nm)**	$\boldsymbol{\nu^{Abs}_{Max}}$ **(cm^{-1})**	$\boldsymbol{\lambda^{Em}_{Max}}$ **(nm)**	$\boldsymbol{\nu^{Em}_{Max}}$ **(cm^{-1})**	$\boldsymbol{\nu_{Stokes}}$ **(cm^{-1})**
0	501.66	19839.72	633.25	15040.81	4798.91
0.05	511.43	19488.95	648.15	14656.67	4832.28
0.10	511.50	19475.48	647.33	14668.35	4807.13
0.20	512.17	19462.30	645.50	14729.61	4732.69
0.50	512.43	19415.25	641.53	14817.43	4597.82
0.80	512.59	19404.33	639.15	14923.80	4480.53
1	513.52	19379.84	631.27	15120.30	4259.54

Table A10 : Steady state properties of D102 in BmimTFSI-ACN mixtures.

$\mathbf{X_{IL}}$	$\boldsymbol{\lambda^{Abs}_{Max}}$ **(nm)**	$\boldsymbol{\nu^{Abs}_{Max}}$ **(cm^{-1})**	$\boldsymbol{\lambda^{Em}_{Max}}$ **(nm)**	$\boldsymbol{\nu^{Em}_{Max}}$ **(cm^{-1})**	$\boldsymbol{\nu_{Stokes}}$ **(cm^{-1})**
0	494.12	20131.16	633.62	15030.10	5101.06
0.05	504.97	19710.85	656.20	14336.38	5374.47
0.10	506.53	19656.47	654.16	14384.70	5271.77
0.20	507.88	19599.06	650.20	14485.64	5113.42
0.50	510.18	19505.96	641.28	14897.62	4608.34
0.80	510.85	19474.31	635.03	15197.57	4276.74
1	512.37	19424.73	630.81	15350.10	4074.63

Table A11 : Steady state properties of D102 in BmimTFSI-γ-BL mixtures.

$\mathbf{X_{IL}}$	$\boldsymbol{\lambda^{Abs}_{Max}}$ **(nm)**	$\boldsymbol{\nu^{Abs}_{Max}}$ **(cm^{-1})**	$\boldsymbol{\lambda^{Em}_{Max}}$ **(nm)**	$\boldsymbol{\nu^{Em}_{Max}}$ **(cm^{-1})**	$\boldsymbol{\nu_{Stokes}}$ **(cm^{-1})**
0	499.52	19923.01	631.62	15311.41	4611.60
0.05	510.89	19497.06	648.30	14731.40	4765.66
0.10	511.00	19495.96	647.52	14693.73	4802.23
0.20	511.00	19493.21	646.53	14767.19	4726.02
0.50	511.07	19487.23	640.00	14955.04	4532.19
0.80	511.13	19483.42	635.45	15182.69	4300.73
1	512.37	19424.73	630.81	15350.10	4074.63

Table A12 : Steady state properties of D102 in BmimTFSI-PC mixtures.

X_{IL}	λ_{Max}^{Abs} (nm)	ν_{Max}^{Abs} (cm^{-1})	λ_{Max}^{Em} (nm)	ν_{Max}^{Em} (cm^{-1})	ν_{Stokes} (cm^{-1})
0	501.66	19839.72	633.25	15040.81	4798.91
0.05	510.38	19518.81	647.38	14646.76	4872.05
0.10	510.98	19484.25	646.58	14657.83	4826.42
0.20	511.22	19475.51	643.14	14823.74	4651.77
0.50	511.31	19470.28	639.59	14984.27	4486.01
0.80	511.63	19467.46	634.51	15220.70	4246.76
1	512.37	19424.73	630.81	15350.10	4074.63

Table A13 : Steady state properties of D149 in $BmimBF_4$-γ-BL mixtures.

X_{IL}	λ_{Max}^{Abs} (nm)	ν_{Max}^{Abs} (cm^{-1})	λ_{Max}^{Em} (nm)	ν_{Max}^{Em} (cm^{-1})	ν_{Stokes} (cm^{-1})
0	538.12	18473.62	661.32	14724.57	3749.05
0.05	540.97	18416.21	664.32	14696.05	3720.16
0.10	541.11	18389.24	665.11	14672.64	3716.60
0.20	541.28	18388.01	661.05	14684.29	3703.72
0.50	541.67	18387.04	656.41	14854.74	3532.30
0.80	542.10	18365.47	648.41	15001.18	3364.29
1	542.30	18353.44	644.00	15025.08	3328.36

Table A14 : Steady state properties of D149 in $BmimBF_4$-PC mixtures.

X_{IL}	λ_{Max}^{Abs} (nm)	ν_{Max}^{Abs} (cm^{-1})	λ_{Max}^{Em} (nm)	ν_{Max}^{Em} (cm^{-1})	ν_{Stokes} (cm^{-1})
0	532.91	18688.22	646.10	14992.65	3695.57
0.05	539.50	18482.19	659.04	14621.76	3860.43
0.10	539.72	18460.01	658.41	14626.25	3833.76
0.20	539.92	18422.88	650.71	14751.28	3671.60
0.50	541.00	18381.21	647.33	14964.37	3416.84
0.80	541.95	18363.28	648.22	15001.65	3361.63
1	542.30	18353.44	644.00	15025.08	3328.36

Table A15 : Steady state properties of D149 in $BmimPF_6$-ACN mixtures.

X_{IL}	λ_{Max}^{Abs} (nm)	ν_{Max}^{Abs} (cm^{-1})	λ_{Max}^{Em} (nm)	ν_{Max}^{Em} (cm^{-1})	ν_{Stokes} (cm^{-1})
0	531.00	18727.60	665.00	14442.10	4285.50
0.05	532.37	18643.07	668.50	14534.88	4108.19
0.10	533.81	18591.08	662.30	14525.51	4065.57
0.20	534.70	18542.06	660.20	14528.60	4013.46
0.50	536.80	18443.38	650.80	14748.60	3694.78
0.80	539.50	18356.10	643.10	15021.10	3335.00
1	542.60	18300.37	637.90	15224.60	3075.77

Table A16 : Steady state properties of D149 in $BmimPF_6$-γ-BL mixtures.

X_{IL}	λ_{Max}^{Abs} (nm)	ν_{Max}^{Abs} (cm^{-1})	λ_{Max}^{Em} (nm)	ν_{Max}^{Em} (cm^{-1})	ν_{Stokes} (cm^{-1})
0	538.12	18473.62	661.32	14724.57	3749.05
0.05	540.00	18422.38	665.64	14536.09	3886.29
0.10	540.28	18408.41	666.22	14535.35	3873.06
0.20	540.71	18404.29	665.17	14548.52	3855.77
0.50	540.85	18364.73	656.93	14731.18	3633.55
0.80	541.75	18330.94	646.19	15184.67	3146.27
1	542.60	18300.37	637.90	15224.60	3075.77

Table A17 : Steady state properties of D149 in $BmimPF_6$-PC mixtures.

X_{IL}	λ_{Max}^{Abs} (nm)	ν_{Max}^{Abs} (cm^{-1})	λ_{Max}^{Em} (nm)	ν_{Max}^{Em} (cm^{-1})	ν_{Stokes} (cm^{-1})
0	532.91	18688.22	646.10	14992.65	3695.57
0.05	539.00	18458.75	663.23	14563.23	3895.52
0.10	539.67	18436.91	663.73	14557.38	3879.53
0.20	540.14	18436.06	662.83	14563.99	3872.07
0.50	541.13	18376.50	655.71	14661.75	3714.75
0.80	542.07	18342.56	645.37	15139.56	3203.00
1	542.60	18300.37	637.90	15224.60	3075.77

Table A18 : Steady state properties of D149 in BmimTFO-ACN mixtures.

X_{IL}	λ_{Max}^{Abs} (nm)	ν_{Max}^{Abs} (cm^{-1})	λ_{Max}^{Em} (nm)	ν_{Max}^{Em} (cm^{-1})	ν_{Stokes} (cm^{-1})
0	531.00	18727.60	665.00	14442.10	4285.50
0.05	535.11	18604.65	665.37	14517.89	4086.76
0.10	535.53	18596.21	664.45	14660.28	3935.93
0.20	537.17	18534.19	659.37	14803.07	3731.12
0.50	540.10	18452.33	652.19	15018.45	3433.88
0.80	540.21	18416.14	645.94	15159.26	3256.88
1	540.53	18402.18	640.71	15285.47	3116.71

Table A19 : Steady state properties of D149 in BmimTFO-γ-BL mixtures.

X_{IL}	λ_{Max}^{Abs} (nm)	ν_{Max}^{Abs} (cm^{-1})	λ_{Max}^{Em} (nm)	ν_{Max}^{Em} (cm^{-1})	ν_{Stokes} (cm^{-1})
0	538.12	18473.62	661.32	14724.57	3749.05
0.05	539.87	18437.66	665.84	14541.40	3896.26
0.10	540.07	18433.79	658.76	14705.11	3728.68
0.20	540.13	18428.76	652.33	14884.29	3544.47
0.50	540.31	18415.80	648.13	14943.28	3472.52
0.80	540.50	18409.52	644.24	15086.34	3323.18
1	540.53	18402.18	640.71	15285.47	3116.71

Table A20 : Steady state properties of D149 in BmimTFO-PC mixtures.

X_{IL}	λ_{Max}^{Abs} (nm)	ν_{Max}^{Abs} (cm^{-1})	λ_{Max}^{Em} (nm)	ν_{Max}^{Em} (cm^{-1})	ν_{Stokes} (cm^{-1})
0	532.91	18688.22	646.10	14992.65	3695.57
0.05	539.28	18478.10	660.59	14647.74	3830.36
0.10	539.46	18467.22	654.12	14808.04	3659.18
0.20	539.50	18459.84	650.80	14893.04	3566.80
0.50	539.76	18450.85	648.54	14977.58	3473.27
0.80	540.09	18447.62	646.38	15061.82	3385.80
1	540.53	18402.18	640.71	15285.47	3116.71

Table A21 : Steady state properties of D149 in BmimTFSI-ACN mixtures.

X_{IL}	λ_{Max}^{Abs} (nm)	ν_{Max}^{Abs} (cm^{-1})	λ_{Max}^{Em} (nm)	ν_{Max}^{Em} (cm^{-1})	ν_{Stokes} (cm^{-1})
0	531.00	18727.60	665.00	14442.10	4285.50
0.05	533.25	18649.55	666.11	14391.46	4258.09
0.10	534.94	18671.38	662.93	14426.68	4244.70
0.20	536.41	18602.23	659.36	14497.13	4105.10
0.50	537.82	18468.76	652.04	14729.40	3739.36
0.80	538.51	18497.00	648.26	14861.73	3635.27
1	540.46	18413.99	643.99	15046.96	3367.03

Table A22 : Steady state properties of D149 in BmimTFSI-γ-BL mixtures.

X_{IL}	λ_{Max}^{Abs} (nm)	ν_{Max}^{Abs} (cm^{-1})	λ_{Max}^{Em} (nm)	ν_{Max}^{Em} (cm^{-1})	ν_{Stokes} (cm^{-1})
0	538.12	18473.62	661.32	14724.57	3749.05
0.05	539.00	18459.79	663.82	14467.98	3991.81
0.10	539.51	18456.49	662.54	14481.01	3975.48
0.20	539.86	18449.10	660.00	14523.82	3925.28
0.50	540.13	18439.34	651.58	14798.07	3641.27
0.80	540.22	18430.40	646.78	14919.19	3511.21
1	540.46	18413.99	643.99	15046.96	3367.03

Table A23 : Steady state properties of D149 in BmimTFSI-PC mixtures.

X_{IL}	λ_{Max}^{Abs} (nm)	ν_{Max}^{Abs} (cm^{-1})	λ_{Max}^{Em} (nm)	ν_{Max}^{Em} (cm^{-1})	ν_{Stokes} (cm^{-1})
0	532.91	18688.22	646.10	14992.65	3695.57
0.05	537.00	18481.62	656.24	14629.87	3851.75
0.10	538.00	18474.87	655.53	14644.74	3830.13
0.20	539.00	18468.28	655.64	14652.94	3815.34
0.50	539.70	18450.18	650.52	14770.19	3679.99

0.80	539.72	18438.95	646.55	14938.95	3500.00
1	540.46	18413.99	643.99	15046.96	3367.03

Table A24 : Steady state properties of D205 in $BmimBF_4$-ACN mixtures.

X_{IL}	λ_{Max}^{Abs} (nm)	ν_{Max}^{Abs} (cm^{-1})	λ_{Max}^{Em} (nm)	ν_{Max}^{Em} (cm^{-1})	ν_{Stokes} (cm^{-1})
0	527.86	18839.37	646.77	14858.41	3980.96
0.05	535.09	18617.65	650.64	14807.25	3810.40
0.10	536.89	18558.62	647.51	14825.02	3733.60
0.20	538.17	18494.57	645.98	14872.29	3622.28
0.50	539.44	18431.47	643.67	14912.63	3518.84
0.80	541.22	18349.35	642.91	14933.78	3415.57
1	543.82	18183.10	641.51	14940.57	3242.53

Table A25 : Steady state properties of D205 in $BmimBF_4$-γ-BL mixtures.

X_{IL}	λ_{Max}^{Abs} (nm)	ν_{Max}^{Abs} (cm^{-1})	λ_{Max}^{Em} (nm)	ν_{Max}^{Em} (cm^{-1})	ν_{Stokes} (cm^{-1})
0	533.91	18647.33	642.33	15161.83	3485.50
0.05	539.22	18507.21	645.73	14774.88	3732.33
0.10	540.90	18447.45	644.96	14793.60	3653.85
0.20	541.33	18424.15	643.11	14840.56	3583.59
0.50	542.25	18370.42	642.36	14881.51	3488.91
0.80	542.77	18310.50	641.83	14906.35	3404.15
1	543.82	18183.10	641.51	14940.57	3242.53

Table A26 : Steady state properties of D205 in $BmimBF_4$-PC mixtures.

X_{IL}	λ_{Max}^{Abs} (nm)	ν_{Max}^{Abs} (cm^{-1})	λ_{Max}^{Em} (nm)	ν_{Max}^{Em} (cm^{-1})	ν_{Stokes} (cm^{-1})
0	534.62	18624.75	643.09	14626.34	3998.41
0.05	535.59	18593.10	646.03	14516.08	4077.02
0.10	540.63	18441.41	645.71	14524.53	3916.88
0.20	541.27	18405.51	644.52	14578.11	3827.40
0.50	542.19	18371.52	643.23	14691.42	3680.10
0.80	542.51	18369.92	642.01	14810.23	3559.69
1	543.82	18183.10	641.51	14940.57	3242.53

Table A27 : Steady state properties of D205 in $BmimPF_6$-ACN mixtures.

X_{IL}	λ_{Max}^{Abs} (nm)	ν_{Max}^{Abs} (cm^{-1})	λ_{Max}^{Em} (nm)	ν_{Max}^{Em} (cm^{-1})	ν_{Stokes} (cm^{-1})
0	527.86	18839.37	646.77	14858.41	3980.96
0.05	533.96	18639.96	653.22	14523.73	4116.23
0.10	535.26	18567.36	652.50	14525.51	4041.85

0.20	536.76	18522.23	651.31	14716.96	3805.27
0.50	540.35	18410.52	647.45	14741.31	3669.21
0.80	541.98	18325.08	644.88	14752.64	3572.44
1	543.22	18254.81	639.11	14877.00	3377.81

Table A28 : Steady state properties of D205 in $BmimPF_6$-γ-BL mixtures.

X_{IL}	λ_{Max}^{Abs} (nm)	ν_{Max}^{Abs} (cm^{-1})	λ_{Max}^{Em} (nm)	ν_{Max}^{Em} (cm^{-1})	ν_{Stokes} (cm^{-1})
0	533.91	18647.33	642.33	15161.83	3485.50
0.05	540.06	18410.96	649.35	14632.22	3778.74
0.10	541.13	18394.93	646.61	14751.99	3642.94
0.20	541.33	18398.26	645.17	14801.82	3596.44
0.50	542.36	18348.53	644.54	14823.78	3524.75
0.80	543.01	18313.11	642.71	14846.57	3466.54
1	543.22	18254.81	639.11	14877.00	3377.81

Table A29 : Steady state properties of D205 in $BmimPF_6$-PC mixtures.

X_{IL}	λ_{Max}^{Abs} (nm)	ν_{Max}^{Abs} (cm^{-1})	λ_{Max}^{Em} (nm)	ν_{Max}^{Em} (cm^{-1})	ν_{Stokes} (cm^{-1})
0	534.62	18624.75	643.09	14626.34	3998.41
0.05	537.52	18368.65	654.16	14561.78	3806.87
0.10	540.01	18350.62	653.18	14567.13	3783.49
0.20	540.89	18348.06	649.97	14602.42	3745.64
0.50	541.50	18328.62	645.09	14710.07	3618.55
0.80	542.70	18315.02	642.23	14825.86	3489.16
1	543.22	18254.81	639.11	14877.00	3377.81

Table A30 : Steady state properties of D205 in BmimTFO-ACN mixtures.

X_{IL}	λ_{Max}^{Abs} (nm)	ν_{Max}^{Abs} (cm^{-1})	λ_{Max}^{Em} (nm)	ν_{Max}^{Em} (cm^{-1})	ν_{Stokes} (cm^{-1})
0	527.86	18839.37	646.77	14858.41	3980.96
0.05	531.18	18730.83	652.61	14652.21	4078.62
0.10	532.70	18626.36	648.63	14672.06	3954.30
0.20	534.83	18541.77	646.31	14793.53	3748.24
0.50	540.01	18453.10	643.93	14961.26	3491.84
0.80	541.34	18342.32	640.36	15021.23	3321.09
1	542.44	18267.51	638.46	15188.65	3078.86

Table A31 : Steady state properties of D205 in BmimTFO-γ-BL mixtures.

X_{IL}	λ_{Max}^{Abs} (nm)	ν_{Max}^{Abs} (cm^{-1})	λ_{Max}^{Em} (nm)	ν_{Max}^{Em} (cm^{-1})	ν_{Stokes} (cm^{-1})
0	533.91	18647.33	642.33	15161.83	3485.50

0.05	540.09	18407.18	650.33	14919.39	3487.79
0.10	540.61	18403.59	648.56	14998.72	3404.87
0.20	540.74	18363.66	645.67	15068.79	3294.87
0.50	541.61	18309.32	643.89	15126.28	3183.04
0.80	542.01	18244.60	641.15	15153.02	3091.58
1	542.44	18267.51	638.46	15188.65	3078.86

Table A32 : Steady state properties of D205 in BmimTFO-PC mixtures.

X_{IL}	λ_{Max}^{Abs} (nm)	ν_{Max}^{Abs} (cm^{-1})	λ_{Max}^{Em} (nm)	ν_{Max}^{Em} (cm^{-1})	ν_{Stokes} (cm^{-1})
0	534.62	18624.75	643.09	14626.34	3998.41
0.05	539.53	18454.68	651.51	14451.03	4003.65
0.10	540.62	18425.69	647.28	14548.26	3877.43
0.20	541.64	18402.46	643.05	14631.05	3771.41
0.50	541.88	18338.32	641.28	14898.45	3439.87
0.80	542.03	18293.25	640.13	15028.13	3265.12
1	542.44	18267.51	638.46	15188.65	3078.86

Table A33 : Steady state properties of D205 in BmimTFSI-ACN mixtures.

X_{IL}	λ_{Max}^{Abs} (nm)	ν_{Max}^{Abs} (cm^{-1})	λ_{Max}^{Em} (nm)	ν_{Max}^{Em} (cm^{-1})	ν_{Stokes} (cm^{-1})
0	527.86	18839.37	646.77	14858.41	3980.96
0.05	536.81	18491.26	646.54	14841.35	3649.91
0.10	537.61	18411.63	644.35	14892.03	3519.60
0.20	538.13	18350.21	643.51	14951.20	3399.01
0.50	539.03	18293.64	642.83	14983.21	3310.43
0.80	540.21	18251.30	641.10	15001.21	3250.09
1	541.66	18195.41	640.13	15021.29	3174.12

Table A34 : Steady state properties of D205 in BmimTFSI-γ-BL mixtures.

X_{IL}	λ_{Max}^{Abs} (nm)	ν_{Max}^{Abs} (cm^{-1})	λ_{Max}^{Em} (nm)	ν_{Max}^{Em} (cm^{-1})	ν_{Stokes} (cm^{-1})
0	533.91	18647.33	642.33	15161.83	3485.50
0.05	535.10	18416.21	652.23	14451.26	3964.95
0.10	536.72	18366.20	650.12	14526.31	3839.89
0.20	537.53	18335.13	649.02	14623.05	3712.08
0.50	538.29	18303.27	647.51	14801.23	3502.04
0.80	539.00	18255.69	643.21	14923.21	3332.48
1	541.66	18195.41	640.13	15021.29	3174.12

Table A35 : Steady state properties of D205 in BmimTFSI-PC mixtures.

X_{IL}	λ_{Max}^{Abs}	ν_{Max}^{Abs}	λ_{Max}^{Em}	ν_{Max}^{Em}	ν_{Stokes}

	(nm)	(cm^{-1})	(nm)	(cm^{-1})	(cm^{-1})
0	534.62	18624.75	643.09	14626.34	3998.41
0.05	537.09	18421.65	653.21	14401.02	4020.63
0.10	538.91	18393.18	647.31	14502.15	3891.03
0.20	539.49	18352.18	643.51	14621.79	3730.39
0.50	540.07	18323.33	642.72	14743.61	3579.72
0.80	540.92	18245.88	641.16	14901.26	3344.62
1	541.66	18195.41	640.13	15021.29	3174.12

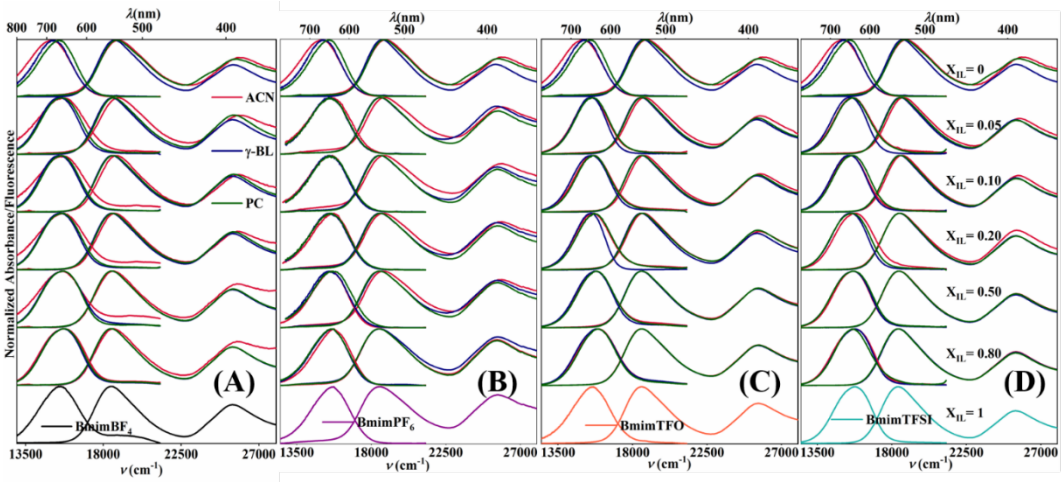

Figure A1: Normalized steady state absorption (right) and emission (left) spectra of D149 in (A) $BmimBF_4$-MS, (B) $BmimPF_6$-MS, (C) BmimTFO-MS and (D) BmimTFSI-MS mixtures ($\lambda_{excitation}$= 460 nm).

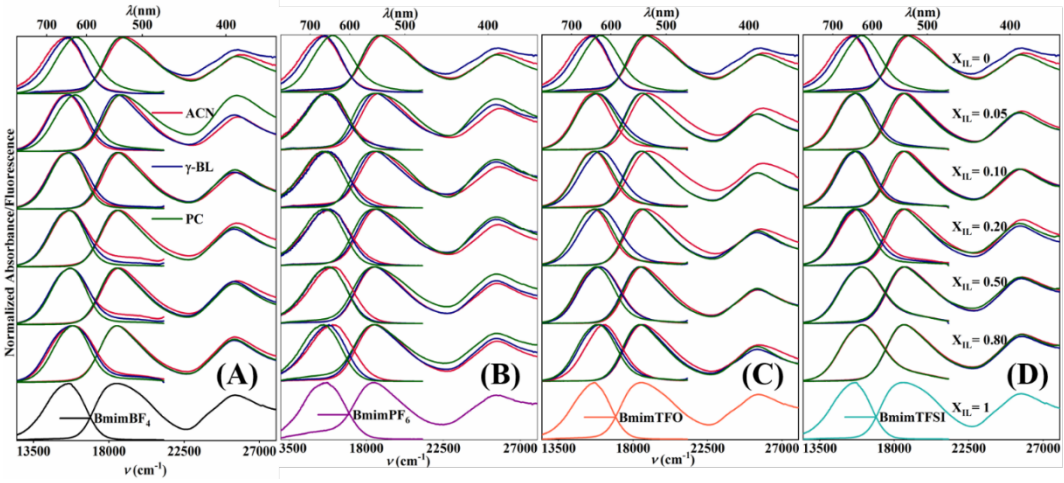

Figure A2: Normalized steady state absorption (right) and emission (left) spectra of D205 in (A) $BmimBF_4$-MS, (B) $BmimPF_6$-MS, (C) BmimTFO-MS and (D) BmimTFSI-MS mixtures ($\lambda_{excitation}$= 460 nm).

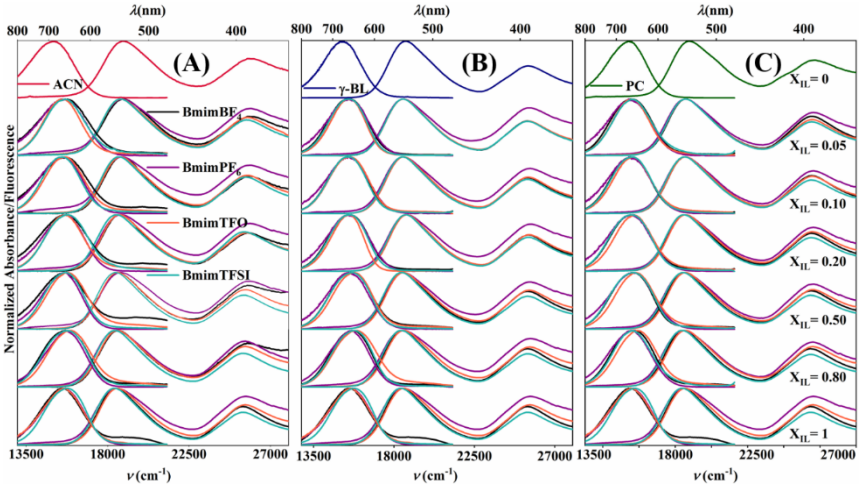

Figure A3: Normalized steady state absorption (right) and emission (left) spectra of D149 in (A) IL-ACN , (B) IL-γ-BL and (C) IL-PC mixtures ($\lambda_{excitation}$= 460 nm).

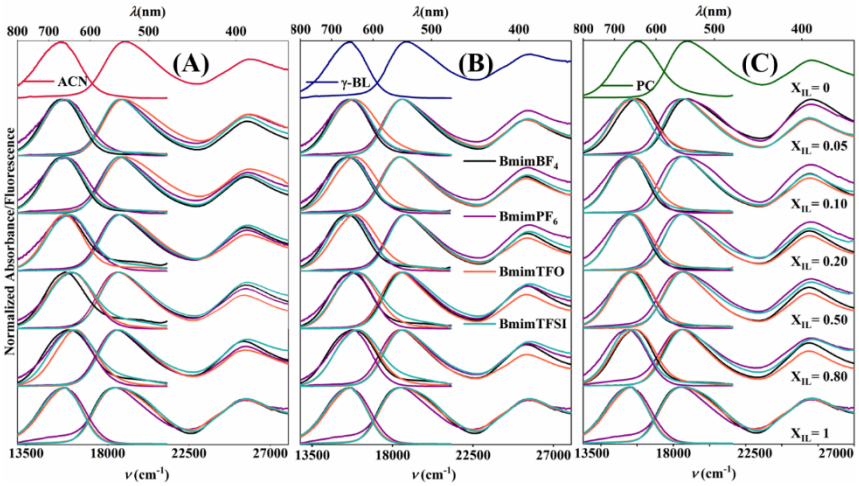

Figure A4: Normalized steady state absorption (right) and emission (left) spectra of D205 in (A) IL-ACN , (B) IL-γ-BL and (C) IL-PC mixtures ($\lambda_{excitation}$= 460 nm).

Appendix B: Transient absorption study in IL-MS mixtures

Table B1: Excited state relaxation times of D102, D149 and D205 in various solvents and ILs.

Solvent /IL	η	Δf	τ_1 (ps)	τ_2 (ps)	τ_3 (ps)	τ_4 (ps)	Ref
			D149				
ACN	0.35	0.71	0.08, 0.16, 0.35, 0.089	0.65, 0.63, 0.77, 1.4	33.34, 18.5, 23, 19	275.65, 320, 220, 280	[1–3]
γ-BL	1.76	0.67	0.14	1.26	13.93	418.65	
PC	2.65	0.70	0.23	2.31	14.67	372.12	
$BmimBF_4$	109	0.53	0.51	10.39	120.71	912.27	
$BmimPF_6$	261	0.53	0.83	11.48	161.06	1595.21	
BmimTFO	89	0.54	0.82	10.46	84.88	878.17	
BmimTFSI	50.05	0.52	1.29	14.88	110.87	835.55	
MeOH	0.54	0.71	0.12	0.99, 2.5	11.9, 13.2	99, 103	[2–4]
EtOH	0.98	0.66	0.39	5.03	29.6	178	[2]
Acetone	0.3	0.65	0.187	1.09		540	
THF	0.46	0.44	0.228	1.52	30	720	
Hexane	0.3	0.003			25	310	[4]
Toluene	0.56	0.024	0.45		40	630	[1]
			D102				
ACN	0.35	0.71	0.11, 0.21	0.84, 0.91	17.37, 17.5	228.92, 310	[3]
γ-BL	1.76	0.67	0.19	1.15	15.85	334.7	
PC	2.65	0.70	0.3	1.72	16.45	324.56	
$BmimBF_4$	109	0.53	0.99	11.23	112.36	891.25	
$BmimPF_6$	261	0.53	0.42	12.46	143.41	1305.22	
BmimTFO	89	0.54	1.01	7.49	102.36	853.55	
BmimTFSI	50.05	0.52	0.49	10.81	72.4	768.13	
MeOH	0.54	0.71	0.1	1.4	11	70	[3]
			D205				
ACN	0.35	0.71	0.12	1.11	16.72	240.75	
γ-BL	1.76	0.67	0.13	1.12	12.5	357.24	
PC	2.65	0.70	0.28	1.78	13.35	354.25	
$BmimBF_4$	109	0.53	0.91	14.29	125.17	1041.96	
$BmimPF_6$	261	0.53	0.96	10.16	166.93	2208.3	
BmimTFO	89	0.54	0.99	12.3	103.62	1014.81	
BmimTFSI	50.05	0.52	0.86	19.9	121.94	973.65	

$\Delta f = \frac{\varepsilon-1}{\varepsilon+2} - \frac{n^2-1}{n^2+2}$;[2] and ε and n are the dielectric constants and refractive indices of pure components

Table B2 : Global analysis time constants of D102 in $BmimBF_4$-ACN mixtures.

X_{IL}	τ_1 (ps)	τ_2 (ps)	τ_3 (ps)	τ_4 (ps)
0	0.11	0.84	17.37	228.92
0.05	0.13	1.01	17.61	163.31
0.10	0.15	1.21	22.88	169.86
0.20	0.17	1.94	26.99	182.13
0.50	0.33	2.27	57.80	372.37
0.80	0.55	6.48	90.97	560.73
1	0.99	11.23	112.36	891.25

Table B3 : Global analysis time constants of D102 in $BmimBF_4$-γ-BL mixtures.

X_{IL}	τ_1 (ps)	τ_2 (ps)	τ_3 (ps)	τ_4 (ps)
0	0.19	1.15	15.85	334.70
0.05	0.21	1.67	15.11	285.35
0.10	0.33	2.67	23.51	300.28
0.20	0.35	3.45	31.85	339.51
0.50	0.64	7.06	61.18	494.08
0.80	0.69	9.92	80.48	671.94
1	0.99	11.23	112.36	891.25

Table B4 : Global analysis time constants of D102 in $BmimBF_4$-PC mixtures.

X_{IL}	τ_1 (ps)	τ_2 (ps)	τ_3 (ps)	τ_4 (ps)
0	0.30	1.72	16.45	324.56
0.05	0.28	2.38	16.59	261.64
0.10	0.27	2.81	20.38	276.85
0.20	0.33	3.42	25.09	301.48
0.50	0.42	5.81	45.26	455.60
0.80	0.76	8.92	72.62	748.63
1	0.99	11.23	112.36	891.25

Table B5 : Global analysis time constants of D102 in $BmimPF_6$-ACN mixtures.

X_{IL}	τ_1 (ps)	τ_2 (ps)	τ_3 (ps)	τ_4 (ps)
0	0.11	0.84	17.37	228.92
0.05	0.15	0.83	9.89	171.64
0.10	0.21	1.68	23.58	164.02
0.20	0.26	2.58	33.33	184.37
0.50	0.30	4.76	39.99	399.92
0.80	0.31	6.40	85.91	908.69
1	0.42	12.46	143.41	1305.22

Table B6 : Global analysis time constants of D102 in $BmimPF_6$-γ-BL mixtures.

X_{IL}	τ_1 (ps)	τ_2 (ps)	τ_3 (ps)	τ_4 (ps)
0	0.19	1.15	15.85	334.70
0.05	0.20	1.78	15.49	304.76
0.10	0.22	1.97	17.97	299.53
0.20	0.25	2.04	20.46	368.39
0.50	0.39	2.56	31.12	649.73
0.80	0.41	6.32	85.77	1042.38
1	0.42	12.46	143.41	1305.22

Table B7 : Global analysis time constants of D102 in $BmimPF_6$-PC mixtures.

X_{IL}	τ_1 (ps)	τ_2 (ps)	τ_3 (ps)	τ_4 (ps)
0	0.30	1.72	16.60	324.56
0.05	0.19	2.52	16.45	315.28
0.10	0.22	2.64	17.21	293.72
0.20	0.22	2.73	18.95	338.53
0.50	0.24	3.89	40.08	613.34
0.80	0.28	7.69	101.56	897.91
1	0.42	12.46	143.41	1305.22

Table B8 : Global analysis time constants of D102 in BmimTFO-ACN mixtures.

X_{IL}	τ_1 (ps)	τ_2 (ps)	τ_3 (ps)	τ_4 (ps)
0	0.11	0.84	17.37	228.92
0.05	0.15	1.27	18.95	176.37
0.10	0.18	1.40	20.14	185.66
0.20	0.25	2.19	25.39	219.20
0.50	0.42	3.66	38.79	377.81
0.80	0.57	5.22	97.25	648.57
1	1.01	7.49	102.36	853.55

Table B9 : Global analysis time constants of D102 in BmimTFO-γ-BL mixtures.

X_{IL}	τ_1 (ps)	τ_2 (ps)	τ_3 (ps)	τ_4 (ps)
0	0.19	1.15	15.85	334.70
0.05	0.23	2.13	24.26	291.48
0.10	0.28	2.76	32.26	288.93
0.20	0.37	4.05	41.60	306.15
0.50	0.52	5.22	51.30	454.32
0.80	0.90	6.26	69.94	745.92
1	1.01	7.49	102.36	853.55

Table B10 : Global analysis time constants of D102 in BmimTFO-PC mixtures.

X_{IL}	τ_1 (ps)	τ_2 (ps)	τ_3 (ps)	τ_4 (ps)
0	0.30	1.72	16.45	324.56
0.05	0.31	2.62	18.93	264.16
0.10	0.32	3.17	22.15	280.94
0.20	0.41	4.23	23.14	303.20
0.50	0.59	5.08	47.66	454.02
0.80	0.84	6.07	107.20	739.10
1	1.01	7.49	102.36	853.55

Table B11 : Global analysis time constants of D102 in BmimTFSI-ACN mixtures.

X_{IL}	τ_1 (ps)	τ_2 (ps)	τ_3 (ps)	τ_4 (ps)
0	0.11	0.84	17.37	228.92

0.05	0.11	0.90	14.88	160.81
0.10	0.23	1.68	19.01	173.61
0.20	0.34	2.68	28.38	198.27
0.50	0.38	5.76	46.71	331.37
0.80	0.44	6.91	62.93	545.72
1	0.49	10.81	72.40	768.13

Table B12 : Global analysis time constants of D102 in BmimTFSI-γ-BL mixtures.

X_{IL}	τ_1 (ps)	τ_2 (ps)	τ_3 (ps)	τ_4 (ps)
0	0.19	1.15	15.85	334.70
0.05	0.20	1.80	16.85	310.95
0.10	0.30	2.05	19.04	284.65
0.20	0.28	2.61	22.86	324.87
0.50	0.31	5.04	34.63	470.41
0.80	0.39	6.29	56.25	661.61
1	0.49	10.81	72.40	768.13

Table B13 : Global analysis time constants of D102 in BmimTFSI-PC mixtures.

X_{IL}	τ_1 (ps)	τ_2 (ps)	τ_3 (ps)	τ_4 (ps)
0	0.30	1.72	16.45	324.56
0.05	0.27	2.71	20.10	257.11
0.10	0.27	2.85	20.72	274.72
0.20	0.32	4.21	32.41	308.05
0.50	0.38	7.19	53.46	436.17
0.80	0.44	9.10	76.58	677.70
1	0.49	10.81	72.40	768.13

Table B14 : Global analysis time constants of D149 in $BmimBF_4$-ACN mixtures.

X_{IL}	τ_1 (ps)	τ_2 (ps)	τ_3 (ps)	τ_4 (ps)
0	0.08	0.65	33.34	275.65
0.05	0.10	0.81	27.92	234.91
0.10	0.14	0.90	16.29	210.72
0.20	0.17	1.04	18.71	248.61
0.50	0.25	2.65	30.23	450.02
0.80	0.27	5.68	69.58	706.73
1	0.51	10.39	120.71	912.43

Table B15 : Global analysis time constants of D149 in $BmimBF_4$-γ-BL mixtures.

X_{IL}	τ_1 (ps)	τ_2 (ps)	τ_3 (ps)	τ_4 (ps)
0	0.14	1.26	13.93	418.65
0.05	0.17	1.35	8.79	326.03
0.10	0.25	2.16	18.58	331.77

0.20	0.27	3.06	22.92	381.11
0.50	0.40	6.76	62.04	492.32
0.80	0.47	8.19	112.20	724.35
1	0.51	10.39	120.71	912.27

Table B16 : Global analysis time constants of D149 in $BmimBF_4$-PC mixtures.

X_{IL}	τ_1 (ps)	τ_2 (ps)	τ_3 (ps)	τ_4 (ps)
0	0.23	2.31	14.67	372.12
0.05	0.20	2.34	13.95	308.16
0.10	0.15	2.95	15.97	312.53
0.20	0.21	3.02	24.09	342.52
0.50	0.27	4.18	40.31	511.25
0.80	0.50	8.75	96.98	681.75
1	0.51	10.39	120.71	912.27

Table B17 : Global analysis time constants of D149 in $BmimPF_6$-ACN mixtures.

X_{IL}	τ_1 (ps)	τ_2 (ps)	τ_3 (ps)	τ_4 (ps)
0	0.08	0.65	33.34	275.65
0.05	0.13	1.01	25.41	213.93
0.10	0.19	1.52	18.71	210.90
0.20	0.25	1.99	24.12	265.95
0.50	0.48	5.81	56.09	659.67
0.80	0.68	8.14	101.95	990.50
1	0.83	11.48	161.06	1595.21

Table B18 : Global analysis time constants of D149 in $BmimPF_6$-γ-BL mixtures.

X_{IL}	τ_1 (ps)	τ_2 (ps)	τ_3 (ps)	τ_4 (ps)
0	0.14	1.26	13.93	418.64
0.05	0.16	1.43	9.44	339.47
0.10	0.25	1.97	12.77	316.66
0.20	0.29	3.55	20.74	343.40
0.50	0.46	4.72	50.91	577.29
0.80	0.77	8.08	92.15	1018.91
1	0.83	11.48	161.06	1595.21

Table B19 : Global analysis time constants of D149 in $BmimPF_6$-PC mixtures.

X_{IL}	τ_1 (ps)	τ_2 (ps)	τ_3 (ps)	τ_4 (ps)
0	0.23	2.31	14.67	372.12
0.05	0.14	2.50	10.19	359.59
0.10	0.15	2.91	14.10	339.17
0.20	0.21	3.58	30.84	413.29
0.50	0.47	4.70	66.63	620.68

0.80	0.79	8.96	91.80	895.28
1	0.83	11.48	161.06	1595.21

Table B20 : Global analysis time constants of D149 in BmimTFO-ACN mixtures.

X_{IL}	τ_1 (ps)	τ_2 (ps)	τ_3 (ps)	τ_4 (ps)
0	0.08	0.65	33.34	275.65
0.05	0.09	1.03	16.98	214.91
0.10	0.17	1.10	13.13	223.44
0.20	0.24	2.32	22.96	250.12
0.50	0.33	4.89	42.73	453.05
0.80	0.55	7.82	78.82	677.52
1	0.82	10.46	84.88	878.17

Table B21 : Global analysis time constants of D149 in BmimTFO-γ-BL mixtures.

X_{IL}	τ_1 (ps)	τ_2 (ps)	τ_3 (ps)	τ_4 (ps)
0	0.14	1.26	13.93	418.65
0.05	0.15	1.56	9.30	333.16
0.10	0.18	2.36	21.39	284.08
0.20	0.24	2.83	24.63	375.23
0.50	0.45	5.75	44.41	498.03
0.80	0.72	9.40	54.78	723.84
1	0.82	10.46	84.88	878.17

Table B22 : Global analysis time constants of D149 in BmimTFO-PC mixtures.

X_{IL}	τ_1 (ps)	τ_2 (ps)	τ_3 (ps)	τ_4 (ps)
0	0.23	2.31	14.67	372.11
0.05	0.18	2.53	14.15	309.91
0.10	0.19	2.92	18.53	282.54
0.20	0.24	3.37	21.43	383.71
0.50	0.24	3.98	32.47	549.72
0.80	0.78	8.87	84.92	670.27
1	0.82	10.46	84.88	878.17

Table B23 : Global analysis time constants of D149 in BmimTFSI-ACN mixtures.

X_{IL}	τ_1 (ps)	τ_2 (ps)	τ_3 (ps)	τ_4 (ps)
0	0.08	0.65	33.34	275.65
0.05	0.12	1.22	13.09	194.55
0.10	0.17	1.67	16.98	220.41
0.20	0.29	2.65	33.39	310.82
0.50	0.57	7.37	50.42	433.79
0.80	1.09	12.25	91.20	684.47
1	1.29	14.88	110.87	835.55

Table B24 : Global analysis time constants of D149 in BmimTFSI-γ-BL mixtures.

X_{IL}	τ_1 (ps)	τ_2 (ps)	τ_3 (ps)	τ_4 (ps)
0	0.14	1.26	13.93	418.65
0.05	0.16	1.69	13.11	324.67
0.10	0.25	2.37	19.46	278.64
0.20	0.40	3.25	27.68	331.55
0.50	0.59	5.40	45.69	505.24
0.80	1.13	13.93	83.88	718.06
1	1.29	14.88	110.87	835.55

Table B25 : Global analysis time constants of D149 in BmimTFSI-PC mixtures.

X_{IL}	τ_1 (ps)	τ_2 (ps)	τ_3 (ps)	τ_4 (ps)
0	0.23	2.31	14.67	372.12
0.05	0.16	2.56	12.79	308.56
0.10	0.24	2.79	21.36	278.08
0.20	0.27	3.15	23.96	356.28
0.50	0.41	6.31	50.91	536.79
0.80	0.76	8.51	83.72	616.15
1	1.29	14.88	110.87	835.55

Table B26 : Global analysis time constants of D205 in $BmimBF_4$-ACN mixtures.

X_{IL}	τ_1 (ps)	τ_2 (ps)	τ_3 (ps)	τ_4 (ps)
0	0.12	1.11	16.72	240.75
0.05	0.16	1.16	14.30	205.09
0.10	0.20	1.29	14.86	233.16
0.20	0.25	2.21	18.91	263.77
0.50	0.33	3.45	32.43	552.11
0.80	0.37	7.41	74.79	837.76
1	0.91	14.29	125.17	1041.96

Table B27 : Global analysis time constants of D205 in $BmimBF_4$-γ-BL mixtures.

X_{IL}	τ_1 (ps)	τ_2 (ps)	τ_3 (ps)	τ_4 (ps)
0	0.13	1.12	12.50	357.24
0.05	0.16	1.65	12.49	318.88
0.10	0.16	2.04	13.48	368.28
0.20	0.21	2.41	16.37	394.13
0.50	0.35	4.49	36.05	548.16
0.80	0.50	5.23	52.76	854.68
1	0.91	14.29	125.17	1041.96

Table B28 : Global analysis time constants of D205 in $BmimBF_4$-PC mixtures.

X_{IL}	τ_1 (ps)	τ_2 (ps)	τ_3 (ps)	τ_4 (ps)
0	0.28	1.78	13.35	354.25
0.05	0.19	2.03	11.80	334.46
0.10	0.20	2.10	21.02	305.32
0.20	0.26	3.32	33.40	317.56
0.50	0.55	7.31	58.51	524.01
0.80	0.81	10.32	92.36	791.42
1	0.91	14.29	125.17	1041.96

Table B29 : Global analysis time constants of D205 in $BmimPF_6$-ACN mixtures.

X_{IL}	τ_1 (ps)	τ_2 (ps)	τ_3 (ps)	τ_4 (ps)
0	0.12	1.11	16.72	240.75
0.05	0.13	1.25	12.50	214.46
0.10	0.14	1.29	33.39	240.86
0.20	0.17	1.70	39.43	374.21
0.50	0.19	2.13	43.38	733.64
0.80	0.91	4.99	77.65	1081.29
1	0.96	10.16	166.93	2208.30

Table B30 : Global analysis time constants of D205 in $BmimPF_6$-γ-BL mixtures.

X_{IL}	τ_1 (ps)	τ_2 (ps)	τ_3 (ps)	τ_4 (ps)
0	0.13	1.12	12.50	357.24
0.05	0.13	1.26	12.34	334.60
0.10	0.15	1.43	14.30	355.24
0.20	0.17	1.72	17.57	403.10
0.50	0.25	2.50	25.05	690.75
0.80	0.46	5.51	98.24	1168.99
1	0.96	10.16	166.93	2208.30

Table B31 : Global analysis time constants of D205 in $BmimPF_6$-PC mixtures.

X_{IL}	τ_1 (ps)	τ_2 (ps)	τ_3 (ps)	τ_4 (ps)
0	0.28	1.78	13.35	354.25
0.05	0.15	1.88	13.00	337.44
0.10	0.17	2.13	13.88	356.10
0.20	0.19	2.67	14.73	380.75
0.50	0.37	2.87	48.90	775.95
0.80	0.59	7.96	104.70	1188.03
1	0.96	10.16	166.93	2208.30

Table B32 : Global analysis time constants of D205 in BmimTFO-ACN mixtures.

X_{IL}	τ_1 (ps)	τ_2 (ps)	τ_3 (ps)	τ_4 (ps)
0	0.12	1.11	16.72	240.75

0.05	0.13	1.15	11.92	228.78
0.10	0.14	1.31	14.91	260.63
0.20	0.17	1.43	16.68	303.31
0.50	0.33	2.86	27.13	594.03
0.80	0.61	7.34	85.92	944.35
1	0.99	12.30	103.62	1014.81

Table B33 : Global analysis time constants of D205 in BmimTFO-γ-BL mixtures.

X_{IL}	τ_1 (ps)	τ_2 (ps)	τ_3 (ps)	τ_4 (ps)
0	0.13	1.12	12.50	357.24
0.05	0.15	1.19	10.50	328.59
0.10	0.17	1.48	16.60	375.43
0.20	0.20	2.20	26.72	464.83
0.50	0.49	5.01	42.08	588.34
0.80	0.65	8.55	81.19	861.82
1	0.99	12.30	103.62	1014.81

Table B34 : Global analysis time constants of D205 in BmimTFO-PC mixtures.

X_{IL}	τ_1 (ps)	τ_2 (ps)	τ_3 (ps)	τ_4 (ps)
0	0.28	1.78	13.35	354.25
0.05	0.27	3.13	13.29	334.01
0.10	0.33	3.45	18.92	361.23
0.20	0.37	3.75	27.57	389.89
0.50	0.49	6.54	62.88	570.69
0.80	0.69	10.23	73.70	818.93
1	0.99	12.30	103.62	1014.81

Table B35 : Global analysis time constants of D205 in BmimTFSI-ACN mixtures.

X_{IL}	τ_1 (ps)	τ_2 (ps)	τ_3 (ps)	τ_4 (ps)
0	0.12	1.11	16.72	240.75
0.05	0.21	1.25	6.29	198.84
0.10	0.25	1.54	15.76	255.74
0.20	0.29	2.55	22.07	305.91
0.50	0.34	4.39	37.80	509.26
0.80	0.55	10.71	78.36	695.53
1	0.86	19.90	121.94	973.65

Table B36 : Global analysis time constants of D205 in BmimTFSI-γ-BL mixtures.

X_{IL}	τ_1 (ps)	τ_2 (ps)	τ_3 (ps)	τ_4 (ps)
0	0.13	1.12	12.50	357.24
0.05	0.19	2.06	11.94	312.59
0.10	0.25	2.81	15.51	344.21

0.20	0.32	3.89	47.77	399.15
0.50	0.37	6.73	65.56	569.07
0.80	0.56	12.33	83.72	733.25
1	0.86	19.90	121.94	973.65

Table B37 : Global analysis time constants of D205 in BmimTFSI-PC mixtures.

X_{IL}	τ_1 (ps)	τ_2 (ps)	τ_3 (ps)	τ_4 (ps)
0	0.28	1.78	13.35	354.25
0.05	0.16	1.95	12.86	290.51
0.10	0.22	2.17	17.79	315.69
0.20	0.26	2.73	22.50	371.06
0.50	0.27	5.08	57.11	520.94
0.80	0.48	10.05	102.14	740.07
1	0.86	19.90	121.94	973.65

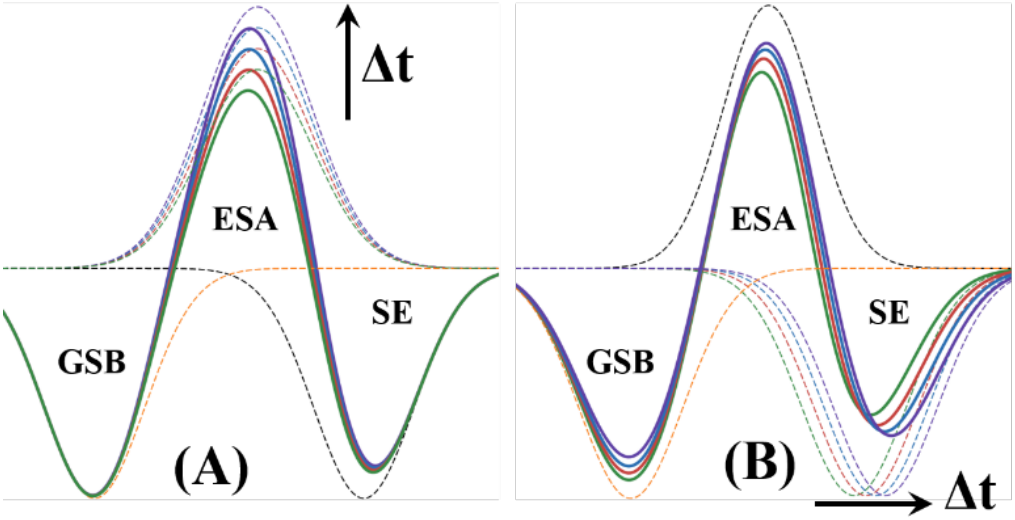

Figure B1: Two different situations to describe the time dependent changes of the TAS, (A) increasing the ESA intensity, (B) Red-shift of SE region of the TA spectra

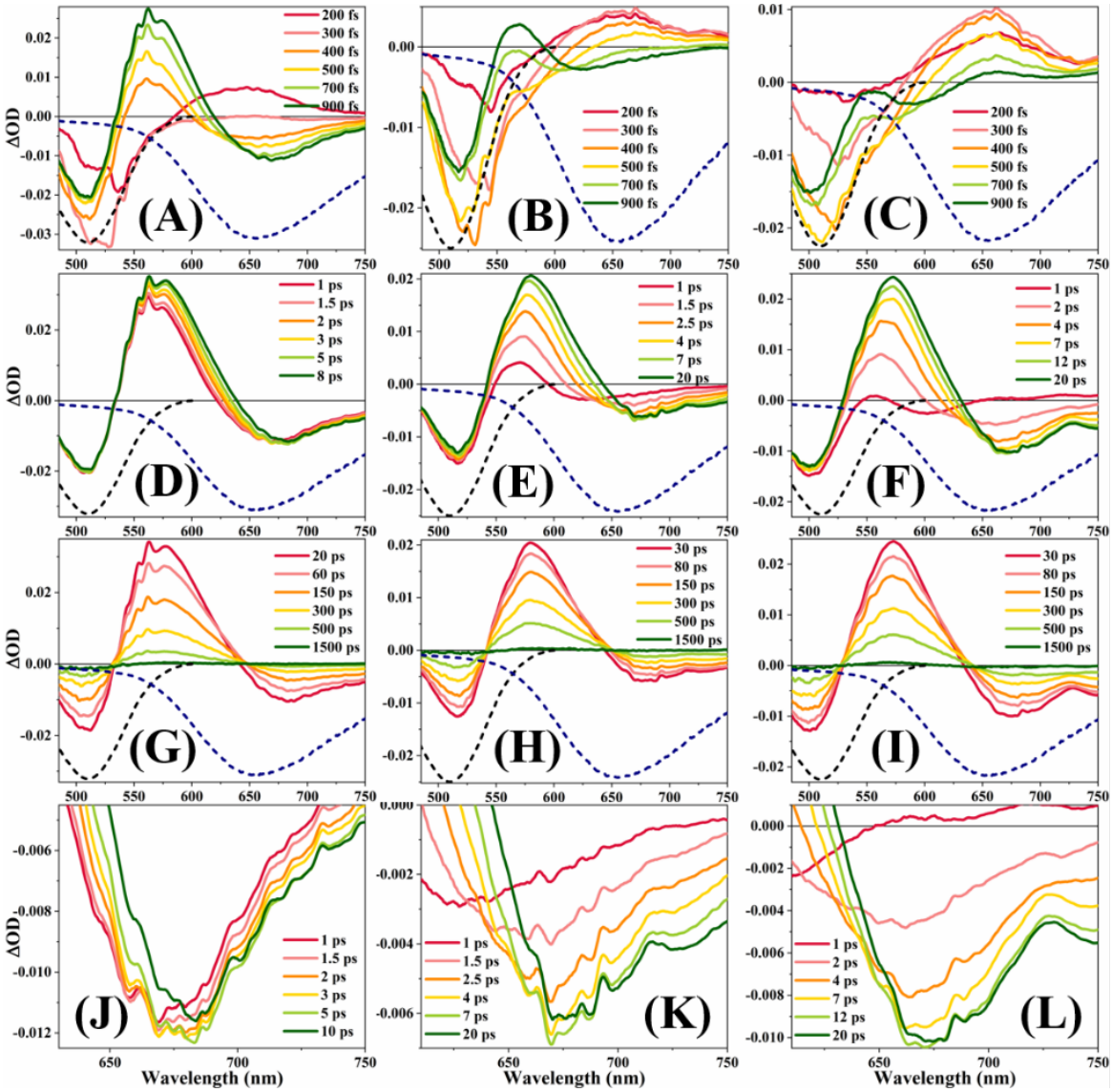

Figure B2: Transient Absorption spectra of D102 in ACN [(A), (D), (G), (J)], γ-BL [(B), (E), (H), (K)] and in PC [(C), (F), (I), (L)]. [(A), (B), (C)] short timescale (200-900 fs), [(D), (E), (F)] middle timescale (1-20 ps), [(G), (H), (I)] long timescale (30-1500 ps) and [(J), (K), (L)] solvation timescale. Dashed spectra are steady state absorption (black) and emission (blue) spectra.

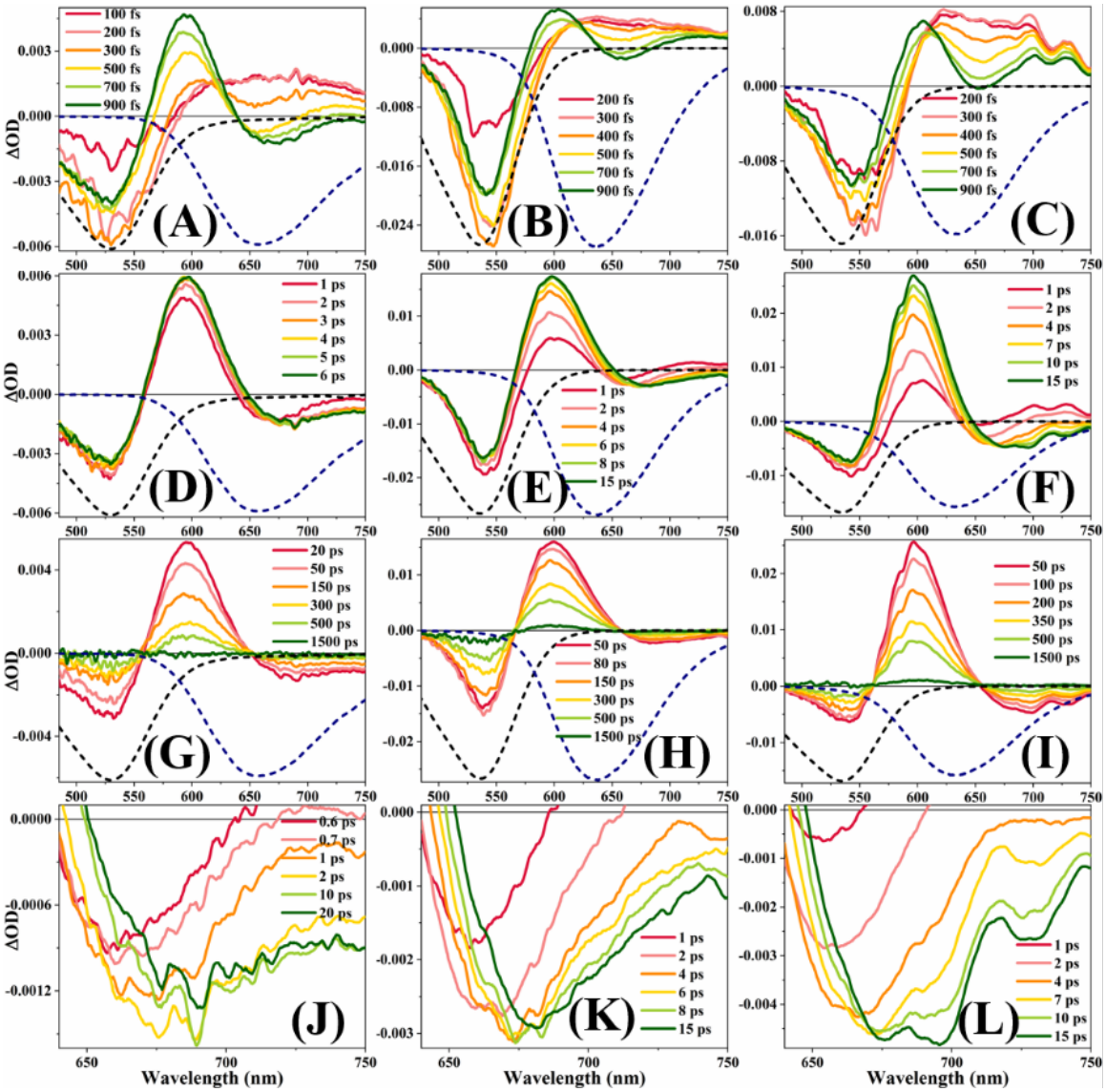

Figure B3: Transient Absorption spectra of D149 in ACN [(A), (D), (G), (J)], γ-BL [(B), (E), (H), (K)] and in PC [(C), (F), (I), (L)]. [(A), (B), (C)] short timescale, [(D), (E), (F)] middle timescale, [(G), (H), (I)] long timescale and [(J), (K), (L)] solvation timescale. Dashed spectra are steady state absorption (black) and emission (blue) spectra.

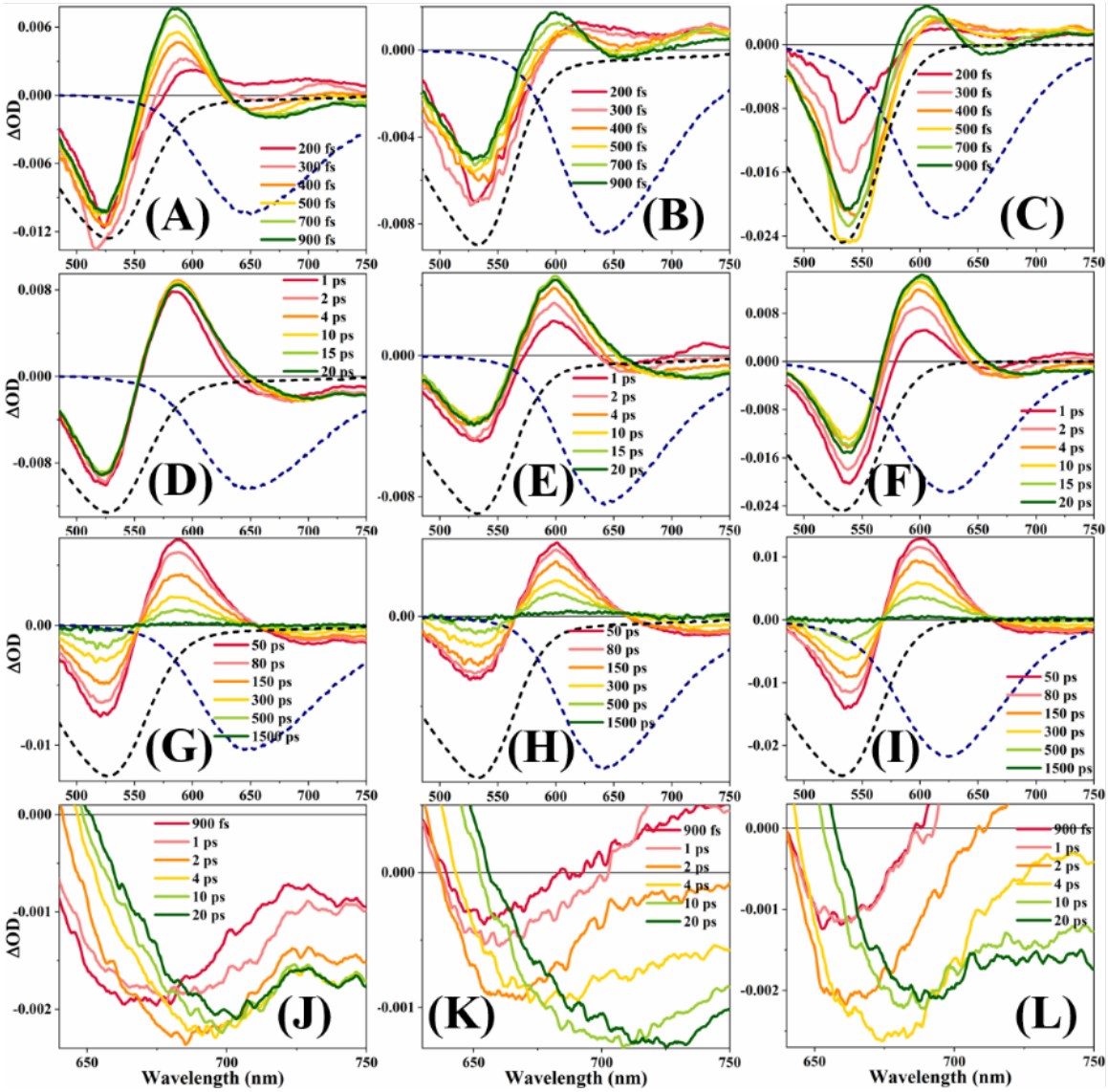

Figure B4: Transient Absorption spectra of D205 in ACN [(A), (D), (G), (J)], γ-BL [(B), (E), (H), (K)] and in PC [(C), (F), (I), (L)]. [(A), (B), (C)] short timescale, [(D), (E), (F)] middle timescale, [(G), (H), (I)] long timescale and [(J), (K), (L)] solvation timescale. Dashed spectra are steady state absorption (black) and emission (blue) spectra.

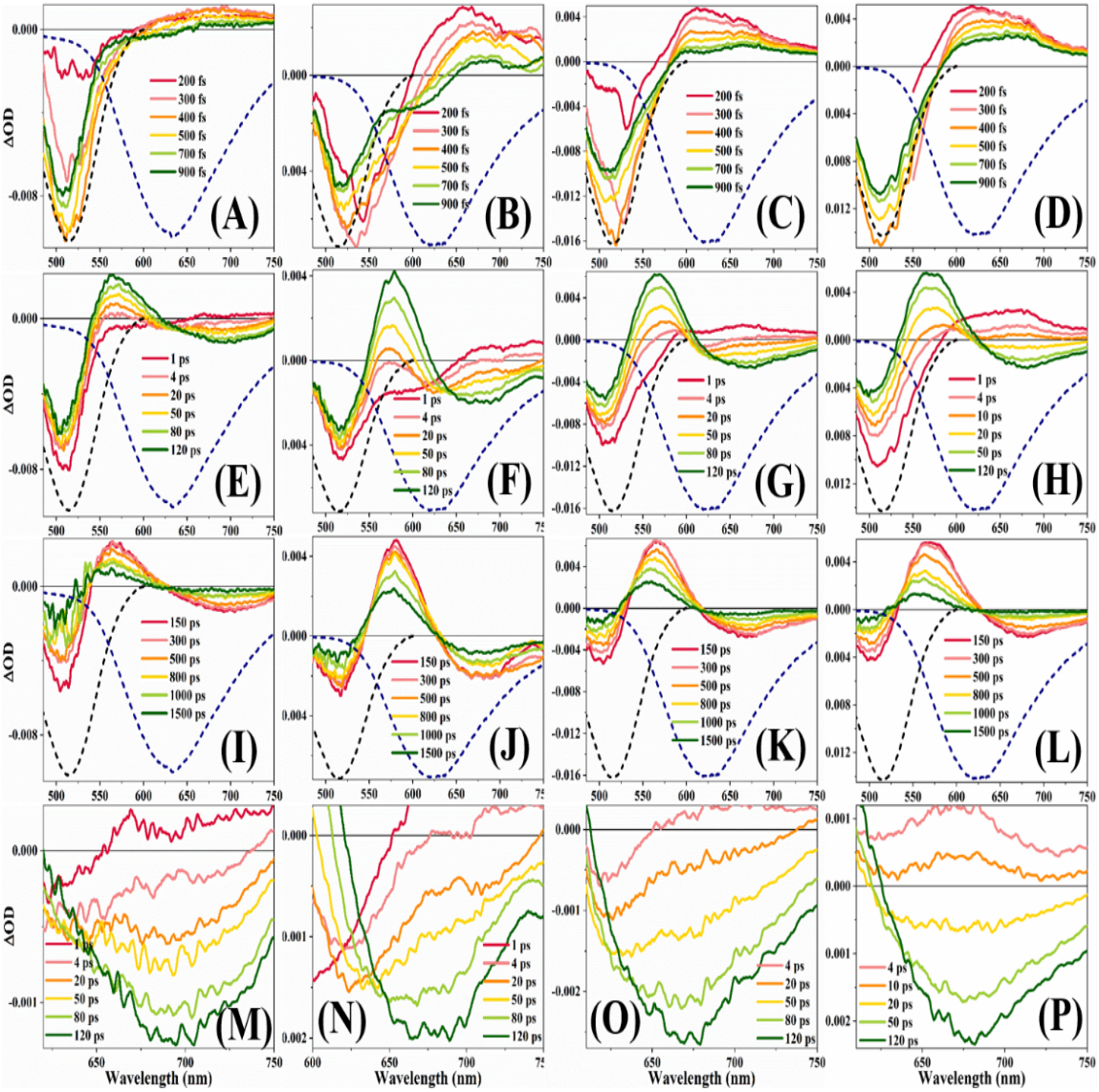

Figure B5: Transient Absorption spectra of D102 in $BmimBF_4$ [(A), (E), (I), (M)], $BmimPF_6$ [(B), (F), (J), (N)], BmimTFO [(C), (G), (K), (O)] and BmimTFSI [(D), (H), (L), (P)]. [(A), (B), (C), (D)] short timescale, [(E), (F), (G), (H)] middle timescale, [(I), (J), (K), (L)] long timescale and [(M), (N), (O), (P)] solvation timescale. Dashed spectra are steady state absorption (black) and emission (blue) spectra.

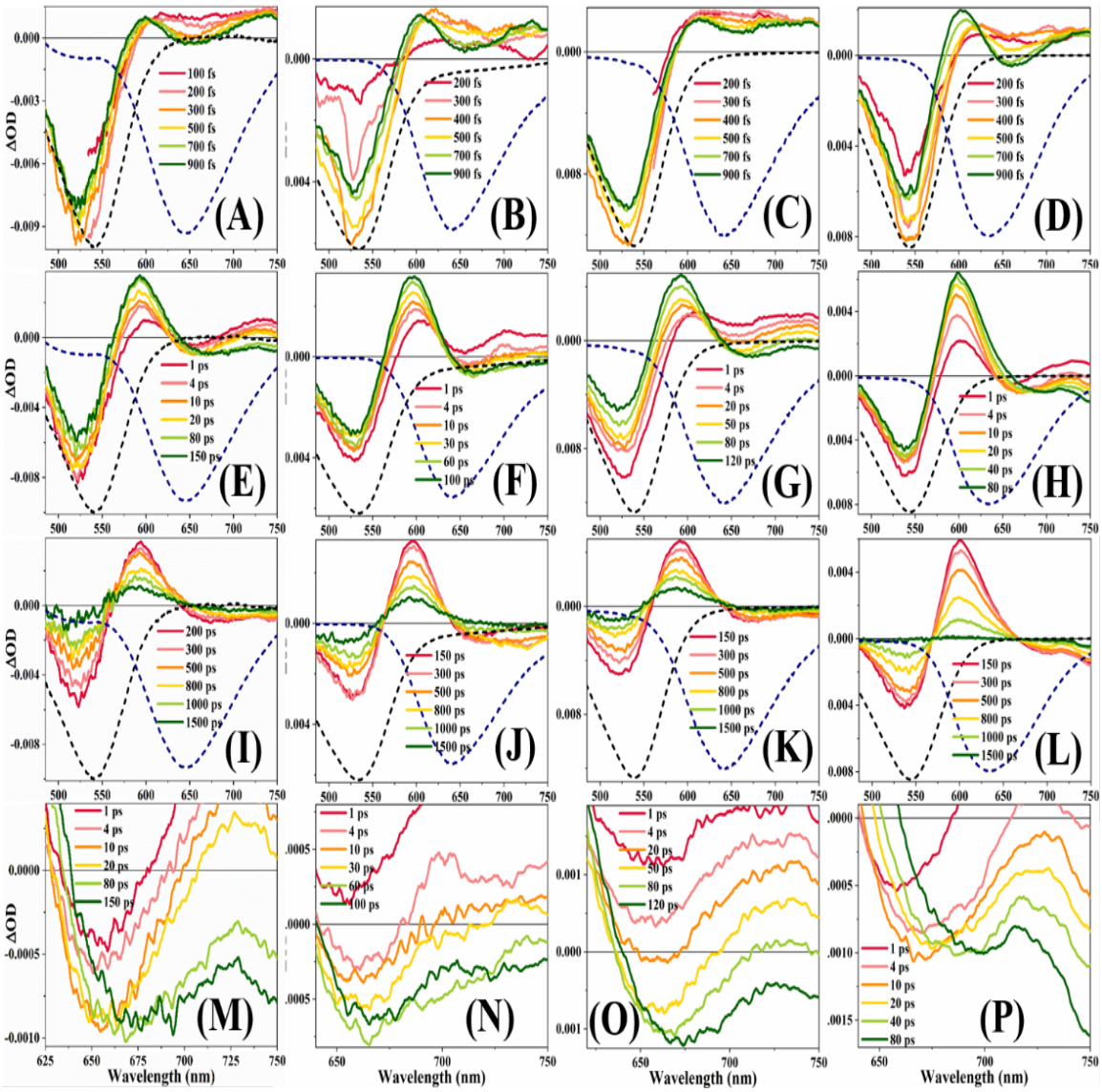

Figure B6: Transient Absorption spectra of D149 in $BmimBF_4$ [(A), (E), (I), (M)], $BmimPF_6$ [(B), (F), (J), (N)], BmimTFO [(C), (G), (K), (O)] and BmimTFSI [(D), (H), (L), (P)]. [(A), (B), (C), (D)] short timescale, [(E), (F), (G), (H)] middle timescale, [(I), (J), (K), (L)] long timescale and [(M), (N), (O), (P)] solvation timescale. Dashed spectra are steady state absorption (black) and emission (blue) spectra.

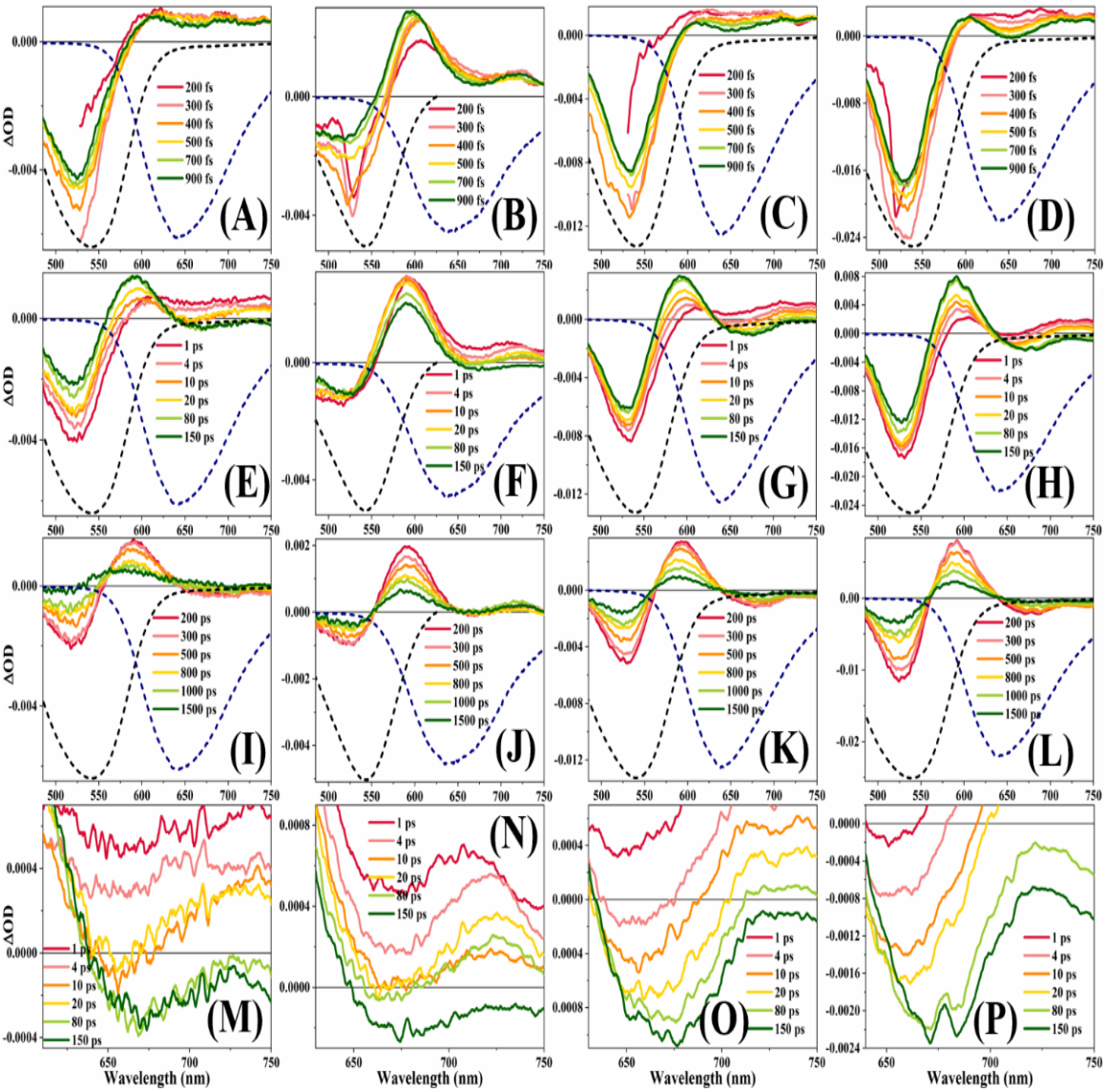

Figure B7: Transient Absorption spectra of D205 in $BmimBF_4$ [(A), (E), (I), (M)], $BmimPF_6$ [(B), (F), (J), (N)], BmimTFO [(C), (G), (K), (O)] and BmimTFSI [(D), (H), (L), (P)]. [(A), (B), (C), (D)] short timescale, [(E), (F), (G), (H)] middle timescale, [(I), (J), (K), (L)] long timescale and [(M), (N), (O), (P)] solvation timescale. Dashed spectra are steady state absorption (black) and emission (blue) spectra.

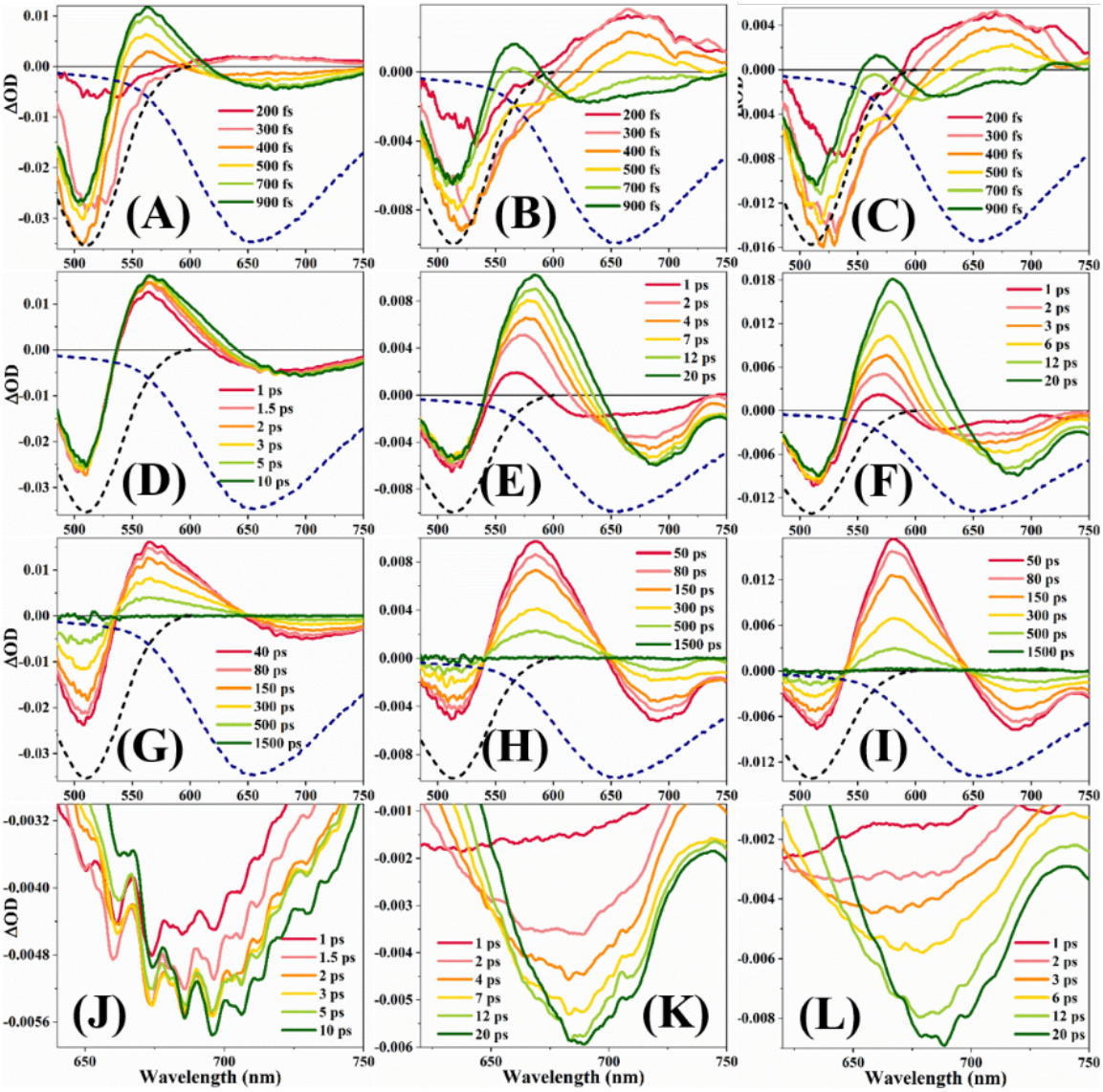

Figure B8: Transient Absorption spectra of D102 in $BmimBF_4$-ACN [(A), (D), (G), (J)], in $BmimBF_4$-γ-BL [(B), (E), (H), (K)] and in $BmimBF_4$-PC [(C), (F), (I), (L)] mixtures (X_{IL}= 0.05). [(A), (B), (C)] short timescale, [(D), (E), (F)] middle timescale, [(G), (H), (I)] long timescale and [(J), (K), (L)] solvation timescale. Dashed spectra are steady state absorption (black) and emission (blue) spectra.

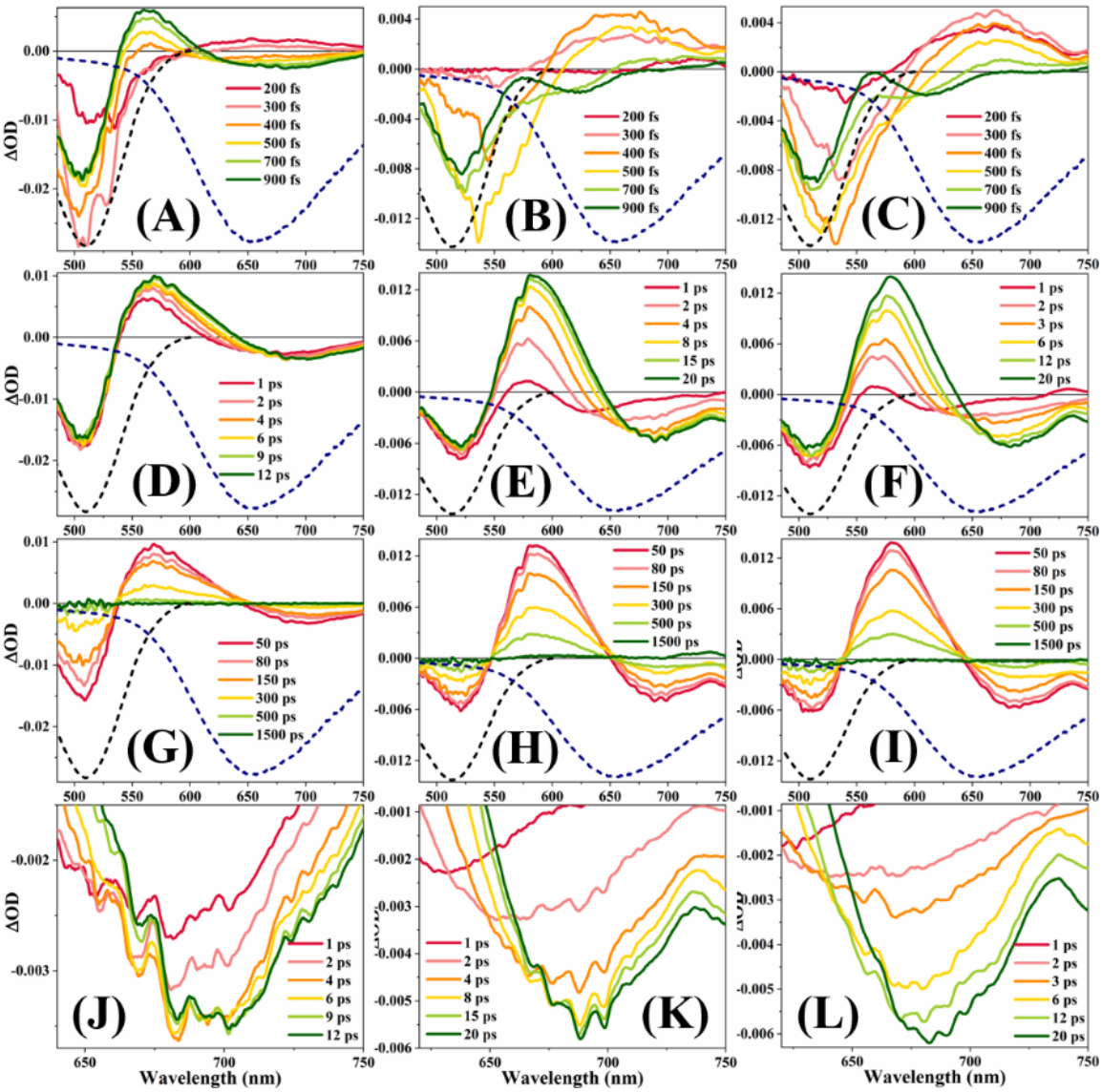

Figure B9: Transient Absorption spectra of D102 in $BmimBF_4$-ACN [(A), (D), (G), (J)], in $BmimBF_4$-γ-BL [(B), (E), (H), (K)] and in $BmimBF_4$-PC [(C), (F), (I), (L)] mixtures (X_{IL}= 0.10). [(A), (B), (C)] short timescale, [(D), (E), (F)] middle timescale, [(G), (H), (I)] long timescale and [(J), (K), (L)] solvation timescale. Dashed spectra are steady state absorption (black) and emission (blue) spectra.

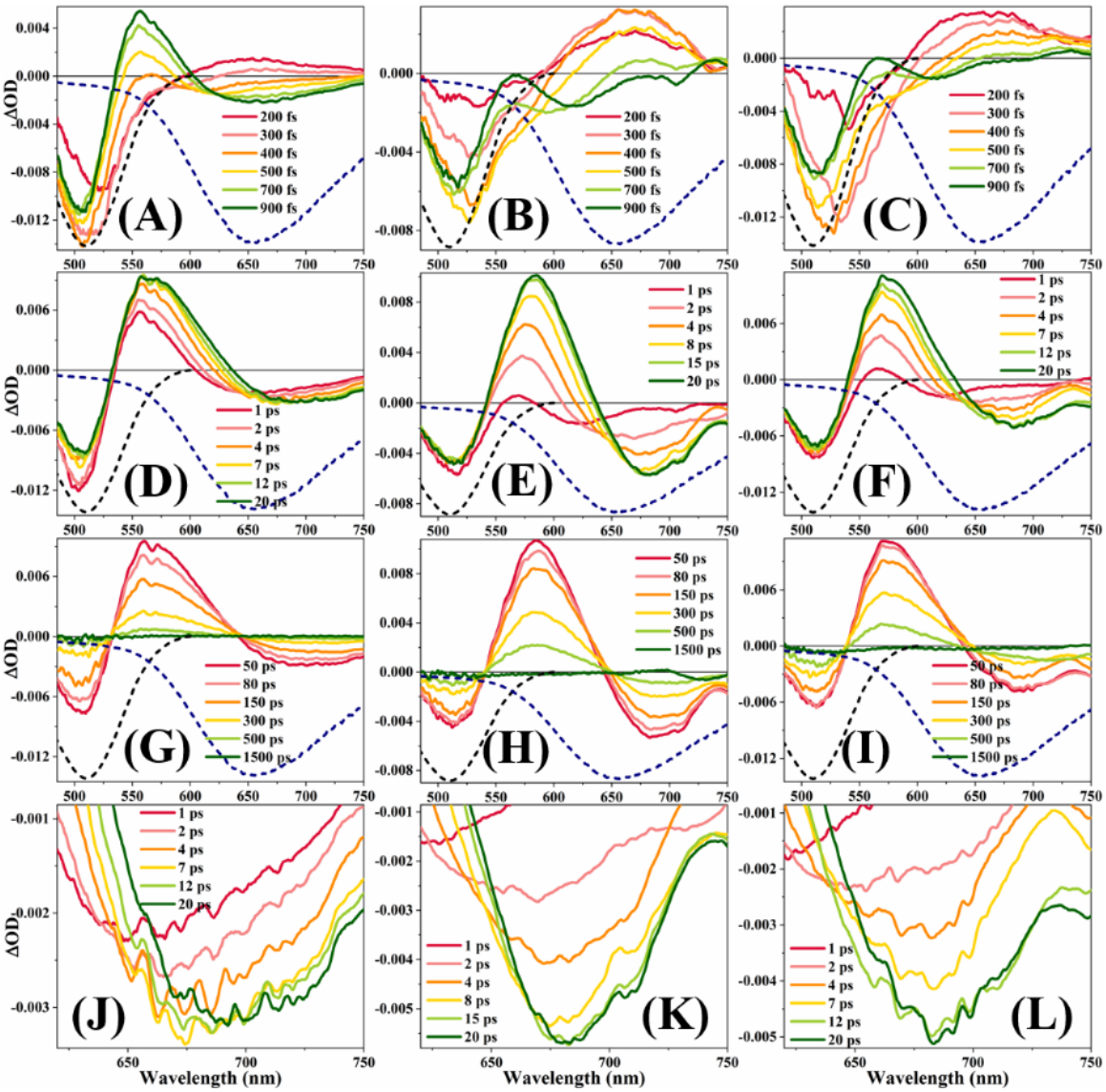

Figure B10: Transient Absorption spectra of D102 in $BmimBF_4$-ACN [(A), (D), (G), (J)], in $BmimBF_4$-γ-BL [(B), (E), (H), (K)] and in $BmimBF_4$-PC [(C), (F), (I), (L)] mixtures (X_{IL}= 0.20). [(A), (B), (C)] short timescale, [(D), (E), (F)] middle timescale, [(G), (H), (I)] long timescale and [(J), (K), (L)] solvation timescale. Dashed spectra are steady state absorption (black) and emission (blue) spectra.

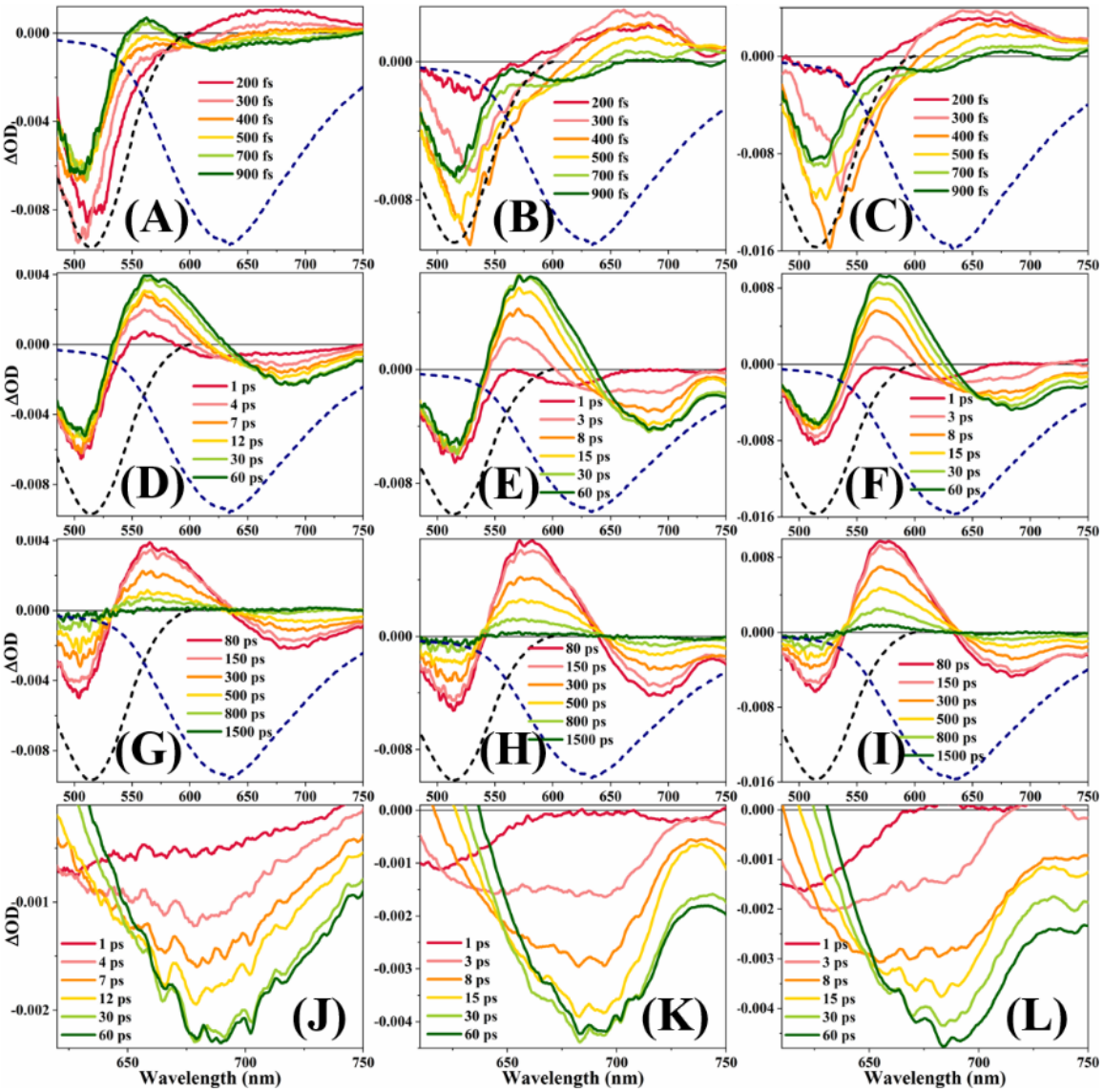

Figure B11: Transient Absorption spectra of D102 in $BmimBF_4$-ACN [(A), (D), (G), (J)], in $BmimBF_4$-γ-BL [(B), (E), (H), (K)] and in $BmimBF_4$-PC [(C), (F), (I), (L)] mixtures (X_{IL}= 0.50). [(A), (B), (C)] short timescale, [(D), (E), (F)] middle timescale, [(G), (H), (I)] long timescale and [(J), (K), (L)] solvation timescale. Dashed spectra are steady state absorption (black) and emission (blue) spectra.

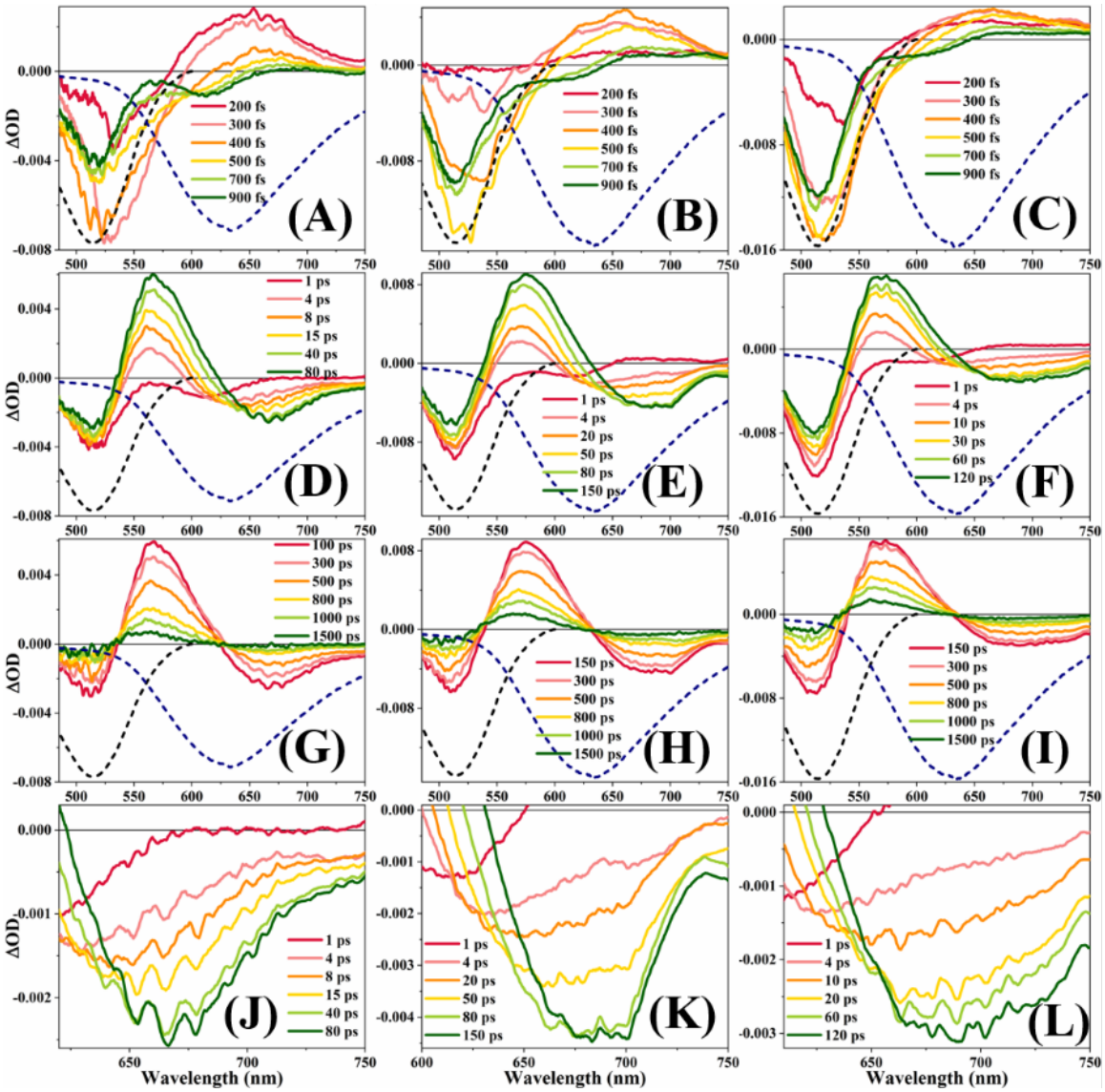

Figure B12: Transient Absorption spectra of D102 in $BmimBF_4$-ACN [(A), (D), (G), (J)], in $BmimBF_4$-γ-BL [(B), (E), (H), (K)] and in $BmimBF_4$-PC [(C), (F), (I), (L)] mixtures (X_{IL}= 0.80). [(A), (B), (C)] short timescale, [(D), (E), (F)] middle timescale, [(G), (H), (I)] long timescale and [(J), (K), (L)] solvation timescale. Dashed spectra are steady state absorption (black) and emission (blue) spectra.

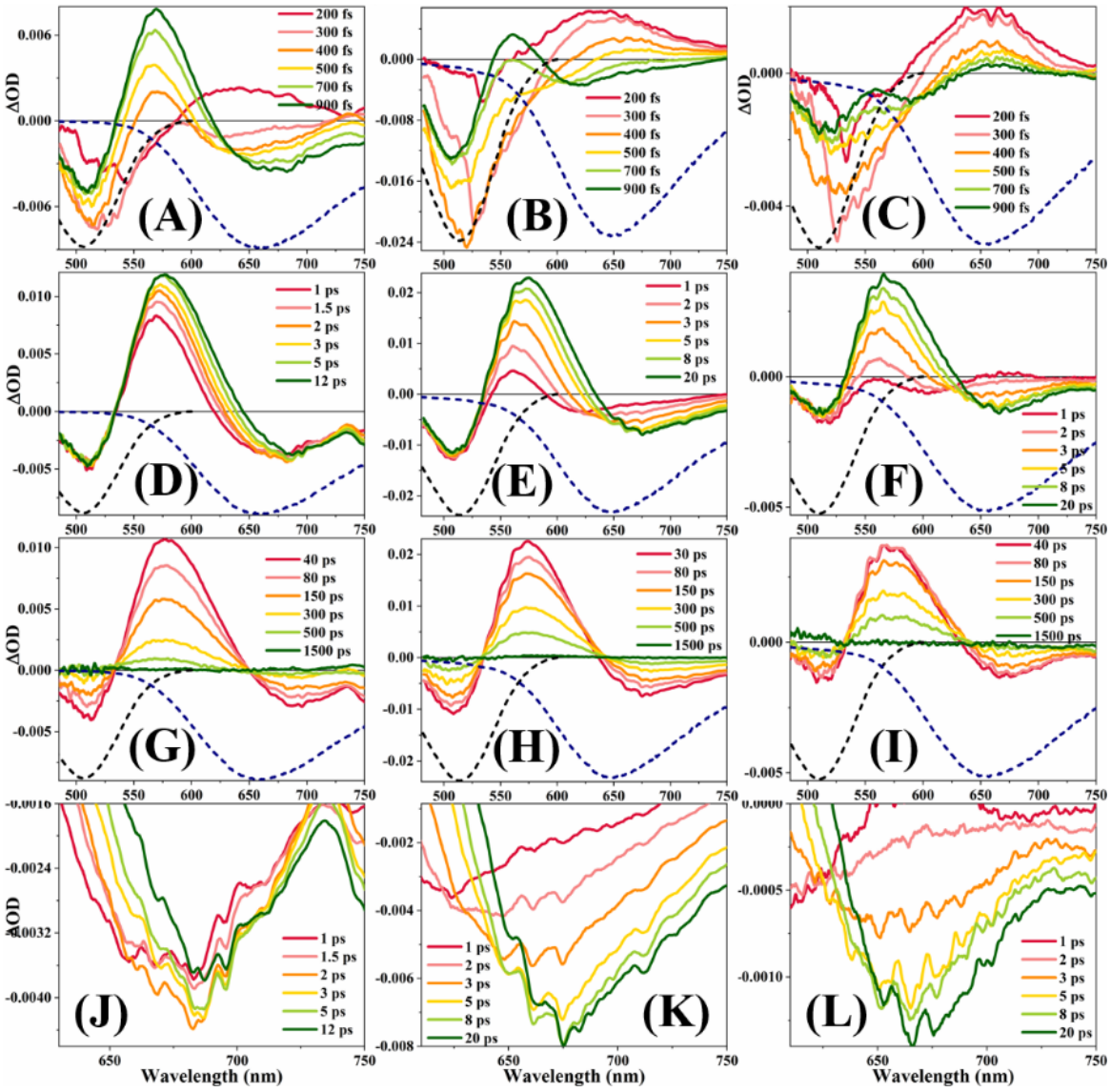

Figure B13: Transient Absorption spectra of D102 in $BmimPF_6$-ACN [(A), (D), (G), (J)], in $BmimPF_6$-γ-BL [(B), (E), (H), (K)] and in $BmimPF_6$-PC [(C), (F), (I), (L)] mixtures (X_{IL}= 0.05). [(A), (B), (C)] short timescale, [(D), (E), (F)] middle timescale, [(G), (H), (I)] long timescale and [(J), (K), (L)] solvation timescale. Dashed spectra are steady state absorption (black) and emission (blue) spectra.

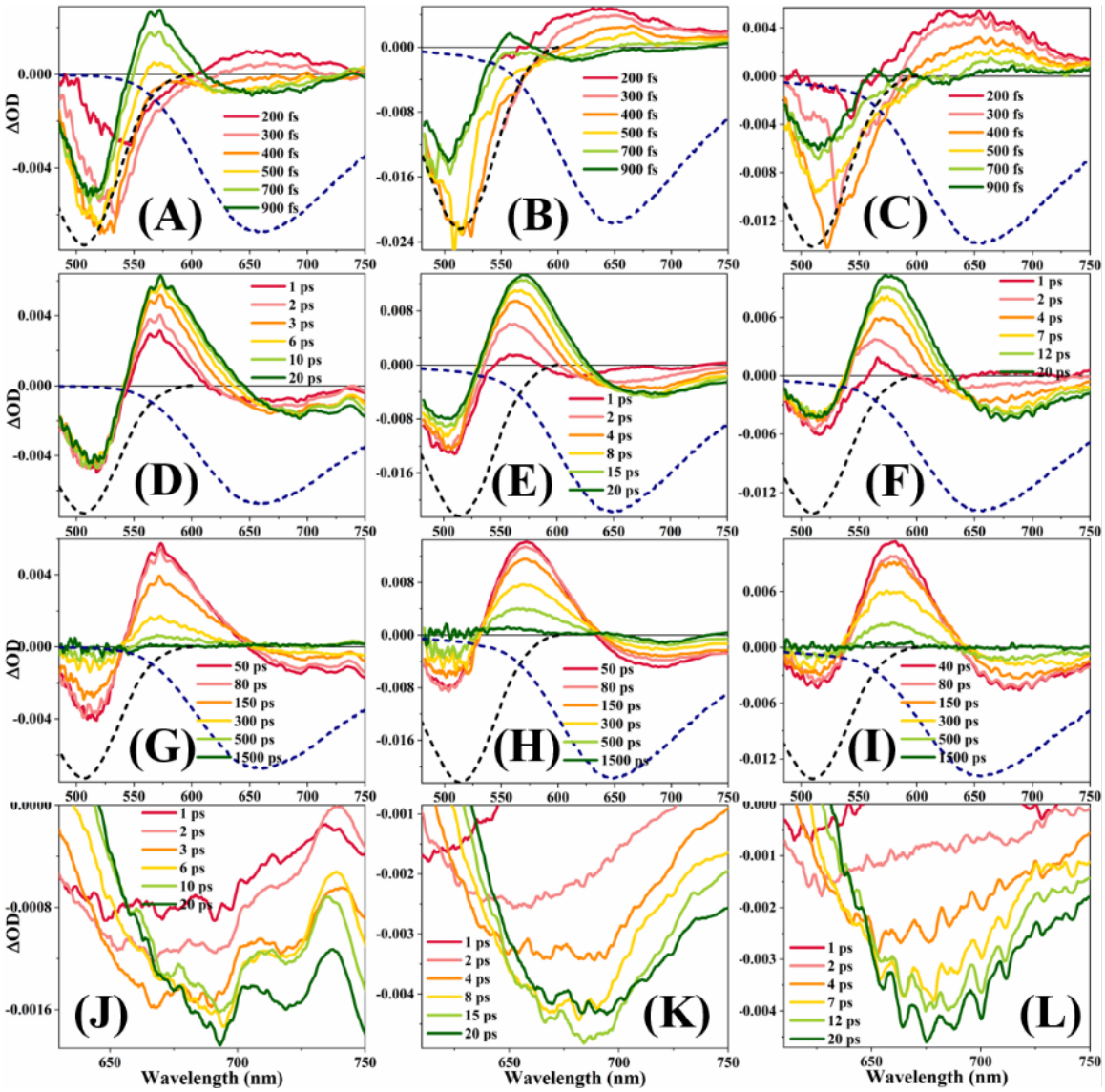

Figure B14: Transient Absorption spectra of D102 in $BmimPF_6$-ACN [(A), (D), (G), (J)], in $BmimPF_6$-γ-BL [(B), (E), (H), (K)] and in $BmimPF_6$-PC [(C), (F), (I), (L)] mixtures (X_{IL}= 0.20). [(A), (B), (C)] short timescale, [(D), (E), (F)] middle timescale, [(G), (H), (I)] long timescale and [(J), (K), (L)] solvation timescale. Dashed spectra are steady state absorption (black) and emission (blue) spectra.

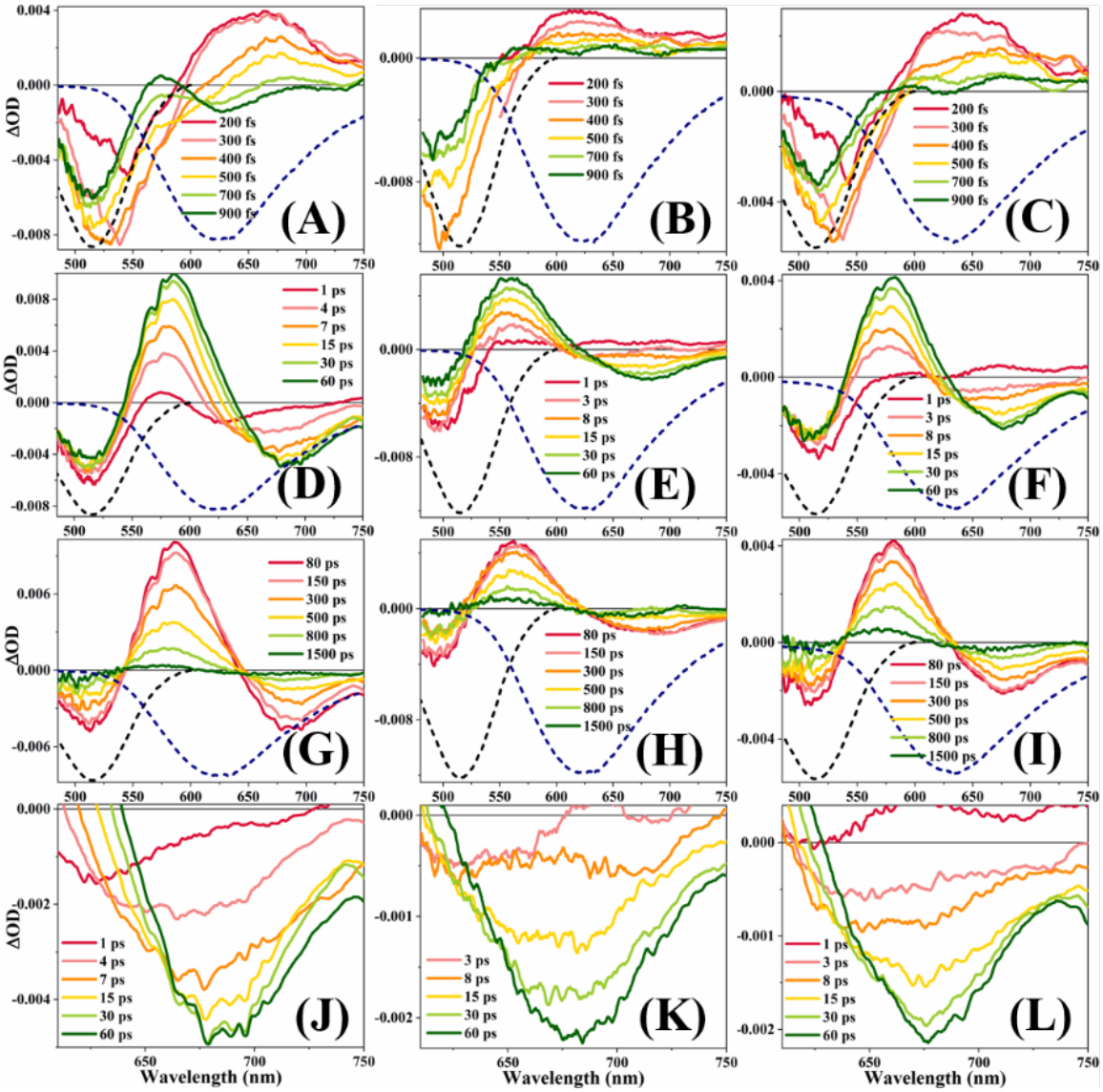

Figure B15: Transient Absorption spectra of D102 in $BmimPF_6$-ACN [(A), (D), (G), (J)], in $BmimPF_6$-γ-BL [(B), (E), (H), (K)] and in $BmimPF_6$-PC [(C), (F), (I), (L)] mixtures (X_{IL}= 0.50). [(A), (B), (C)] short timescale, [(D), (E), (F)] middle timescale, [(G), (H), (I)] long timescale and [(J), (K), (L)] solvation timescale. Dashed spectra are steady state absorption (black) and emission (blue) spectra.

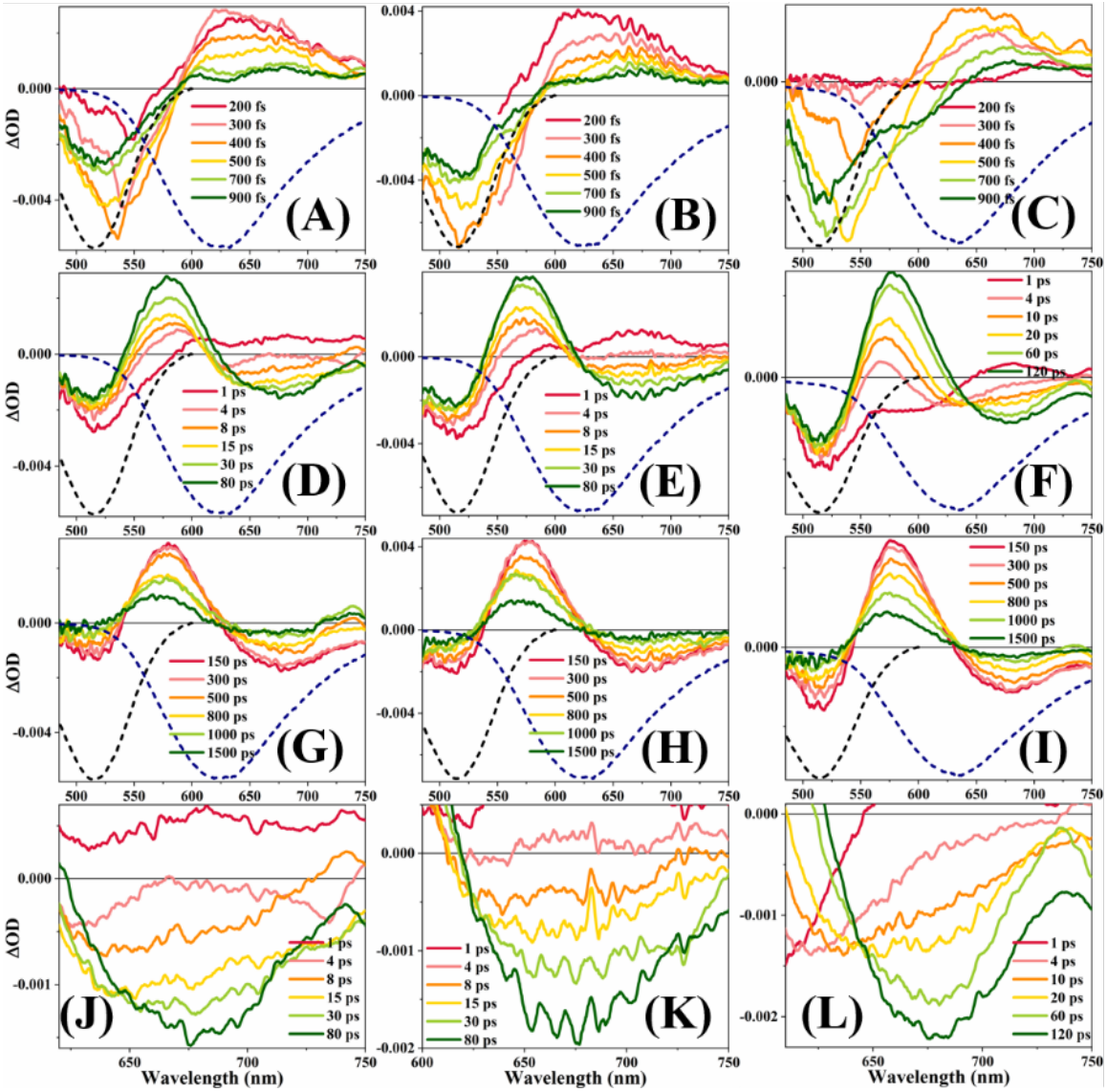

Figure B16: Transient Absorption spectra of D102 in $BmimPF_6$-ACN [(A), (D), (G), (J)], in $BmimPF_6$-γ-BL [(B), (E), (H), (K)] and in $BmimPF_6$-PC [(C), (F), (I), (L)] mixtures (X_{IL}= 0.80). [(A), (B), (C)] short timescale, [(D), (E), (F)] middle timescale, [(G), (H), (I)] long timescale and [(J), (K), (L)] solvation timescale. Dashed spectra are steady state absorption (black) and emission (blue) spectra.

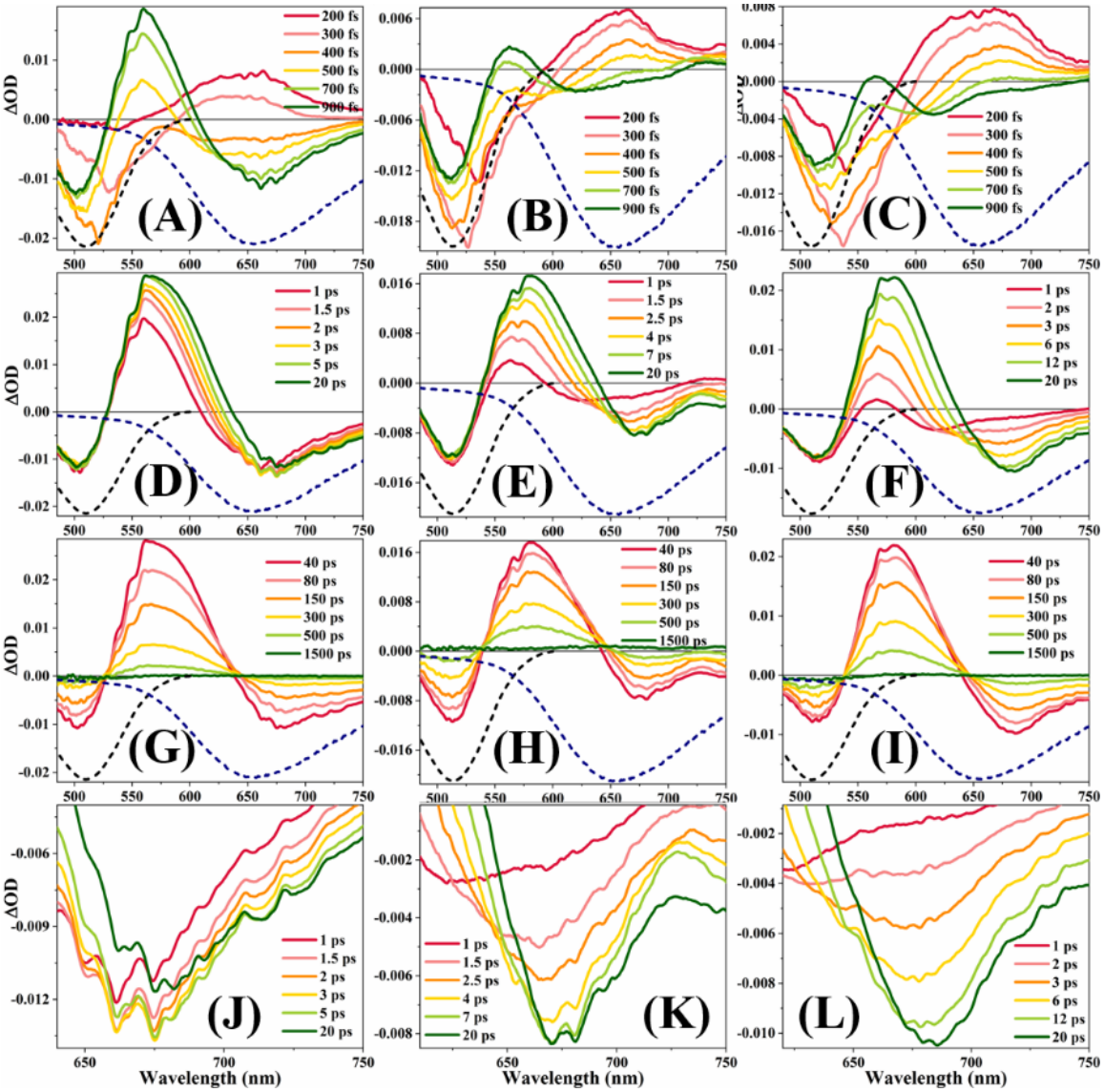

Figure B17: Transient Absorption spectra of D102 in BmimTFO-ACN [(A), (D), (G), (J)], in BmimTFO-γ-BL [(B), (E), (H), (K)] and in BmimTFO-PC [(C), (F), (I), (L)] mixtures (X_{IL}= 0.05). [(A), (B), (C)] short timescale, [(D), (E), (F)] middle timescale, [(G), (H), (I)] long timescale and [(J), (K), (L)] solvation timescale. Dashed spectra are steady state absorption (black) and emission (blue) spectra.

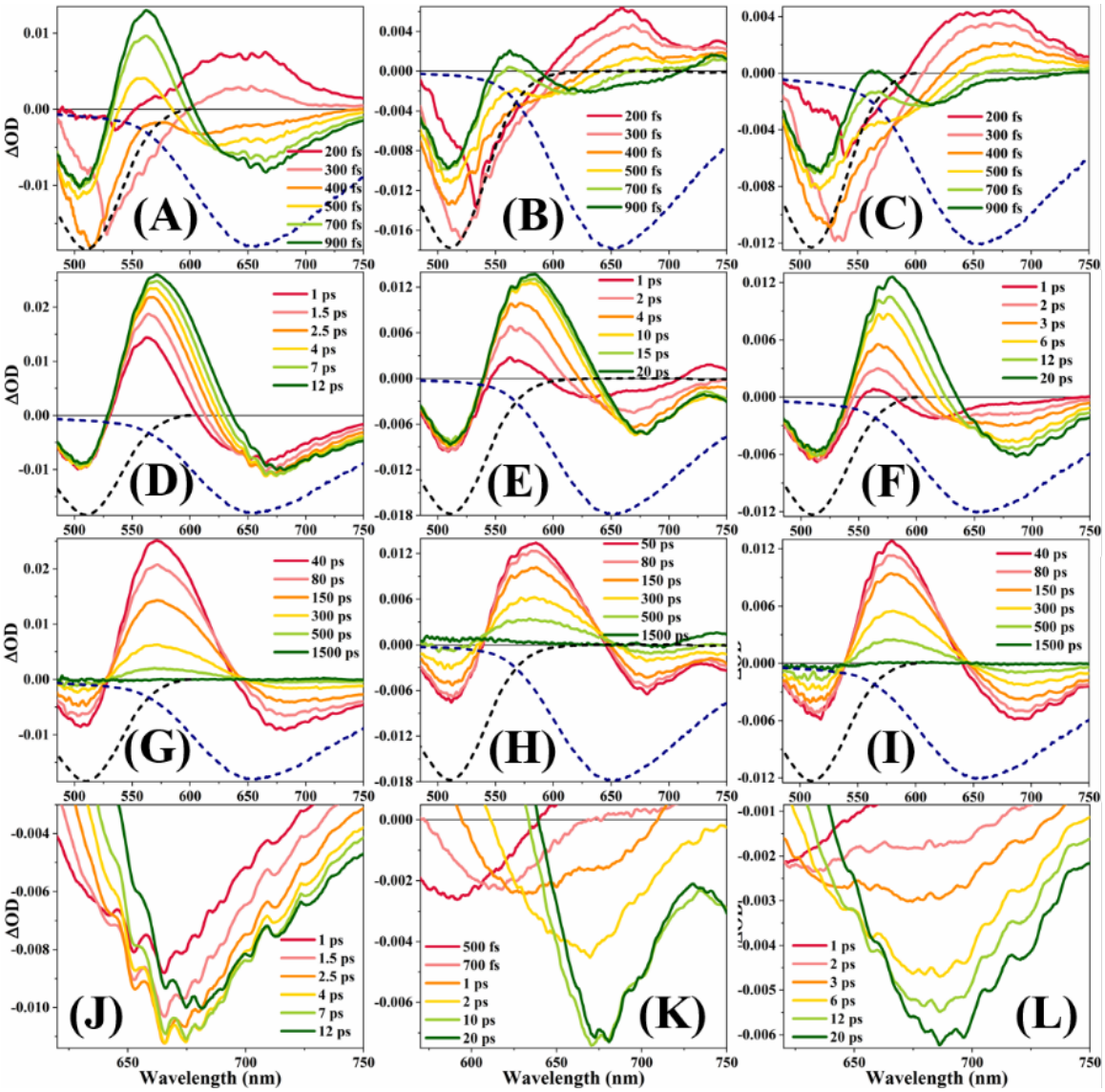

Figure B18: Transient Absorption spectra of D102 in BmimTFO-ACN [(A), (D), (G), (J)], in BmimTFO-γ-BL [(B), (E), (H), (K)] and in BmimTFO-PC [(C), (F), (I), (L)] mixtures (X_{IL}= 0.10). [(A), (B), (C)] short timescale, [(D), (E), (F)] middle timescale, [(G), (H), (I)] long timescale and [(J), (K), (L)] solvation timescale. Dashed spectra are steady state absorption (black) and emission (blue) spectra.

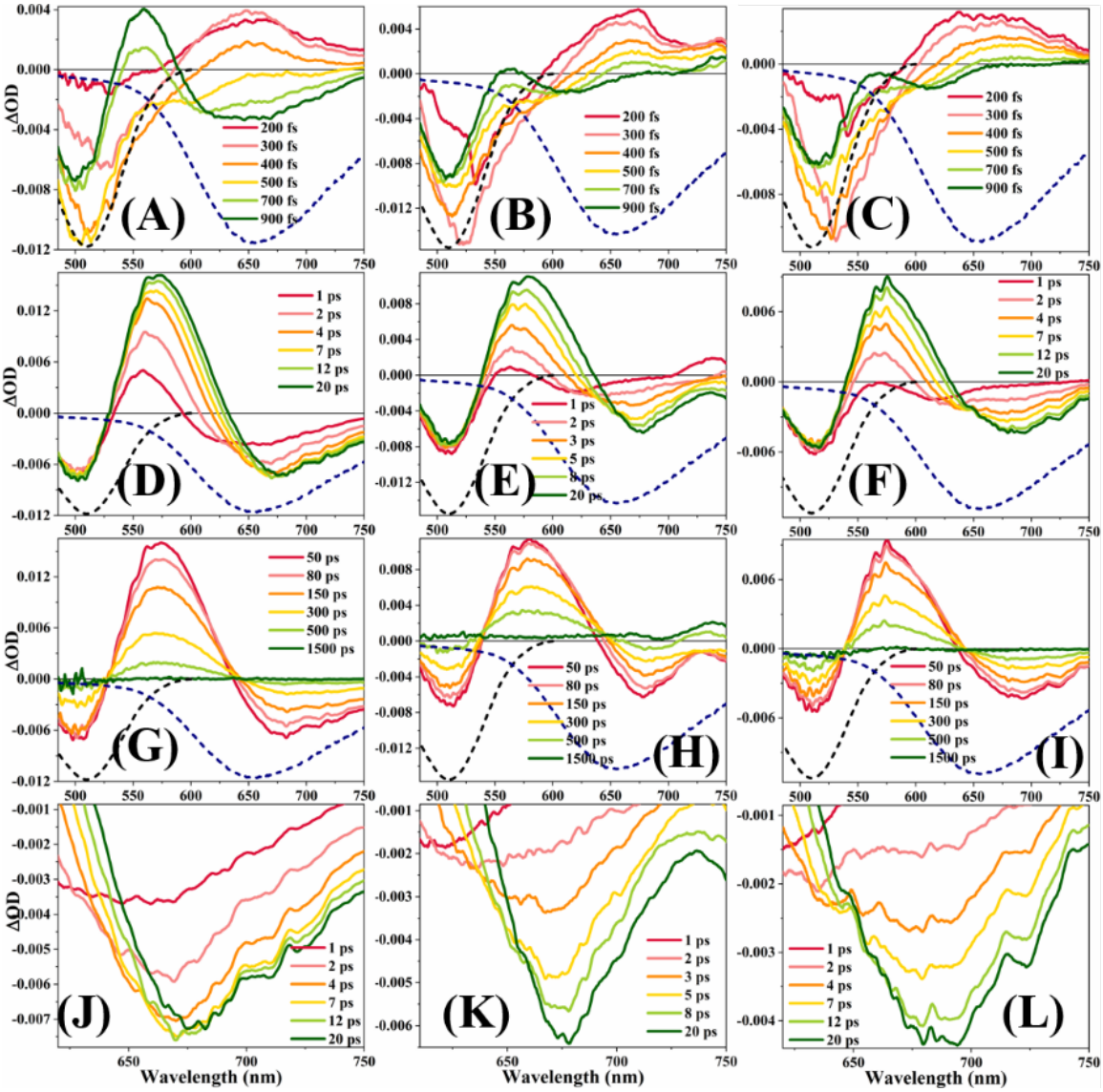

Figure B19: Transient Absorption spectra of D102 in BmimTFO-ACN [(A), (D), (G), (J)], in BmimTFO-γ-BL [(B), (E), (H), (K)] and in BmimTFO-PC [(C), (F), (I), (L)] mixtures (X_{IL}= 0.20). [(A), (B), (C)] short timescale, [(D), (E), (F)] middle timescale, [(G), (H), (I)] long timescale and [(J), (K), (L)] solvation timescale. Dashed spectra are steady state absorption (black) and emission (blue) spectra.

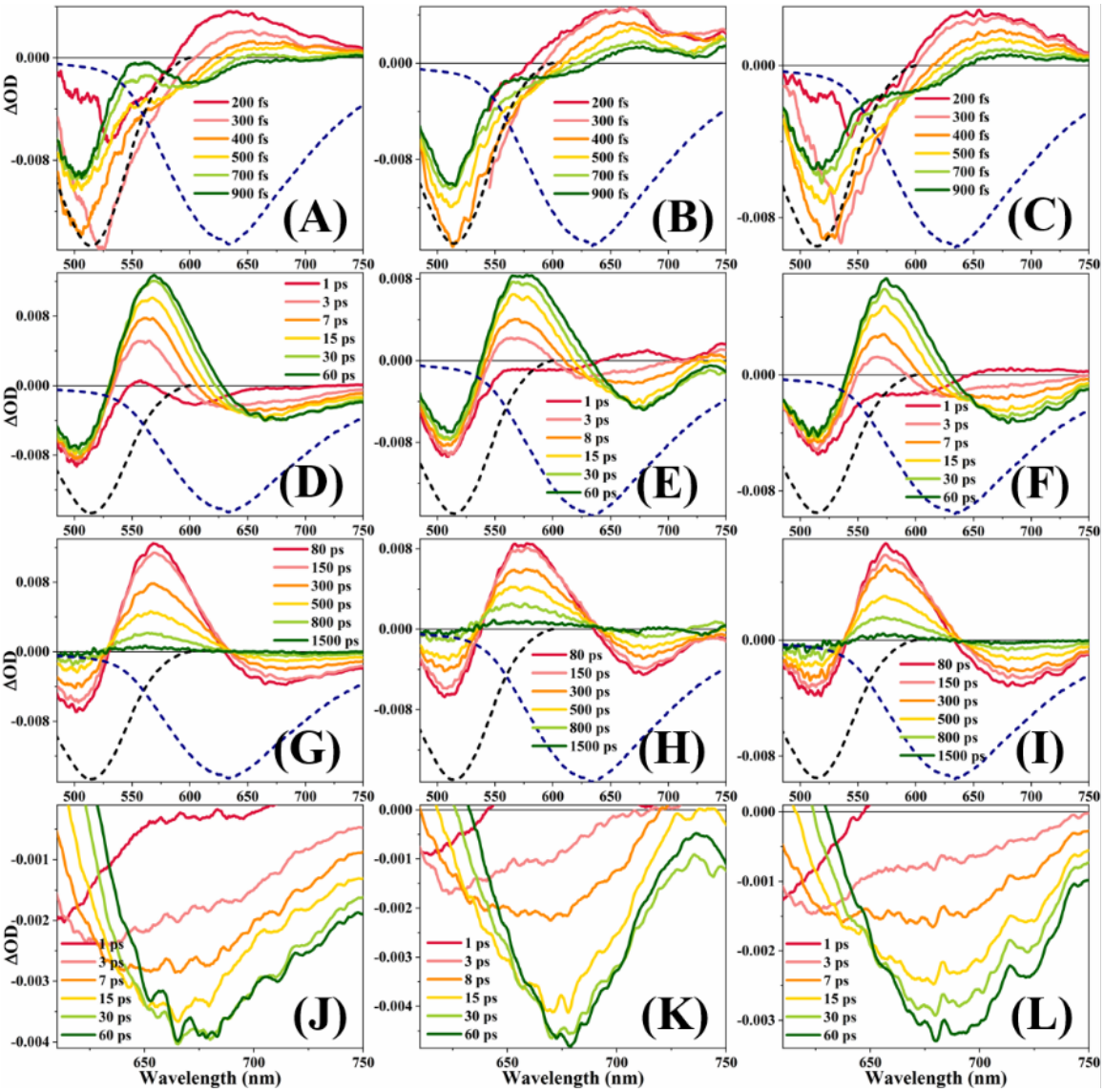

Figure B20: Transient Absorption spectra of D102 in BmimTFO-ACN [(A), (D), (G), (J)], in BmimTFO-γ-BL [(B), (E), (H), (K)] and in BmimTFO-PC [(C), (F), (I), (L)] mixtures (X_{IL}= 0.50). [(A), (B), (C)] short timescale, [(D), (E), (F)] middle timescale, [(G), (H), (I)] long timescale and [(J), (K), (L)] solvation timescale. Dashed spectra are steady state absorption (black) and emission (blue) spectra.

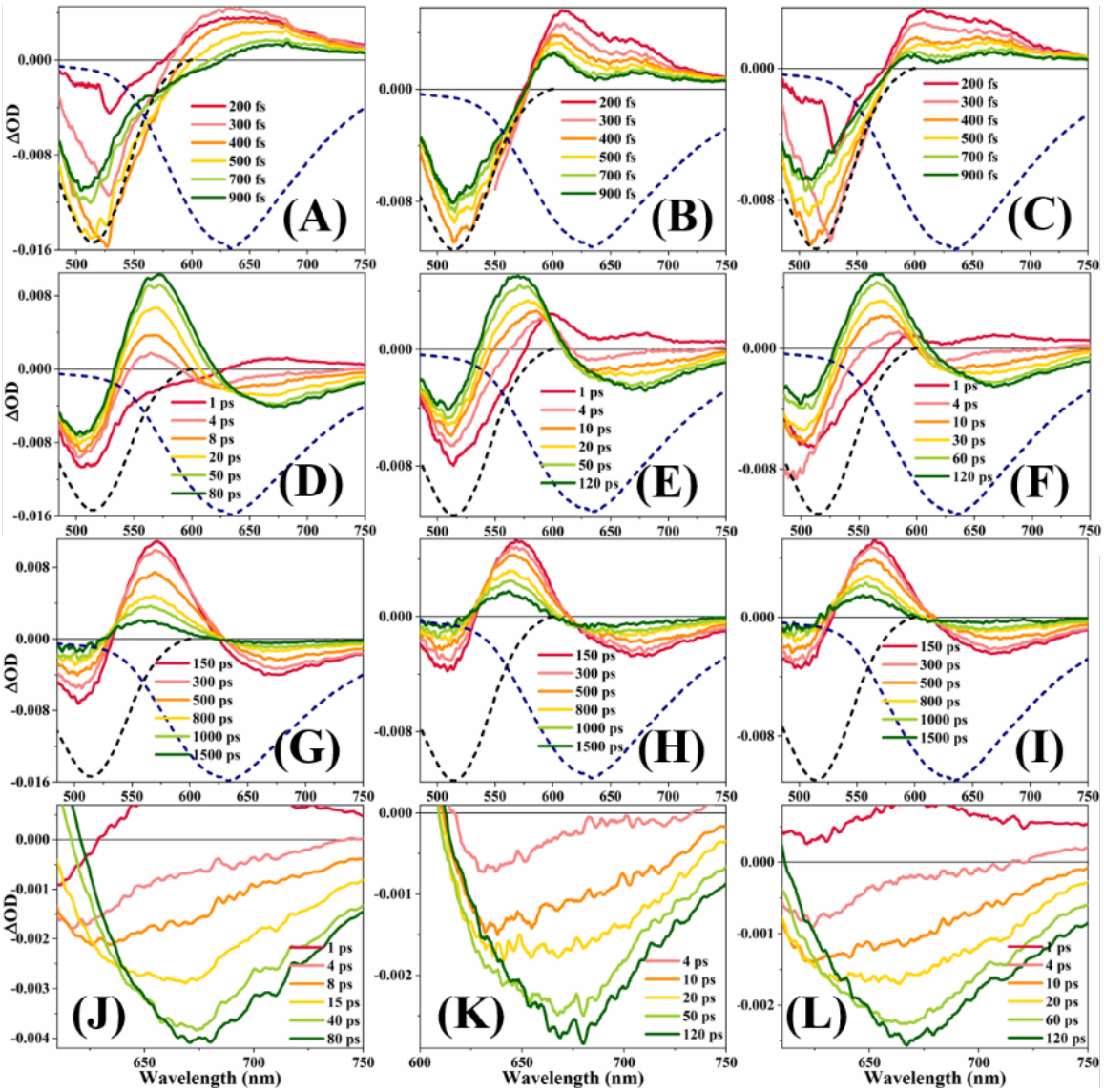

Figure B21: Transient Absorption spectra of D102 in BmimTFO-ACN [(A), (D), (G), (J)], in BmimTFO-γ-BL [(B), (E), (H), (K)] and in BmimTFO-PC [(C), (F), (I), (L)] mixtures (X_{IL}= 0.80). [(A), (B), (C)] short timescale, [(D), (E), (F)] middle timescale, [(G), (H), (I)] long timescale and [(J), (K), (L)] solvation timescale. Dashed spectra are steady state absorption (black) and emission (blue) spectra.

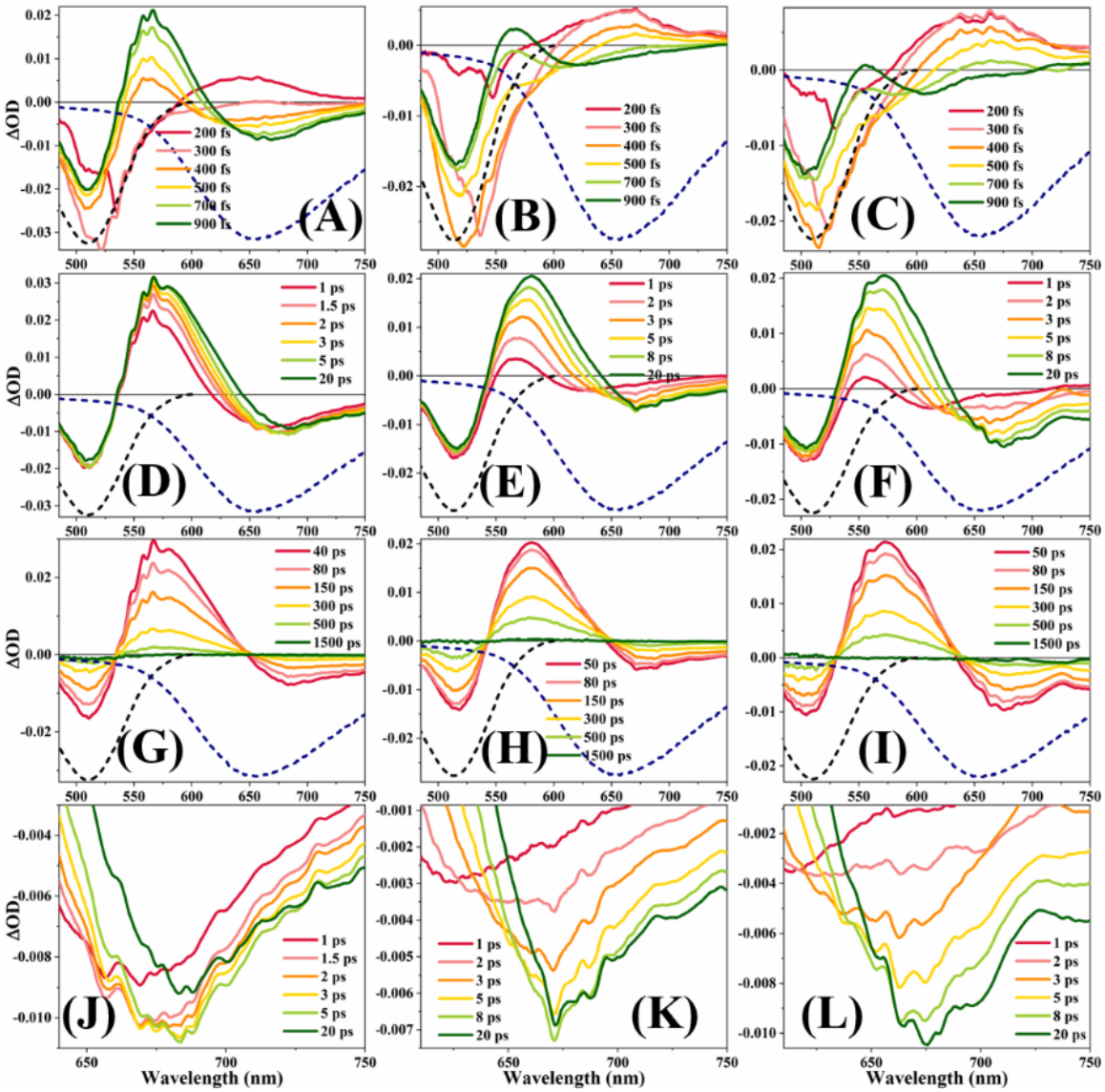

Figure B22: Transient Absorption spectra of D102 in BmimTFSI-ACN [(A), (D), (G), (J)], in BmimTFSI-γ-BL [(B), (E), (H), (K)] and in BmimTFSI-PC [(C), (F), (I), (L)] mixtures (X_{IL}= 0.05). [(A), (B), (C)] short timescale, [(D), (E), (F)] middle timescale, [(G), (H), (I)] long timescale and [(J), (K), (L)] solvation timescale. Dashed spectra are steady state absorption (black) and emission (blue) spectra.

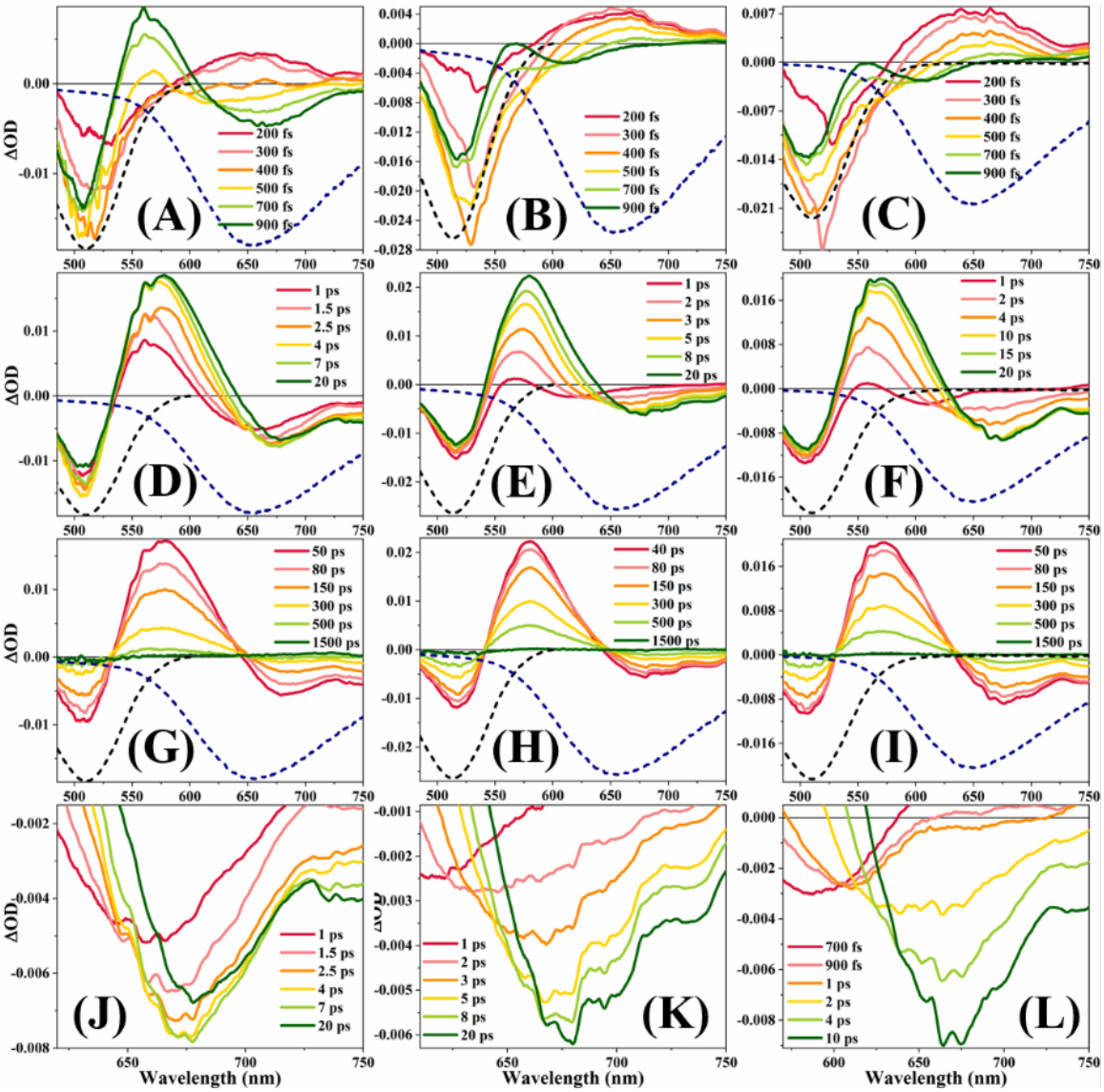

Figure B23: Transient Absorption spectra of D102 in BmimTFSI-ACN [(A), (D), (G), (J)], in BmimTFSI-γ-BL [(B), (E), (H), (K)] and in BmimTFSI-PC [(C), (F), (I), (L)] mixtures (X_{IL}= 0.10). [(A), (B), (C)] short timescale, [(D), (E), (F)] middle timescale, [(G), (H), (I)] long timescale and [(J), (K), (L)] solvation timescale. Dashed spectra are steady state absorption (black) and emission (blue) spectra.

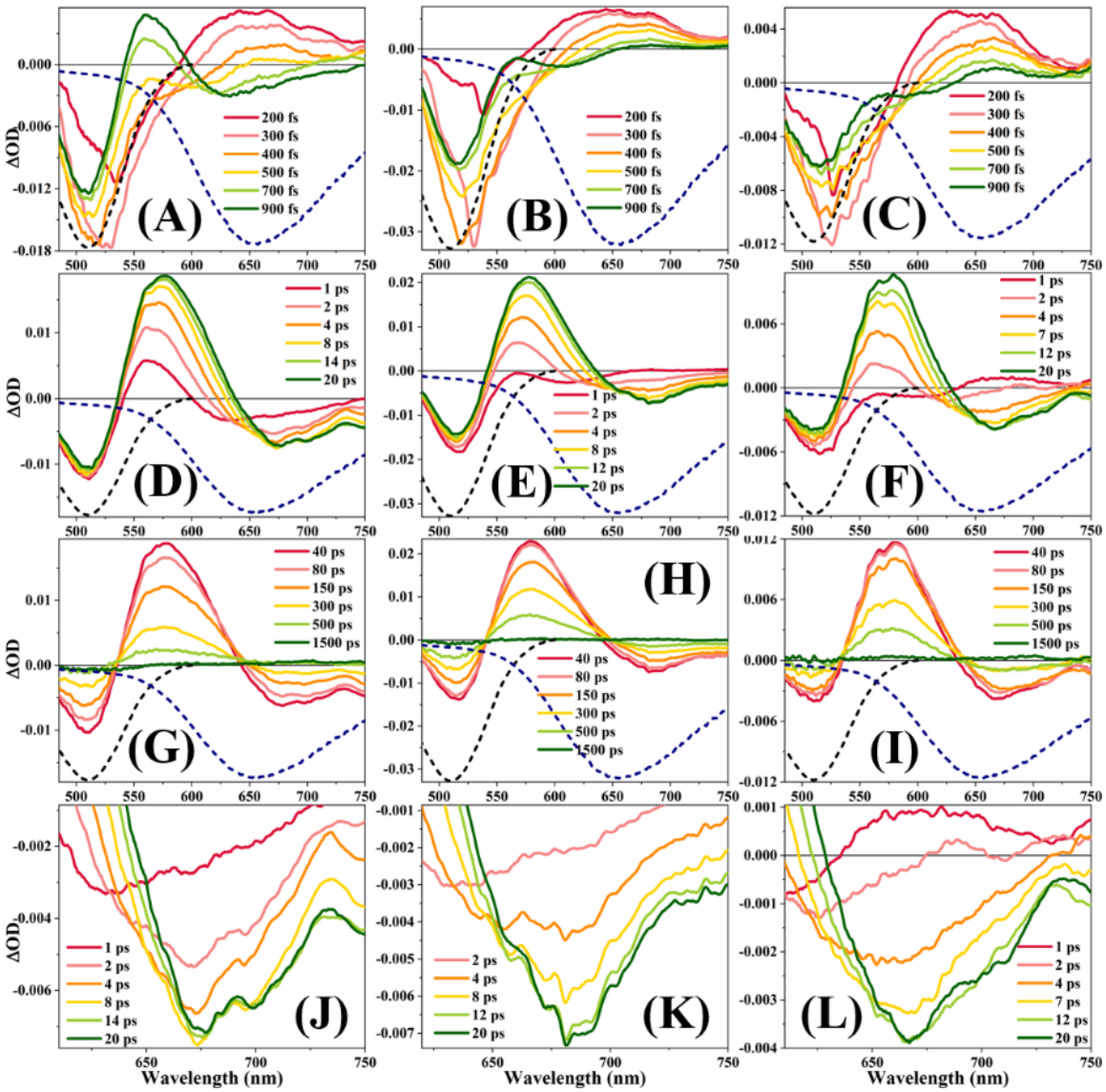

Figure B24: Transient Absorption spectra of D102 in BmimTFSI-ACN [(A), (D), (G), (J)], in BmimTFSI-γ-BL [(B), (E), (H), (K)] and in BmimTFSI-PC [(C), (F), (I), (L)] mixtures (X_{IL}= 0.20). [(A), (B), (C)] short timescale, [(D), (E), (F)] middle timescale, [(G), (H), (I)] long timescale and [(J), (K), (L)] solvation timescale. Dashed spectra are steady state absorption (black) and emission (blue) spectra.

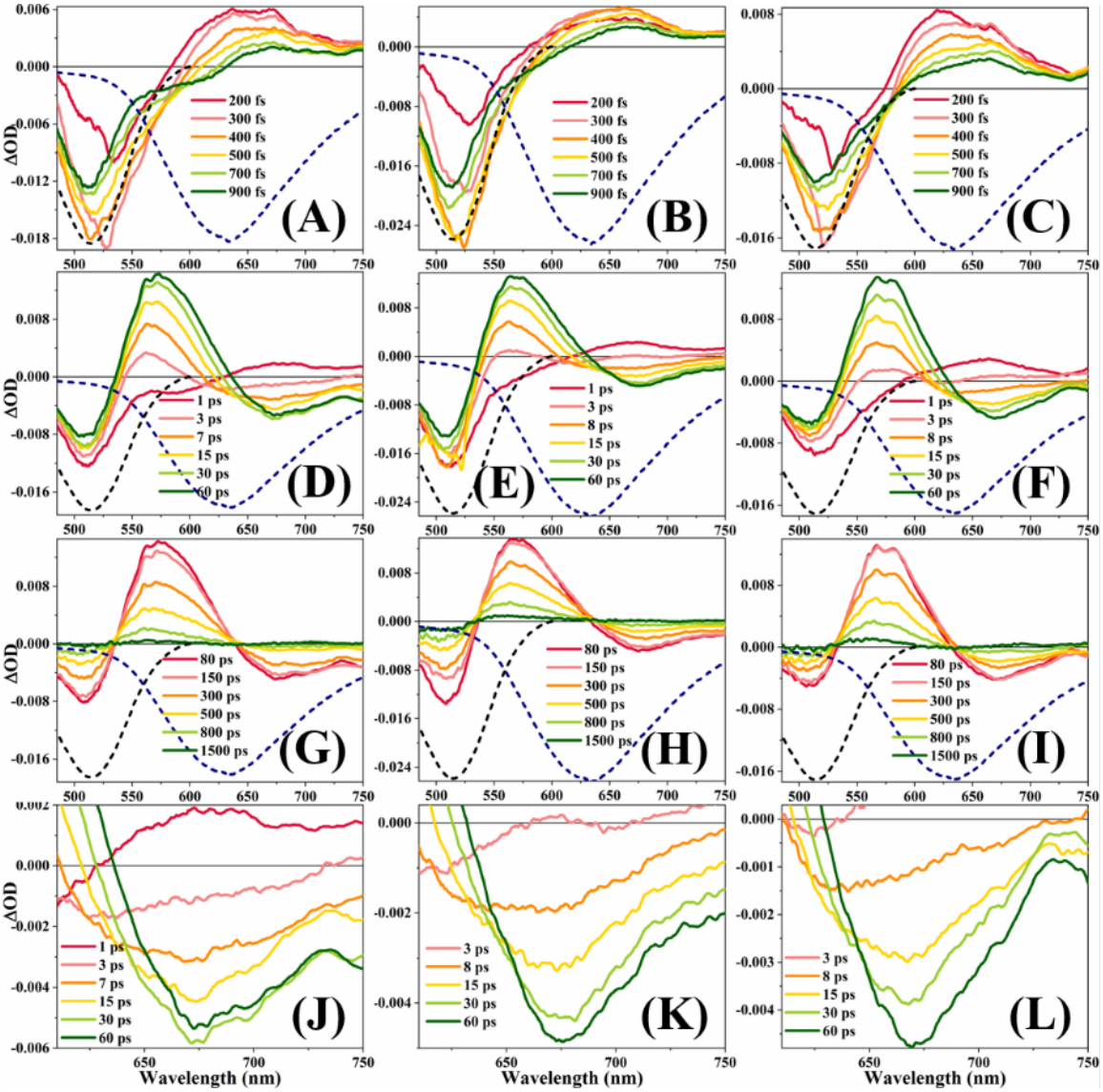

Figure B25: Transient Absorption spectra of D102 in BmimTFSI-ACN [(A), (D), (G), (J)], in BmimTFSI-γ-BL [(B), (E), (H), (K)] and in BmimTFSI-PC [(C), (F), (I), (L)] mixtures (X_{IL}= 0.50). [(A), (B), (C)] short timescale, [(D), (E), (F)] middle timescale, [(G), (H), (I)] long timescale and [(J), (K), (L)] solvation timescale. Dashed spectra are steady state absorption (black) and emission (blue) spectra.

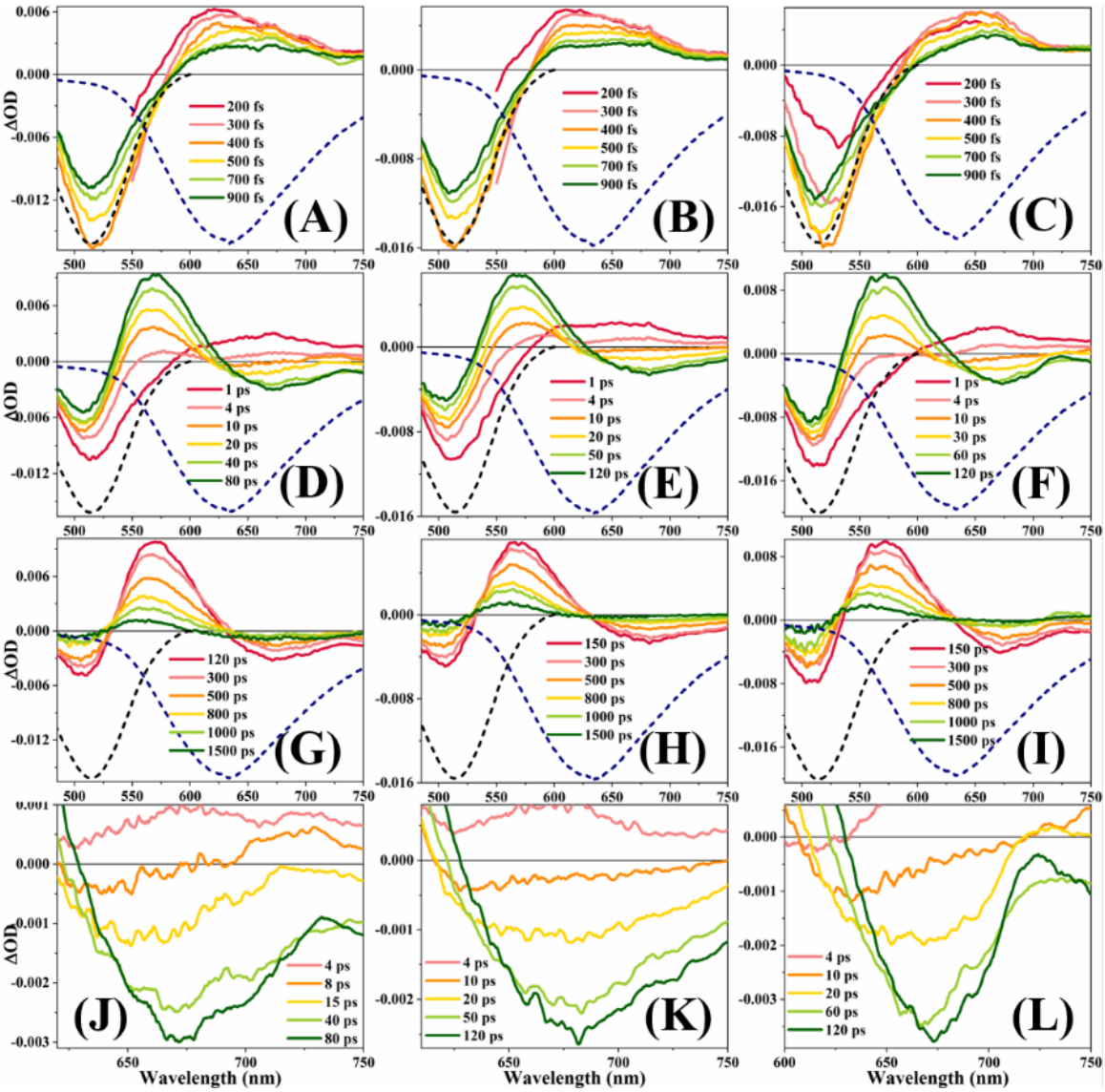

Figure B26: Transient Absorption spectra of D102 in BmimTFSI-ACN [(A), (D), (G), (J)], in BmimTFSI-γ-BL [(B), (E), (H), (K)] and in BmimTFSI-PC [(C), (F), (I), (L)] mixtures (X_{IL}= 0.80). [(A), (B), (C)] short timescale, [(D), (E), (F)] middle timescale, [(G), (H), (I)] long timescale and [(J), (K), (L)] solvation timescale. Dashed spectra are steady state absorption (black) and emission (blue) spectra.

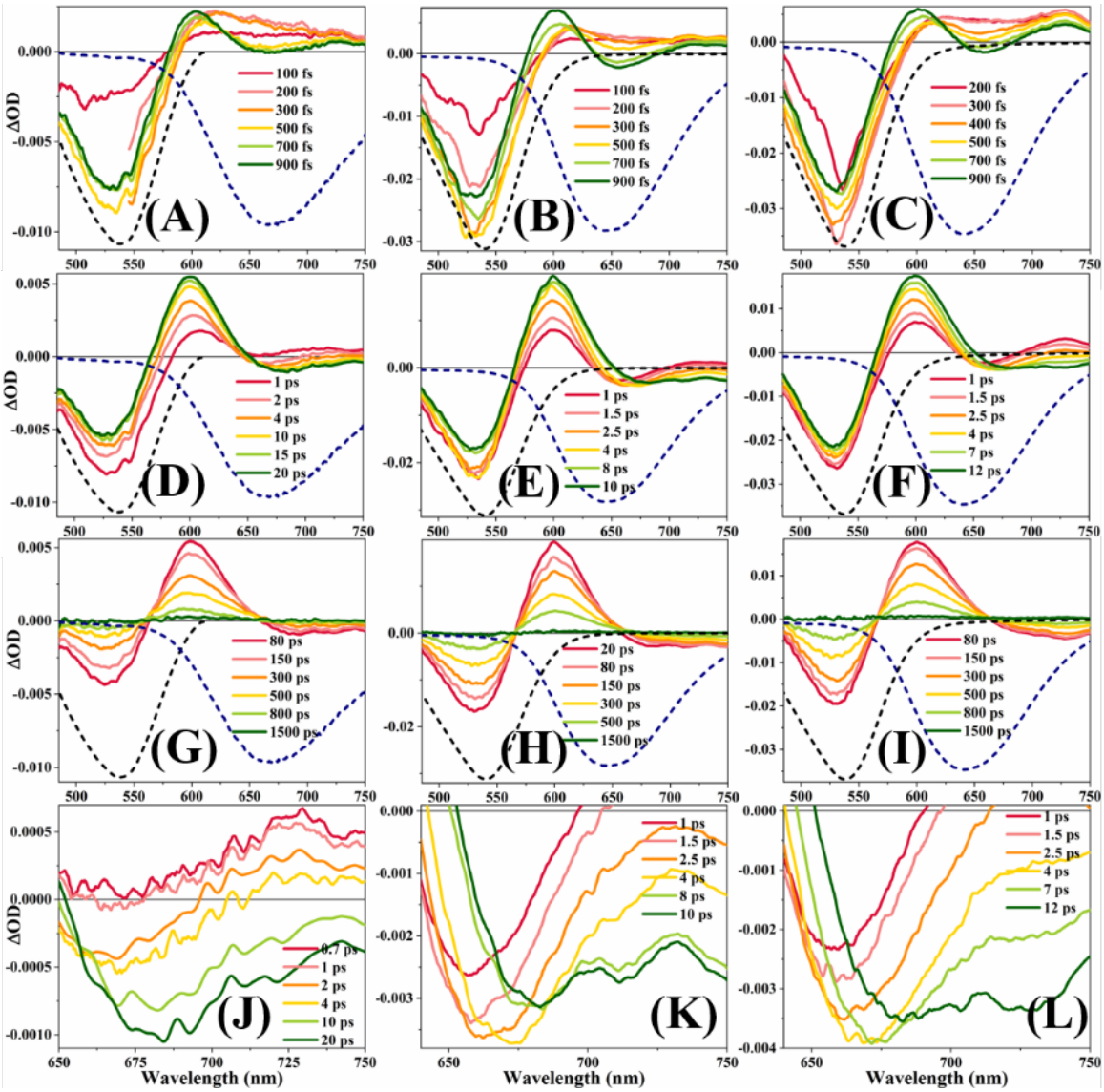

Figure B27: Transient Absorption spectra of D149 in $BmimBF_4$-ACN [(A), (D), (G), (J)], in $BmimBF_4$-γ-BL [(B), (E), (H), (K)] and in $BmimBF_4$-PC [(C), (F), (I), (L)] mixtures (X_{IL}= 0.05). [(A), (B), (C)] short timescale, [(D), (E), (F)] middle timescale, [(G), (H), (I)] long timescale and [(J), (K), (L)] solvation timescale. Dashed spectra are steady state absorption (black) and emission (blue) spectra.

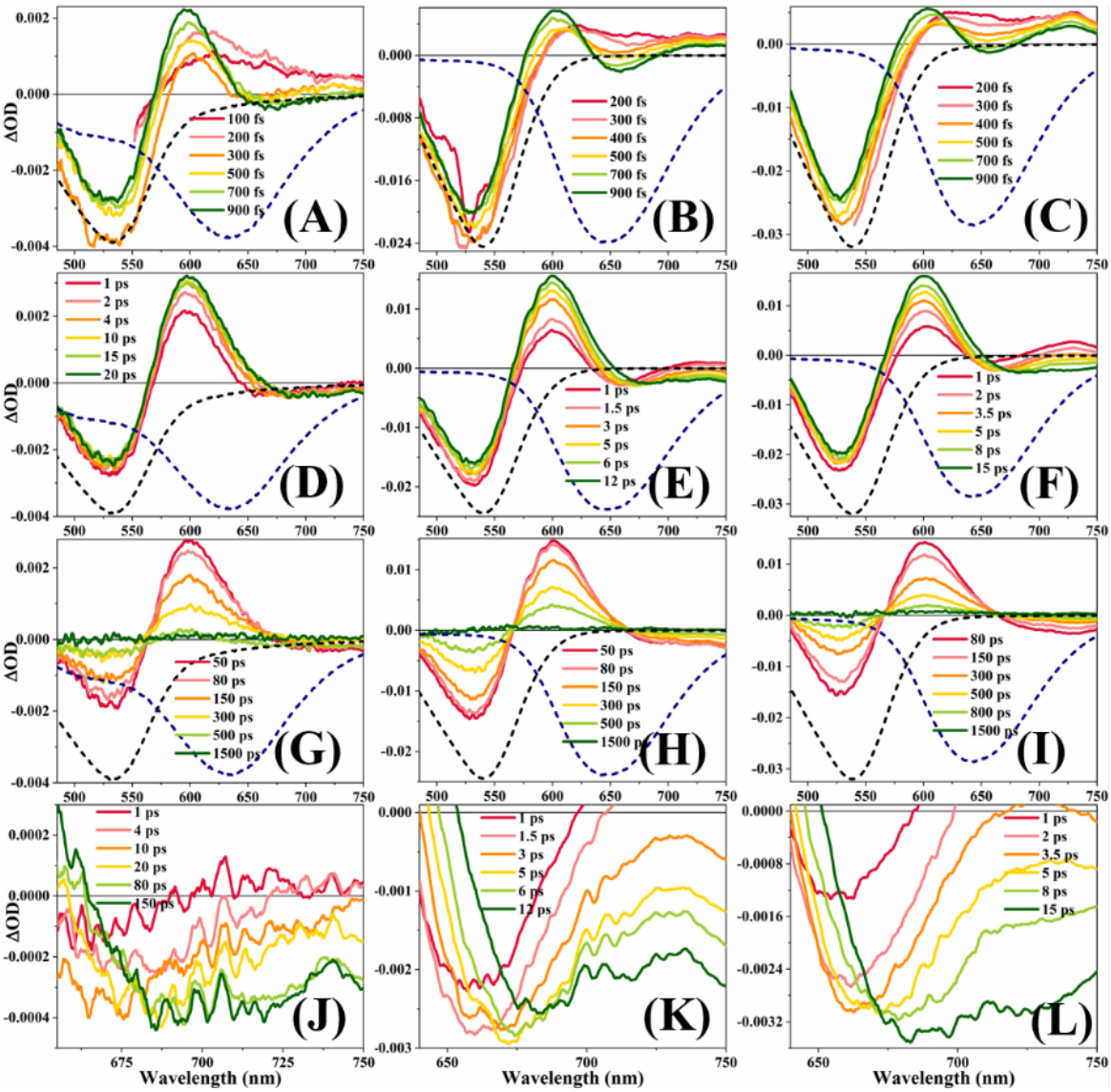

Figure B28: Transient Absorption spectra of D149 in $BmimBF_4$-ACN [(A), (D), (G), (J)], in $BmimBF_4$-γ-BL [(B), (E), (H), (K)] and in $BmimBF_4$-PC [(C), (F), (I), (L)] mixtures (X_{IL}= 0.10). [(A), (B), (C)] short timescale, [(D), (E), (F)] middle timescale, [(G), (H), (I)] long timescale and [(J), (K), (L)] solvation timescale. Dashed spectra are steady state absorption (black) and emission (blue) spectra.

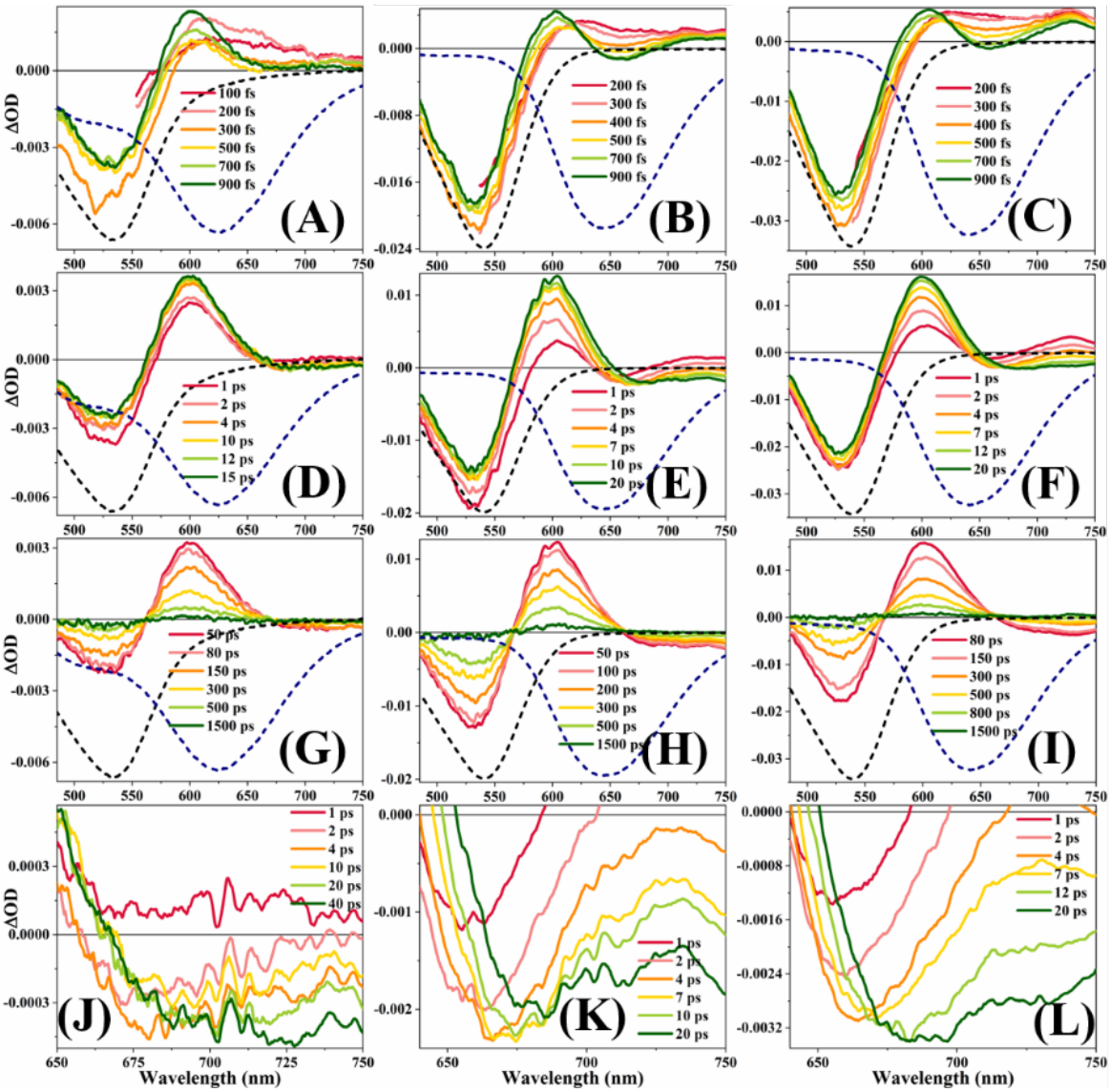

Figure B29: Transient Absorption spectra of D149 in $BmimBF_4$-ACN [(A), (D), (G), (J)], in $BmimBF_4$-γ-BL [(B), (E), (H), (K)] and in $BmimBF_4$-PC [(C), (F), (I), (L)] mixtures (X_{IL}= 0.20). [(A), (B), (C)] short timescale, [(D), (E), (F)] middle timescale, [(G), (H), (I)] long timescale and [(J), (K), (L)] solvation timescale. Dashed spectra are steady state absorption (black) and emission (blue) spectra.

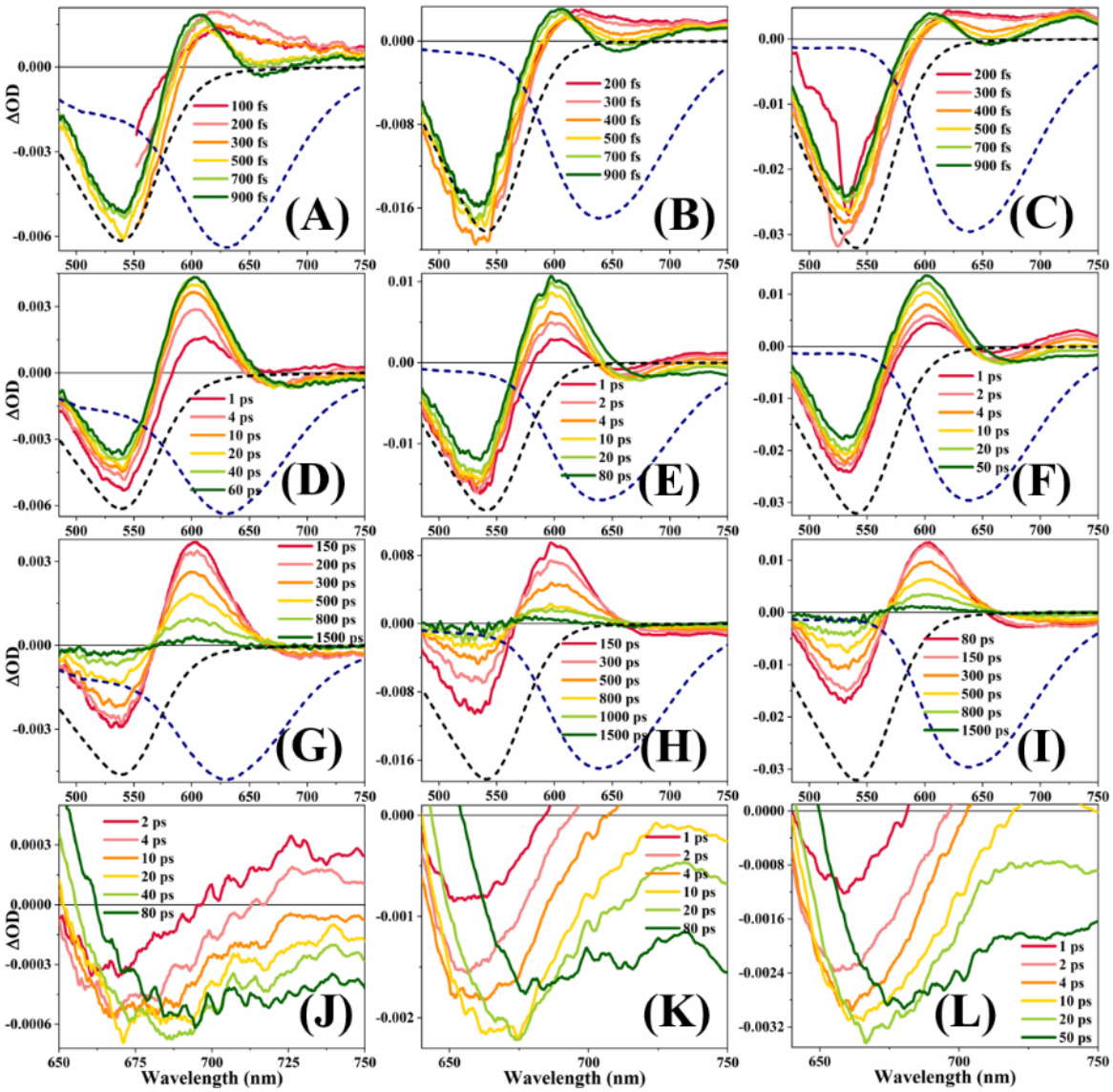

Figure B30: Transient Absorption spectra of D149 in $BmimBF_4$-ACN [(A), (D), (G), (J)], in $BmimBF_4$-γ-BL [(B), (E), (H), (K)] and in $BmimBF_4$-PC [(C), (F), (I), (L)] mixtures (X_{IL}= 0.50). [(A), (B), (C)] short timescale, [(D), (E), (F)] middle timescale, [(G), (H), (I)] long timescale and [(J), (K), (L)] solvation timescale. Dashed spectra are steady state absorption (black) and emission (blue) spectra.

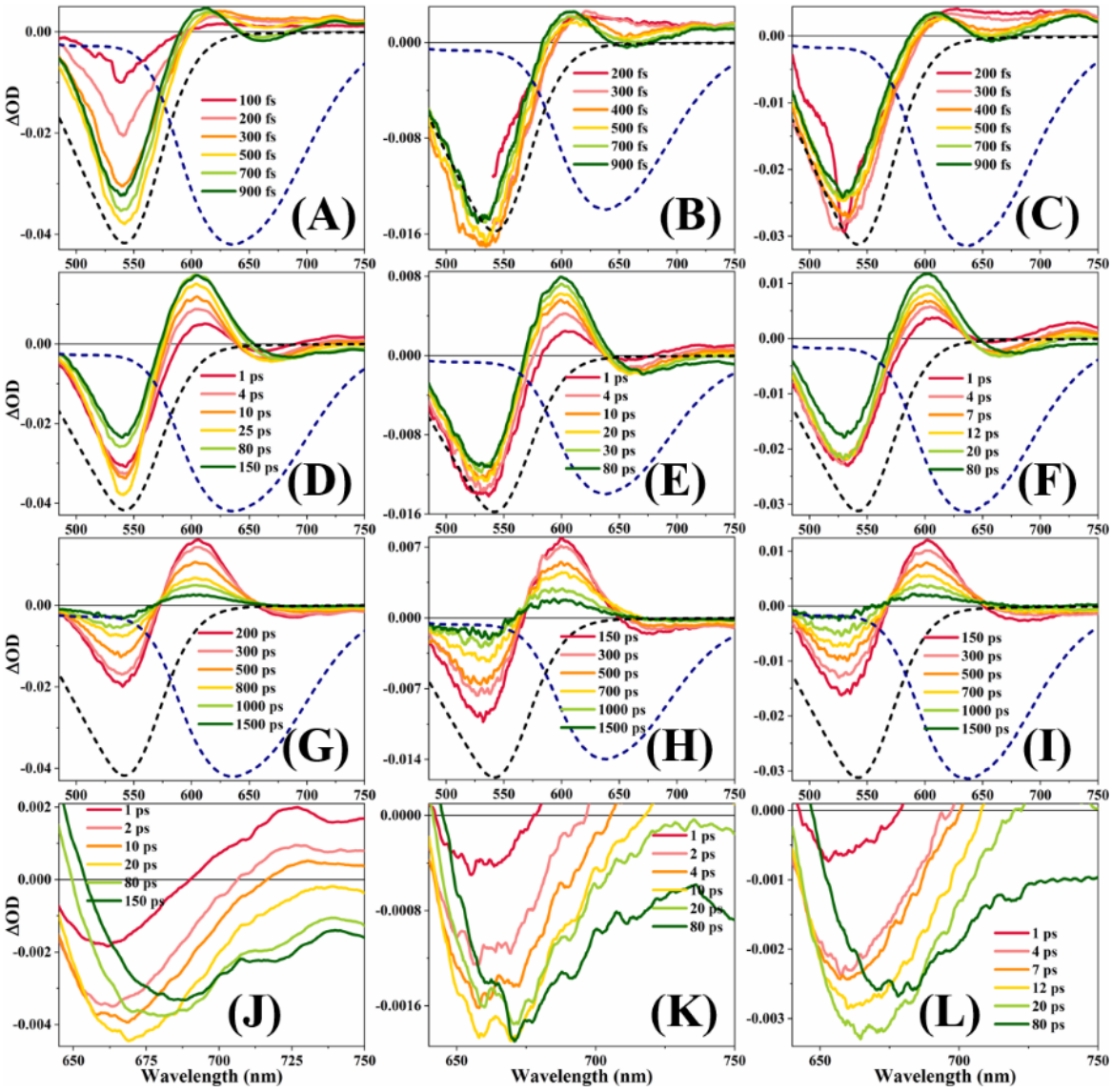

Figure B31: Transient Absorption spectra of D149 in $BmimBF_4$-ACN [(A), (D), (G), (J)], in $BmimBF_4$-γ-BL [(B), (E), (H), (K)] and in $BmimBF_4$-PC [(C), (F), (I), (L)] mixtures (X_{IL}= 0.80). [(A), (B), (C)] short timescale, [(D), (E), (F)] middle timescale, [(G), (H), (I)] long timescale and [(J), (K), (L)] solvation timescale. Dashed spectra are steady state absorption (black) and emission (blue) spectra.

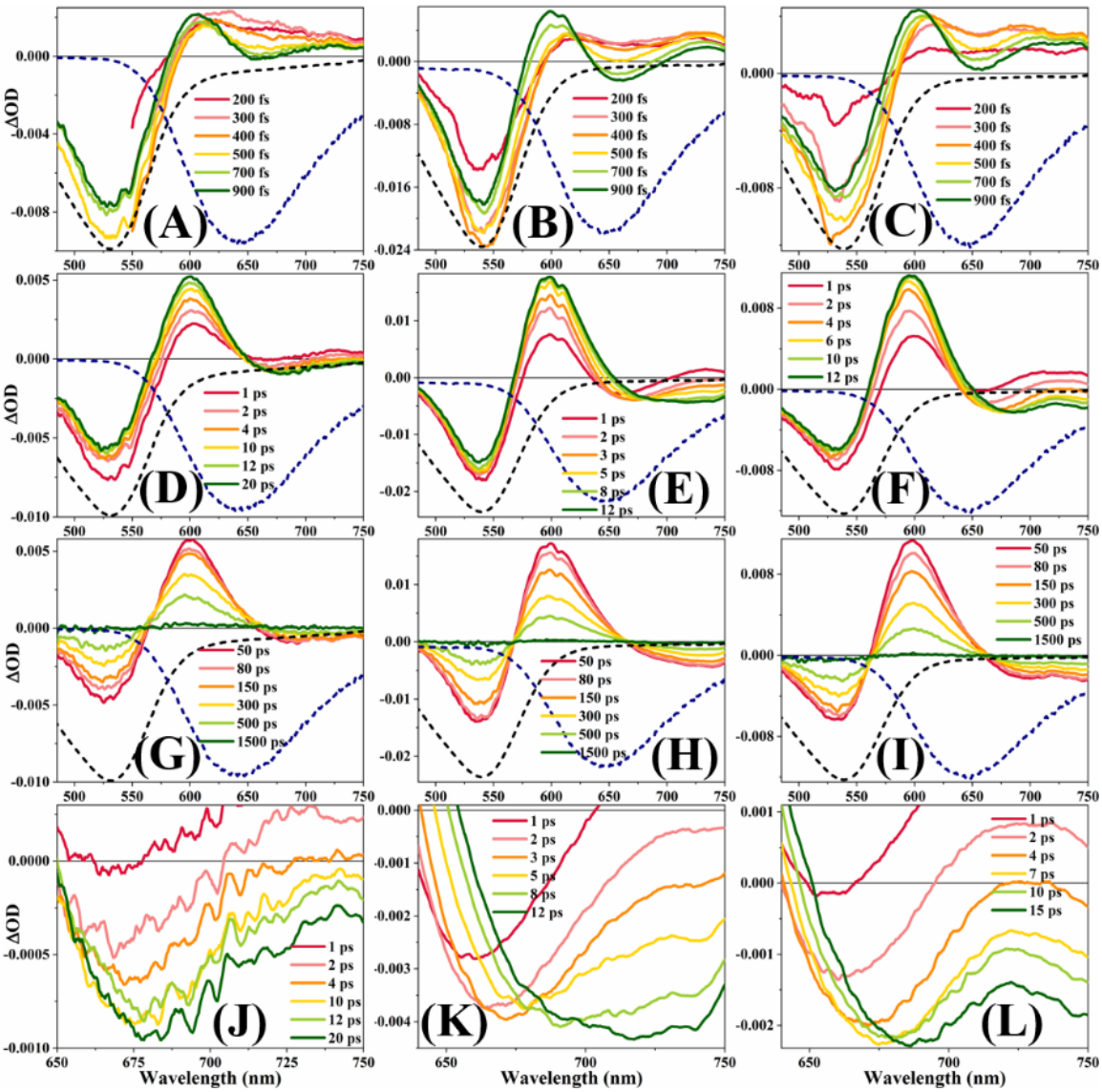

Figure B32: Transient Absorption spectra of D149 in $BmimPF_6$-ACN [(A), (D), (G), (J)], in $BmimPF_6$-γ-BL [(B), (E), (H), (K)] and in $BmimPF_6$-PC [(C), (F), (I), (L)] mixtures (X_{IL}= 0.05). [(A), (B), (C)] short timescale, [(D), (E), (F)] middle timescale, [(G), (H), (I)] long timescale and [(J), (K), (L)] solvation timescale. Dashed spectra are steady state absorption (black) and emission (blue) spectra.

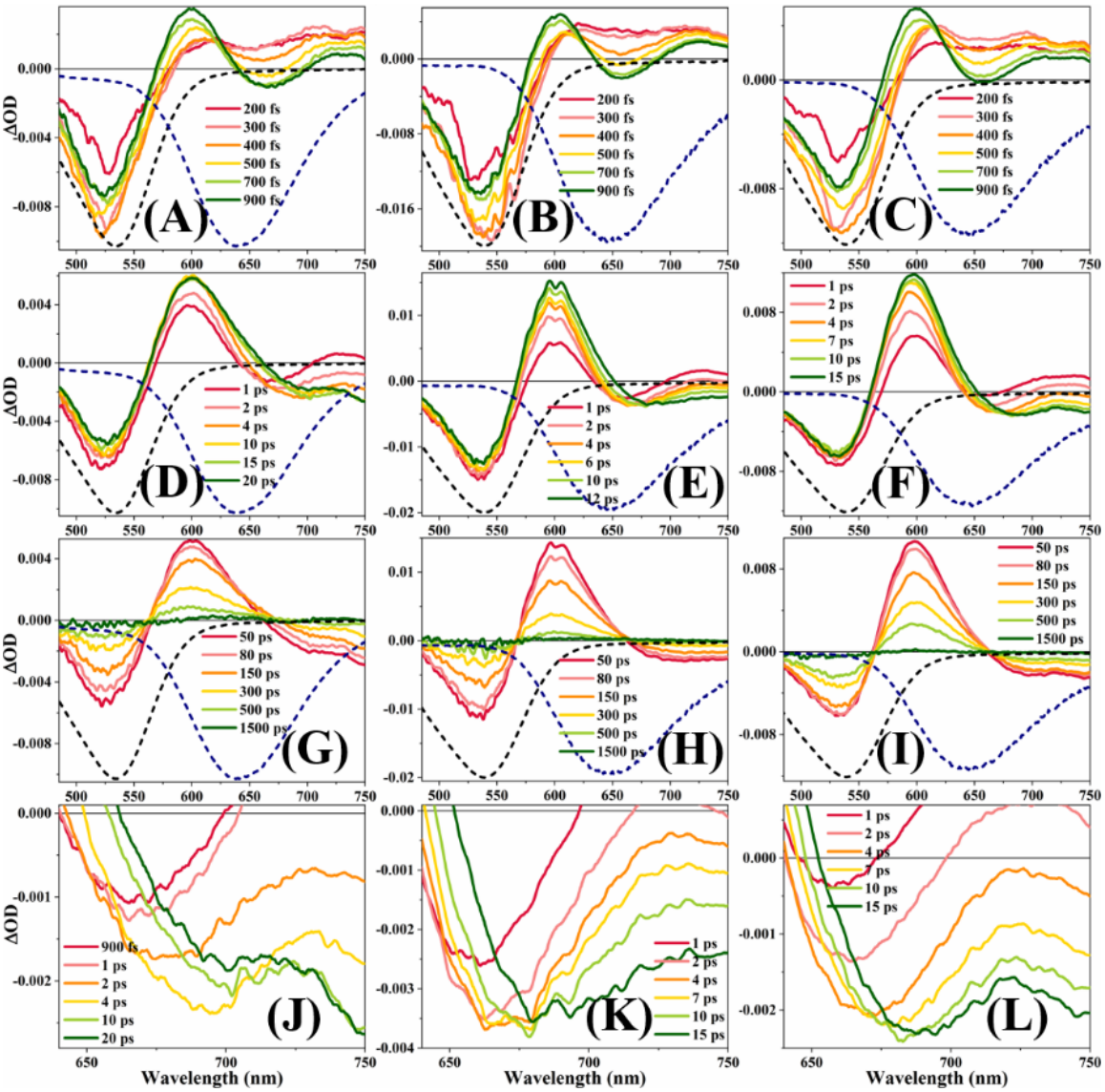

Figure B33: Transient Absorption spectra of D149 in BmimPF$_6$-ACN [(A), (D), (G), (J)], in BmimPF$_6$-γ-BL [(B), (E), (H), (K)] and in BmimPF$_6$-PC [(C), (F), (I), (L)] mixtures (X_{IL}= 0.10). [(A), (B), (C)] short timescale, [(D), (E), (F)] middle timescale, [(G), (H), (I)] long timescale and [(J), (K), (L)] solvation timescale. Dashed spectra are steady state absorption (black) and emission (blue) spectra.

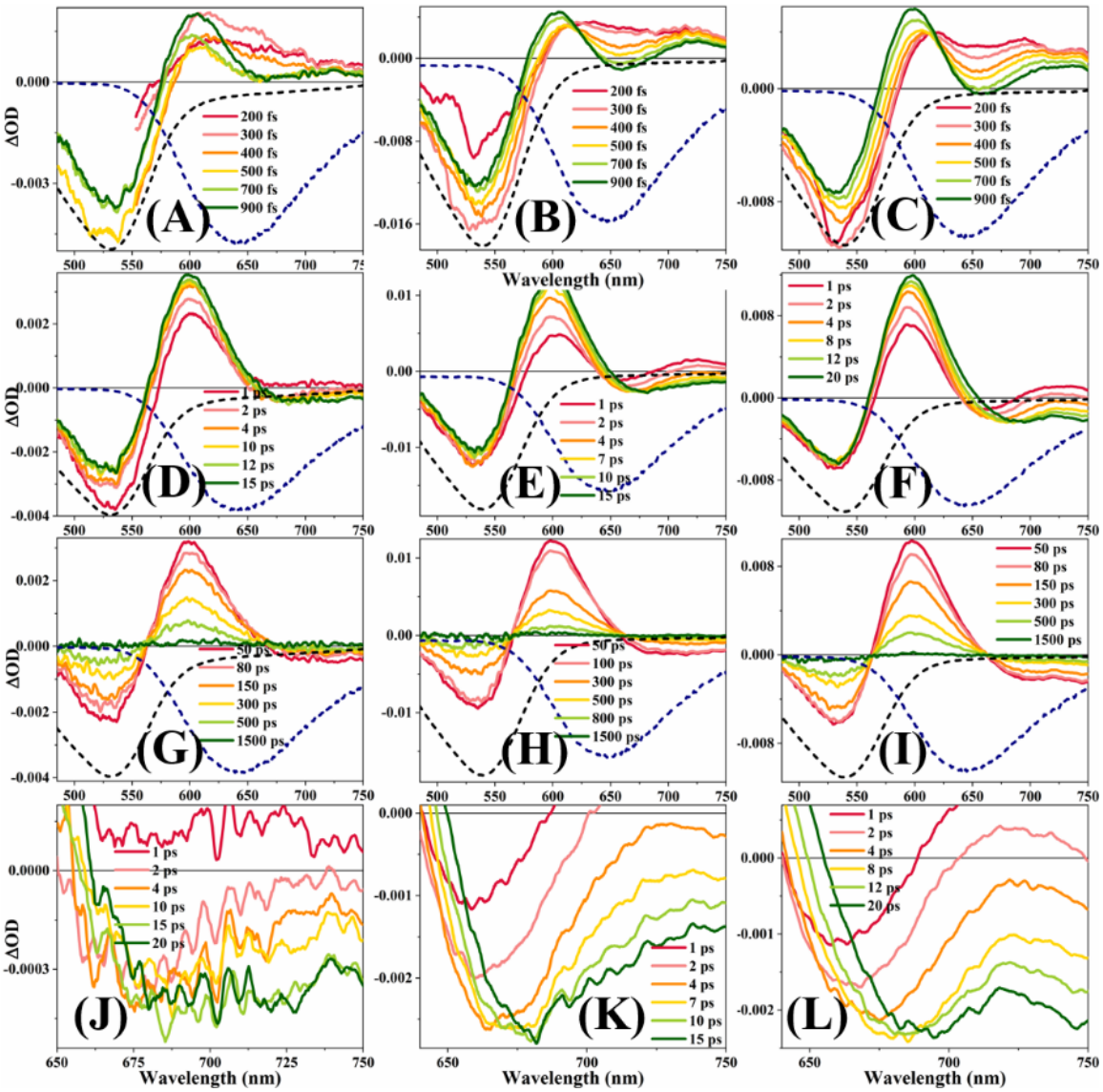

Figure B34: Transient Absorption spectra of D149 in $BmimPF_6$-ACN [(A), (D), (G), (J)], in $BmimPF_6$-γ-BL [(B), (E), (H), (K)] and in $BmimPF_6$-PC [(C), (F), (I), (L)] mixtures (X_{IL}= 0.20). [(A), (B), (C)] short timescale, [(D), (E), (F)] middle timescale, [(G), (H), (I)] long timescale and [(J), (K), (L)] solvation timescale. Dashed spectra are steady state absorption (black) and emission (blue) spectra.

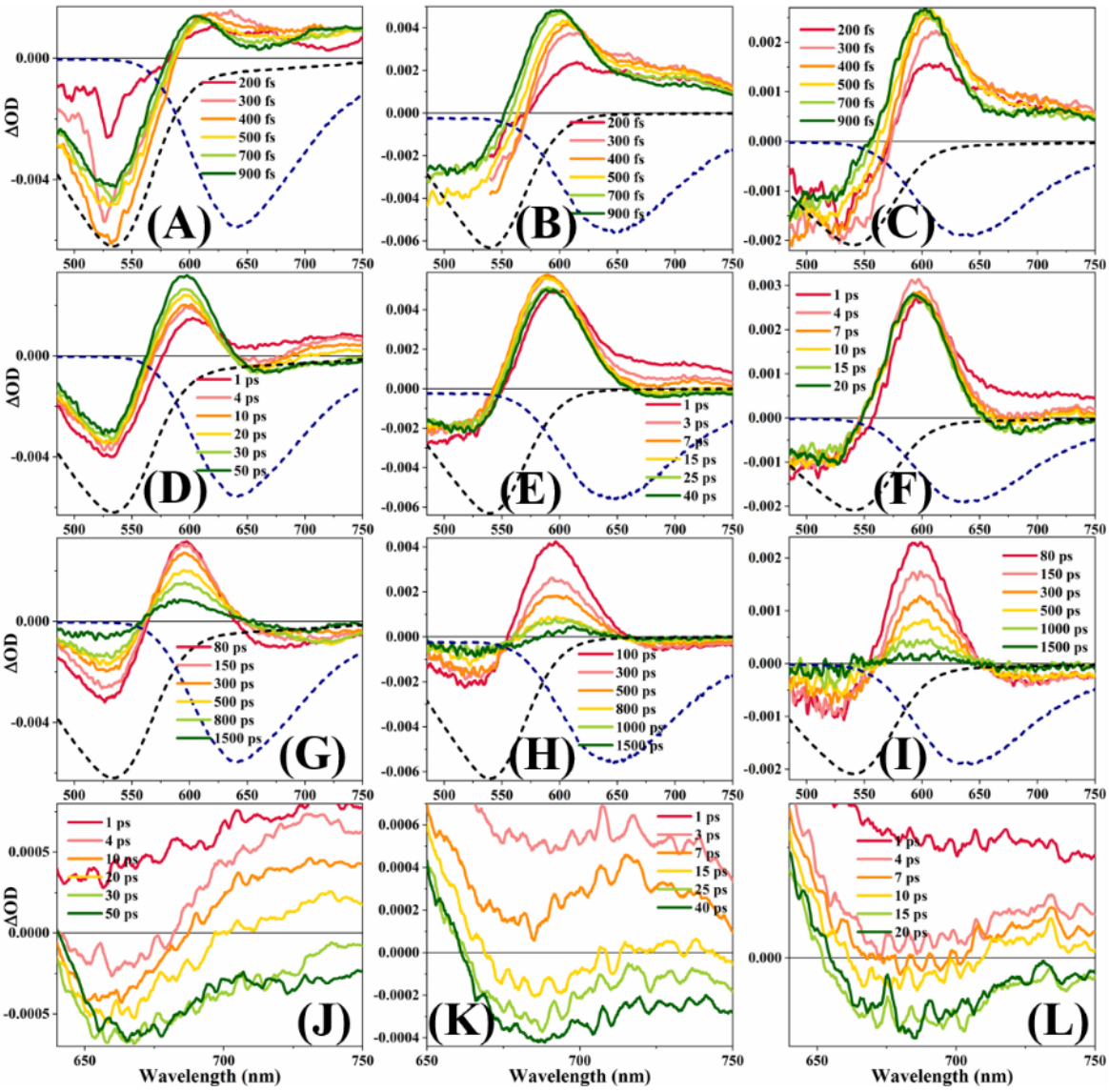

Figure B35: Transient Absorption spectra of D149 in $BmimPF_6$-ACN [(A), (D), (G), (J)], in $BmimPF_6$-γ-BL [(B), (E), (H), (K)] and in $BmimPF_6$-PC [(C), (F), (I), (L)] mixtures (X_{IL}= 0.50). [(A), (B), (C)] short timescale, [(D), (E), (F)] middle timescale, [(G), (H), (I)] long timescale and [(J), (K), (L)] solvation timescale. Dashed spectra are steady state absorption (black) and emission (blue) spectra.

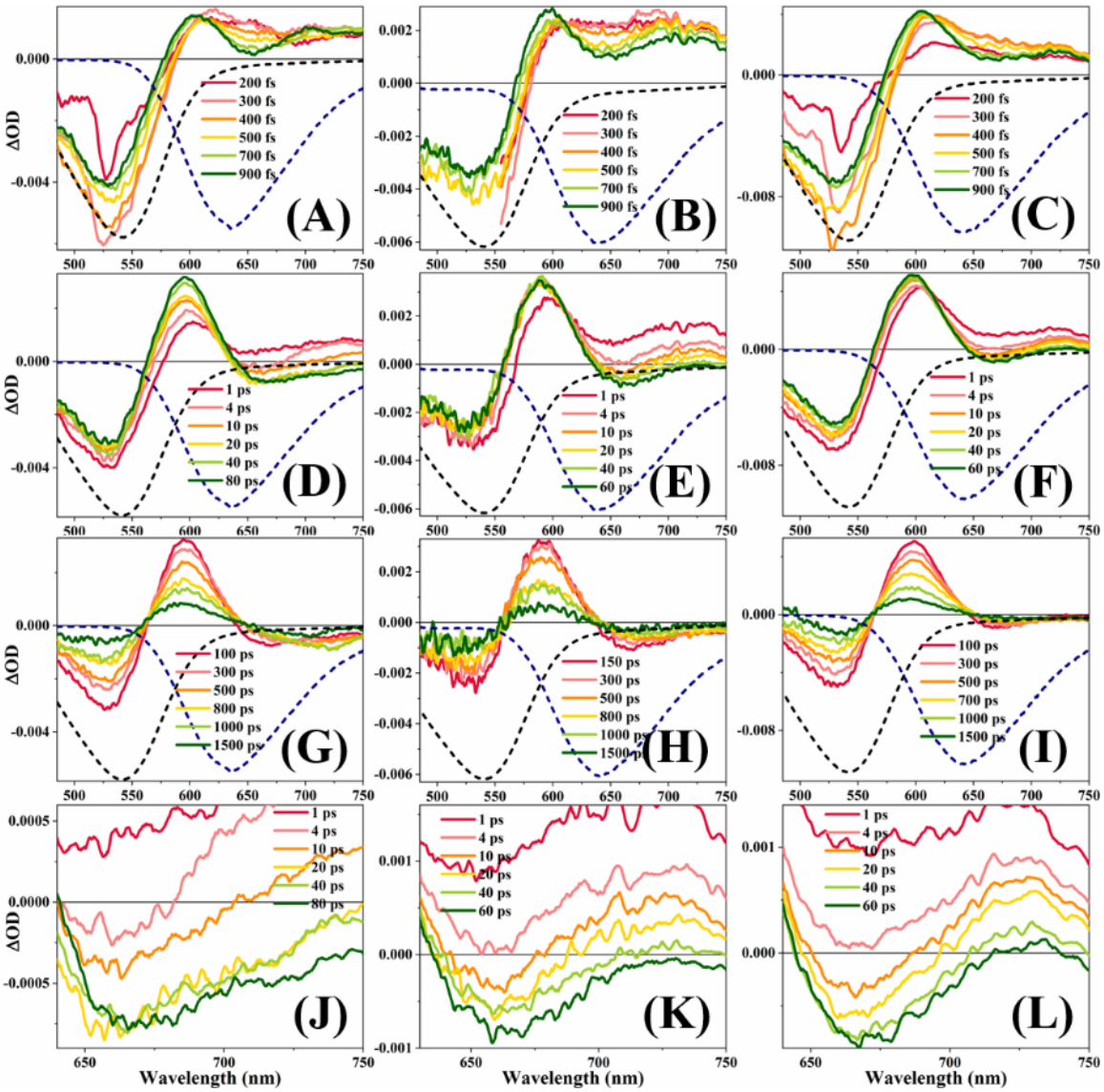

Figure B36: Transient Absorption spectra of D149 in $BmimPF_6$-ACN [(A), (D), (G), (J)], in $BmimPF_6$-γ-BL [(B), (E), (H), (K)] and in $BmimPF_6$-PC [(C), (F), (I), (L)] mixtures (X_{IL}= 0.80). [(A), (B), (C)] short timescale, [(D), (E), (F)] middle timescale, [(G), (H), (I)] long timescale and [(J), (K), (L)] solvation timescale. Dashed spectra are steady state absorption (black) and emission (blue) spectra.

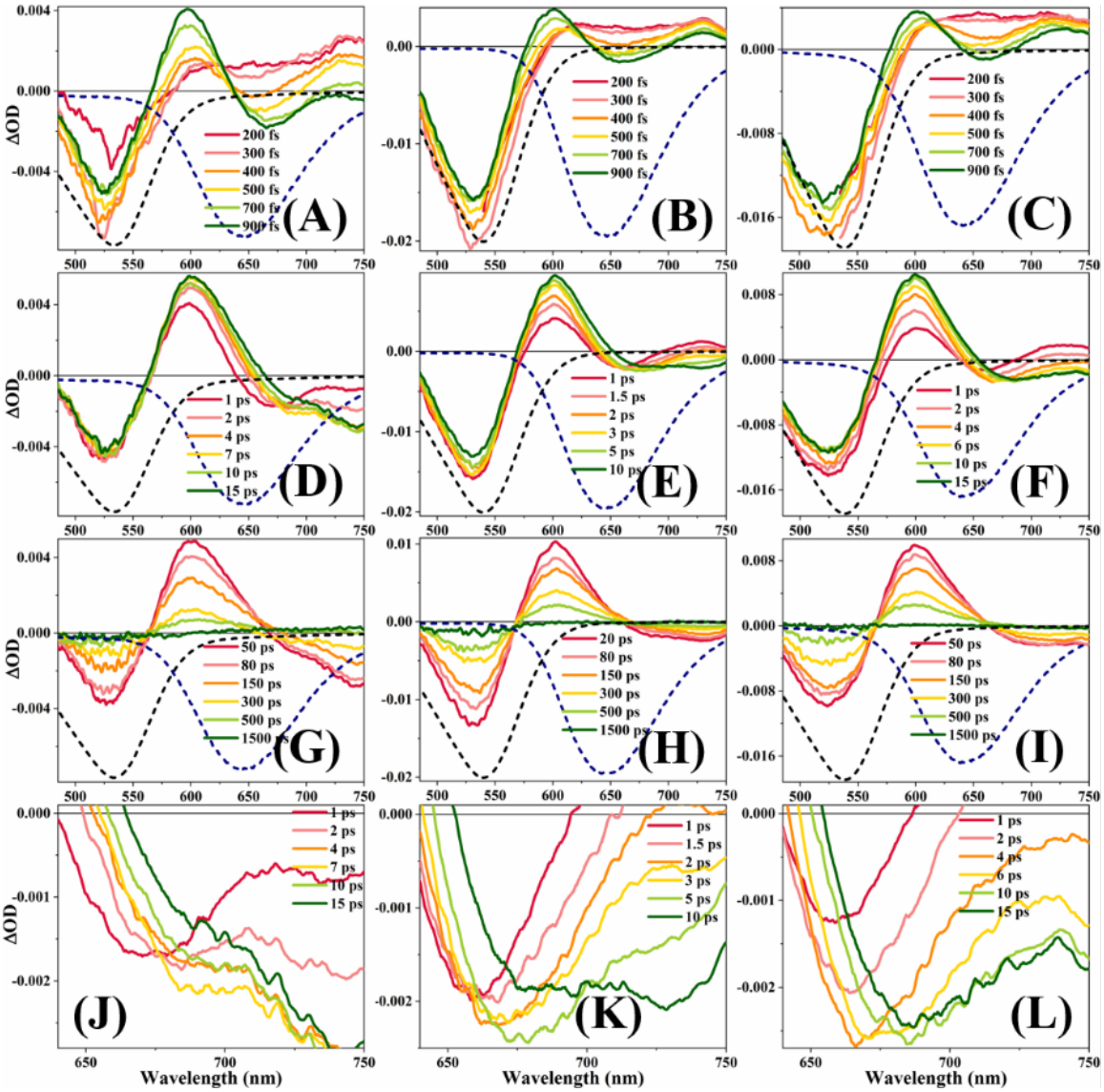

Figure B37: Transient Absorption spectra of D149 in BmimTFO-ACN [(A), (D), (G), (J)], in BmimTFO-γ-BL [(B), (E), (H), (K)] and in BmimTFO-PC [(C), (F), (I), (L)] mixtures (X_{IL}= 0.05). [(A), (B), (C)] short timescale, [(D), (E), (F)] middle timescale, [(G), (H), (I)] long timescale and [(J), (K), (L)] solvation timescale. Dashed spectra are steady state absorption (black) and emission (blue) spectra.

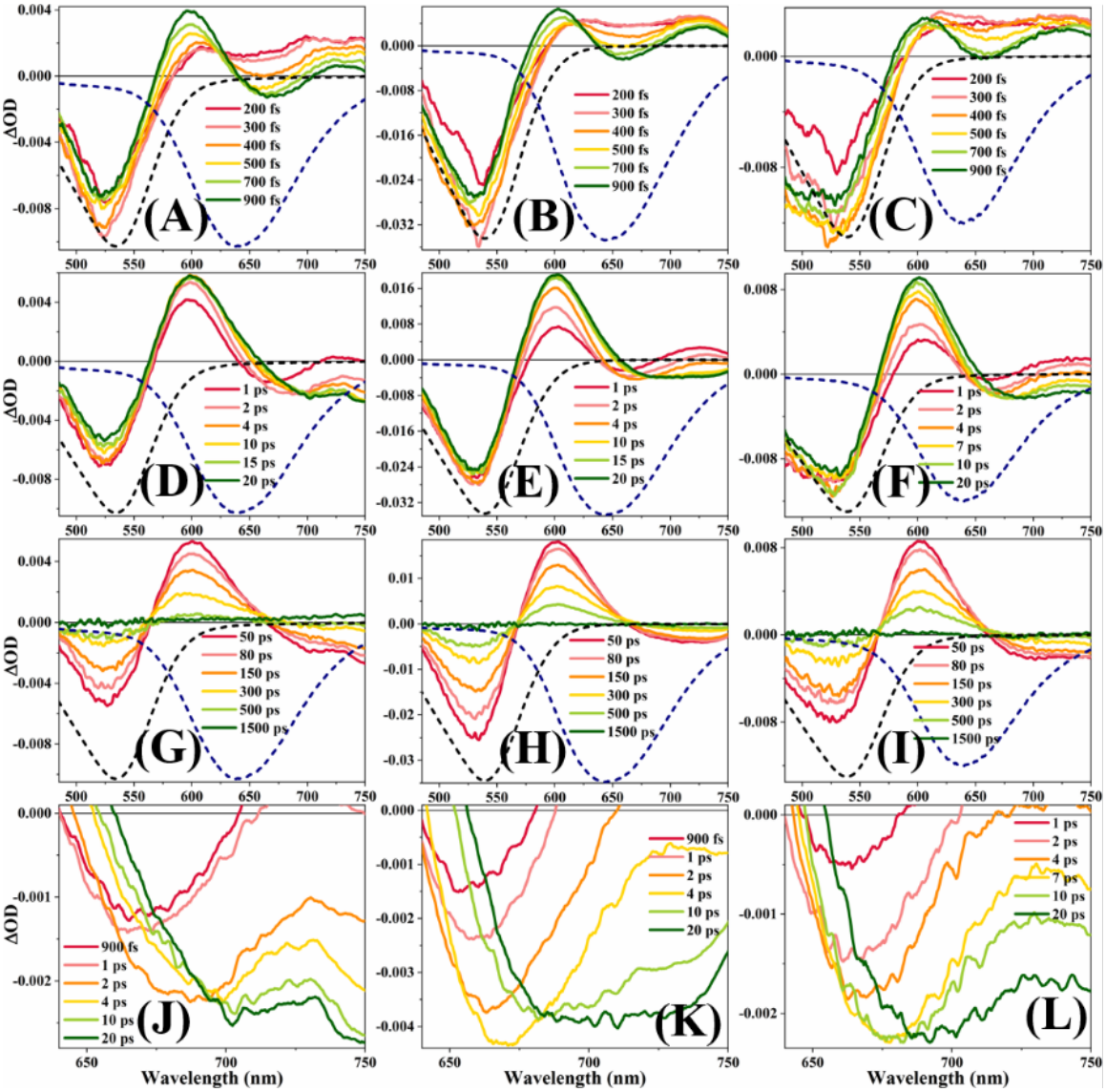

Figure B38: Transient Absorption spectra of D149 in BmimTFO-ACN [(A), (D), (G), (J)], in BmimTFO-γ-BL [(B), (E), (H), (K)] and in BmimTFO-PC [(C), (F), (I), (L)] mixtures (X_{IL}= 0.10). [(A), (B), (C)] short timescale, [(D), (E), (F)] middle timescale, [(G), (H), (I)] long timescale and [(J), (K), (L)] solvation timescale. Dashed spectra are steady state absorption (black) and emission (blue) spectra.

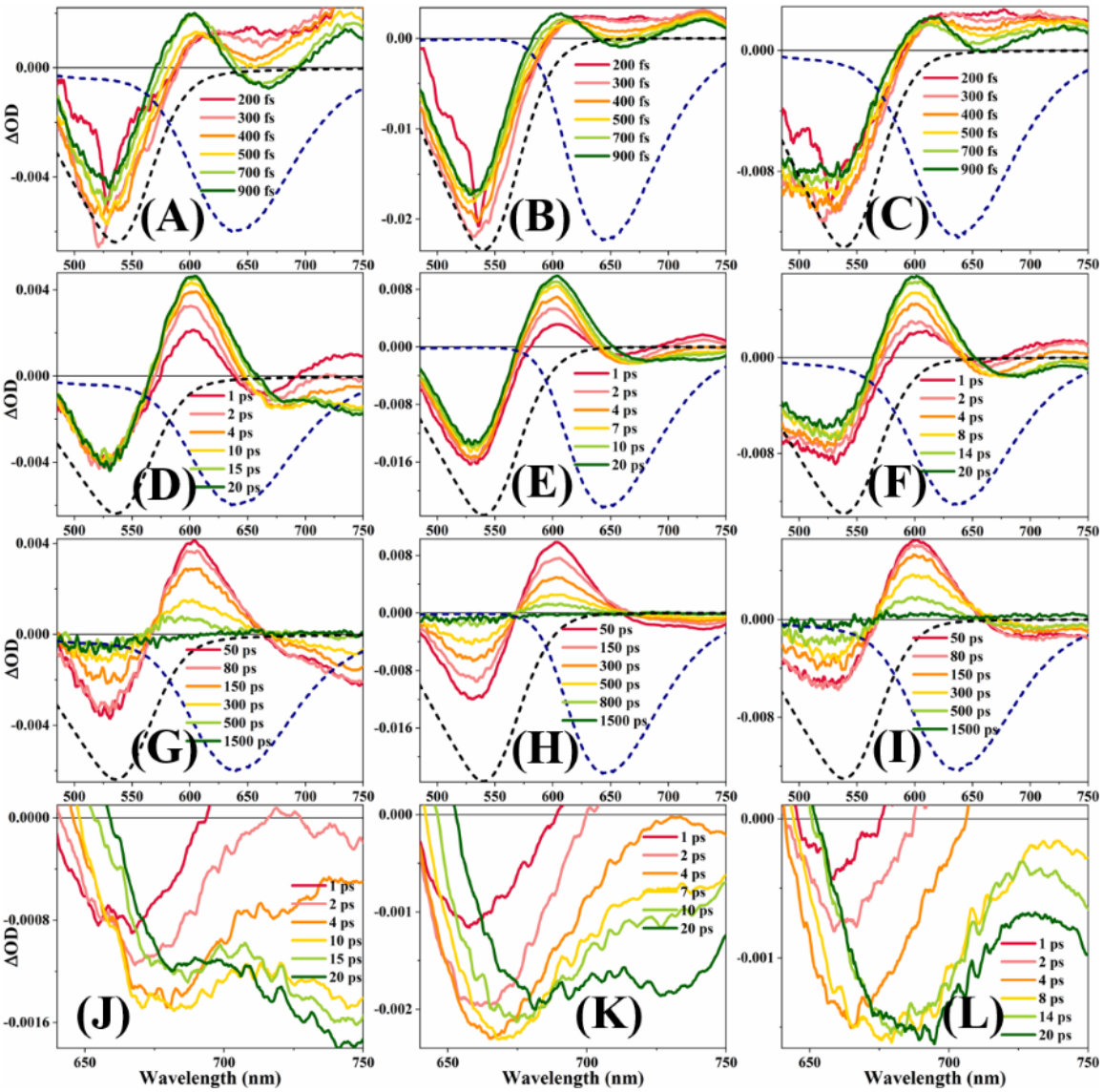

Figure B39: Transient Absorption spectra of D149 in BmimTFO-ACN [(A), (D), (G), (J)], in BmimTFO-γ-BL [(B), (E), (H), (K)] and in BmimTFO-PC [(C), (F), (I), (L)] mixtures (X_{IL}= 0.20). [(A), (B), (C)] short timescale, [(D), (E), (F)] middle timescale, [(G), (H), (I)] long timescale and [(J), (K), (L)] solvation timescale. Dashed spectra are steady state absorption (black) and emission (blue) spectra.

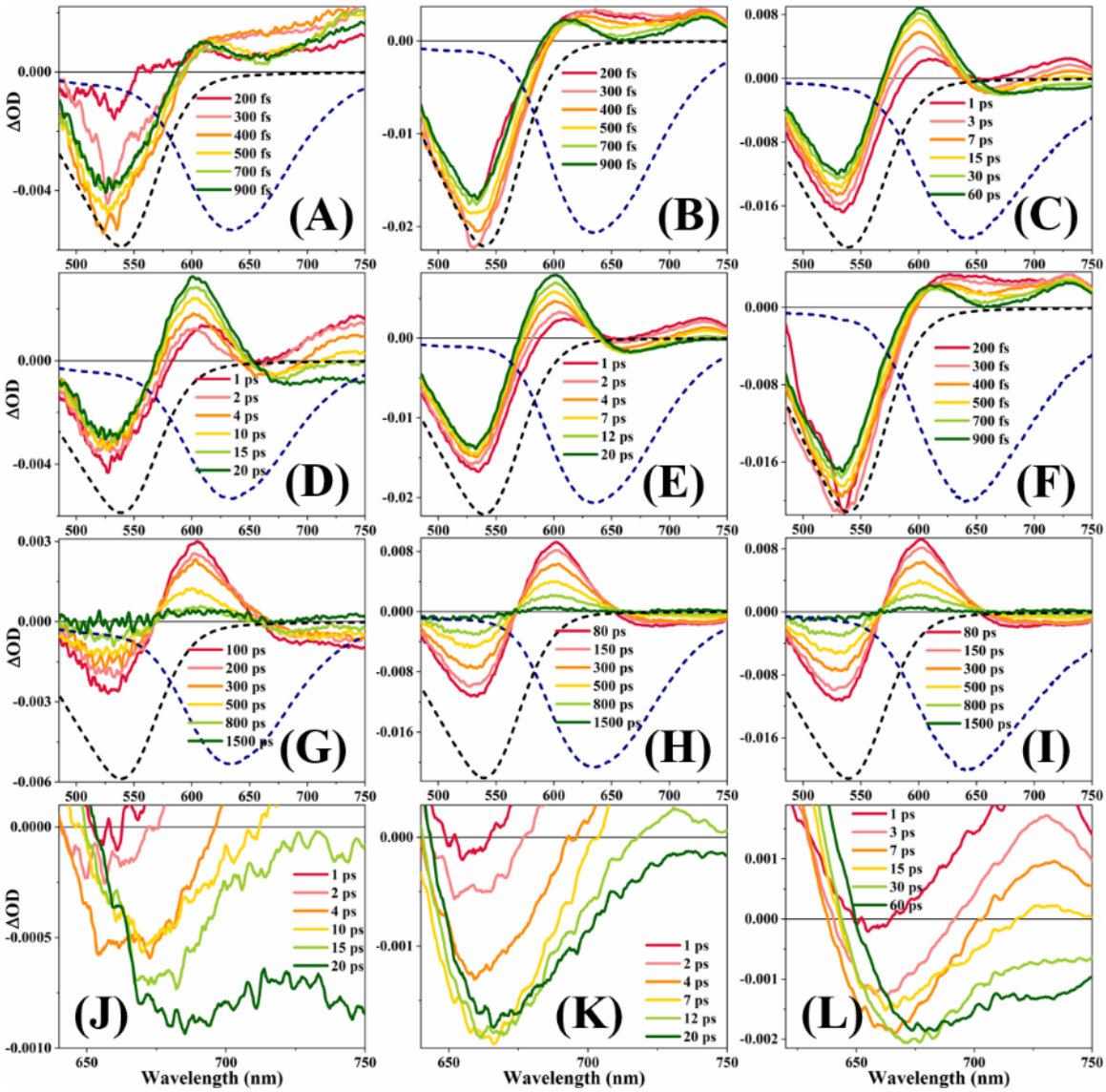

Figure B40: Transient Absorption spectra of D149 in BmimTFO-ACN [(A), (D), (G), (J)], in BmimTFO-γ-BL [(B), (E), (H), (K)] and in BmimTFO-PC [(C), (F), (I), (L)] mixtures (X_{IL}= 0.50). [(A), (B), (C)] short timescale, [(D), (E), (F)] middle timescale, [(G), (H), (I)] long timescale and [(J), (K), (L)] solvation timescale. Dashed spectra are steady state absorption (black) and emission (blue) spectra.

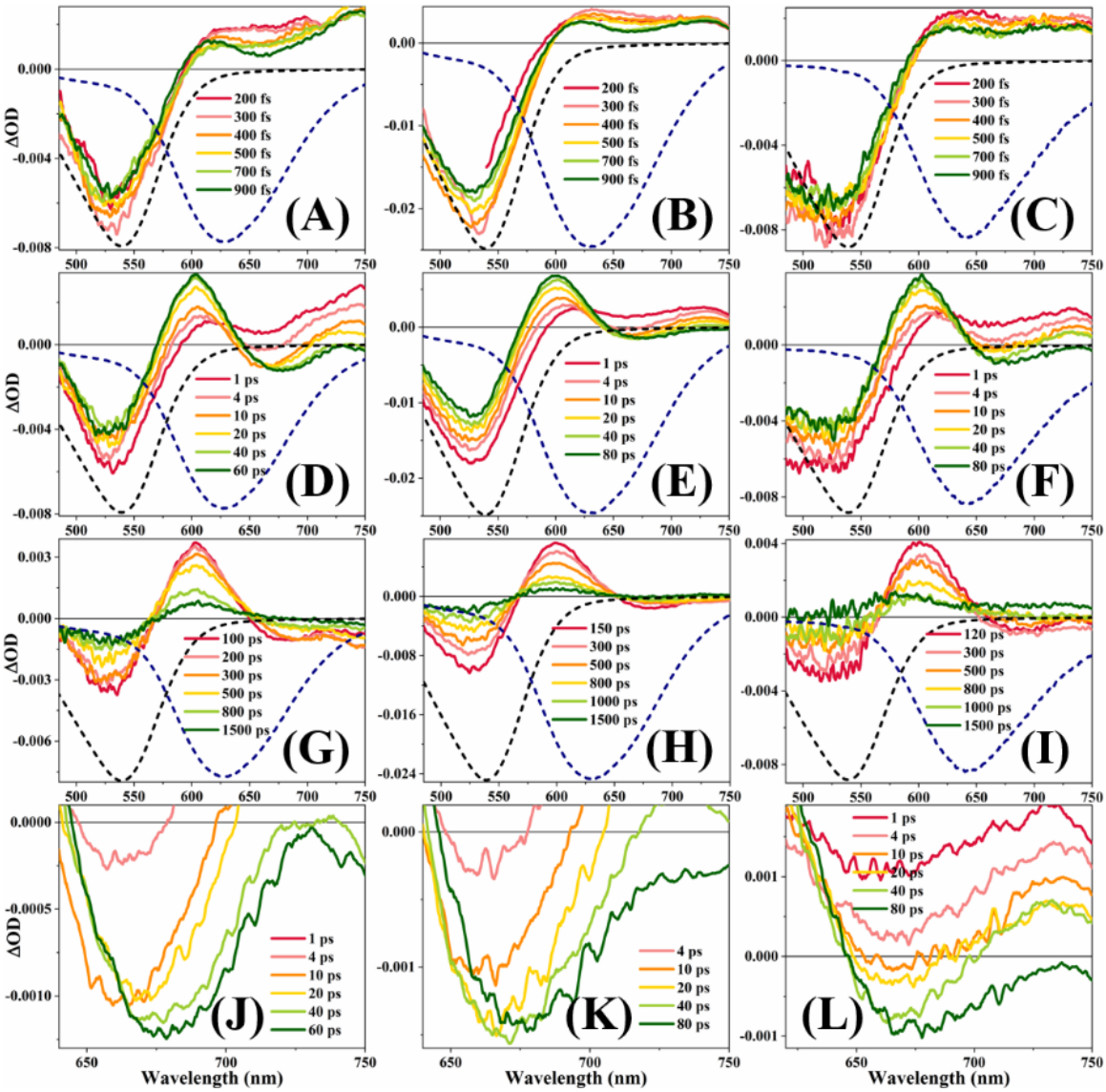

Figure B41: Transient Absorption spectra of D149 in BmimTFO-ACN [(A), (D), (G), (J)], in BmimTFO-γ-BL [(B), (E), (H), (K)] and in BmimTFO-PC [(C), (F), (I), (L)] mixtures (X_{IL}= 0.80). [(A), (B), (C)] short timescale, [(D), (E), (F)] middle timescale, [(G), (H), (I)] long timescale and [(J), (K), (L)] solvation timescale. Dashed spectra are steady state absorption (black) and emission (blue) spectra.

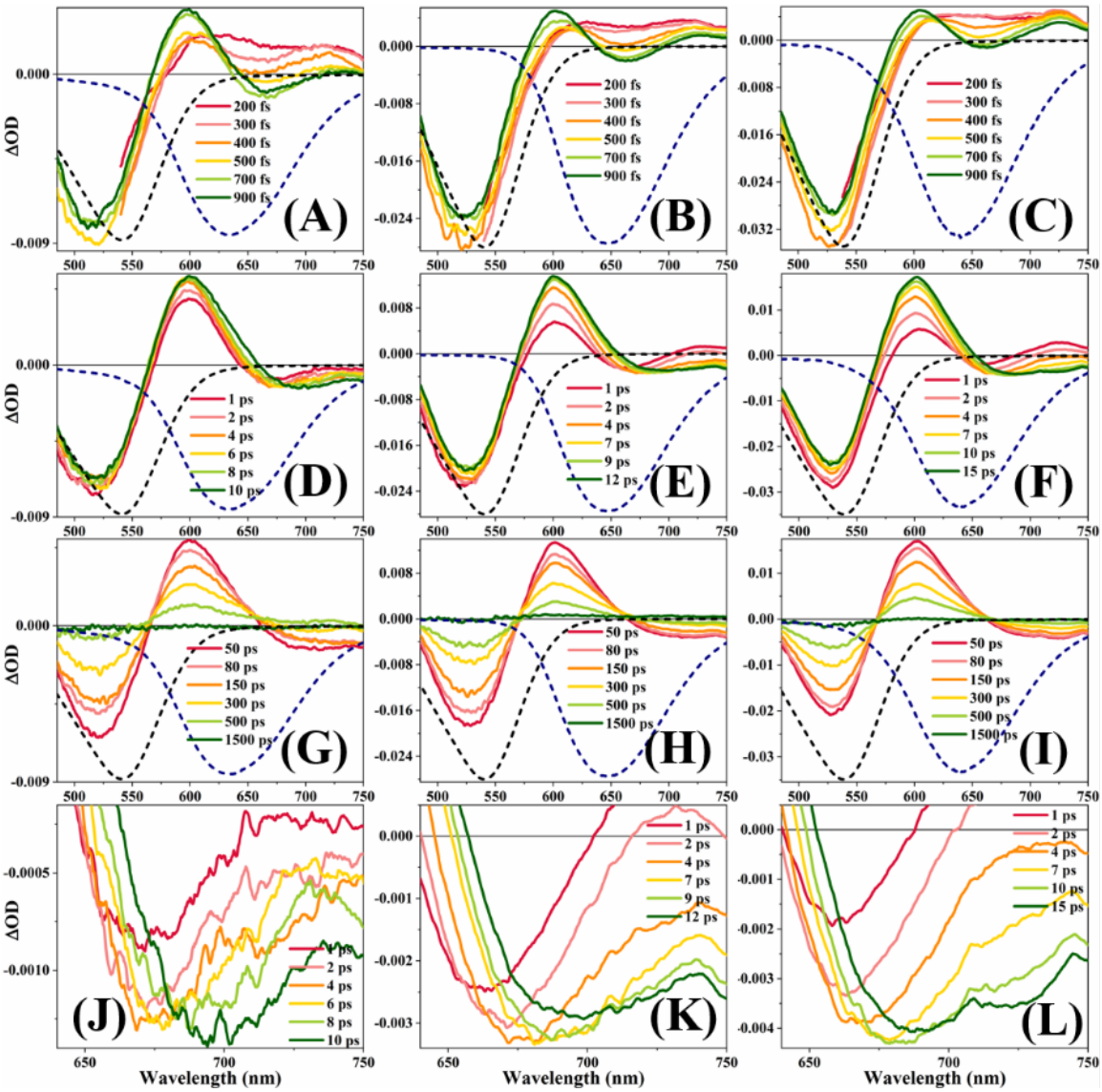

Figure B42: Transient Absorption spectra of D149 in BmimTFSI-ACN [(A), (D), (G), (J)], in BmimTFSI-γ-BL [(B), (E), (H), (K)] and in BmimTFSI-PC [(C), (F), (I), (L)] mixtures (X_{IL}= 0.05). [(A), (B), (C)] short timescale, [(D), (E), (F)] middle timescale, [(G), (H), (I)] long timescale and [(J), (K), (L)] solvation timescale. Dashed spectra are steady state absorption (black) and emission (blue) spectra.

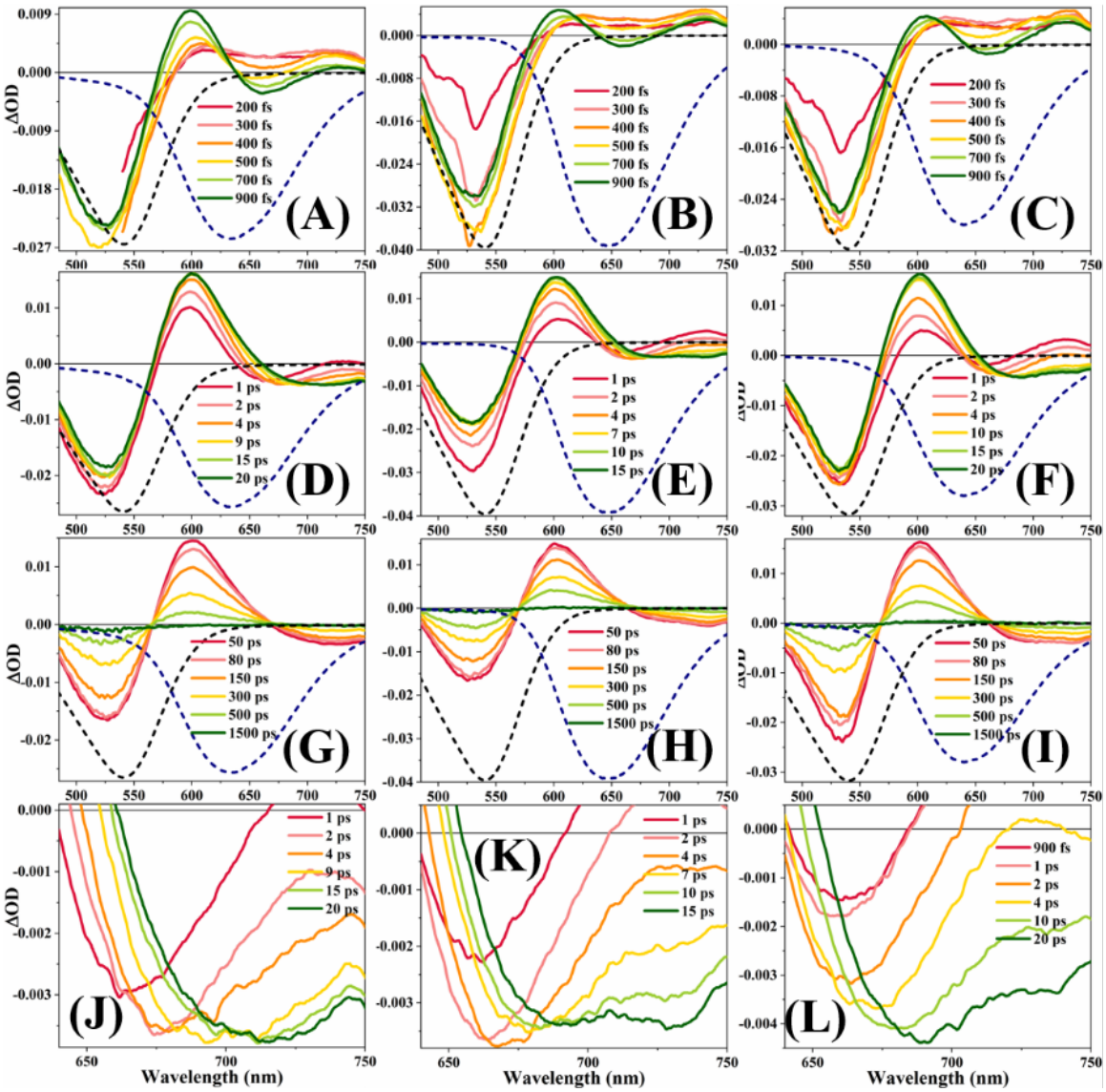

Figure B43: Transient Absorption spectra of D149 in BmimTFSI-ACN [(A), (D), (G), (J)], in BmimTFSI-γ-BL [(B), (E), (H), (K)] and in BmimTFSI-PC [(C), (F), (I), (L)] mixtures (X_{IL}= 0.10). [(A), (B), (C)] short timescale, [(D), (E), (F)] middle timescale, [(G), (H), (I)] long timescale and [(J), (K), (L)] solvation timescale. Dashed spectra are steady state absorption (black) and emission (blue) spectra.

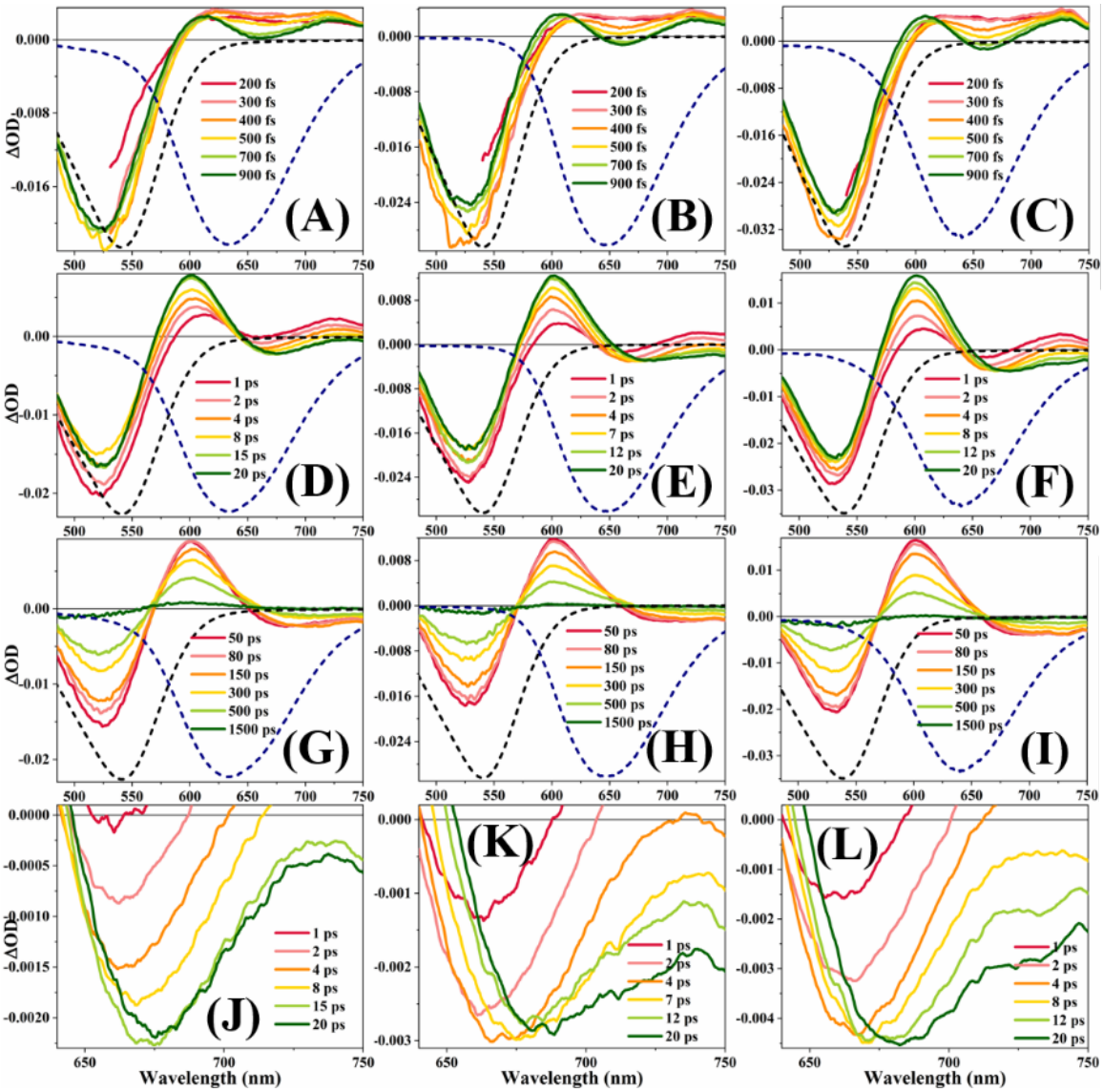

Figure B44: Transient Absorption spectra of D149 in BmimTFSI-ACN [(A), (D), (G), (J)], in BmimTFSI-γ-BL [(B), (E), (H), (K)] and in BmimTFSI-PC [(C), (F), (I), (L)] mixtures (X_{IL}= 0.20). [(A), (B), (C)] short timescale, [(D), (E), (F)] middle timescale, [(G), (H), (I)] long timescale and [(J), (K), (L)] solvation timescale. Dashed spectra are steady state absorption (black) and emission (blue) spectra.

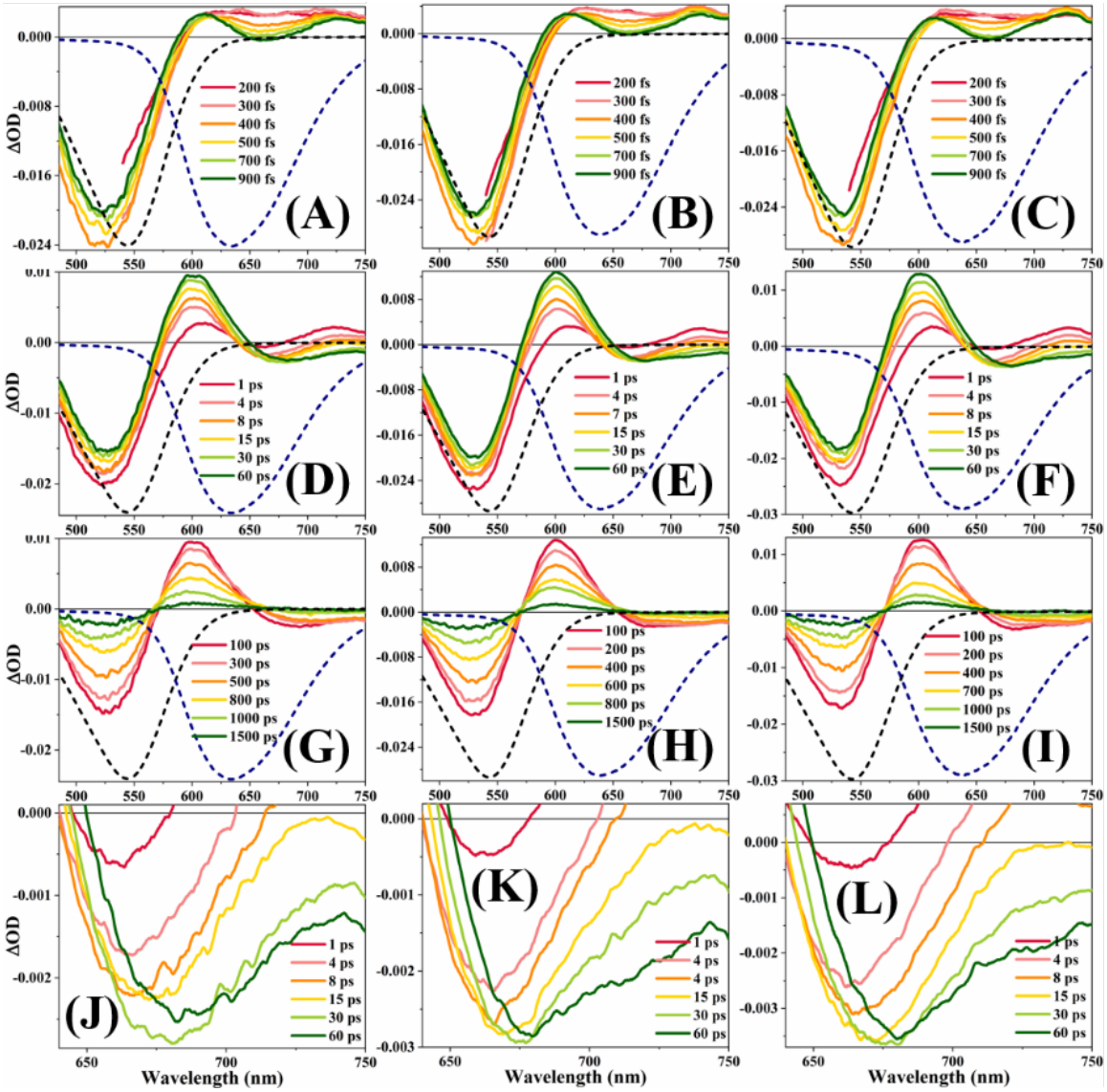

Figure B45: Transient Absorption spectra of D149 in BmimTFSI-ACN [(A), (D), (G), (J)], in BmimTFSI-γ-BL [(B), (E), (H), (K)] and in BmimTFSI-PC [(C), (F), (I), (L)] mixtures (X_{IL}= 0.50). [(A), (B), (C)] short timescale, [(D), (E), (F)] middle timescale, [(G), (H), (I)] long timescale and [(J), (K), (L)] solvation timescale. Dashed spectra are steady state absorption (black) and emission (blue) spectra.

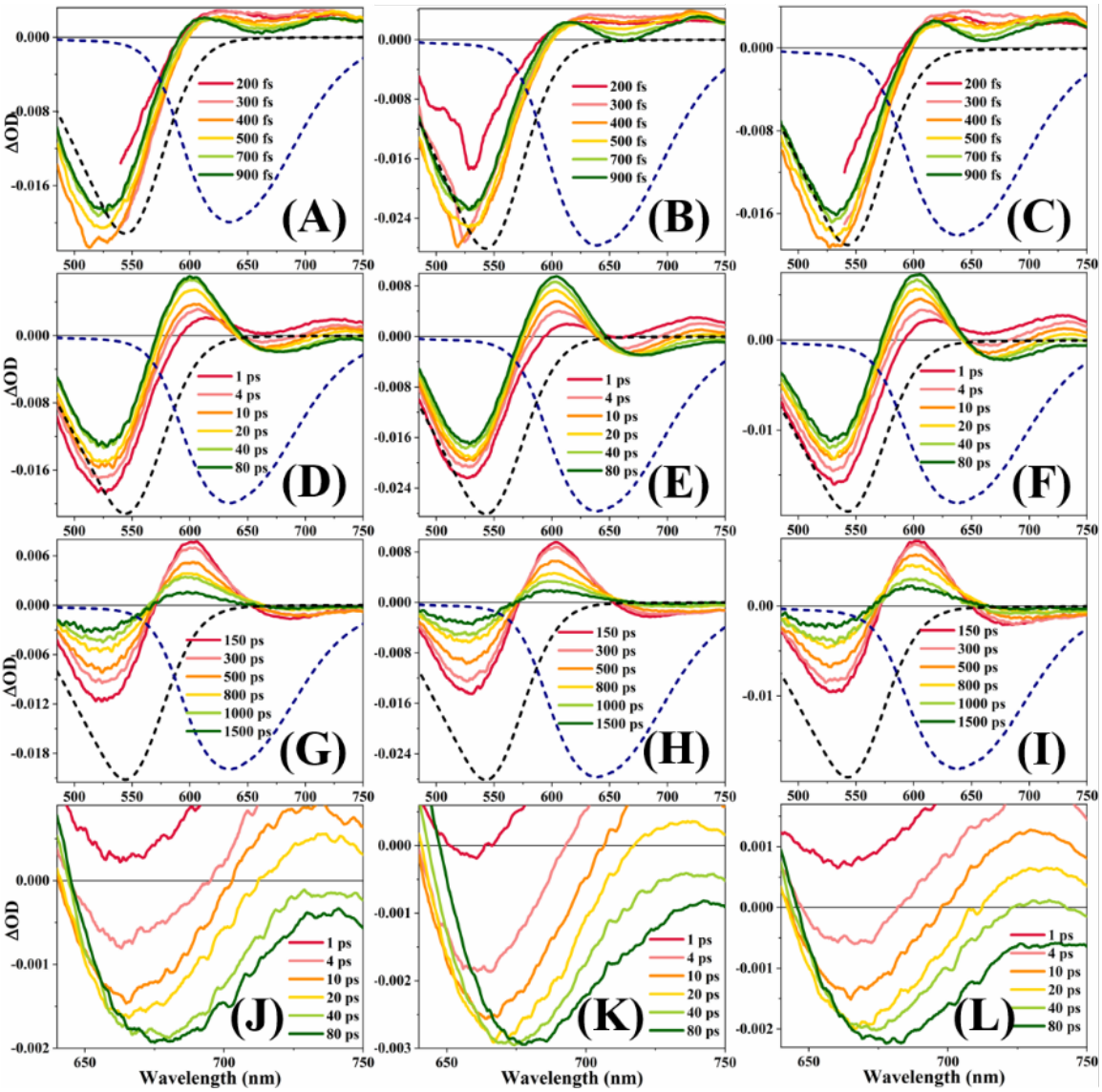

Figure B46: Transient Absorption spectra of D149 in BmimTFSI-ACN [(A), (D), (G), (J)], in BmimTFSI-γ-BL [(B), (E), (H), (K)] and in BmimTFSI-PC [(C), (F), (I), (L)] mixtures (X_{IL}= 0.80). [(A), (B), (C)] short timescale, [(D), (E), (F)] middle timescale, [(G), (H), (I)] long timescale and [(J), (K), (L)] solvation timescale. Dashed spectra are steady state absorption (black) and emission (blue) spectra.

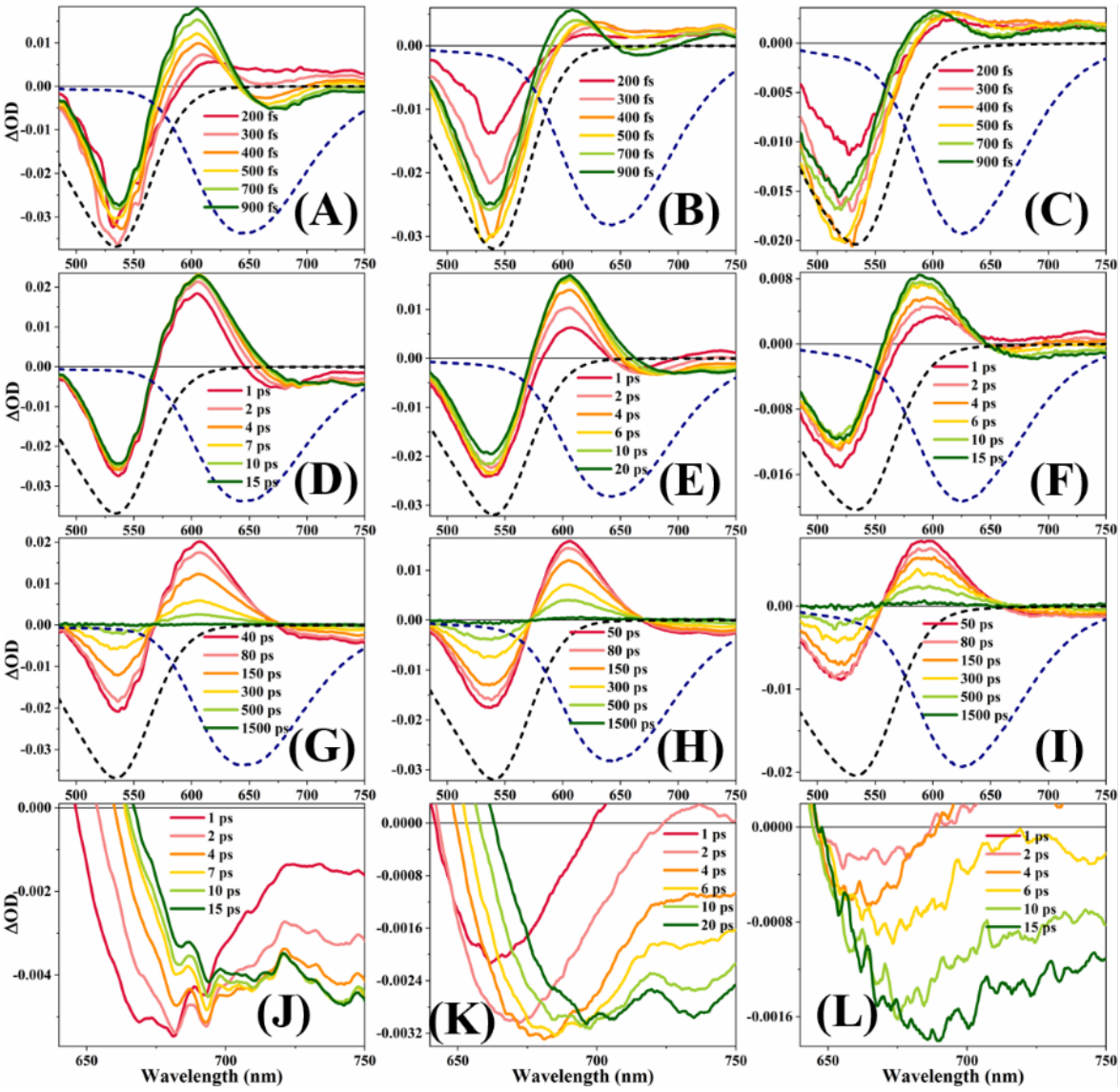

Figure B47: Transient Absorption spectra of D205 in $BmimBF_4$-ACN [(A), (D), (G), (J)], in $BmimBF_4$-γ-BL [(B), (E), (H), (K)] and in $BmimBF_4$-PC [(C), (F), (I), (L)] mixtures (X_{IL}= 0.05). [(A), (B), (C)] short timescale, [(D), (E), (F)] middle timescale, [(G), (H), (I)] long timescale and [(J), (K), (L)] solvation timescale. Dashed spectra are steady state absorption (black) and emission (blue) spectra.

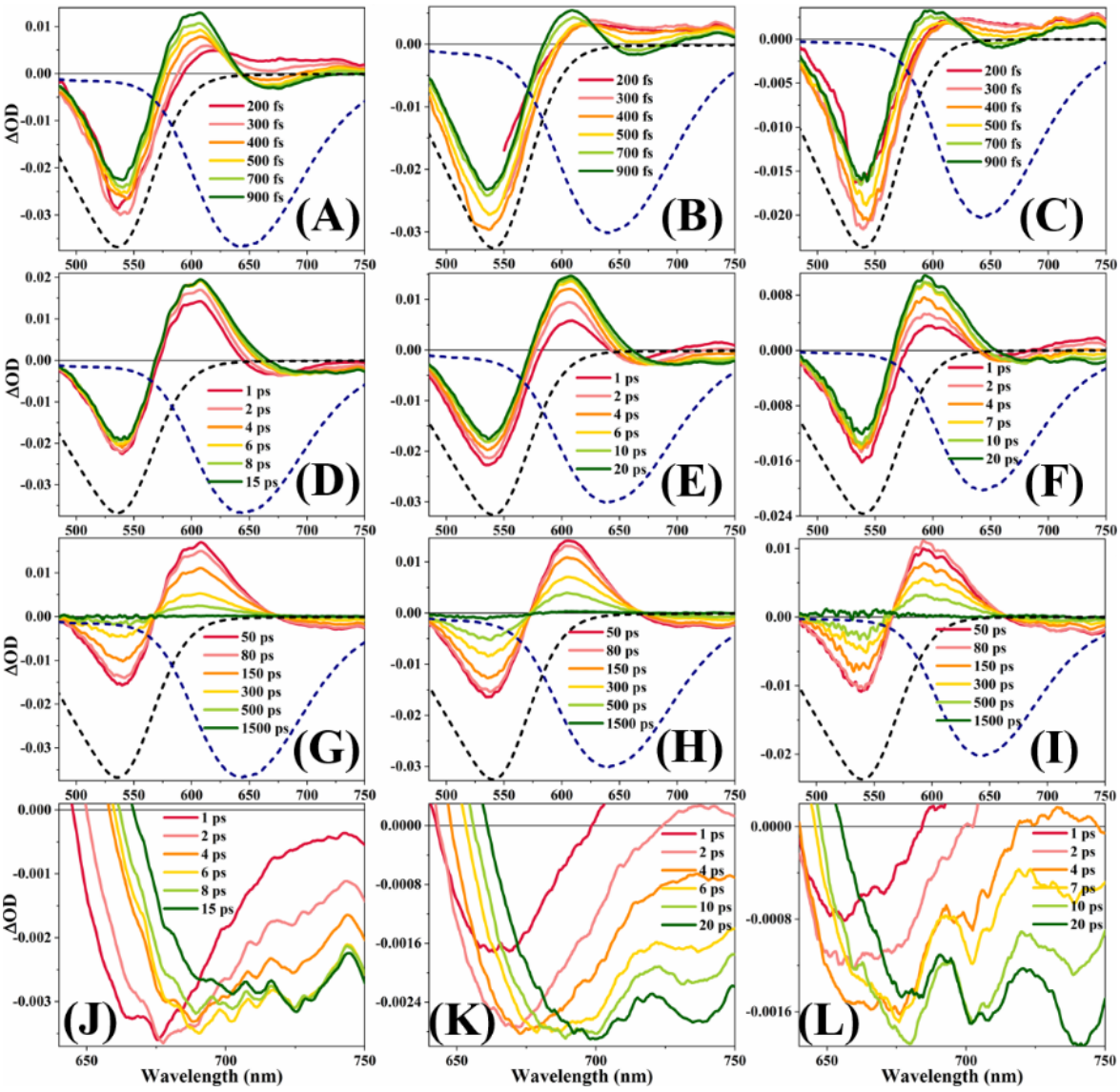

Figure B48: Transient Absorption spectra of D205 in $BmimBF_4$-ACN [(A), (D), (G), (J)], in $BmimBF_4$-γ-BL [(B), (E), (H), (K)] and in $BmimBF_4$-PC [(C), (F), (I), (L)] mixtures (X_{IL}= 0.10). [(A), (B), (C)] short timescale, [(D), (E), (F)] middle timescale, [(G), (H), (I)] long timescale and [(J), (K), (L)] solvation timescale. Dashed spectra are steady state absorption (black) and emission (blue) spectra.

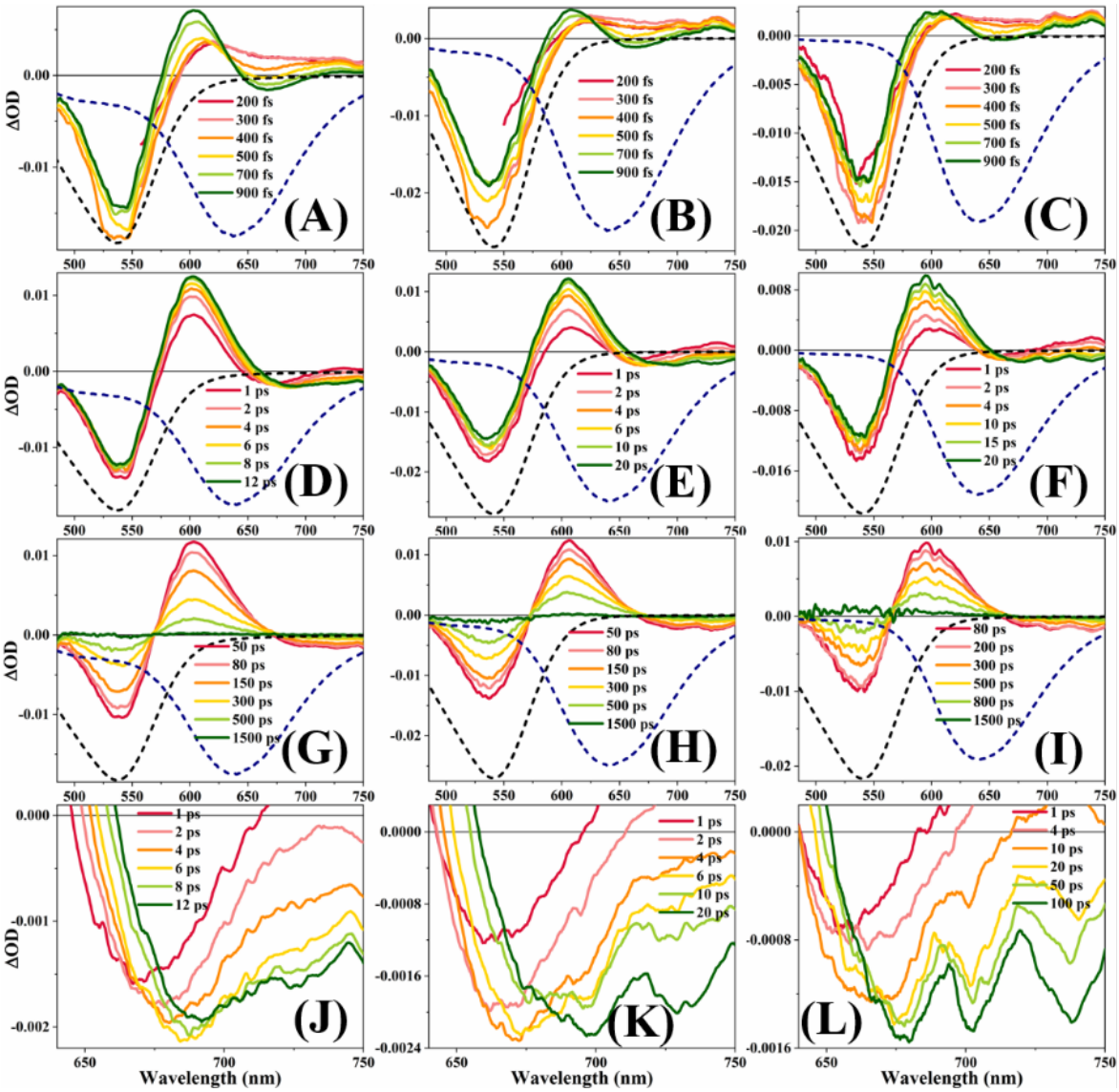

Figure B49: Transient Absorption spectra of D205 in $BmimBF_4$-ACN [(A), (D), (G), (J)], in $BmimBF_4$-γ-BL [(B), (E), (H), (K)] and in $BmimBF_4$-PC [(C), (F), (I), (L)] mixtures (X_{IL}= 0.20). [(A), (B), (C)] short timescale, [(D), (E), (F)] middle timescale, [(G), (H), (I)] long timescale and [(J), (K), (L)] solvation timescale. Dashed spectra are steady state absorption (black) and emission (blue) spectra.

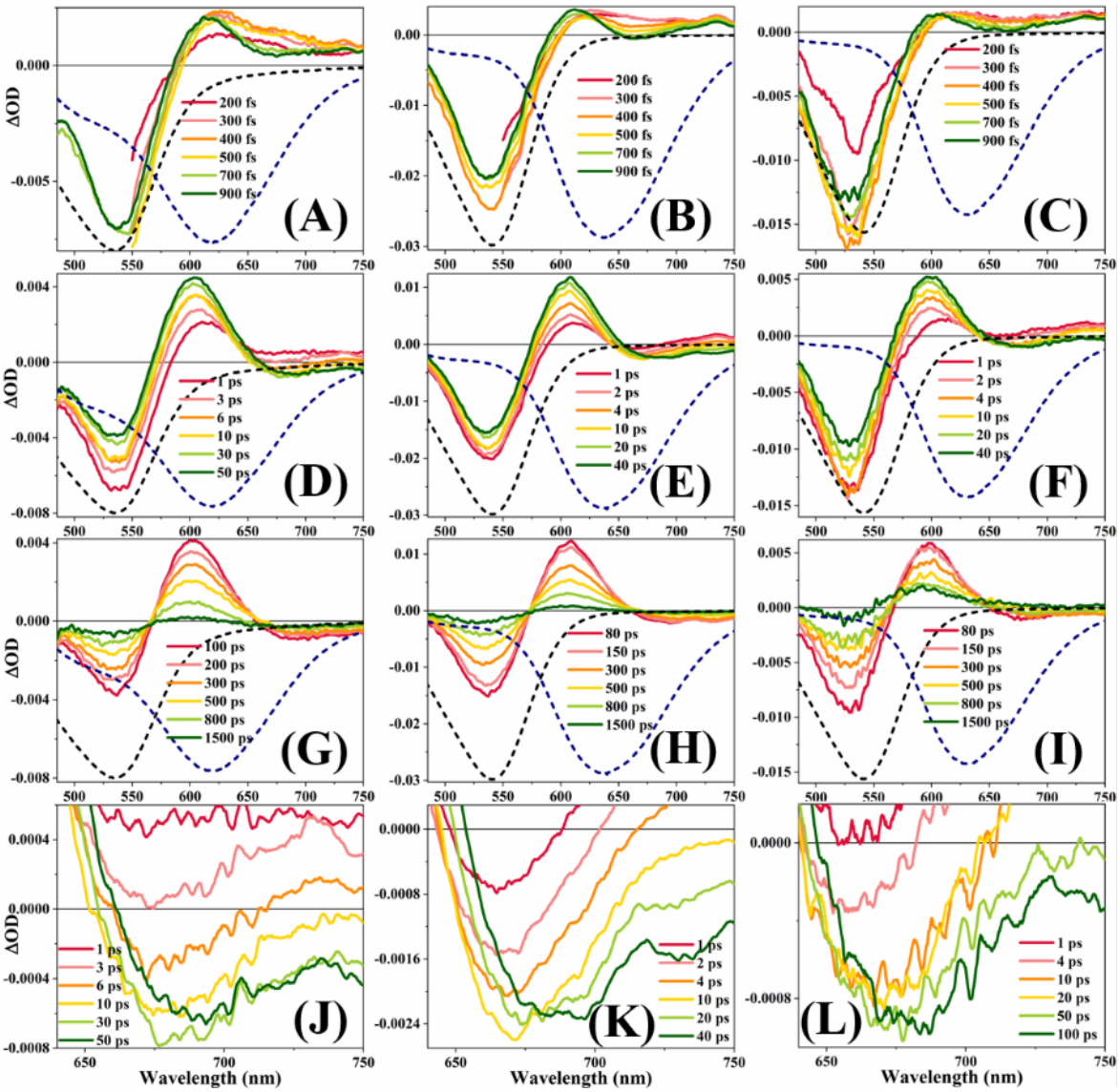

Figure B50: Transient Absorption spectra of D205 in $BmimBF_4$-ACN [(A), (D), (G), (J)], in $BmimBF_4$-γ-BL [(B), (E), (H), (K)] and in $BmimBF_4$-PC [(C), (F), (I), (L)] mixtures (X_{IL}= 0.50). [(A), (B), (C)] short timescale, [(D), (E), (F)] middle timescale, [(G), (H), (I)] long timescale and [(J), (K), (L)] solvation timescale. Dashed spectra are steady state absorption (black) and emission (blue) spectra.

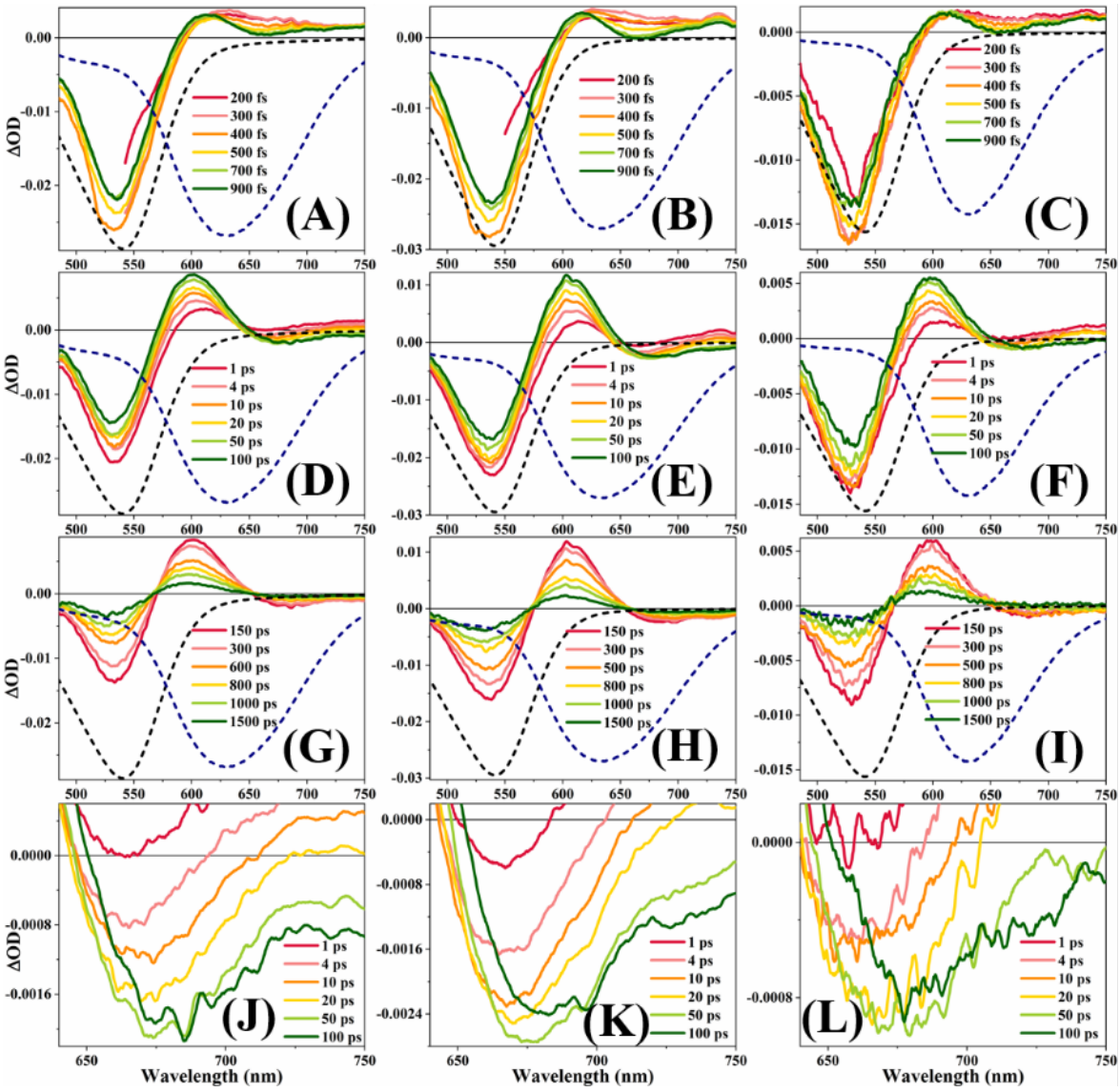

Figure B51: Transient Absorption spectra of D205 in $BmimBF_4$-ACN [(A), (D), (G), (J)], in $BmimBF_4$-γ-BL [(B), (E), (H), (K)] and in $BmimBF_4$-PC [(C), (F), (I), (L)] mixtures (X_{IL}= 0.80). [(A), (B), (C)] short timescale, [(D), (E), (F)] middle timescale, [(G), (H), (I)] long timescale and [(J), (K), (L)] solvation timescale. Dashed spectra are steady state absorption (black) and emission (blue) spectra.

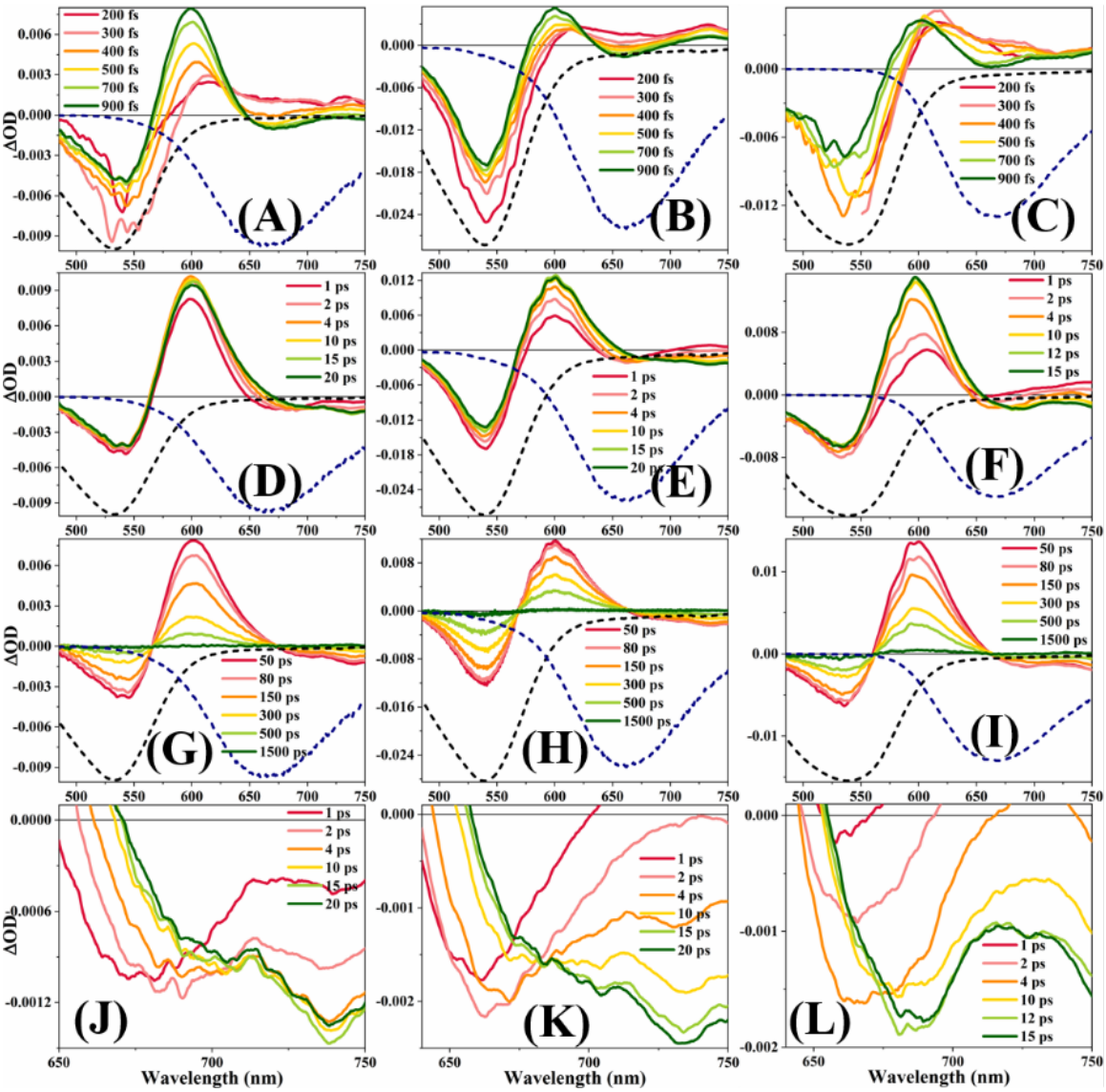

Figure B52: Transient Absorption spectra of D205 in $BmimPF_6$-ACN [(A), (D), (G), (J)], in $BmimPF_6$-γ-BL [(B), (E), (H), (K)] and in $BmimPF_6$-PC [(C), (F), (I), (L)] mixtures (X_{IL}= 0.05). [(A), (B), (C)] short timescale, [(D), (E), (F)] middle timescale, [(G), (H), (I)] long timescale and [(J), (K), (L)] solvation timescale. Dashed spectra are steady state absorption (black) and emission (blue) spectra.

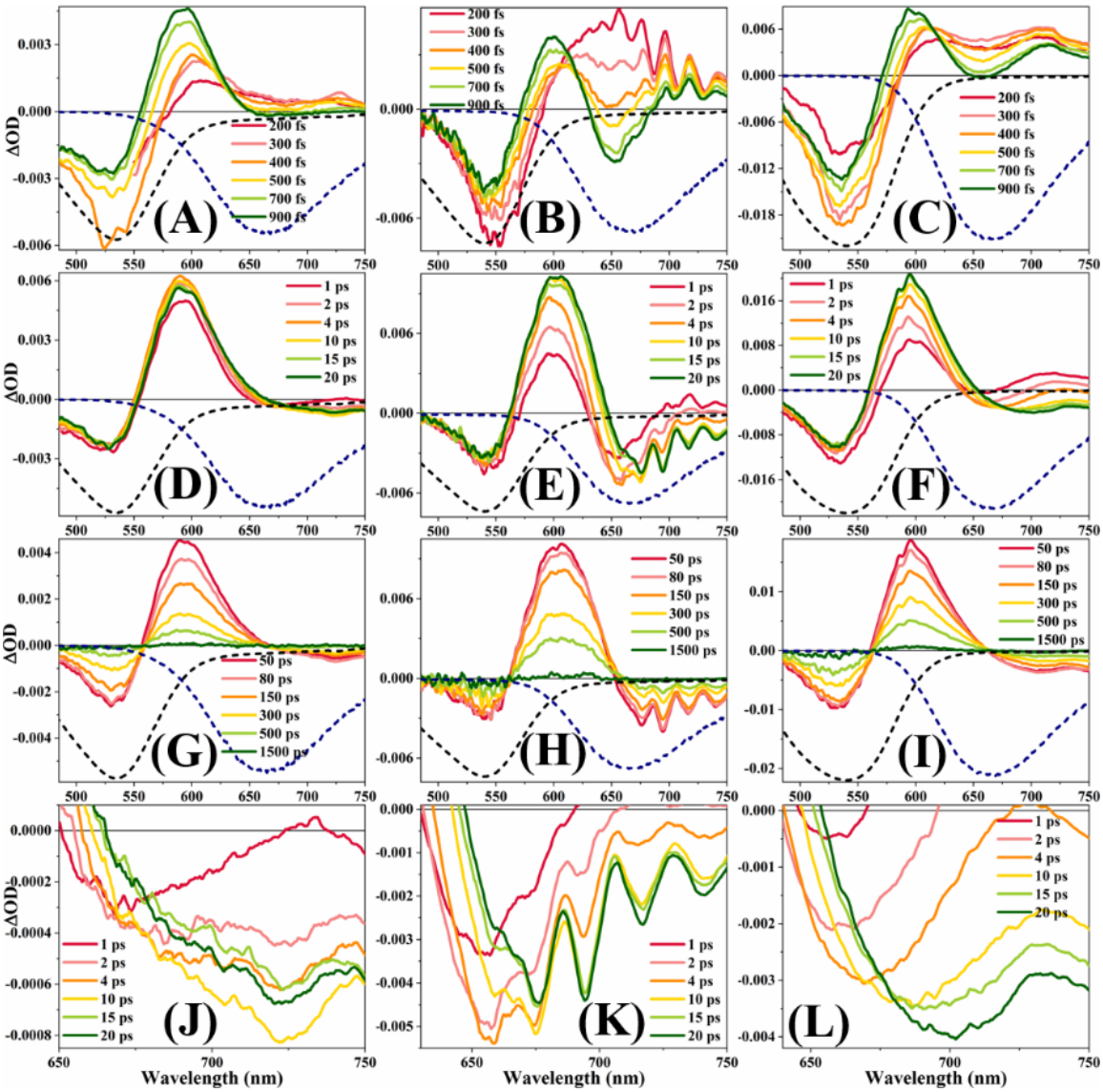

Figure B53: Transient Absorption spectra of D205 in $BmimPF_6$-ACN [(A), (D), (G), (J)], in $BmimPF_6$-γ-BL [(B), (E), (H), (K)] and in $BmimPF_6$-PC [(C), (F), (I), (L)] mixtures (X_{IL}= 0.10). [(A), (B), (C)] short timescale, [(D), (E), (F)] middle timescale, [(G), (H), (I)] long timescale and [(J), (K), (L)] solvation timescale. Dashed spectra are steady state absorption (black) and emission (blue) spectra.

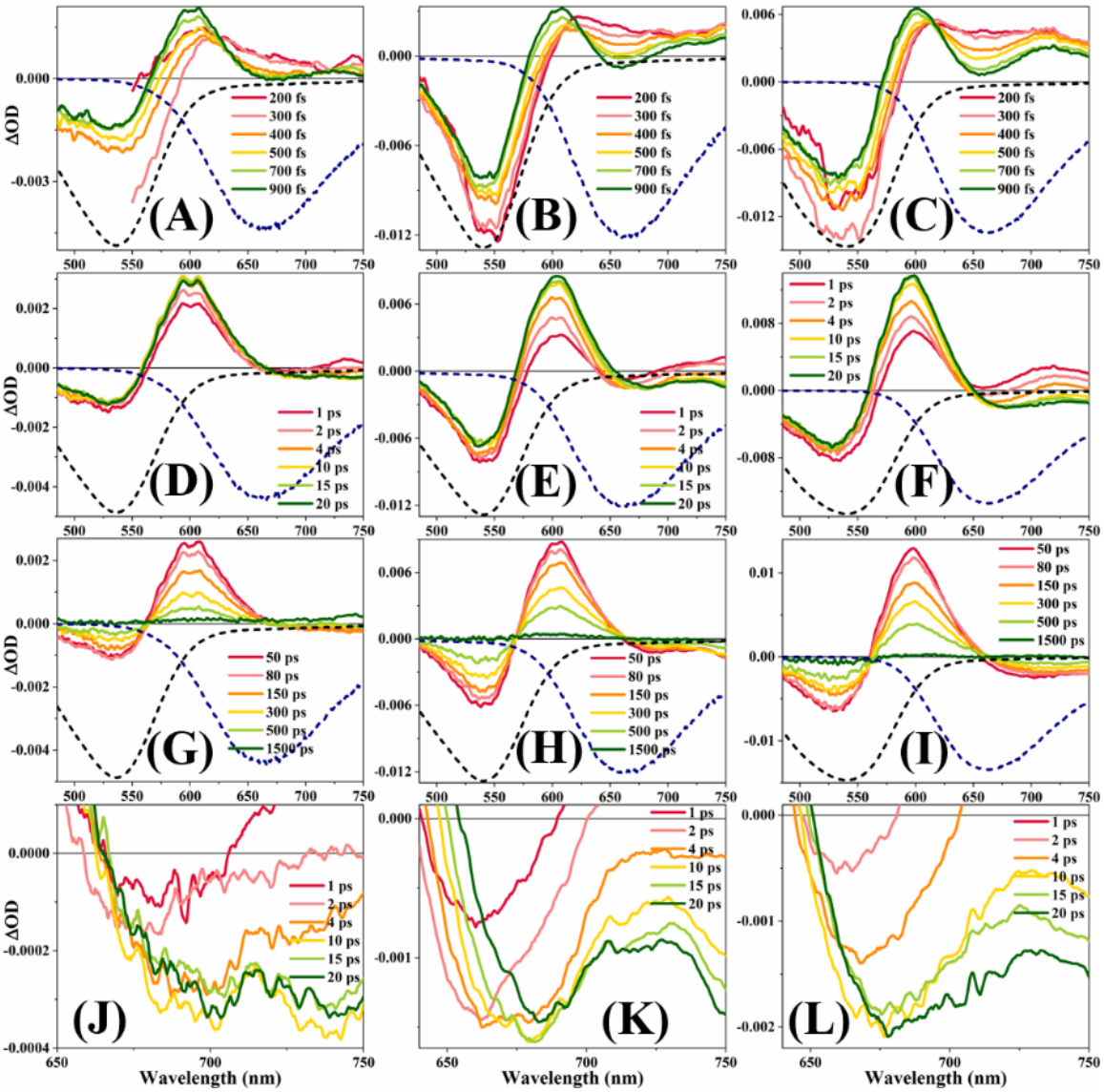

Figure B54: Transient Absorption spectra of D205 in $BmimPF_6$-ACN [(A), (D), (G), (J)], in $BmimPF_6$-γ-BL [(B), (E), (H), (K)] and in $BmimPF_6$-PC [(C), (F), (I), (L)] mixtures (X_{IL}= 0.20). [(A), (B), (C)] short timescale, [(D), (E), (F)] middle timescale, [(G), (H), (I)] long timescale and [(J), (K), (L)] solvation timescale. Dashed spectra are steady state absorption (black) and emission (blue) spectra.

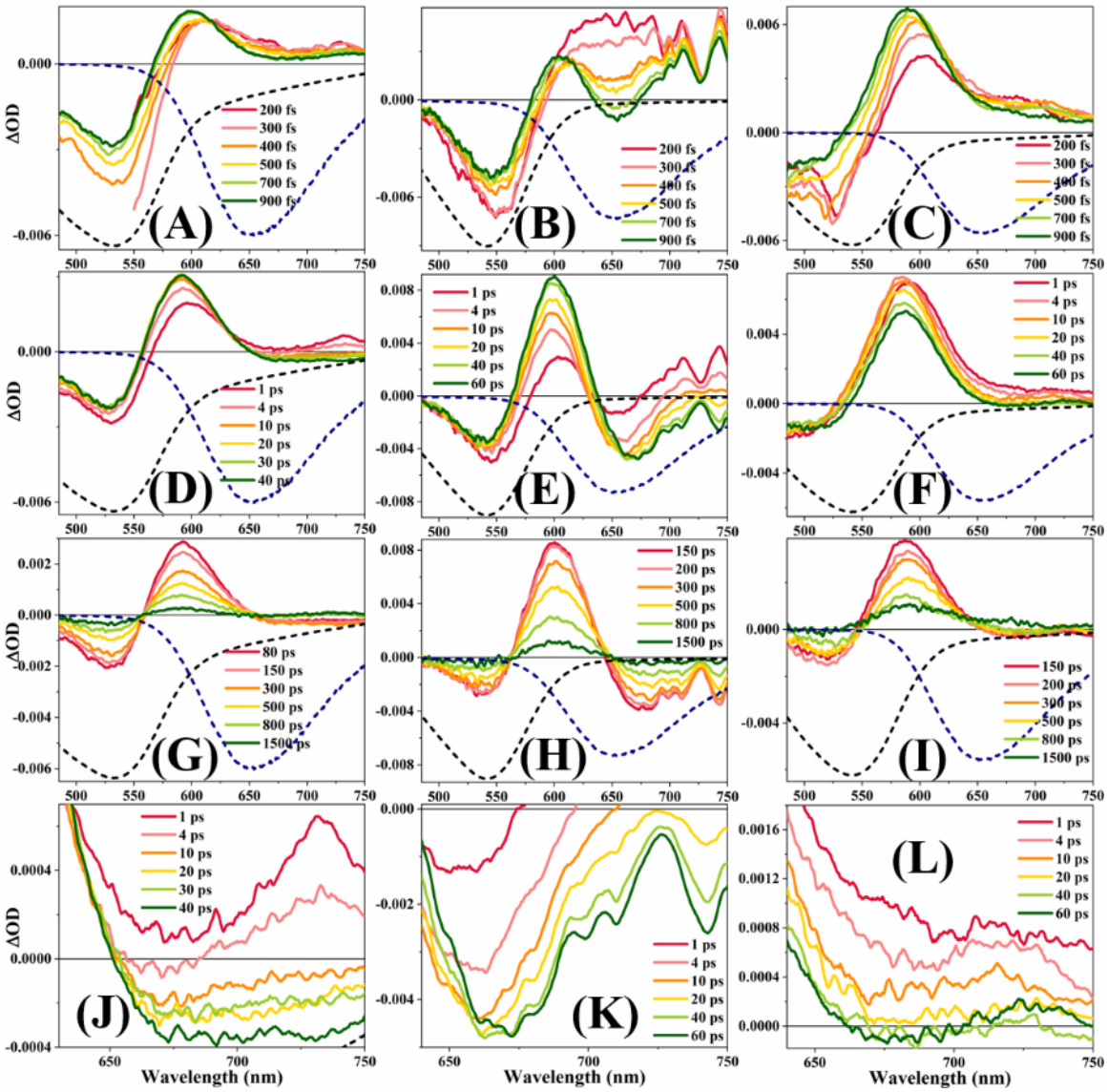

Figure B55: Transient Absorption spectra of D205 in BmimPF$_6$-ACN [(A), (D), (G), (J)], in BmimPF$_6$-γ-BL [(B), (E), (H), (K)] and in BmimPF$_6$-PC [(C), (F), (I), (L)] mixtures (X_{IL}= 0.50). [(A), (B), (C)] short timescale, [(D), (E), (F)] middle timescale, [(G), (H), (I)] long timescale and [(J), (K), (L)] solvation timescale. Dashed spectra are steady state absorption (black) and emission (blue) spectra.

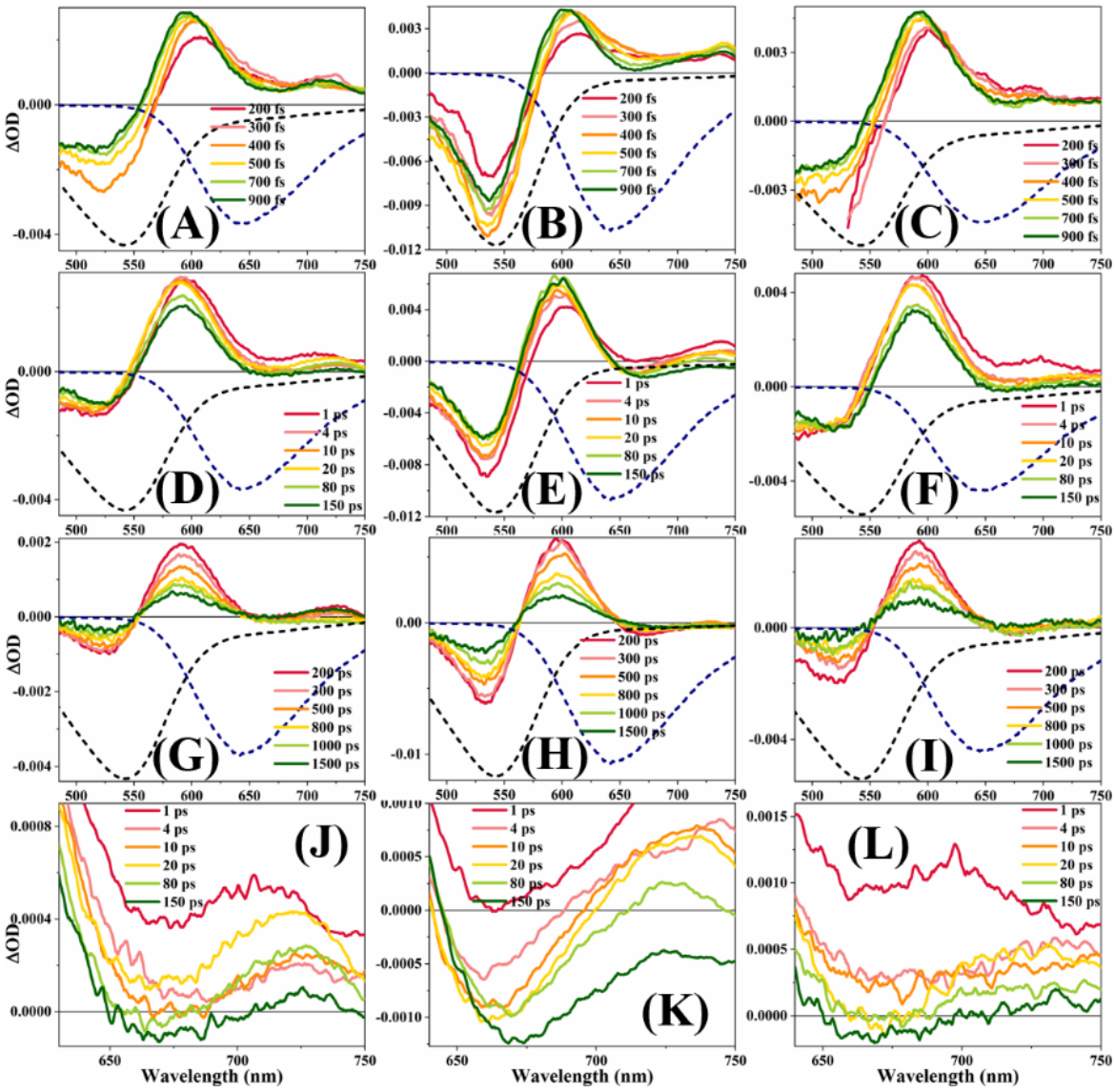

Figure B56: Transient Absorption spectra of D205 in $BmimPF_6$-ACN [(A), (D), (G), (J)], in $BmimPF_6$-γ-BL [(B), (E), (H), (K)] and in $BmimPF_6$-PC [(C), (F), (I), (L)] mixtures (X_{IL}= 0.80). [(A), (B), (C)] short timescale, [(D), (E), (F)] middle timescale, [(G), (H), (I)] long timescale and [(J), (K), (L)] solvation timescale. Dashed spectra are steady state absorption (black) and emission (blue) spectra.

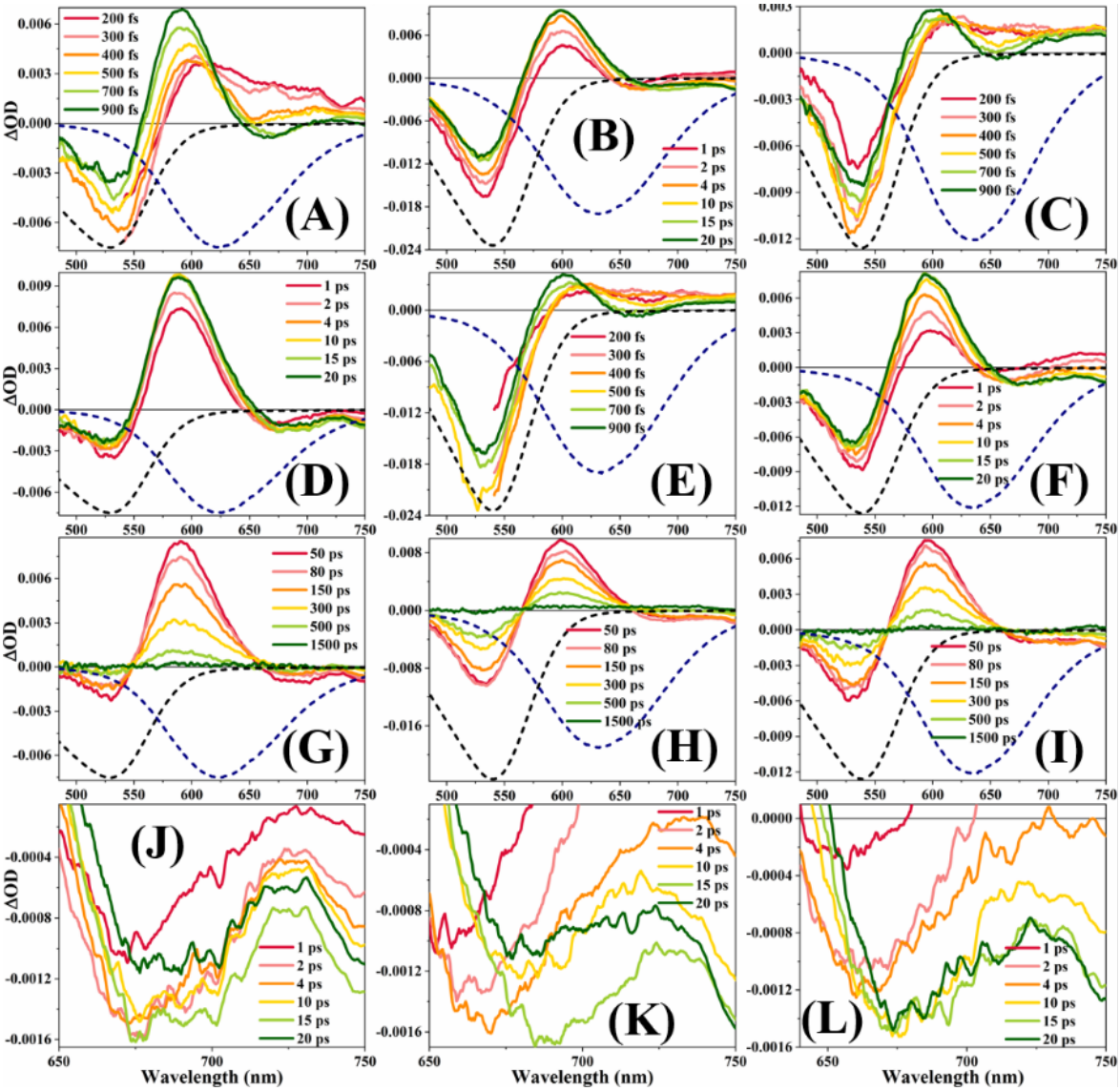

Figure B57: Transient Absorption spectra of D205 in BmimTFO-ACN [(A), (D), (G), (J)], in BmimTFO-γ-BL [(B), (E), (H), (K)] and in BmimTFO-PC [(C), (F), (I), (L)] mixtures (X_{IL}= 0.05). [(A), (B), (C)] short timescale, [(D), (E), (F)] middle timescale, [(G), (H), (I)] long timescale and [(J), (K), (L)] solvation timescale. Dashed spectra are steady state absorption (black) and emission (blue) spectra.

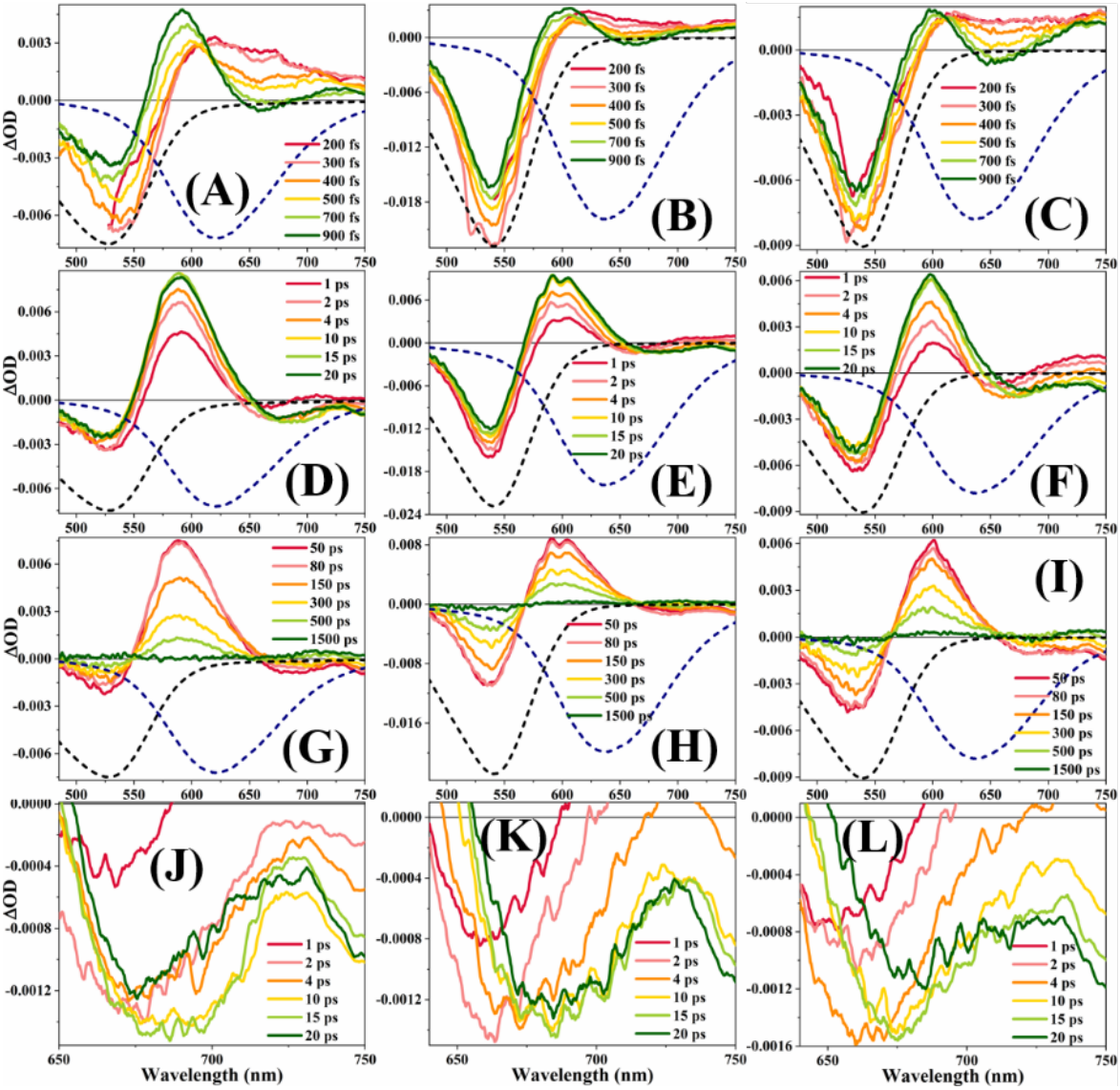

Figure B58: Transient Absorption spectra of D205 in BmimTFO-ACN [(A), (D), (G), (J)], in BmimTFO-γ-BL [(B), (E), (H), (K)] and in BmimTFO-PC [(C), (F), (I), (L)] mixtures (X_{IL}= 0.10). [(A), (B), (C)] short timescale, [(D), (E), (F)] middle timescale, [(G), (H), (I)] long timescale and [(J), (K), (L)] solvation timescale. Dashed spectra are steady state absorption (black) and emission (blue) spectra.

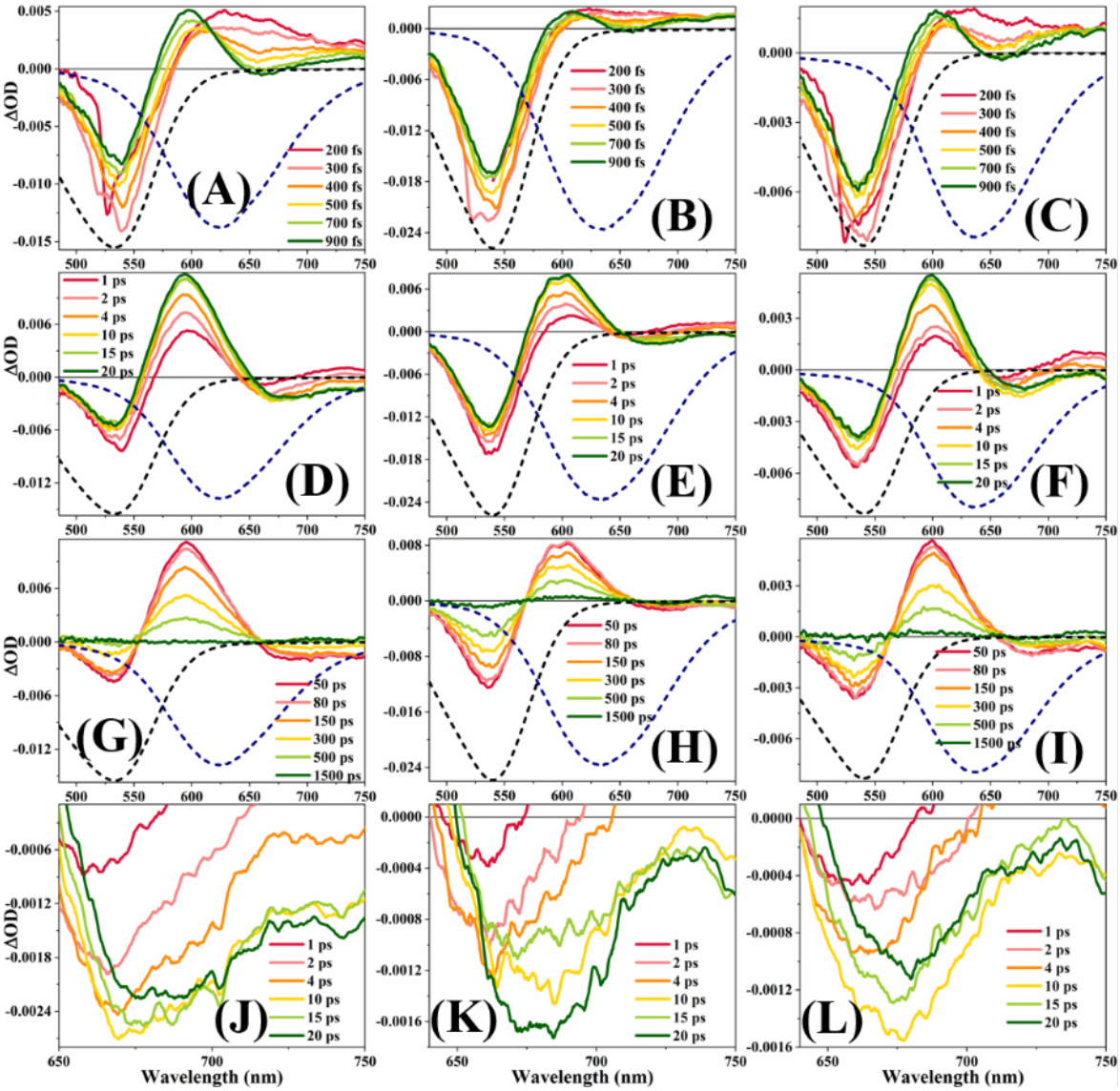

Figure B59: Transient Absorption spectra of D205 in BmimTFO-ACN [(A), (D), (G), (J)], in BmimTFO-γ-BL [(B), (E), (H), (K)] and in BmimTFO-PC [(C), (F), (I), (L)] mixtures (X_{IL}= 0.20). [(A), (B), (C)] short timescale, [(D), (E), (F)] middle timescale, [(G), (H), (I)] long timescale and [(J), (K), (L)] solvation timescale. Dashed spectra are steady state absorption (black) and emission (blue) spectra.

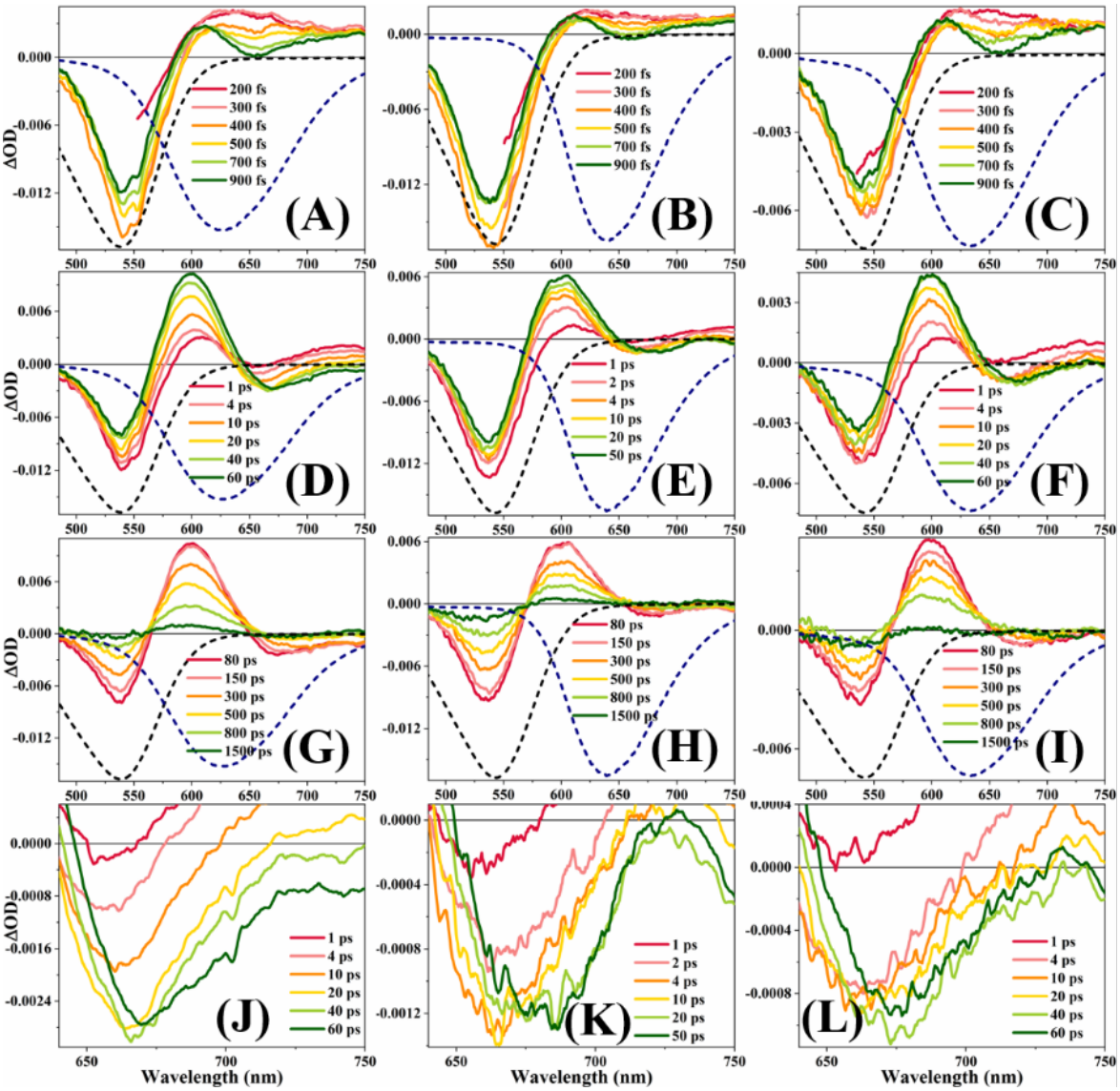

Figure B60: Transient Absorption spectra of D205 in BmimTFO-ACN [(A), (D), (G), (J)], in BmimTFO-γ-BL [(B), (E), (H), (K)] and in BmimTFO-PC [(C), (F), (I), (L)] mixtures (X_{IL}= 0.50). [(A), (B), (C)] short timescale, [(D), (E), (F)] middle timescale, [(G), (H), (I)] long timescale and [(J), (K), (L)] solvation timescale. Dashed spectra are steady state absorption (black) and emission (blue) spectra.

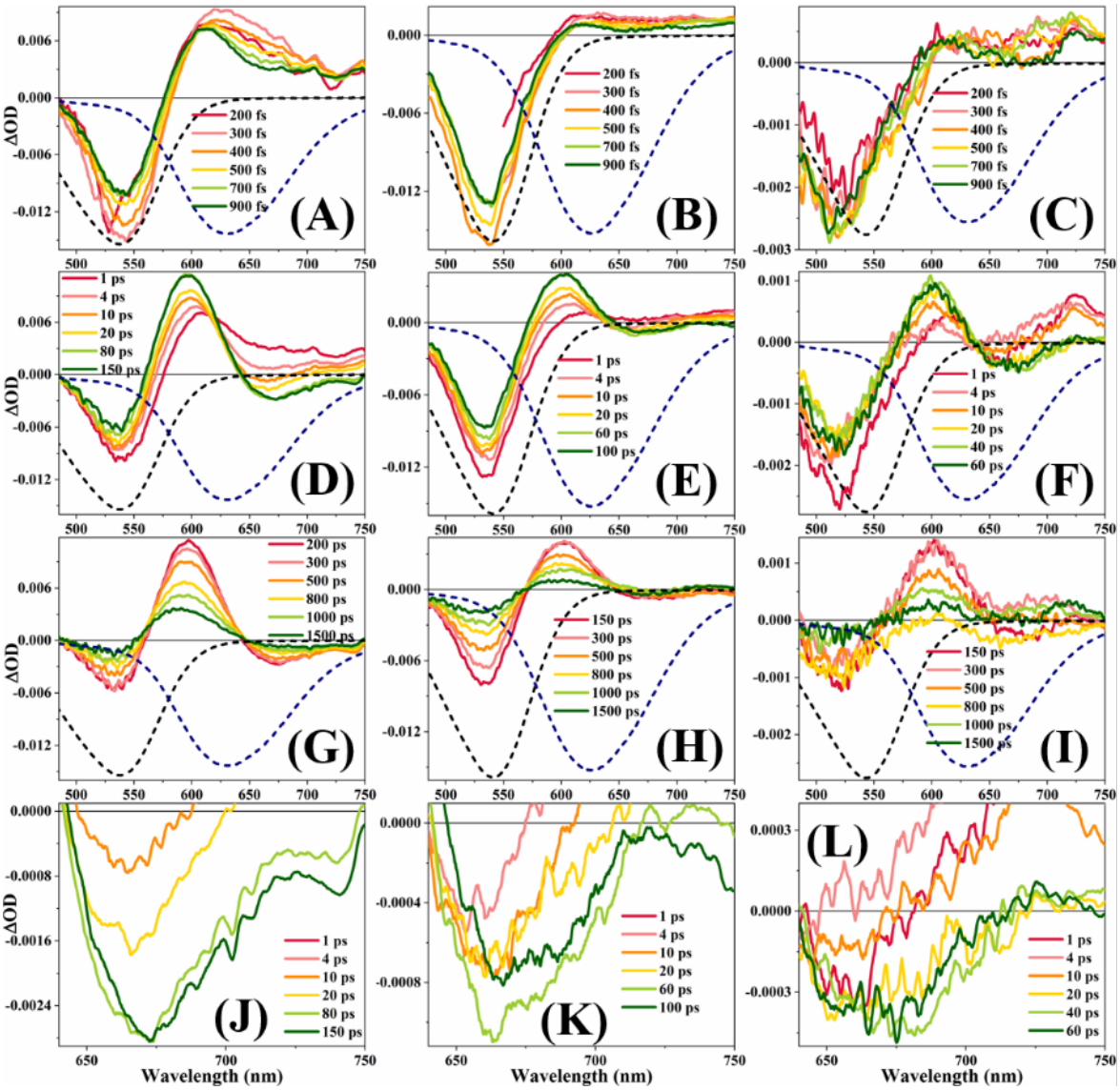

Figure B61: Transient Absorption spectra of D205 in BmimTFO-ACN [(A), (D), (G), (J)], in BmimTFO-γ-BL [(B), (E), (H), (K)] and in BmimTFO-PC [(C), (F), (I), (L)] mixtures (X_{IL}= 0.80). [(A), (B), (C)] short timescale, [(D), (E), (F)] middle timescale, [(G), (H), (I)] long timescale and [(J), (K), (L)] solvation timescale. Dashed spectra are steady state absorption (black) and emission (blue) spectra.

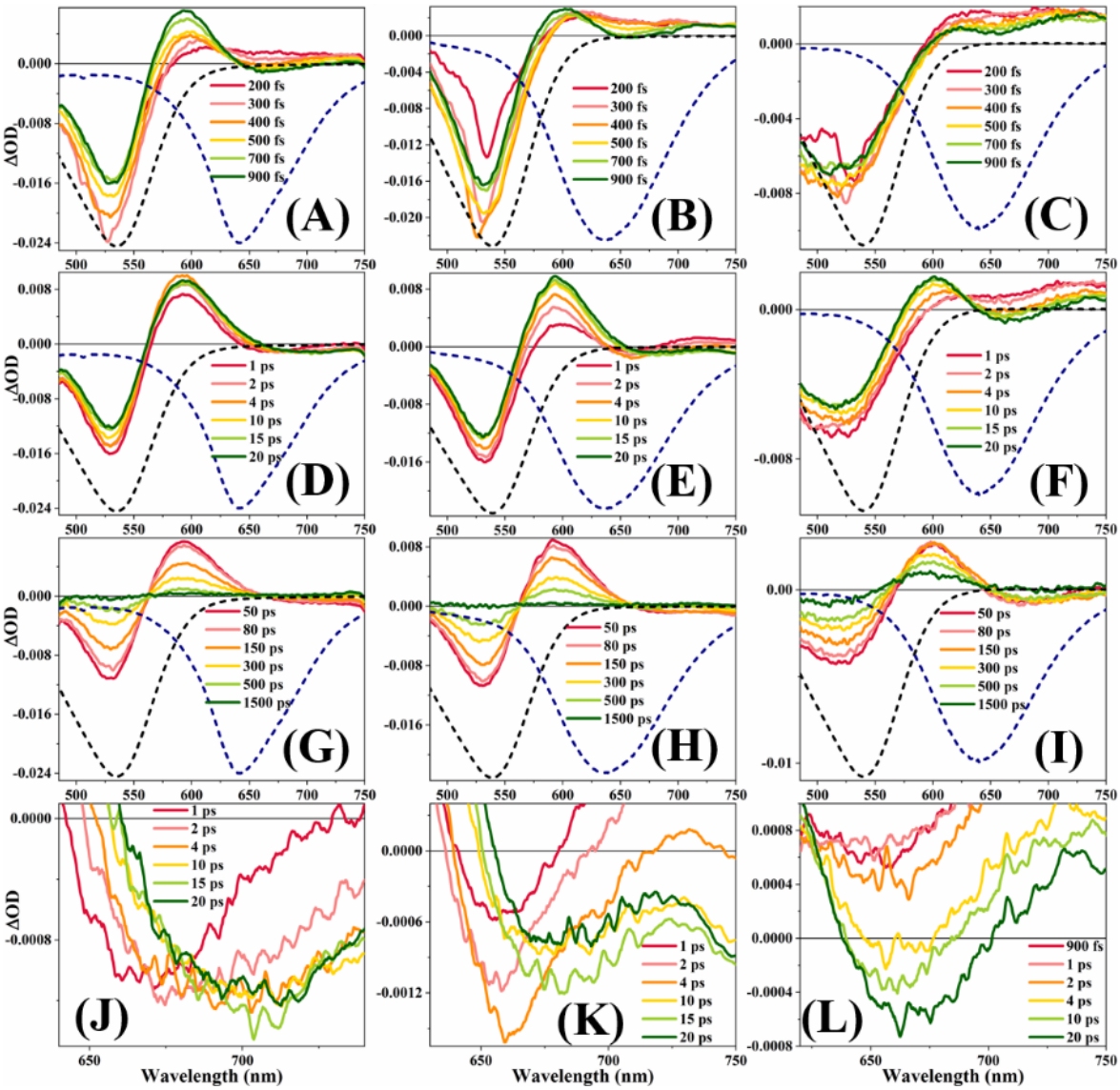

Figure B62: Transient Absorption spectra of D205 in BmimTFSI-ACN [(A), (D), (G), (J)], in BmimTFSI-γ-BL [(B), (E), (H), (K)] and in BmimTFSI-PC [(C), (F), (I), (L)] mixtures (X_{IL}= 0.05). [(A), (B), (C)] short timescale, [(D), (E), (F)] middle timescale, [(G), (H), (I)] long timescale and [(J), (K), (L)] solvation timescale. Dashed spectra are steady state absorption (black) and emission (blue) spectra.

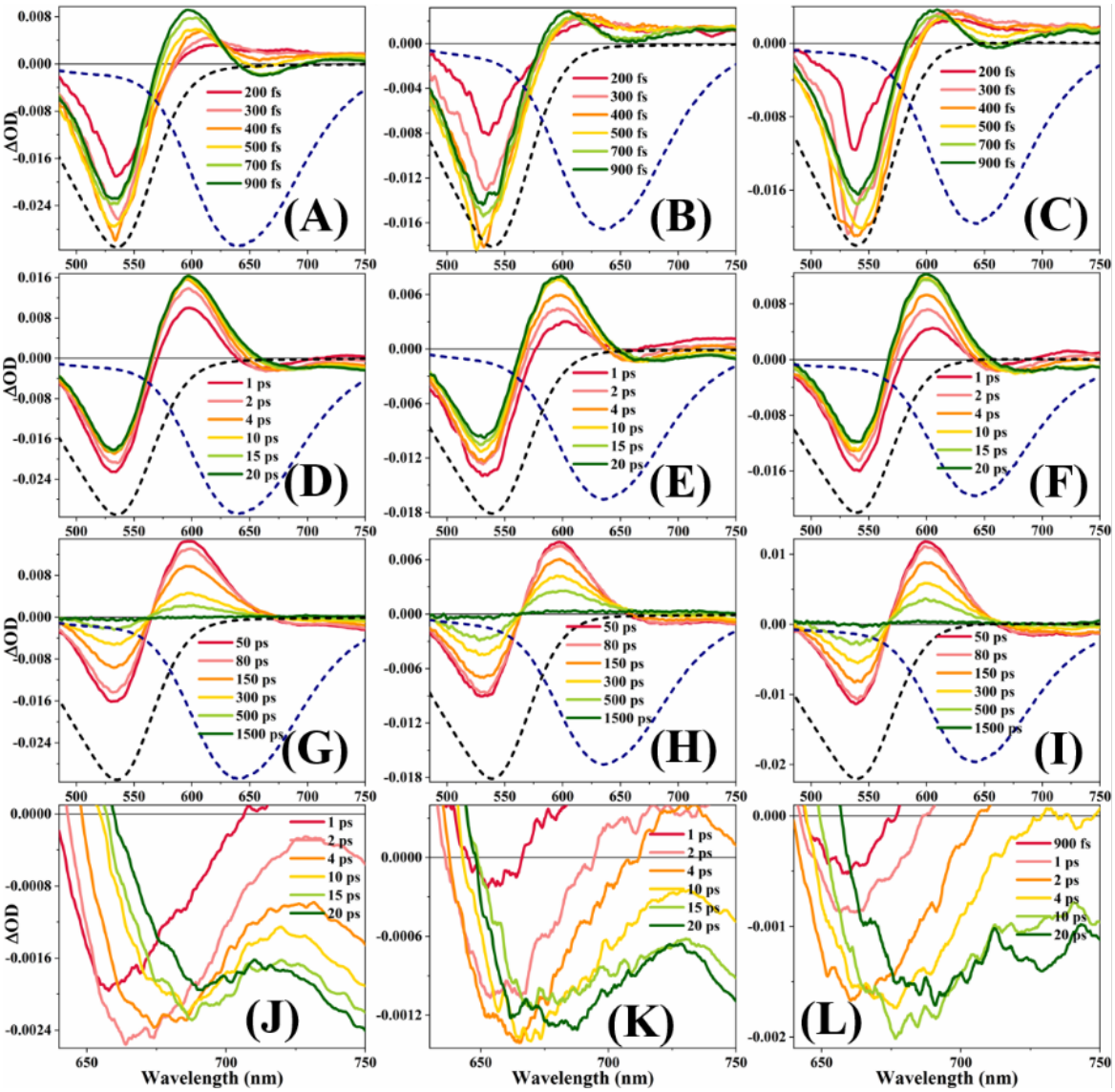

Figure B63: Transient Absorption spectra of D205 in BmimTFSI-ACN [(A), (D), (G), (J)], in BmimTFSI-γ-BL [(B), (E), (H), (K)] and in BmimTFSI-PC [(C), (F), (I), (L)] mixtures (X_{IL}= 0.10). [(A), (B), (C)] short timescale, [(D), (E), (F)] middle timescale, [(G), (H), (I)] long timescale and [(J), (K), (L)] solvation timescale. Dashed spectra are steady state absorption (black) and emission (blue) spectra.

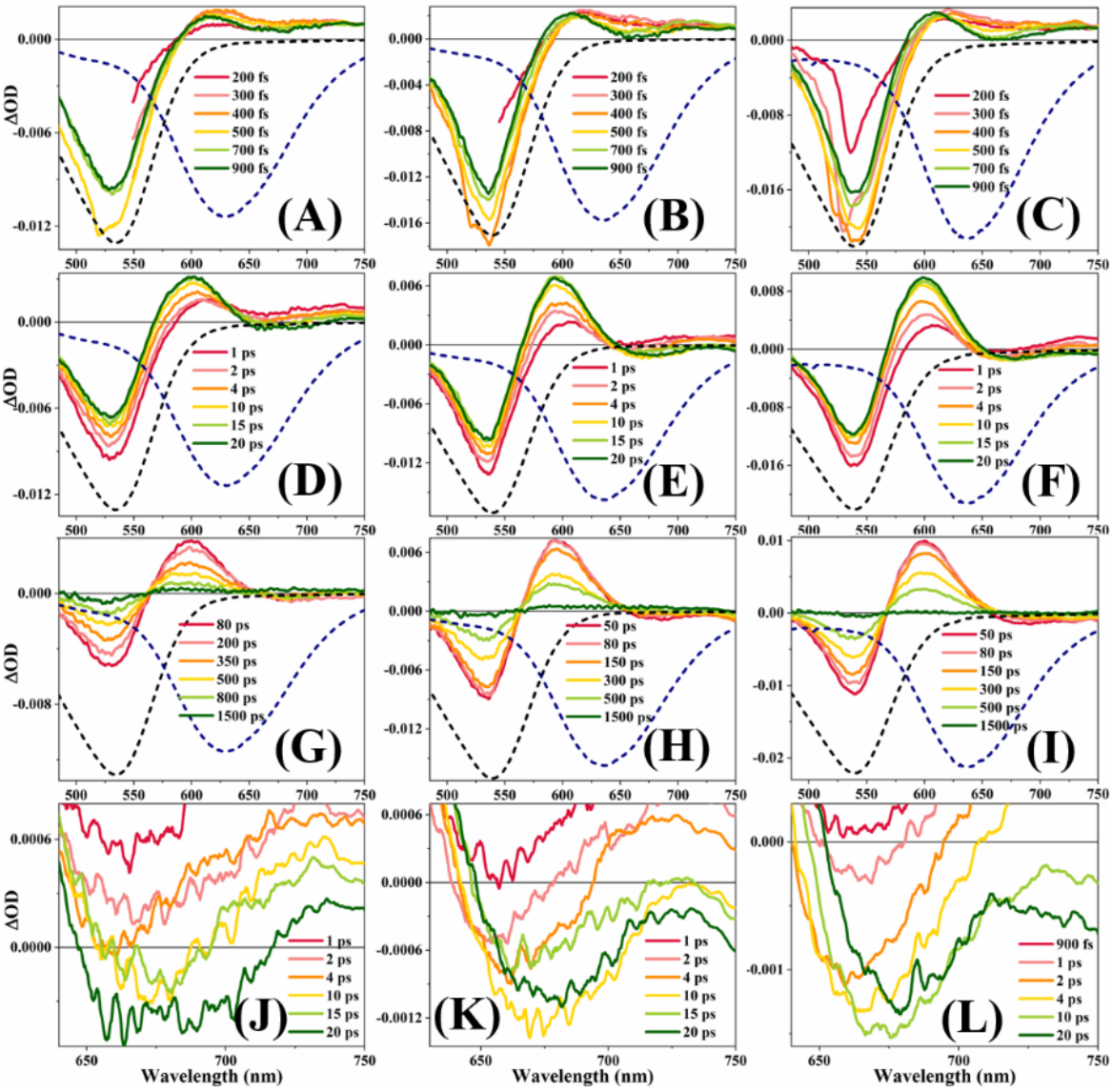

Figure B64: Transient Absorption spectra of D205 in BmimTFSI-ACN [(A), (D), (G), (J)], in BmimTFSI-γ-BL [(B), (E), (H), (K)] and in BmimTFSI-PC [(C), (F), (I), (L)] mixtures (X_{IL}= 0.20). [(A), (B), (C)] short timescale, [(D), (E), (F)] middle timescale, [(G), (H), (I)] long timescale and [(J), (K), (L)] solvation timescale. Dashed spectra are steady state absorption (black) and emission (blue) spectra.

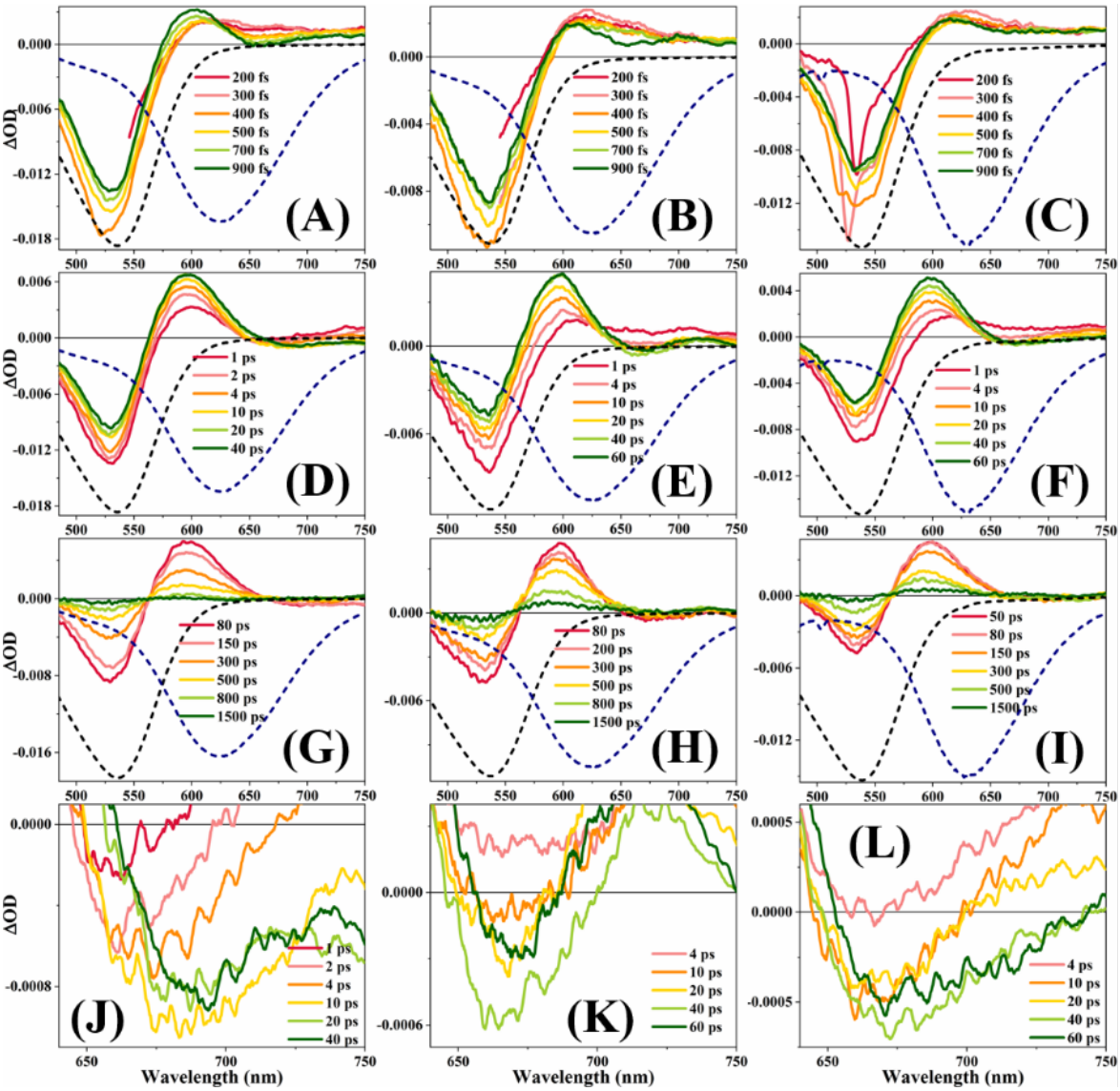

Figure B65: Transient Absorption spectra of D102 in BmimTFSI-ACN [(A), (D), (G), (J)], in BmimTFSI-γ-BL [(B), (E), (H), (K)] and in BmimTFSI-PC [(C), (F), (I), (L)] mixtures (X_{IL}= 0.50). [(A), (B), (C)] short timescale, [(D), (E), (F)] middle timescale, [(G), (H), (I)] long timescale and [(J), (K), (L)] solvation timescale. Dashed spectra are steady state absorption (black) and emission (blue) spectra.

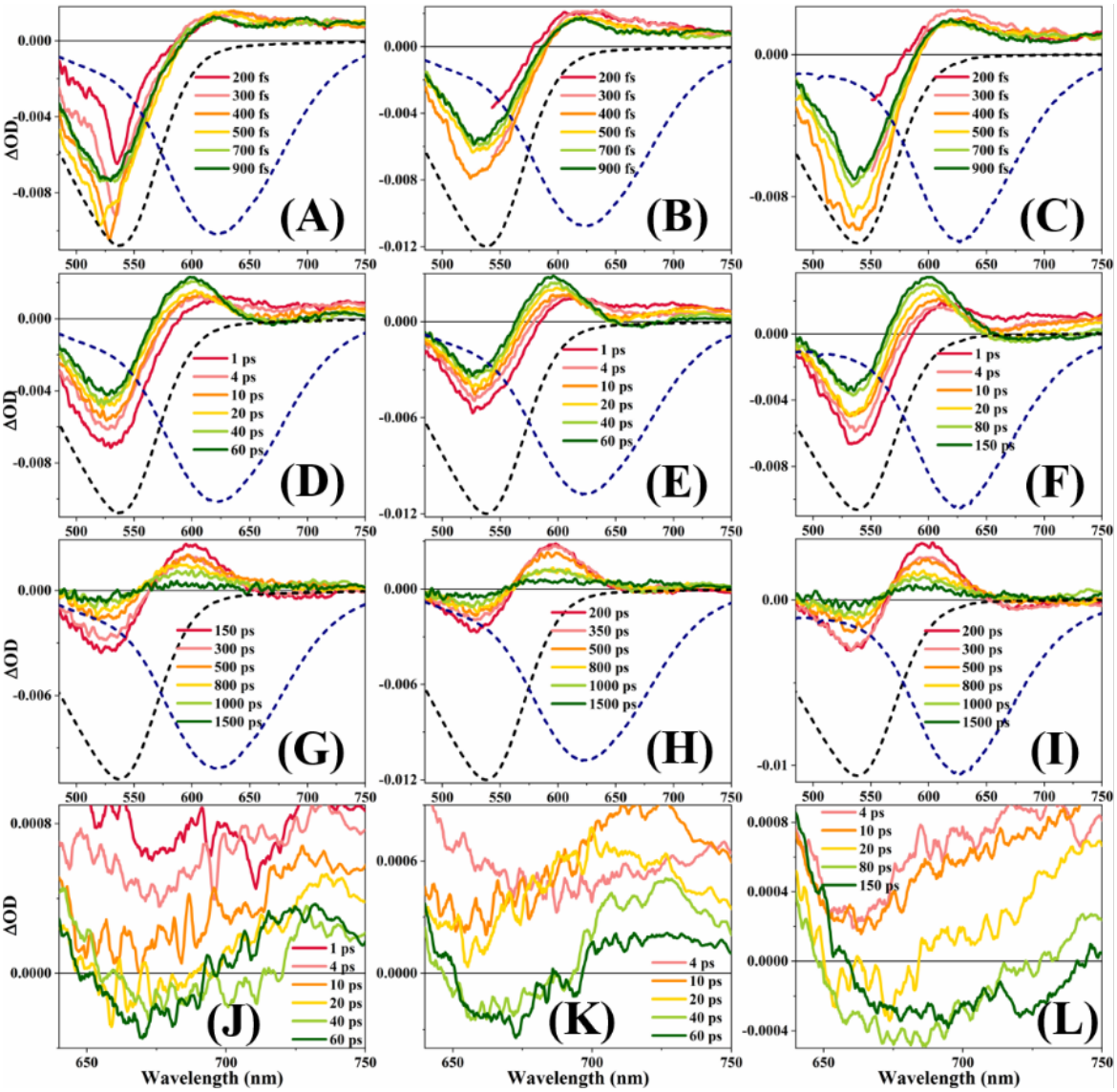

Figure B66: Transient Absorption spectra of D205 in BmimTFSI-ACN [(A), (D), (G), (J)], in BmimTFSI-γ-BL [(B), (E), (H), (K)] and in BmimTFSI-PC [(C), (F), (I), (L)] mixtures (X_{IL}= 0.80). [(A), (B), (C)] short timescale, [(D), (E), (F)] middle timescale, [(G), (H), (I)] long timescale and [(J), (K), (L)] solvation timescale. Dashed spectra are steady state absorption (black) and emission (blue) spectra.

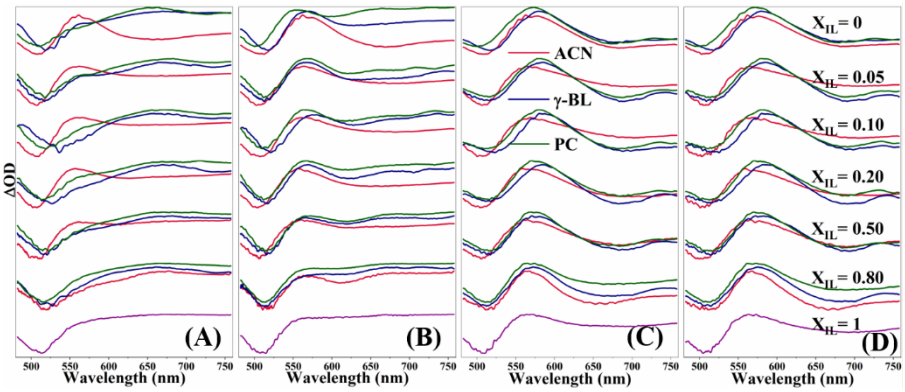

Figure B67: Composition dependent TAS of D102 in $BmimBF_4$-MS mixtures at (A) 500 fs, (B) 1 ps, (C) 30 ps and (D) 150 ps

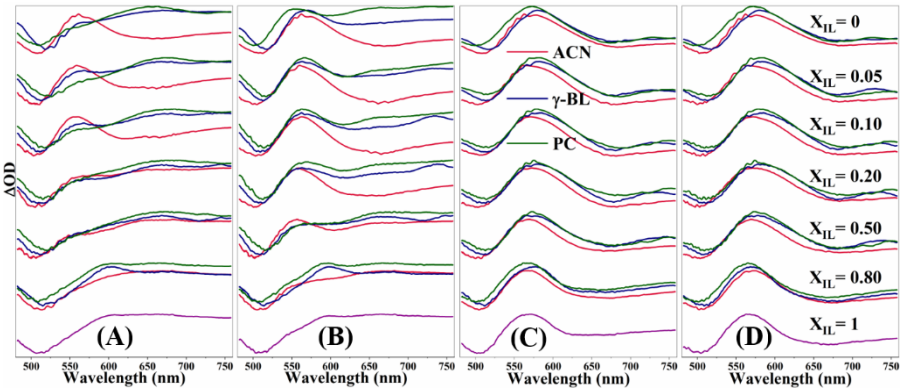

Figure B68: Composition dependent TAS of D102 in BmimTFO-MS mixtures at (A) 500 fs, (B) 1 ps, (C) 30 ps and (D) 150 ps

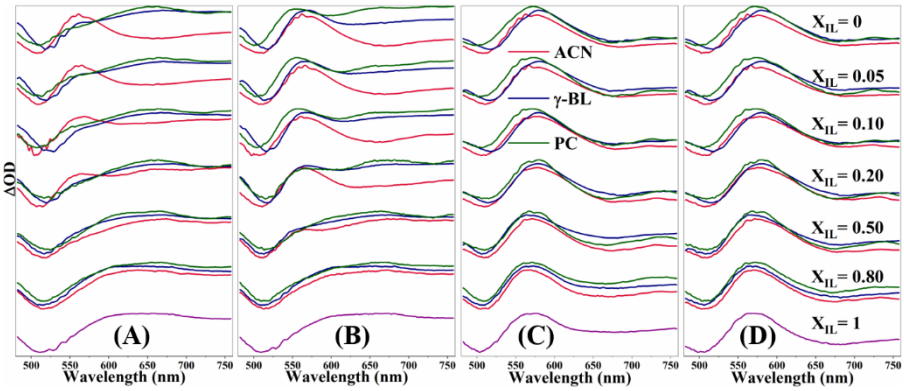

Figure B69: Composition dependent TAS of D102 in BmimTFSI-MS mixtures at (A) 500 fs, (B) 1 ps, (C) 30 ps and (D) 150 ps

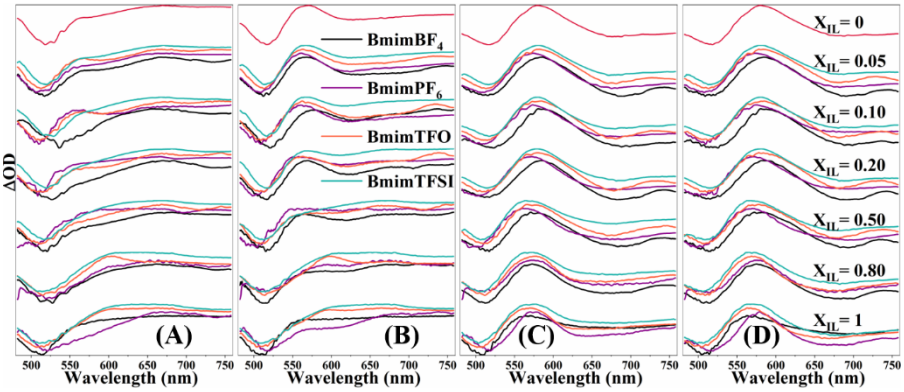

Figure B70: Composition dependent TAS of D102 in IL-γ-BL mixtures at (A) 500 fs, (B) 1 ps, (C) 30 ps and (D) 150 ps

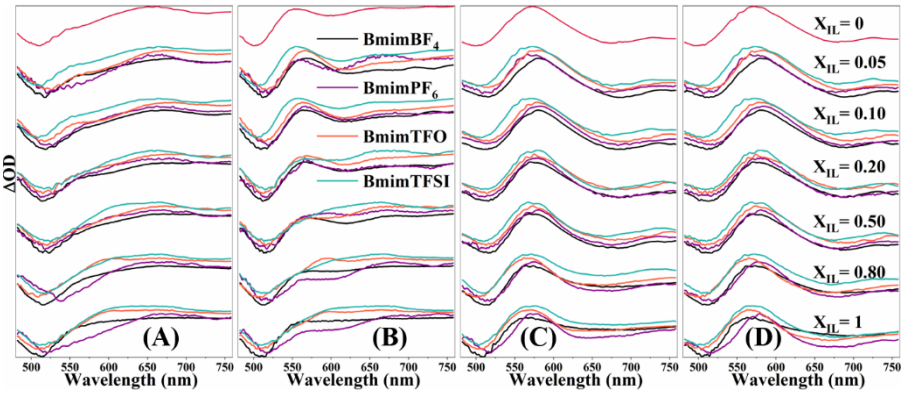

Figure B71: Composition dependent TAS of D102 in IL-PC mixtures at (A) 500 fs, (B) 1 ps, (C) 30 ps and (D) 150 ps

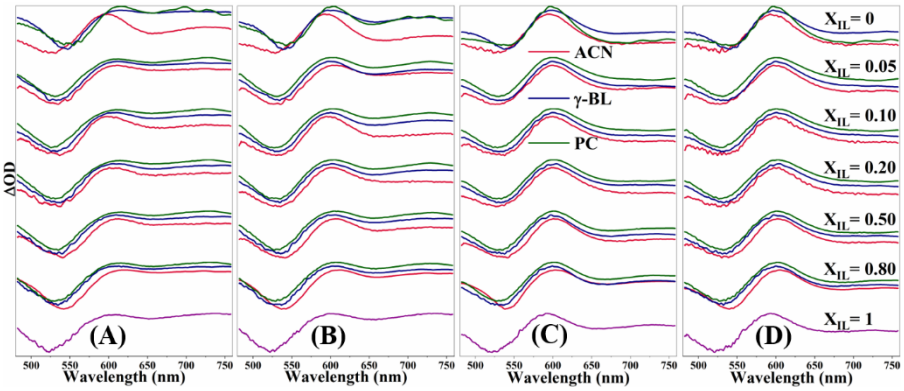

Figure B72: Composition dependent TAS of D149 in $BmimBF_4$-MS mixtures at (A) 500 fs, (B) 1 ps, (C) 30 ps and (D) 150 ps

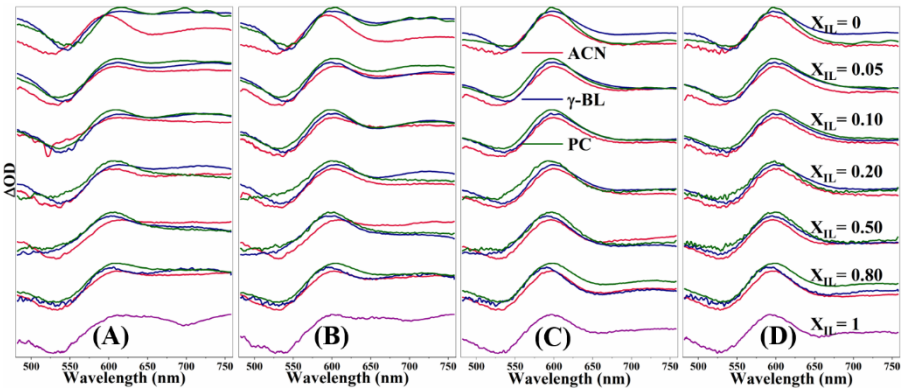

Figure B73: Composition dependent TAS of D149 in $BmimPF_6$-MS mixtures at (A) 500 fs, (B) 1 ps, (C) 30 ps and (D) 150 ps

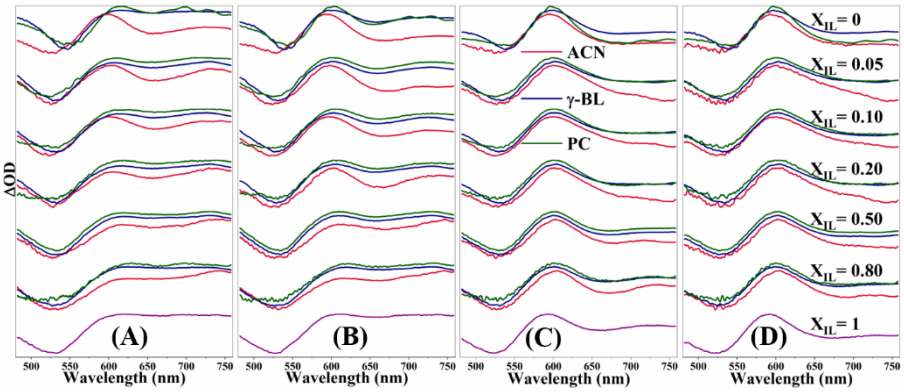

Figure B74: Composition dependent TAS of D149 in BmimTFO-MS mixtures at (A) 500 fs, (B) 1 ps, (C) 30 ps and (D) 150 ps

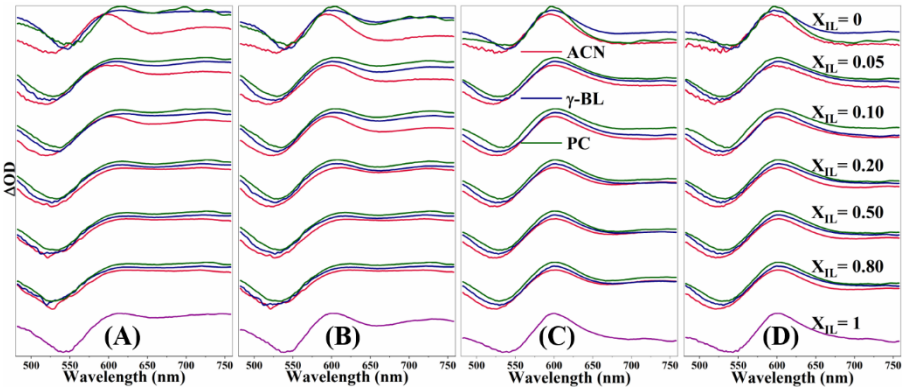

Figure B75: Composition dependent TAS of D149 in BmimTFSI-MS mixtures at (A) 500 fs, (B) 1 ps, (C) 30 ps and (D) 150 ps

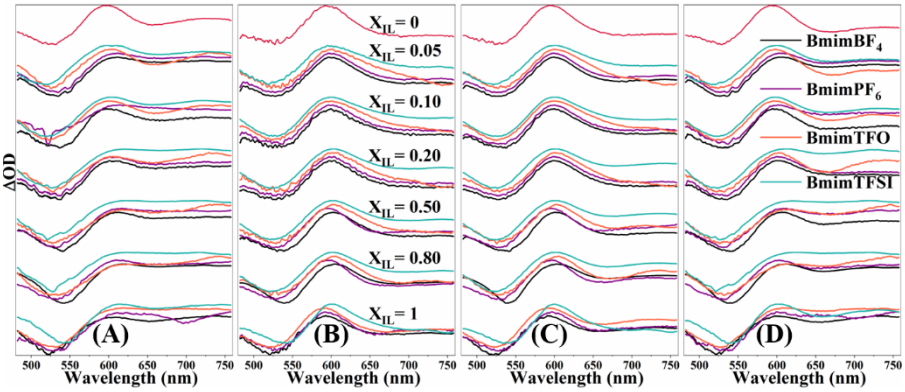

Figure B76: Composition dependent TAS of D149 in IL-ACN mixtures at (A) 500 fs, (B) 1 ps, (C) 30 ps and (D) 150 ps

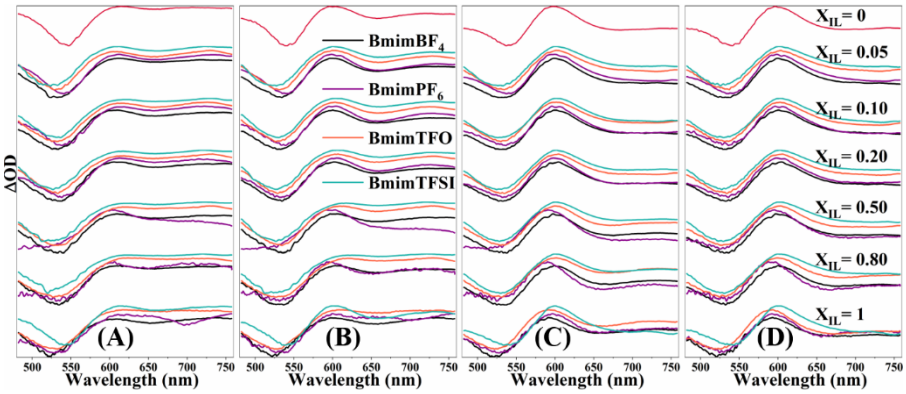

Figure B77: Composition dependent TAS of D149 in IL-γ-BL mixtures at (A) 500 fs, (B) 1 ps, (C) 30 ps and (D) 150 ps

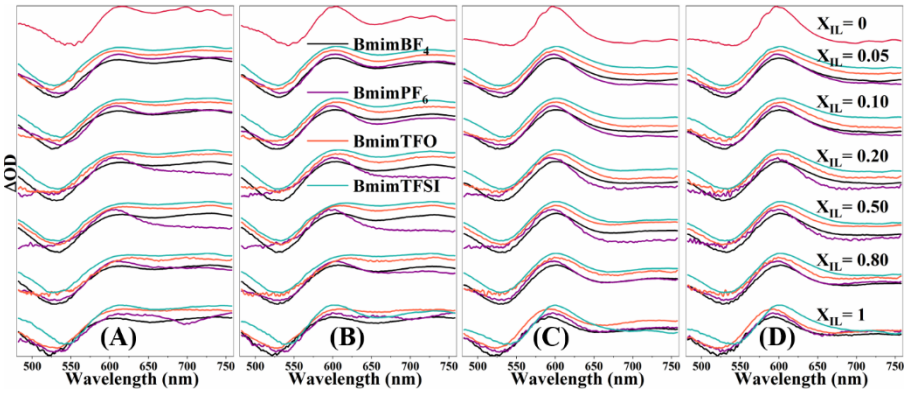

Figure B78: Composition dependent TAS of D149 in IL-PC mixtures at (A) 500 fs, (B) 1 ps, (C) 30 ps and (D) 150 ps

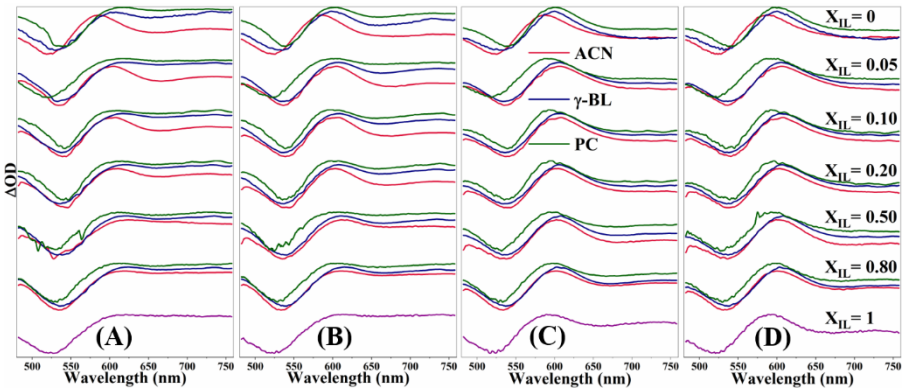

Figure B79: Composition dependent TAS of D205 in $BmimBF_4$-MS mixtures at (A) 500 fs, (B) 1 ps, (C) 30 ps and (D) 150 ps

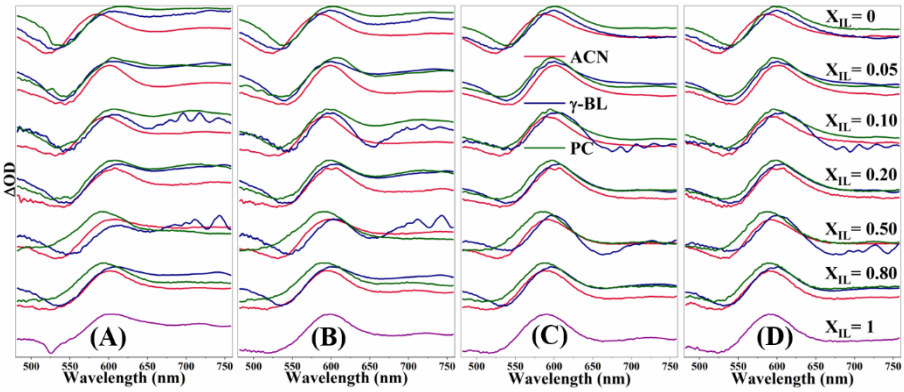

Figure B80: Composition dependent TAS of D205 in BmimPF$_6$-MS mixtures at (A) 500 fs, (B) 1 ps, (C) 30 ps and (D) 150 ps

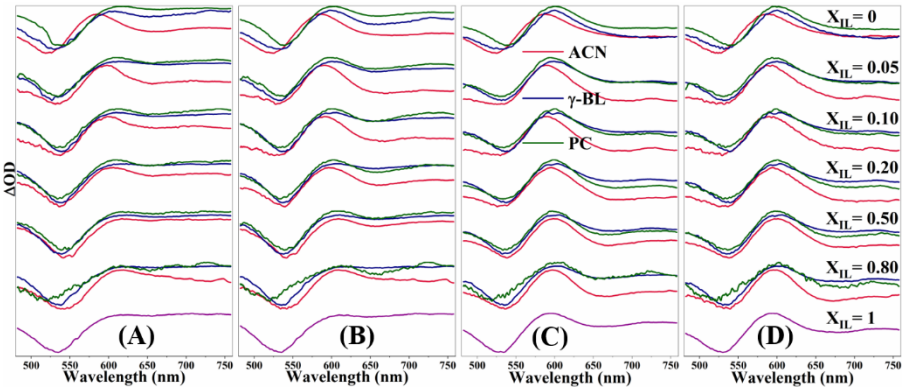

Figure B81: Composition dependent TAS of D205 in BmimTFO-MS mixtures at (A) 500 fs, (B) 1 ps, (C) 30 ps and (D) 150 ps

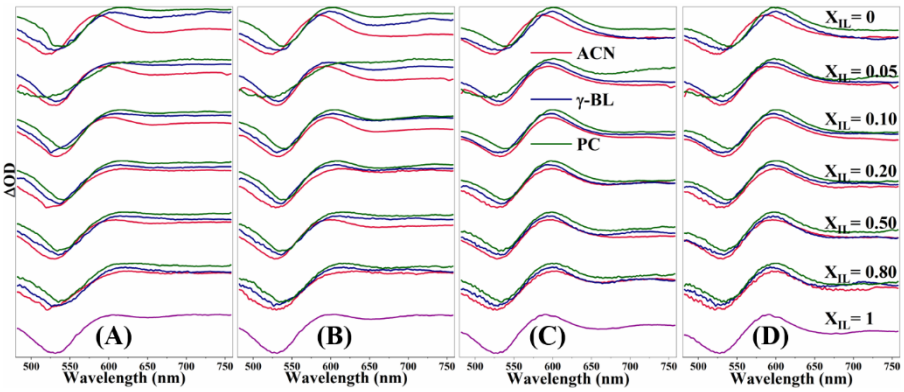

Figure B82: Composition dependent TAS of D205 in BmimTFSI-MS mixtures at (A) 500 fs, (B) 1 ps, (C) 30 ps and (D) 150 ps

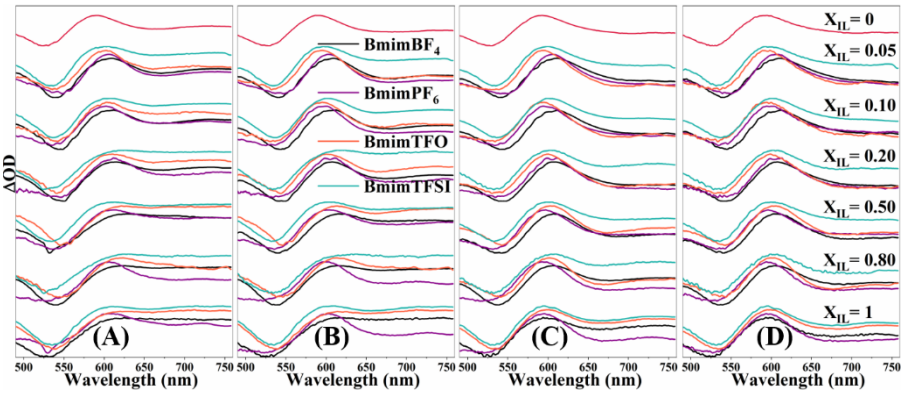

Figure B83: Composition dependent TAS of D205 in IL-ACN mixtures at (A) 500 fs, (B) 1 ps, (C) 30 ps and (D) 150 ps

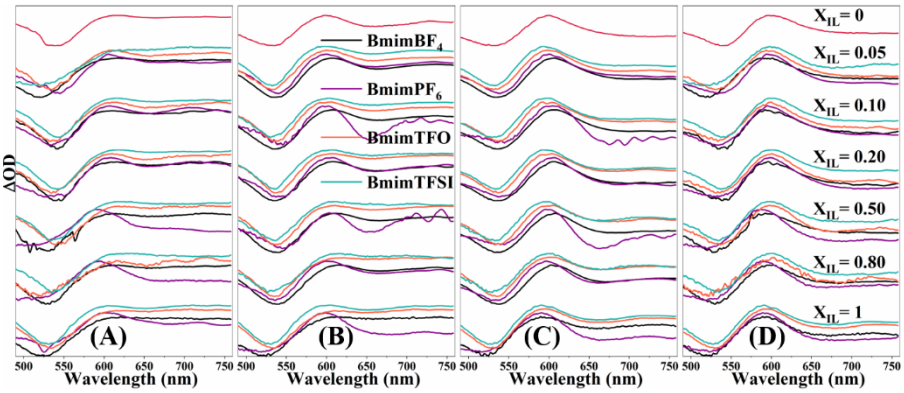

Figure B84: Composition dependent TAS of D205 in IL-γ-BL mixtures at (A) 500 fs, (B) 1 ps, (C) 30 ps and (D) 150 ps

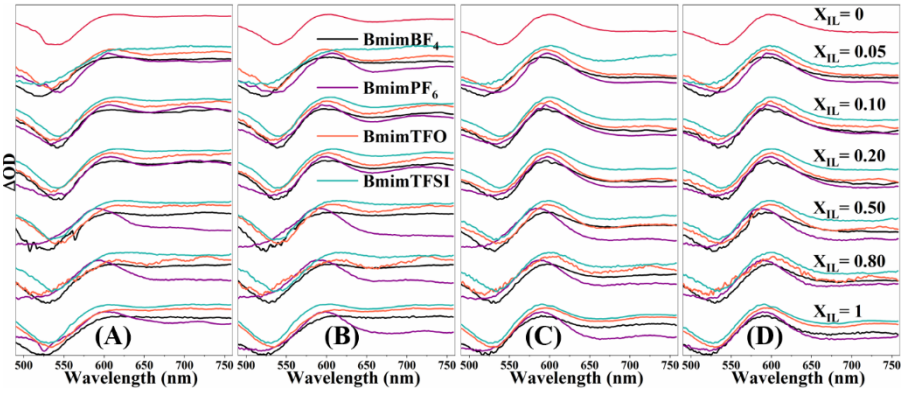

Figure B85: Composition dependent TAS of D205 in IL-PC mixtures at (A) 500 fs, (B) 1 ps, (C) 30 ps and (D) 150 ps

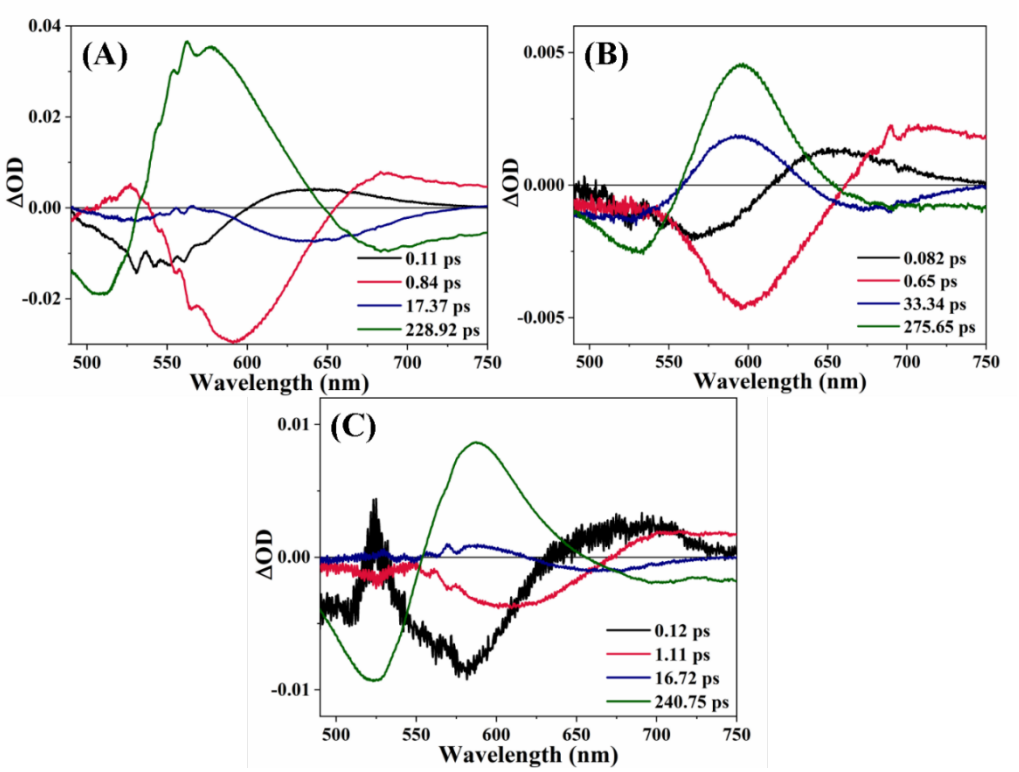

Figure B86: DAS of (A) D102, (B) D149 and (C) D205 in pure ACN

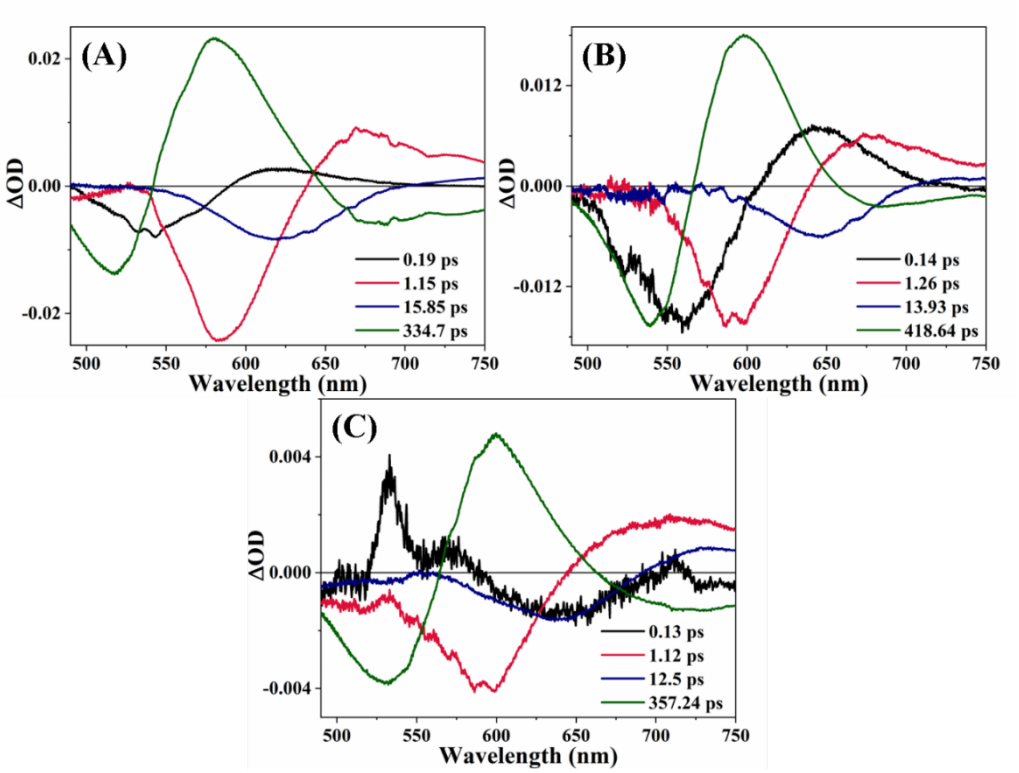

Figure B87: DAS of (A) D102, (B) D149 and (C) D205 in pure γ-BL

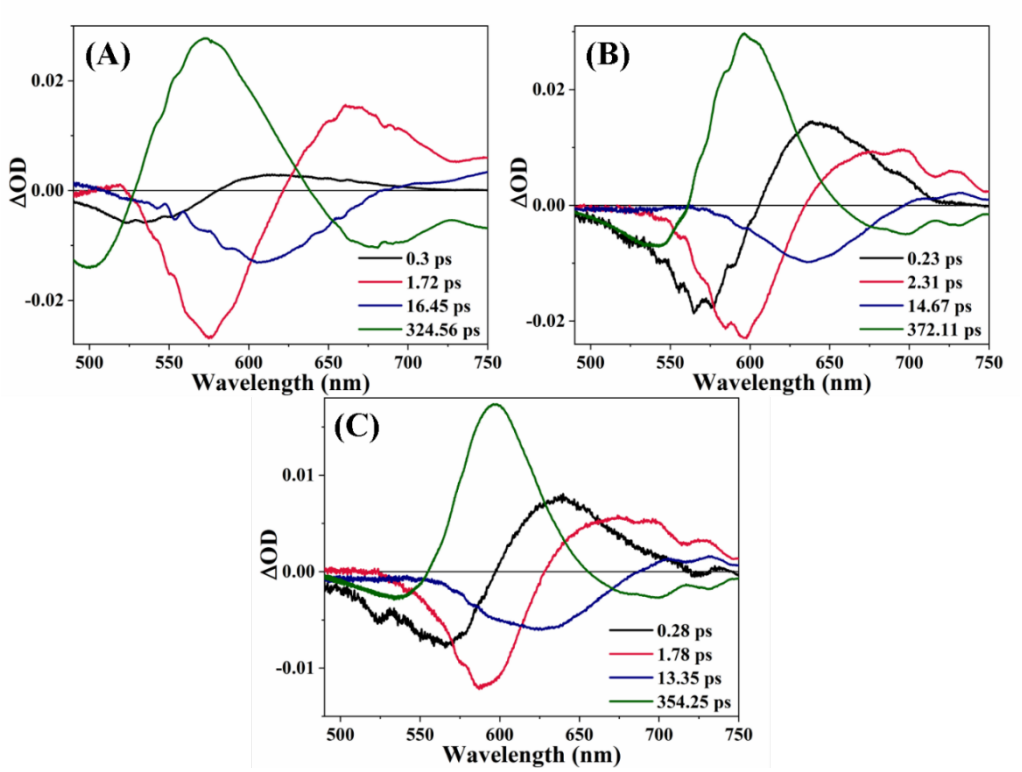

Figure B88: DAS of (A) D102, (B) D149 and (C) D205 in pure PC

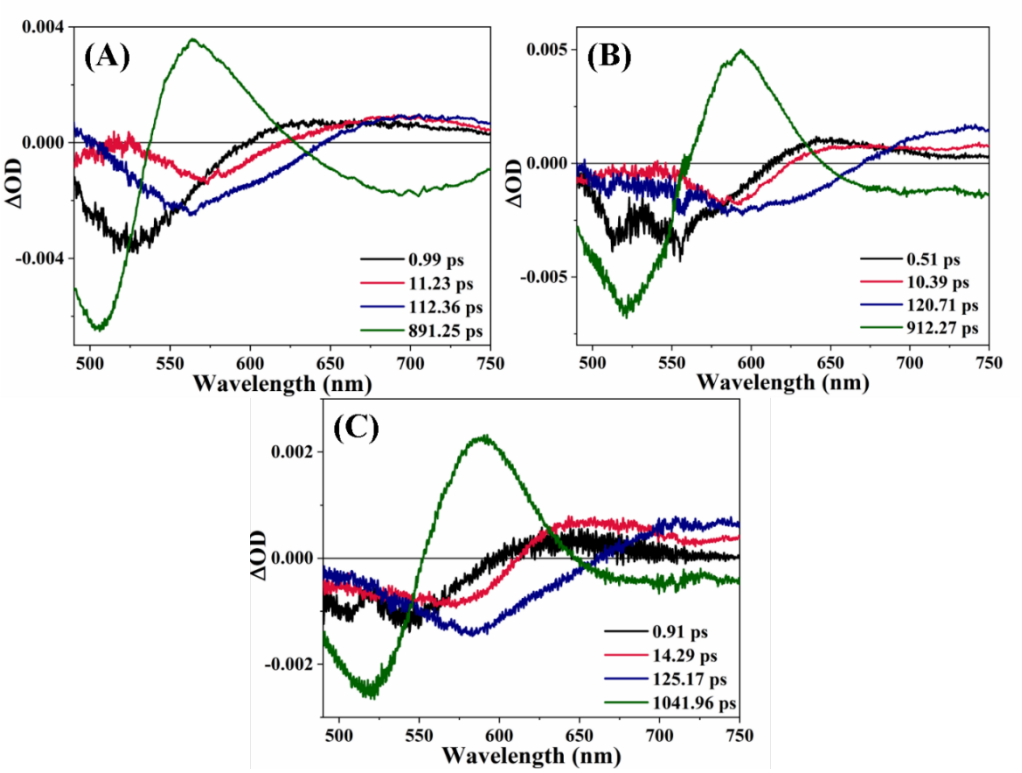

Figure B89: DAS of (A) D102, (B) D149 and (C) D205 in pure $BmimBF_4$

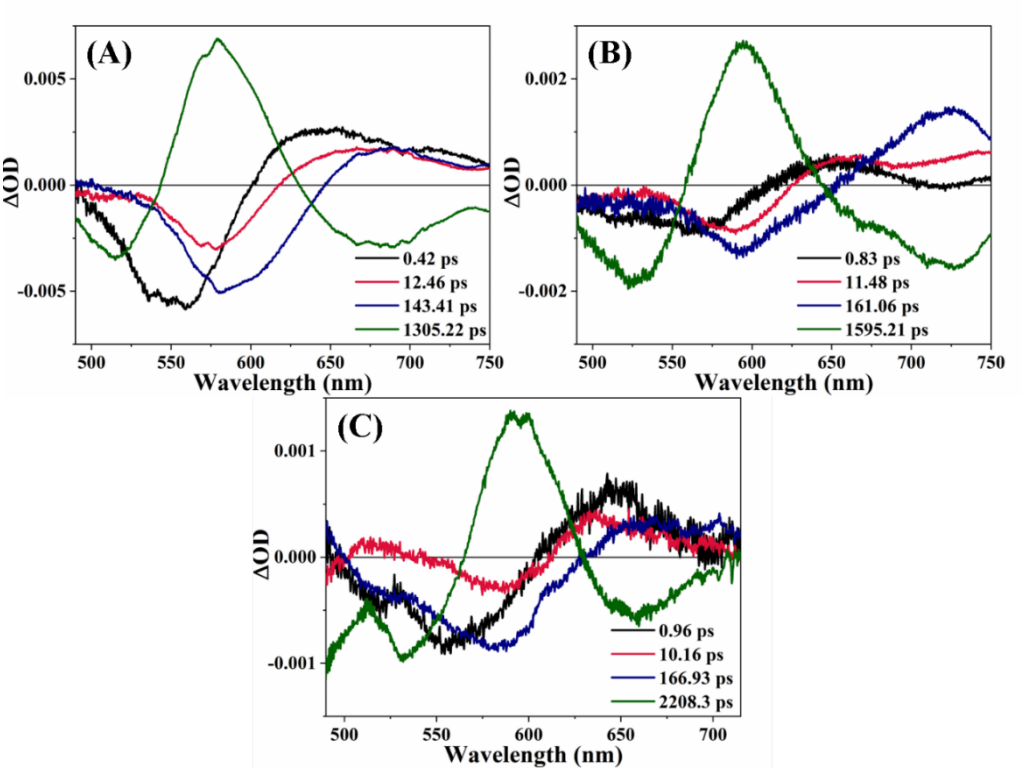

Figure B90: DAS of (A) D102, (B) D149 and (C) D205 in pure $BmimPF_6$

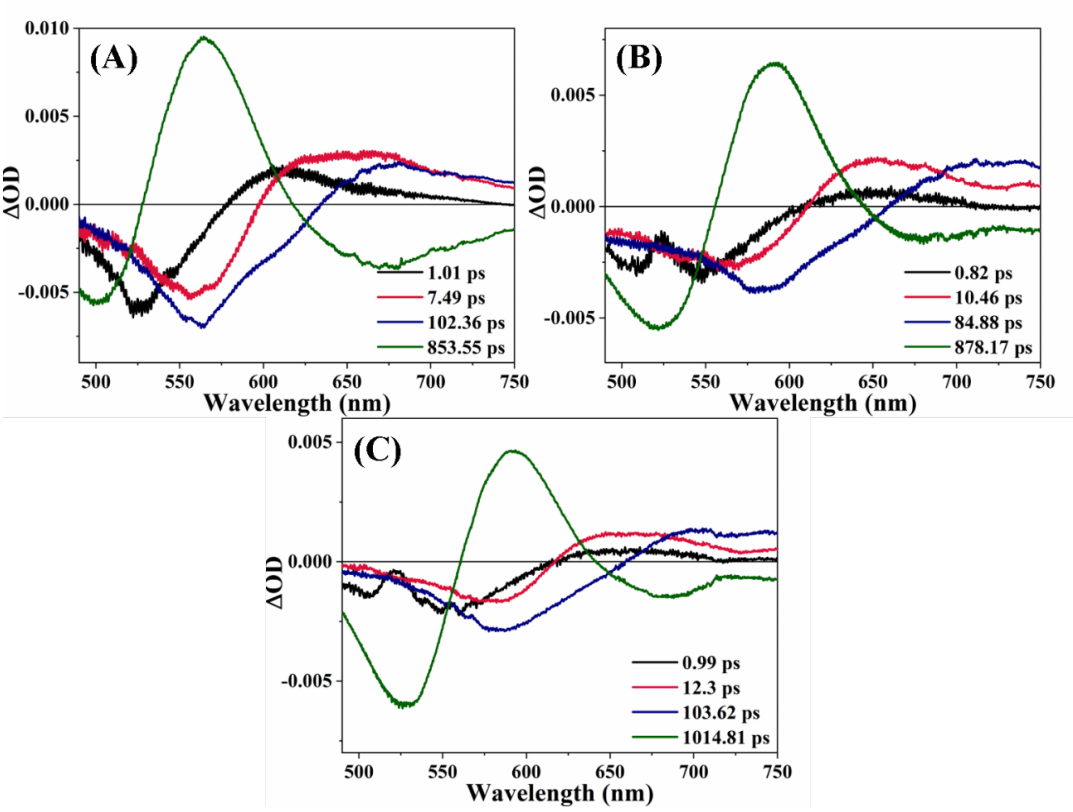

Figure B91: DAS of (A) D102, (B) D149 and (C) D205 in pure BmimTFO

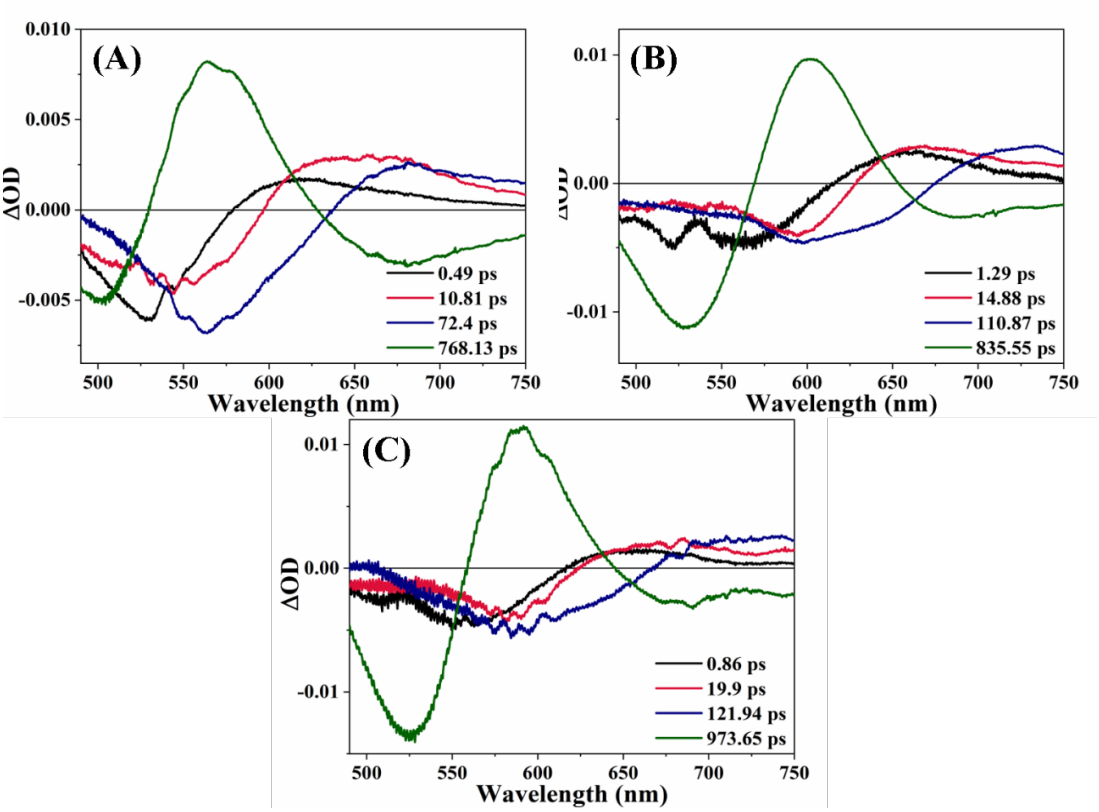

Figure B92: DAS of (A) D102, (B) D149 and (C) D205 in pure BmimTFSI

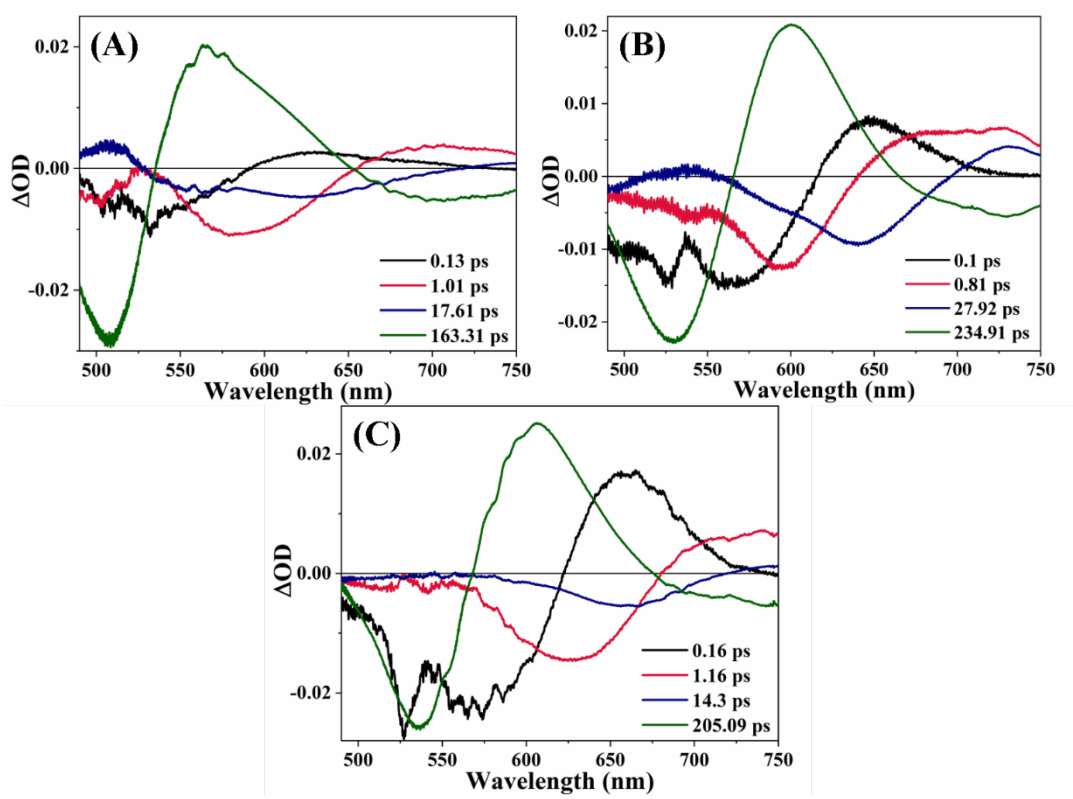

Figure B93: DAS of (A) D102, (B) D149 and (C) D205 in $BmimBF_4$-ACN mixture (X_{IL} = 0.05)

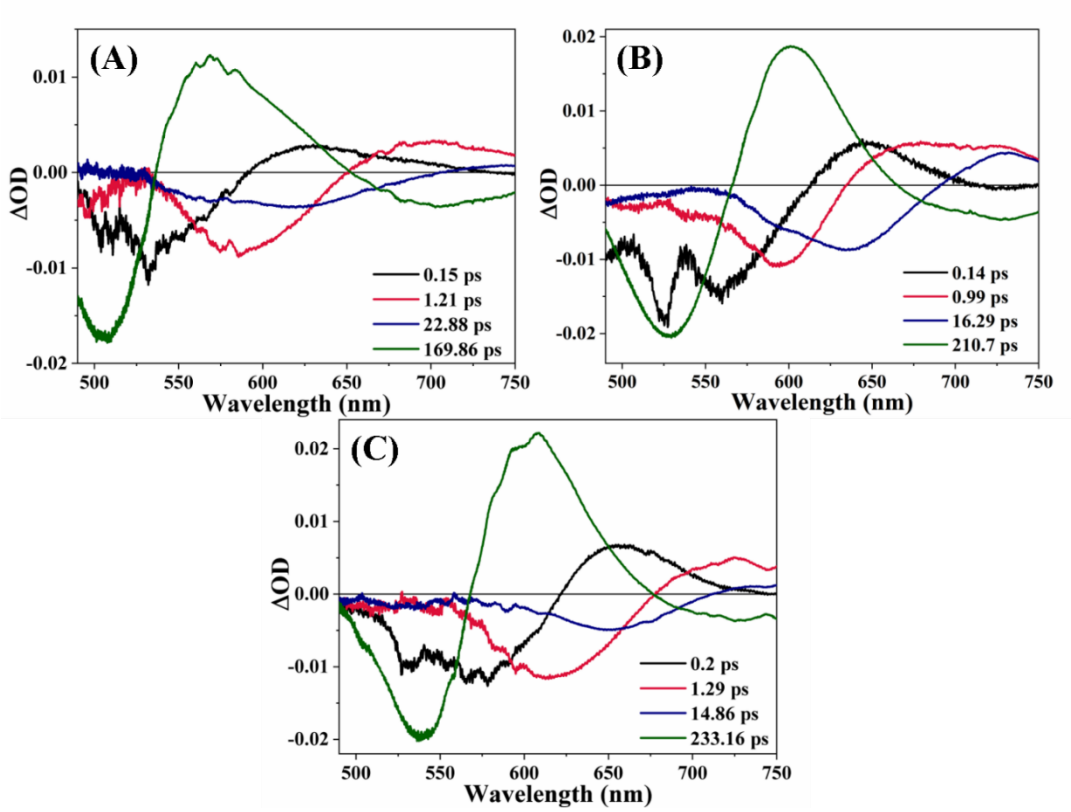

Figure B94: DAS of (A) D102, (B) D149 and (C) D205 in $BmimBF_4$-ACN mixture (X_{IL} = 0.10)

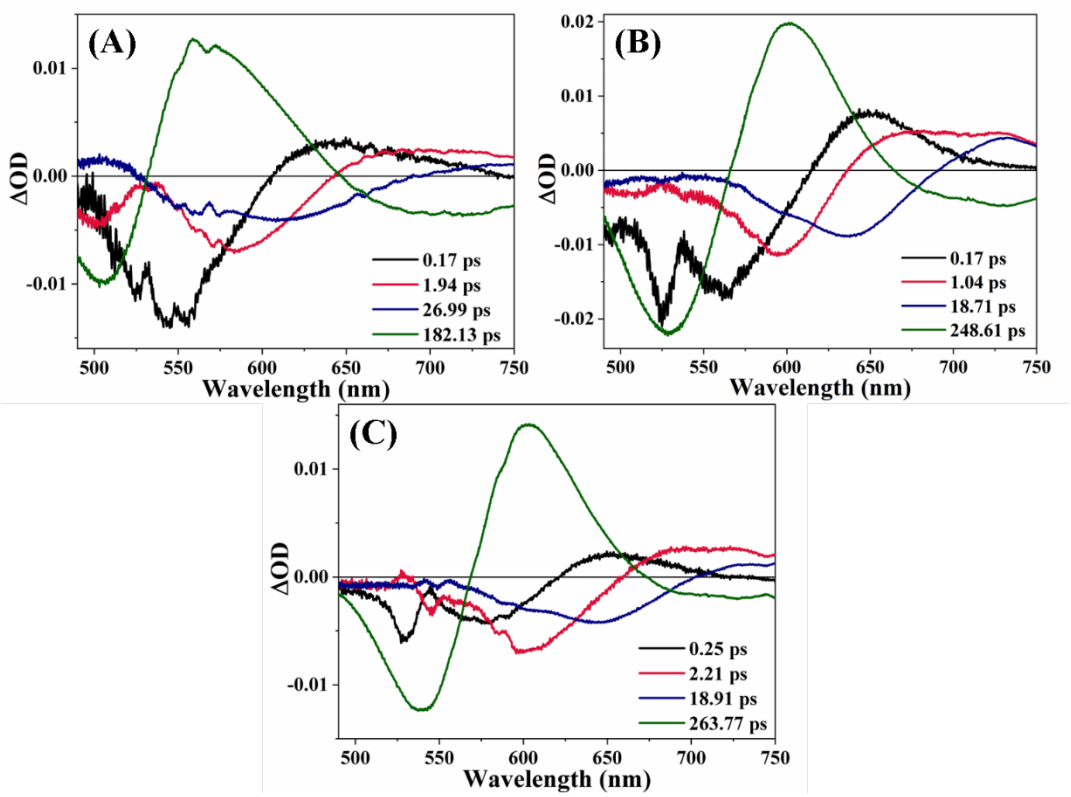

Figure B95: DAS of (A) D102, (B) D149 and (C) D205 in $BmimBF_4$-ACN mixture (X_{IL} = 0.20)

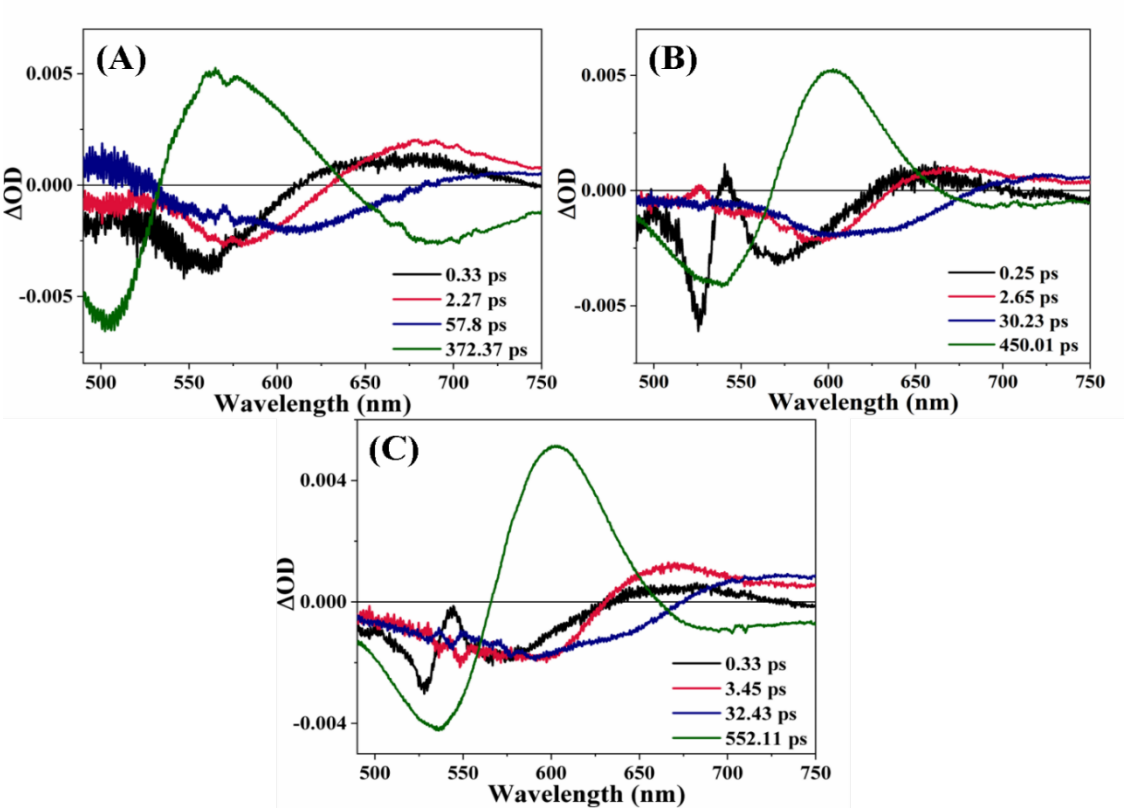

Figure B96: DAS of (A) D102, (B) D149 and (C) D205 in $BmimBF_4$-ACN mixture (X_{IL} = 0.50)

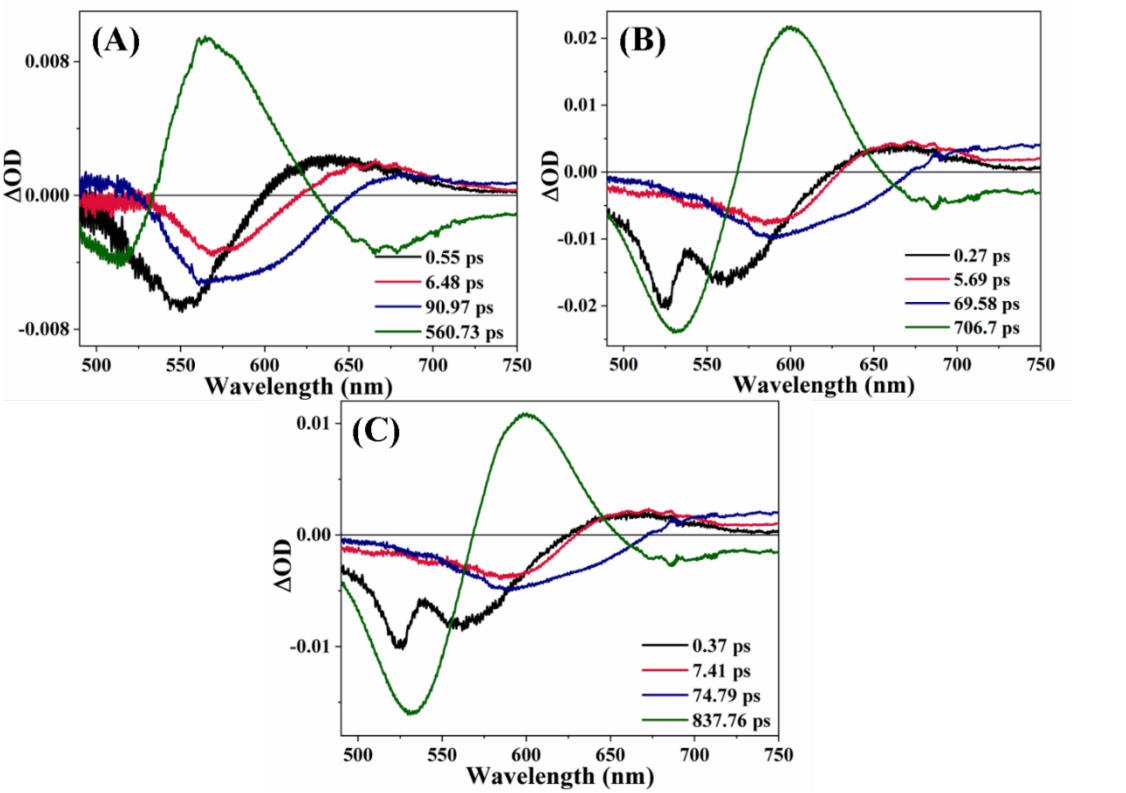

Figure B97: DAS of (A) D102, (B) D149 and (C) D205 in $BmimBF_4$-ACN mixture (X_{IL} = 0.80)

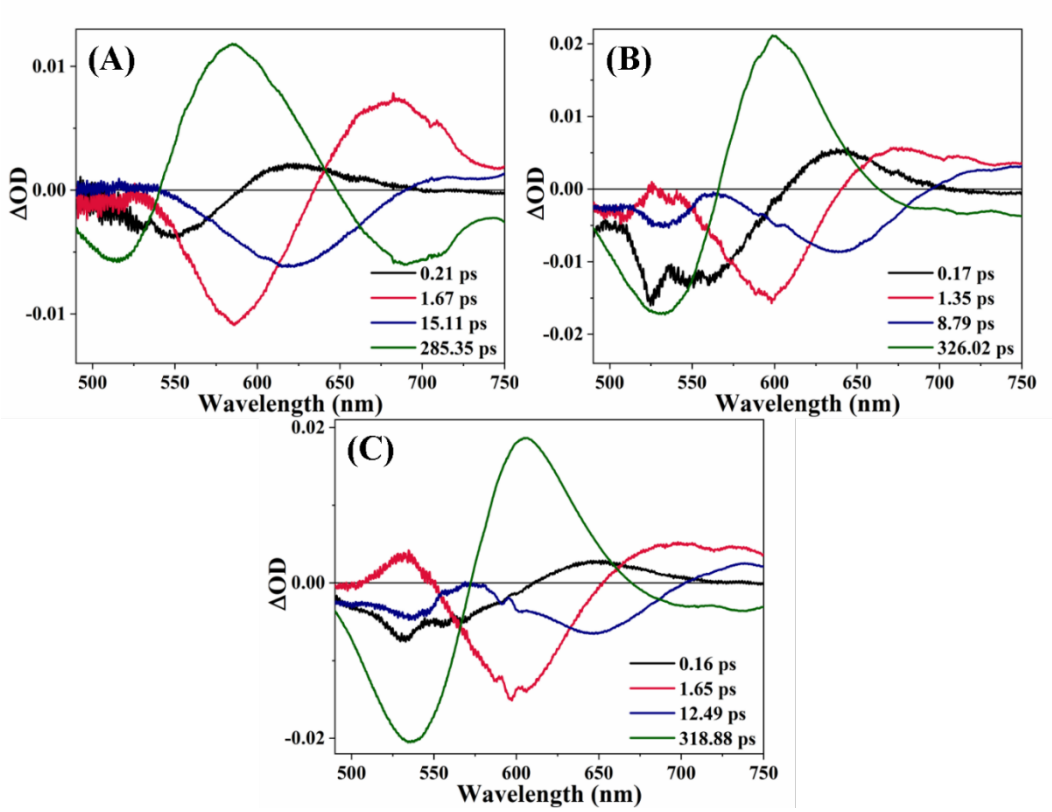

Figure B98: DAS of (A) D102, (B) D149 and (C) D205 in $BmimBF_4$-γ-BL mixture (X_{IL} = 0.05)

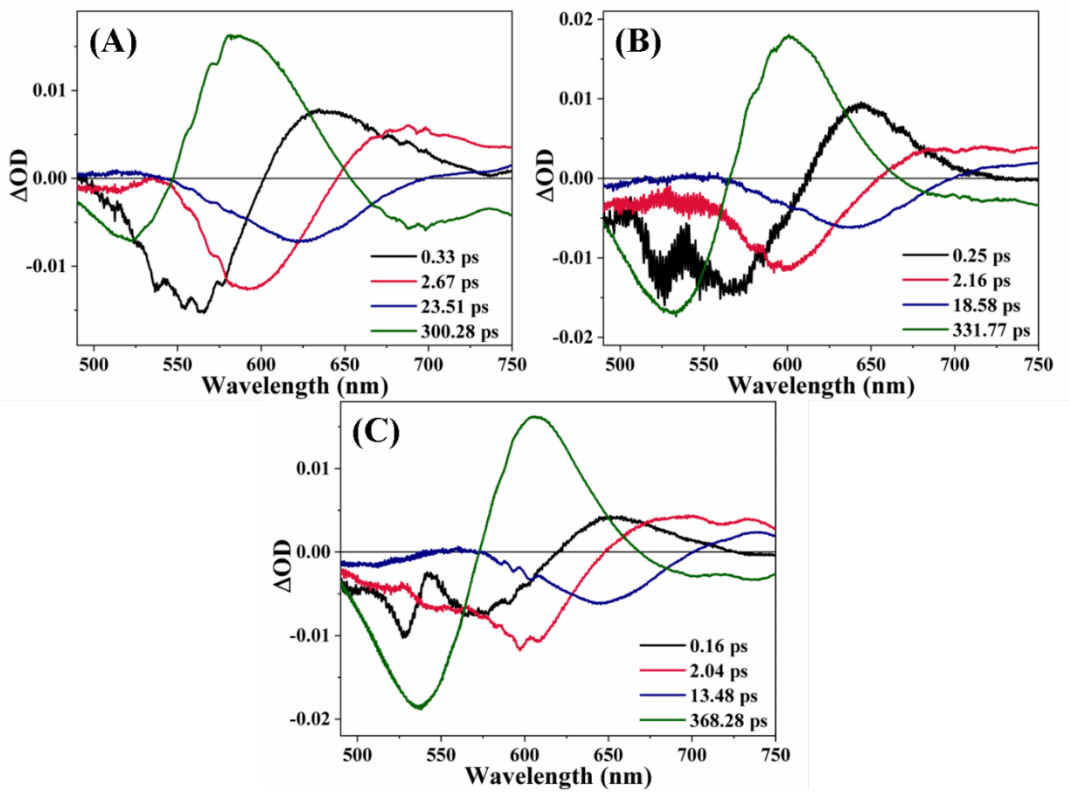

Figure B99: DAS of (A) D102, (B) D149 and (C) D205 in $BmimBF_4$-γ-BL mixture (X_{IL} = 0.10)

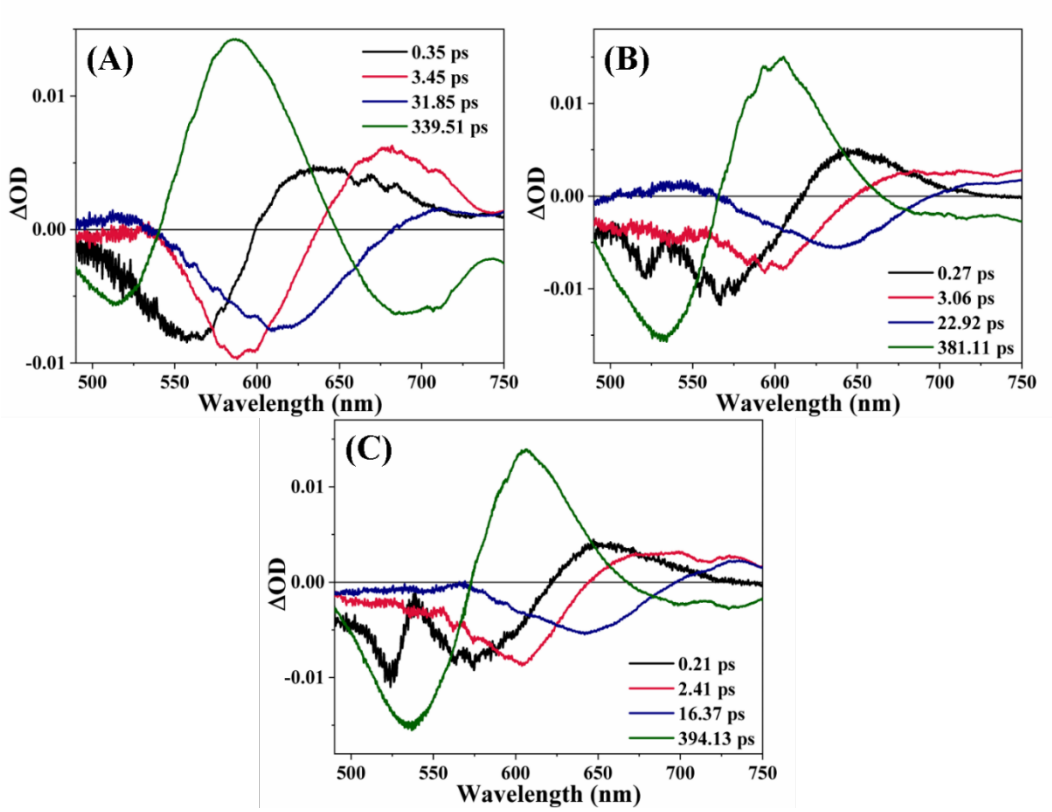

Figure B100: DAS of (A) D102, (B) D149 and (C) D205 in $BmimBF_4$-γ-BL mixture (X_{IL} = 0.20)

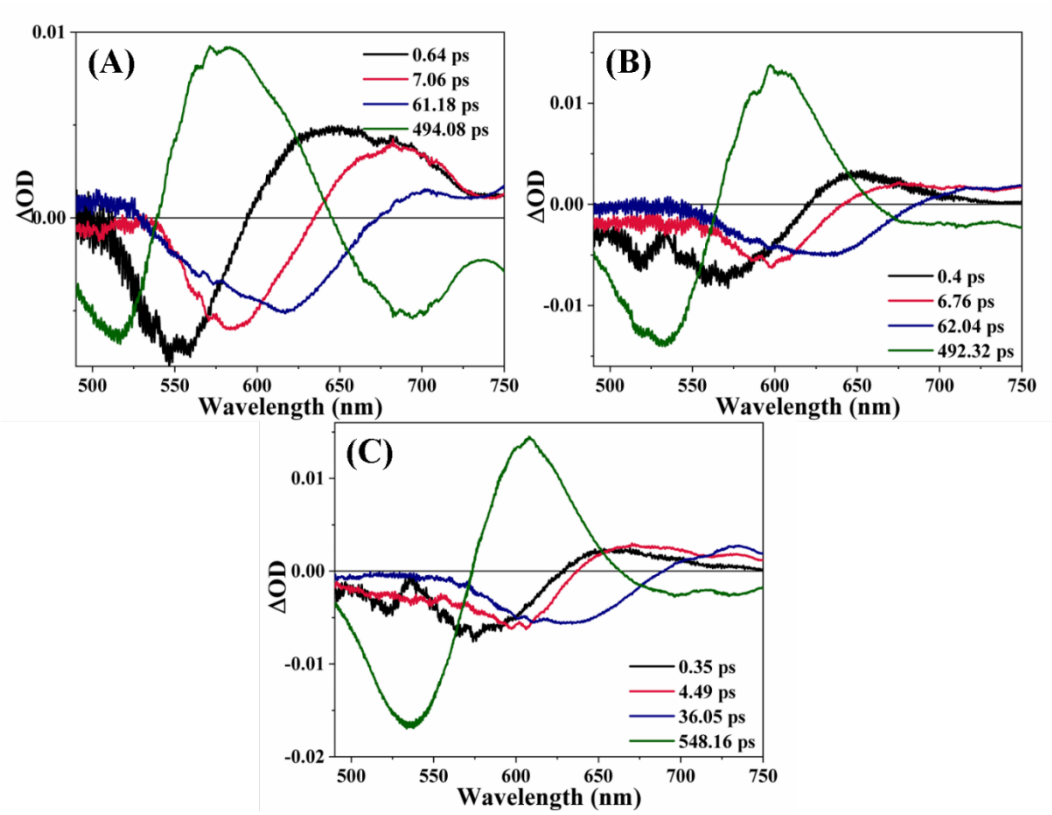

Figure B101: DAS of (A) D102, (B) D149 and (C) D205 in $BmimBF_4$-γ-BL mixture (X_{IL} = 0.50)

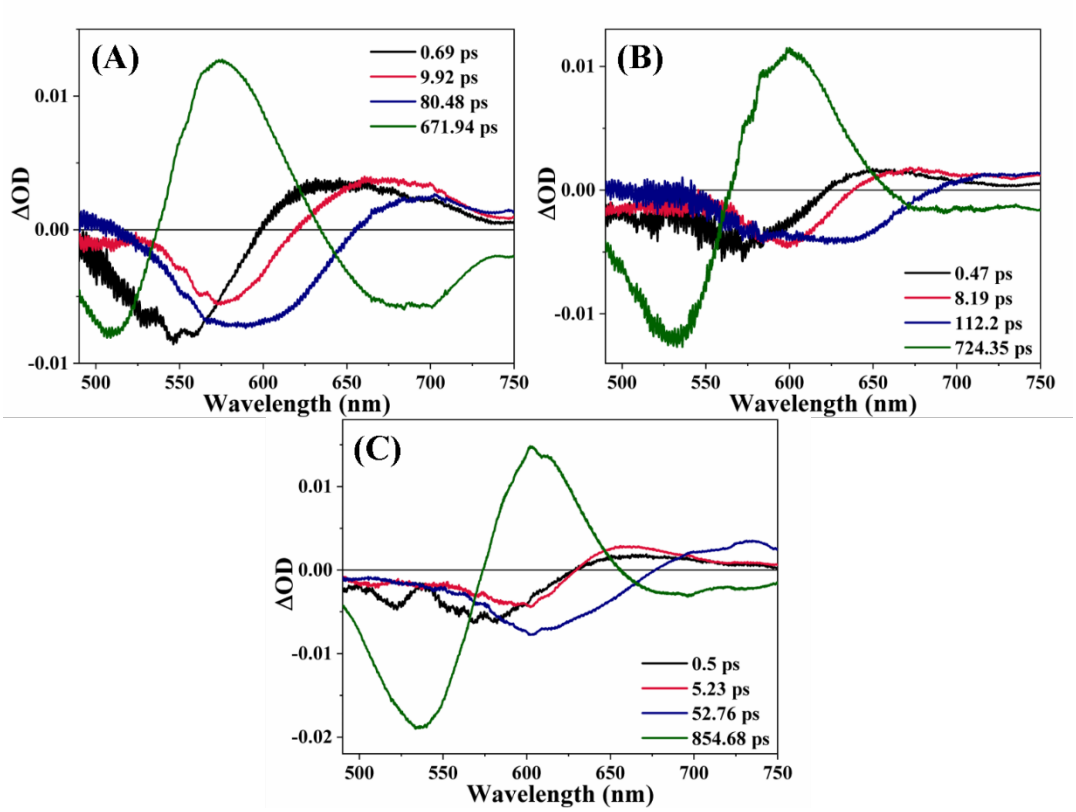

Figure B102: DAS of (A) D102, (B) D149 and (C) D205 in $BmimBF_4$-γ-BL mixture (X_{IL} = 0.80)

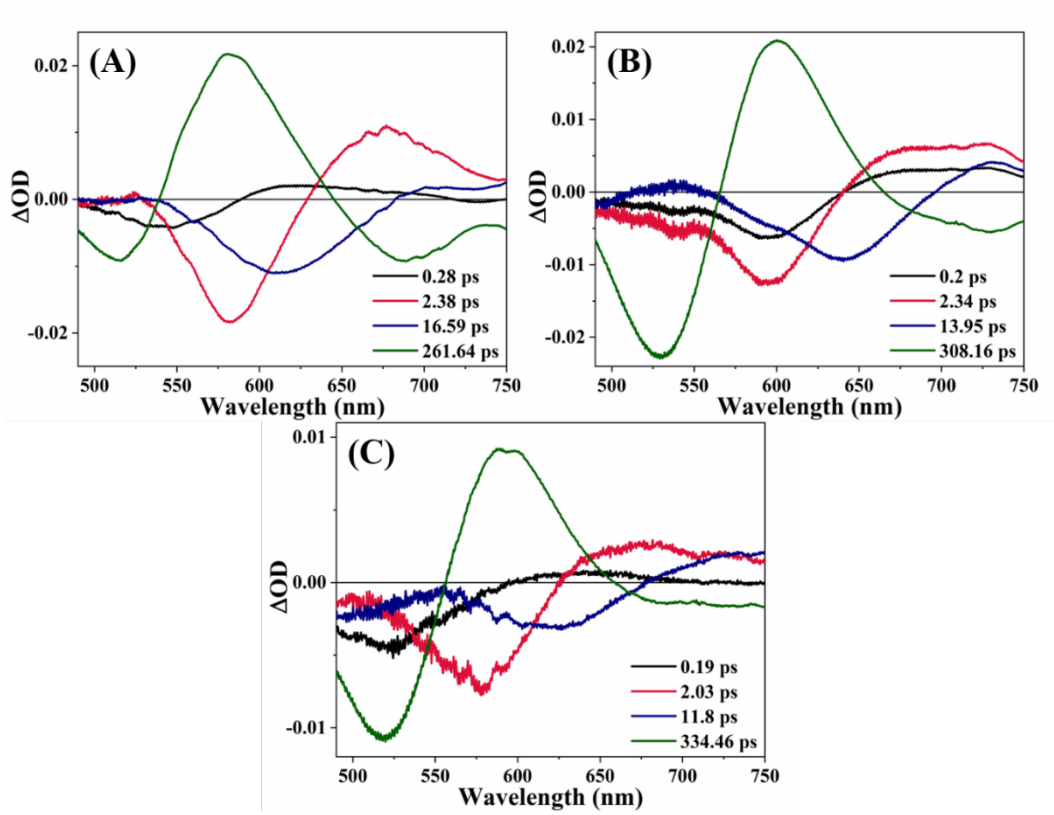

Figure B103: DAS of (A) D102, (B) D149 and (C) D205 in $BmimBF_4$-PC mixture (X_{IL} = 0.05)

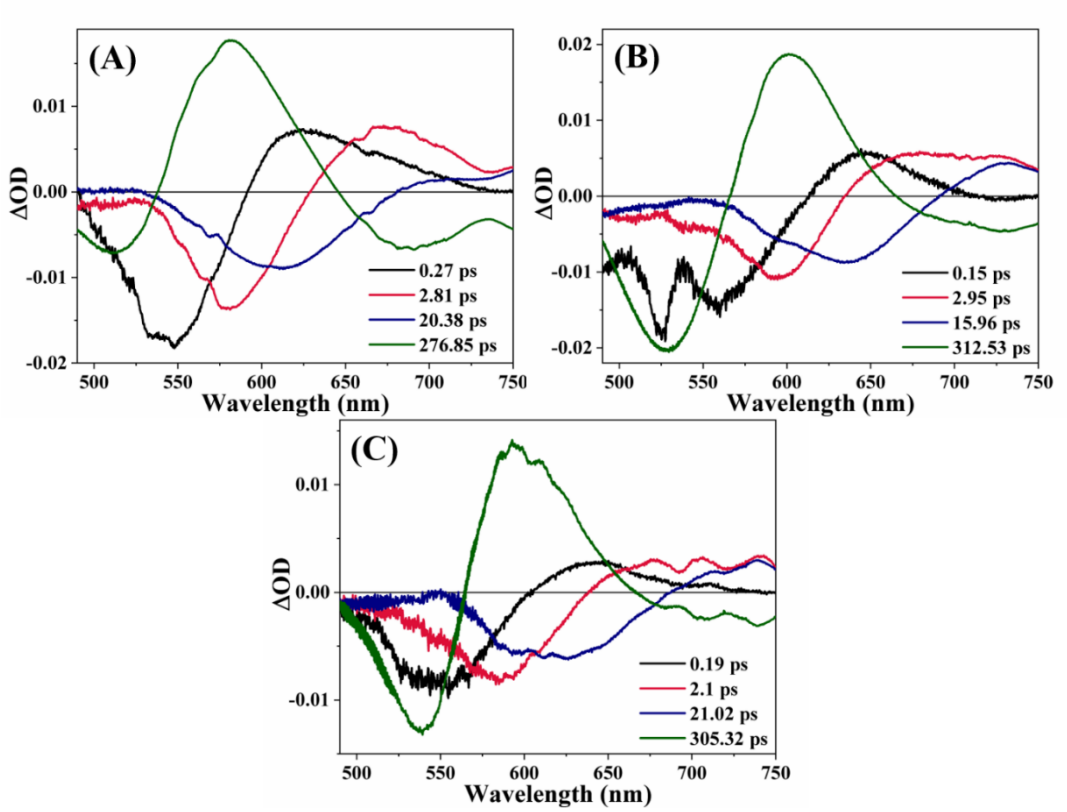

Figure B104: DAS of (A) D102, (B) D149 and (C) D205 in $BmimBF_4$-PC mixture (X_{IL} = 0.10)

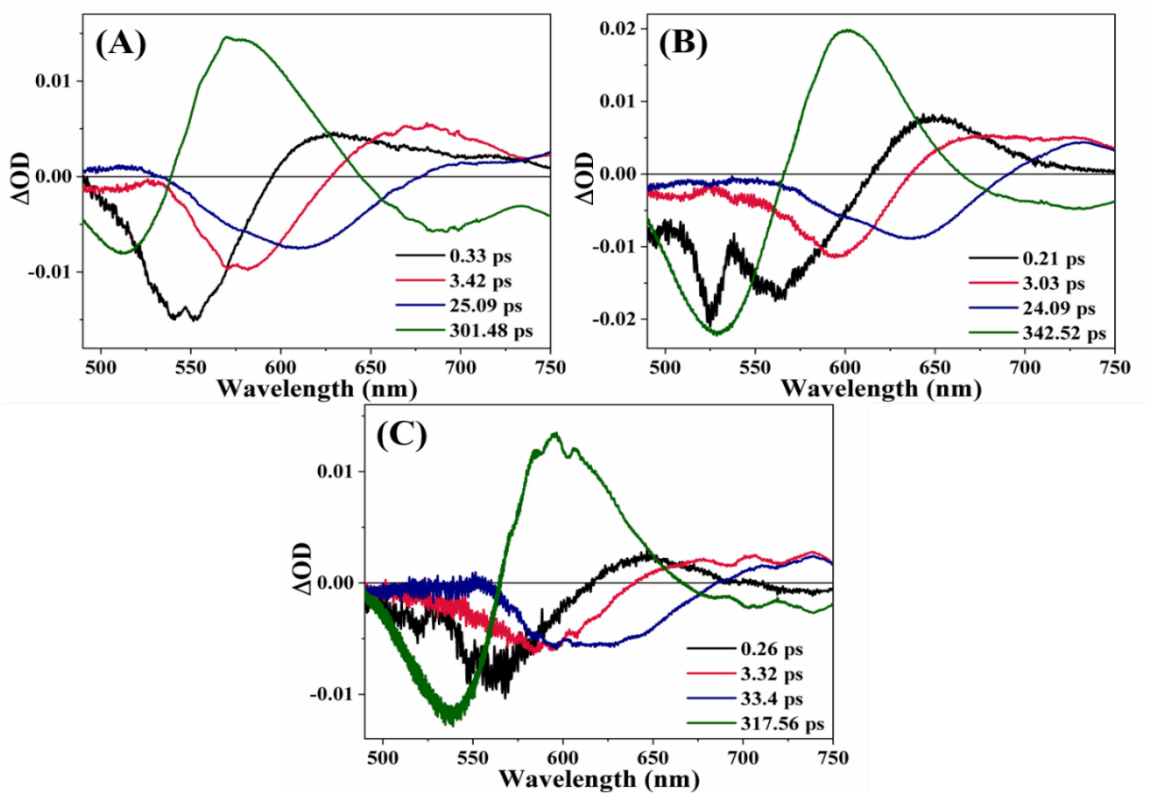

Figure B105: DAS of (A) D102, (B) D149 and (C) D205 in $BmimBF_4$-PC mixture (X_{IL} = 0.20)

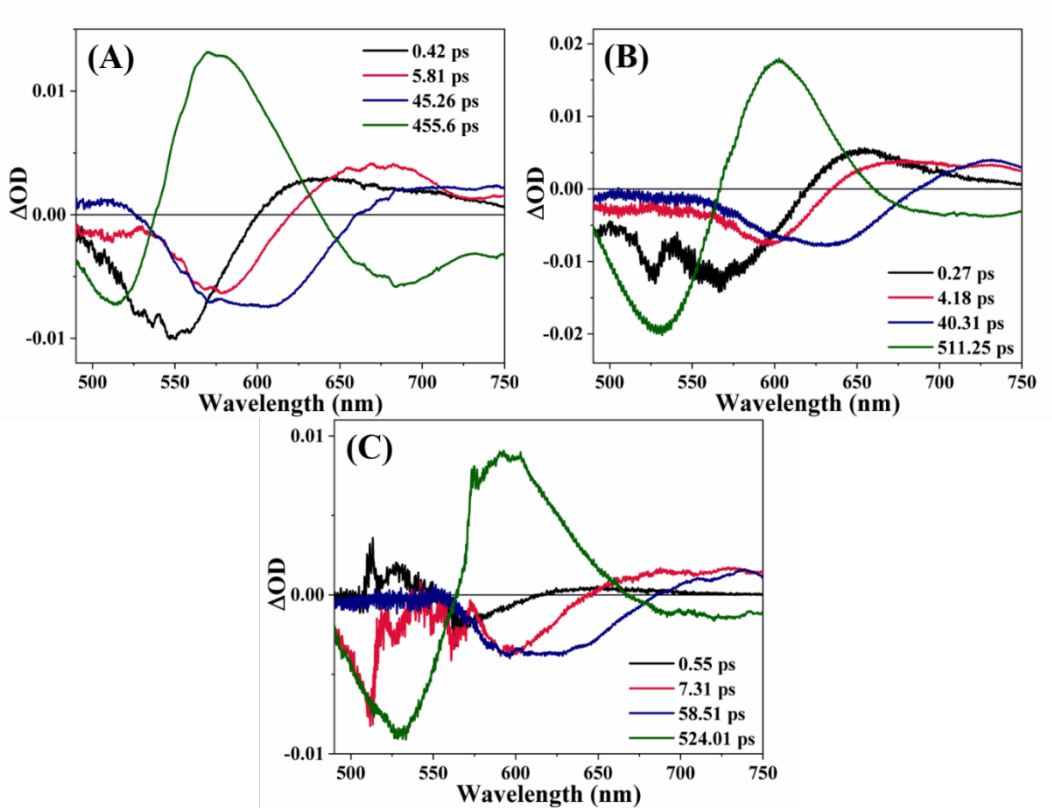

Figure B106: DAS of (A) D102, (B) D149 and (C) D205 in $BmimBF_4$-PC mixture (X_{IL} = 0.50)

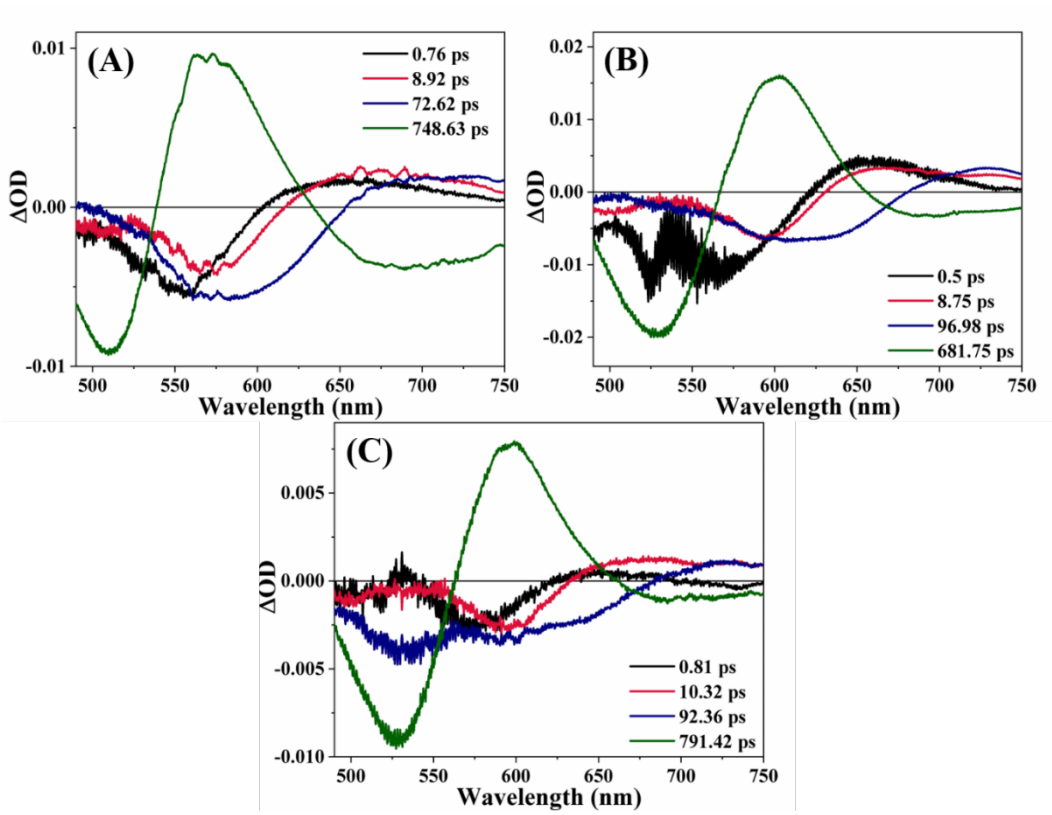

Figure B107: DAS of (A) D102, (B) D149 and (C) D205 in $BmimBF_4$-PC mixture (X_{IL} = 0.80)

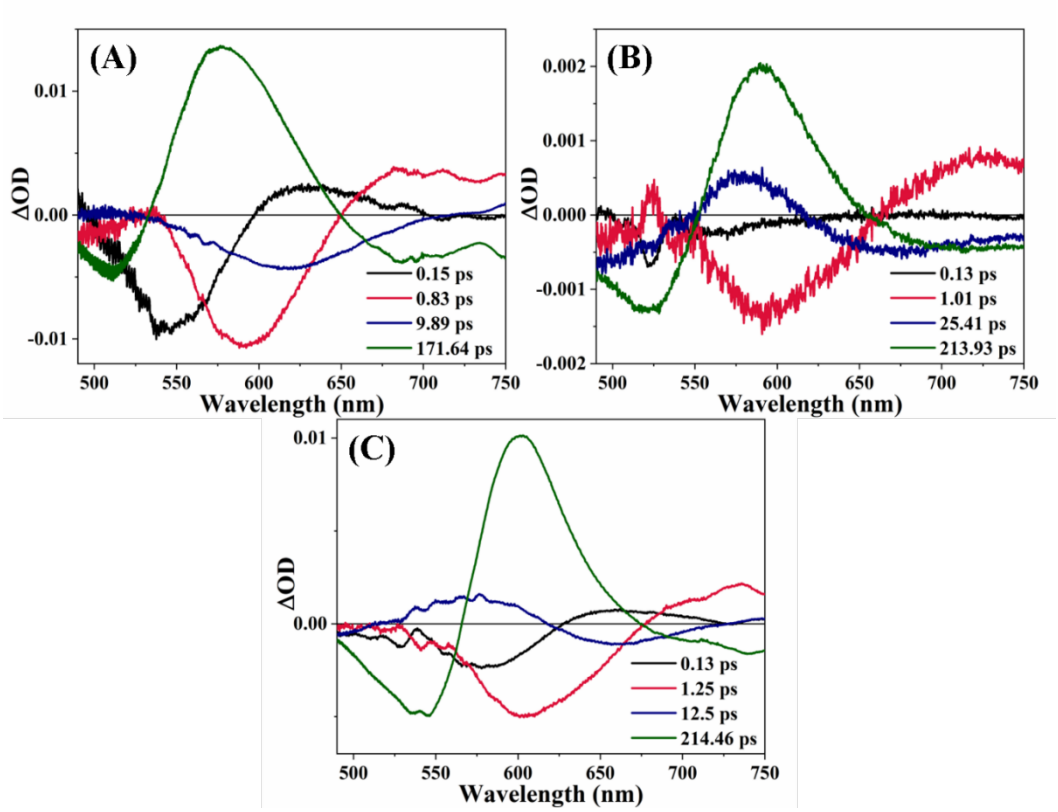

Figure B108: DAS of (A) D102, (B) D149 and (C) D205 in $BmimPF_6$-ACN mixture (X_{IL} = 0.05)

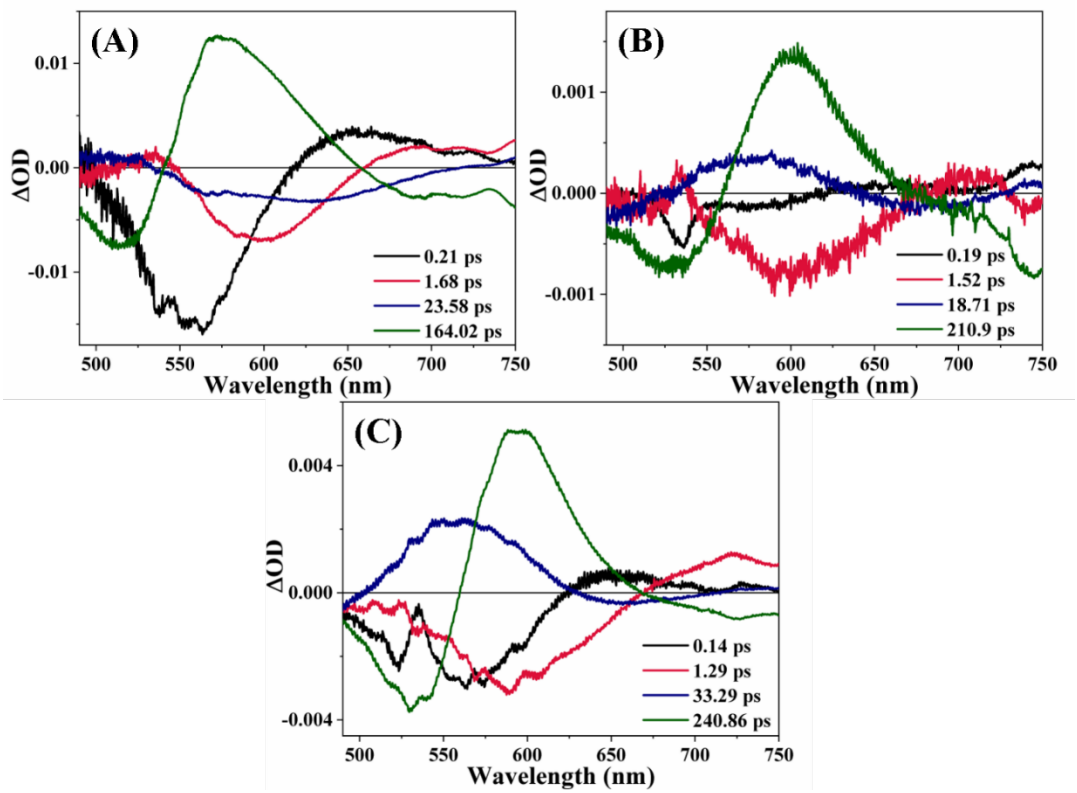

Figure B109: DAS of (A) D102, (B) D149 and (C) D205 in $BmimPF_6$-ACN mixture (X_{IL} = 0.10)

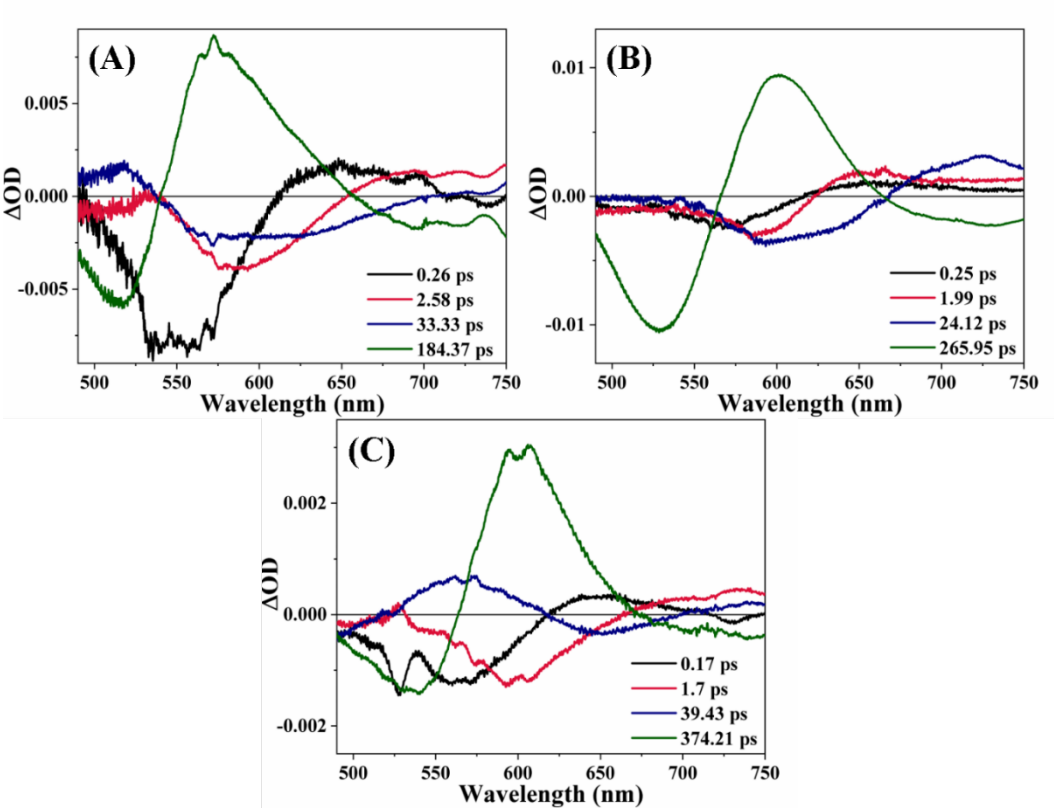

Figure B110: DAS of (A) D102, (B) D149 and (C) D205 in $BmimPF_6$-ACN mixture (X_{IL} = 0.20)

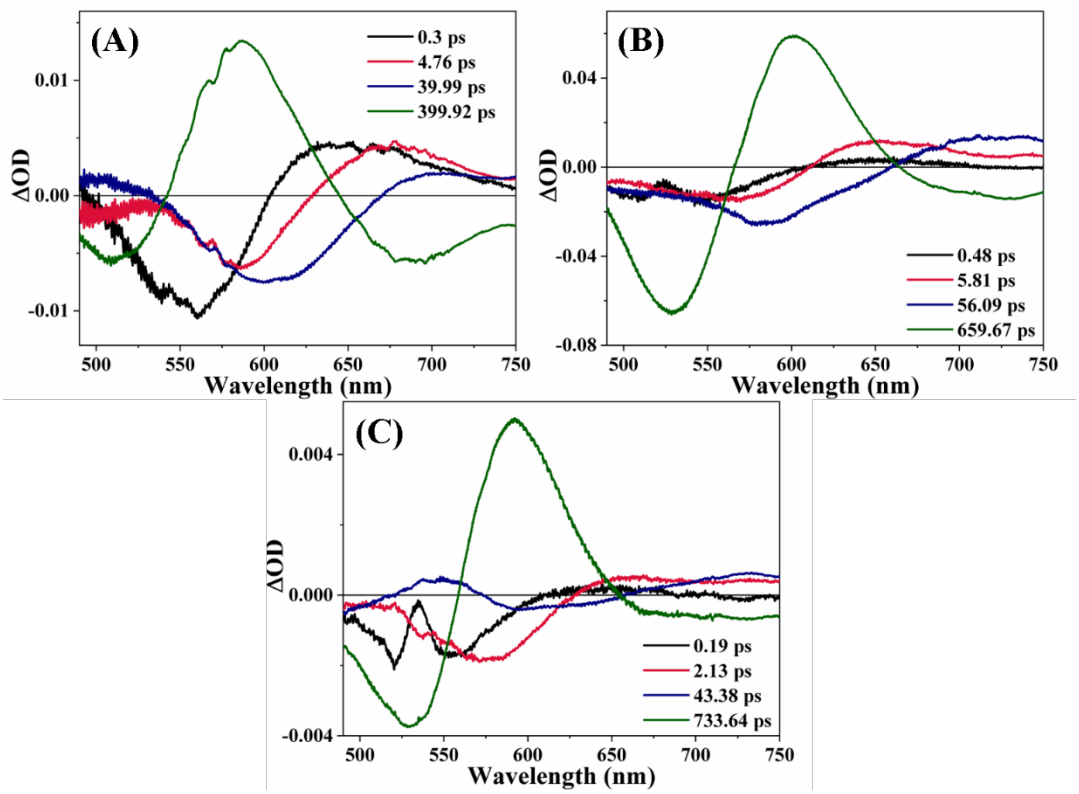

Figure B111: DAS of (A) D102, (B) D149 and (C) D205 in $BmimPF_6$-ACN mixture (X_{IL} = 0.50)

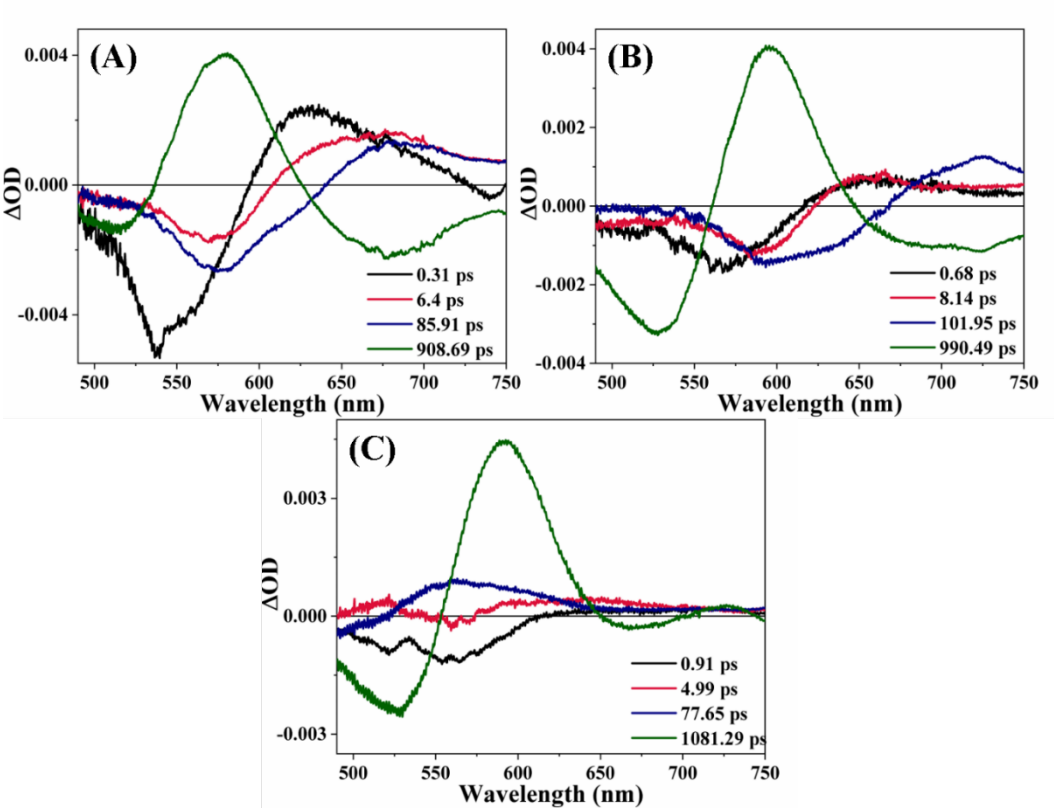

Figure B112: DAS of (A) D102, (B) D149 and (C) D205 in BmimPF$_6$-ACN mixture (X_{IL} = 0.80)

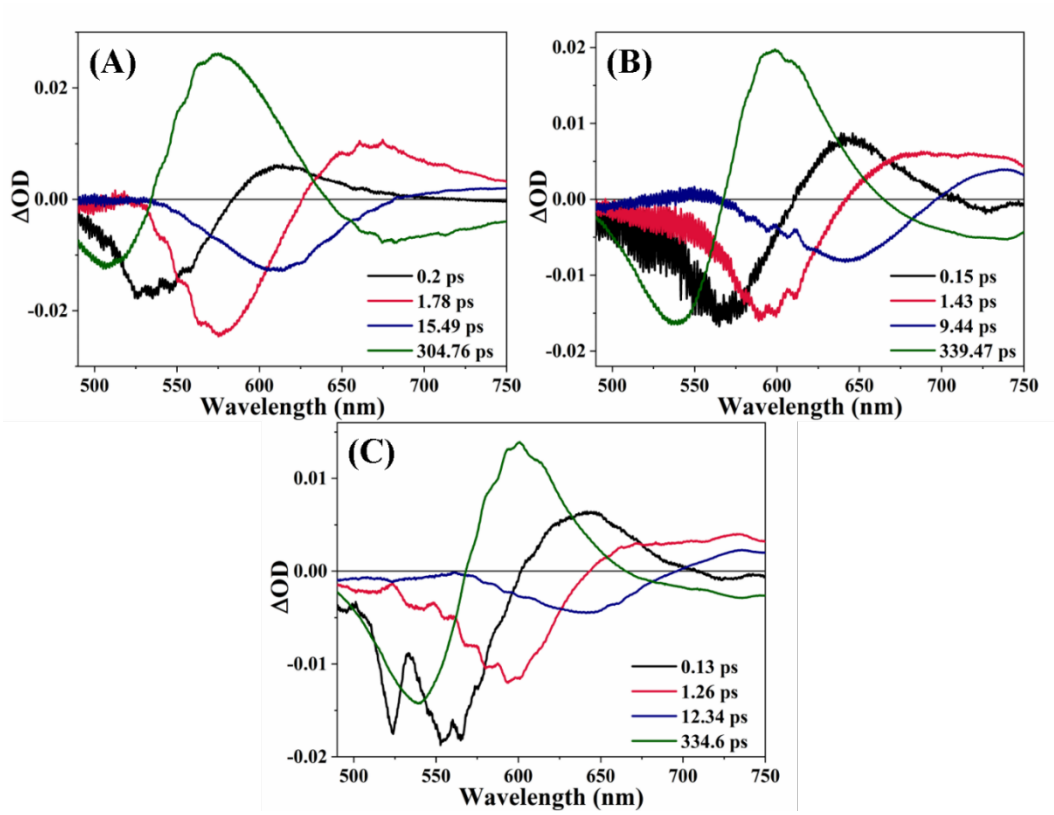

Figure B113: DAS of (A) D102, (B) D149 and (C) D205 in BmimPF$_6$-γ-BL mixture (X_{IL} = 0.05)

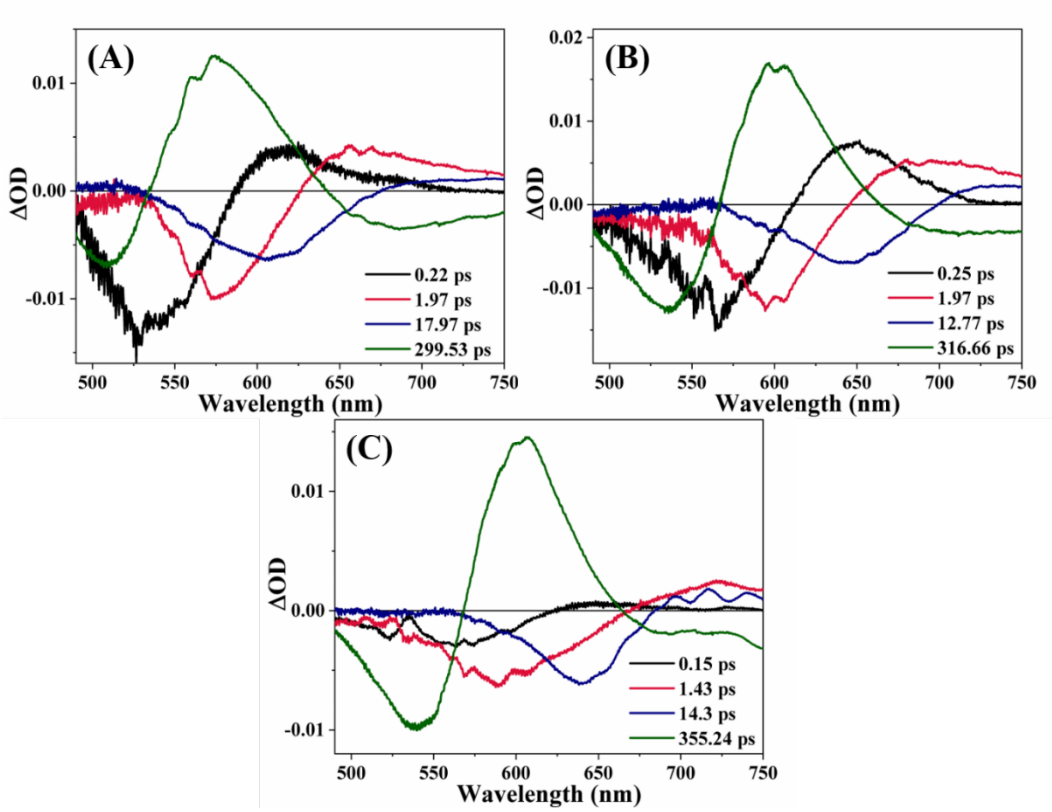

Figure B114: DAS of (A) D102, (B) D149 and (C) D205 in $BmimPF_6$-γ-BL mixture (X_{IL} = 0.10)

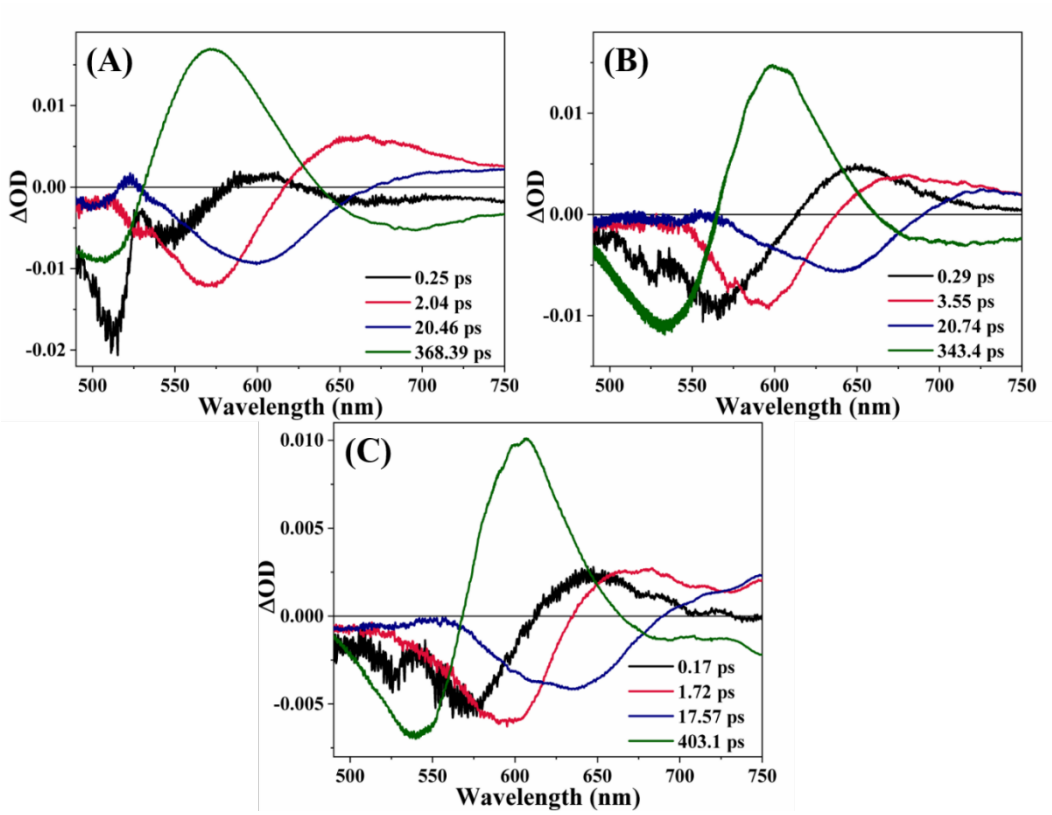

Figure B115: DAS of (A) D102, (B) D149 and (C) D205 in $BmimPF_6$-γ-BL mixture (X_{IL} = 0.20)

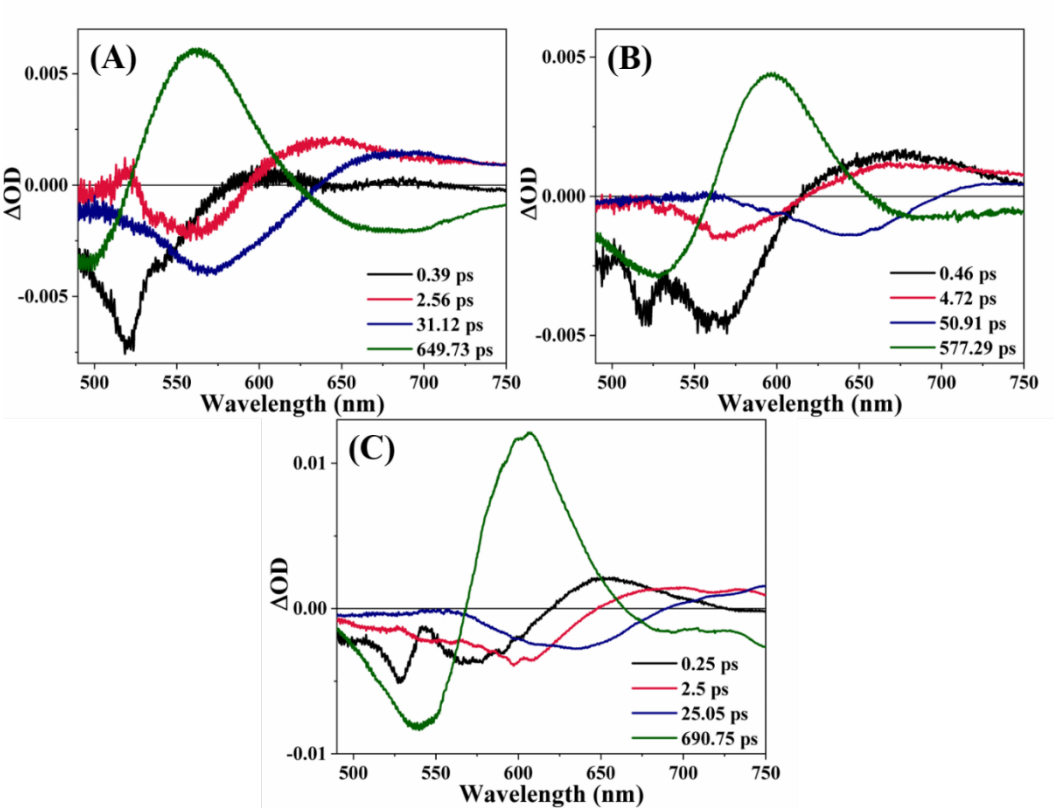

Figure B116: DAS of (A) D102, (B) D149 and (C) D205 in $BmimPF_6$-γ-BL mixture (X_{IL} = 0.50)

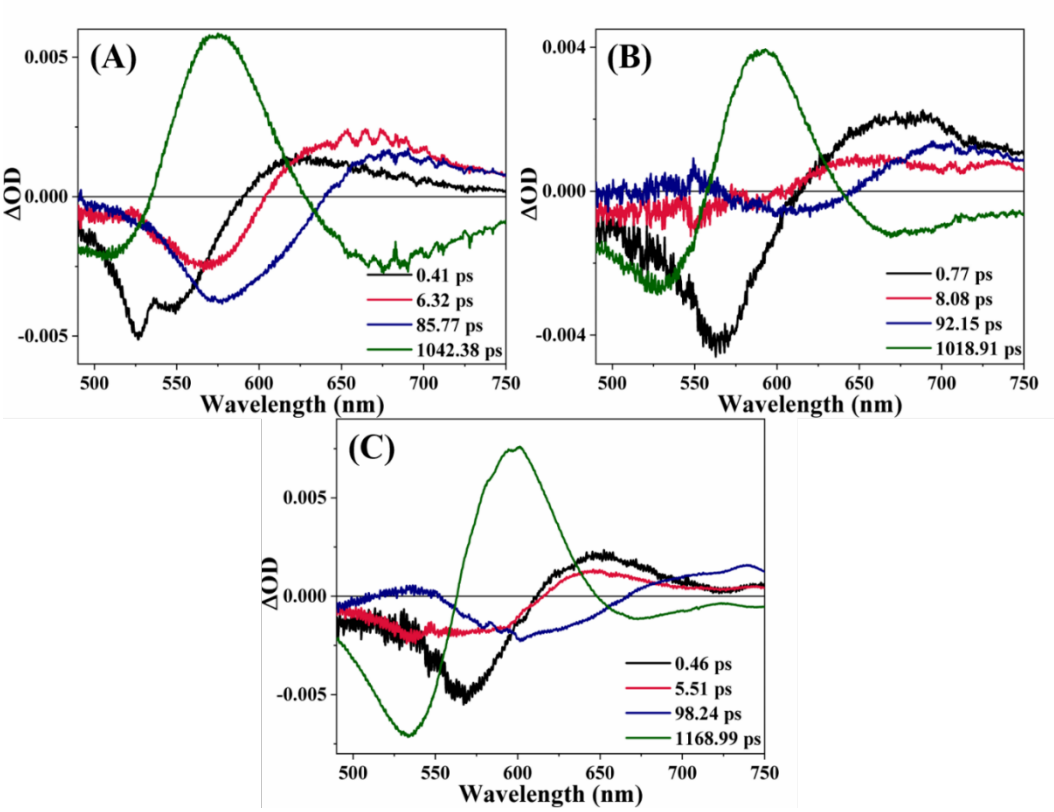

Figure B117: DAS of (A) D102, (B) D149 and (C) D205 in $BmimPF_6$-γ-BL mixture (X_{IL} = 0.80)

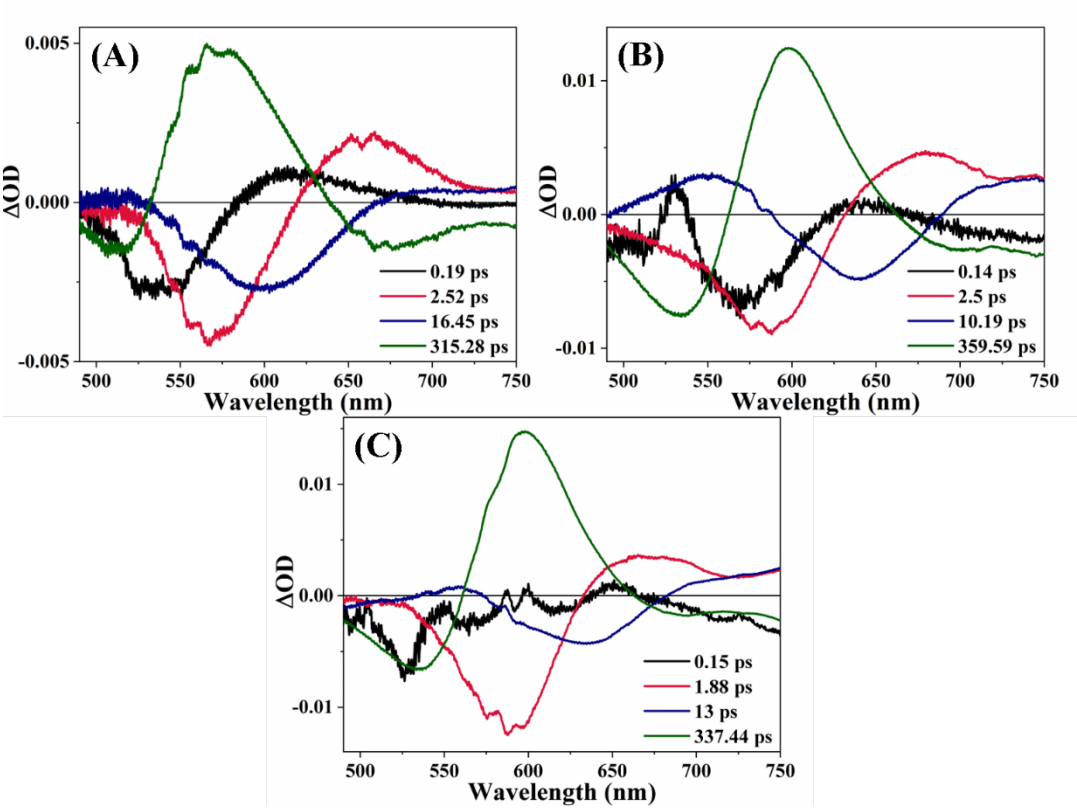

Figure B118: DAS of (A) D102, (B) D149 and (C) D205 in $BmimPF_6$-PC mixture (X_{IL} = 0.05)

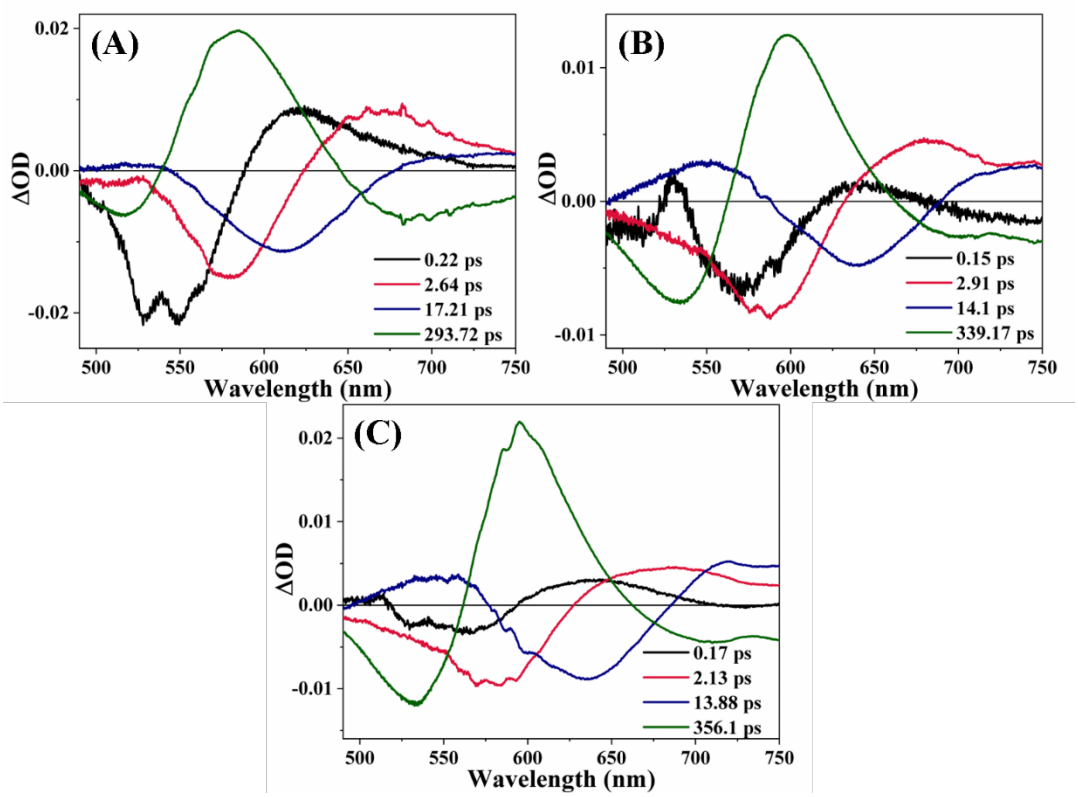

Figure B119: DAS of (A) D102, (B) D149 and (C) D205 in $BmimPF_6$-PC mixture (X_{IL} = 0.10)

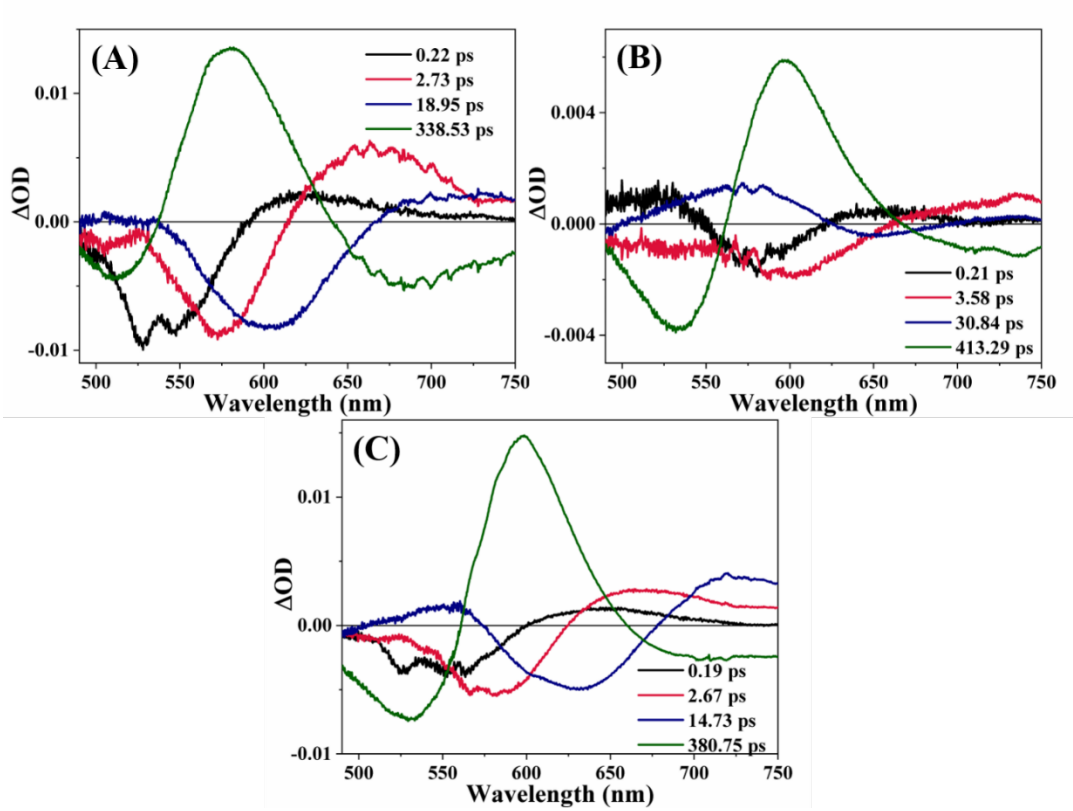

Figure B120: DAS of (A) D102, (B) D149 and (C) D205 in $BmimPF_6$-PC mixture (X_{IL} = 0.20)

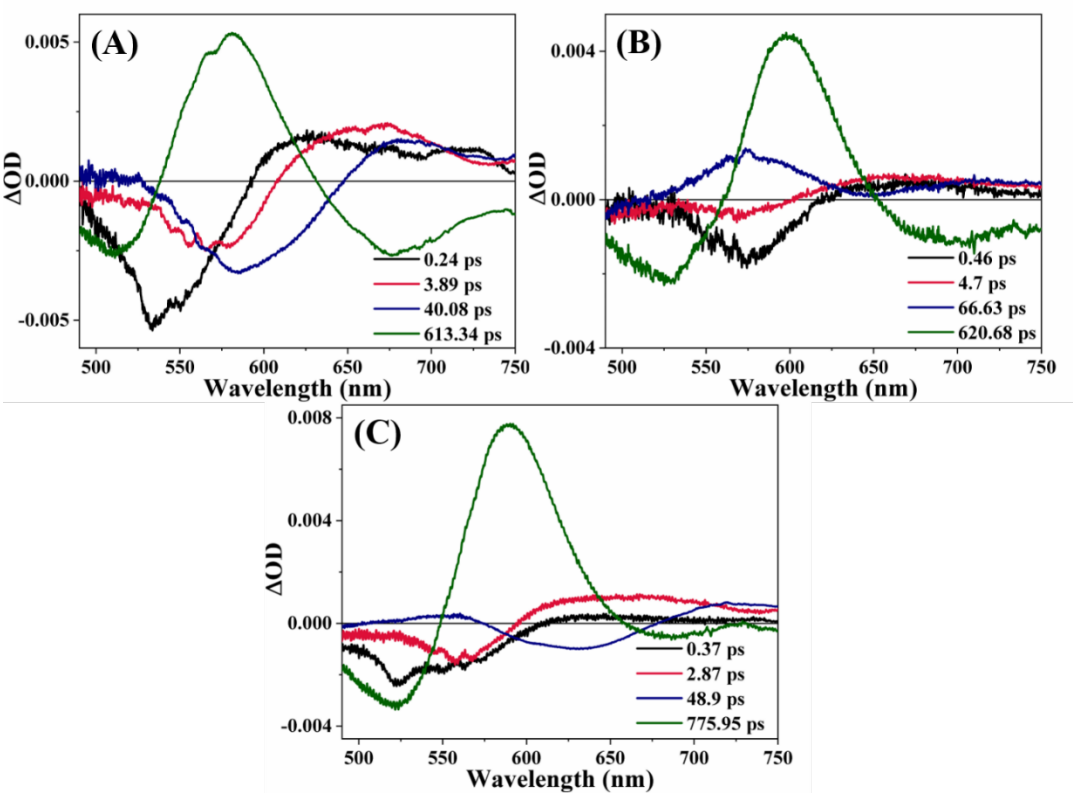

Figure B121: DAS of (A) D102, (B) D149 and (C) D205 in $BmimPF_6$-PC mixture (X_{IL} = 0.50)

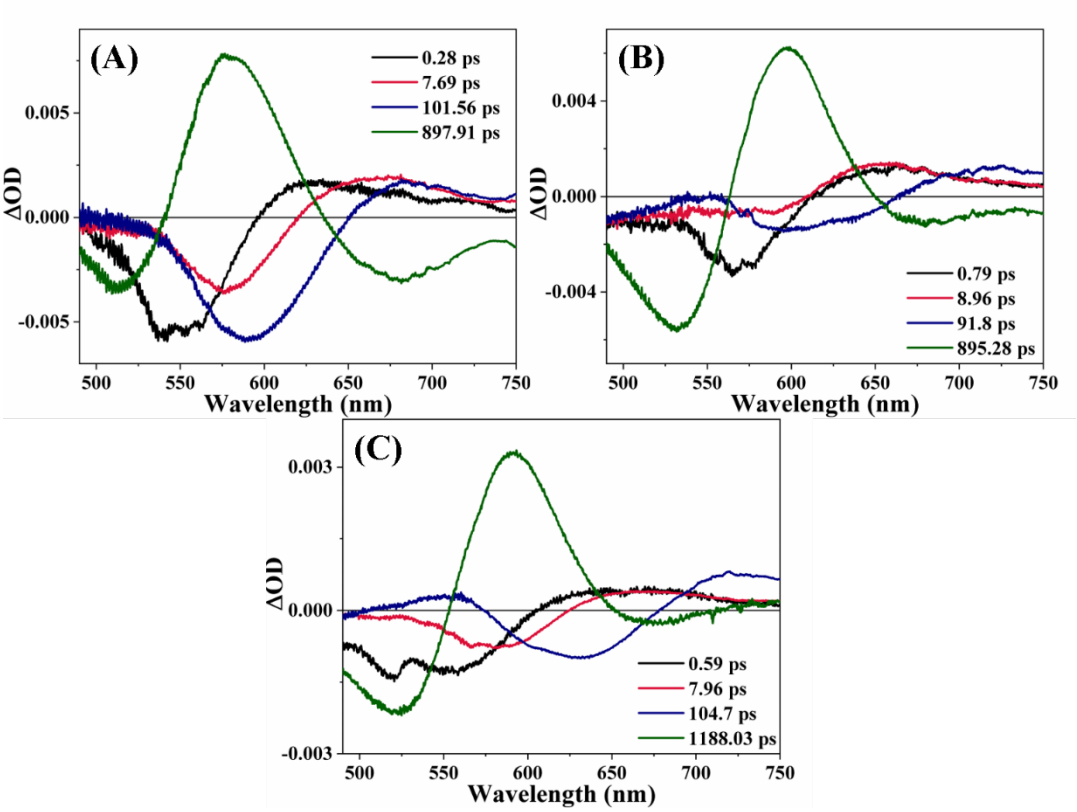

Figure B122: DAS of (A) D102, (B) D149 and (C) D205 in $BmimPF_6$-PC mixture (X_{IL} = 0.80)

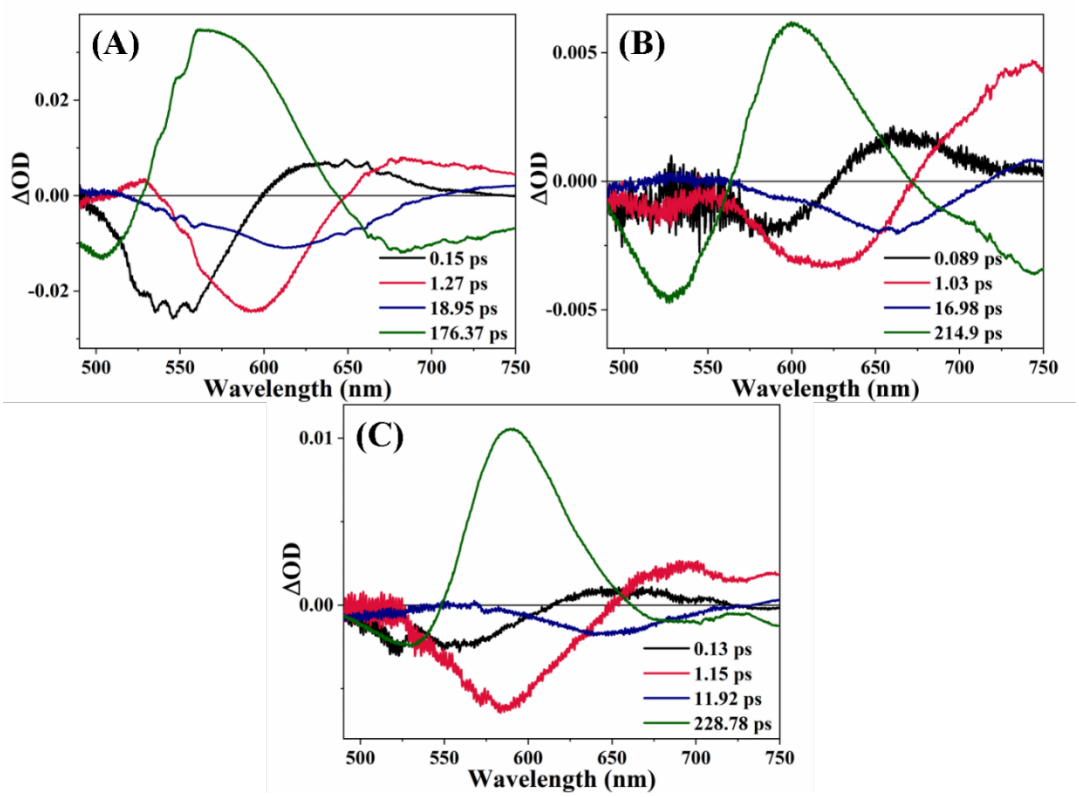

Figure B123: DAS of (A) D102, (B) D149 and (C) D205 in BmimTFO-ACN mixture (X_{IL} = 0.05)

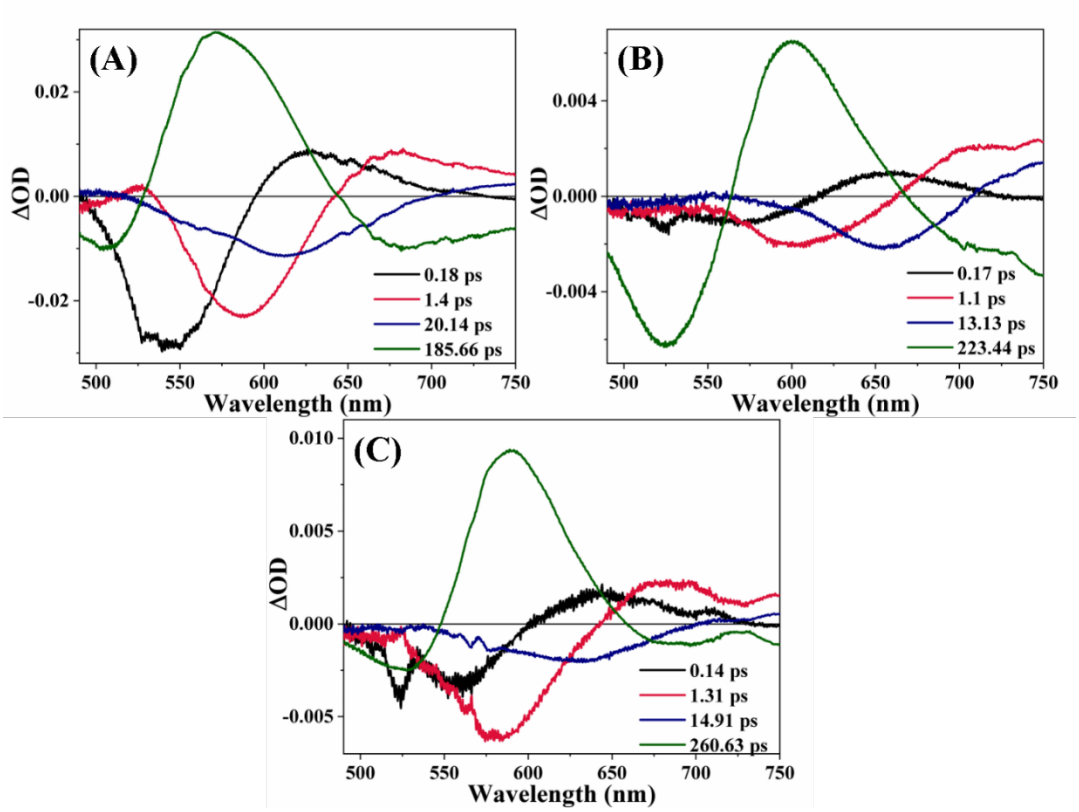

Figure B124: DAS of (A) D102, (B) D149 and (C) D205 in BmimTFO-ACN mixture (X_{IL} = 0.10)

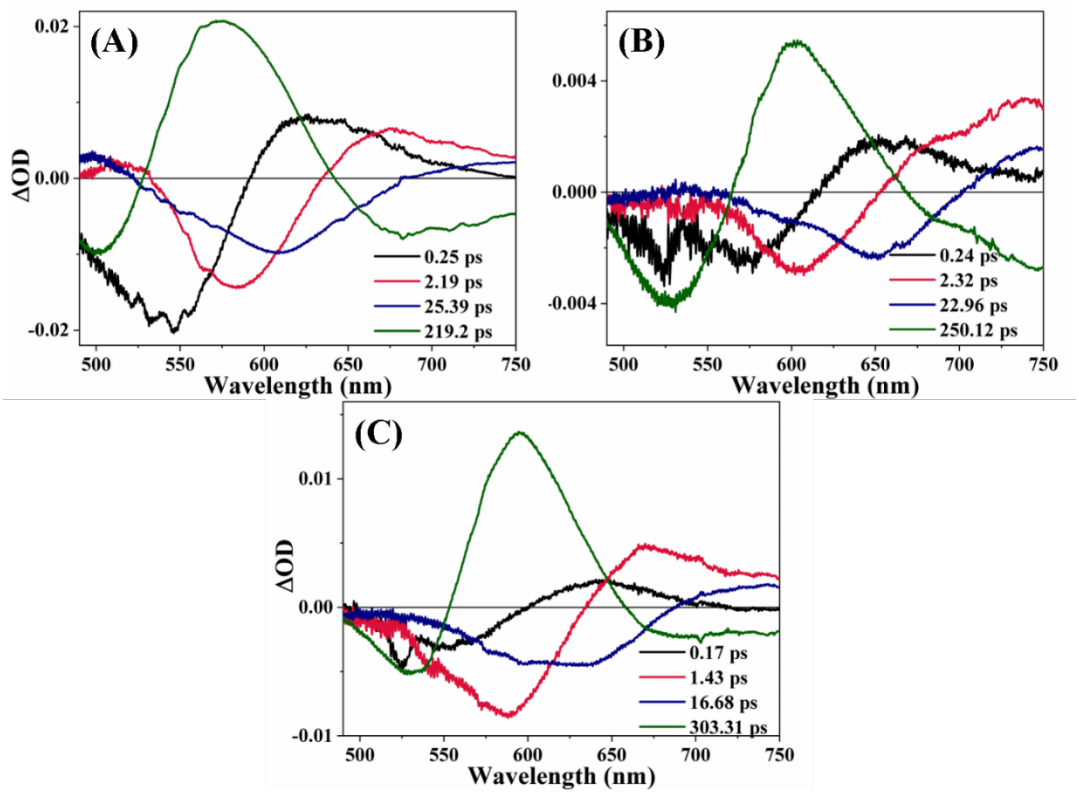

Figure B125: DAS of (A) D102, (B) D149 and (C) D205 in BmimTFO-ACN mixture (X_{IL} = 0.20)

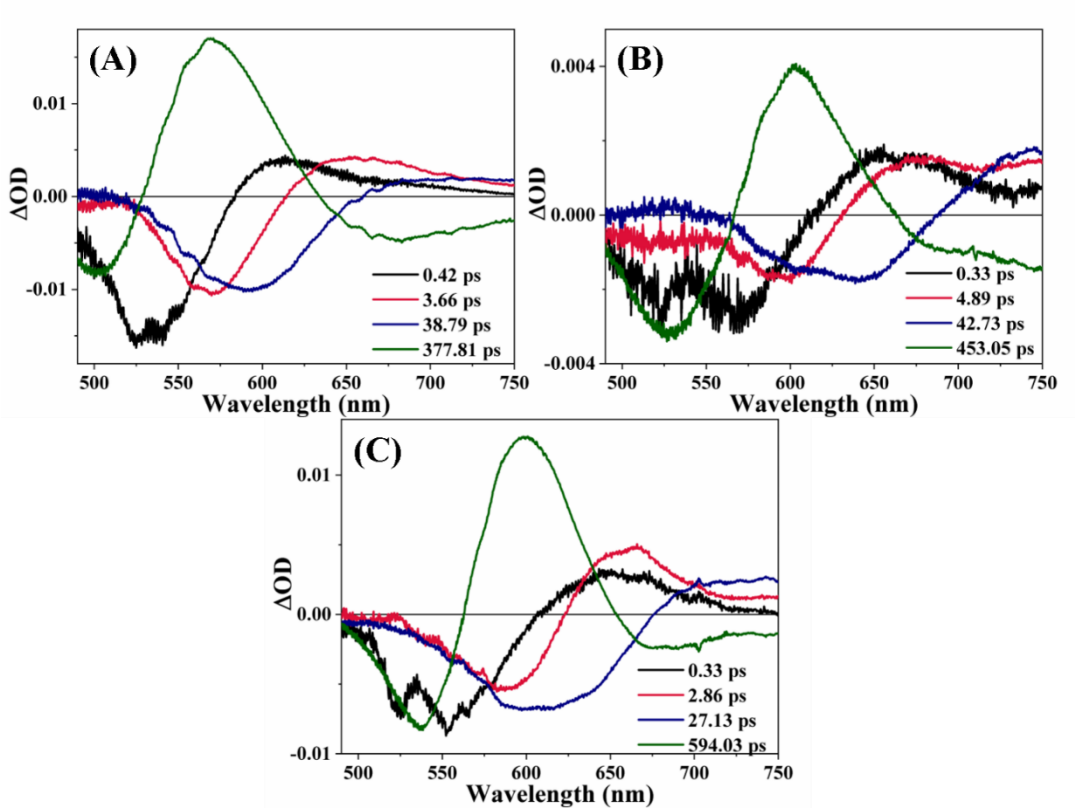

Figure B126: DAS of (A) D102, (B) D149 and (C) D205 in BmimTFO-ACN mixture (X_{IL} = 0.50)

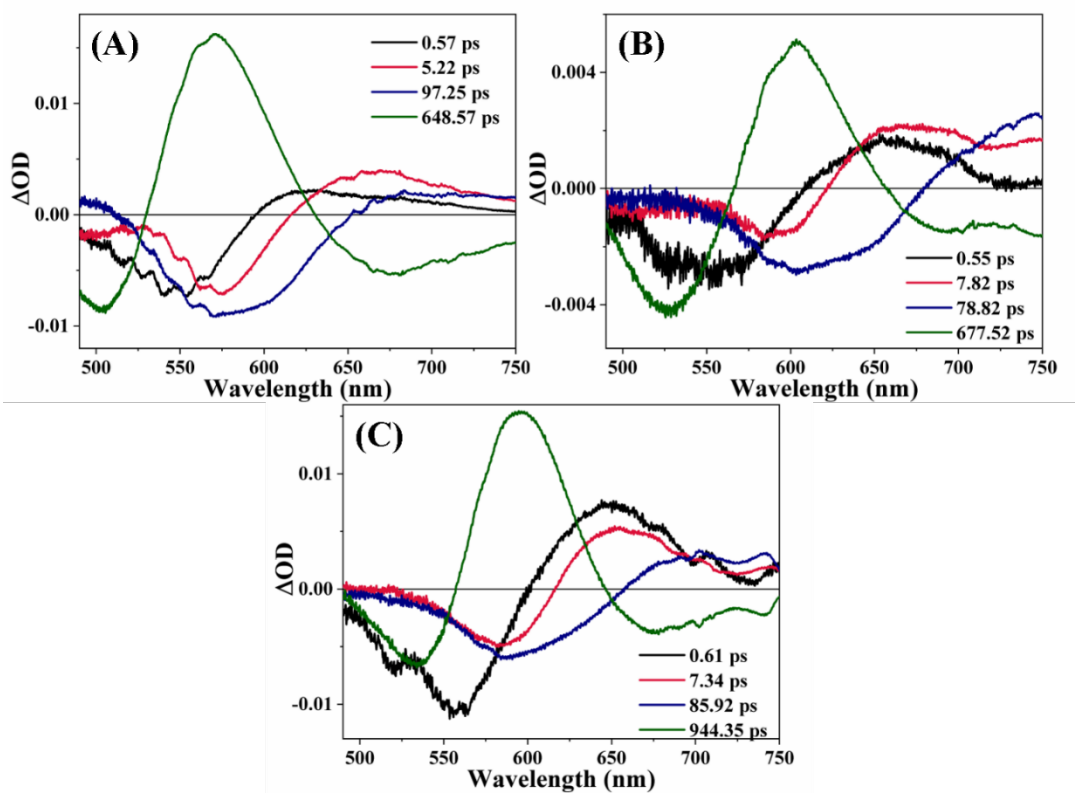

Figure B127: DAS of (A) D102, (B) D149 and (C) D205 in BmimTFO-ACN mixture (X_{IL} = 0.80)

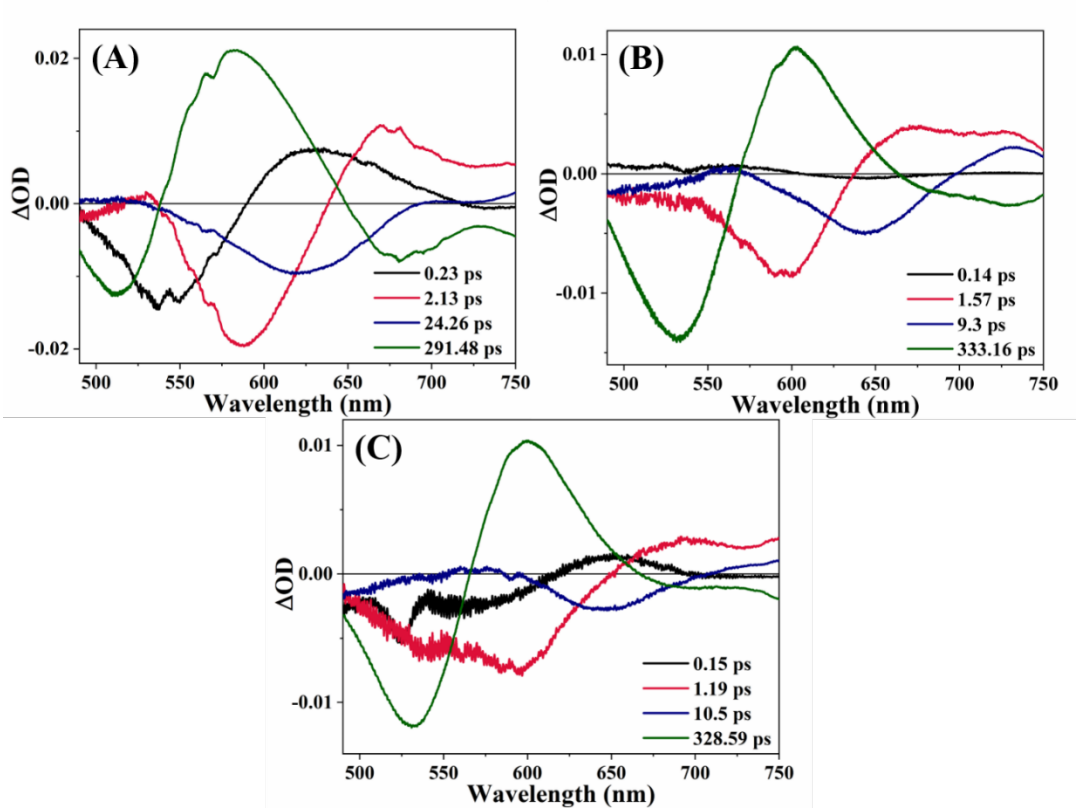

Figure B128: DAS of (A) D102, (B) D149 and (C) D205 in BmimTFO-γ-BL mixture (X_{IL} = 0.05)

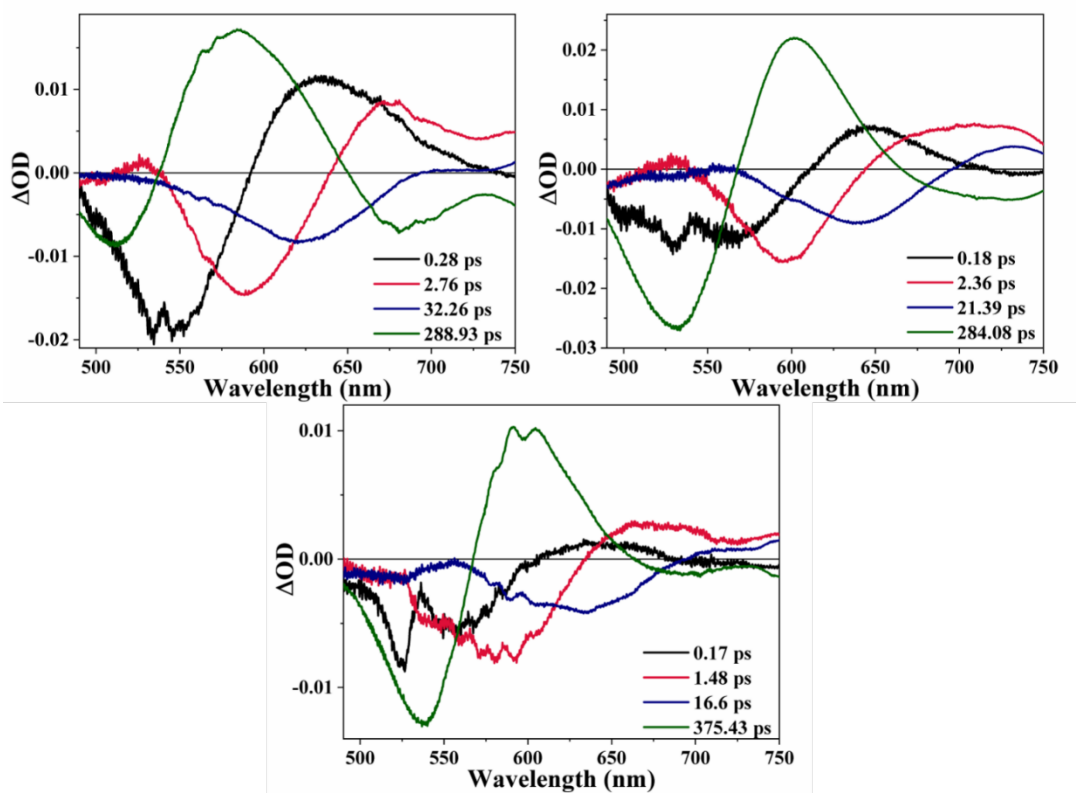

Figure B129: DAS of (A) D102, (B) D149 and (C) D205 in BmimTFO-γ-BL mixture (X_{IL} = 0.10)

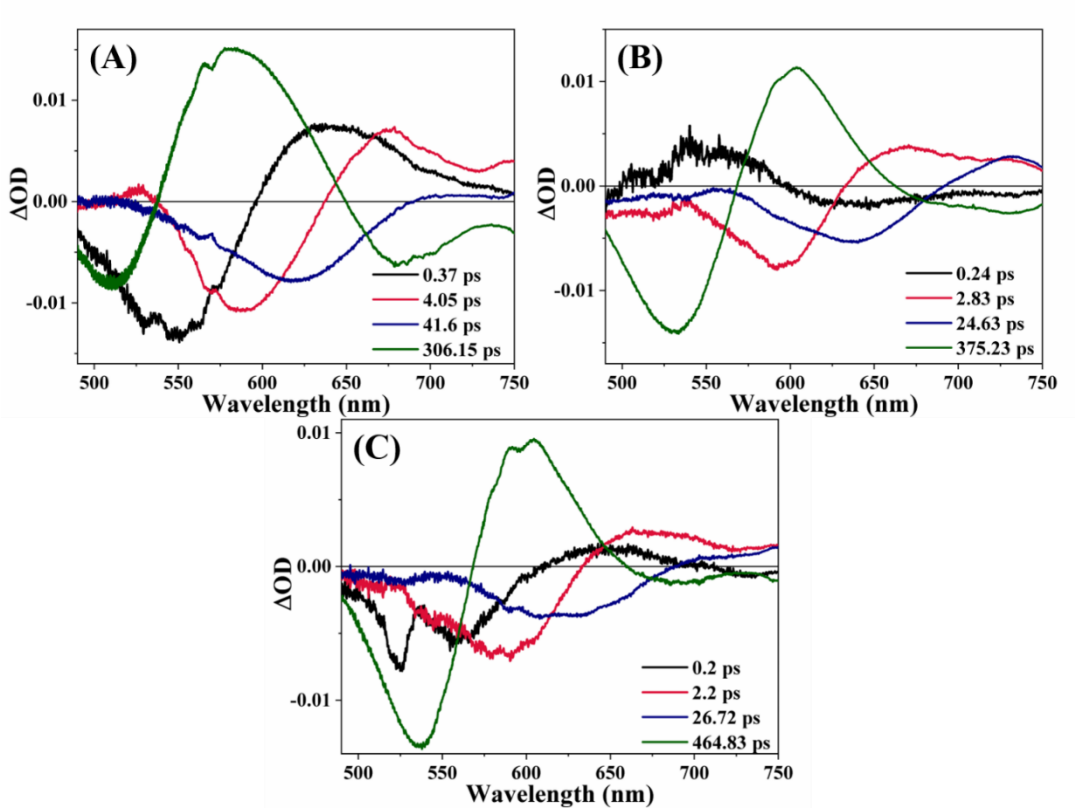

Figure B130: DAS of (A) D102, (B) D149 and (C) D205 in BmimTFO-γ-BL mixture (X_{IL} = 0.20)

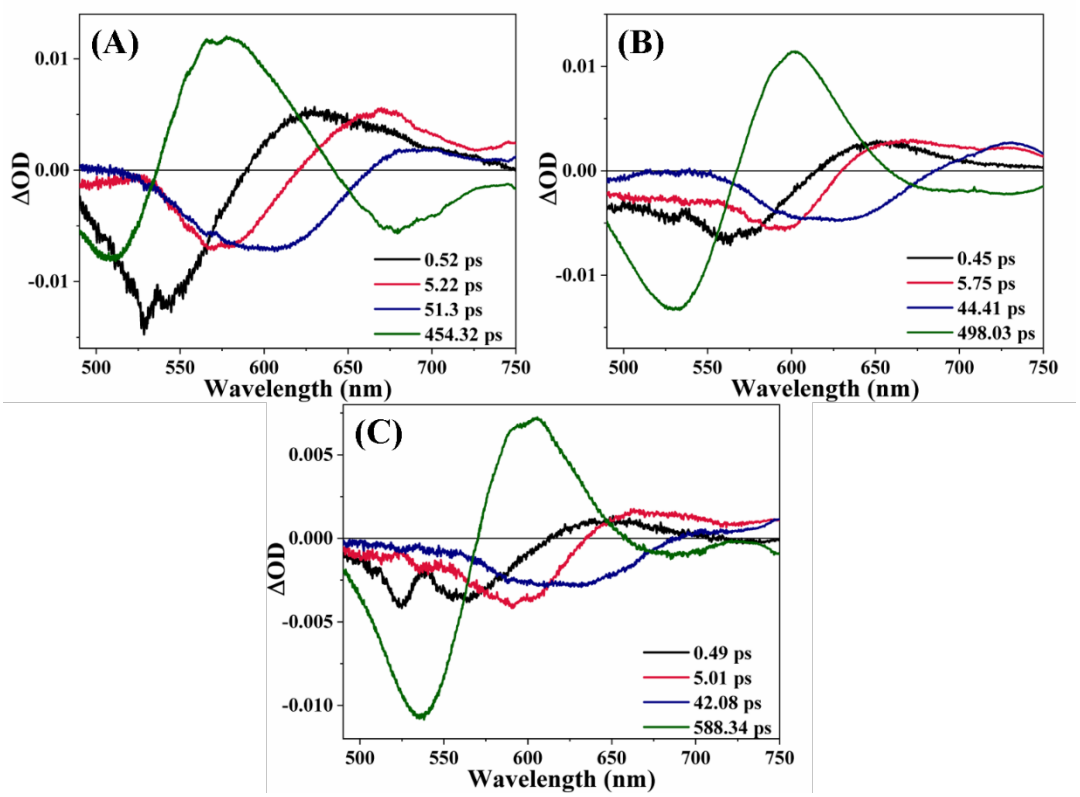

Figure B131: DAS of (A) D102, (B) D149 and (C) D205 in BmimTFO-γ-BL mixture (X_{IL} = 0.50)

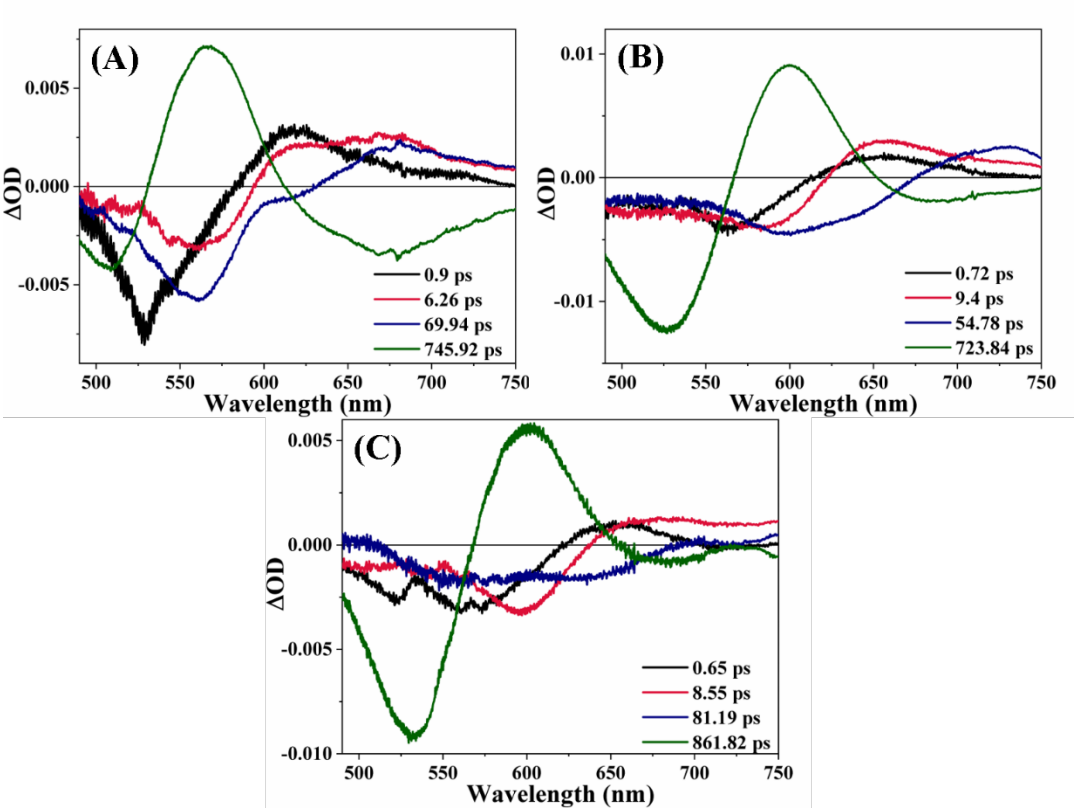

Figure B132: DAS of (A) D102, (B) D149 and (C) D205 in BmimTFO-γ-BL mixture (X_{IL} = 0.80)

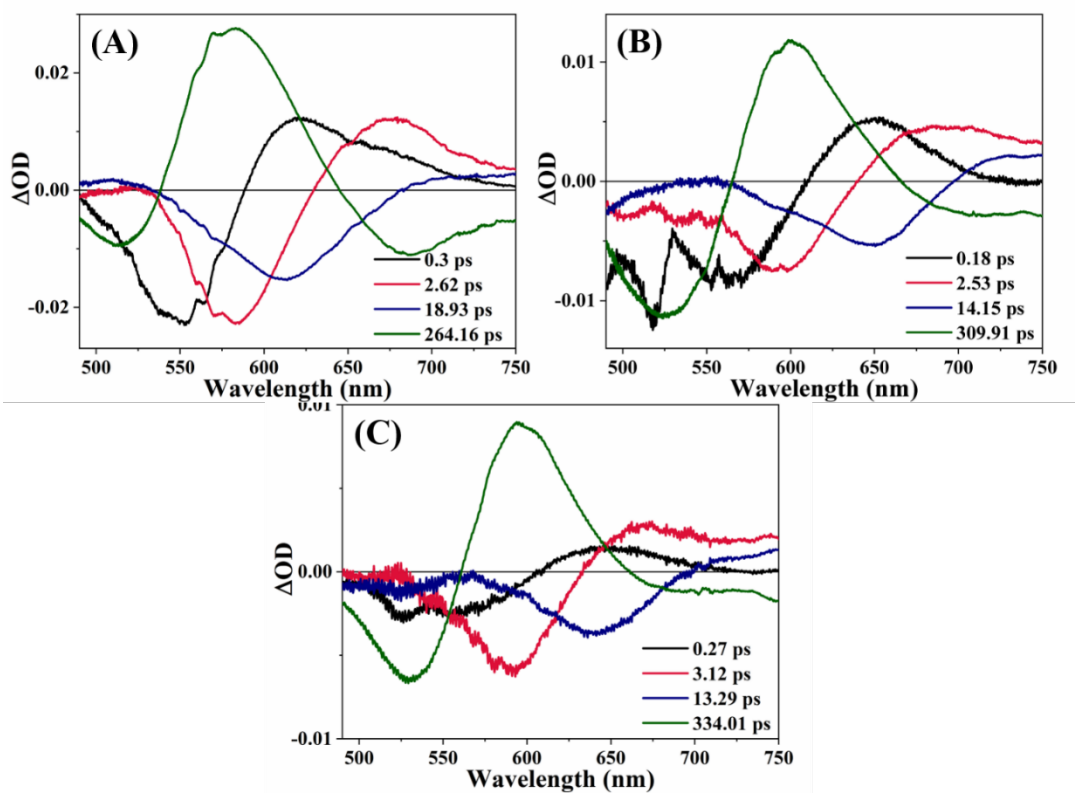

Figure B133: DAS of (A) D102, (B) D149 and (C) D205 in BmimTFO-PC mixture (X_{IL} = 0.05)

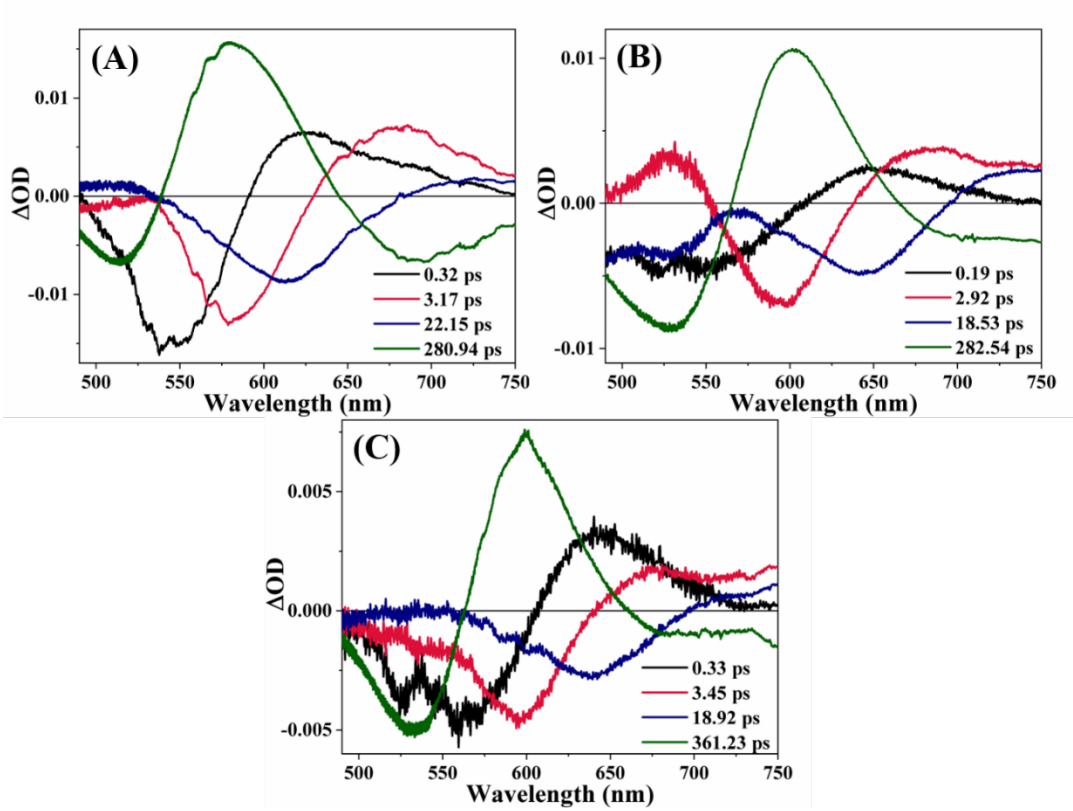

Figure B134: DAS of (A) D102, (B) D149 and (C) D205 in BmimTFO-PC mixture (X_{IL} = 0.10)

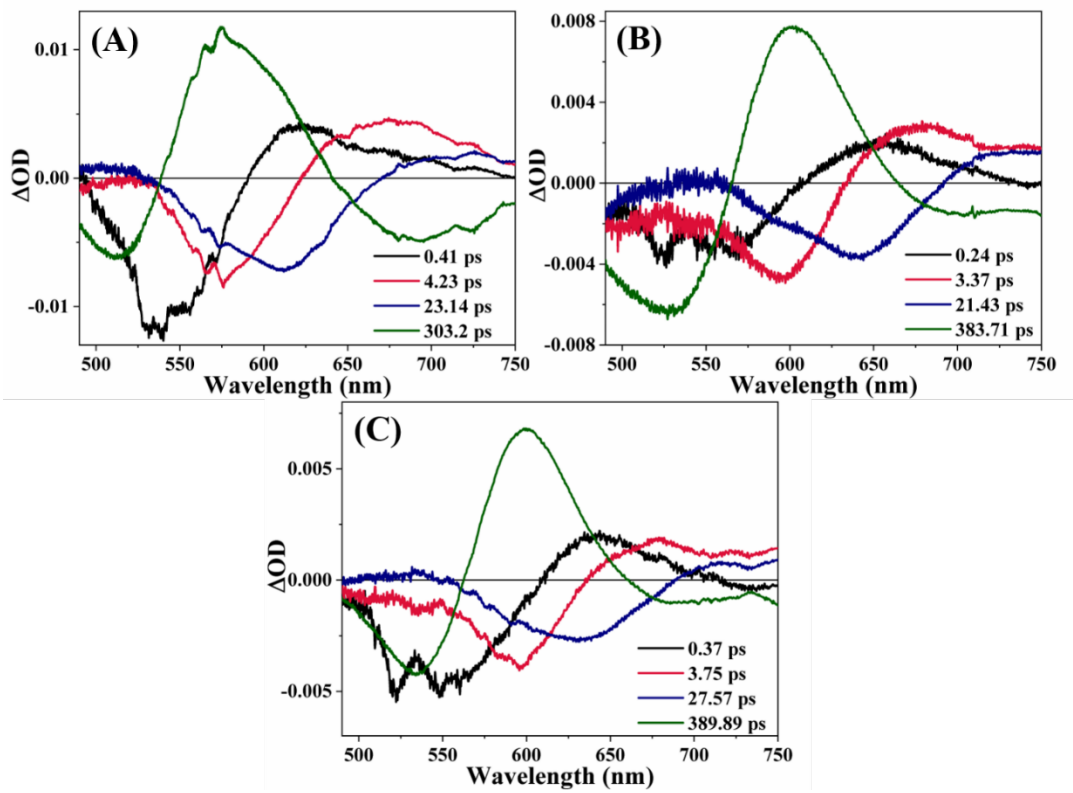

Figure B135: DAS of (A) D102, (B) D149 and (C) D205 in BmimTFO-PC mixture (X_{IL} = 0.20)

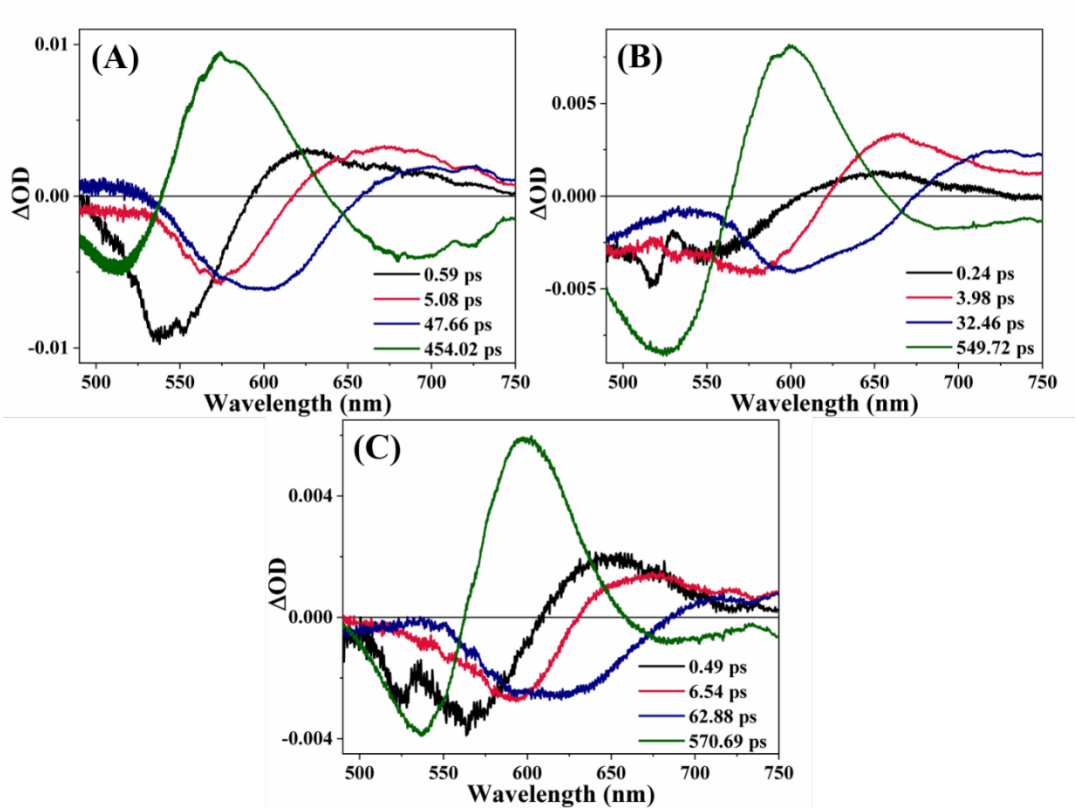

Figure B136: DAS of (A) D102, (B) D149 and (C) D205 in BmimTFO-PC mixture (X_{IL} = 0.50)

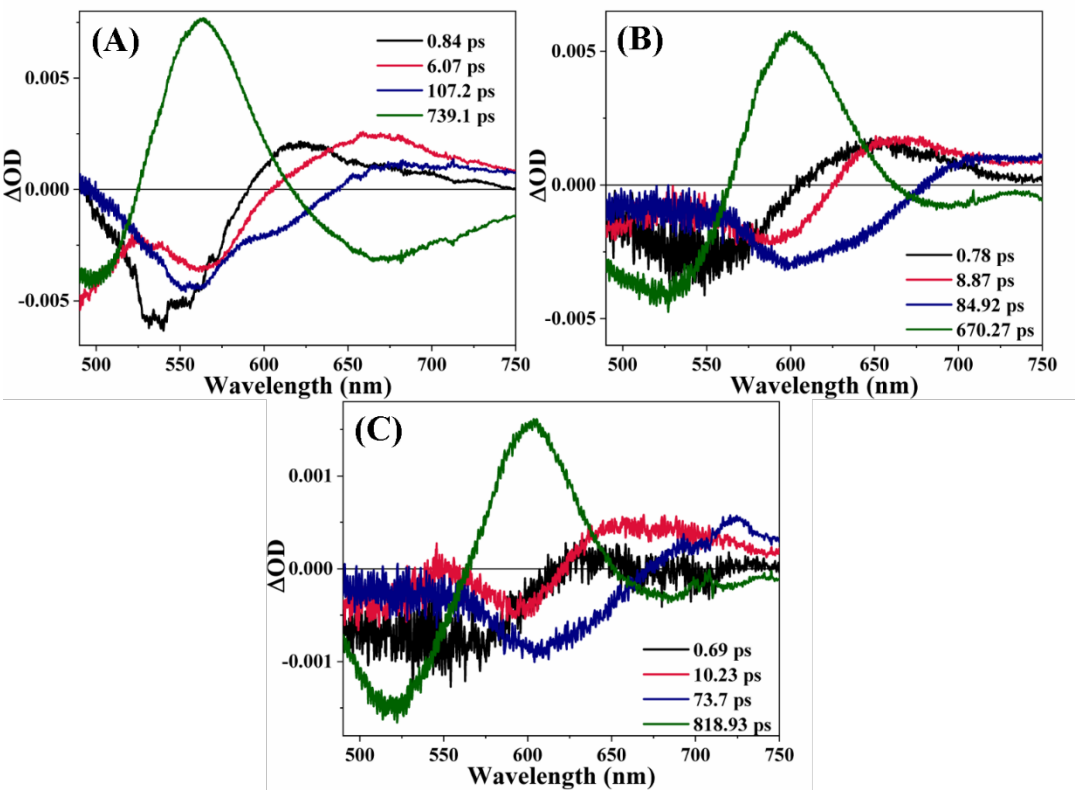

Figure B137: DAS of (A) D102, (B) D149 and (C) D205 in BmimTFO-PC mixture (X_{IL} = 0.80)

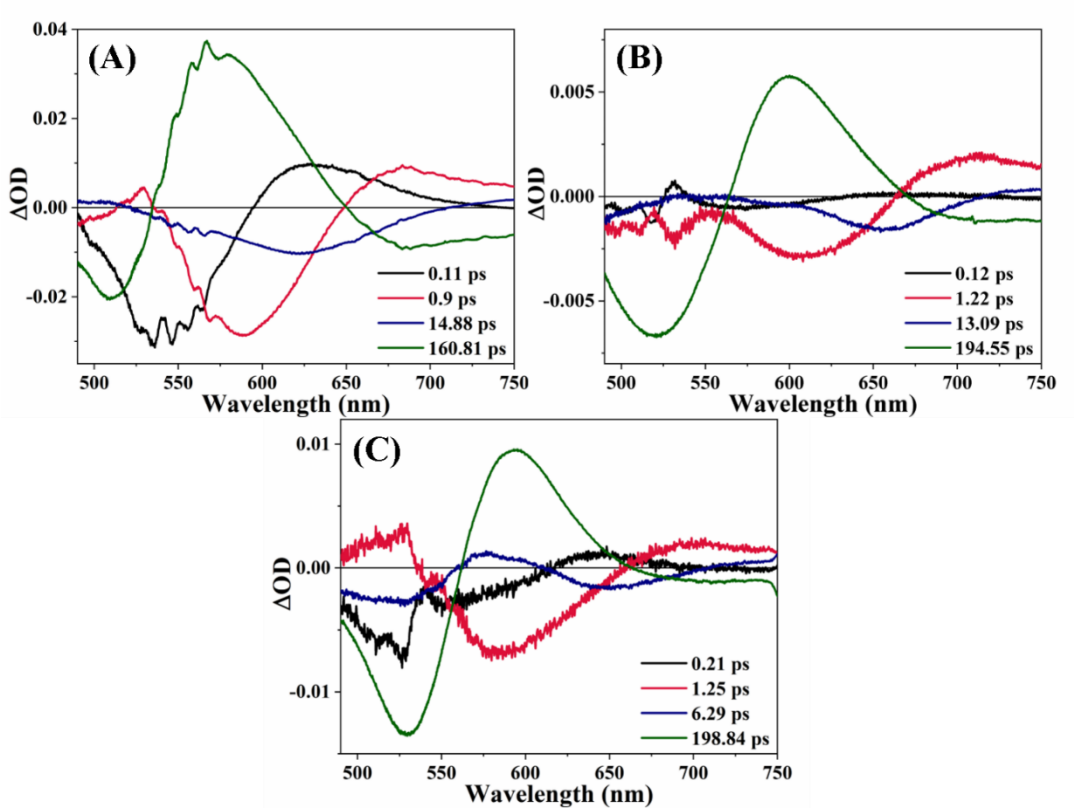

Figure B138: DAS of (A) D102, (B) D149 and (C) D205 in BmimTFSI-ACN mixture (X_{IL} = 0.05)

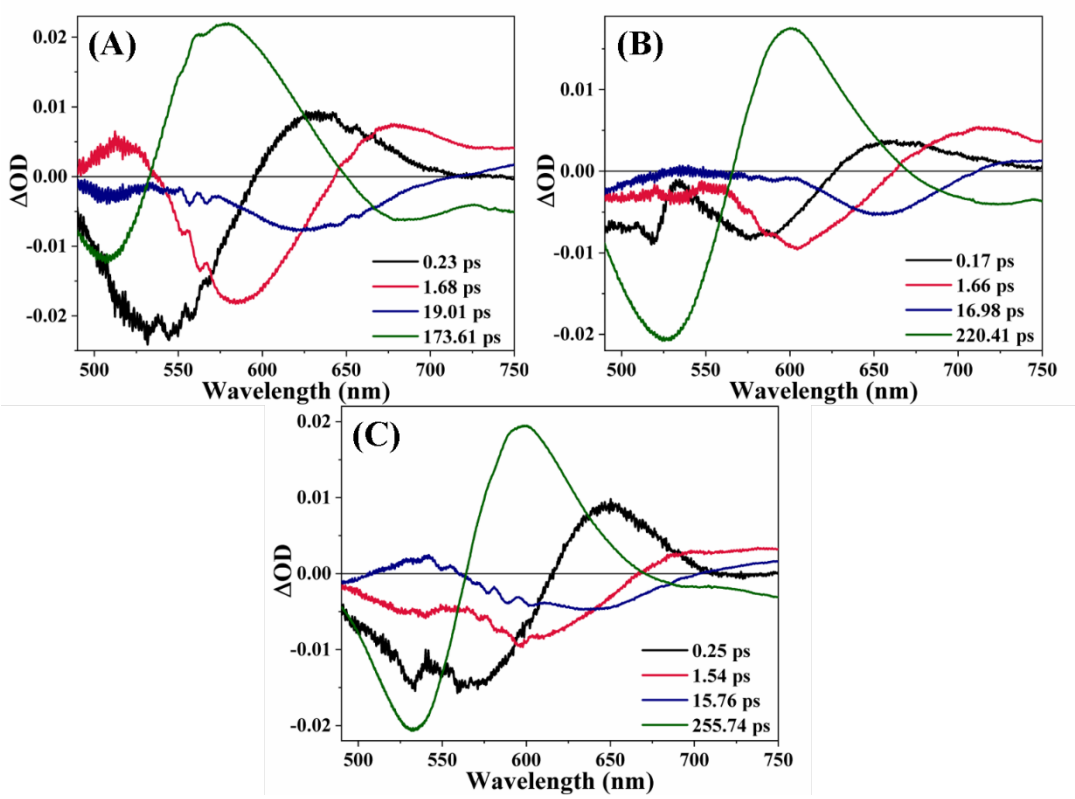

Figure B139: DAS of (A) D102, (B) D149 and (C) D205 in BmimTFSI-ACN mixture (X_{IL} = 0.10)

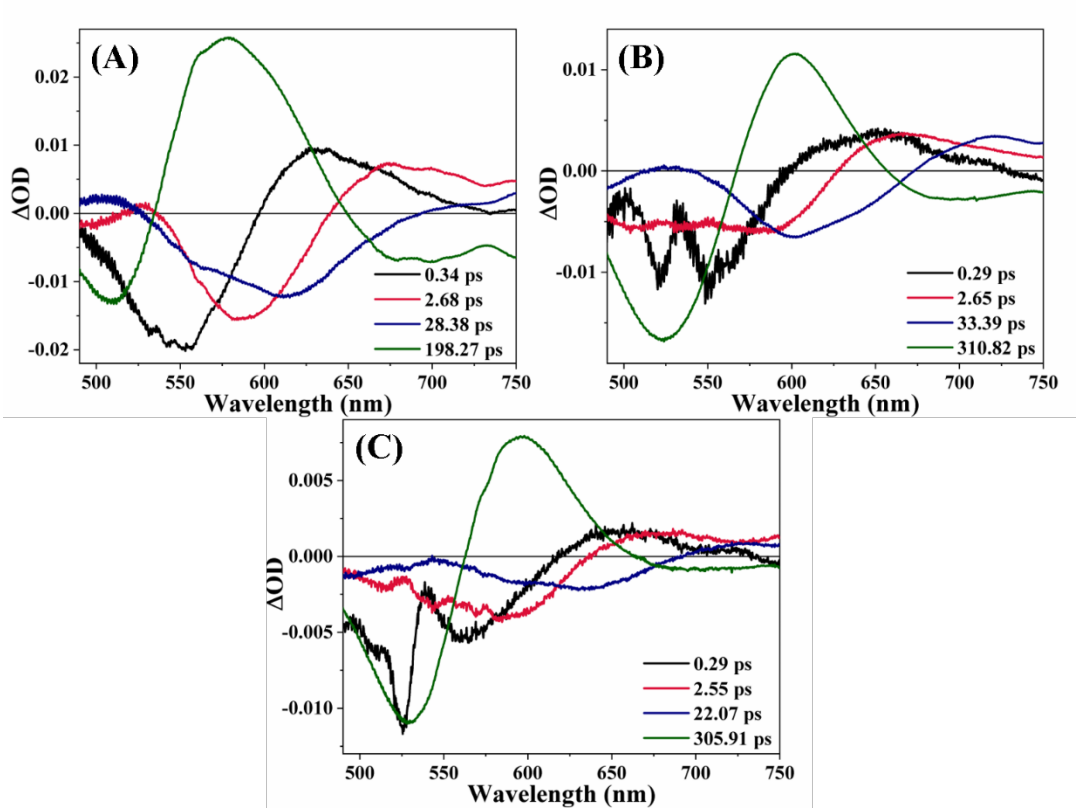

Figure B140: DAS of (A) D102, (B) D149 and (C) D205 in BmimTFSI-ACN mixture (X_{IL} = 0.20)

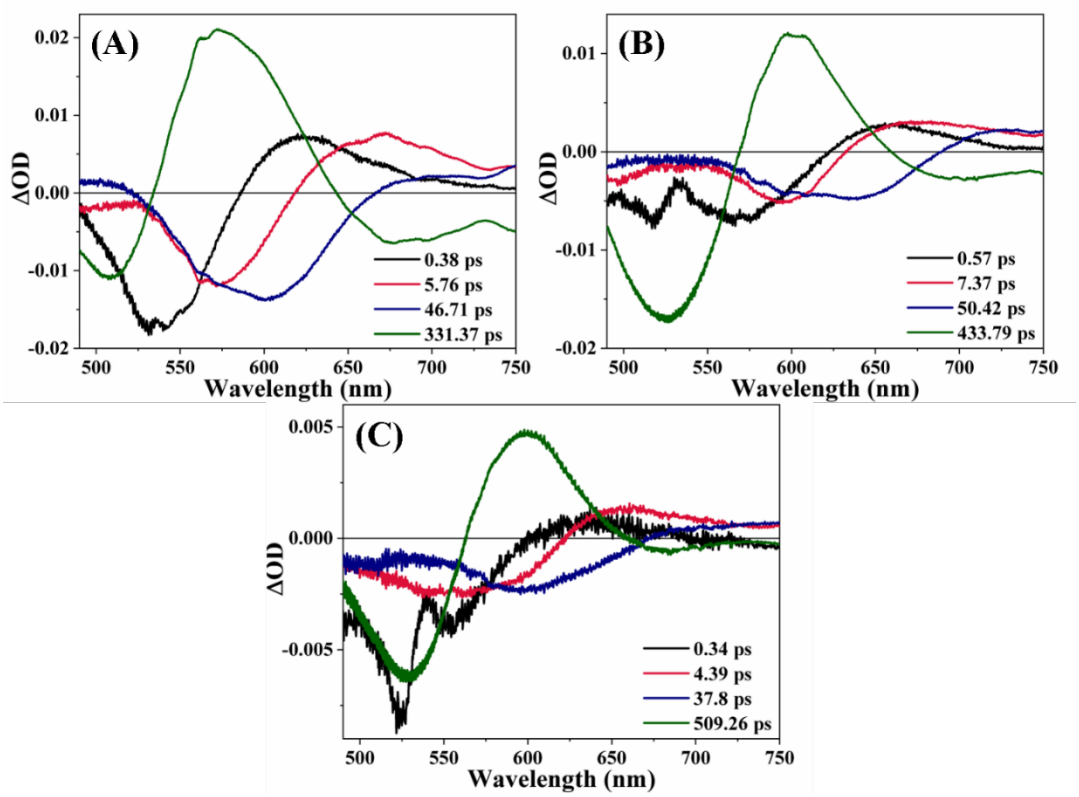

Figure B141: DAS of (A) D102, (B) D149 and (C) D205 in BmimTFSI-ACN mixture (X_{IL} = 0.50)

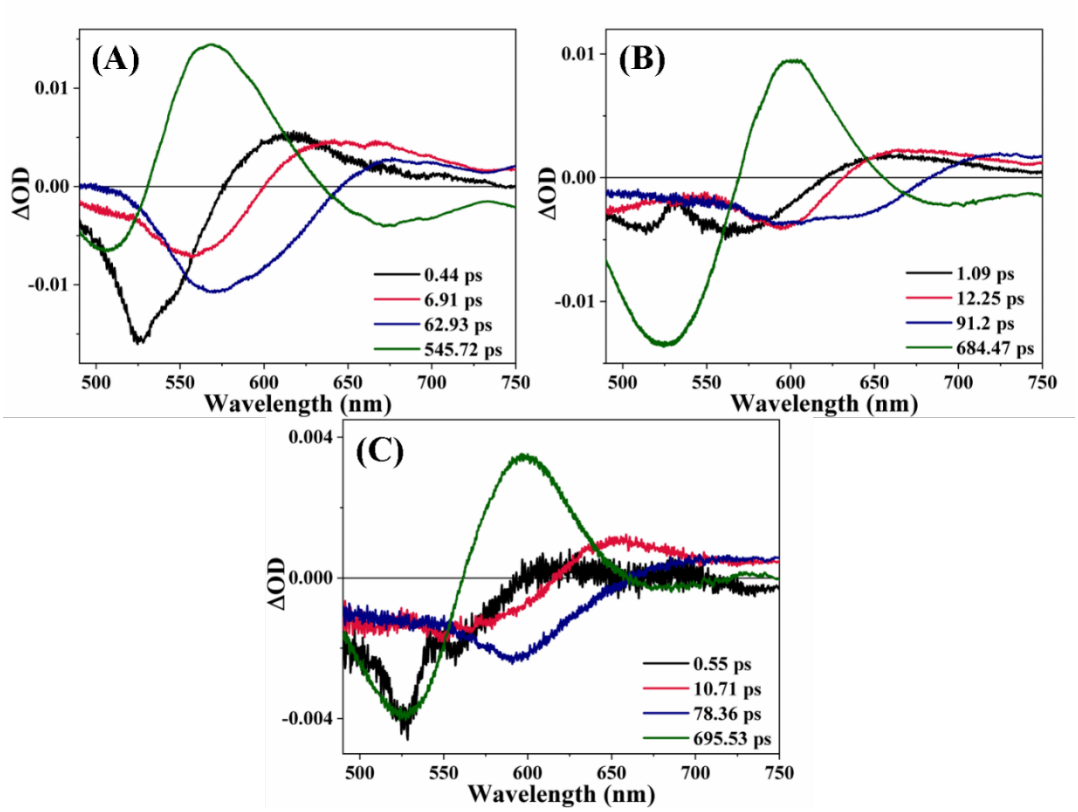

Figure B142: DAS of (A) D102, (B) D149 and (C) D205 in BmimTFSI-ACN mixture (X_{IL} = 0.80)

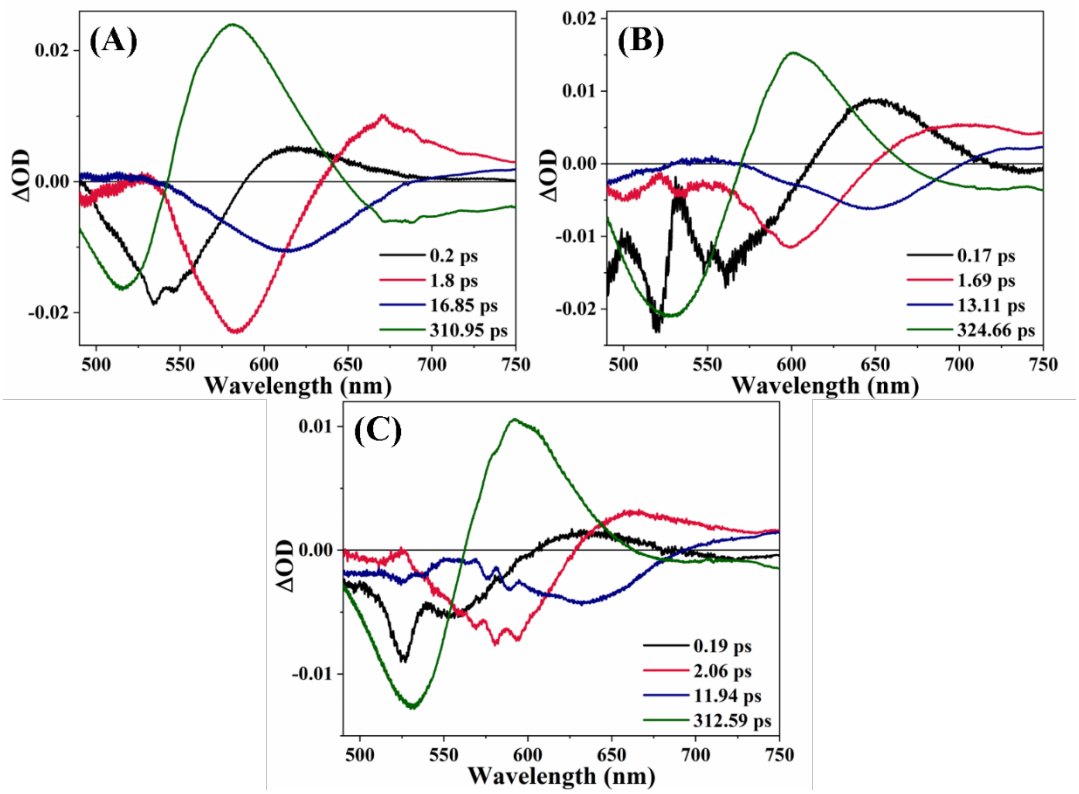

Figure B143: DAS of (A) D102, (B) D149 and (C) D205 in BmimTFSI-γ-BL mixture (X_{IL} = 0.05)

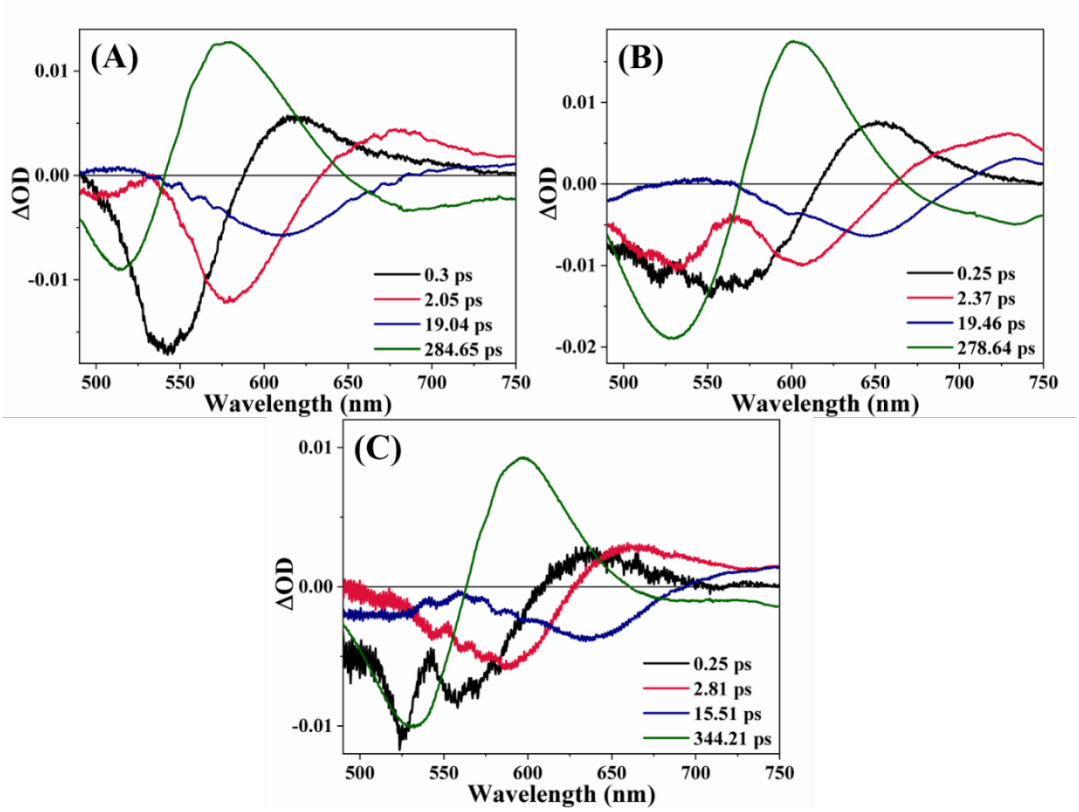

Figure B144: DAS of (A) D102, (B) D149 and (C) D205 in BmimTFSI-γ-BL mixture (X_{IL} = 0.10)

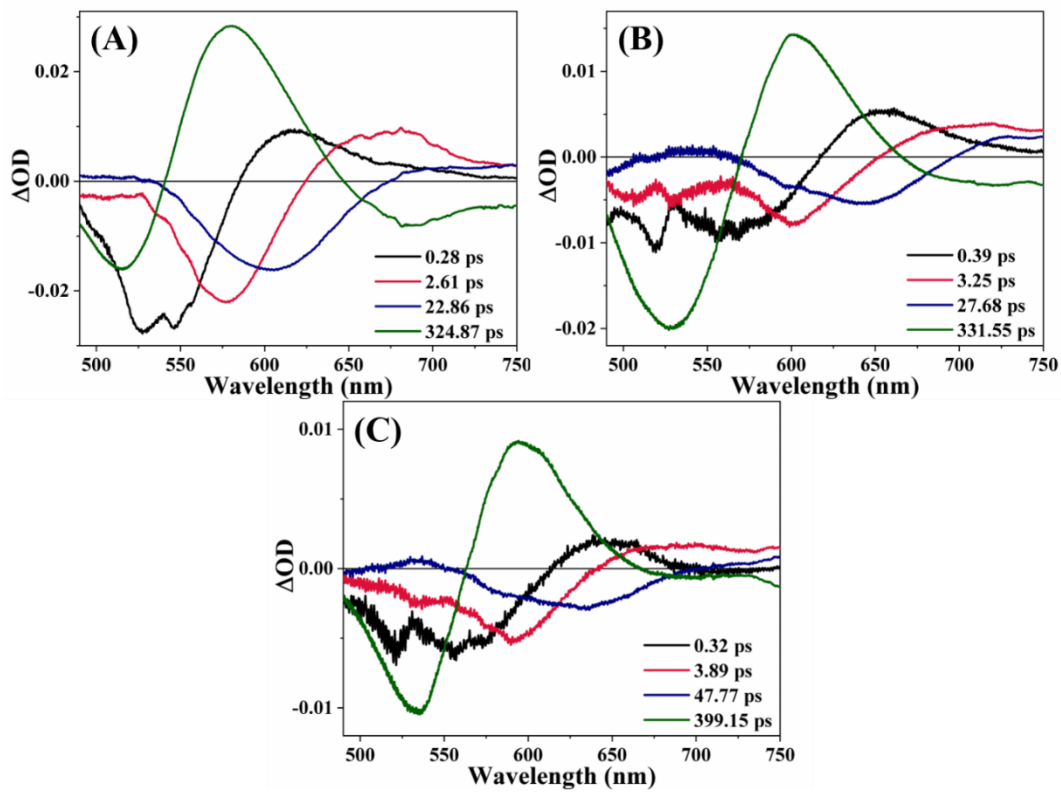

Figure B145: DAS of (A) D102, (B) D149 and (C) D205 in BmimTFSI-γ-BL mixture (X_{IL} = 0.20)

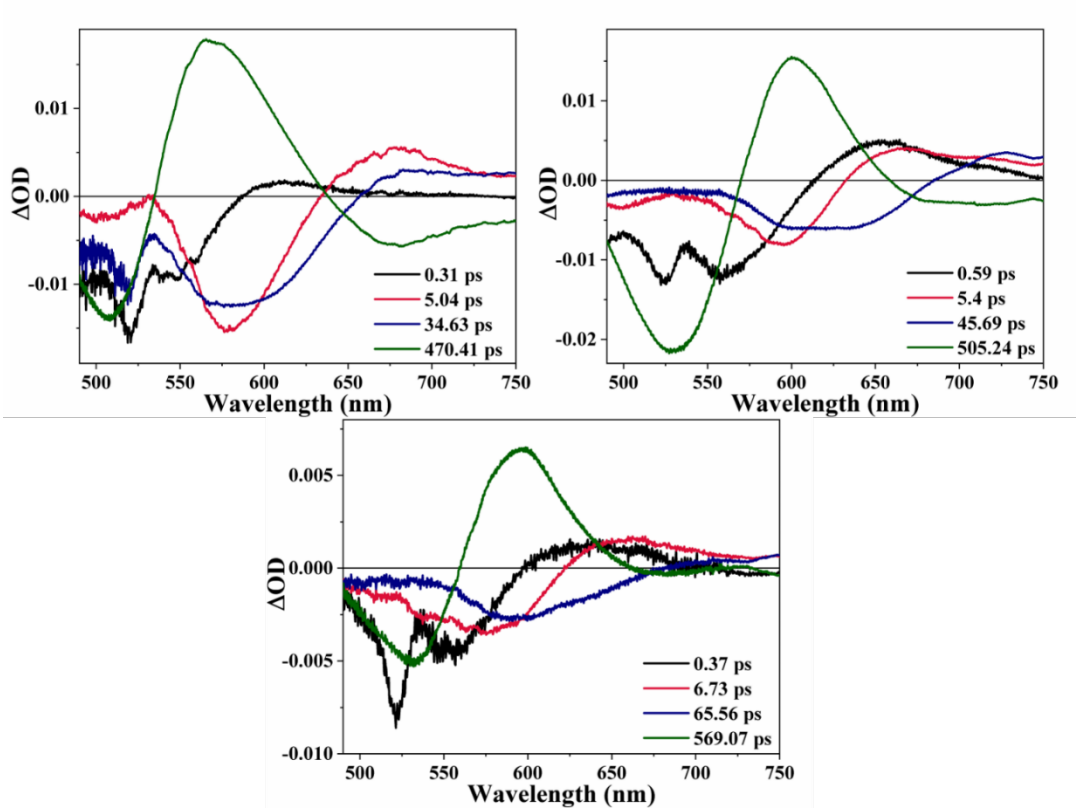

Figure B146: DAS of (A) D102, (B) D149 and (C) D205 in BmimTFSI-γ-BL mixture (X_{IL} = 0.50)

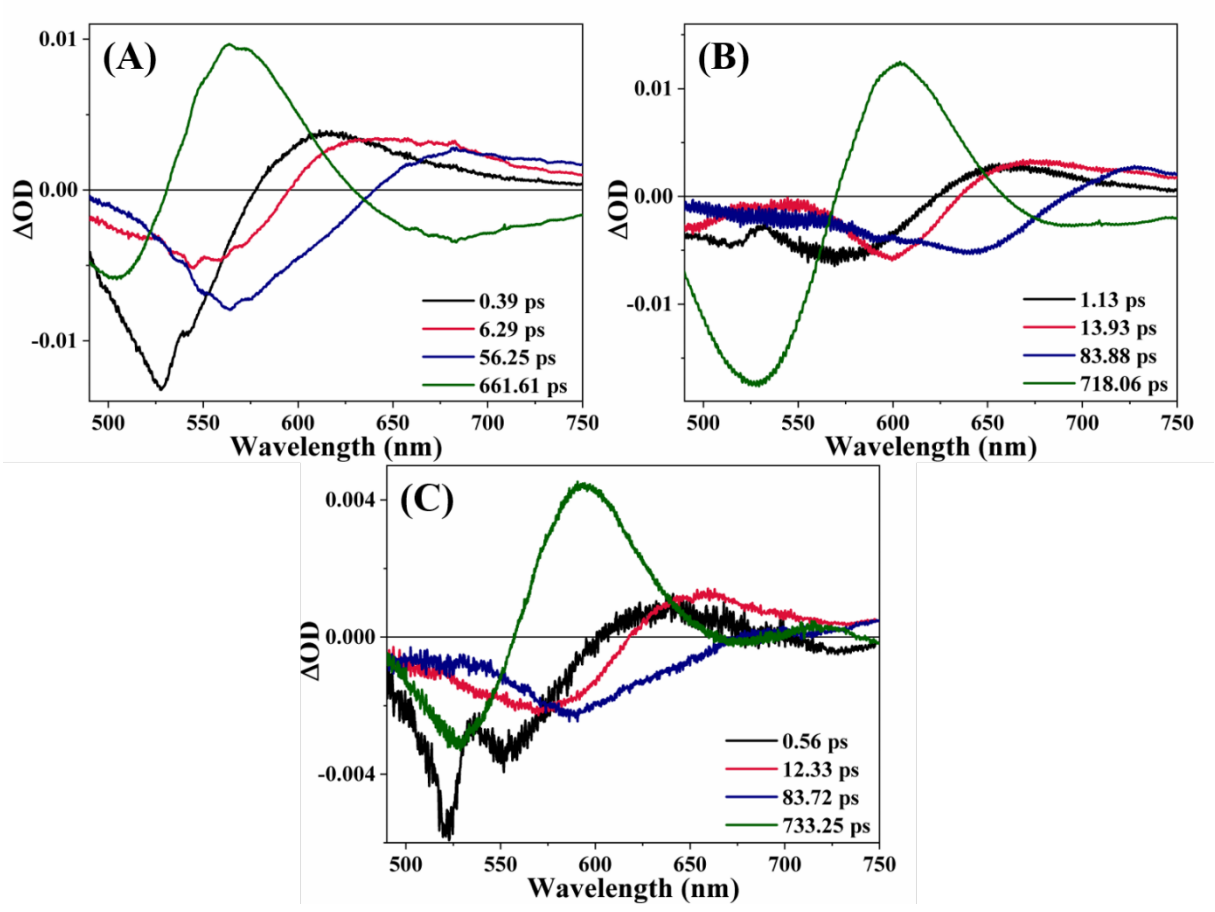

Figure B147: DAS of (A) D102, (B) D149 and (C) D205 in BmimTFSI-γ-BL mixture (X_{IL} = 0.80)

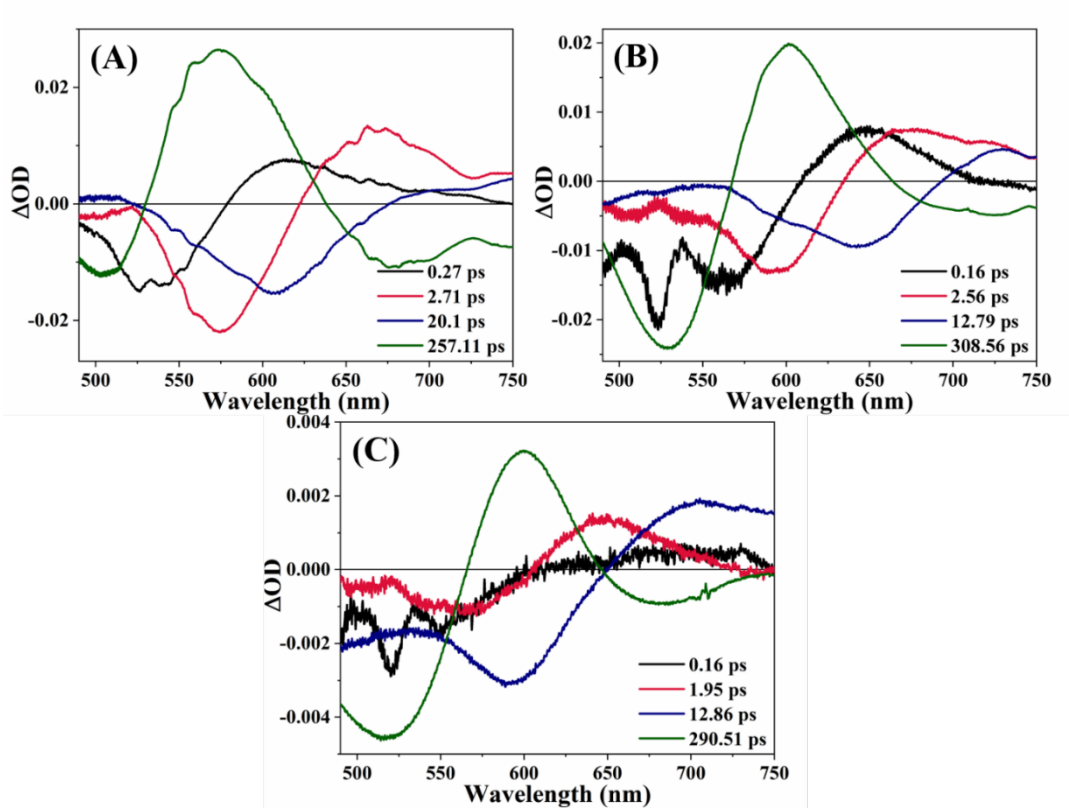

Figure B148: DAS of (A) D102, (B) D149 and (C) D205 in BmimTFSI-PC mixture (X_{IL} = 0.05)

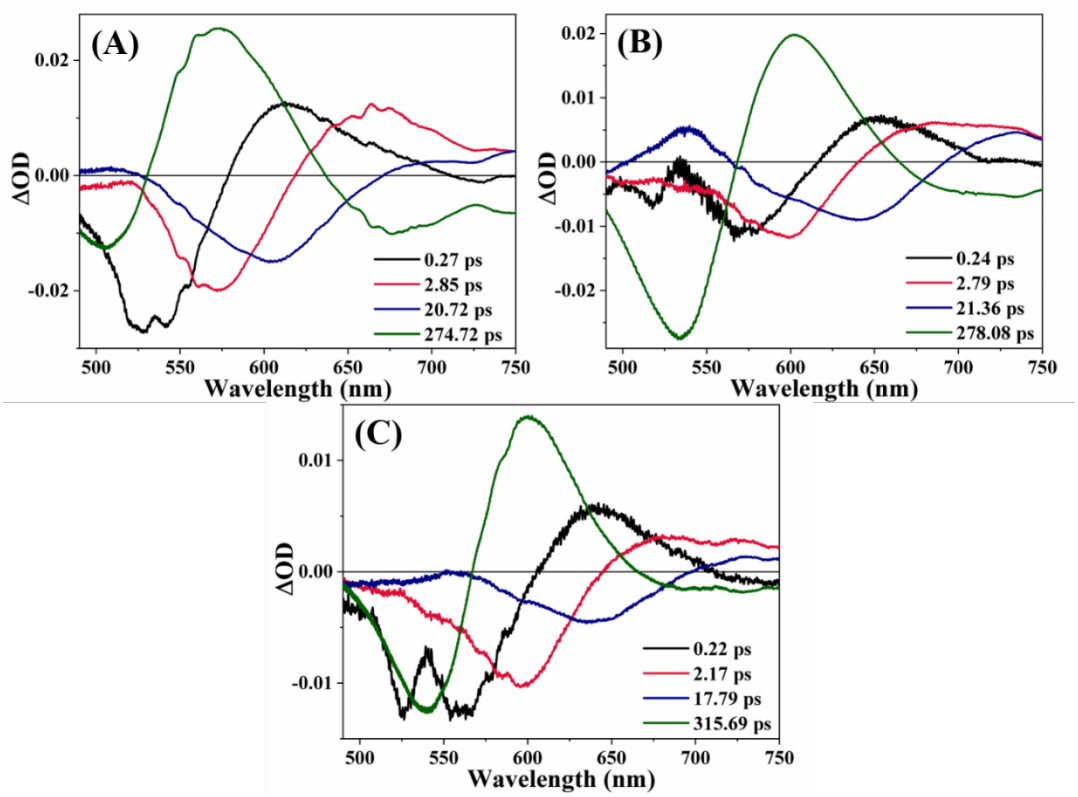

Figure B149: DAS of (A) D102, (B) D149 and (C) D205 in BmimTFSI-PC mixture (X_{IL} = 0.10)

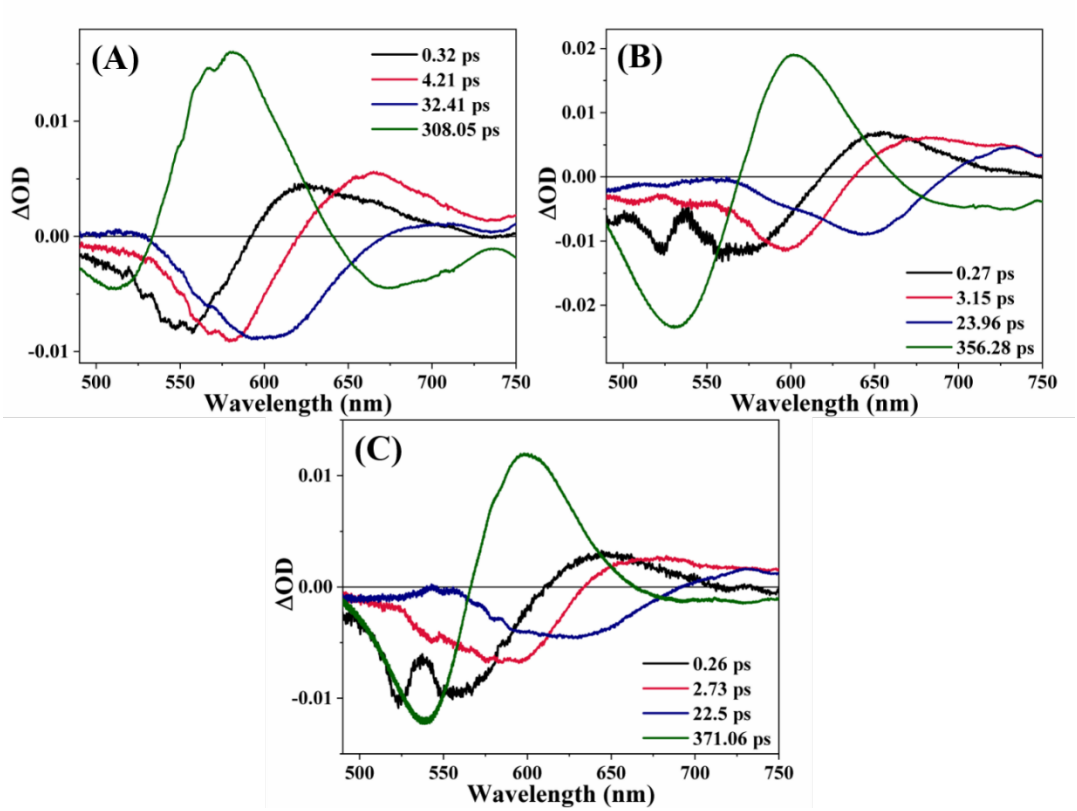

Figure B150: DAS of (A) D102, (B) D149 and (C) D205 in BmimTFSI-PC mixture (X_{IL} = 0.20)

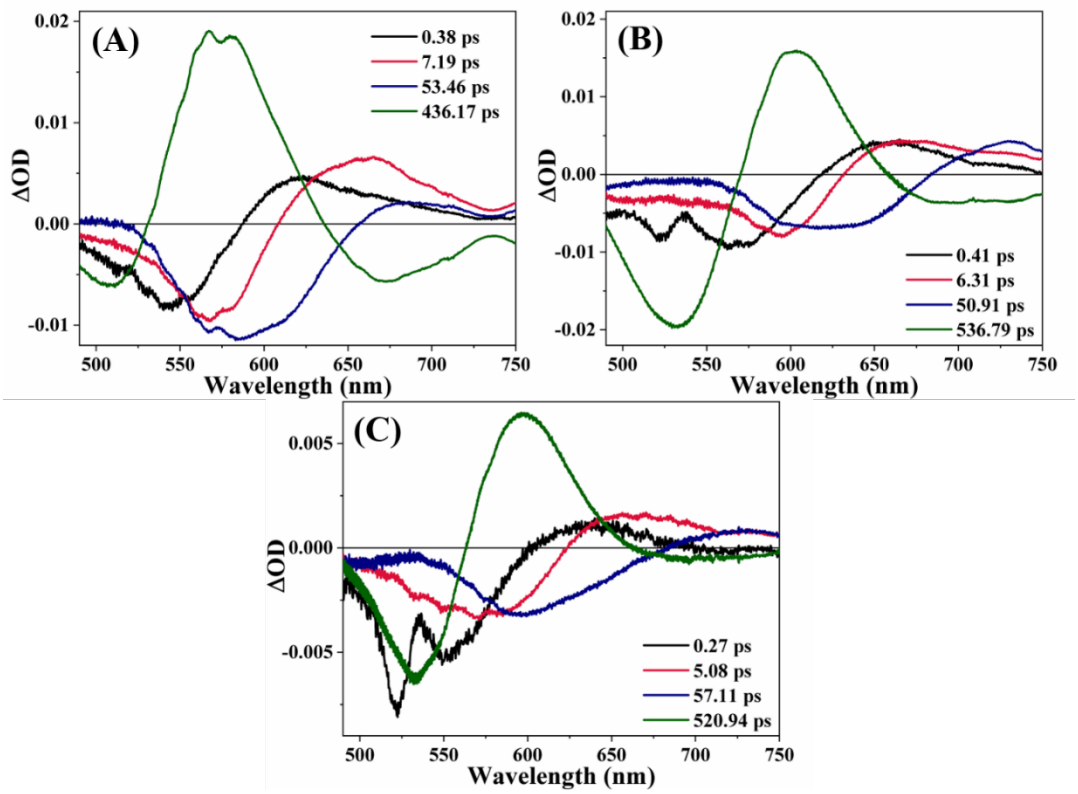

Figure B151: DAS of (A) D102, (B) D149 and (C) D205 in BmimTFSI-PC mixture (X_{IL} = 0.50)

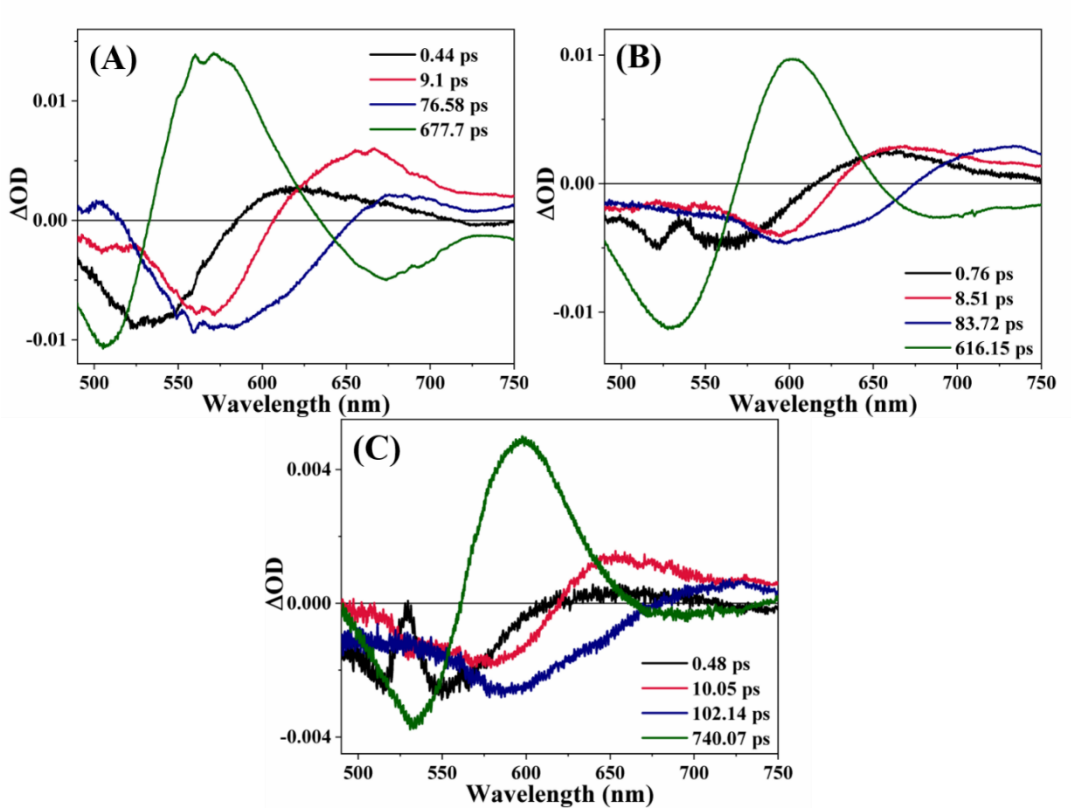

Figure B152: DAS of (A) D102, (B) D149 and (C) D205 in BmimTFSI-PC mixture (X_{IL} = 0.80)

Appendix C: CW-EPR Study in IL-MS mixtures

Table C1: Values of A_N and τ_R values of TEMPO in pure ILs including previous studies

Solvent/IL	A_N (G)	τ_R (ns)
$BmimBF_4$	16.17[5], 15.9[6], 15.99[7–9], 15.91[10],	2.3[7],1.1[8],
$BmimPF_6$	16.3[5], 15.99[6], 16.11[7,8], 15.98[10]	2.19[8]
BmimTFO	15.98[7]	1.2[8]
BmimTFSI	16.03[10], 15.82	0.11

Table C2: Values of A_N of TEMPO after fitting EPR spectra in the studied IL-MS mixtures

X_{IL}	A_N(G)											
	$BmimBF_4$			**$BmimPF_6$**			**BmimTFO**			**BmimTFSI**		
	ACN	**γ-BL**	**PC**	**ACN**	**γ-BL**	**PC**	**ACN**	**γ-BL**	**PC**	**ACN**	**γ-BL**	**PC**
0	15.86	15.85	15.85	15.86	15.85	15.85	15.86	15.85	15.85	15.86	15.85	15.85
0.01	15.88	15.85	15.87	15.87	15.85	15.90	15.87	15.85	15.88	15.90	15.85	15.90
0.05	15.92	15.87	15.91	15.91	15.90	15.93	15.93	15.87	15.92	15.97	15.91	15.92
0.1	15.97	15.90	15.93	15.95	15.92	15.93	15.94	15.88	15.95	16.01	15.94	15.96
0.15	15.97	15.92	15.95	15.99	15.93	15.95	15.96	15.90	15.96	16.03	15.96	15.96
0.2	16.00	15.97	15.96	16.02	15.95	16.01	15.97	15.93	15.97	16.04	15.98	15.99
0.25	16.03	15.98	15.98	16.03	15.98	16.01	15.99	15.95	16.00	16.06	16.00	16.02
0.3	16.04	15.98	15.99	16.05	16.01	16.02	16.00	15.96	16.02	16.06	16.03	16.03
0.4	16.07	16.02	16.03	16.07	16.03	16.05	16.03	15.99	16.03	16.07	16.05	16.07
0.6	16.07	16.03	16.05	16.08	16.06	16.07	16.05	16.02	16.05	16.09	16.06	16.08
0.8	16.08	16.06	16.06	16.09	16.07	16.08	16.08	16.06	16.08	16.10	16.07	16.09
1	16.09	16.09	16.09	16.11	16.11	16.11	16.12	16.12	16.12	16.12	16.12	16.12

Table C3: Values of τ_R of TEMPO after fitting EPR spectra in the studied IL-MS mixtures

X_{IL}	τ_R(ns)											
	$BmimBF_4$			**$BmimPF_6$**			**BmimTFO**			**BmimTFSI**		
	ACN	**γ-BL**	**PC**	**ACN**	**γ-BL**	**PC**	**ACN**	**γ-BL**	**PC**	**ACN**	**γ-BL**	**PC**
0	0.02	0.06	0.09	0.02	0.06	0.09	0.02	0.06	0.09	0.02	0.06	0.09
0.01	0.02	0.12	0.19	0.02	0.07	0.17	0.10	0.12	0.15	0.08	0.12	0.16
0.05	0.22	0.17	0.23	0.06	0.12	0.17	0.12	0.15	0.17	0.10	0.13	0.17
0.1	0.31	0.20	0.27	0.08	0.15	0.21	0.15	0.18	0.22	0.12	0.14	0.23
0.15	0.34	0.26	0.35	0.09	0.16	0.24	0.21	0.23	0.24	0.16	0.19	0.25
0.2	0.40	0.32	0.39	0.11	0.20	0.32	0.22	0.25	0.29	0.17	0.20	0.32
0.25	0.65	0.33	0.42	0.15	0.32	0.35	0.26	0.29	0.35	0.20	0.25	0.45
0.3	0.82	0.40	0.46	0.21	0.40	0.39	0.31	0.37	0.60	0.36	0.39	0.55
0.4	1.37	0.57	0.56	0.39	0.47	0.57	0.50	0.53	0.63	0.50	0.46	0.83
0.6	1.67	0.62	0.91	1.02	1.13	1.29	0.88	0.84	0.85	0.99	1.26	1.32
0.8	2.39	1.46	1.78	1.66	2.19	2.35	1.23	1.37	1.26	1.37	1.50	1.72
1	2.85	2.85	2.85	3.65	3.65	3.65	2.50	2.50	2.50	2.35	2.35	2.35

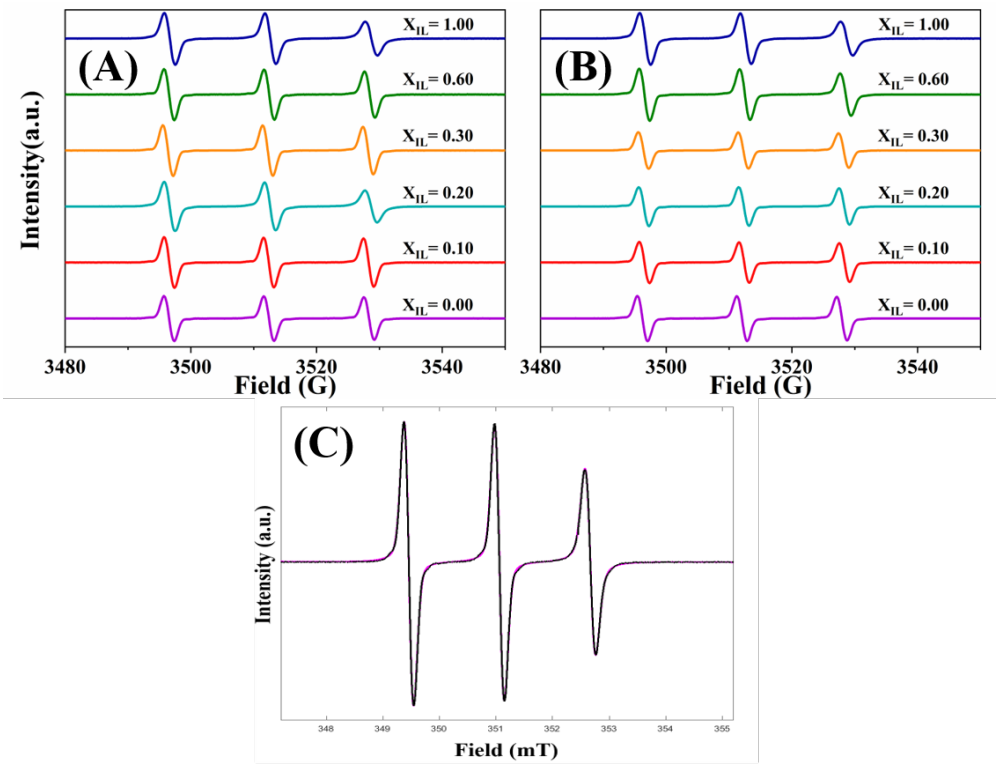

Figure C1: EPR signal of TEMPO in (A) $BmimBF_4$-γ-BL, (B) $BmimBF_4$-PC mixtures and (C) Experimental (Black) and fitted (Pink) spectra of TEMPO in pure $BmimBF_4$

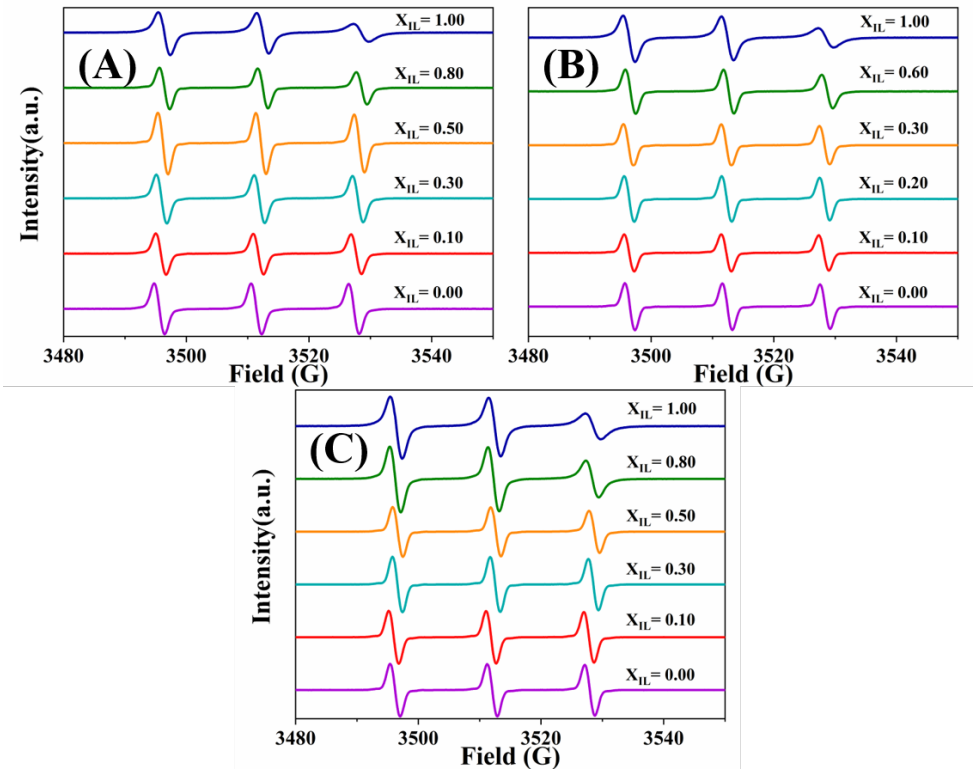

Figure C2: EPR signal of TEMPO in (A) $BmimPF_6$-ACN, (B) $BmimPF_6$-γ-BL and (C) $BmimPF_6$-PC mixtures

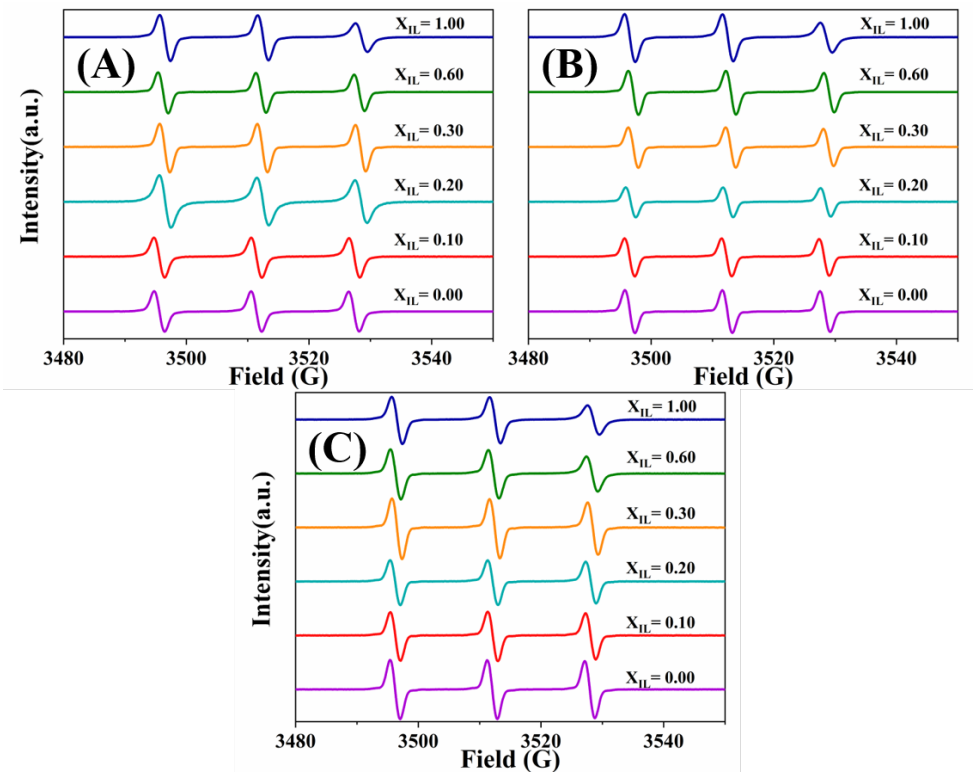

Figure C3: EPR signal of TEMPO in (A) BmimTFO-ACN, (B) BmimTFO-γ-BL and (C) BmimTFO-PC mixtures

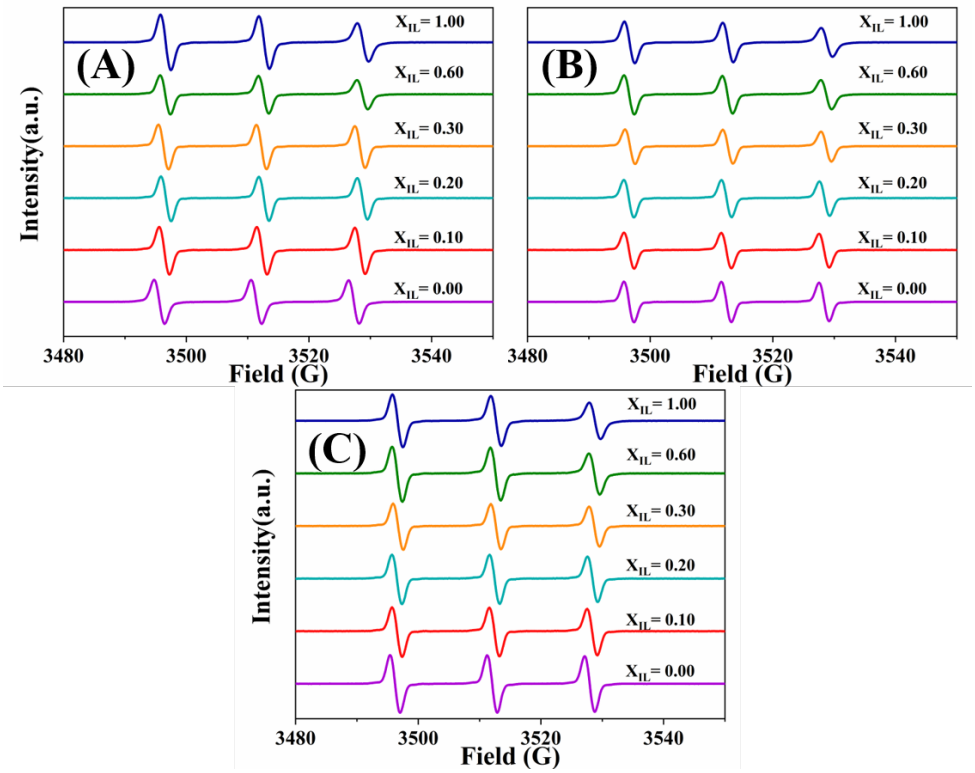

Figure C4: EPR signal of TEMPO in (A) BmimTFSI-ACN, (B) BmimTFSI-γ-BL and (C) BmimTFSI-PC mixtures

C.1: Calculation of modified Onsager equation used in $BmimBF_4$-ACN mixture

According to modified Onsagar equation-

$$A_N = A_{N_0} + K.\frac{R}{a^3} \quad \text{(C.1.1)}$$

A_{N_0} is values of hyperfine coupling constant without external electric fields, K is a constant for a particular probe, a is the radius of the field and $R = \frac{\varepsilon-1}{2\varepsilon+1}$

$a = r_2 + 2r_1$, where r_2 is radius of probe (TEMPO in our case) and r_1 is the radius of solvent molecule

For ACN,

$V_M = 52.86\ cm^3mol^{-1}$ [11]

$$\frac{4}{3}\pi R^3 = \frac{52.86 * 10^{21}}{6.022 * 10^{23}}\ nm^3$$

$$R^3 = 0.02095\ nm^3$$

$$R_{ACN} = 0.2757\ nm$$

Similarly,
$R_{TEMPO} = 0.39\ nm$ and $R_{BmimBF_4} = 0.2314\ nm$ ($V_{M,TEMPO} = 156.25\ cm^3mol^{-1}$, $V_{M,BmimBF_4} = 31.25\ cm^3mol^{-1}$ [12])

Now,

$$a_{ACN} = R_{TEMPO} + (2 \times R_{ACN}) = 0.9414\ nm$$

$$a_{BmimBF_4} = R_{TEMPO} + \left(2 \times R_{BmimBF_4}\right) = 0.8528\ nm$$

$$a^3_{ACN} = 0.5024 \times 10^3\ cm^3mol^{-1}$$

$$a^3_{BmimBF_4} = 0.3735 \times 10^3\ cm^3mol^{-1}$$

$R_{ACN} = 0.47645, R_{BmimBF_4} = 0.45033$ (ε values are taken from Stoppa et al.[13])

Putting the values in equation C.1.1 for ACN and $BmimBF_4$,

$$15.86 = A_{N_0} + K \times \frac{0.47945}{502.4} \quad \text{(C.1.2)}$$

$$16.09 = A_{N_0} + K \times \frac{0.45033}{373.5} \quad \text{(C.1.3)}$$

Solving equation C.1.2 and C.1.3,

One can easily find out that, $A_{N_0} = 14.987\ G$ and $K = 914.94\ G\ mol\ cm^{-3}$

Now we can modify equation C.1.1 to obtain a general form by putting these calculated values of A_{N_0} and K in it. The modified form of equation C.1.1 is the following-

$$A_N = 14.987 + 914.94 \times {}^{R}/_{a^3} \quad \text{(C.1.4)}$$

We can apply this equation (C.1.4) in $BmimBF_4$-ACN mixtures and get the values of a (radius of reaction field which is nothing but radius of primary solvation shell plus radius of TEMPO)

Appendix D: Study of Solvation and Reorientation Dynamics in $BmimPF_6$-ACN mixture

Table D1: Composition dependence of the decay times after fitting the molecular contributions to the total polarizability of the system due to Bmim cation at different mixture compositions in $BmimPF_6$-ACN mixture.

X_{IL}	τ_1(ps)	τ_2(ps)	$a_1.10^3$	$a_2.10^3$
0.01	10.7	4.06	3.92	1.54
0.05	15.7	7.32	10.1	10.7
0.1	20.2	7.87	16.8	14.7
0.15	26.2	7.54	19.9	22.1
0.2	36.9	11.2	16.5	23.5
0.25	42.7	9.5	19.8	23.3
0.3	57.3	12.1	16.9	21.2
0.4	99.3	26.6	12.1	10.4
0.5	157	30.1	8.89	13.8
0.6	232	47	6.65	9.66
0.7	333	50.3	5.41	7.79
0.8	454	55.7	4.64	7.08
0.9	610	54.8	3.74	7.07
1	1219	192	3.6	7.25

Table D2: Composition dependence of the decay times after fitting the molecular contributions to the total polarizability of the system due to ACN at different mixture compositions in $BmimPF_6$-ACN mixture.

X_{IL}	τ_1(ps)	τ_2(ps)	$a_1.10^3$	$a_2.10^3$
0	-	1.6	-	145
0.01	-	1.85	-	123
0.05	15.6	2.32	0.82	87.9
0.1	19.0	3.54	1.14	40.8
0.15	23.9	4.88	1.06	25.8
0.2	23.7	5.73	1.67	17.5
0.25	33.6	6.59	1.08	15.9
0.3	36.0	8.06	1.22	10.5
0.4	59.9	13.1	0.59	4.84
0.5	80.4	16.7	0.47	2.42
0.6	126.0	28.4	0.21	1.07
0.7	260.0	57.9	0.05	0.44
0.8	295.0	72.9	0.04	0.17
0.9	444.0	98.2	0.01	0.07

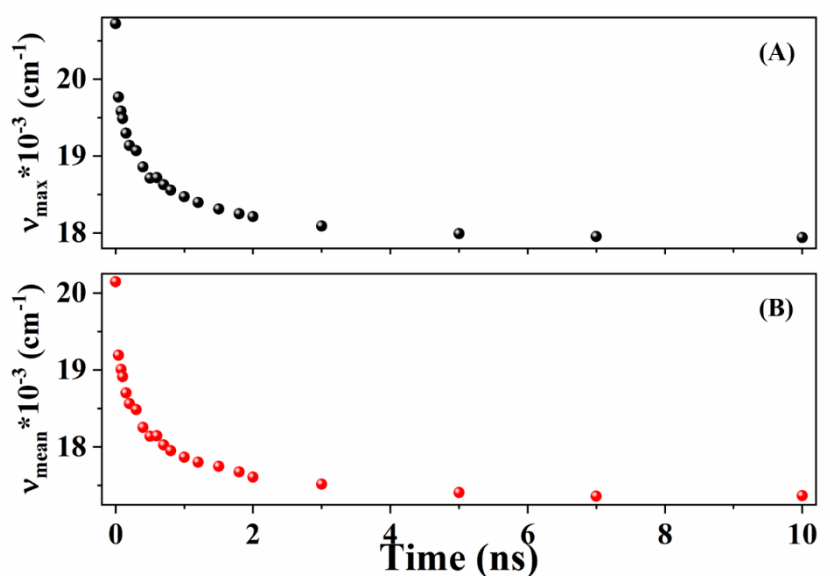

Figure D1: Time dependent evolution of (A) ν_{max} (t) and (B) ν_{mean} (t) of C153 in pure $BmimPF_6$ using TCSPC technique

Bibliography

(1) Fakis, M.; Stathatos, E.; Tsigaridas, G.; Giannetas, V.; Persephonis, P. Femtosecond Decay and Electron Transfer Dynamics of the Organic Sensitizer D149 and Photovoltaic Performance in Quasi-Solid-State Dye-Sensitized Solar Cells. *J. Phys. Chem. C* **2011**, *115* (27), 13429–13437. https://doi.org/10.1021/jp201143n.

(2) Lohse, P. W.; Kuhnt, J.; Druzhinin, S. I.; Scholz, M.; Ekimova, M.; Oekermann, T.; Lenzer, T.; Oum, K. Ultrafast Photoinduced Relaxation Dynamics of the Indoline Dye D149 in Organic Solvents. *Phys. Chem. Chem. Phys.* **2011**, *13* (43), 19632. https://doi.org/10.1039/c1cp22429h.

(3) El-Zohry, A. M.; Roca-Sanjuán, D.; Zietz, B. Ultrafast Twisting of the Indoline Donor Unit Utilized in Solar Cell Dyes: Experimental and Theoretical Studies. *J. Phys. Chem. C* **2015**, *119* (5), 2249–2259. https://doi.org/10.1021/jp505649s.

(4) El-Zohry, A.; Orthaber, A.; Zietz, B. Isomerization and Aggregation of the Solar Cell Dye D149. *J. Phys. Chem. C* **2012**, *116* (50), 26144–26153. https://doi.org/10.1021/jp306636w.

(5) Ivanov, M. Y.; Veber, S. L.; Prikhod'ko, S. A.; Adonin, N. Y.; Bagryanskaya, E. G.; Fedin, M. V. Probing Microenvironment in Ionic Liquids by Time-Resolved EPR of Photoexcited Triplets. *J. Phys. Chem. B* **2015**, *119* (42), 13440–13449. https://doi.org/10.1021/acs.jpcb.5b06792.

(6) Dhale, R. S.; Sahu, P. K.; Sarkar, M. Understanding the Microscopic Behavior of the Mixture of Ionic Liquid/Ethylene Glycol/Lithium Salt through Time-Resolved Fluorescence, Nuclear Magnetic Resonance (NMR), and Electron Paramagnetic Resonance (EPR) Studies. *J. Phys. Chem. B* **2017**, *121* (33), 7934–7945. https://doi.org/10.1021/acs.jpcb.7b04585.

(7) Strehmel, V.; Berdzinski, S.; Rexhausen, H. Interactions between Ionic Liquids and Radicals. *J. Mol. Liq.* **2014**, *192*, 153–170. https://doi.org/10.1016/j.molliq.2013.12.007.

(8) Strehmel, V.; Rexhausen, H.; Strauch, P. Synthesis of 4-Trimethylammonio-2,2,6,6-Tetramethylpiperidine-1-Yloxyl with Various Anions for Investigation of Ionic Liquids. *Tetrahedron Lett.* **2008**, *49* (20), 3264–3267. https://doi.org/10.1016/j.tetlet.2008.03.073.

(9) Strehmel, V.; Rexhausen, H.; Strauch, P.; Görnitz, E.; Strehmel, B. Temperature Dependence of Interactions between Stable Piperidine-1-Yloxyl Derivatives and an Ionic Liquid. *ChemPhysChem* **2008**, *9* (9), 1294–1302. https://doi.org/10.1002/cphc.200800068.

(10) Chakraborty, M.; Ahmed, T.; Dhale, R. S.; Majhi, D.; Sarkar, M. Understanding the Microscopic Behavior of Binary Mixtures of Ionic Liquids through Various Spectroscopic Techniques. *J. Phys. Chem. B* **2018**, *122* (50), 12114–12130. https://doi.org/10.1021/acs.jpcb.8b09699.

(11) Wang, X.; Dao, R.; Yao, J.; Peng, D.; Li, H. Modification of the Onsager Reaction Field and Its Application on Spectral Parameters. *ChemPhysChem* **2017**, *18* (7), 763–771. https://doi.org/10.1002/cphc.201601093.

(12) Wang, X.; Zhang, S.; Yao, J.; Li, H. The Polarity of Ionic Liquids: Relationship between Relative Permittivity and Spectroscopic Parameters of Probe. *Ind. Eng. Chem. Res.* **2019**, *58* (17), 7352–7361. https://doi.org/10.1021/acs.iecr.9b00485.

(13) Stoppa, A.; Hunger, J.; Hefter, G.; Buchner, R. Structure and Dynamics of 1- N -Alkyl-3- N -Methylimidazolium Tetrafluoroborate + Acetonitrile Mixtures. *J. Phys. Chem. B* **2012**, *116* (25), 7509–7521. https://doi.org/10.1021/jp3020673.